Bitlis Eren Üniversitesi
Fen Bilimleri Dergisi

Bitlis Eren University
Journal of Science

Dergi Hakkında / *About Journal*

Bitlis Eren Üniversitesi Fen Bilimleri Dergisi, mühendislik ve temel bilimler alanlarındaki gelişmeleri ve yenilikleri takip etmek, meslek kuruluşlarının, araştırmacıların ve bireylerin ulusal ve uluslararası gelişimlerine katkıda bulunmak ve bu alanlarda elektronik bir kaynak oluşturmak amacıyla yayımlanmaktadır. Derginin yazım dili Türkçe veya İngilizcedir. Fen Bilimleri Dergisi, Bitlis Eren Üniversitesi Lisansüstü Eğitim Enstitüsü yayını olup, 2012 yılından bu yana ücretsiz ve açık erişimli olarak yayın hayatına devam etmektedir. Mühendislik ve temel bilimlerin bilgi tabanına ve teknolojik gelişmelere ışık tutması amacıyla bu alanlarda yapılmış deneysel ve teorik ilerlemeleri konu alan özgün araştırma makalelerine yer verilmektedir. Dergiye gönderilen çalışmaların benzerlik oranı %25'i geçmemelidir. Yazım kurallarına uymayan makaleler, hakemlere gönderilmeden önce düzeltilmek üzere yazara geri gönderilir. Bu nedenle, derginin yazım kuralları dikkate alınmalıdır. Ayrıca, editörlerden yazarlara iletilen düzeltmelere veya taleplere 30 gün içerisinde cevap verilmediği takdirde ilgili makaleler reddedilir. Makaleler şekiller ve tablolar dâhil 20 sayfayı geçmemelidir. Dergiye yayın için gönderilen makaleler en az iki hakem tarafından değerlendirilir. Yazarlardan hakem önerisi talep edilmemektedir. Makalelerin dergide yayımlanabilmesi için hakemler tarafından olumlu görüş bildirilmesi gerekmektedir. Dergi Editör Kurulu, hakem raporlarını (*en aziki hakemin değerlendirmeleri geldikten sonra*) dikkate alarak makalelerin yayımlanmak üzere kabul edilip edilmemesine karar verir. Fen Bilimleri Dergisi, yılda dört defa (*Mart, Haziran, Eylül, Aralık*) yayımlanmaktadır. **Dergimiz Tübitak-Ulakbim Mühendislik ve Temel Bilimler Veri Tabanı Dergi Listesinde taranmaktadır.**

B.E.Ü. Fen Bilimleri Dergisi 13(3), 2024 / *B.E.U. Journal of Science 13(3), 2024*
İÇİNDEKİLER / *CONTENTS*

Biosorption of Methylene Blue into Pumpkin Seed: Isotherm, Kinetic and Thermodynamics Studies

İlhan KÜÇÜK[1*]

[1]*Rektorship, Muş Alparslan University, Muş, Türkiye*

(ORCID: 0000-0003-2876-3942)

Keywords: Biosorption, Methylene blue, Pumpkin seed, Kinetic, Isotherm.

Abstract

This work has demonstrated the potential utility of pumpkin seed shells (PSS) as a low-cost solid adsorbent for methylene blue (MB) adsorption. PSS have investigated surface functional groups with FTIR (after and before adsorption), crystal structure with XRD, and surface morphology with SEM-EDX. Biosorption parameters were examined contact time, pH, solution temperature, and initial concentration. This research was conducted to analyze adsorption processes involved in adsorption of MB onto crude PSS by gaining essential knowledge from the study of equilibrium adsorption kinetics, isotherms, and thermodynamics. It was determined whether four models-Langmuir, Temkin, Freundlich, and D-R models-fit experimental data derived from adsorption isotherms. In addition, the accuracy of fits of three models to experimental data derived from adsorption kinetics were tested, namely, the Elovich, pseudo-first order, and pseudo-second order models. Biosorption of MB on PSS is exothermic and spontaneous according to thermodynamic analysis. FTIR (Fourier transform infrared spectroscopy) studies show significant changes in the absorption values, shapes and positions of bands both before and after solute adsorption. It was found that there are two MB adsorption mechanisms: electrostatic attraction and hydrogen bonding

1. Introduction

Because of their harmful effects on a wide variety of life forms, dyes in wastewater are of great concern. Into the environment, the release of dyes raises both toxicological and esthetic issues. Industries such as plastics, leather, textiles, and paper use dyes to colour their products and consume a lot of water in the process. Consequently, they emerge a remarkable amount of colored wastewater [1]. It is well known that color has an important impact on how the public perceives water quality. Color is first contaminant in wastewater that can be detected. In water, even very low amounts of some dyes—less than 1 ppm— are undesirable and extremely visible [2]. Methylene blue dye (MB), with the molecular formula C16H18N3SCl, also referred to as methyl thioninium chloride, is heterocyclic aromatic chemical substance. It falls under the cationic dye category. It is usually used dye for silk, wood, and cotton [3]. It may cause eye burns that can lead to permanent eye damage in both humans and animals. When ingested by mouth, it produces a burning sensation and may cause vomiting, nausea, mental confusion, excessive sweating, and methemoglobinemia. It can also cause brief, rapid, or laboured breathing when inhaled. Because of its adverse effects on receiving water, treatment of wastewater containing this dye is of great importance [4].

A variety of treatment methods is used to remove dyes from wastewater, including adsorption, integrated chemical-biological degradation, cation exchange

membranes, sonochemical degradation, micelle-assisted ultrafiltration, solar photo-Fenton, electrochemical degradation, fenton biological treatment scheme, integrated iron (III)-photo-assisted biological treatment, and biological processes [5,6]. Adsorption of synthetic dyes on affordable and effective solid supports was considered a cost-effective and simple method to remove them from wastewater and water, since conventional methods cannot effectively decolorize synthetic dyes in wastewater. A well-known equilibrium separation technique, adsorption is well suited for the decontamination of water. Compared to other methods of reusing water, adsorption has proven to be more advantageous due to its low initial cost, adaptability and ease of construction, and resistance to toxic pollutants. In addition, adsorption is not lead to formation of hazardous substances [7,8].

A biotechnological approach to sustainable development has a practical application branch, biosorption [9]. It is considered an economical, effective, and environmentally friendly method of water treatment. It keeps concentration of various water pollutants below limits recommended by various regulations. The principles of green chemistry are consistent with this protocol. It is important to understand the complex fundamentals of the biosorption process in terms of its various components. Shortly, it is metabolically independent process (passive uptake) based on the use of biowaste to remove various types of water pollutants [10]. The recycling of these biomasses (biowastes) generally brings a number of benefits. Their use in their natural or/and modified forms contributes directly to reduction of waste. Numerous ecological and environmental problems can be solved in this way. It is characterized by exceptional properties such as high efficiency and low operating and manufacturing costs [11].

The aim of this study is to utilize pumpkin seed, which can be considered as agricultural waste, as an adsorbent. Specifically, the focus is on the removal of pollutants such as methylene blue, which are harmful to human health and commonly used in industry, from aqueous environments. The research was conducted under various temperature conditions, different initial concentrations, varying contact times, and various pH levels. The impact of these factors ensured a detailed examination of their effects on the efficiency of methylene blue removal. Comprehensive experimental studies were conducted to determine important parameters such as the adsorption capacity and adsorption kinetics of pumpkin seed. The results highlight the potential of pumpkin seed husks as an effective adsorbent. This study not only presents an environmentally sustainable approach to waste management but also contributes to the development of new and effective treatment methods in fields such as water treatment industry.

2. Material and Method

2.1. Preparation of the biosorbent

The PSS were get from commercial (Muş/Turkey). The obtained pumpkin seeds had their interiors removed, and only the husks were utilized in this study. The pumpkin seeds were taken and dried in air until constant weight. They were then crushed with laboratory blender and sieved with 1.6-mm sieve. Pumpkin seed shells (PSS) remaining under the sieve were used as biosorbent

Figure 1. Pumpkin Seeds (Biosorbent)

2.2. Preparation of the adsorbate

0.5 g of methylene blue (Isolab C.I. 52015) was weighed and dissolved in 1liter of distilled water to prepare stock solution (500 ppm or 500 mg/L). The methylene blue solutions used in adsorption experiments were prepared by dilution from stock solution.

2.3. Adsorption procedure

In the isothermal experiments, fixed amount of GP (0.10 g) was added to five 100 mL erlenmeyer flasks containing 100 mL dilute solutions (10–50 mg/L). The Erlenmeyer flasks were capped and placed in water bath shaker, where they were shaken at 22, 30 and 40°C for 90 minutes. UV/vis spectrophotometer was used to measure final dye concentration in the solution at a maximum wavelength of 666 nm.

The kinetic tests followed a process almost identical to equilibrium tests. Aqueous samples were collected at predetermined times, and dye concentrations were assessed similarly.

The amount of MB at time qt, was calculated as follows:

$$q_t = \frac{(C_0 - C_t)V}{w} \qquad (1)$$

2.3.1 Effect of contact time and initial concentration

Each 500 mL volume of MB solution contained 0.5 g of the PSS sample. Experiments were performed at 295 K for 90 minutes at initial dye solution concentrations of 30, 40, and 50 mg/L.

2.3.2 Effect of temperature

0.5 g of the PSS sample was added to each 500 mL volume of MB aqueous solution at initial concentration of 30 mg/L. Experiments were performed at 22, 30 and 40°C for 90 minutes.

2.3.3 Effect of pH

The solution's pH was studied at pH 2, 3, 4, 5, 6, 7, 8, 9, 10, 11, and 12. At a constant adsorption time of 90 minutes, 0.1 g of PSS sample was added to each 100 mL of the aqueous solution MB with initial concentration of 20 mg/L.

3. Results and Discussion

3.1. Characterization of adsorbent

3.1.1 FTIR analysis

Using ATR-FTIR spectroscopy, the surface chemistry of PSS was investigated both before and after MB adsorption. Both the surface groups of the PSS and the nature of the interactions between PSS and MB were investigated using ATR-FTIR spectroscopy. By comparing the IR spectra obtained after and before the interaction of MB with PSS, much can be learned about the interactions that take place. The ATR spectra of the biosorbent PSS are shown in Fig. 2 A. The hydroxyl group in lignin, hemicellulose, cellulose, and adsorbed water on the surface of adsorbent exhibits an O-H stretching vibration associated with broad peak at 3290 cm^{-1}. In general, the methoxyl groups in cellulose, lignin, hemicellulose, and aliphatic acids show symmetric and asymmetric C-H stretching vibrations, respectively, as indicated by the peaks at 2890 and 2865 cm^{-1} [12]. The band at 1742 cm^{-1} is due to stretching of carbonyl or carboxyl groups. Due to carboxylate and phenol groups in the chemical structures of aliphatic/phenolic carboxyl molecules, the peak at 1654 cm^{-1} was determined to be of intensity and width for C=C stretching in aromatic rings. C=C or C-O vibrations are responsible for peak at 1511 cm^{-1}, while aromatic C=C stretching

vibrations occurred peaks at 1445 and 1226 cm^{-1} [13]. In carboxylate groups C-O stretching vibrations (alkyl groups and alkanes) are assumed to be responsible for observed peak at 1367 cm^{-1}. In spectral region, bands in 1030 cm^{-1}, which were present in all spectra with only slight variations in peak intensity and width, indicated presence of -glycosidic bonds in cellulose and hemicellulose and C-O stretching vibration of aliphatic ethers and alcoholic groups. Same bands also evidenced presence of general carboxyl groups, lactones, and lignin structure in the adsorbents of the study [14].

Based on the FTIR spectra indicating presence of -OH and C-O bonds of alcohols, esters, ethers, and phenols, on the surface of PSS the mechanism of MB adsorption was deduced. On surface of PSS, oxygen-containing functional groups (negatively charged or acidic groups) and dye species are electrostatically attracted to each other, in the adsorption process. Another possible component is hydrogen bonding contact between N atoms in the MB and H atoms on PSS surface. In addition, aromatic rings of MB and the hexagonal structure of PSS may interact as p-p electron donors and acceptors. This type of interaction was regularly observed when the dye MB was adsorbed onto various carbon-based materials [15].

3.1.2 XRD analysis

The crystalline morphology of PSS was examined by powder X-ray diffraction (Fig. 2 B). In XRD, the PSS shows distinct peaks at $2\theta = 27.3, 31.6, 45.4, 56.4, 66.2,$ and 75.2. This clearly shows that the PSS has high crystallinity. The six peaks mentioned above have d-spacings of 3.27, 2.82, 1.99, 1.63, 1.41 and 1.26 A°, respectively. These peaks are formed from NaCl in the structure (RRUFF ID: R070292.1. Crystal System: cubic). In addition to, one peak is existed at around 22° which is assigned to the reflection from the 200 planes. This peak consists of cellulose in the structure [16].

3.1.1 SEM analysis

In research, the PSS investigated by scanning electron microscopy (SEM). The SEM images of PSS and PSS-MB-loaded samples are shown in Fig. 3. They prove that the adsorption of the studied solutes changed the PSS structure. The PSS-MB-loaded samples tended to form spherical aggregates, as can be seen in the SEM micrographs. In addition, S atom was found in the structure after MB adsorption in

EDX analysis. This confirms that the structure adsorbs MB.
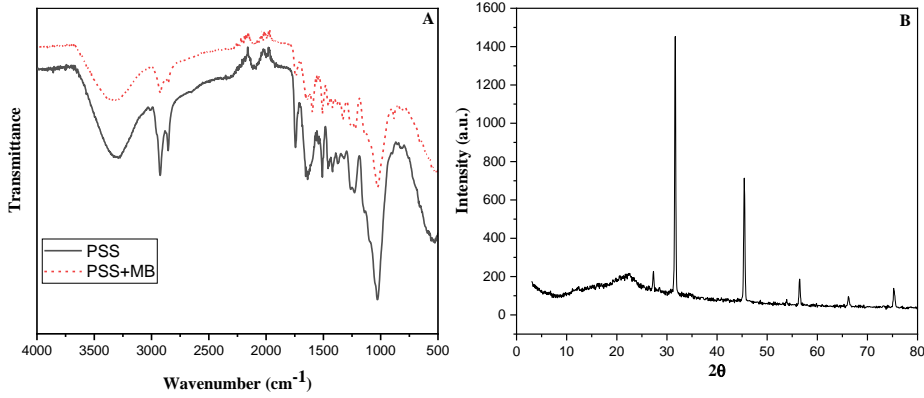
Figure 2. A. Fourier-transform infrared spectroscopy spectrum **B.** XRD spectrum
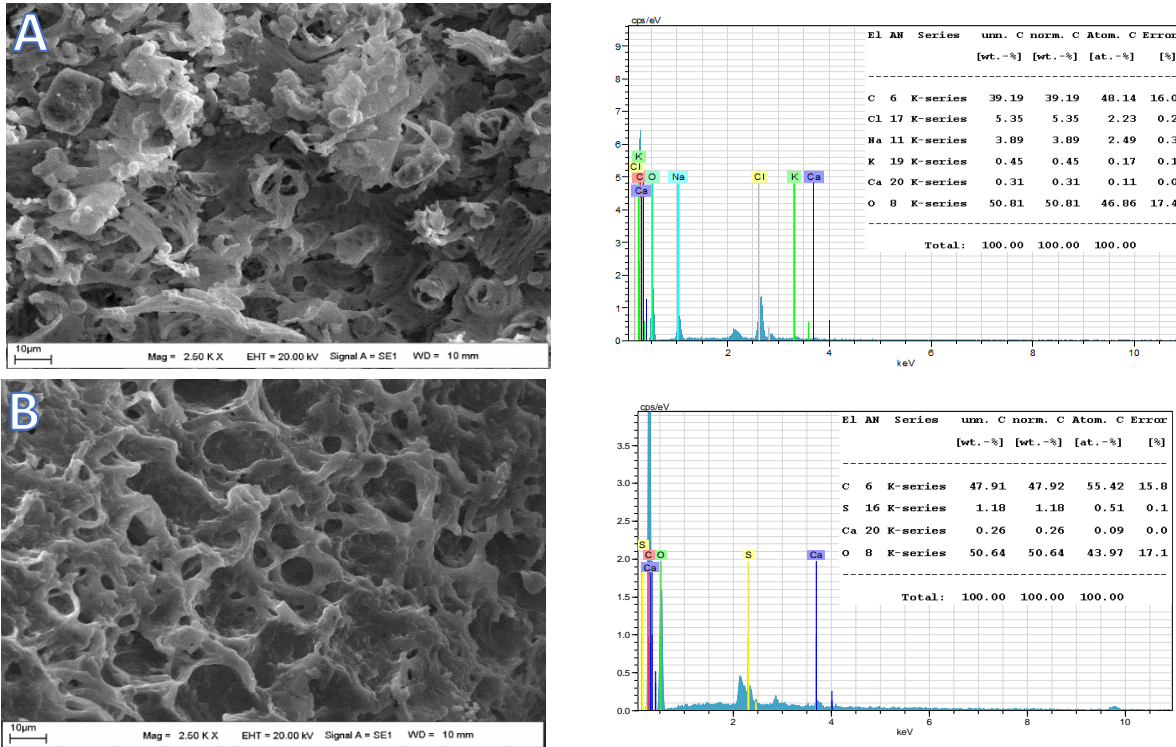
Figure 3. SEM İmages and EDX results **A.** PSS **B.** PSS (After Adsorption)

3.2. Adsorption Study

3.2.1 Effect of initial concentration and contact time

Fig. 4. A shows adsorption of dye MB on fixed amount of 0.5 g per 500 mL of PSS as a function of exposure time at a constant pH of 5.8. The dye MB

was initially rapidly adsorbed. Approximately half of the MB dye was absorbed in the first 5 minutes. Furthermore, the uptake of the dye MB gradually increased up to 90 minutes of increased contact time between adsorbent and adsorbate before reaching a plateau at a maximum update of 16 mg/g with 53.3% removal (initial concentration 30 mg/L). The rapid initial adsorption rate can be ascribed to increased number of active sites in the form of functional groups and pores on surface of PSS during the first phase of the adsorption process. The accumulation of dye molecules on surface of PSS causes adsorption process to proceed slowly because it stops the molecules from diffusing into the pores. In addition, initial concentration of pollutants in the system has a significant effect on adsorbent's ability to bind pollutants. In this situation, initial concentration of the MB was chosen between 30 mg/L and 50 mg/L. As shown in Fig. 4. A, the uptake of MB on PSS increased from 16 mg/g to 20.6 mg/g by changing initial concentration from 30 mg/L to 50 mg/L. Later, it was found that required equilibrium time for the MB increased with an increase in initial concentration.

3 .2.2 Effect of Temperature

Temperature is important and effective parameters in the adsorption process and affects both transfer process and adsorption kinetics of dye. In Fig. 4 B, impact of temperature on adsorption effectiveness of MB dyes was examined using PSS biosorbent in temperature range of 22 to 40 °C. The results demonstrated that when temperature increased from 22 °C to 40 °C, the adsorption efficiency of MB dye

employing PSS biosorbent reduced from 53.3% to 48%. This shows that use of adsorbent in MB adsorption process is exothermic [17]. The increased solubility of MB in an aqueous solution causes interactions between dye molecule and solvent to be stronger than those between dye molecule and the adsorbent, which may lead to a decrease in efficiency of adsorption process with increasing temperature [18]. Therefore, PSS biosorbent was found to work best at a temperature of 22 °C for MB dye adsorption process.

3.2.3 Effect of pH

Capacity of PSS to remove MB was found to be more effective at higher pH values. Fig. 4. C shows the removal of MB for a study performed under 2-12 pH. The removal efficiency was lower at an acidic pH. This result shows that protonation of carbonyl and hydroxyl groups on surface of PSS repels positively charged MB ions and negatively affects removal efficiency. However, as pH increases, surface of PSS material becomes negatively charged, making it easier to attract and remove positively charged MB ions from water. Analysis of the pH_{pzc} can help confirm this conclusion. The calculated pH_{pzc} of PSS was 5.66 (Fig. 4. D). Consequently, the surfaces of these materials below this pH are known to be positively charged [19]. This confirms our earlier conclusion. Other researchers who studied the removal of MB from water using biomass reported a similar impact of pH on removal of MB [20]. MB increased with an increase in initial concentration.
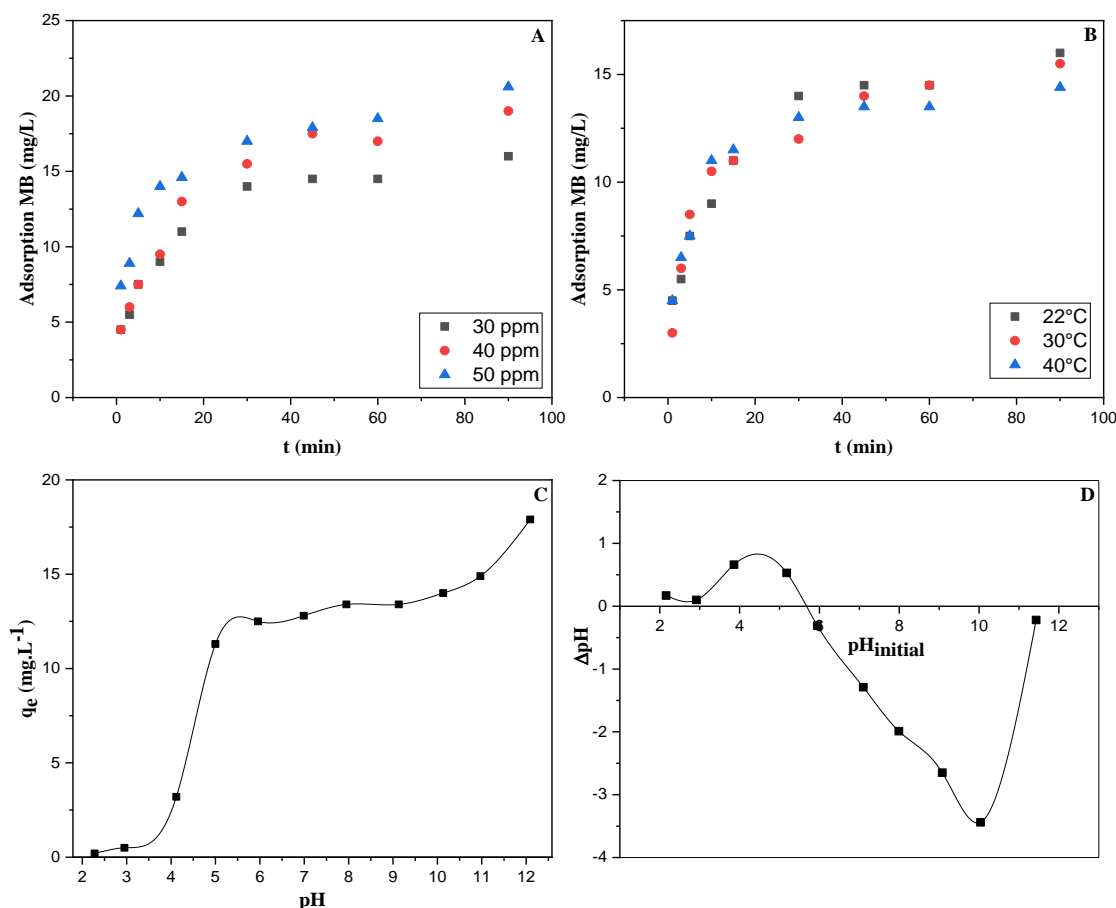
Figure 4. A. Effect of contact time and initial ion concentration of MB on PSS biosorbent **B.** Effect of temperature of MB on PSS biosorbent C_0= 30 mg/L **C.** Effect of solution pH of MB on PSS biosorbent **D.** pHpzc graph

3.2.4 Isotherm studies

Adsorption isotherm models explain the interactions between pollutants and adsorbents. To explain this interaction, isotherm models were investigated in research.

Langmuir isotherm model, defined to compare adsorption capacities and performances of different biosorbents, assumes single-layer adsorption. This isotherm model states that adsorption can only take place in a finite (constant) number of equal and equivalent localized patches that have lateral contact and are not steric [21]. Adsorption is not ideal, is reversible, and is not just confined to the creation of monolayers, according to the Freundlich isotherm. According to this model, the amount adsorbed represents the total amount of adsorption on all sites (each of which has a bond energy), with stronger binding sites being occupied first until the adsorption process is complete and the adsorption energy is exponentially reduced [21]. The Temkin isotherm

model takes into account interactions between adsorbate and adsorbent assumes that the heat of adsorption (temperature function) decreases linearly rather than logarithmically with coating. This model does not take into account extremely low and high values of the concentrations [22]. Nonlinear equations of Langmuir, Freundlich, and Temkin are shown in Eq. 2,3,4 respectively.

$$q_e = \frac{q_m K_L C_e}{1 + K_L C_e} \tag{2}$$

$$q_e = K_F C_e^{\frac{1}{n}} \tag{3}$$

$$q_e = B_T \ln(A_T C_e) \tag{4}$$

The experimental data were applied to isotherm equations, and graphs shown in Fig. 5 A were obtained. Isotherm constants were calculated using obtained graphs and listed in Table 1.

Equilibrium concentration of adsorbate, C_e (mg/L), amount of dye adsorbed per gram of adsorbent at equilibrium, q_t (mg/g), maximum monolayer coverage capacity, q_m (mg/g), initial concentration,

C_0, constant related to energy of adsorption (Langmuir Constant), K_L (L/mg), Freundlich isotherm constant, K_F (mg/g)/(mg/L)^n, adsorption intensity, A_T(L/g), Temkin isotherm constant, n, Temkin isotherm equilibrium binding constant, B_T (j/mol).

Table 1 lists constants for the Langmuir model, which were determined. Other important parameter defining properties of the Langmuir model is the adsorption intensity (R_L). This parameter determines mode and quality of isothermal model. Respectively, for $R_L > 1$, $R_L = 0$, $R_L = 1$ and $0 > R_L > 1$, the adsorption process is undesirable, irreversible, linear, and favorable, [23]. R_L value of the adsorption process of MB, which ranged from 0 to 1, was in the ideal range. Adsorption capacities of MB were calculated at 38.6.

Table 1 lists the constants for the Freundlich model, which were determined. While 1/n is a function of strength of adsorption in adsorption process, the constant K_F is a rough measure of adsorption capacity. Separation between two phases is independent of concentration when n = 1. Normal adsorption occurs when the value of 1/n is less than one. On the other hand, cooperative adsorption is indicated when 1/n is greater than one. When the pressure increases without constraints, the function reaches an asymptotic maximum. The constants K_F and n change with temperature to account for empirical finding that adsorbed amount increases more slowly and larger pressures are required to saturate surface. However, linear regression is often used to determine parameters of the kinetic and isothermal models, while K_F and n are parameters specific to the system of sorbent and sorbate and must be determined by data fitting. Because 1/n is heterogeneity parameter and smaller 1/n is, higher predicted heterogeneity, linear least squares approach and linear transformed equations is usually used to correlate sorption data. When 1/n = 1, this formula simplifies to a linear adsorption isotherm. A favorable sorption process is given when n is between one and ten. According to the data in Table 3, the biosorption of MP is favorable, and the R^2 value is 0.978, with the value of 1/n = 0.6, when n=1.66.

Table 1 lists constants for Temkin model, which were determined. The equilibrium binding constant of Temkin isotherm is A_T, while the heat constant of sorption (J/mol) is B_T. $A_T = 0.47$ L/g, B = 8.51, J/mol, a measure of the heat of sorption, and $R^2 = 0.996$ indicate a physical adsorption process.

Table 1. The parameters of the selected adsorption isotherm models obtained from Fig. 5.

Langmuir		Freundlich		Temkin	
q_m	38.6	K_F	3.06	B_T	8,51
K_L	0.04	n	1.66	A_T	0.47
R^2	0,993	R^2	0.978	R^2	0.996

3.2.5 Kinetics studies

Adsorption kinetics of MB onto PSS were investigated using pseudo-first-order (PFO), pseudo-second-order (PSO), Elovic, and intraparticle diffusion methods.

PFO model equation is applied to adsorption in a liquid-solid system. In this equation, the differences in saturation levels of concentration are directly proportional to adsorbate uptake [24]. The PFO model equation is known as follows:

$$q_t = q_e(1 - \exp(-k_1 t)) \qquad (5)$$

Chemisorption is usually described by pseudo-second-order (PSO) model and Elovich model. More specifically, The pseudo-second-order model depicts the participation of valence forces through the exchange of electrons between the adsorbate and the adsorbent as covalent forces and ion exchange, whereas the Elovich model explains the kinetics of chemisorption on an adsorbent with a heterogeneous surface [21]. The PSO model and Elovich equation are respectively known as follows:

$$q_t = \frac{q_e^2 k_2 t}{1 + k_2 q_e t} \qquad (6)$$

$$q_t = \frac{1}{b} In(abt + 1) \qquad (7)$$

The rate-limiting step in the adsorption process is intraparticle diffusion, which produces a straight line when plotting amount of metal ions adsorbed against square root of contact time. [25]. For an adsorption system, the following is intraparticle diffusion equation that is most frequently used.

$$q_t = k_p t^{1/2} + C \qquad (8)$$

q_t (mg g^{-1}) is adsorption capacity at time t and k_1 (min^{-1}) is rate constant of the pseudo-first order adsorption. Rate constant of pseudo-second order adsorption, k_2 (g mg^{-1} min^{-1}). k_p (mg g^{-1} min$^{-1/2}$) is intraparticle diffusion rate constant and C (mg g^{-1}) is a constant. a (mg/g ·min) is initial adsorption rate, and the desorption constant, b, depends on amount of surface covering and the chemisorption's activation energy.

Based on higher R^2 values compared to PFO and PSO models, the results show that adsorption process of the dye MB follows Elovich model. The results show that a chemisorption mechanism controls the adsorption of the dye MB by PSS. Additionally, the q_e value closest to the C_0 values was determined in the PSO model. Fig. 5 D and Table 2 contain the plots and the analyzed parameters of intraparticle diffusion, respectively. In Fig. 5 D, a linearity segment can be seen, indicating that the only rate-regulating phase in adsorption process was intraparticle diffusion of dye MB by PSS.
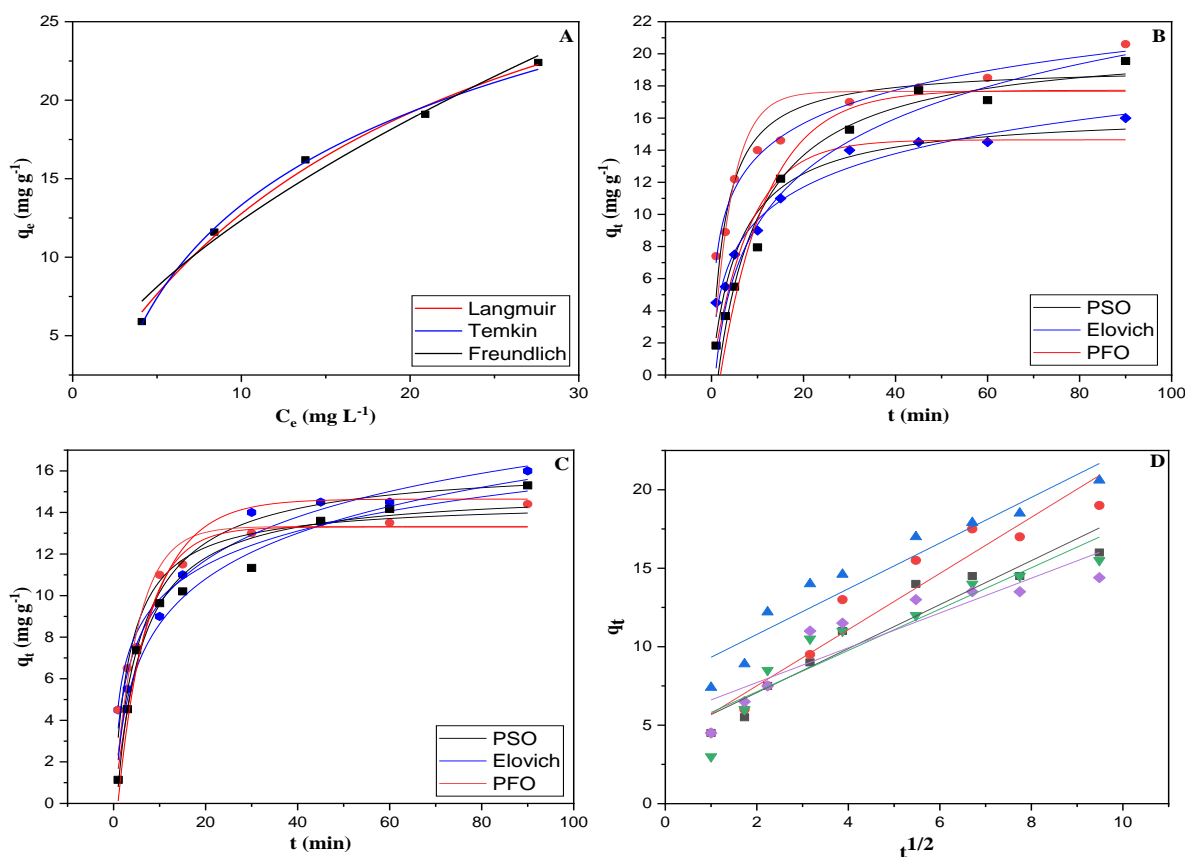
Figure 5. A. Isotherm models **B.** Kinetic models of the initial concentration **C.** Kinetic models of the temperature **D.** Intraparticle Diffusion

Table 2. The parameters of the selected adsorption kinetic models at different solution temperatures and initial concentration.

		Pseudo-First Order			Pseudo-Second Order		
°C	C_0	k_1	q_e	R^2	k_2	q_e	R^2
22	30	0.12	14.6	0.897	0.01	16.3	0.949
22	40	0.09	17.5	0.927	0.006	20	0.960
22	50	0.23	17.6	0.786	0.017	19.23	0.910
30	30	0.16	13.7	0.918	0.013	15.3	0.974
40	30	0.19	13.3	0.919	0.019	14.5	0.969
		Elovich			Intraparticle Diffusion		
°C	C_0	a	b	R^2	k_p	C	R^2
22	30	6.90	0.32	0.976	1.40	4.27	0.915
22	40	5.18	0.24	0.975	1.79	3.93	0.927
22	50	27.6	0.33	0.983	1.45	7.87	0.914
30	30	14.5	0.41	0.962	1.31	4.49	0.869
40	30	8.15	0.35	0.978	1.10	5.50	0.825

3.2.4 Thermodynamics of adsorption

Adsorption capacity of adsorbents and transport/kinetic mechanism of adsorption are significantly affected by temperature. The following equations 10 and 11 were used to calculate the thermodynamic parameters, adsorption free energy ($\Delta G°$), standard enthalpy ($\Delta H°$) and entropy changes ($\Delta S°$).

$$\Delta G° = -RT\ln (K_c) \tag{10}$$

K_c was calculated as follows: Langmuir constant multiplied by the molar mass of methylene blue, then multiplied by the molecular mass of methylene blue, and finally multiplied by 1000. R ($8.314\ JK^{-1}mol^{-1}$) is

universal gas constant, T(K) is temperature. $\Delta S°$ and $\Delta H°$ values were calculated with the Van't Hoff (eq. 21).

$$\ln K_C = \frac{\Delta S^0}{R} - \frac{\Delta H^0}{RT} \tag{11}$$

Table 3, the thermodynamic parameters are shown. Positive value of $\Delta G°$ indicates unspontaneous nature of adsorption of MB onto PSS surface at given experimental conditions [26]. Exothermic character of adsorption process is shown by negative enthalpy ($\Delta H°$) of process. The decrease randomness at solid/liquid boundary during dye adsorption on PSS is shown by the negative value of $\Delta S°$ [27].

Table 3. Thermodynamic parameters

$\Delta G°$ (kJ/mol)			$\Delta H°$ (kJ/mol)	$\Delta S°$ (kJ/mol·K)
22°C	30°C	40°C		
23.618	22.294	21.859	-53.237	-0.101

4. Conclusion and Suggestions

In this study, cheap, renewable, and waste material pumpkin seed shells were used as an adsorbent. Methylene blue, which is used in many sectors and pollutes the environment, was selected as the adsorbate. The study aimed to determine kinetic and isotherm properties of adsorbent. The parameters of pH, initial concentration, temperature, and contact time were investigated for removal of methylene blue. Although a significant increase in initial concentration, pH, and contact time was observed, the removal of methylene blue decreased with increasing temperature. This

decrease was confirmed by a thermodynamic study, which established that biosorption is an exothermic process. The obtained results were applied to different isotherm models, and the Temkin model (R2= 0.996) was found to be the most suitable. Kinetic studies demonstrated that biosorption followed Elovich model (R2=0.983). Consistent with these results, it was concluded that pumpkin seed shells can be effectively used as a renewable adsorbent.

Statement of Research and Publication Ethics
The study is complied with research and publication ethics

References

[1] Y. Zhou, J. Lu, Y. Zhou, and Y. Liu, "Recent advances for dyes removal using novel adsorbents: A review," *Environ. Pollut*., vol. 252, pp. 352–365, 2019.

[2] M. Rafatullah, O. Sulaiman, R. Hashim, and A. Ahmad, "Adsorption of methylene blue on low-cost adsorbents: A review," *J. Hazard. Mater*., vol. 177, no. 1–3, pp. 70–80, 2010.

[3] A. M. Elgarahy, K. Z. Elwakeel, S. H. Mohammad, and G. A. Elshoubaky, "A critical review of biosorption of dyes, heavy metals and metalloids from wastewater as an efficient and green process," *Clean. Eng. Technol*., vol. 4, no. 100209, p. 100209, 2021.

[4] Y. Wang, Q. Peng, N. Akhtar, X. Chen, and Y. Huang, "Microporous carbon material from fish waste for removal of methylene blue from wastewater," *Water Sci. Technol*., vol. 81, no. 6, pp. 1180–1190, 2020.

[5]   M. Onay and Ç. Sarici Özdemir, "Equilibrium studies for dye adsorption onto Red Clay," *Naturengs MTU Journal of Engineering and Natural Sciences Malatya Turgut Ozal University*, vol.3, no. 2, pp. 36-45, 2022.

[6]   N. Kaya, Z. Yıldız, and S. Ceylan, "Preparation and characterisation of biochar from hazelnut shell and its adsorption properties for methylene blue dye," *J. Polytech.*, vol. 21, no. 4, pp. 765-776, 2018.

[7]   S. Savcı and F. Karadağ, "Fast adsorption of methylene blue by filter coffee waste," *NWSA-Eng. Sci.*, vol. 15, no. 4, pp. 111–120, 2020.

[8]   Z. Ciğeroğlu and E. Yildirir, "Vermicompost as a Potential Adsorbent for the Adsorption of Methylene Blue Dye from Aqueous Solutions," *JOTCSA*, vol. 7, no. 3, pp. 893–902, 2020.

[9]   T. Satır and İ. Erol, "Calcined Eggshell for the Removal of Victoria Blue R Dye from Wastewater Medium by Adsorption," *JOTCSA*, vol. 8, no. 1, pp. 31–40, 2021.

[10]   V. Krstić, T. Urošević, and B. Pešovski, "A review on adsorbents for treatment of water and wastewaters containing copper ions," *Chem. Eng. Sci.*, vol. 192, pp. 273–287, 2018.

[11]   N. K. Gupta, A. Gupta, P. Ramteke, H. Sahoo, and A. Sengupta, "Biosorption-a green method for the preconcentration of rare earth elements (REEs) from waste solutions: A review," *J. Mol. Liq.*, vol. 274, pp. 148–164, 2019.

[12]   A. Stavrinou, C. A. Aggelopoulos, and C. D. Tsakiroglou, "Exploring the adsorption mechanisms of cationic and anionic dyes onto agricultural waste peels of banana, cucumber and potato: Adsorption kinetics and equilibrium isotherms as a tool," *J. Environ. Chem. Eng.*, vol. 6, no. 6, pp. 6958–6970, 2018.

[13]   K. Komnitsas, D. Zaharaki, I. Pyliotis, D. Vamvuka, and G. Bartzas, "Assessment of pistachio shell biochar quality and its potential for adsorption of heavy metals," *Waste Biomass Valorization*, vol. 6, no. 5, pp. 805–816, 2015.

[14]   D. Angın, T. E. Köse, and U. Selengil, "Production and characterization of activated carbon prepared from safflower seed cake biochar and its ability to absorb reactive dyestuff," *Appl. Surf. Sci.*, vol. 280, pp. 705–710, 2013.

[15]   B. Hu et al., "Efficient elimination of organic and inorganic pollutants by biochar and biochar-based materials," *Biochar*, vol. 2, no. 1, pp. 47–64, 2020.

[16]   Z. Zhang, M. Zhu, and D. Zhang, "A Thermogravimetric study of the characteristics of pyrolysis of cellulose isolated from selected biomass," *Appl. Energy*, vol. 220, pp. 87–93, 2018.

[17]   M. Naushad, A. A. Alqadami, Z. A. AlOthman, I. H. Alsohaimi, M. S. Algamdi, and A. M. Aldawsari, "Adsorption kinetics, isotherm and reusability studies for the removal of cationic dye from aqueous medium using arginine modified activated carbon," *J. Mol. Liq.*, vol. 293, no. 111442, p. 111442, 2019.

[18]   R. Foroutan, S. J. Peighambardoust, S. H. Peighambardoust, M. Pateiro, and J. M. Lorenzo, "Adsorption of crystal Violet dye using activated carbon of lemon wood and activated carbon/Fe3O4 magnetic nanocomposite from aqueous solutions: A kinetic, equilibrium and thermodynamic study," *Molecules*, vol. 26, no. 8, p. 2241, 2021

[19]   S. Manna, D. Roy, P. Saha, D. Gopakumar, and S. Thomas, "Rapid methylene blue adsorption using modified lignocellulosic materials," *Process Saf. Environ. Prot.*, vol. 107, pp. 346–356, 2017.

[20]   P. M. Thabede, N. D. Shooto, and E. B. Naidoo, "Removal of methylene blue dye and lead ions from aqueous solution using activated carbon from black cumin seeds," *S. Afr. J. Chem. Eng.*, vol. 33, pp. 39–50, 2020.

[21]   M. Choudhary, R. Kumar, and S. Neogi, "Activated biochar derived from Opuntia ficus-indica for the efficient adsorption of malachite green dye, Cu+2 and Ni+2 from water," *J. Hazard. Mater.*, vol. 392, no. 122441, p. 122441, 2020.

[22]   K. Y. Foo and B. H. Hameed, "Insights into the modeling of adsorption isotherm systems," *Chem. Eng. J.*, vol. 156, no. 1, pp. 2–10, 2010.

[23]   E. Ajenifuja, J. A. Ajao, and E. O. B. Ajayi, "Adsorption isotherm studies of Cu (II) and Co (II) in high concentration aqueous solutions on photocatalytically modified diatomaceous ceramic adsorbents," *Appl. Water Sci.*, vol. 7, no. 7, pp. 3793–3801, 2017.

[24]   J. Wang and X. Guo, "Adsorption kinetic models: Physical meanings, applications, and solving methods," *J. Hazard. Mater.*, vol. 390, no. 122156, p. 122156, 2020.

[25]   A. Pholosi, E. B. Naidoo, and A. E. Ofomaja, "Intraparticle diffusion of Cr(VI) through biomass and magnetite coated biomass: A comparative kinetic and diffusion study," *S. Afr. J. Chem. Eng.*, vol. 32, pp. 39–55, 2020.

[26]   P. Nautiyal, K. A. Subramanian, and M. G. Dastidar, "Kinetic and thermodynamic studies on biodiesel production from Spirulina platensis algae biomass using single stage extraction–transesterification process," *Fuel (Lond.)*, vol. 135, pp. 228–234, 2014.

[27]   M. Toprak, A. Salci, and A. R. Demirkiran, "Comparison of adsorption performances of vermiculite and clinoptilolite for the removal of pyronine Y dyestuff," *React. Kinet. Mech. Catal.*, vol. 111, no. 2, pp. 791–804, 2014.

Effect of Pulse Width and Intensity on Cell Death in Reversible Electroporation of Cancerous Cells

Mehmet Eşref ALKIŞ[1*], Yusuf ALAN[2], Erhan ESER[3]

[1]*Muş Alparslan University, Faculty of Health Sciences, Department of Occupational Health and Safety, Muş, Türkiye*
[2]*Bitlis Eren University, Vocational School of Health Services, Department of Medical Services and Techniques, Bitlis, Türkiye*
[3]*Ankara Hacı Bayram Veli University, Polatlı Faculty of Arts and Sciences, Department of Physics, Ankara, Türkiye*
(ORCID: 0000-0002-3321-2873) (ORCID: 0000-0003-0007-0212) (ORCID: 0000-0003-3207-818X)

Abstract
Electroporation (EP) is the process of increasing the permeability of a biological cell or tissue by applying a short-term and sufficient external electric field. The utilization of proper pulse settings is required for EP-based treatments to be successful. Our aim in this study was to examine the effect of different electrical pulse widths and strength on EP efficiency. Human osteosarcoma cells (U2OS) were used in the study. Eight-square-pulses with a frequency of 1Hz at 10μs, 1ms, 5ms, 10ms, and 20ms widths with low electric fields (20-500V/cm) were applied to U2OS cells. 10-15 minutes after the applications, the cells were incubated in 96-well plates with 10 thousand cells in each well for 24 hours. Efficiency of pulses of different intensity and width was evaluated by MTT analysis method. The percent inhibition of U2OS cancer cells elevated as the pulse width increased in almost all electric field values. The highest cell inhibition (%) occurred in pulses with an electric field of 500 V/cm and a width of 20ms (inhibition ratio: 76.25%). No inhibition was observed in the cells at 10μs, 1ms, 5ms, 10ms width pulses with 20 V/cm electric field and 10μs, 1ms width pulses with 50V/cm electric field. In conclusion, our findings show that the electric field intensity and pulse width used in electroporation play an important role in U2OS cancer cell death. According to our results, it may be more appropriate to use high-voltage short-width pulses or low-voltage long-width pulses in reversible EP studies.

1. Introduction

Electroporation (EP) is a biophysical process in which the membrane permeability is elevated by increasing the transmembrane voltage of the cell membrane above the threshold level (0.2-1V) with electrical pulses [1]. Large molecules and ions that unable to pass through the membrane can enter the cell by EP [2]. Tumor treatment techniques include irreversible electroporation (IRE) and chemotherapy+reversible electroporation (electrochemotherapy, ECT). In the IRE technique, high voltage (>600 V/cm) and short duration electrical pulses are used (no anticancer drug administration) to change the membrane potential of the cancer cell, resulting in permanent holes and apoptosis [3]. Since this technique uses larger number of high amplitude pulses, neuromuscular blockade and general anesthesia are required [4]. IRE therapy shows promise for the treatment of malignancies such as cardiac catheter ablation and intra-abdominal cancers. As for the reversible electroporation approach, microelectropores form on the cell membrane during electric field application and these pores close again shortly after the electroporation process. Therefore, this approach allows the cells to live, while IRE destroys the cells directly [5].

Some cancer medications are designed to cause DNA damage. These drugs can show cytotoxic effects only if they easily pass through the cancer cell membrane and reach their targets inside the cell. Unfortunately, many of the highly cytotoxic anticancer drugs pass little or practically no penetration across the cell membrane [6,7]. Electrochemotherapy (ECT) is a treatment technique in which reversible EP is utilized to enhance the transport of anticancer agents into cancer cells [8]. In ECT, a reversible effect with strong permeabilization is desired. Therefore, cell death and permeability threshold impact, which is controlled by electrical pulse characteristics and type of cell, is necessary [9,10]. It is critical to select the proper amplitude, frequency, and number of pulses for the transitory effect. In many previous studies, the effect of different parameters like the electric field magnitude of the pulse, its frequency, and the number of pulses on the efficiency of electroporation have been investigated [11-13]. For various electroporation applications, a large variety of distinct pulse procedures have been documented to date. Most of the studies for ECT have used 1 or 8 square wave pulse trains with a width of 100 µs and a frequency of 1Hz or 5kHz [4,11,14,15]. While investigating the optimum electroporation conditions, generally keeping these parameters constant, only the electric field was changed [16,17]. In some studies, when the electric field is reduced, the pulse width is increased [18,19]. The appropriate pulse width to be applied in current ECT protocols has not been fully elucidated and there is still some debate about the effectiveness of pulse width and strength in treatment. Osteosarcoma is the most common bone tumor in children and adolescents and is more common in men [20]. In recent years, different modern treatment strategies have been developed for osteosarcoma patients [21]. However, since the negative effects of radio and chemotherapy cause significant morbidities, more studies are needed to eliminate these effects [22]. The aim of the present study was to determine the most suitable electric field and pulse width for human osteosarcoma (U2OS) cells by trying pulses of different widths with different electric fields keeping the pulse frequency (1 Hz) and number (8 pulses) constant.

2. Material and Method

2.1. Cell culture

In this study, U2OS were used as a model. The cell line was provided by Muş Alparslan University Application and Research Center. U2OS cells were seeded in culture flasks with a surface area of 75 cm2 in Dulbecco's Modified Eagle Medium (DMEM) (Gibco™, USA) with 1% Pen-Strep and 10% FBS, then left to incubate at 37 °C, 75–85% humid and 5% CO_2 environment. They were fed 3 times a week until the cells reached sufficient numbers.

2.2. Electroporation Applications

When U2OS cells were approximately 70% confluent, they were taken out using trypsin and then centrifuged for 5 minutes at 1300 rpm. The cells were re-suspended at a density of $1x10^6$ cells/l in fresh media. After 400 µl of cell solution was placed in each electroporation cuvette (4mm gap), the cuvettes were put in the electroporation and currents were applied. ECT applications were performed using Gene Pulser Xcell TM (Bio-Rad, Hercules, CA, USA) [23]. In the electroporation application, pulses with different electric field intensities of 20 V/cm, 50 V/cm, 250 V/cm and 500 V/cm were used while keeping the 1 Hz frequency and eight square wave parameters constant. Five different pulses with pulse widths of 10µs, 1ms, 5ms, 10ms and 20ms were used in each electric field application. No electric field was applied to the control cells placed in 4 mm EP cuvettes. After the applications, the cells were kept at room environment for 12-15 minutes, then placed into 96-well plates with 10 thousand cells/well and allowed to incubate for one day. The MTT assay was conducted to measure cell viability. Ethics committee approval is not required as the study was performed on a commercially purchased cell line.

2.3. MTT assay

U2OS cells viability was determined by 3(4,5-dimethylthiazol-2-yl)-2,5-diphenyltetrazolium bromide (MTT) test after exposure to different electric fields. Cells that were left to incubate after electric field application were removed from the incubator after 24 hours, and 20 µl of MTT solution was applied to the wells. The cells were then incubated for another 4 hours at 37°C. After which, the liquids in the wells were emptied, 100 µl of DMSO was put instead and mixed. After 15 minutes, the optical density formed in the wells was measured at 540 nm by a Multiscan ELISA reader (Labsystems Multiscan MS, U.K.).

2.4. Statistical analysis

The data presented in the study were expressed as averages with standard error of the mean (mean±SEM), and the graphs presented in the study were created using these values. Tests were performed in at least three replicates.

3. Results and Discussion

The Pulses with different electric fields and widths were applied to U2OS cancer cells. In EP applications, 8 square wave electrical pulses with a frequency of 1 Hz were used. The effect of different pulses applied in EP on cell viability was determined and was given in Table 1.

The % inhibition values caused by electric field pulses with different electric field intensities (20V/cm, 50V/cm, 250V/cm and 500V/cm) and widths (10 μs, 1 ms, 5 ms, 10 ms and 20 ms) in U2OS cancer cells were given in Figure 1.
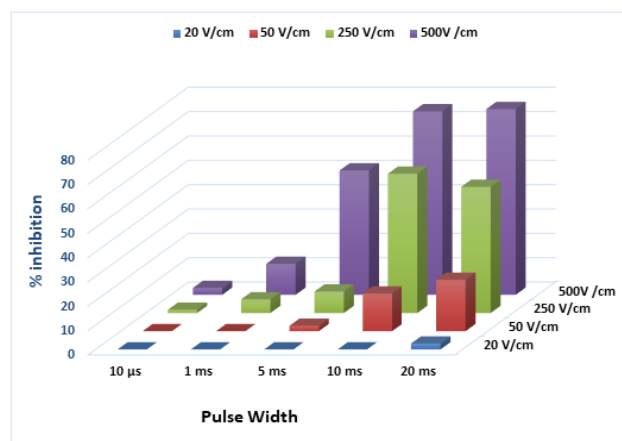
Figure 1. The inhibition (%) of U2OS cancer cells 24 hours after EP.

Table 1. Cell viability (%) of U2OS cancer cells 24 hours after applying pulses with different electric fields and widths

Electric field strength	Pulse width 10 μs	Pulse width 1 ms	Pulse width 5 ms	Pulse width 10 ms	Pulse width 20 ms
20 V/cm	100±0.5	100±0.7	100±1.62	100±2.72	97.59±2.75
50 V/cm	100±1.20	100±2.35	97.76±2.54	84.54±3.23	78.92±1.52
250 V/cm	98.97±2.35	94.4±3.45	91.2±1.45	42.83±1.95	48.19±1.42
500V /cm	97.2±1.33	87.3±1.23	48.95±2.43	24.67±2.43	23.75±2.44

The inhibition (%) of U20S cancer cells increased as the pulse width increased in almost all electric field values (Figure 1, Table 1). The increase of the electric field also increased the cell inhibition percentage in a similar way. The highest cell inhibition (%) occurred in pulses with an electric field of 500 V/cm and a width of 20 ms (inhibition ratio: 76.25 %). No inhibition was observed in the cells at 10 μs, 1 ms, 5 ms, 10 ms width pulses with 20 V/cm electric field and 10 μs, 1 ms width pulses with 50 V/cm electric field. Our data show that the pulse width should be reduced at high electric field pulses and increased at low electric field pulses.

Membrane permeability is increased transiently when cells are subjected to high-intensity electrical impulses via electroporation (EP) [24]. The use of EP in medicine and biotechnology has resulted in new therapeutic techniques for drug delivery, gene therapy and cancer treatment [22]. ECT (anticancer agent+EP) is a therapy approach that uses reversible EP to help anticancer medicines enter cancer cells [25,26]. Much research has been undertaken to determine the efficacy of EP in cancer treatment. Bicek et al. [27] reported that New Anti-Tumor Metastasis Inhibitor-A (NAMI-A) treatment decreased the cell viability by 10 % when used alone

and by 90 % when used in combination with EP in the mouse melanoma (B16F1) cells. Mali et al. [28] conducted an investigation on the findings of the previous studies that examined the effectiveness of ECT application with various drugs in treating head/neck tumors, malignant melanoma, and breast cancer. They discovered that in all tumor types, ECT exhibited an objective response percentage of 84.1% and an entire remission rate of 59.4%. In addition, ECT contributes to the efficiency of therapy with its vascular lock, that is, keeping the high drug concentrations near the cancer cell for many hours [29,30]. Unlike the chemo- and radiotherapy, ECT is highly selective and has less negative side effects [30]. Being effective for subcutaneous and cutaneous tumors in humans [31], ECT has recently been used for the therapy of tumors in the internal organs and brain [32].

In ECT treatment technique, EP is expected to induce a strong permeability while causing minimal cell death. Therefore, it is very important to properly select parameters such as the width, amplitude, repetition frequency, waveforms and number of pulses of the electric field. Because these parameters have a significant effect on the efficiency of EP [33]. In the current research, we investigated the

toxicity of the electric pulse in U2OS cancer cells as a function of electric field strength and pulse width. As seen in Figure 1, the inhibition (%) of U2OS cancer cells increased as the pulse width increased in almost all electric field values. Cell inhibition was maximized when pulses with a high electric field (500 V/cm) and long pulse width (20 ms) were used in EP. No inhibition was observed in the cells at 10 µs, 1 ms, 5 ms, 10 ms width pulses with 20 V/cm electric field and 10 µs, 1 ms width pulses with 50 V/cm electric field. Our data suggest that high-voltage short-width pulses or low-voltage long-width pulses should be used in reversible electroporation studies [34]. The electric field strength and pulse width used in electroporation play an important role in pore formation. Sulaeman and Widita [35] showed that high electric field density and long-width pulses would yield high pore intensity in the cell membrane. Increasing the electric field intensity with a long pulse width can cause a condition in which the pores can coalesce, resulting in cell death [36]. Some studies have suggested that EP plays a major role in transporting molecules across the cell membrane and that the pulse duration long enough for adequate uptake is crucial [37]. Our findings show that a change in pulse amplitude used in EP can be compensated for by another parameter such as pulse duration. Also, cell death is maximized when high electric field (500 V/cm) and long width (20 ms) pulses are used in EP.

4. Conclusion and Suggestions

In conclusion, our findings show that the electric field intensity and pulse width used in electroporation play an important role in U2OS cancer cell death. According to our results, it may be more appropriate to use high-voltage short-width pulses or low-voltage long-width pulses in reversible EP studies. More research is needed with different EP parameters to determine the width and strength of electric field pulses to be used in EP for different cancer cell lines.

Contributions of the authors

M.E.A and Y.A designed the study, performed the experiments and wrote the article. E.E performed the calculations, checked the language and contributed to the writing of the manuscript.

Conflict of Interest Statement

There is no conflict of interest between the authors.

Statement of Research and Publication Ethics

The study is complied with research and publication ethics.

References

[1] Y. Lv, Z. Feng, S. Chen, X. Cheng, J. Zhang, and C. Yao, "A fundamental theoretical study on the different effect of electroporation on tumor blood vessels and normal blood vessels," *Bioelectrochemistry*, vol. 144, no. 108010, p. 108010, 2022.

[2] A. Groselj, M. Bosnjak, P. Strojan, M. Krzan, M. Cemazar, and G. Sersa, "Efficiency of electrochemotherapy with reduced bleomycin dose in the treatment of nonmelanoma head and neck skin cancer: Preliminary results," *Head Neck*, vol. 40, no. 1, pp. 120–125, 2018.

[3] P. Gupta et al., "Efficacy and safety of irreversible electroporation for malignant liver tumors: a systematic review and meta-analysis," *Eur. Radiol.*, vol. 31, no. 9, pp. 6511–6521, 2021.

[4] L. G. Campana et al., "Electrochemotherapy of superficial tumors - Current status: Basic principles, operating procedures, shared indications, and emerging applications," *Semin. Oncol.*, vol. 46, no. 2, pp. 173–191, 2019.

[5] A. Zupanic, B. Kos, and D. Miklavcic, "Treatment planning of electroporation-based medical interventions: electrochemotherapy, gene electrotransfer and irreversible electroporation," *Phys. Med. Biol.*, vol. 57, no. 17, pp. 5425–5440, 2012.

[6]   M. E. Alkış, K. Buldurun, N. Turan, Y. Alan, Ü. K. Yılmaz, and A. Mantarcı, "Synthesis, characterization, antiproliferative of pyrimidine based ligand and its Ni(II) and Pd(II) complexes and effectiveness of electroporation," *J. Biomol. Struct. Dyn.*, vol. 40, no. 9, pp. 4073–4083, 2022.

[7]   V. Novickij et al., "Electrochemotherapy using doxorubicin and nanosecond electric field pulses: A pilot in vivo study," *Molecules*, vol. 25, no. 20, p. 4601, 2020.

[8]   O. Kozak, S. Haċ, J. Pieńkowska, and M. Studniarek, "Benefitial role of electrochemotherapy in locally advanced pancreatic cancer - radiological perspective," *Pol. J. Radiol.*, vol. 87, no. 1, pp. e30–e42, 2022.

[9]   G. Sersa, D. Miklavcic, M. Cemazar, Z. Rudolf, G. Pucihar, and M. Snoj, "Electrochemotherapy in treatment of tumours," *Eur. J. Surg. Oncol.*, vol. 34, no. 2, pp. 232–240, 2008.

[10]   Z. Shankayi, S. M. P. Firoozabadi, and Z. S. Hassan, "Optimization of electric pulse amplitude and frequency in vitro for low voltage and high frequency electrochemotherapy," *J. Membr. Biol.*, vol. 247, no. 2, pp. 147–154, 2014.

[11]   G. Pucihar, J. Krmelj, M. Reberšek, T. B. Napotnik, and D. Miklavčič, "Equivalent pulse parameters for electroporation," *IEEE Trans. Biomed. Eng.*, vol. 58, no. 11, pp. 3279–3288, 2011.

[12]   J. C. Weaver, K. C. Smith, A. T. Esser, R. S. Son, and T. R. Gowrishankar, "A brief overview of electroporation pulse strength-duration space: a region where additional intracellular effects are expected," *Bioelectrochemistry*, vol. 87, pp. 236–243, 2012.

[13]   M. E. Alkış, Ü. Keleştemür, Y. Alan, N. Turan, and K. Buldurun, "Cobalt and ruthenium complexes with pyrimidine based schiff base: Synthesis, characterization, anticancer activities and electrochemotherapy efficiency," *J. Mol. Struct.*, vol. 1226, no. 129402, p. 129402, 2021.

[14]   M. E. Alkış, N. Turan, Y. Alan, S. Irtegun Kandemir, and K. Buldurun, "Effects of electroporation on anticancer activity of 5-FU and newly synthesized zinc(II) complex in chemotherapy-resistance human brain tumor cells," *Med. Oncol.*, vol. 38, no. 11, p. 129, 2021.

[15]   V. Novickij et al., "Effects of time delay between unipolar pulses in high frequency nano-electrochemotherapy," *IEEE Trans. Biomed. Eng.*, vol. 69, no. 5, pp. 1726–1732, 2022.

[16]   M. A. Esmekaya, H. Kayhan, M. Yagci, A. Coskun, and A. G. Canseven, "Effects of electroporation on tamoxifen delivery in estrogen receptor positive (ER+) human breast carcinoma cells," *Cell Biochem. Biophys.*, vol. 75, no. 1, pp. 103–109, 2017.

[17]   M. E. Alkis, K. Buldurun, Y. Alan, N. Turan, and A. Altun, "Electroporation enhances the anticancer effects of novel Cu(II) and Fe(II) complexes in chemotherapy-resistant glioblastoma cancer cells," *Chem. Biodivers.*, vol. 20, no. 2, p. e202200710, 2023.

[18]   M. Cemazar, I. Hreljac, G. Sersa, and M. Filipic, "Construction of EGFP expressing HepG2 cell line using electroporation," in *IFMBE Proceedings, Berlin, Heidelberg: Springer Berlin Heidelberg*, 2009, pp. 128–131.

[19]   C. H. Lu, S. H. Lin, C. H. Hsieh, W. T. Chen, and C. Y. Chao, "Enhanced anticancer effects of low-dose curcumin with non-invasive pulsed electric field on PANC-1 cells," *Onco. Targets. Ther.*, vol. 11, pp. 4723–4732, 2018.

[20]   Y. Q. Chen, T. Q. Yang, B. Zhou, M. X. Yang, H. J. Feng, and Y. L. Wang, "HOXA5 overexpression promotes osteosarcoma cell apoptosis through the p53 and p38α MAPK pathway," *Gene*, vol. 689, pp. 18-23, 2019.

[21] Y. N. Hsu, H. W. Shyu, T. W. Hu, J. P. Yeh, Y. W. Lin, L. Y. Lee, and S. J. Su, "Anti-proliferative activity of biochanin A in human osteosarcoma cells via mitochondrial-involved apoptosis," *Food Chem. Toxicol.*, vol. 112, pp. 194-204, 2018.

[22] T. Wang, X. Gong, R. Jiang, H. Li, W. Du, and G. Kuang, "Ferulic acid inhibits proliferation and promotes apoptosis via blockage of PI3K/Akt pathway in osteosarcoma cell," *Am. J. Transl. Res.*, vol. 8, no. 2, pp. 968-980, 2016.

[23] B. Bute and M. E. Alkis, "Anticancer activity of methotrexate in electrochemotherapy and electrochemotherapy plus ionizing radiation treatments in human breast cancer cells," *Med. Oncol.*, vol. 40, no. 1, p. 28, 2022.

[24] T. Polajžer, J. Dermol-Černe, M. Reberšek, R. O'Connor, and D. Miklavčič, "Cancellation effect is present in high-frequency reversible and irreversible electroporation," *Bioelectrochemistry*, vol. 132, no. 107442, p. 107442, 2020.

[25] D. E. Chafai, A. Mehle, A. Tilmatine, B. Maouche, and D. Miklavčič, "Assessment of the electrochemical effects of pulsed electric fields in a biological cell suspension," *Bioelectrochemistry*, vol. 106, no. Pt B, pp. 249–257, 2015.

[26] M. E. Alkış, "Investigation of treatment potential of O-vanillin containing Schiff base ligand and pd(II) complex in glioblastoma multiforme cells and efficiency of electroporation," *Van Med. J.*, vol. 29, no. 1, pp. 69–75, 2022.

[27] A. Bicek, I. Turel, M. Kanduser, and D. Miklavcic, "Combined therapy of the antimetastatic compound NAMI-A and electroporation on B16F1 tumour cells in vitro," *Bioelectrochemistry*, vol. 71, no. 2, pp. 113–117, 2007.

[28] B. Mali, T. Jarm, M. Snoj, G. Sersa, and D. Miklavcic, "Antitumor effectiveness of electrochemotherapy: a systematic review and meta-analysis," *Eur. J. Surg. Oncol.*, vol. 39, no. 1, pp. 4–16, 2013.

[29] T. Jarm, M. Cemazar, D. Miklavcic, and G. Sersa, "Antivascular effects of electrochemotherapy: implications in treatment of bleeding metastases," *Expert Rev. Anticancer Ther.*, vol. 10, no. 5, pp. 729–746, 2010.

[30] J. Saczko et al., "Combination of therapy with 5-fluorouracil and cisplatin with electroporation in human ovarian carcinoma model in vitro," *Biomed. Pharmacother.*, vol. 68, no. 5, pp. 573–580, 2014.

[31] V. De Giorgi, F. Scarfì, E. Saqer, A. Gori, G. M. Tomassini, and P. Covarelli, "The use of cisplatin electrochemotherapy in nonmelanoma skin cancers: A single-center study," *Dermatol. Ther.*, vol. 33, no. 4, p. e13547, 2020.

[32] B. Agerholm-Larsen et al., "Preclinical validation of electrochemotherapy as an effective treatment for brain tumors," *Cancer Res.*, vol. 71, no. 11, pp. 3753–3762, 2011.

[33] R. Fusco, E. Di Bernardo, V. D'Alessio, S. Salati, and M. Cadossi, "Reduction of muscle contraction and pain in electroporation-based treatments: An overview," *World J. Clin. Oncol.*, vol. 12, no. 5, pp. 367–381, 2021.

[34] V. Stankevic et al., "Compact square-wave pulse electroporator with controlled electroporation efficiency and cell viability," *Symmetry (Basel)*, vol. 12, no. 3, p. 412, 2020.

[35] M. Y. Sulaeman and R. Widita, "The effect of electric field intensity, pulse width, and pulse rise time on conventional and supra electroporation," *The 5th International Conference on Mathematics and Natural Sciences*, 2–3 November 2014 Bandung, Indonesia. AIP Conf. Proc. 1677, 100008, 2015.

[36] I. Hyder, S. Eghbalsaied, and W. A. Kues, "Systematic optimization of square-wave electroporation conditions for bovine primary fibroblasts," *BMC Mol. Cell Biol.*, vol. 21, no. 1, p. 9, 2020.

[37] M. P. Rols and J. Teissié, "Electropermeabilization of mammalian cells to macromolecules: control by pulse duration," *Biophys. J.*, vol. 75, no. 3, pp. 1415–1423, 1998.

Machine Learning-Assisted Wearable Thermo-Haptic Device for Creating Tactile Sensation

Mine BOZ[1*], Yeliz DURGUN[2]

[1]Tokat Gaziosmanpaşa University, Department of Bioengineering, 60100, Tokat, Türkiye
[2] Tokat Gaziosmanpaşa University, Biomedical Device Technology Program, 60100, Tokat, Turkey
(ORCID: 0000-0002-0692-8809) (ORCID: 0000-0003-3834-5533)

Abstract
The tactile modality is an important source of human experience and emotional expression, either on its own or by intensifying and complementing other senses, influencing our interactions with objects, people, animals and other beings. Following this, developed haptic devices transmit information to the user using tactile stimuli to increase or change sensory input. Haptics are an important factor that makes virtual worlds and remote interpersonal interaction tangible. Haptic feedback consists of more components that make an experience physically perceptible and realistic. Haptic feedbacks are widely used in mobile and wearable devices to convey various types of notifications to users. In this study, it was aimed to develop a new generation of wearable gloves against the hypoesthesia problem by combining artificial intelligence and thermohaptic, which are popular in many fields.

1. Introduction

The survival of all organisms (plants, animals, fungi, etc.) depends on their ability to sense touch, perceive and respond to various external stimuli [1]. Touch is the sensation experienced when the skin interacts mechanically or thermally with an object [2]. Chemicals, mechanical force, temperature and pH are clues that provide information about safe and dangerous environments through pain sensations [1]. A basic biological function of pain sensations; It is to direct the organism's attention to injury and damage and to protect it from further injuries by triggering or blocking movement [3]. For many years, human skin has been considered as information-transmitting receptors. Skin sensations such as pressure values and stretching transmit tactile messages that are carried to the brain via afferent nerves. [4].

Tactile information is collected on the skin by numerous receptors, which are special end organs of the peripheral nervous system. Numerous receptors help convert thermal, noxious, itching or chemical stimuli into neural information. [5]. Tactile sensation and tactile perception change proportionally with age.

Starting from the age of 20, people gradually lose their sensitivity to external stimuli such as touch, pressure and vibration. These changes that occur with age depend on both skin characteristics and the central nervous system. The structure and number of sensory receptors in the skin, including the most sensitive receptors, change as the person ages. Changes in brain map areas can affect tactile perception in individuals with conditions such as stroke and diabetes. Approximately 3/4 of stroke patients occur in people over the age of 65. However, in addition to age, stroke may cause abnormal somatosensory function in 50-80% of cases. [6]. Stroke is the 3rd cause of disability and the 2nd cause of death worldwide. The most common disability that occurs after a stroke is hemiparesis of the upper extremity. This situation affects the life activity and peace of mind of 50%-70% of paralyzed individuals. While approximately 80% of sick individuals experience acute hemiparesis, 40% may experience this condition chronically. [7]. Individuals who experience this condition chronically may have lower skin perception, which impairs their ability to touch, perceive and press. It can reduce sensitivity to emotions. [6]. Among the most common

effects of stroke is the impairment of hand functions. People who have a stroke often experience permanent movement disorders. [8]. Severe hand or upper extremity weakness occurs in approximately 87% of stroke patients [7]. Treatment methods for sensory deficits are inadequate, and these have traditionally been addressed with compensatory strategies in physical therapy [9]. As the average age of the world population increases, it is predicted that these problems will increase, considering the tendency of the elderly population to sensory disorders. Due to the lack of treatment that fully restores sensory functions, approaches that aim to increase the standard of living or replace deficiencies can serve as effective alternatives. [4].

Previous work on haptic devices; showed that user preference for touch communication is haptic devices rather than vibration [10]. The term haptic; It allows us to manipulate objects and textures around us, temperature, pain, etc. It is defined as allowing us to detect sensations and perceive emotions [11]. Haptic feedback consists of more components that make a behavior physically detectable and realistic [12]. Tactile feedback is widespread in wearable technologies and mobile applications by providing various types of notifications to individuals [13]. These devices generally lack thermal feedback, although they are not separated from the sense of touch [10]. Temperature is an effective communication tool in our lives because human skin perceives a wide temperature range with high resolution [14]. Lack of temperature sensitivity or lack of sensation leads to avoidance of useful tactile information such as avoidance of extreme temperature and psychological comfort. Additionally, the lack of temperature feedback causes tissue damage through exposure to high temperatures [15]. Therefore, "thermo-haptic" devices are important for people with hypoesthesia.

Thermo-haptic technology is a method that allows people to sense temperature changes [16]. This technology is used especially in wearable devices such as gloves, allowing the user to sense the temperature of objects around them. Temperature perception plays an important role in daily life; for example, knowing whether something is too hot or feeling the surface temperature of an object. By providing this type of sensory information, thermo-haptic technology helps people experience their environment in a richer way.

Today, many wearable device studies are being carried out to overcome the difficulties caused by sensory loss and to enable patients with tissue loss to perceive their environment with their hands [14].

Wearable devices are in physical contact with human skin and convey different sensations to users through sensory feedback. Sensory feedback generally includes the senses of hearing, sight, taste, smell and touch. [12]. Chen suggested that temperature is one of the important factors when defining the material in thermal haptic feedback research [17]. Ho et al. conducted a study to verify the role of temperature information in material identification and positioning. [18]. Peiris et al. [19] by integrating the Peltier device into the 'Head Mounted Display (HMD)' device, it provided temperature feedback directly to the user's face [20]. To simulate the sensation of penetrating the body, Peng and others used thermal feedback. Existing studies have enabled people to truly feel tactile information in virtual environments by stimulating various sensory receptors on the skin and to reproduce this interaction to the user [21]. Yunus et al. developed a new wearable edge device to automatically calculate clinically important gait features in real time, as mobility features collected in daily life better reflect a person's walking capacity and complement clinical gait analysis [22]. These thermal technology-based studies demonstrate augmented reality (AR) / virtual reality (VR), but there are deficiencies in temperature transfer between limbs. In order to fill the gap in the literature, it is aimed that during the interaction, the user sends thermal information about an object and the temperature is felt by the thermistor sensor on the glove, and the temperature is detected from the other hand, where there is no hypoesthesia, and the hand reacts.

It is difficult to understand how patients with hypoesthesia detect extreme temperatures and pain, and therefore it is important to investigate these areas in future studies to improve the quality of life of these patients. The importance of tactile technologies is increasing with the acceleration of the technological and industrial revolution that has emerged with the spread of new generation information and communication technologies such as artificial intelligence, IoT (internet of things) and blockchain technology. [23]. The Internet of Things (IoT), which entered our lives with Industry 4.0, is a collection of devices that can detect environmental situations with various sensors and hardware that communicate between electronic devices and produce data [24]. The effective use of artificial intelligence (AI) and machine learning (ML) techniques in this study is innovative and importantMachine learning, especially deep learning and artificial neural networks, have been used to perform a variety of cognitive tasks. These technologies are used to increase the ability of

thermo-haptic devices to detect temperature and create tactile sensations.

Machine learning is a branch of artificial intelligence developed so that computers can learn from experience and make predictions based on given data. This technology can produce accurate results for new situations by learning from examples and using algorithms. Machine learning is used in various fields today, and in this study it was used to improve the temperature sensing capabilities of thermo-haptic devices. In summary, machine learning is a technology that allows computers to learn and develop like humans.

2. Haptic Feedback

The human touch system, with the skin at its center, has an advanced structure. Considering the location of the sensory input, the sense of touch is grouped as cutaneous and kinesthetic sense. [25]. Tactile sense is our ability to feel objects through our skin. Thanks to this sense, we can perceive the texture, hardness, temperature and other physical properties of objects around us. Tactile sense plays an important role in daily life; for example, when holding a glass or writing. Thermo-haptic devices mimic tactile sensation, allowing users to feel objects in virtual environments or in the real world. Skin sensation focused on in this study; It has different sensory receptors such as mechanoreceptors, thermoreceptors and nociceptors. The skin is full of different types of mechanoreceptors that can convert tactile stimuli into electrical nerve impulses that are transmitted to the brain. These stimuli are defined as information that is encoded as action potentials and then interpreted in the brain. After the stimulus comes into contact with the skin, it is encoded by the relevant mechanoreceptors. It is then transmitted to the synapses through nerve fibers, and the synapses transmit it to the brain for processing and interpretation. As a result of the rich features of the touch system, people use it as a useful and successful communication tool in transferring auditory, visual and thermal information.

3. Materyal and Method

Artificial Intelligence (AI) aims to design machines that can perform many cognitive tasks at a level similar to or higher than human intelligence. It is a very rapidly developing branch of computing [27] , [28] . Machine learning (ML) is a subfield of artificial intelligence that involves computer algorithms [28] It is aimed at the development of artificial neural networks, designed to train and teach a machine to solve a problem or pre-perform complex tasks without special programming and is shown in Fig.1 (Deep Learning, Machine Learning and Artificial intelligence) [29].
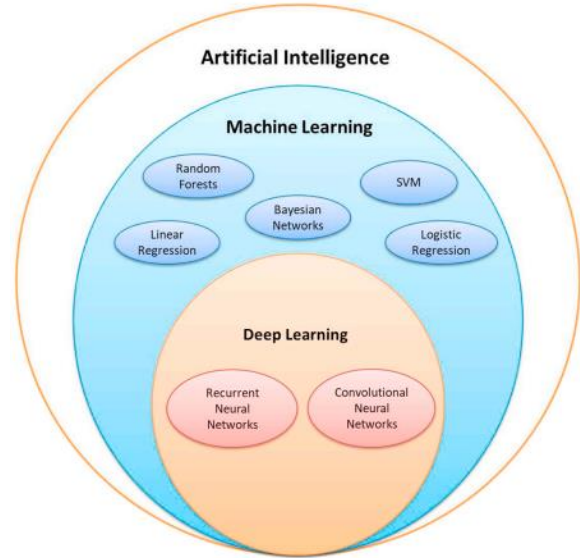
Figure 1. Artificial intelligence, machine learning and deep learning

Artificial intelligence, which has revolutionized many fields, continues its development in medical technology without slowing down. It can cope with different medical problems by developing applications in many fields that often contain large amounts of data [30]. AI applications are developing and shed light on the development of medicine by guiding the course, prevention and personalized treatment of patients in a shorter time [31]. Glove and Edge Machine Learning with Piezoelectric Sensors Fazio et al., a wearable glove enables gesture and object recognition using piezoelectric sensors. This glove classifies detected signals using machine learning algorithms and provides different tactile feedback. This provides an example of how machine learning can be used in wearable haptic devices [32]. Use of Machine Learning in Smart Gloves Ravenscroft et al. , a wearable patch records and decodes non-sound signals using machine learning algorithms. This patch can predict spoken words by detecting throat movements and transmits these predictions to the user with haptic feedback. This work is a concrete example of how machine learning can be integrated in haptic devices [33]. Machine Learning for Haptic Feedback Wang et al. examined new sensing, actuation and control techniques for haptic interaction and teleoperation. This study shows how machine learning can be used in the design of

haptic devices. She studied new sensing, actuation and control techniques in haptic interaction and teleoperation and demonstrated the potential of this field. [34]. However, our current work focuses on improving real-world interactions of individuals with tactile sensory loss by applying these technologies to thermo-haptic feedback devices.

In addition, while existing research in the literature generally focuses on a specific type of sensory loss, this study provides a much broader range of applications using the combination of thermo-haptic sensing and machine learning. In conclusion, the current study provides a new and effective solution for individuals with tactile sensory loss by filling gaps in the literature and extending the findings of previous research. This should be considered a novelty in our field and open new avenues for future research.

3.1. System Design

The temperature sensing system will detect the object temperature and ensure that the measured temperature is felt by the user. The temperature sensing system used in the study has a structure that detects object temperatures and makes them felt to the user. The developed system consists of hardware and software components. Hardware components include ESP32 and ESP8266 microcontroller modules, DS18B20 temperature sensors, Converter, Relay and Peltier components. Hardware components are shown in Figure.2 and Figure.3 (system hardware components).

To implement this idea, we need to use microcontrollers that can support wireless interfaces. Controllers with the required features are ESP32 and ESP8266. In this proposed system, while the materials and methods were being developed, preferences in the element base were given to microcontrollers with internal transmission modules (Wi-Fi, Bluetooth) [35]. Based on this, the components used are; ESP32 and ESP8266 as primary controllers, 2 DS18B20 sensors for object temperature measurement, Peltier to sense the temperature, Converter to provide the high current and low voltage required by the Peltier, Relay to keep the temperature at the desired level, DC12V 3A Power Supply for the operation of the system. The system hardware content consists of two parts: "Data Collection" and "Data Processing".
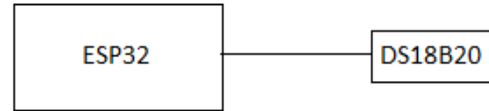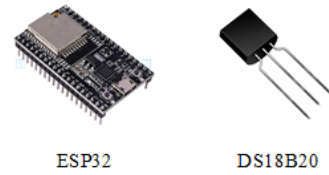
Figure 2. Hardware components and circuit diagram used for the data acquisition and preprocessing system.

Figure 3. Hardware components and circuit diagram used for the data processing system.

3.1.1 Data Collection and Preprocessing

The data acquisition section is the section where the object temperature is taken. The data acquisition circuit is designed using ESP32 module and DS18B20 temperature sensor. System hardware components and circuit diagram are shown in Figure 2.

ESP32 Microcontroller module

In a short time since its launch, the ESP32 microcontroller has been deployed especially in embedded systems and has been fully integrated into different IoT tasks [36]. Being a price-performance product, its circuit structure offers unique use for creating applications in addition to the possibility of connecting peripheral units, IoT modules and other sensors used. ESP32 module is well implemented as a web server, using Wi-Fi and Bluetooth communication to exchange messages in the environment [37].

DS18B20 Temperature Sensor

DS18B20 is a digital body temperature sensor that gives accurate temperature values and does not require ADC [38]. This sensor helps measure temperature between -55°C and +125°C (-67°F and +257°F). Data received from a single cable ranges

from 9-bit to 12-bit. DS18B20 can be controlled by a single pin of the microcontroller after connecting this sensor to GND. Each DS18B20 sensor is equipped with a 64-bit serial code that helps control multiple sensors through a single pin of the microcontroller. In simple terms, it assigns different addresses to all connected sensors and allows us to get the value of those sensors by calling the address. DS18B20 sensor has 3 pins in total, these are;

Pin 1: VCC (+5 V is the pin that should be supplied.)

Pin 2: Data Pin (This is the pin where we will get temperature readings.)

Pin 3: GND (This is the pin where the ground connection is made.) [39]

The most important feature of this sensor and the reason why it is preferred is that it allows reading data, that is, body temperature, directly from the skin and sending it to the microcontroller without the need for a different power source [40].

3.1.2 Data Processing

The data processing section is the section where object temperature is felt. The data processing circuit is designed using ESP8266 module, DS18B20 temperature sensor, Converter, Relay, Peltier and Power Supply. Data processing system hardware components and circuit diagram are shown in Figure 3.

ESP8266 Microcontroller Module

The ESP8266 module provides a unique and standalone Wi-Fi networking solution. It can be used to keep applications or transfer Wi-Fi network tasks from another application module. When the application is launched, it starts directly from the external flash and has the feature of transferring it to the built-in cache to increase the system working level with these applications. It is one of the most available and integrated Wi-Fi chips in this field [41]. This microcontroller produced by Espressif has become the preferred component due to its very low price, very few external components on the module and its Wi-Fi connectivity feature. ESP8266 plays a very important role in reducing the hardware of the system [42].

Peltier

The Peltier component used in the study is defined as a device that is used as a heat source on both sides and has the appearance of a thin plate. In the component, the thermocouple principle applies direct current voltage to two different devices. Depending on the direction of the current, heat is absorbed on one side while heat is produced on the other side, and this is called the Peltier effect. Additionally, heat is absorbed at low temperatures and released at high temperatures. Thus, Peltier acts as a heat pump, sending heat from the low-temperature region to the high-temperature region. Temperature changes the direction and current of the heat pump. Therefore, the Peltier component acts as a semiconductor element that changes the amount of heat pumped to provide free cooling, heating and temperature control. Among the reasons why it is preferred are its small size, lightness, possibility of manufacturing according to desired dimensions, lifespan and reliability. It reacts instantly to temperature changes. In addition, it is preferred because it does not contain any parts that could cause mechanical fatigue or damage [44]. In the study, TEC1 4905 peltier model was used to physically convert the temperature signal received from Data Collection into temperature. The temperature value felt in the transmitter was adjusted with the temperature sensor (DS18B20) mounted on the hot surface. It is a thermoelectric element that can quickly heat or cool according to temperature change. In this study, it was used to observe how quickly Peltier reacts to temperature changes of hot or cold objects touched by the glove.

Relay

The relay, which acts as a source, consists of a console inlet that is fixed to one end and operated laterally, and 3 fixed side electrodes: drain, gate and body. It serves as a contact to pass drainage current. Used to run gates. The body is used for a constant DC bias voltage to reduce the effective tripping threshold voltage of the relay [45]. The relay coil with current passing through it creates a magnetic field and attracts the contacts. Thus, the relay contacts change position. In the study, a relay with contact current of 5A, coil voltage of 5VDc and coil current of 40mA was used. The relay aims to keep the temperature at the desired level. The converter energy was controlled by a relay and used to energize and heat the peltier when the

temperature increase signal from the data collector reached the data processing. For cooling, the relay energy was cut off, leaving the peltier without energy and a natural cooling process was achieved.

Converter

In this study, a DC-DC converter based on the use of LM2596 adjustable voltage step-down power module was preferred to control the output voltage. This module is a converter voltage regulator that can drive a 3A load with high efficiency, excellent linearity and load regulation [46]. The converter was used to provide the high current and low voltage required by Peltier.

Power Source

A 12 Volt 3 Ampere power supply was preferred to provide the energy needed to operate the device. The purpose of choosing this power supply is to convert high voltage to low voltage and alternating current to direct current. It protects the Data Processing system from voltage or current fluctuations.

3.1.3 Software Components

Computer programming has become an essential tool for academic and professional development. Traditional programming languages like C/C++ are much slower in terms of writing code and detecting errors. Computer programming that detects and corrects errors in software codes can cost approximately 20/25% of the software project [47]. Because of this , it is very important to choose an appropriate programming considering the cost of the project. In the software development process, the speed of writing and debugging code is also important. For this purpose, MikroPython was used because this language offers faster results than traditional programming languages. ESP32 and ESP8266 microcontrollers were programmed with MicroPython and Thonny IDE and uPyCraft Integrated Development Environments (IDE) were used. In terms of code writing and error detection speed, Micropython works 5-10 times faster than traditional programming languages [48].

MikroPython is defined as an open source, simpler and more effective implementation of the Python 3 programming language. It is an interpreter optimized to run on small embedded development cards. It has clean and simple syntax to take control of the

hardware with 93% code coverage. REPL stands for read evaluation print cycle. It is a MikroPython interactive command prompt that allows you to connect it to the board just to experiment with the hardware without any editing or installation process. The codes work meaningfully and robustly. This implements logical concepts with fewer lines of code [49]. In this study, uPyCraft Integrated Development Environments (IDE) and Thonny IDE were preferred to program ESP32 and ESP8266 boards with MikroPython. The software component consists of 2 parts: Data Collection Software Part and Data Processing Software Part. System Codes are shown in Figure 4. and Figure 5.

```python
verio.py

1  import network
2  import socket
3  import time
4  import machine, onewire, ds18x20,time

6  ds = ds18x20.DS18X20(onewire.OneWire(machine.Pin(4)))
7  roms = ds.scan()

9  UDP_IP = "192.168.43.17"
10 UDP_PORT = 10086

12 port=10086
13 wlan = network.WLAN(network.STA_IF)
14 wlan.active(True)
15 wlan.connect('X', 'Y')
16 while(wlan.isconnected() == False):
17     time.sleep(1)
18 ip = wlan.ifconfig()[0]
19 print(ip)
20 s=socket.socket(socket.AF_INET, socket.SOCK_DGRAM)
21 s.setsockopt(socket.SOL_SOCKET,socket.SO_REUSEADDR,1)
22 s.bind((ip,port))
23 print('Baglanti bekleniyor')

25 while True:
26     time.sleep(1)
27     try:
28         ds.convert_temp()
29         for rom in roms:
30             tmp=(ds.read_temp(rom))
31         print(tmp)
32         output = str(tmp)
33         message = output
34         sock = socket.socket(socket.AF_INET, #internet
35                         socket.SOCK_DGRAM) #UDP
36         sock.sendto(message.encode(), (UDP_IP, UDP_PORT))
37         sock.close()
38         #print ("Sicaklik Gonderildi")
39     except:
40         print ("Ag Hatasi")
```

Figure 4. Data acquisition software code

Figure 5. Data processing software code

The data collection and processing section of the system are the main parts where temperature readings are taken and temperature values are processed. These sections are supported by software codes that send data to predefined IP addresses and process the received data.

Data Acquisition Software Section

Thonny IDE coding tool makes it easy to create, debug and test code. It offers a number of useful features, including code completion, grammar highlighting, debugging tools, variable explorers, visualization tools, and others [49]. Thonny is a simple and easy-to-use IDE for Python with MicroPython support. In this section, the ESP32 module was programmed with MikroPython using Thonny IDE. Data collection software codes are shown in Figure 4.

Data Processing Software Codes

An integrated development environment called uPyCraft IDE can be preferred to program development devices in the MicroPython programming language. It simplifies firmware development and code debugging [49]. UpyCraft IDE is designed specifically for use with MikroPython. In this section, the ESP8266 module was programmed with MikroPython using UpyCraft Ide. Data Processing software codes are shown in Figure 5.

System Operating Steps

When the system data processing code is run, the IP address "192.168.43.48" seen on the screen is written to the "UDP_IP = " " " section in the data collection code to specify which address the data will be sent to. Operation of the data acquisition system: Temperature readings are taken by connecting to Wi-Fi. The data collection flow chart is shown in Figure 6. The collected data begins to be processed according to the flow chart shown in Figure 7. If the temperature value read from the transmitter is less than the measured temperature value, the system turns off the heater. If the temperature value received is greater than the measured temperature value, the heater is turned on and reaches the temperature value read on the transmitter.
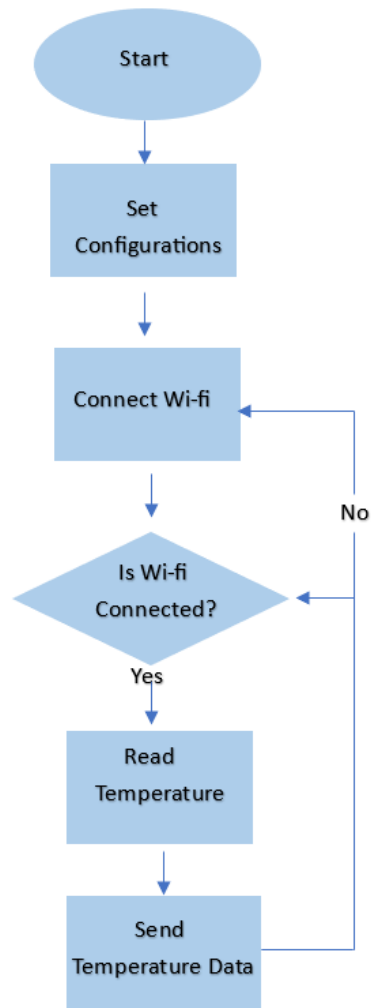
Figure 6. Data collection flow chart
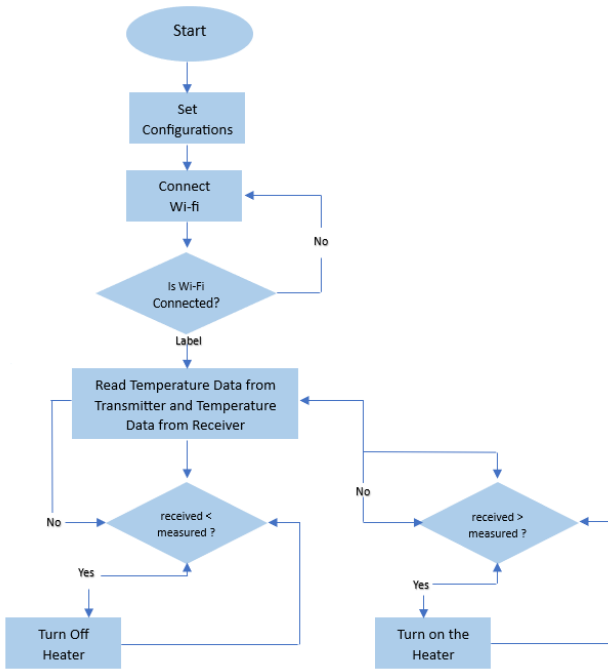
Figure 7. Data processing flow chart

Figure 8. Glove that can measure real-time temperature

Figure 9. Peltier that can react in real time

4. Findings

A glove capable of real-time temperature measurement with a built-in temperature sensor, shown in Figure 8, was used. In the experiments, how temperature changes were detected and how the Peltier element reacted to these changes were examined by using a glove containing a temperature sensor. This involved recording temperature changes when hot and cold objects were touched. An experiment was conducted to measure these temperature changes when the glove touches hot and cold objects and to determine how long and how a thermoelectric element called Peltier responds to these temperature changes. Temperature values were recorded when the glove touched a hot object (e.g. a teapot at 70°C) or a cold object (e.g. chicken taken from the freezer at -14°C). It was recorded how long and how the Peltier reacted, shown in Figure 9, according to the temperature changes of the object touched by the glove.

Soft Pneumatic Actuator Use The soft pneumatic actuator device developed by Sonar, Huang and Paik, provides realistic haptic feedback by simulating different textures and recreating the contour of various shapes in the VR environment. This device was able to simulate physical interaction with 83% accuracy. By using a similar actuator technology in our study, it could further improve tactile perception [50]. Energy Efficiency and Skin Compatibility A study by Lindsay et al, developed a vibrotactile system that increases energy efficiency and consumes less power by adapting to skin impedance. This technology offers new avenues for miniaturization and development of wearable haptic devices. In your

article, by using similar energy-efficient designs, it will be possible to improve the performance and user experience of your wearable devices [51]. Imitation of Mechanoreceptors In the research conducted by Shimada, artificial haptic sensors that imitate the mechanoreceptors of human skin were developed. This work presents methods to predict fast and slow adaptation in haptic sensing, and this approach can be used to increase the sensitivity and accuracy of your wearable devices [52].

Application of Haptic Wearable Devices in Individuals with Hypothesis A review by Shull and Damian, highlights the potential of haptic wearable devices to increase functionality for individuals with sensory disabilities. These devices can be used as sensory replacement, sensory augmentation, and trainer. The use of similar devices to increase tactile perception in individuals with hypoesthesia can improve the quality of life and accelerate rehabilitation processes [4]. Haptic Performance Diagnostic Device for Children with Hypostesis A haptic performance diagnostic device developed by Chikai and Miyake is a hypostasis and/or Designed for children with symptoms of hyperesthesia. This device can be used to identify and treat tactile perception disorders by presenting a variety of tactile sensations (e.g. itching, tremors). Such devices have the potential to demonstrate practical effects and benefits for individuals with hypoesthesia, offering a similar approach to your wearable device in your article [53]. Sensory Substitution and Augmentation A study by Wheeler et al, demonstrated through rotary skin stretching examined the effectiveness of a haptic device that provides proprioceptive feedback. This device reduced aiming errors in blind movements and reduced visual demand in situations where vision was occupied. Using a similar device in your article, it can enhance the sensory perception of individuals with hypoesthesia and assist them with daily activities [54].

4.1 Analyzes

To see how the temperature changes over time, the temperature values are shown in Figure 10. Time Series Plot.
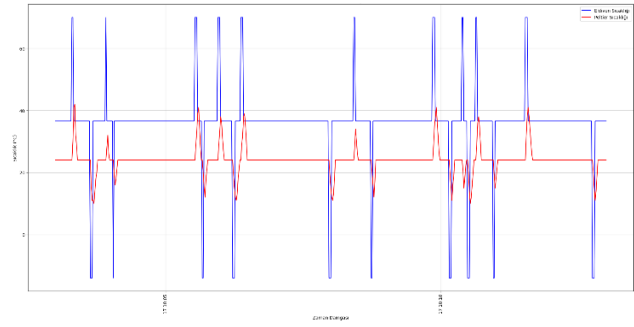
Figure 10. Time series analysis

To determine how quickly Peltier reacts to temperature changes, the time between the moment the glove touches a hot or cold object and the moment Peltier responds to this change is measured and shown in Figure 11. Response Time Analysis.
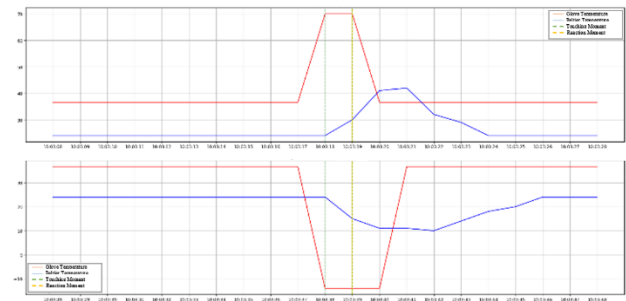
Figure 11. Response time analysis

Histograms were used to show the distributions of glove and Peltier temperature values. Temperature Distributions are shown in Figure 12.
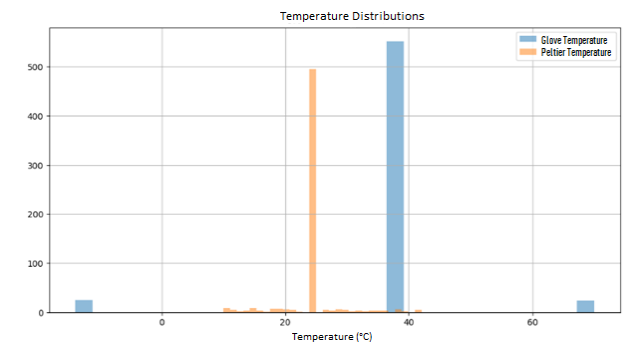
Figure 12. Temperature distributions

Glove Average Temperature	:	35.83°C
Peltier Average Temperature	:	24.00°C
Glove Temperature Standard Deviation	:	12.28
Peltier Temperature Standard Deviation	:	3.94
Glove Min-Max Temperature	:	-14.0°C - 70.0°C
Peltier Min-Max Temperature	:	10°C - 42°C
Glove and Peltier Temperature Correlation	:	0.29
Average Reaction Time	:	2.90 seconds

The relationship between temperature changes of the glove and Peltier's responses was measured. It is shown in Figure 13.
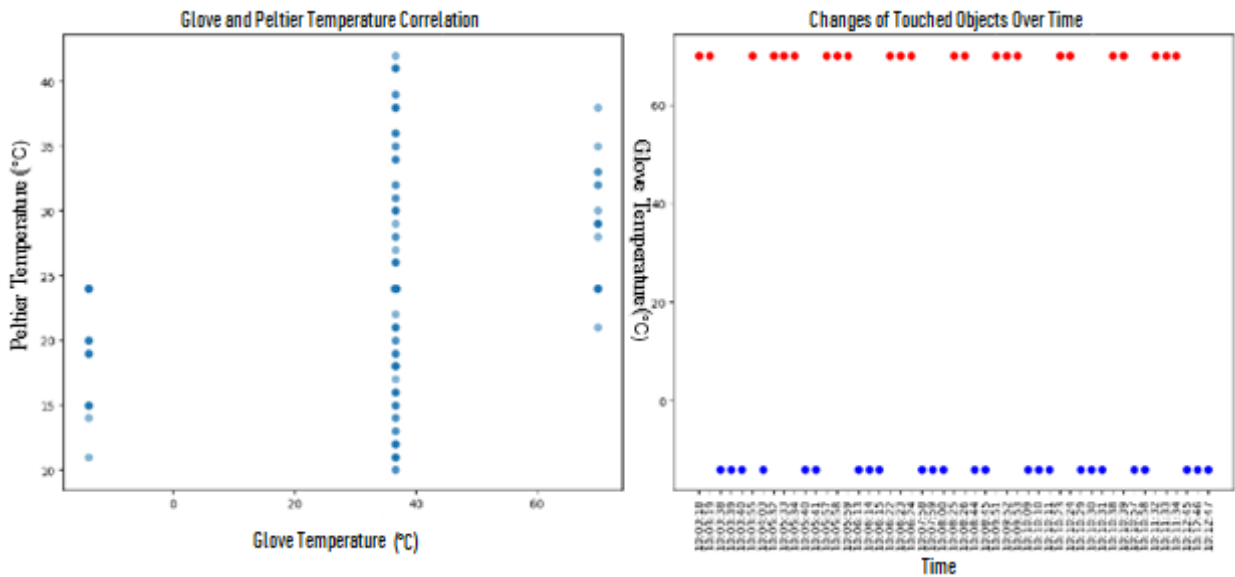
Figure 13. Correlation analysis

The data obtained were analyzed using time series graphs, response time analyzes and histograms of temperature distributions. These analyzes reveal the relationship between temperature changes of the glove and the responses of the Peltier element. In conclusion, a new model that can detect thermal noxious stimuli to accelerate the withdrawal reflex of hypoesthesia patients is proposed.

Flexible and Bi-directional Heating/Cooling Features give originality to the work. For example, Lee et al. , which provides flexible and bi-directional heating/cooling for realistic virtual reality (VR) environments, can make fast and accurate temperature adjustment with 230% stretchability. Your article demonstrates the potential of the device for use in VR applications, highlighting features such as higher flexibility and temperature adjustment sensitivity than similar devices [14]. However, while these studies generally focus on thermo-haptic feedback only on temperature perception, our current study addresses a broader spectrum of haptic sensation.

Applicability to Multiple Body Regions is important. Introduced by Maeda and Kurahashi , TherModule can be worn on multiple body parts such as wrist, arm, ankle, and neck. The device in your article has similar versatility, increasing its applicability for different use scenarios [55]. PneuMod, developed by Zhang and Sra , is a modular haptic device that has a simple, user-friendly design and can be integrated into different parts of the body. In your article, you can point out wide usage areas and easy adaptation by providing a similar user experience [10].

5. Conclusion

The thermo-haptic wearable device developed in this study and its integration with machine learning offer significant improvements for individuals with tactile sensory loss. Our main findings show that this type of device can precisely simulate temperature perception and enrich real-world interactions. In particular, the device's ability to produce real-time responses when interacting with hot and cold objects is a significant advance in the field.

In terms of practical applications, this model can play an important role in rehabilitation and daily living activities for stroke patients and individuals with other sensory limitations. The use of the device can allow these individuals to perceive their environment more effectively and therefore live a more independent life.

Our research expands the existing literature on thermo-haptic sensing and machine learning. This study has established a foundation that will guide future research and encourage the integration of these technologies into broader areas of application. In particular, it offers new opportunities for the use of wearable technologies in medical rehabilitation and virtual reality applications.

In conclusion, a new model has been proposed to detect thermal harmful stimuli using a haptic feedback stimulation system responsible for rapidly initiating withdrawal reflexes in patients with conditions like diabetes and paralysis, who over time experience hypoesthesia. The proposed model, based on the literature review conducted, represents the first endeavor aimed at designing, evaluating, and sensing through other parts of the body a thermal haptic feedback stimulation system. The experiments conducted have successfully demonstrated how the Peltier element perceives hot and cold touches made with the glove and responds to these perceptions. The reaction times and temperature change dynamics of the Peltier have been successfully analyzed through touches performed with the glove. This research has taken an important step towards improving the quality of life of individuals with tactile sensory loss, taking into account both technological innovations and practical applications. The findings of this study provide a strong basis for future technological developments and open new doors for research in this field.

Conflict of Interest Statement

There was no conflict of interest between the authors.

Statement of Research and Publication Ethics

There is no need for ethics committee permission for the edited article and there is no conflict of interest with any person/institution in the article.

References

[1] R. Z. Hill and D. M. Bautista, "Getting in Touch with Mechanical Pain Mechanisms," *Trends Neurosci*, vol. 43, no. 5, pp. 311–325, May 2020, doi: 10.1016/J.TINS.2020.03.004.

[2] E. H. Lee, S. H. Kim, and K. S. Yun, "Three-Axis Pneumatic Haptic Display for the Mechanical and Thermal Stimulation of a Human Finger Pad," *Actuators, vol. 10,* no. 3, p. 60, Mar. 2021, doi: 10.3390/ACT10030060.

[3] X. Lu, X. Yao, W. F. Thompson, and L. Hu, "Movement-induced hypoalgesia: behavioral characteristics and neural mechanisms," *Ann N Y Acad Sci*, vol. 1497, no. 1, pp. 39–56, Aug. 2021, doi: 10.1111/NYAS.14587.

[4] P. B. Shull and D. D. Damian, "Haptic wearables as sensory replacement, sensory augmentation and trainer - A review," *J Neuroeng Rehabil*, vol. 12, no. 1, pp. 1–13, Jul. 2015, doi: 10.1186/S12984-015-0055-Z/FIGURES/7.

[5] S. Biswas and Y. Visell, "Haptic Perception, Mechanics, and Material Technologies for Virtual Reality," *Adv Funct Mater*, vol. 31, no. 39, Sep. 2021, doi: 10.1002/ADFM.202008186.

[6] L. A. Connell, N. B. Lincoln, and K. A. Radford, "Somatosensory impairment after stroke: frequency of different deficits and their recovery," *Clin. Rehabil.,* vol. 22, no. 8, pp. 758–767, Aug. 2008, doi: 10.1177/0269215508090674.

[7] M. A. Choukou, S. Mbabaali, J. B. Hani, and C. Cooke, "Haptic-Enabled Hand Rehabilitation in Stroke Patients: A Scoping Review," *Applied Sciences,* vol. 11, no. 8, p.3712, Apr. 2021, doi: 10.3390/APP11083712.

[8] S. M. Lai, S. Studenski, P. W. Duncan, and S. Perera, "Persisting Consequences of Stroke Measured by the Stroke Impact Scale," *Stroke*, vol. 33, no. 7, pp. 1840–1844, Jul. 2002, doi: 10.1161/01.STR.0000019289.15440.F2.

[9] C. E. Seim, B. Ritter, K. E. Flavin, M. G. Lansberg, and A. M. Okamura, "Affective Ratings of Vibrotactile Signals in Older Adults with and without History of Stroke," *2021 IEEE World Haptics Conference, WHC 2021*, pp. 457–462, Jul. 2021, doi: 10.1109/WHC49131.2021.9517216.

[10] B. Zhang and M. Sra, "PneuMod: A Modular Haptic Device with Localized Pressure and Thermal Feedback," *in Proceedings of the 27th ACM Symposium on Virtual Teality Software and Thechnology*, 2021, doi: 10.1145/3489849.3489857.

[11] J. J. Huaroto, E. Suárez, and E. A. Vela, "Wearable mechatronic devices for upper-limb amputees," *in Control Theory in Biomedical Engineering*, 2020, pp. 205–234, doi: 10.1016/B978-0-12-821350-6.00008-1.

[12] S. Günther, "Somatosensory Interaction: Investigating Mechanoreception, Thermoception, and Proprioception for On-Body Haptic Feedback," 2022, doi: 10.26083/TUPRINTS-00021617.

[13] A. Nasser, K. Zheng, and K. Zhu, "ThermEarhook: Investigating Spatial Thermal Haptic Feedback on the Auricular Skin Area," *ICMI 2021 - Proceedings of the 2021 International Conference on Multimodal Interaction*, pp. 662–672, Oct. 2021, doi: 10.1145/3462244.3479922.

[14] J. Lee *et al.*, "Stretchable Skin-Like Cooling/Heating Device for Reconstruction of Artificial Thermal Sensation in Virtual Reality," *Adv Funct Mater*, vol. 30, no. 29, p. 1909171, Jul. 2020, doi: 10.1002/ADFM.201909171.

[15] A. I. Abdullah, N. Mat Isa, M. A. Al-Mashhadani, O. M. Al-Moayed, and A. K. Kareem, "Design of a Hybrid Haptic Wearable Device for Upper Limb Amputees to Recover the Missing Sensation," *International Journal of Mechanical Engineering*, vol. 7, no. 1, 2022.

[16] J. Lee, D. Kim, H. Sul, & S. H. Ko, "Thermo-haptic materials and devices for wearable virtual and augmented reality," *Advanced Functional Materials*, vol. 31, no.39, p. 2007376, 2021.

[17] C. Chen and S. Qiu, "Influence of temperature profiles on thermal tactile sensation," *Adv. Robot*, vol. 28, no. 1, pp. 53–61, 2014, doi: 10.1080/01691864.2013.854460.

[18] H. N. Ho and L. A. Jones, "Contribution of thermal cues to material discrimination and localization," *Percept Psychophys*, vol. 68, no. 1, pp. 118–128, 2006, doi: 10.3758/BF03193662/METRICS.

[19] R. L. Peiris, W. Peng, Z. Chen, L. Chan, and K. Minamizawa, "ThermoVR: Exploring integrated thermal haptic feedback with head mounted displays," *Conference on Human Factors in Computing Systems - Proceedings*, vol. 2017-May, pp. 5452–5456, May 2017, doi: 10.1145/3025453.3025824.

[20] W. Peng, R. L. Peiris, and K. Minamizawa, "Exploring of simulating passing through feeling on the wrist: Using thermal feedback," *in Adjunct Publication of the 30th Annual ACM Symposium on User Interface Software and Technology*, pp. 187–188, Oct. 2017, doi: 10.1145/3131785.3131819.

[21] S. Li, X. Tong, J. Huang, X. Wu, W. Yang, and Z. Pan, "A Thermal and Vibrational Feedback Glove Based on the Tactile Characteristics of Human Hand Skin," *IEEE Access*, vol. 8, pp. 226671-226684, 2020, doi: 10.1109/ACCESS.2020.3045614.

[22] Y. Celik, J. Moore, M. Durgun, S. Stuart, W. L. Woo, & A. Godfrey, "Gait on the edge: A proposed wearable for continuous real-time monitoring beyond the laboratory." *IEEE Sensors J.,* vol. 23, no. 23, pp. 29656-29666, 2023, doi: 10.1109/JSEN.2023.3328054

[23] C. Zhang and Y. Lu, "Study on artificial intelligence: The state of the art and future prospects," *J Ind Inf Integr*, vol. 23, p. 100224, Sep. 2021, doi: 10.1016/J.JII.2021.100224.

[24] M. Kışlakçı and M. Durgun, "Anomaly Diagnosis Using Autoencoder in Edge Computing Systems", *ISVOS,* vol. 6, no. 1, pp. 41–50, 2022, doi: 10.47897/bilmes.1132562.

[25] R. S. Dahiya and M. Valle, "Robotic tactile sensing: Technologies and system," *Robotic Tactile Sensing: Technologies and System*, vol. 9789400705791, pp. 1–245, Jan. 2014, doi: 10.1007/978-94-007-0579-1/COVER.

[26] O. Ozioko and R. Dahiya, "Smart Tactile Gloves for Haptic Interaction, Communication, and Rehabilitation," *Advanced Intelligent Systems*, vol. 4, no. 2, p. 2100091, Feb. 2022, doi: 10.1002/AISY.202100091.

[27] L. M. Davidovic, D. Laketic, J. Cumic, E. Jordanova, and I. Pantic, "Application of artificial intelligence for detection of chemico-biological interactions associated with oxidative stress and DNA damage," *Chem Biol Interact*, vol. 345, p. 109533, Aug. 2021, doi: 10.1016/J.CBI.2021.109533.

[28] N. Maffulli *et al.*, "Artificial intelligence and machine learning in orthopedic surgery: a systematic review protocol," *J Orthop Surg Res*, vol. 15, no. 1, Dec. 2020, doi: 10.1186/S13018-020-02002-Z.

[29] J. Wang and X. Hu, "Convolutional Neural Networks With Gated Recurrent Connections," *IEEE Trans Pattern Anal Mach Intell*, vol. 44, no. 7, pp. 3421–3435, Jul. 2022, doi: 10.1109/TPAMI.2021.3054614.

[30] T. M. Maddox, J. S. Rumsfeld, and P. R. O. Payne, "Questions for Artificial Intelligence in Health Care," *JAMA*, vol. 321, no. 1, pp. 31–32, Jan. 2019, doi: 10.1001/JAMA.2018.18932.

[31] G. M. Minopoulos, V. A. Memos, K. D. Stergiou, C. L. Stergiou, and K. E. Psannis, "A Medical Image Visualization Technique Assisted with AI-Based Haptic Feedback for Robotic Surgery and Healthcare," *Applied Sciences,* vol. 13, no. 6, p. 3592, Mar. 2023, doi: 10.3390/APP13063592.

[32] R. De Fazio, V. M. Mastronardi, M. Petruzzi, M. De Vittorio, and P. Visconti, "Human–Machine Interaction through Advanced Haptic Sensors: A Piezoelectric Sensory Glove with Edge Machine Learning for Gesture and Object Recognition," *Future Internet 2023,* vol. 15, no. 1, p. 14, Dec. 2022, doi: 10.3390/FI15010014.

[33] D. Ravenscroft, I. Prattis, T. Kandukuri, Y. A. Samad, and L. G. Occhipinti, "A Wearable Graphene Strain Gauge Sensor with Haptic Feedback for Silent Communications," *FLEPS 2021 - IEEE International Conference on Flexible and Printable Sensors and Systems*, Jun. 2021, doi: 10.1109/FLEPS51544.2021.9469728.

[34] D. Wang, K. Ohnishi, and W. Xu, "Novel emerging sensing, actuation, and control techniques for haptic interaction and teleoperation," *IEEE Transactions on Industrial Electronics*, vol. 67, no. 1, pp. 624–626, Jan. 2020, doi: 10.1109/TIE.2019.2927784.

[35] Д. Л. Овчинников, А. Ю. Тычков, Д. С. Чернышов, А. Д. Сашина, and П. Государственный Университет, "РАЗРАБОТКА ПРОТОТИПА 'УМНОЙ' ОДЕЖДЫ С ДИСТАНЦИОННЫМ КОНТРОЛЕМ И УПРАВЛЕНИЕМ ТЕМПЕРАТУРОЙ ПОСРЕДСТВОМ МИКРОЭЛЕКТРОННОГО ИСПОЛНЕНИЯ," *Измерение. Мониторинг. Управление. Контроль*, vol. 4, no.42, 2022, doi: 10.21685/2307-5538-2022-4-13.

[36] A. Puliafito, A. Celesti, M. Villari, and M. Fazio, "Towards the integration between IoT and cloud computing: An approach for the secure self-configuration of embedded devices," *Int J Distrib Sens Netw*, vol. 2015, 2015, doi: 10.1155/2015/286860.

[37] P. F. Folty´nek, M. Babiuch, and P. S. ˇ Uránek, "Measurement and data processing from Internet of Things modules by dual-core application using ESP32 board," *Measurement and Control*, vol. 52, no. 8, pp. 970–984, 2019, doi: 10.1177/0020294019857748.

[38] J. Kaur, N. Batra, and S. Goyal, "SmartEmoDetect: An Internet of Things Based Emotion Monitoring Wearable Technology for Drivers Lightweight Operating System Framework for IoT Devices View project Integrated platform for innovation and smart product designs View project SmartEmoDetect: An IoT Based Emotion Monitoring Wearable Technology for Drivers," *Article in Journal of Computational and Theoretical Nanoscience*, vol. 16, pp. 1–5, 2019, doi: 10.1166/jctn.2019.8279.

[39] M. Fezari and A. Al Dahoud, "Exploring One-wire Temperature sensor 'DS18B20' with Microcontrollers", Accessed: Jun. 02, 2023. [Online]. Available: https://www.researchgate.net/publication/330854061

[40] H. K. Naji, N. Goga, A. J. M. Karkar, H. A. Ali, M. Falahi, and A. T. H. Al-Rawi, "Design and Development of a Bracelet to Monitor Vital signs of COVID-19 Patients," *IICETA 2022 - 5th International Conference on Engineering Technology and its Applications*, pp. 109–114, 2022, doi: 10.1109/IICETA54559.2022.9888696.

[41] S. Miah, G. M. Jahedul Islam, S. K. Das, S. Islam, M. Islam, and K. K. Islam, "Internet of Things (IoT) based automatic electrical energy meter billing system," vol. 14, no. 4, pp. 39–50, doi: 10.9790/2834-1404013950.

[42] H. Hanan, A. A. N. Gunawan, and M. Sumadiyasa, "Water level detection system based on ultrasonic sensors HC-SR04 and ESP8266-12 modules with telegram and buzzer communication media," *Instrum. mes. métrol.*, vol. 18, no. 3, pp. 305–309, 2019, doi: 10.18280/i2m.180311.

[43] K. N. Swaroop, K. Chandu, R. Gorrepotu, and S. Deb, "A health monitoring system for vital signs using IoT," *Internet of Things*, vol. 5, pp. 116–129, Mar. 2019, doi: 10.1016/J.IOT.2019.01.004.

[44] E.-B. Park, S. J. M. Yazdi, and J.-H. Lee, "Development of wearable temperature sensor based on Peltier thermoelectric device to change human body temperature," *Sens. Mater.*, vol. 32, no. 9, p. 2959, 2020, doi: 10.18494/SAM.2020.2741.

[45] R. Li and H. Fariborzi, "Design and Demonstration of MEM Relay-Based Arithmetic and Sequential Circuit Blocks," *IEEE Trans Electron Devices*, vol. 68, no. 12, pp. 6415–6421, Dec. 2021, doi: 10.1109/TED.2021.3118663

[46] M. O. Alsumady, Y. K. Alturk, A. Dagamseh, and M. Tantawi, "Controlling of DC-DC buck converters using microcontrollers," *Int. J. Circuits Syst. Signal Process.*, vol. 15, pp. 197–202, 202, doi: 10.46300/9106.2021.15.22.

[47] C. Du, "Empirical study on college students' debugging abilities in computer programming," in *2009 First International Conference on Information Science and Engineering*, 2009, doi: 10.1109/ICISE.2009.550.

[48] R. K. Kodali and K. S. Mahesh, "Low cost ambient monitoring using ESP8266," in *2016 2nd International Conference on Contemporary Computing and Informatics (IC3I)*, 2016, doi: 10.1109/IC3I.2016.7918788.

[49] M. S. Gowri R, R. R. Gowsika S, and M. D. Assistant Professor, "Prepaid Energy Meter with Automatic Billing and Theft Detection," *International Journal of New Innovations in Engineering and Technology*, vol. 22, p. 619, 2023.

[50] H. A. Sonar, J.-L. Huang, and J. Paik, "Soft Touch using Soft Pneumatic Actuator–Skin as a Wearable Haptic Feedback Device," *Advanced Intelligent Systems*, vol. 3, no. 3, Mar. 2021, doi: 10.1002/AISY.202000168.

[51] J. I. C. Lindsay, I. Jiang, E. Larson, R. Adams, S. N. Patel, and B. Hannaford, "Good vibrations: An evaluation of vibrotactile impedance matching for low power wearable applications," in *Proceedings of the 26th annual ACM symposium on User interface software and technology*, 2013, doi: 10.1145/2501988.2502051.

[52] K. Shimada, "Estimation of Fast and Slow Adaptions in the Tactile Sensation of Mechanoreceptors Mimicked by Hybrid Fluid (HF) Rubber with Equivalent Electric Circuits and Properties," *Sensors*, vol. 23, no. 3, p. 1327, Jan. 2023, doi: 10.3390/S23031327.

[53] M. Chikai and H. Miyake, "Development of a Haptic Performance Diagnostics Device for Children with Developmental Disorder," *Iryou kikigaku (The Japanese journal of medical instrumentation)*, vol. 84, no. 1, pp. 18–22, 2014, doi: 10.4286/JJMI.84.18.

[54] J. Wheeler, K. Bark, J. Savall, and M. Cutkosky, "Investigation of rotational skin stretch for proprioceptive feedback with application to myoelectric systems," *IEEE Transactions on Neural Systems and Rehabilitation Engineering*, vol. 18, no. 1, pp. 58–66, Feb. 2010, doi: 10.1109/TNSRE.2009.2039602.

[55] T. Maeda and T. Kurahashi, "TherModule: Wearable and modular thermal feedback system based on a wireless platform," in *Proceedings of the 10th Augmented Human International Conference 2019*, 2019., doi: 10.1145/3311823.3311826.

Prebiotic Chemistry and Sepiolite: A Density Functional Theory Approach

Deniz KARATAŞ[1*]

[11]*Bioengineering Department, Manisa Celal Bayar University, Yunusemre, Manisa, 45140, Turkey*

(ORCID: 0000-0002-8176-4883)

Abstract

Sepiolite, a natural clay mineral, offers a large surface area due to its fibrous structure, allowing it to exhibit adsorption properties. In this study, the molecular interactions of sepiolite, a biocompatible clay mineral known as a biomaterial, and purine and pyrimidine molecules forming the bases of deoxyribonucleic acid (DNA) and ribonucleic acid (RNA) molecules were modeled by Density Functional Theory. In addition to geometry optimization, calculations of interaction energy, bond critical points, and electrostatic potential revealed that essential molecules for our source of life interact with basal surface of the clay. For example, the best interaction energies between bases/sepiolite were found to be -127.47 kJ/mol for guanine and -121.35 kJ/mol for cytosine, respectively. Looking at the modeling results, one of the most important factors affecting the interaction energies is hydrogen bonding. To reveal this, bond critical point analysis was performed, and it was computed that a large amount of intermolecular interaction energies came from hydrogen bonds. For example, it was calculated that approximately 70% of the total energy in the guanine/TOT (two tetrahedra and one octahedron) model comes from hydrogen bonds. Furthermore, this value for the cytosine/TOT model was found to be around 72%. The most effective indices in these two models are 145 and 135, with the H-bond energies recorded as -22.41 and -31.41 kJ/mol, respectively. Considering all analyses, it can be concluded that basal surfaces of sepiolite serve as suitable hosts for nitrogenous bases, which are the basic components of life. The aim of this study is to show that sepiolite offers an important surface feature to protect and stabilize DNA and RNA nucleic acid bases, which are necessary for the existence of living organisms, and to reveal the existence of a robust adsorption interaction between sepiolite and bases, thanks to the surface and chemical properties of sepiolite.

1. Introduction

Sepiolite is a clay mineral belonging to the serpentinite family, which is abundant and produced in the Eskişehir region of Turkey. There are two different types of minerals belonging to the clay mineral family: serpentinite and smectite. The main difference between serpentinite and smectite minerals is that serpentinites are fibrous and contain both crystalline water and zeolitic water. Another important feature of serpentinites is that they consist of channels and tunnels resulting from their fibrous structure. This makes them suitable surface areas for molecules of certain sizes, such as drugs, DNA, and RNA bases. Considering these unique structural and textural features, sepiolite mineral consists of magnesium hydrosilicate, and its general formula is $Mg_4Si_6O_{15}(OH)_2 \cdot 6(H_2O)$. When examining the literature, it is evident that sepiolite is extensively utilized in the healthcare sector. For instance, Hermosin et al. demonstrated the potential utility of sepiolite as a pharmaceutical excipient for drugs

susceptible to oxidative degradation through hydrogen bonds (H-bond) [1, 2]. In another study, it was revealed that drug molecules can be adsorbed onto sepiolite due to the presence of silanol groups, and the clay is instrumental in the controlled release of the drug [3, 4]. It was generalized in another study that sepiolite is also a good drug carrier in the presence of biocompatible and biodegradable polymers [5]. In addition, it was emphasized that biohybrid nanomaterials containing sonicated sepiolite in the presence of various polyvalent cations could serve as an alternative carrier for DNA transfer [6]. Smirnov et al., demonstrated, that sepiolite can be a DNA carrier mediator through their experimental study and stated that sepiolite can facilitate the delivery of bound molecules such as DNA to cells, especially through clathrin-mediated endocytosis and macropinocytosis [7]. Due to the physical and mechanical properties of sepiolite, it has been proven to interact by breaking the double strands of DNA in incubated *Escherichia coli* bacteria. As a result, it has been demonstrated that the mutagenic effect of sepiolite fibers increases antibiotic resistance when combined with antibiotics. This increase stems from the friction generated by the peristalsis of farm animals' intestines, in addition to horizontal gene transfer. [8]. The aforementioned experimental studies also indicate that investigations into the interaction between sepiolite and DNA have been very popular in recent years. However, the important point is where the bases of the DNA really adsorb to the clay, this is a very curious situation. Computational studies on DNA-RNA/clay, especially with layered clays apart from sepiolite, have been discussed in recent years. For example, Robinson et al. and Mignon et al. explained in two different studies that due to the H-bond interactions nucleobases can be adsorbed on the surfaces of the clay minerals at the atomistic level with Density Functional Theory (DFT) [9, 10]. Since the representative clay surfaces selected in this study were chosen quite small, and thus the atoms were frozen, which may have changed the amount of adsorption and perhaps the type of interaction. Mignon et al. studied the adsorption of all nucleobases on sodium montmorillonite clay using periodic plane wave DFT [11]. The effect of atomic positions of bases in different configurations on adsorption was investigated in the presence of sodium cations [11]. In the presence of sodium cations, it was revealed that the contribution of intermolecular interaction driving force can vary for different configurations. For instance, while the dispersion contribution was higher for cation-pi interactions, the electrostatic interaction contribution was greater for cation-pi/displaced orientations [11, 12]. In another study by the same team, two different montmorillonite models, substituted in tetrahedral and octahedral sheets, were used to investigate the adsorption type and shape of DNA bases onto the external surfaces of clay [13]. In their DFT study, it was revealed that bases can adsorb parallel or perpendicular to the surfaces and octahedral substitution contributes to 10 kcal/mol more interaction than tetrahedral [13]. Michalkova et al. investigated the adsorption of uracil and thymine bases in the presence of sodium on frozen hydrated and non-hydrated tetrahedral and octahedral kaolin sheets [14]. The most important shortcoming of this study is that all clay atoms were frozen. In this non-periodic study, freezing of atoms prevented possible repulsive forces. If the atoms were unfrozen, distortions would be observed in representative clay models, and this would change the amount of the intermolecular interaction. Bhatt et al. conducted a study regarding cytosine adsorption onto montmorillonite in the absence and presence of the metal ions and concluded that adsorption can be enhanced due to the especially transition metals [15]. Pedreira-Segade et al. carried out experimental and theoretical studies with layered clays such as nontronite, lizardite, montmorillonite, chlorite and profilite under different pH, temperature, and salinity conditions. In these studies, adsorption of nucleotides on the lateral, basal and interlayer surfaces of the clay in different salt ratios and solvent compositions has been demonstrated. It has been reported that these mechanisms arise from physicochemical reactions and manifest in the form of ligand exchange and hydrogen bonds [16-18].

It is obvious that in all of these studies, adsorption of prebiotic building blocks on clay surfaces once again emphasizes the emergence of life. To support this, the adsorption of building blocks with sepiolite, a fibrous clay that has been little studied, was demonstrated in this study. The literature in question identifies the formation of hydrogen bonds as one of the most significant adsorption mechanisms. For the first time, an analysis of atoms in molecules (AIM) topology with electronic wave function was conducted to elucidate the contribution of hydrogen bonding to the binding energy.

2. Computational Setup

The process flow diagram of all DFT stages of this study, which was theoretically designed with the basic theories of computational chemistry, is presented in Figure 1.
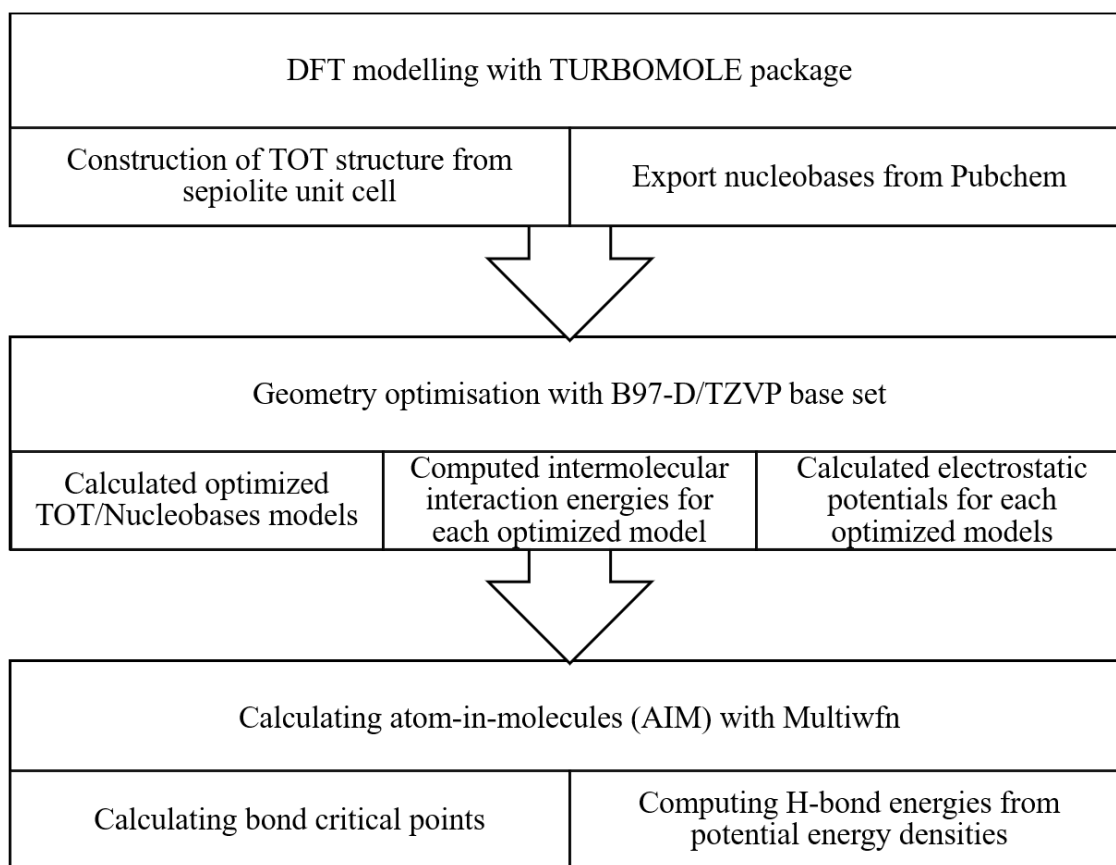
Figure 1. Process flow chart for each steps run

As mentioned in Figure 1, the representation of sepiolite clay was constructed using a published sepiolite crystal structure [19]. All dangling bonds in the model were saturated with hydrogen, as used in our previous studies [20-22]. The ball-and-stick representation of the structure consisting of 2 tetrahedra and 1 octahedron (TOT) was obtained from the sepiolite unit cell [19].

Input files were created by arbitrarily and randomly placing nitrogenous base molecules separately on the basal surface of the structure. After the creation of the input files, modeling was performed with the TURBOMOLE V6.1 package program [23]. Geometry optimization of each model was computed by using the B97-D functional to consider the dispersion contribution with the TZVP basis set. Binding energies of the optimized structures obtained as a result of geometry optimization were calculated with Equation 1 using Counter-Poise (CP) correction [24, 25]. Binding energies were corrected against the basis set superposition error (BSSE) with CP method. The negative interaction energies were obtained using the following formula:

$$E_{BE}^{CP} = E_{TOT+bases}^{(TOT+bases)} - (E_{TOT}^{(TOT+bases)} + E_{bases}^{(TOT+bases)}) \qquad (1)$$

where E_{BE}^{CP} is the CP corrected binding energy, $E_{TOT+bases}^{(TOT+bases)}$, $E_{TOT}^{(TOT+bases)}$ and $E_{bases}^{(TOT+bases)}$ the total energies of the TOT+bases, TOT, and the bases of each molecules were calculated using the basis set of the complete system (TOT+bases).

After the geometry optimization, the electrostatic potentials of the optimized models were calculated. Electrostatic potentials (EPs) were visualized using TmoleX, a graphical user interface for Turbomole program [26].

In the final stage, topological analyses were also conducted to determine the types of interaction bonds and the energies of the hydrogen bonds. One of the topology bond critical points (BCP) was calculated using the Multiwfn program [27]. Multiwfn gives very fast and successful results in the calculation of cage and ring critical points in addition to the BCPs belonging to complex models; it has been used quite frequently in recent years [28, 29]. Therefore, detailed information about atoms in molecules (AIM) and the electron density topology can be obtained. In the case where two eigenvalues of the Hessian matrix of the function are negative, a BCP is formed. Electron density at the BCP can be reliably used to predict hydrogen bond binding energies [30]. H-bond [R-H----O (R=C, N, O)] energies, the relationship between bond energy E_{HB} and potential

energy density $V(r)$ at the corresponding BCP (3,-1) can be approximately described as [31, 32]:

$$E_{HB} = V(r_{BCP})/2 \qquad (2)$$

where, E_{HB} is the H-bond energy and $V(r_{BCP})$ is the potential energy density at a certain BCP.

3. Results and Discussion

Electrostatic potential (EP) maps are highly productive in obtaining information about adsorption on mineral surfaces and revealing the regions of H-bond formation. Therefore, to understand the interactions of molecules with each other and therefore to follow the adsorption process, the electrostatic potentials of each structure used in the modeling were calculated with B97-D/TZVP base set and exhibited in Figure 2.

Optimized TOT 3D structure	EPs for optimized TOT structure
ADENINE	GUANINE
THYMINE	CYTOSINE
URACIL	
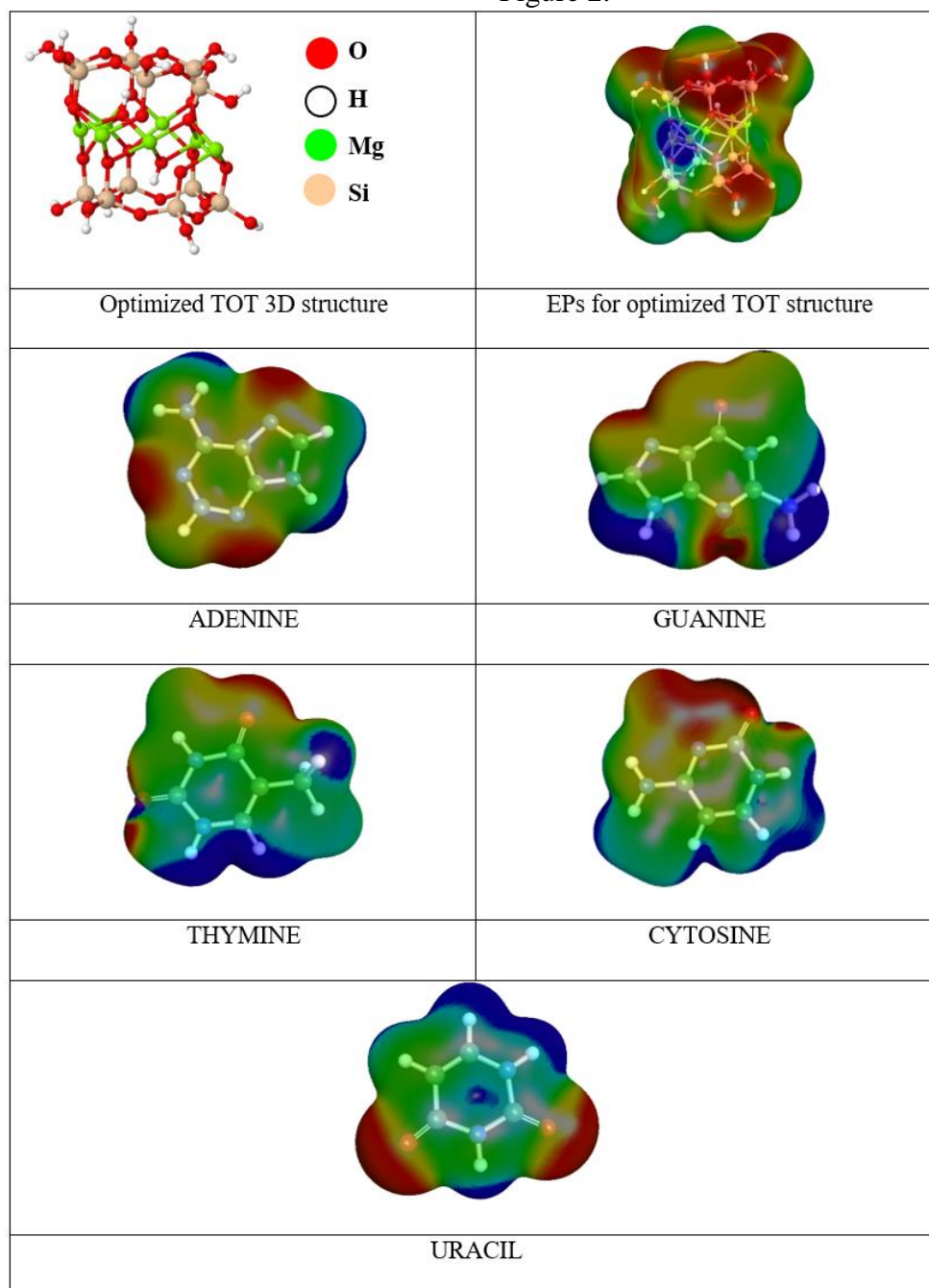
Figure 2. Maps of electrostatic potential of each structure. EPs are mapped onto electron density isosurfaces (0.007 e/au^3) at the B97-D/TZVP level

From the electrostatic potentials of the TOT model in Figure 2, it is seen that the electron accumulation increases in the groups belonging to the silanol groups (Si–O–H). In nitrogenous bases, on the other hand, it is understood that the regions with oxygen atoms become more negative due to the formation of red tones around them. The EP maps depicting the interactions of these adsorbate and adsorbent molecules are shown in Figure 3.
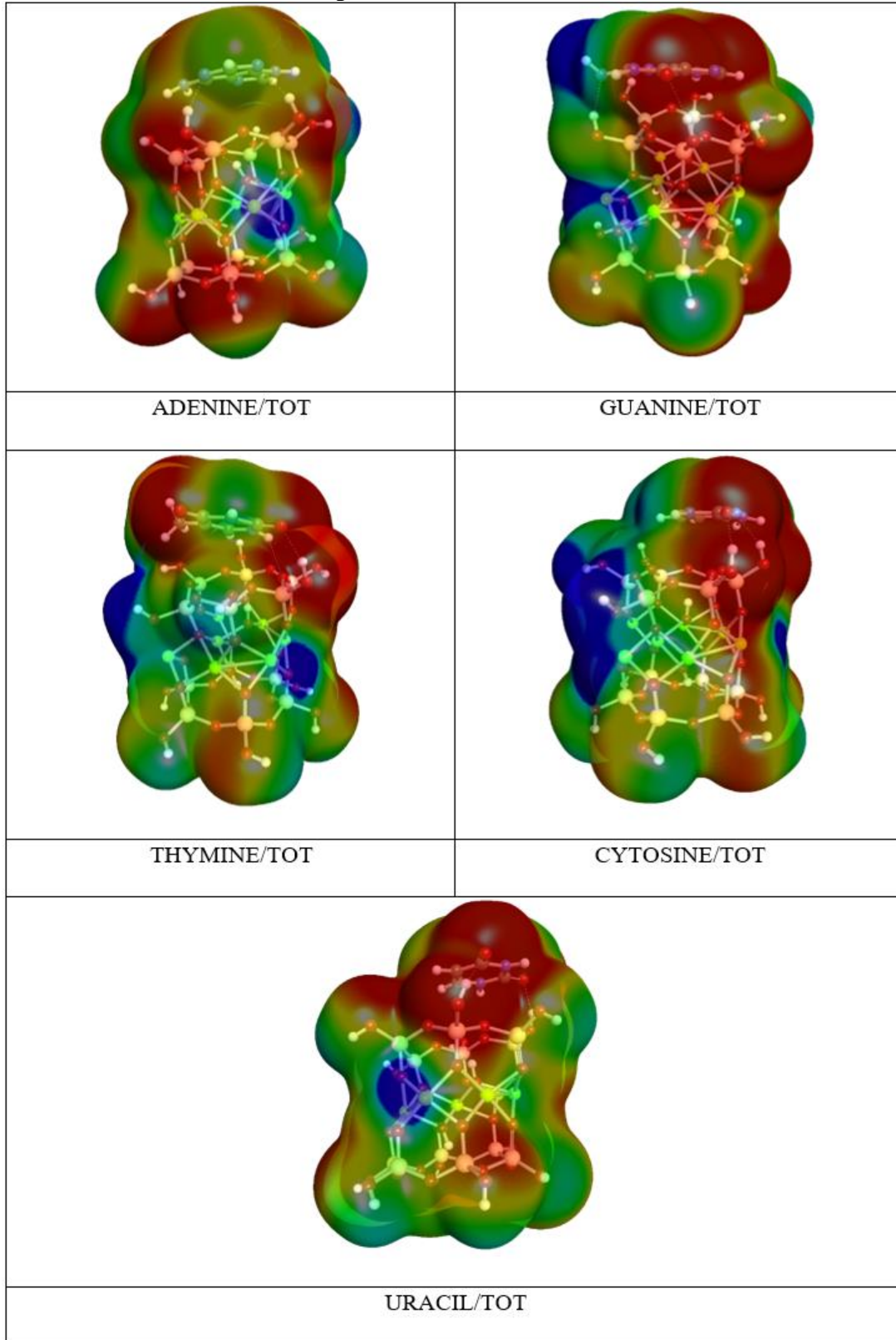
Figure 3. Maps of electrostatic potential for each model

In Figure 3, it is observed that the interaction is concentrated in the tetrahedral region where the bases are located on the electrostatic surfaces visualized with Tmolex [26]. On the other hand, in the octahedral region, it is understood that the interaction decreases with the increase in blue color tones. The reason for this is that the relatively more negative oxygen atoms interact electrostatically with the neighboring cationic atoms [14, 33, 34]. The most important formations affecting adsorption is the H-bonds between oxygen, nitrogen and hydrogen atoms with partial negative and positive charges. These H-bond distances range from 2-3 Å. In terms of the formation sites of H-bond interactions, it is seen that guanine and cytosine are almost parallel and the others are placed on the surfaces as slightly tilted. These formations cause charge distribution and polarization in electrostatic potentials. The resulting H-bonds and charge polarization affect the amount of adsorption on the basal surface of the sepiolite as well as the formation of adsorption, and therefore, calculated energies as CP and non-CP for intermolecular interactions are shown in Table 1.

Table 1. CP and non-CP energies for nucleobases/TOT models in kJ/mol

NUCLEOBASES	MODEL	CP	non-CP
PURINES	ADENINE/TOT	-95.59	-107.86
	GUANINE/TOT	-127.47	-142.46
PYRIMIDINES	THYMINE/TOT	-81.79	-90.01
	CYTOSINE/TOT	-121.35	-133.20
	URACIL/TOT	-87.99	-97.57

The first thing that stands out from the results in Table 1 is that guanine interacts with TOT more than other purines and pyrimidines, which structurally contain very few atoms. As a matter of fact, while the interaction energy of guanine was -127.47 kJ/mol, the energy of the nearest base was calculated as -121.35 kJ/mol. Similarly, Mignon et al. reported that guanine and cytosine were more adsorbed onto the basal surfaces of montmorillonite [11]. On the other hand, the second striking result is that the interaction energy of adenine, structurally most similar to guanine, is very high and is calculated as -95.59 kJ/mol. The last interesting result is that uracil, the smallest and relatively planar structure, has lower in energy than thymine. Using the final coordinates obtained at the end of the geometry optimization, Bond Critical Points (BCPs) were calculated to reveal the H-bond contribution of interactions between molecules, and the images of the obtained points are shown in Figure 4.
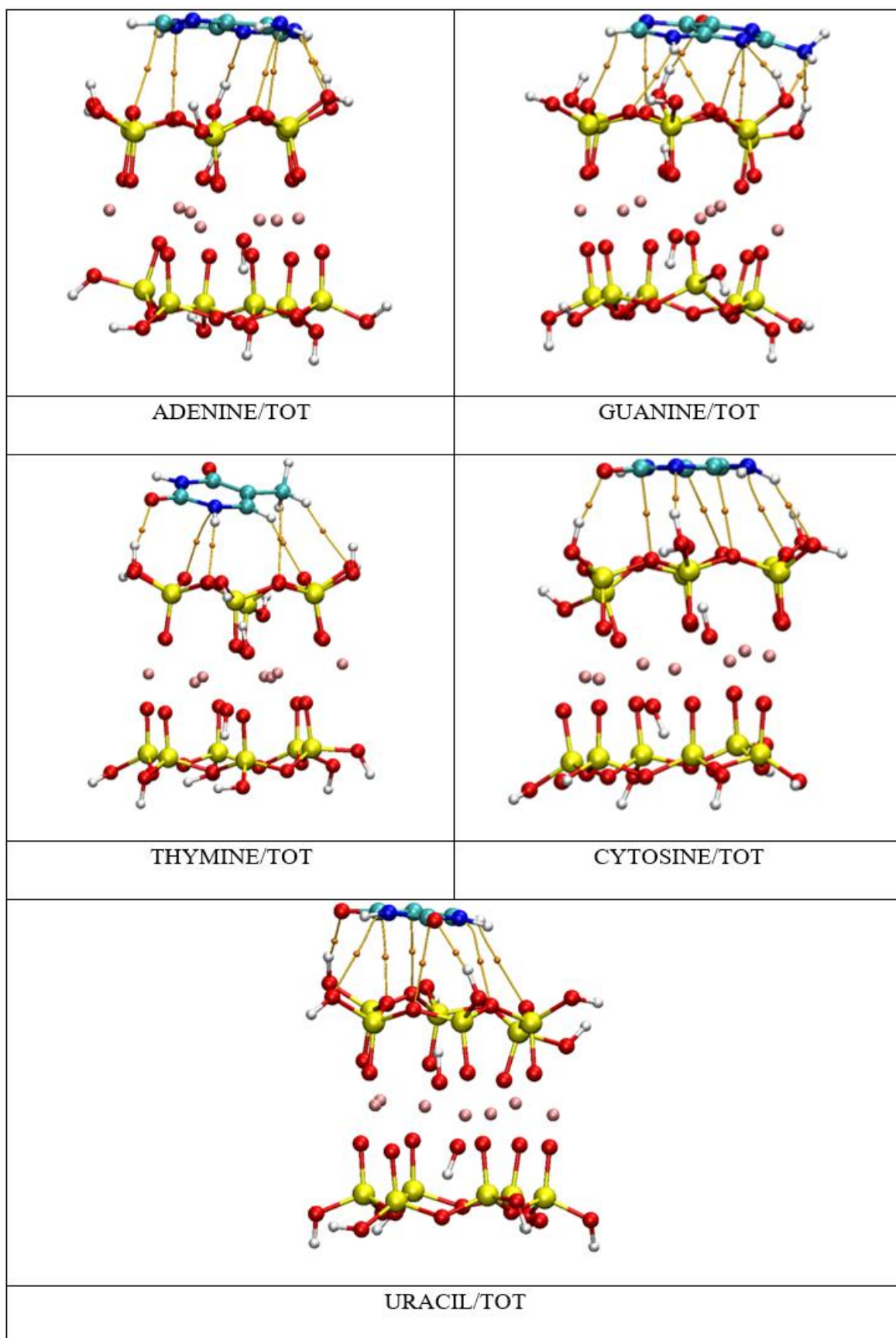
Figure 4. BCPs for nucleobases/TOT models. Yellow, red, blue, white, tile bergere, and aqua green colors are silicon (Si), oxygen (O), nitrogen (N), hydrogen (H), magnesium (Mg), and carbon (C), respectively

In Figure 4, BCPs of nucleobases/TOT models visualized using the VMD program are shown as yellow knotted threads. It is also observed that there is a tight relationship between the partially positive charged cation (–H$^+$) and the partial negative charged (–O$^-$ and –N$^-$) anions on the sepiolite basal surfaces. The number of BCPs for adenine and guanine is counted as 7 and 10, respectively, while it is 6, 7, and 8 for thymine, cytosine, and uracil,

respectively. Compared to the results in Table 1, guanine, which exhibits the most binding, also stands out with the highest number of BCPs. Another striking result is the presence of 8 BCPs in the thymine/TOT model. It is understood that the H-bond contribution may be high in both models. To reveal this, the binding energies of each BCP index were calculated and presented in Table 2.

Table 2. Indices of BCPs and their H-bonds energies computed by potential energy densities

MODEL	indexes of BCPs	V(r)	BE, kJ/mol	MODEL	indexes of BCPs	V(r)	BE, kJ/mol
ADENINE/TOT	116	-1.65E-03	-2.16	THYMINE / TOT	102	-3.29E-03	-4.32
	137	-4.01E-03	-5.26		104	-2.31E-03	-3.04
	193	-1.12E-02	-14.72		162	-4.76E-03	-6.26
	217	-6.31E-03	-8.28		183	-5.83E-03	-7.65
	225	-3.77E-03	-4.95		218	-7.79E-03	-10.23
	255	-3.90E-03	-5.13		233	-2.29E-02	-30.03
	256	-2.16E-02	-28.34	CYTOSINE / TOT	128	-1.73E-03	-2.27
GUANINE/TOT	107	-4.37E-03	-5.74		135	-2.39E-02	-31.41
	111	-6.33E-03	-8.31		158	-5.52E-03	-7.24
	129	-4.21E-03	-5.53		189	-1.72E-03	-2.26
	141	-2.28E-03	-3.00		206	-2.31E-02	-30.38
	143	-6.83E-03	-8.97		209	-6.19E-03	-8.12
	145	-1.71E-02	-22.41		246	-4.07E-03	-5.34
	216	-4.91E-03	-6.45	URACIL / TOT	110	-9.31E-04	-1.22
	217	-4.68E-03	-6.14		137	-5.73E-03	-7.52
	233	-4.13E-03	-5.43		163	-3.84E-03	-5.04
	263	-1.35E-02	-17.73		178	-2.53E-03	-3.33
					199	-4.68E-03	-6.14
					208	-5.31E-03	-6.97
					238	-1.52E-02	-20.00
					246	-2.41E-03	-3.17

The index with the highest H-bond energy (-31.41 kJ/mol) in Table 2 belongs to the cytosine/TOT model, numbered 135. This is followed by the one with index number 206, which has -30.38 kJ/mol in the same model. The one that is slightly above these is the one with the index number 233 in the thymine/TOT model with an energy of -30.03 kJ/mol, while the other one belongs to the Adenine/TOT model with the index number 256, which is

approximately 2 kJ/mol larger. On the other hand, in the Guanine/TOT model, the energies of 2 H-bonds were recorded as -22.41 and -17.73 kJ/mol for the index numbers 145 and 263, respectively, considerably lower than the others. In Uracil/TOT, it has the lowest energy index with the number 238 and an energy of -20.00 kJ/mol, as well.

4. Conclusion and Suggestions

In this study, the atomistic modeling of key molecules of life and sepiolite is investigated using DFT. It has been revealed that the basic building blocks of DNA and RNA, the indispensable molecules of life, are adsorbed on the basal surfaces of sepiolite. It has been revealed by both CP-corrected and BCP analyzes that the most important parameter playing a key role in this adsorption is H-bond. Considering the intermolecular interactions obtained as a result of the analyzes, it can be stated that the guanine/TOT model is the most stable model. As a result, the fibrous clay crystals such as sepiolite which possess abundant silanol groups, can be potential carriers in the transport of nucleotides. On the other hand, there are certain limitations within the scope of this study. Computational modeling methods such as DFT are utilized in the analysis of surface adsorption between sepiolite mineral and DNA bases. However, while theoretical calculations provide important insights, they oversimplify physical and chemical interactions. Consequently, there is a possibility of less accurate analysis of molecular properties by neglecting some obstacles that may occur in the reaction. Nonetheless, such theoretical studies still contribute to our understanding, complementing experimental studies. This study aimed to highlight the adsorption feature of purine and pyrimidine, the nucleic acid bases, on the surface of sepiolite mineral through DFT. The originality of this study lies in assessing the interaction capacity of the biocompatible clay mineral with DNA and RNA bases, fundamental molecules for life, and revealing the potential contributions of these interactions to biochemical processes. While there are numerous studies in the literature on the use of sepiolite in healthcare, this study explores the interaction of DNA and RNA bases with sepiolite mineral, investigating the contribution of sepiolite to prebiotic chemistry from the perspective of molecular modeling and computational chemistry.

Statement of Research and Publication Ethics

The study is complied with research and publication ethics

References

[1] G. Biddeci, G. Spinelli, P. Colomba, and F. Di Blasi, "Halloysite Nanotubes and Sepiolite for Health Applications," *Int J Mol Sci,* vol. 24, Mar 2 2023.

[2] M. C. Hermosin, J. Cornejo, J. L. White, and S. L. Hem, "Sepiolite, a potential excipient for drugs subject to oxidative degradation," *J Pharm Sci,* vol. 70, pp. 189-92, Feb 1981.

[3] C. Aguzzi, P. Cerezo, C. Viseras, and C. Caramella, "Use of clays as drug delivery systems: Possibilities and limitations," *Applied Clay Science,* vol. 36, pp. 22-36, 2007.

[4] D. E. Bayraktepe, K. Polat, C. Yıldız, and Z. Yazan, "Electrochemical detection of bicalutamide in sepiolite clay sensing platform: Its possible electrooxidation mechanism, determination, and DNA interaction," *Electroanalysis,* vol. 36, no. 7, pp.1-12, 2024.

[5] M. D. Eduardo Ruiz-Hitzky, Francisco M. Fernandes, Bernd Wicklein, Ana C. S. Alcântara, and Pilar Aranda, "Bionanocomposites of sepiolite and palygorskite and their Medical issues," in *Natural Mineral Nanotubes: Properties and Applications*, G. J. C. Pooria Pasbakhsh, Ed., 1st Edition ed New York: Taylor & Francis Group, 2015.

[6] F. A. Castro-Smirnov, O. Pietrement, P. Aranda, J. R. Bertrand, J. Ayache, E. Le Cam*, et al.*, "Physical interactions between DNA and sepiolite nanofibers, and potential application for DNA transfer into mammalian cells," *Sci Rep,* vol. 6, p. 36341, Nov 3 2016.

[7]   F. A. Castro-Smirnov, J. Ayache, J. R. Bertrand, E. Dardillac, E. Le Cam, O. Pietrement, *et al.*, "Cellular uptake pathways of sepiolite nanofibers and DNA transfection improvement," *Sci Rep,* vol. 7, p. 5586, Jul 17 2017.

[8]   E. Gonzalez-Tortuero, J. Rodriguez-Beltran, R. Radek, J. Blazquez, and A. Rodriguez-Rojas, "Clay-induced DNA breaks as a path for genetic diversity, antibiotic resistance, and asbestos carcinogenesis," *Sci Rep,* vol. 8, p. 8504, May 31 2018.

[9]   P. Mignon, G. Corbin, S. Le Crom, V. Marry, J. Hao, and I. Daniel, "Adsorption of nucleotides on clay surfaces: Effects of mineral composition, pH and solution salts," *Applied Clay Science,* vol. 190, p. 105544, 2020.

[10]   T. L. Robinson, A. Michalkova, L. Gorb, and J. Leszczynski, "Hydrogen bonding of thymine and uracil with surface of dickite: An ab initio study," *Journal of Molecular Structure,* vol. 844-845, pp. 48-58, 2007.

[11]   P. Mignon, P. Ugliengo, and M. Sodupe, "Theoretical Study of the Adsorption of RNA/DNA Bases on the External Surfaces of Na+-Montmorillonite," *The Journal of Physical Chemistry C,* vol. 113, pp. 13741-13749, 2009.

[12]   S. A. Villafane-Barajas, J. P. T. Bau, M. Colin-Garcia, A. Negron-Mendoza, A. Heredia-Barbero, T. Pi-Puig, *et al.*, "Salinity Effects on the Adsorption of Nucleic Acid Compounds on Na-Montmorillonite: a Prebiotic Chemistry Experiment," *Orig Life Evol Biosph,* vol. 48, pp. 181-200, Jun 2018.

[13]   P. Mignon and M. Sodupe, "Theoretical study of the adsorption of DNA bases on the acidic external surface of montmorillonite," *Phys Chem Chem Phys,* vol. 14, pp. 945-54, Jan 14 2012.

[14]   A. Michalkova, T. L. Robinson, and J. Leszczynski, "Adsorption of thymine and uracil on 1:1 clay mineral surfaces: comprehensive ab initio study on influence of sodium cation and water," *Phys Chem Chem Phys,* vol. 13, pp. 7862-81, May 7 2011.

[15]   P. Bhatt, C. K. Pant, P. Pandey, Y. Pandey, S. C. Sati, and M. S. Mehata, "Adsorption of cytosine on prebiotic siliceous clay surface induced with metal dications: Relevance to origin of life," *Materials Chemistry and Physics,* vol. 291, p. 126720, 2022.

[16]   U. Pedreira-Segade, C. Feuillie, M. Pelletier, L. J. Michot, and I. Daniel, "Adsorption of nucleotides onto ferromagnesian phyllosilicates: Significance for the origin of life," *Geochimica et Cosmochimica Acta,* vol. 176, pp. 81-95, 2016.

[17]   U. Pedreira-Segade, J. Hao, A. Razafitianamaharavo, M. Pelletier, V. Marry, S. Le Crom, *et al.*, "How do Nucleotides Adsorb Onto Clays?," *Life (Basel),* vol. 8, Nov 27 2018.

[18]   U. Pedreira-Segade, L. J. Michot, and I. Daniel, "Effects of salinity on the adsorption of nucleotides onto phyllosilicates," *Phys Chem Chem Phys,* vol. 20, pp. 1938-1952, Jan 17 2018.

[19]   J. E. Post, D. L. Bish, and P. J. Heaney, "Synchrotron powder X-ray diffraction study of the structure and dehydration behavior of sepiolite," *American Mineralogist,* vol. 92, pp. 91-97, 2007.

[20]   D. Karataş, D. Senol-Arslan, and O. Ozdemir, "Experimental and Atomic Modeling of the Adsorption of Acid Azo Dye 57 to Sepiolite," *Clays and Clay Minerals,* vol. 66, pp. 426-437, 2018.

[21]   D. Karataş, A. Tekin, and M. S. Çelik, "Adsorption of quaternary amine surfactants and their penetration into the intracrystalline cavities of sepiolite," *New Journal of Chemistry,* vol. 37, p. 3936, 2013.

[22]   D. Karataş, A. Tekin, and M. Sabri Çelik, "Density functional theory computation of organic compound penetration into sepiolite tunnels," *Clays and Clay Minerals,* vol. 65, pp. 1-13, 2017.

[23]   S. G. Balasubramani, G. P. Chen, S. Coriani, M. Diedenhofen, M. S. Frank, Y. J. Franzke, *et al.*, "TURBOMOLE: Modular program suite for ab initio quantum-chemical and condensed-matter simulations," *J Chem Phys,* vol. 152, p. 184107, May 14 2020.

[24]   S. F. Boys and F. Bernardi, "The calculation of small molecular interactions by the differences of separate total energies. Some procedures with reduced errors," *Molecular Physics,* vol. 19, pp. 553-566, 2006.

[25]   J. Villard, M. P. Bircher, and U. Rothlisberger, "Plane Waves Versus Correlation-Consistent Basis Sets: A Comparison of MP2 Non-Covalent Interaction Energies in the Complete Basis Set Limit," *J Chem Theory Comput,* vol. 19, pp. 9211-9227, Dec 26 2023.

[26]   C. Steffen, K. Thomas, U. Huniar, A. Hellweg, O. Rubner, and A. Schroer, "TmoleX--a graphical user interface for TURBOMOLE," *J Comput Chem,* vol. 31, pp. 2967-70, Dec 2010.

[27]   T. Lu and F. Chen, "Multiwfn: a multifunctional wavefunction analyzer," *J Comput Chem,* vol. 33, pp. 580-92, Feb 15 2012.

[28]   L. Ismahan, N. Leila, M. Fatiha, G. Abdelkrim, C. Mouna, B. Nada, *et al.*, "Computational study of inclusion complex of l-Glutamine/beta-Cycldextrin: Electronic and intermolecular interactions investigations," *Journal of Molecular Structure,* vol. 1206, p. 127740, 2020.

[29]   A. Mehranfar, M. Izadyar, and A. N. Shamkhali, "A joint MD/QM study on the possibility of alkaloids detection by cucurbiturils and graphene oxide-cucurbituril composites," *Journal of Molecular Liquids,* vol. 272, pp. 963-972, 2018.

[30]   S. Emamian, T. Lu, H. Kruse, and H. Emamian, "Exploring Nature and Predicting Strength of Hydrogen Bonds: A Correlation Analysis Between Atoms-in-Molecules Descriptors, Binding Energies, and Energy Components of Symmetry-Adapted Perturbation Theory," *J Comput Chem,* vol. 40, pp. 2868-2881, Dec 15 2019.

[31]   E. Espinosa, E. Molins, and C. Lecomte, "Hydrogen bond strengths revealed by topological analyses of experimentally observed electron densities," *Chemical Physics Letters,* vol. 285, pp. 170-173, 1998.

[32]   H. Yang, P. Boulet, and M.-C. Record, "A rapid method for analyzing the chemical bond from energy densities calculations at the bond critical point," *Computational and Theoretical Chemistry,* vol. 1178, p. 112784, 2020.

[33]   W. F. Bleam, "The Nature of Cation-Substitution Sites in Phyllosilicates," *Clays and Clay Minerals,* vol. 38, no. 5, pp. 527-536, 1990.

[34]   C. Nomicisio, M. Ruggeri, E. Bianchi, B. Vigani, C. Valentino, C. Aguzzi, *et al.*, "Natural and Synthetic Clay Minerals in the Pharmaceutical and Biomedical Fields," *Pharmaceutics,* vol. 15, no. 5, pp. 1368, Apr 29 2023.

Investigation of the Effects of Kombucha Mushroom on Mycelium Growth of Agaricus bisporus Using Artificial Neural Networks

Fatih KUTLUER[1*], Ramazan GÜNGÜNEŞ[2]

[1] Department of Herbal and Animal Production, Kırıkkale Vocational School, Kırıkkale University, Kırıkkale, Turkiye
[2] Department of Electricity and Energy, Kırıkkale Vocational School, Kırıkkale University, Kırıkkale, Turkiye

(ORCID: 0000-0001-7035-0995) (ORCID: 0000-0001-6722-7275)

Abstract
The effects of Kombu mushroom extract on Agaricus bisporus mycelia development were the subject of this study. To prepare kombu mushroom extract; 60 g of sugar and black tea were added to 1 liter of water and fermentation of Kombu mushroom was achieved in this environment. The obtained extract was added to the potato dextrose agar medium at 0, 50, 75, 100cc. Mycelial agar discs of Agaricus bisporus with prepared agar were inoculated, developed at 23°C for 10 days, and mycelial development was examined. At the end of the incubation period, it was observed that mycelial development in the groups to which Kombucha mushroom extract was added was much better than the control group.

1. Introduction

Manchurian mushroom, also known as Kombucha or Kombu Tea, is popular in Far Eastern Countries and has been used for many years. Although it has not yet received enough attention in Western countries, it has been the subject of some research in recent years and its popularity is gradually increasing. It is used in the food industry, cosmetics and alternative medicine around the world. Although it is not well known in some countries, Kombucha mushroom has been examined in many studies [1], [2]. Studies show that the Kombu mushroom forms a symbiotic association with bacteria and yeast, which is quite intriguing. [3], [4]. Investigate antimicrobial activities against many organisms such as Staphylococcus aureus, Shigella sonnei, Escherichia coli, Aeromonas hydrophila, Yersinia enterolitica, Pseudomonas aeruginosa, Enterobacter cloacae, Staphylococcus epidermis, Campylobacter jejuni, Salmonella enteritidis, Salmonella typhimurium, Bacillus cereus, Helicobacter pylori and Listeria monocytogenes [5]. Unfortunately, studies on kombu mushroom are almost non-existent in our country. Apart from 1-2 studies on antimicrobial effects, not much research has been done on this subject in our country. In a master's thesis conducted at Marmara University, the fibrinolytic system and antibacterial effects of Kombu mushroom extract were examined, and in another study conducted at Gazi University, its effect against gram positive and gram negative bacteria was investigated [6], [7].

In a master's study conducted at Kırıkkale University, the cultural properties and antibacterial effects of Kombucha mushroom were investigated. Measurement of sugar reduction has been examined [8]. Agaricus bisporus production in Turkey has shown rapid development, especially in recent years. While the production amount of Agaricus bisporus was 80 tons in 1973 [9]., this value increased to 18,000 tons in the 2000s and 65,000 tons in 2018 [10]. As of 2020, it is around 75000 tons. Agaricus bisporus cultivation, which has become widespread especially in the Mediterranean, Marmara, Aegean and Central Anatolia regions, has started to be practiced in almost all our regions in recent years. The development of

the sector continues rapidly with the increase in support given to Agaricus bisporus cultivation in recent years. 75% of our mushroom production in our country consists of Agaricus genus mushrooms [9]. Agaricus bisporus cultivation is quite different from other agricultural cultivation branches due to its structure. Cultivation is done with a bag system on bunk beds and shelves, and in recent years, block-pressed mycelial-grown ready-made composts have been used. Today, in many countries that grow Agaricus bisporus, production is carried out using variations of the bag/block system [11]. Commercial mushroom cultivation in Turkey started in the 1980s. [12]. Since it is a newly developing sector, full efficiency has not yet been achieved and there is very little research done in this field. In this study, the effects of Kombucha mushroom on Agaricus bisporus productivity were determined by measuring zone ages and it was determined that Kombucha mushroom had a positive effect on Agaricus bisporus mycelial development. In the following stages, the amount of Kombucha to be added was determined using the artificial intelligence program.

The effects of Kombu mushroom extract on Agaricus bisporus mycelia development were the subject of this study. To prepare kombu mushroom extract; 60 g of sugar and black tea were added to 1 liter of water and fermentation of Kombu mushroom was achieved in this environment. The obtained extract was added to the potato dextrose agar medium at 0, 50, 75, 100cc. Mycelial agar discs of Agaricus bisporus with prepared agar were inoculated,

developed at 23°C for 10 days, and mycelial development was examined. At the end of the incubation period, it was observed that mycelial development in the groups to which Kombucha mushroom extract was added was much better than the control group.

2. Material and Method

2.1. Preparation of Kombucha Mushroom

Pre-sterilized glass containers should be used to prevent contamination of Kombucha from pathogenic organisms during preparation. Kombucha is usually brewed by adding black tea products (1.5 g/L) to fresh boiling water, sweetening with 50-150 g/L (5-15%) sucrose (tea sugar) and brewing for about 10-15 minutes. Preparation of infusion. The recommended tea is used to ensure that the tea leaves are prevented from cleaning later. After the prepared tea reaches room temperature, approximately 10-15% of the existing kombucha culture is added. It is then covered with a clean cotton cloth and left at room temperature for approximately 10-14 days. If this period is exceeded, the acidity level may be at a level that may be damaged in order for fermentation to continue. After fermentation, the baby mushrooms that form on the surface are removed and kept in a glass bottle with a small amount of tea to prevent them from drying out. Ready-to-drink Kombucha is stored in a glass bottle at 4 o C. Recommended daily consumption amounts are 100-250 ml [13], [14].

Figure 1. Preperation of Kombucha Mushroom

2.2. Application of Machine Learning Algorithms

Python programming language and the related modules such as TensorFlow [15], scipy [16] are used in this section. The basic modules are numpy [17], pandas [18] and seaborn [19]. The array structures and linear algebra is run by using numpy module. We can define data frame structures with the pandas module. The seaborn module is used for the statistical calculations. All of them are open source.

Machine learning process is the job that we can teach the knowledge to machines by using the data everywhere. We used the Agaricus bisporus data in this study. We applied two different machine learning applications to the problem. The first one is the regression algorithm. The algorithm is ready to use in numpy module. We define the independent and the dependent variables, and the algorithm tries to determine a polynomial with whose coefficients, which use the least square method [20]. The polynomial approximation for interpolation in numerical analysis has two important advantages. The former is that the derivatives and the indefinite integrals can be determined easily. The latter is that the algebraic polynomials uniformly approximate the functions.

Our first application for machine learning is the polynomial regression. It is obvious that the more data, the better results are obtained. We have ten experimental data, and we could get reasonable results in this study.

After the regression analysis we can find the following relation,

$$y = f(x) \approx \sum_{i=0}^{N} a_i x_i \qquad (1)$$

where the variable, which is the independent variable and corresponds to the day data, the dependent variable, which is the zone diameter, we called them as target in the program, corresponds to the coefficients of the polynomial approximation.

We tried to study different polynomials orders to get the best results. The fourth and the 5th polynomial order are seeming as the best results. Therefore, we tabulated these results, and we added the graphics of them. We have four data set control data, 50 cc data, 75 cc data and 100 cc data. The Table 1 represents the experimental data. Table 2 represents the coefficients of the polynomials and the values of each polynomial approximations. R-squared is a statistical measure which represents the proportion of the variance for a dependent variable. The closer its value to unity, the better the results.

Table 1. The experimental data

Day1	Control	50cc	75cc	100cc
1	9.05	9.08	9.20	9.65
2	9.15	9.22	9.59	10.26
3	9.31	9.45	10.05	11.01
4	9.94	10.06	10.66	11.92
5	11.12	11.25	11.86	12.93
6	13.71	14.02	14.81	14.98
7	14.62	15.01	16.02	16.65
8	16.02	16.83	17.32	17.92
9	18.36	19.26	20.05	20.69
10	19.93	20.28	21.24	22.05

.

Table 2. The polynomial regression coefficients

4th order approximation				
	Control	50cc	75cc	100cc
a_0	10.28750000	9.65250000	9.64583333	9.04833333
a_1	-1.62442113	-0.66104701	-0.55459984	0.68338384
a_2	0.53260927	0.13834936	0.19626603	-0.10828963
a_3	-0.03672980	0.02497183	0.01117036	0.03749611
a_4	0.00093677	-0.00215181	-0.00136218	-0.00204254
R^2	0.99333389	0.99396541	0.99216048	0.99698312

5th order approximation				
a_0	8.44133333	8.71933333	7.86200000	9.11800000
a_1	1.41895664	0.87726410	2.38602238	0.56853939
a_2	-1.06503496	-0.66919872	-1.34743590	-0.04800117
a_3	0.32045396	0.20551457	0.35629429	0.02401748
a_4	-0.03456643	-0.02009732	-0.03566667	-0.00070280
a_5	0.00129103	0.00065256	0.00124744	-0.00004872
R^2	0.99422560	0.99416806	0.99284030	0.99698419
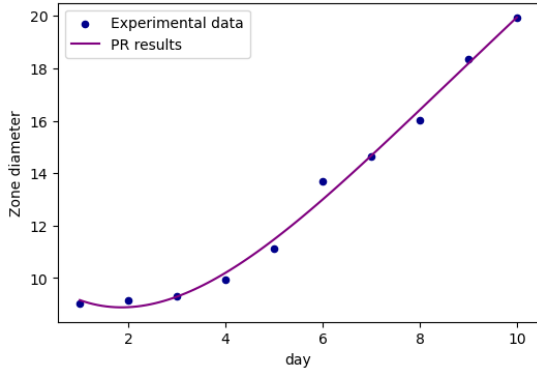
Figure 2. The 4ᵗʰ polynomial regression for control
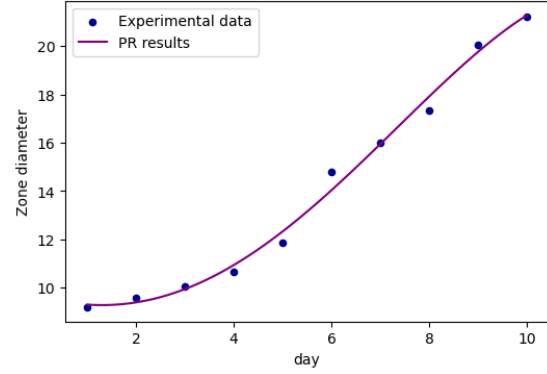
Figure 6. The 4th polynomial regression for 75cc data
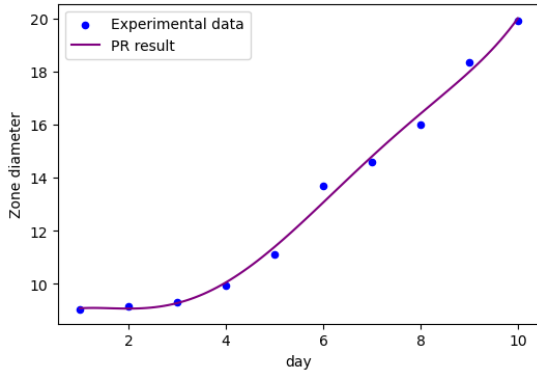
Figure 3. 5th polynomial regression for control
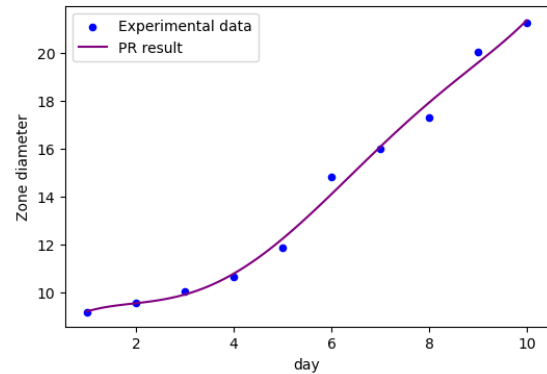
Figure 7. The 4th polynomial regression for 75cc data
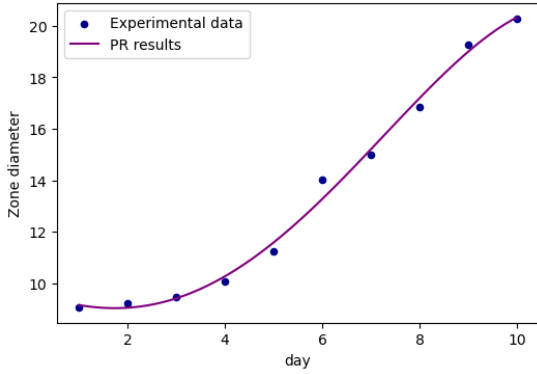
Figure 4. The 4th polynomial regression for 50cc data
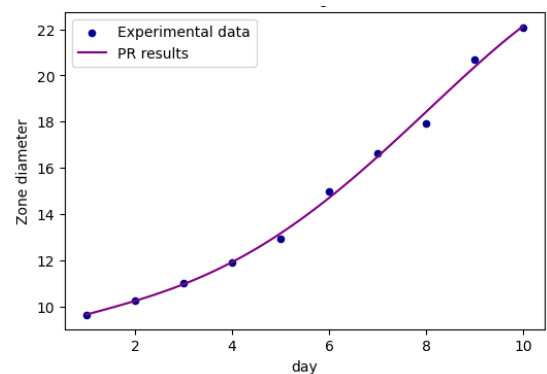
Figure 8. The 4th polynomial regression for 100cc data
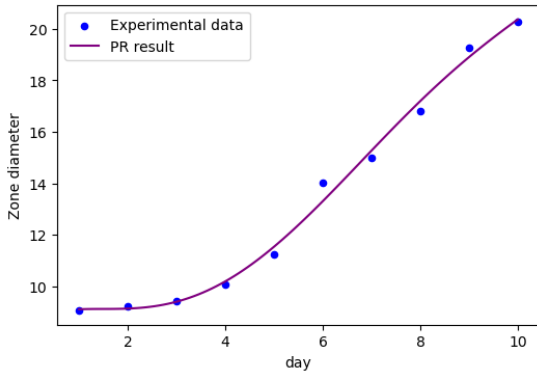
Figure 5. The 5th polynomial regression for 50cc data
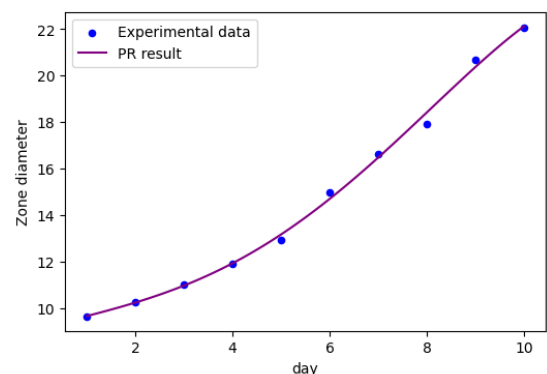
Figure 9. The 4th polynomial regression for 100cc data

The Artificial Neural Network (ANN) is another Machine Learning algorithm. It is called as ANN since the transmission of the information process to the next neuron is so similar to the biological neural network. The basic of artificial neural networks is based on logistic regression [20]. The logistic regression, which is given Figure 10, consists of an input layer, a summation layer, and an output layer.

An activation function is applied to the summation. If the activation value is bigger than a threshold value, then the output is determined. The output gives only two different results. Therefore, the logistic regression is also called as binary classification. This structure runs as a biological neuron cell.
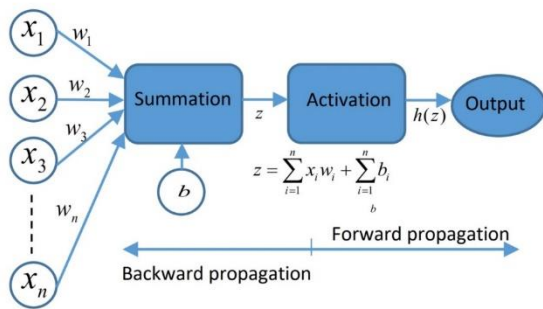
Figure 10. The structure of the logistic regression and the application of.
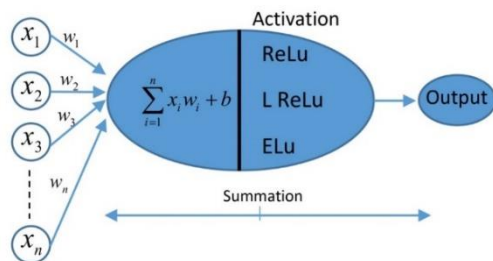
Figure 11. An artificial neuron cell in ANN

ANN is made of three layers. The first layer is called as the input layer. An artificial neural cell in Figure 11 works similarly to a biological cell. The next layer is called as hidden layers, and the number of the hidden layers is a hyperparameter. The final layer is called as the output layer. A schematic representation is given in Figure 11.
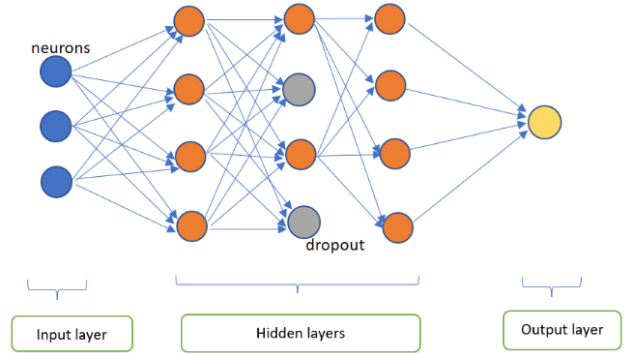
Figure 12. The structure of an Artificial Neural Network

The hyperparameter word is used for certain quantities in the ANN, which we can change these parameters. The number of neurons in the layers, the number of hidden layers are two of these hyperparameters. In the ANN calculations there are also different hyperparameters such as, the optimization function, the number of epoch, the batch size etc. The used hyperparameters in this study are given in Table 3

.

Table 3. The ANN hyperparameters used in this study

	Control	50cc	75cc	100cc
Hyperparameters	100	100	100	100
Number of neurons	1000	1000	1000	1000
Epoch number	4	4	4	4
Batch size	0.2	0.2	0.2	0.2
Test size	0.2	0.2	0.2	0.2
Validation split	12	10	10	10
Number of hidden layers for LRelu	12	10	12	10
Number of hidden layers for Elu (a=0.1)	msle	msle	msle	Msle
Loss function	adam	adam	adam	Adam
Optimization function	LRelu / Elu	LRelu / Elu	LRelu / Elu	LRelu / Elu)
Activation function	Control	50cc	75cc	100cc
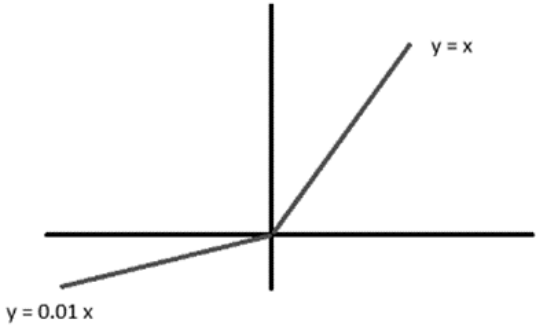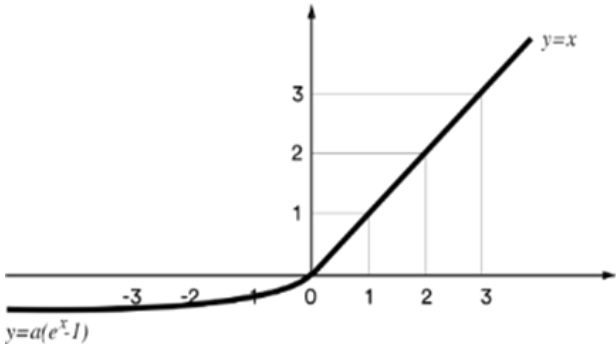
msle: Mean square logarithmic error

There are different models in Machine Learning process. These models are selected for the studied dataset such as an image, data prediction. Here we used the sequential model. A Sequential model is appropriate for a plain stack of layers where each layer has exactly one input tensor and one output tensor [21]. Epoch term is used the number of passes of the entire training dataset. Dataset is used grouped into batches. If the dataset belongs to a huge dataset, then the batch number especially becomes important. Epoch could be thought as the iteration number. The dataset can be randomly chopped to the validation set and test size. There are also activation function and the optimization function. The activation function decides the activation of the next neuron according to the value of neuron. We used two different activation function, Leaky Relu (Leaky Rectified Linear Unit) [22] and Elu (Exponential Linear Unit) [23] in this study. Leaky Relu activation function is focused to zero, and there are no killed neurons. The function has 0.01x for the negative value. Elu activation function includes an exponential term with an parameter and there are no killed neurons. was selected as 0.1 in this study. However, it runs slowly in terms of the calculation time since it includes an exponential term.

Table 4. Activation functions and its properties

Mathematical definition of the activation function 1	The behaviour of the activation function 2
$h_{Leaky\mathrm{ReL}}(x) = \max(0.01x, x)$	
$h_{ELu} = \begin{cases} a(e^x - 1), & x < 0 \\ x & , x \geq 0 \end{cases}$	

The optimization function is selected as adam (adaptive moment estimation) [24] optimization function. Adam is a replacement optimization algorithm for stochastic gradient descent for training deep learning models. It combines the best properties of the AdaGrad and RMSProp algorithms to provide the optimization algorithm which can handle sparse gradients on noisy problems. Another hyperparameter is the loss function. This function calculates the error per epoch. According to the error value the weights and bias are rearranged to get minimum error. The loss function behaviours are given every ANN result for the interested in data.
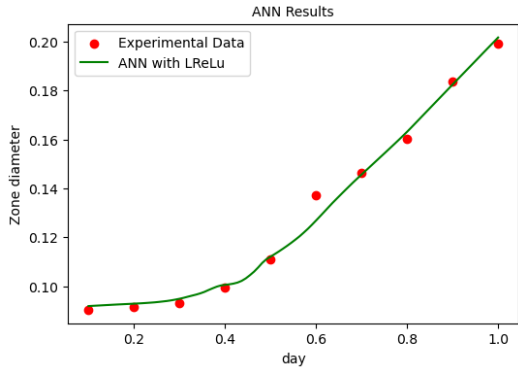
Figure 13 The ANN result for control data with LReLu
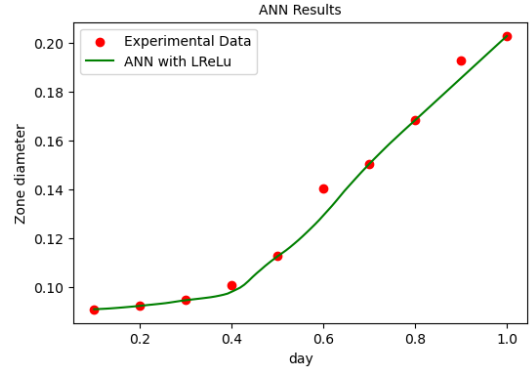
Figure 17 The ANN result for 50cc data with LReLu
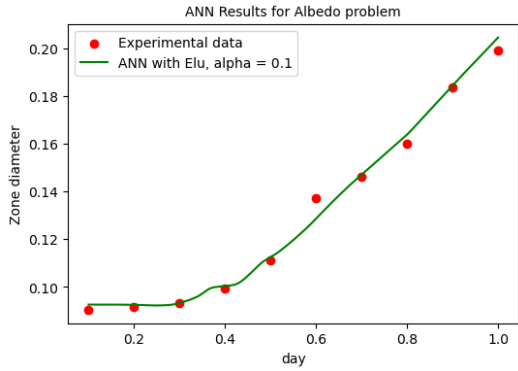
Figure 14 The ANN result for control data with ELu
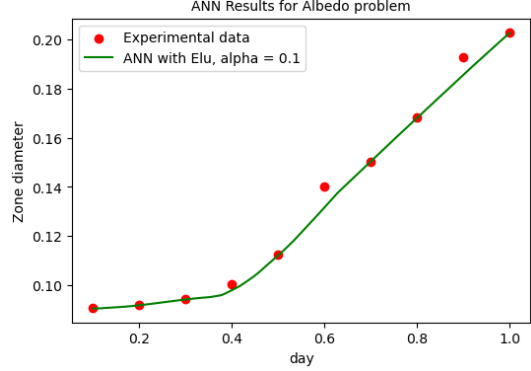
Figure 18 The ANN result for 50cc data with Elu
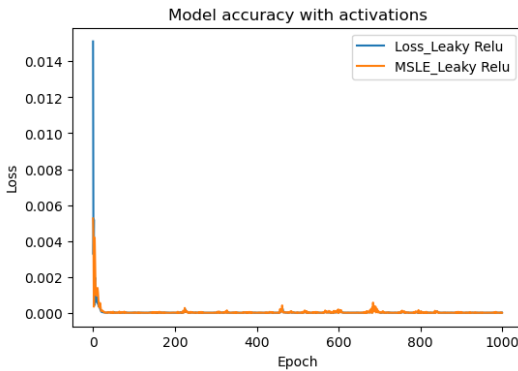
Figure 15 The Loss for control data with LReLu
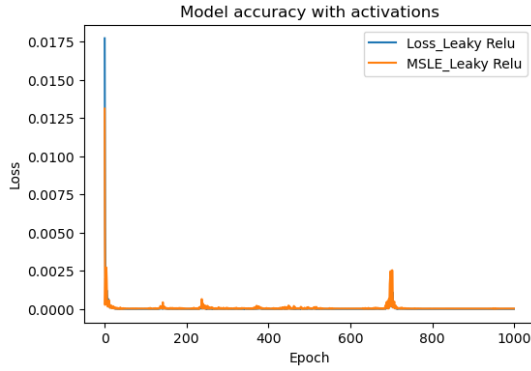
Figure 19 The Loss for 50cc data with LReLu
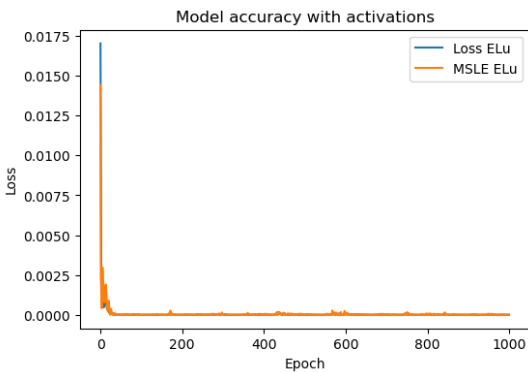
Figure 16 The Loss for control data with Elu
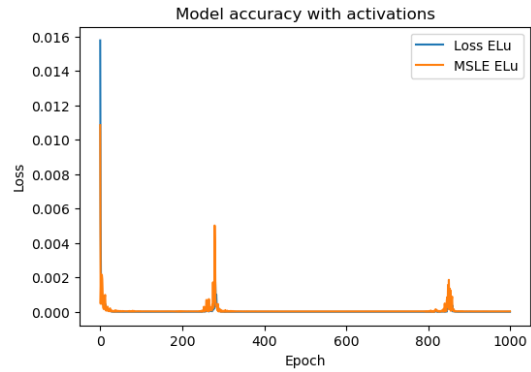
Figure 20 The Loss for 50cc data with Elu
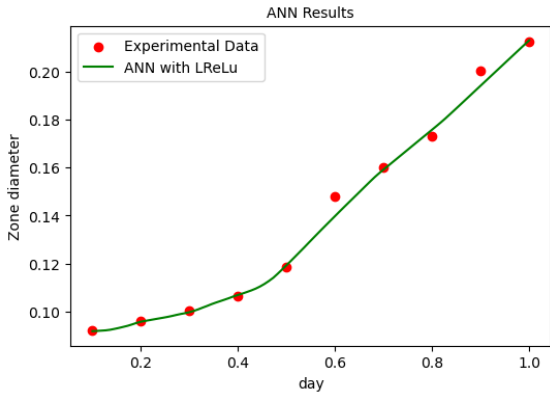
Figure 21 The ANN result for 75cc data with LReLu
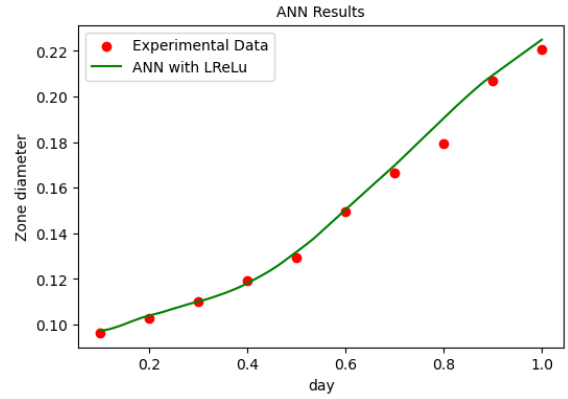
Figure 25 The ANN result for 100cc data with LReLu
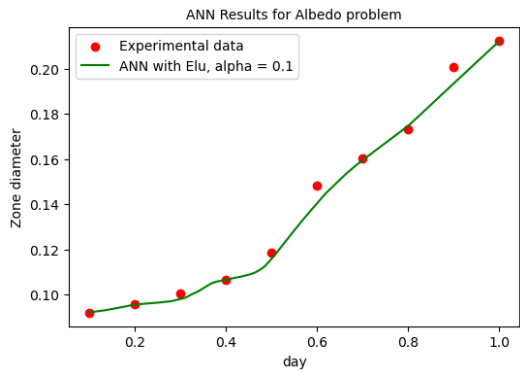
Figure 22 The ANN result for 75cc data with ELu
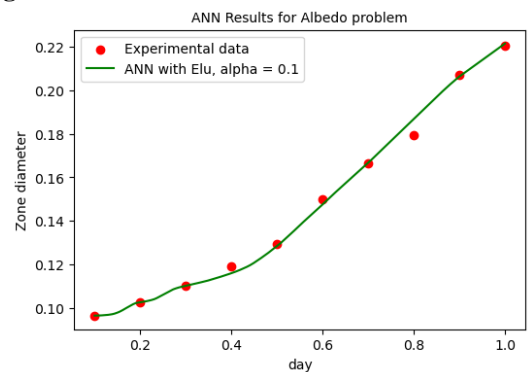
Figure 26 The ANN result for 100cc data with Elu
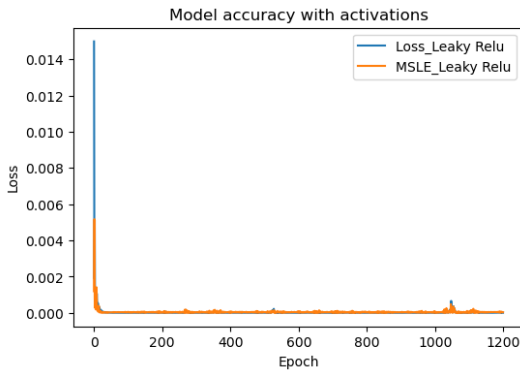
Figure 23 The Loss for 75cc data with LReLu
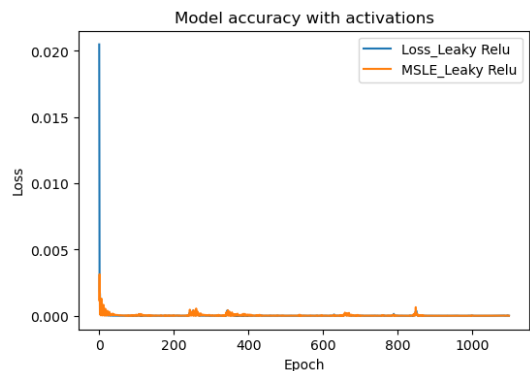
Figure 27 The Loss for 100cc data with LReLu
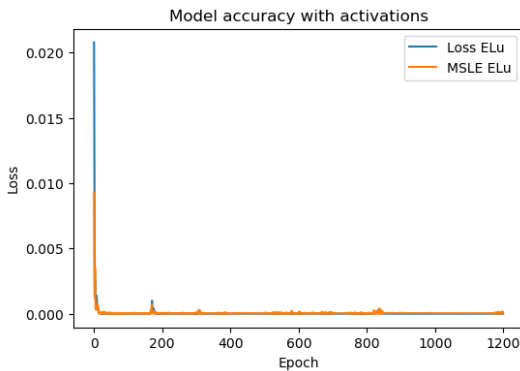
Figure 24 The Loss for 75cc data with Elu
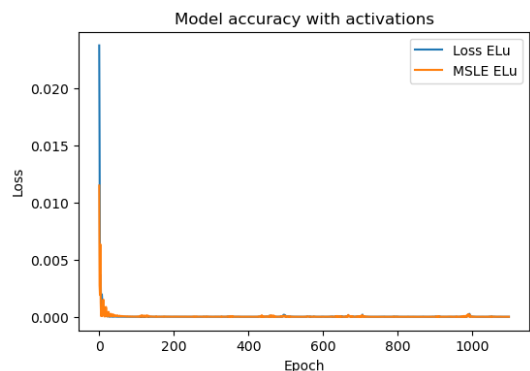
Figure 28 The Loss for 100cc data with Elu

Tables 5-8 represent the comparison of the training data (experimental data) and the predicted data both PR and ANN. We can predict the data for different times. The predictions are given in Tables 9-12

Table 5. Possible flood flow rates of E26A010 AGI

Day	Target	PR 4th	PR 5th	ANN LeakyRelu	ANN Elu
1	9.05	9.159895	9.082434	9.051624	9.050000
2	9.15	8.890245	9.070988	9.164109	9.086722
3	9.31	9.291894	9.278984	9.31168	9.309999
4	9.94	10.20067	10.05866	9.94251	9.940000
5	11.12	11.47488	11.39742	11.12378	11.12000
6	13.71	12.99533	13.07279	12.82565	12.81362
7	14.62	14.66527	14.80729	14.62633	14.62000
8	16.02	16.41048	16.42339	16.42755	16.44286
9	18.36	18.1792	17.99845	18.22413	18.23862
10	19.93	19.94213	20.01959	19.93881	19.93000

Table 6. The comparison of the experimental data, PR and ANN predictions for 50cc

Day	Target	PR 4th	PR 5th	ANN LeakyRelu	ANN Elu
1	9.08	9.152622	9.113469	9.081257	9.061183
2	9.22	9.049149	9.140508	9.221422	9.199373
3	9.45	9.414446	9.407921	9.452195	9.434942
4	10.06	10.26924	10.19745	9.800414	9.805772
5	11.25	11.5826	11.54345	11.25175	11.22337
6	14.02	13.27197	13.31112	12.93047	13.16891
7	15.01	15.20314	15.27492	15.03398	15.03921
8	16.83	17.19026	17.19679	16.82635	16.80187
9	19.26	18.99584	18.90448	18.5477	18.5489
10	20.28	20.33073	20.36989	20.27195	20.25528

Table 7. The comparison of the experimental data, PR and ANN predictions for 75cc

Day	Target	PR 4th	PR 5th	ANN LeakyRelu	ANN Elu
1	9.2	9.297308	9.222462	9.189361	9.214143
2	9.59	9.389266	9.563907	9.58306	9.556547
3	10.05	9.939691	9.927217	9.980069	9.803448
4	10.66	10.93388	10.79666	10.69566	10.65839
5	11.86	12.32442	12.24957	11.93395	11.58418
6	14.81	14.03122	14.10607	13.97941	14.04297
7	16.02	15.94151	16.07873	15.91545	15.94393
8	17.32	17.9098	17.92227	17.5758	17.46046
9	20.05	19.75791	19.58327	19.40751	19.33819
10	21.24	21.275	21.34985	21.29476	21.20565

Table 8. The comparison of the experimental data, PR and ANN predictions for 100cc

Day	Target	PR 4th	PR 5th	ANN LeakyRelu	ANN Elu
1	9.65	9.658881	9.661804	9.737173	9.643672
2	10.26	10.24923	10.24241	10.39709	10.25676
3	11.01	10.97083	10.97131	11.01324	11.01534
4	11.92	11.9261	11.93145	11.82436	11.59534
5	12.93	13.16844	13.17136	13.19254	12.84031
6	14.98	14.70224	14.69931	15.04465	14.75891
7	16.65	16.48286	16.4775	16.98433	16.67183
8	17.92	18.41663	18.41614	19.04833	18.68821
9	20.69	20.36089	20.36771	20.93521	20.63604
10	22.05	22.12392	22.12099	22.49164	22.15119

Table 9. The predictions for control

Predictions-Day	PR 4th	PR 5th	ANN LeakyRelu	ANN Elu
1.00	9.159895	9.082434	9.051624	9.050000
1.25	9.019725	9.096348	9.073997	9.050697
1.50	8.930018	9.089783	9.10161	9.054023
1.75	8.887816	9.077265	9.133728	9.064962
2.00	8.890245	9.070988	9.164109	9.086722
2.25	8.934520	9.080964	9.195367	9.116143
2.50	9.017945	9.115175	9.232083	9.159989
2.75	9.137910	9.179723	9.26773	9.221025
3.00	9.291894	9.278984	9.31168	9.309999
3.25	9.477464	9.415756	9.372495	9.402710
3.50	9.692274	9.591412	9.508907	9.513886
3.75	9.934066	9.806054	9.732154	9.720457
4.00	10.20067	10.05866	9.94251	9.940000
4.25	10.49000	10.34723	10.12466	10.16175
4.50	10.80007	10.66895	10.47141	10.44006
4.75	11.12897	11.02035	10.82195	10.77727
5.00	11.47488	11.39742	11.12378	11.12000
5.25	11.83607	11.79580	11.43860	11.49753
5.50	12.21090	12.21090	11.84305	11.92394
5.75	12.59781	12.63808	12.32830	12.36770
6.00	12.99533	13.07279	12.82565	12.81362
6.25	13.40208	13.51070	13.30147	13.26153
6.50	13.81678	13.94790	13.74257	13.72082
6.75	14.23822	14.38099	14.18311	14.17253
7.00	14.66527	14.80729	14.62633	14.62000
7.25	15.09693	15.22494	15.07411	15.06778
7.50	15.53223	15.63309	15.52544	15.52705
7.75	15.97034	16.03205	15.97673	15.98751
8.00	16.41048	16.42339	16.42755	16.44286
8.25	16.85199	16.81017	16.87808	16.8967
8.50	17.29426	17.19703	17.32834	17.34991
8.75	17.7368	17.59036	17.77746	17.80065
9.00	18.1792	17.99845	18.22413	18.23862
9.25	18.62112	18.43167	18.66617	18.67267
9.50	19.06234	18.90257	19.1027	19.09695
9.75	19.5027	19.42607	19.52349	19.51821

Table 10. The predictions for 50cc

Predictions-Day	PR 4th	PR 5th	ANN LeakyRelu	ANN Elu
1.00	9.152622	9.113469	9.081257	9.061183
1.25	9.085882	9.124612	9.104403	9.083791
1.50	9.045602	9.126357	9.137318	9.112902
1.75	9.033014	9.128774	9.176832	9.148807
2.00	9.049149	9.140508	9.221422	9.199373
2.25	9.094834	9.168856	9.270057	9.252855
2.50	9.170696	9.219842	9.318975	9.310759
2.75	9.277159	9.298294	9.384991	9.369883
3.00	9.414446	9.407921	9.452195	9.434942
3.25	9.582579	9.551388	9.506618	9.48294
3.50	9.781377	9.730395	9.563956	9.524736
3.75	10.01046	9.945752	9.646337	9.598458
4.00	10.26924	10.19745	9.800414	9.805772
4.25	10.55693	10.48476	10.05346	10.07586
4.50	10.87255	10.80627	10.48546	10.40646
4.75	11.2149	11.16	10.89019	10.81675
5.00	11.5826	11.54345	11.25175	11.22337

Continuation of Table 10

Predictions-Day	PR 4th	PR 5th	ANN LeakyRelu	ANN Elu
5.25	11.97405	11.95369	11.59031	11.66359
5.50	12.38746	12.38746	11.99102	12.15025
5.75	12.82083	12.84119	12.43789	12.66101
6.00	13.27197	13.31112	12.93047	13.16891
6.25	13.73847	13.79337	13.45685	13.69178
6.50	14.21774	14.28401	14.01626	14.14508
6.75	14.70696	14.77913	14.53596	14.588
7.00	15.20314	15.27492	15.03398	15.03921
7.25	15.70307	15.76778	15.50601	15.48676
7.50	16.20334	16.25432	15.96201	15.92571
7.75	16.70034	16.73153	16.39946	16.36376
8.00	17.19026	17.19679	16.82635	16.80187
8.25	17.66909	17.64795	17.25533	17.23946
8.50	18.1326	18.08346	17.68609	17.67636
8.75	18.57639	18.50237	18.11666	18.11259
9.00	18.99584	18.90448	18.5477	18.5489
9.25	19.38612	19.29036	18.97897	18.98155
9.50	19.74221	19.66146	19.41024	19.40719
9.75	20.05889	20.02016	19.8415	19.83278

Table 11. The predictions for 75cc

Predictions-Day	PR 3th order	PR 4th	PR 5th	ANN LeakyRelu	ANN Elu
1.00	9.356154	9.297308	9.222462	9.189361	9.214143
1.25	9.28351	9.277741	9.351777	9.218353	9.278126
1.50	9.254001	9.286336	9.440706	9.302257	9.362338
1.75	9.265866	9.323439	9.506491	9.42391	9.459305
2.00	9.317343	9.389266	9.563907	9.58306	9.556547
2.25	9.406668	9.483907	9.625407	9.674099	9.599531
2.50	9.53208	9.607323	9.701271	9.763546	9.642313
2.75	9.691816	9.759349	9.799751	9.87405	9.693686
3.00	9.884114	9.939691	9.927217	9.980069	9.803448
3.25	10.10721	10.14793	10.0883	10.1518	10.01678
3.50	10.35935	10.38351	10.28605	10.34624	10.27865
3.75	10.63876	10.64576	10.52207	10.51768	10.54749
4.00	10.94368	10.93388	10.79666	10.69566	10.65839
4.25	11.27236	11.24692	11.10897	10.86683	10.75988
4.50	11.62302	11.58384	11.45715	11.09962	10.87912
4.75	11.99391	11.94344	11.83849	11.4507	11.10683
5.00	12.38326	12.32442	12.24957	11.93395	11.58418
5.25	12.78932	12.72532	12.6864	12.43985	12.2034
5.50	13.21031	13.14457	13.14457	12.95821	12.8421
5.75	13.64448	13.58048	13.6194	13.47318	13.45736
6.00	14.09007	14.03122	14.10607	13.97941	14.04297
6.25	14.54531	14.49484	14.5998	14.48046	14.59396
6.50	15.00844	14.96926	15.09595	14.9752	15.07872
6.75	15.47769	15.45226	15.59021	15.47092	15.53709
7.00	15.95132	15.94151	16.07873	15.91545	15.94393
7.25	16.42754	16.43454	16.55823	16.33059	16.32511
7.50	16.90461	16.92877	17.02623	16.74572	16.70478
7.75	17.38076	17.42147	17.4811	17.16082	17.08292
8.00	17.85422	17.9098	17.92227	17.5758	17.46046
8.25	18.32324	18.39077	18.35037	18.00028	17.92745
8.50	18.78605	18.86129	18.76734	18.46383	18.39868
8.75	19.24088	19.31812	19.17662	18.9355	18.86893
9.00	19.68599	19.75791	19.58327	19.40751	19.33819
9.25	20.1196	20.17717	19.99412	19.87963	19.8065

Continuation of Table 11

Predictions-Day	PR 3th order	PR 4th	PR 5th	ANN LeakyRelu	ANN Elu
9.50	20.53996	20.57229	20.41792	20.35176	20.27383
9.75	20.94529	20.93952	20.86549	20.8238	20.74022
10.00	21.33385	21.275	21.34985	21.29476	21.20565

Table 12 . The predictions for 100cc

Predictions-Day	PR 4th	PR 5th	ANN LeakyRelu	ANN Elu
1.00	9.658881	9.66180	9.73717	9.643672
1.25	9.801609	9.79872	9.84296	9.670229
1.50	9.945966	9.93994	10.02869	9.783303
1.75	10.09442	10.08727	10.23185	10.06459
2.00	10.24923	10.24241	10.39709	10.25676
2.25	10.41249	10.40696	10.54101	10.36320
2.50	10.58607	10.58240	10.70776	10.61037
2.75	10.77168	10.77011	10.86871	10.87412
3.00	10.97083	10.97131	11.01324	11.01534
3.25	11.18481	11.18714	11.17180	11.13578
3.50	11.41477	11.41857	11.35488	11.26510
3.75	11.66161	11.66644	11.56670	11.42306
4.00	11.92610	11.93145	11.82436	11.59534
4.25	12.20876	12.21415	12.10944	11.80192
4.50	12.50996	12.51491	12.42146	12.08020
4.75	12.82986	12.83396	12.79208	12.44222
5.00	13.16844	13.17136	13.19254	12.84031
5.25	13.52547	13.52699	13.60130	13.29994
5.50	13.90055	13.90055	14.06532	13.80419
5.75	14.29307	14.29155	14.55486	14.27680
6.00	14.70224	14.69931	15.04465	14.75891
6.25	15.12707	15.12297	15.53171	15.25207
6.50	15.56640	15.56145	16.01779	15.73215
6.75	16.01885	16.01346	16.49954	16.20307
7.00	16.48286	16.47750	16.98433	16.67183
7.25	16.95668	16.95185	17.49714	17.17154
7.50	17.43837	17.43456	18.01591	17.67681
7.75	17.92579	17.92347	18.53261	18.18273
8.00	18.41663	18.41614	19.04833	18.68821
8.25	18.90836	18.90994	19.56341	19.19452
8.50	19.39828	19.40195	20.05232	19.70020
8.75	19.88349	19.88901	20.52439	20.18993
9.00	20.36089	20.36771	20.93521	20.63604
9.25	20.82720	20.83435	21.32573	21.01559
9.50	21.27895	21.28498	21.71568	21.39460
9.75	21.71247	21.71537	22.10367	21.77313
10.00	22.12392	22.12099	22.49164	22.15119

3. Conclusion and Suggestions

The fact that the mycelial development of the groups to which kombucha mushroom was added was good, the mushroom mycelia were more resistant to diseases and pests and the mushroom mycelia developed faster, and as a result, it will provide serious advantages in producing mycelia that are more resistant to both time and diseases when used in seed mycelia production [25]. With the increase in commercial cultivation of Agaricus bisporus in Turkey, the need to both increase its yield and develop species that are resistant to diseases and pests has emerged. In this study, the addition of Kombucha mushroom at the seed mycelium stage contributed to both the development of durable mycelia and increased yield. There are limited studies in this field. Our study will lead to future studies.

The PR and the ANN application is used to teach the machine. After this teaching process we can

ask the predictions of new data. This new data can be used to improve the Agaricus bisporus cultivation. Thus, the cultivation efficiency can be improved. Moreover, similar studies can be investigated without any numerical analysis methods. Although we have restricted data, the founded results are good.

Although PR results may seem better, PR results are not good the out of range. But its results can be used for only the dataset range. While ANN results are good both the dataset range and the out of the range of the dataset according to the results. We could have better results but then ANN but then the ANN becomes overflow. This overflow is an unwanted situation. If we compare the ANN results in terms of the activation function, it can be seen that the results with the Elu activation function is better. The reason of that the activation of the next neuron in the network.

Contributions of the authors

Fatih Kutluer : investigation, Methodology, Visualization, Writing- Review&Editing. Ramazan Güngüneş: Investigation, Methodology, Software, Visualization, Writing-Review&Editing.

Conflict of Interest Statement

There is no conflict of interest between the authors.

Statement of Research and Publication Ethics

The study is complied with research and publication ethics

References

[1]   C. J. Greenwalt, K. H. Steinkraus,and R. A. Ledford, "Kombucha, the fermented tea: microbiology, composition, and claimed health effects", *J. Food Prot.*, vol. 63, no 7, pp. 976–981, 2000.

[2]   I. Jankovic and M. Stojanovic, "Microbial and chemical composition, growth, therapeutical and antimicrobial characteristics of tea fungus", *Mikrobiol.*, vol. 31, no 1, 1994.

[3]   C. P. Kurtzman, C. J. Robnett, ve E. Basehoar-Powers, "Zygosaccharomyces kombuchaensis, a new ascosporogenous yeast from 'Kombucha tea'", *FEMS Yeast Res.*, vol. 1, no 2, pp. 133–138, 2001.

[4]   C.-H. Liu, W.-H. Hsu, F.-L. Lee, and C.-C. Liao, "The isolation and identification of microbes from a fermented tea beverage, Haipao, and their interactions during Haipao fermentation", *Food Microbiol.*, vol. 13, no. 6, pp. 407–415, 1996.

[5]   G. Sreeramulu, Y. Zhu, ve W. Knol, "Characterization of antimicrobial activity in Kombucha fermentation", *Acta Biotechnol.*, vol. 21, no. 1, pp. 49–56, 2001.

[6]   N. C. Sesal, "Kombu mantarı ve ekstresinin fibrinolitik sistem ve antibakteriyal etkisinin incelenmesi". Marmara Universitesi (Turkey), 1998.

[7]   N. Mercan, Z. N. Yüksekdağ, H. Katırcıoğlu, and Y. Beyatlı, "The antibacterial activity of Kombucha tea, kefir and Turkish yoghurt", içinde *International Dairy Symposium*, 2004, pp. 313–317.

[8]   F. Kutluer, "Kombucha mantarının kültürel özellikleri ve şeker redüksiyonunun incelenmesi". Yüksek Lisans Tezi (Kırıkkale Üniversitesi, Fen Bilimleri Enstitüsü), 2009.

[9]   S. Erkal and Ş. Aksu, "Türkiye'de kültür mantarı sektöründeki gelişmeler ve işletmelerin yapısal özellikleri, Türkiye 6", *Yemeklik Mantar Kongresi, Bildir. ve Posterleri. Sayfa*, ss. 55–66, 2000.

[10]   E. Eren and A. Pekşen, "Türkiye'de kültür mantarı üretimi ve teknolojik gelişmeler", *Mantar Derg.*, vol. 10, no 3, pp. 225–233, 2019.

[11]   R. Samp, "The bag or block system of Agaricus mushroom growing", *Edible Med. Mushrooms Technol. Appl.*, pp. 175–195, 2017.

[12]   A. Günay, "Mantar yetiştiriciliği", *İlke Kitabevi Yayınları*, vol. 2, p. 469, 1995.

[13]   C. Dufresne and E. Farnworth, "Tea, Kombucha, and health: a review", *Food Res. Int.*, vol. 33, no 6, pp. 409–421, 2000.

[14]   J. Reiss, "Influence of different sugars on the metabolism of the tea fungus", *Zeitschrift für Leb. Und-forsch.*, vol. 198, no 3, pp. 258–261, 1994.

[15]   Tensorflow, "Index @ Tensorflow.Org", 2021. https://www.tensorflow.org/ Retrieved May 2023

[16]   Scipy, "Index @ Scipy.Org". https://scipy.org/ Retrieved May 2023.

[17]   Numpy, "Index @ Numpy.Org". https://numpy.org/doc/stable/user/index.html#user Retrieved May

2023

[18]   Pandas, "Index @ Pandas.Pydata.Org". pandas - Python Data Analysis Library (pydata.org) Retrieved May 2023

[19]   Seaborn, "Index @ seaborn.pydata.org". https://seaborn.pydata.org/ Retrieved May 2023

[20]   C.-Y. J. Peng, K. L. Lee, ve G. M. Ingersoll, "An introduction to logistic regression analysis and reporting", *J. Educ. Res.*, c. 96, sayı 1, ss. 3–14, 2002.

[21]   I. Sutskever, "Sequence to Sequence Learning with Neural Networks", *arXiv Prepr. arXiv1409.3215*, 2014.

[22]   D. P. Kingma, "Adam: A method for stochastic optimization", *arXiv Prepr. arXiv1412.6980*, 2014.

[23]   B. Xu, "Empirical evaluation of rectified activations in convolutional network", *arXiv Prepr. arXiv1505.00853*, 2015.

[24]   D.-A. Clevert, T. Unterthiner, and S. Hochreiter, "Fast and accurate deep network learning by exponential linear units (elus)", *arXiv Prepr. arXiv1511.07289*, 2015.

[25]   P. Güler, E. Yalçın, ve F. Kutluer, "Kombucha Mantarının Fungus Misel Gelişimine Etkileri", *Ecol. Life Sci.*, vol. 5, no 3, pp. 268–273, 2010.

Enhancing Radar Image Classification with Autoencoder-CNN Hybrid System

Kürşad UÇAR[1*]

[1]Department of Electrical-Electronics Engineering, Faculty of Technology, Selcuk University, Konya, Turkey
(ORCID: 0000- 0001-5521-2447)

Abstract

The tracking, analysis, and classification of human movements can be crucial, particularly in areas such as elderly care, healthcare, and infant care. Typically, such tracking is done remotely with cameras. However, radar systems have emerged as significant methods and tools for these tasks due to their advantages such as privacy, wireless operation, and the ability to work through walls. By converting reflected radar signals from targets into images, human activities can be classified using powerful classification tools like deep learning. In this study, range-Doppler images of behind-the-wall human movements obtained with a radar system consisting of one transmitter and four receiver antennas were classified. Since the data collected from the four receiver antennas are in different positions, the collected reflection signals also differ. The signals collected with the range-time matrix content were divided into positive and negative parts, resulting in eight images from the four antennas. Instead of using all the data in CNN training, the images were first subjected to a reconstruction process with an autoencoder to reduce differences. The reproduced images were then classified with CNN. Moreover, the classification success is increased by 8.50% with the proposed method compared to classification only with CNN. In conclusion, it was observed that the classification success of radar images can be increased by using a hybrid system with an autoencoder to reconstruct the images before classification with CNN.

1. Introduction

Electronic devices have begun to play an active role in daily life, such as machines, robots, and cameras, due to their more effective operation compared to humans in various fields [1]-[3]. These devices are advantageous due to their speed, continuity, lower energy consumption, and reduced errors. Additionally, they can prioritize important values such as privacy, confidentiality, and security over humans [4]. Given all these advantages, leveraging technology in critical tasks such as monitoring the elderly, children, and patients is highly appealing. It requires constant monitoring of individuals who may be in dangerous situations or require immediate intervention. Continuous monitoring implies observing every moment of these individuals, potentially violating their private spaces. Therefore, radar devices and systems have started to be used in such tasks as an alternative to devices like cameras that directly display people.

Radar (Radio Detection and Ranging) is a system that uses electromagnetic waves to determine the position and movement of objects [5], [6]. Radars are commonly used in various fields such as aircraft, ships, vehicles, and airports. Radar begins its operation by emitting electromagnetic waves at a specific frequency. These waves are typically radio waves or microwaves. When these emitted waves encounter target objects, reflection occurs. The reflected waves travel back from the object and are received by the radar. The collected waves are

processed by the radar system. This process involves analyzing the timing, frequency, and power of the waves to determine the position, distance, and speed of the target object [7], [8]. Additionally, inference can be made based on the converted signals into images [9]-[11].

Radar systems, by converting radar signals into images, have become an area of interest for researchers in classifying human movements [11]-[14]. Since reflections in collected signals differ based on movements, motion analysis can be performed from the generated images [15]-[17]. However, due to the different semantic relationships between neighboring pixels in such images compared to classical images, feature extraction or image enhancement cannot be performed using classical image processing methods [18]. Although these images may be meaningless to humans, deep learning methods can establish meaningful relationships between pixels thanks to their strong structures. Therefore, deep learning tools developed for image processing play a critical role in achieving effective results on radar images [15]. Among these algorithms, autoencoders have become preferred due to their powerful features such as noise reduction and image reconstruction. Autoencoders, with their deep learning structure, have the ability to reproduce an image similar to the target images.

While a human can understand real-world images by examining them and easily identify shapes, activities, or objects in the image, radar or frequency domain images showing different features of the environment do not make sense to humans. It is very difficult for individuals to make an inference from such images at first glance. Even non-experts would perceive these images as completely meaningless. However, with powerful classification algorithms, it is possible for machines to understand such images. In this context, many studies have been conducted to classify radar images using machine learning algorithms [11], [19], [20]. Radar signals reflected from the human chest have been used to perform tasks such as detecting living beings or counting pulses [21], [22]. Radar signals have also been used to detect instances of individuals in need of care, such as monitoring breathing and detecting falls [23]-[25]. Additionally, it has been shown that different movements can be detected using images created with radar signals [26], [27].

In [11], it was shown that images of signals from different antennas for human activities could be classified with CNN. It was reported that interference and noise differences in signals received with 4 antennas were suitable for data augmentation for CNN, known to provide better results with more data, and the amount of data was increased eightfold with the structure created. In this study, instead of using all the data for CNN training, an autoencoder-CNN hybrid system was proposed to improve images by reconstructing them with an autoencoder [28]. Three different combinations were created for training and testing the autoencoder, and to compare the results, the CNN structure used in [11] was employed.

The contributions of this study are as follows.

• Classification of images obtained with a multi-antenna structure by increasing the similarity to each other in the classification of human movements behind walls,

• Improving classification performance with fewer images.

The rest of the paper is organized as follows: Section 2 provides the autoencoder and dataset. Section 3 presents the experiments and results. The last section concludes the study.

2. Material and Method

2.1. Autoencoder

Autoencoders, unsupervised learning techniques that utilize neural networks for representation learning [29]. Essentially, it is a type of artificial neural network that attempts to learn the original representation of input data. Autoencoder can be used in many applications such as data compression, noise reduction, dimensionality reduction, and feature learning.

Autoencoder consists of two main components:

Encoder: The part that transforms the input data into a lower-dimensional representation.

Decoder: The part that reconstructs the original input data from the lower-dimensional representation generated by the encoder.

During the training of the autoencoder, the model first transforms the input data into a lower-dimensional representation with the encoder and then attempts to reconstruct the original data using the decoder. In this process, the model tries to minimize the difference between the input and output. Thus, the model learns the original representation of the input data.

Autoencoder is used to compress multi-dimensional data into hidden space first and then reconstruct the compressed data from the compressed hidden space [30]. The network

architecture consists of a neural network that creates a compressed representation of the original input and then recreates it. When input features are independent of each other, this compression and subsequent reconstruction become a very challenging task. However, if there is a kind of learnable structure in the data, this structure can be learned and used to force the input through the bottleneck of the network.

The network takes an unlabeled dataset as input and can be summarized as the reconstruction of the original input x in the framework of a supervised learning problem that produces the output x̂. The training of the network can be achieved by minimizing the reconstruction error L(x,x̂), which measures the differences between the original input and the reconstruction [31]. The bottleneck is a crucial step in the network; with the bottleneck, the input cannot directly pass to the output, thus preventing memorization.

The ideal autoencoder model should be sensitive enough to the inputs when reconstructing the outputs based on inputs. At the same time, sensitivity should not be too excessive for problems such as memorizing or overfitting the training data. This balance forces the model to preserve variations in the data required to reconstruct the input without retaining redundancies in the input. In most cases, this involves creating a loss function that encourages the model to be sensitive to the inputs (i.e., reconstruction loss L(x,x̂)) and another term that discourages memorization/overfitting (i.e., an additional regularizer).

Figure 1 shows the autoencoder structure used. A 104x40 pixel input image passes through two convolution layers with 3x3 kernel sizes to reach the fully connected layer. Then, the convolution operations are repeated in reverse, and the image is reconstructed. Here, the training process aims to obtain images similar to the target image from the input image. Two hidden layers are used in autoencoder. Layer sizes consist of 8 and 16 neurons, respectively. This structure was determined based on trial and error method and cross-validation results.
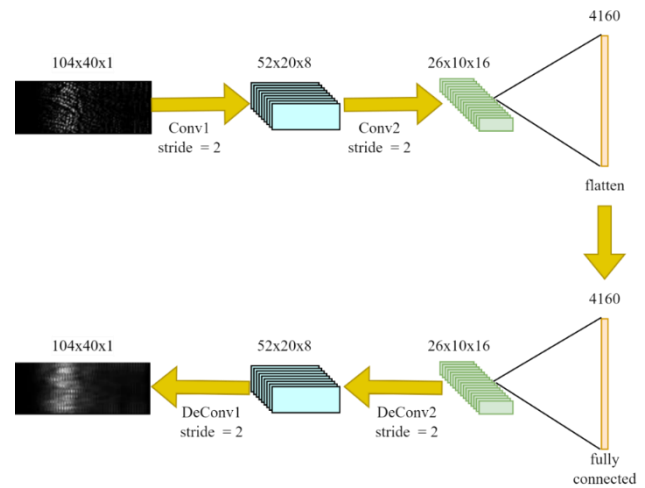
Figure 1. Autoencoder structure

2.2. CNN

Convolutional Neural Network (CNN) is a deep learning architecture widely used especially in image and video recognition, image classification, object detection and similar tasks. CNNs, unlike classical artificial neural networks, are much more successful in learning spatial and temporal relationships within data. Convolutional layer, activation function, pooling layer, fully connected layer are the basic components of CNN. The convolutional layer is applied by shifting filters (kernels) of certain sizes on the input data. Each filter is used to recognize certain features in the image, such as edges, corners. Each application of the filter produces an output called a feature map. Activation function is generally used to produce the output of the layer after convolutional layers. Pooling layer reduces the size of feature maps. Thus, computational cost and memory usage are reduced. The most commonly used type of pooling is Max Pooling, this type of pooling selects the maximum value in a particular region. The last layer, the fully connected layer, connects all neurons to each other, as in classical artificial neural networks. A flattened vector of feature maps is given as input to this layer. This layer is used as the last layer in classification tasks and provides probability distribution between classes with the softmax activation function [32]. The CNN architecture used in [11] is as shown in Figure 2. After 2 convolutional and pooling layers, output estimation is performed in the fully connected layer. The numbers of 3x3 sized kernels in the convolutional layers are 32 and 64, respectively.
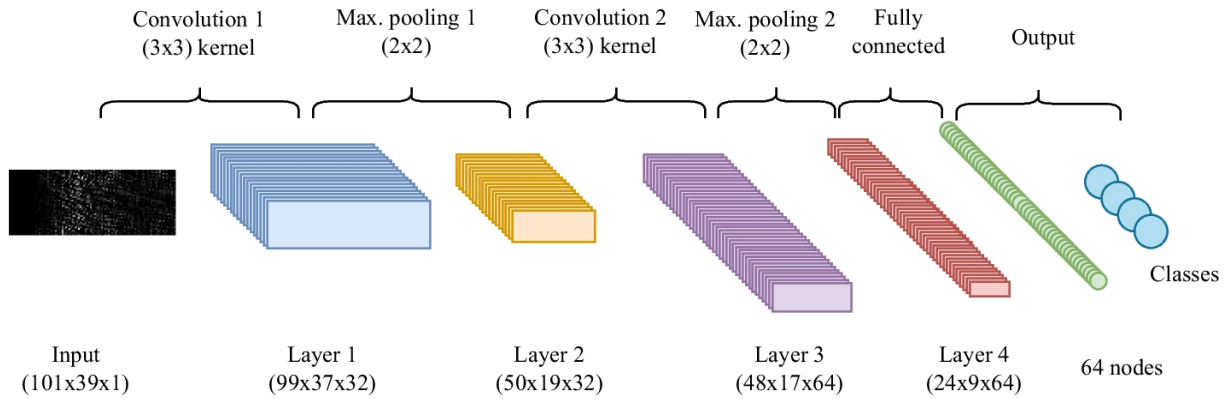
Figure 2. Used CNN model [11]

2.3. Dataset

The dataset used [11] consists of four human activities: running, walking with swinging arms, waving, and walking with steady arms. 50 samples were collected for each activity using 4 antennas. After obtaining grayscale images from the 4 antennas, the method described in Figure 3 [33] was used to double the signals using the negative and positive parts. Thus, there are a total of 1600 images in the dataset, with 400 images for each class. While the image dimensions are 101x39 pixels, they are resized to 104x40 pixels with zero padding to fit the input of the autoencoder. Due to the structure of the autoencoder, the images are reconstructed to be of size 104x40 pixels. Therefore, the original images are given to the autoencoder with zero padding to match the output size. Figure 4 shows the input and output images of the autoencoder for each class. Although the generated images may appear different from the original images, they will only be used in the training and testing of the classifier (CNN) in the study, hence they will not have a detrimental effect on the classification.
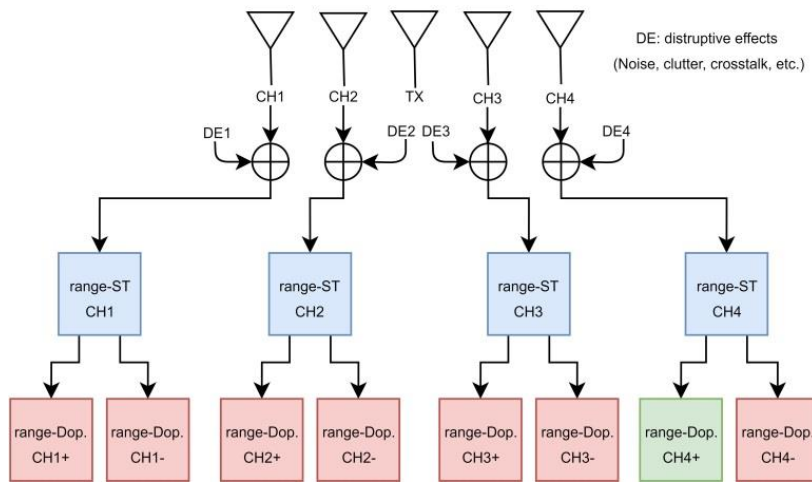
Figure 3. Antenna array [11]
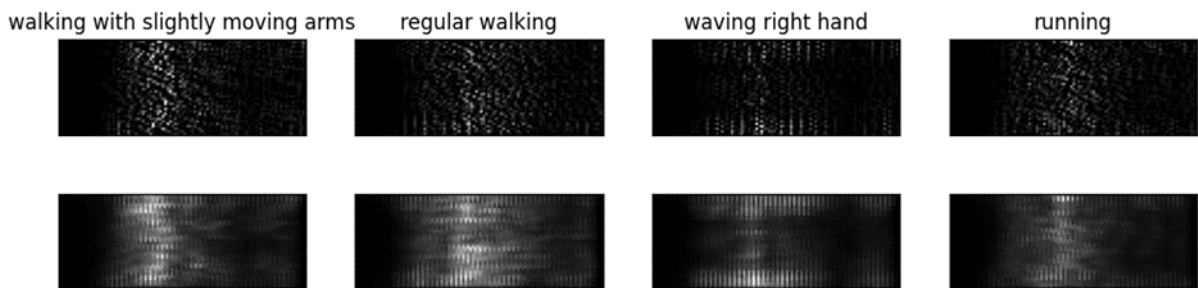
Figure 4. Original images (first row) and images created with autoencoder (last row)

2.4. Proposed Method

The proposed autoencoder-CNN architecture is as shown in Figure 5. The system reconstructs the images with Autoencoder before classification. The output of the Autoencoder is fed into CNN for classification, and as a result, the classes of the movements are obtained.
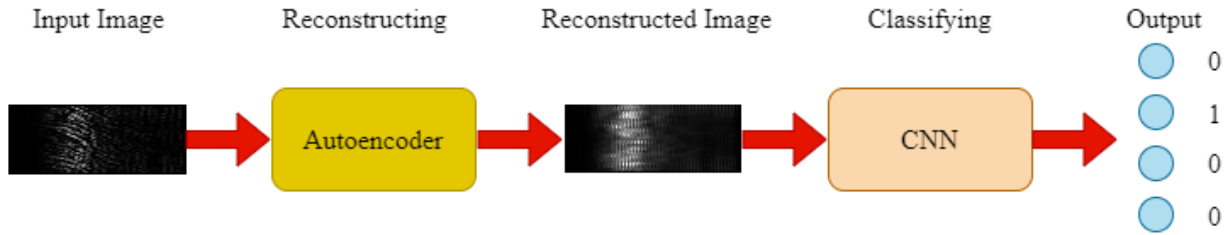
Figure 5. Proposed autoencoder-CNN hybrid model

3. Experimental Result and Discussion

For both the training and testing of the autoencoder, the dataset is further divided into two groups: one for reconstructing the input images and the other for the target images. To investigate the effect of image reconstruction by the autoencoder on CNN classification, the dataset [11] is divided into different groups and three approaches are tried. In [11], it is stated that during classification, ch4+ (the positive signal part of the 4th receiver antenna) yields better results compared to other channels. From this statement, it can be inferred that positive channels may perform better for classification compared to negatives. Therefore, in the experiments, the positive parts of the channels are used as target images for the autoencoder, while the negatives are used as input images to be reconstructed. In other words, the negative region images are attempted to be made similar to the positive ones. Additionally, care has been taken to ensure that the target and input images are taken from the same sample. Table 1 provides the images used for autoencoder training and testing for the three experiments. Table 2 presents the image channels and numbers classified with CNN in these experiments.

Table 1. Autoencoder train and test image channels

Experiment no	Train input	Train target	Test input	Test target
Experiment 1	Ch1-, Ch4-	Ch1+, Ch4+	Ch2-, Ch3-	Ch2+, Ch3+
Experiment 2	Ch1-, Ch4-	Ch1+, Ch4+	Ch2-, Ch3-	Ch2+, Ch3+
Experiment 3	Ch1-, Ch2-	Ch1+, Ch2+	Ch3-	Ch3+

Table 2. CNN train, test images channel and number

Experiment no	Used channels	Number of images
Experiment 1	Ch1+, Ch2+, Ch3+, Ch4+, Ch1-, Ch2-, Ch3-, Ch4-	1600
Experiment 2	Ch2-, Ch3-, Ch2+, Ch3+	800
Experiment 3	Ch4+	200

Table 3. Autoencoder parameters

Parametre	Chosen parameter
Epoch	15
Optimizer	Adam
Loss func	Mean Squerad Error (MSE)
Padding	Same
Activation func.	ReLu

In the three experiments for the autoencoder, the parameters listed in Table 3 have been utilized.

In Experiment 1, the classification success of the entire dataset, as observed in [11], was monitored. The dataset was divided into four parts for both training and testing of the autoencoder. According to the antenna arrangement depicted in Figure 3, the images from the two antennas farthest from each other were used for training, while the images from the other antennas were used for testing. After 15 epochs, the training error was 0.0060, and the test error was 0.0085. Following the training of the autoencoder, the

images from the entire dataset were reconstructed. These reconstructed images were randomly distributed and used for training and testing of the CNN.

In Experiment 1, since the first and fourth channels were used for training the autoencoder, when fed back into the autoencoder for classification in the CNN, there might be more similarity compared to the second and third channels. In other words, after successful autoencoder training, the channels used in training would be more similar to the ones used in testing. This similarity could lead to inconsistencies in the data. Therefore, performing classification in the CNN using data not used in the autoencoder training ensures balanced similarity across all data. In Experiment 2, the aim was to classify only the images used in the testing of the autoencoder. Thus, the success of classifying images not included in the training data of the autoencoder was monitored. After 15 epochs, the training error was 0.0047, and the test error was 0.0070. Since [11] did not present the classification results using only these images, the CNN from [11] was trained and tested using the original images.

In the final experiment, the effect of reconstructing the ch4+ images with the autoencoder, which exhibited the highest classification success in [11], was demonstrated. In this experiment, images from channels other than the fourth channel were used for both training and testing of the autoencoder, while the CH4- images were not used in either the autoencoder or the CNN. After 15 epochs, the training error was 0.0036, and the test error was 0.0065. The results of all experiments are presented in Table 4, based on the classification results of the images used in [11].

Table 4. Classification accuracy of CNN

Experiment no	Original images	Reconstructed images
Experiment 1	90.25% [11]	91.87%
Experiment 2	85.88%	91.12%
Experiment 3	84.50% [11]	93.00%

Upon examination of Table 4, it is observed that as the amount of data decreases in the original images, the classification success also decreases. Conversely, with the proposed method, the situation is reversed. Overall, in all experiments, it is evident that the images reconstructed with the autoencoder improve the classification success. In Experiment 1, where classification was performed with all images from [11], the accuracy rate increased by 1.62%. In Experiment 2, where only the test images

reconstructed by the autoencoder were used, significantly higher accuracy rates were achieved compared to the original images. With the proposed autoencoder-CNN hybrid method in this study, approximate values were obtained with less data in terms of accuracy. Since the training target images were also included in the CNN training and test data in Experiment 1, it is natural to observe higher classification success. The effect of the proposed method is very clear in Experiment 3. With only 200 ch4+ images, 8.50% higher accuracy was achieved compared to the original images. The accuracy value achieved in Experiment 3 is quite high compared to the results presented in [11]. It has been demonstrated that high accuracy can be achieved with the autoencoder without requiring a large amount of data.

Autoencoders can perform data cleaning by reducing noise. This can improve classification performance by reducing interference and noise in radar images. The hybrid model provides the combination of both low-dimensional feature representation and spatial features. This allows for a more powerful and effective data representation. Because hybrid models can learn both low-dimensional features and spatial layout, their generalization ability is generally high. This can be effective in recognizing different types of human movements.

Hybrid models generally require more computing power and memory. Training both Autoencoder and CNNs can be computationally intensive. The complexity of the hybrid model can create challenges during the design and training of the model. This requires careful adjustment of the model's settings and hyperparameters. Hybrid models generally require more data. Without a sufficient amount and variety of data, the model's ability to generalize may be limited.

Autoencoder training took approximately 10.45 seconds with NVIDIA Tesla K80 with 12GB of VRAM GPU. Memory usage was 1543.55 MB. Reconstructing an image with the autoencoder took approximately 0.55 μs. Classifying the reconstructed image with CNN takes 0.83 μs.

4. Conclusion and Suggestions

Autoencoders are deep learning methods used to reconstruct images. They take an input image, pass it through a convolution process, and then through a bottleneck before reconstructing the image through reverse convolution. In this study, an autoencoder-based approach is proposed to enhance the classification accuracy of radar images generated

with stepped-frequency continuous-wave (SFCWR) and Uniform Linear Array (ULA) structures. In the previous study [11], it was mentioned that when all images were used in CNN training and testing, the classification accuracy increased. However, in this study, unlike [11], the augmented data was used for training and testing the autoencoder. As a result, this paper demonstrates that the proposed autoencoder-CNN hybrid approach can achieve significantly higher accuracy with less data compared to the previous study.

Acknowledgment

Statement of Research and Publication Ethics

The study is complied with research and publication ethics.

References

[1] W. Heng, S. Solomon, and W. Gao, "Flexible electronics and devices as human–machine interfaces for medical robotics," *Advanced Materials*, vol. 34, no. 16, p. 2107902, 2022.

[2] M. Javaid, A. Haleem, S. Rab, R. P. Singh, and R. Suman, "Sensors for daily life: A review," *Sensors International*, vol. 2, p. 100121, 2021.

[3] D. S. Nunes, P. Zhang, and J. S. Silva, "A survey on human-in-the-loop applications towards an internet of all," *IEEE Communications Surveys & Tutorials*, vol. 17, no. 2, pp. 944-965, 2015.

[4] J. B. Awotunde, R. G. Jimoh, S. O. Folorunso, E. A. Adeniyi, K. M. Abiodun, and O. O. Banjo, "Privacy and security concerns in IoT-based healthcare systems," in *Internet of Things*, Cham: Springer International Publishing, 2021, pp. 105-134.

[5] A. E. Onoja, A. M. Oluwadamilola, and L. A. Ajao, "Embedded system based radio detection and ranging (RADAR) system using Arduino and ultra-sonic sensor," *American Journal of Embedded Systems and Applications*, vol. 5, no. 1, pp. 7-12, 2017.

[6] A. Biswas, S. Abedin, and M. A. Kabir, "Moving object detection using ultrasonic radar with proper distance, direction, and object shape analysis," *Journal of Information Systems Engineering and Business Intelligence*, vol. 6, no. 2, pp. 99-111, 2020.

[7] M. I. Skolnik, "Introduction to radar," *Radar handbook*, vol. 2, p. 21, 1962.

[8] A. M. Ponsford, L. Sevgi, and H. C. Chan, "An integrated maritime surveillance system based on high-frequency surface-wave radars. 2. Operational status and system performance," *IEEE Antennas and Propagation Magazine*, vol. 43, no. 5, pp. 52-63, 2001.

[9] A. Reigber et al., "Very-high-resolution airborne synthetic aperture radar imaging: Signal processing and applications," *Proceedings of the IEEE*, vol. 101, no. 3, pp. 759-783, 2012.

[10] S. Hazra and A. Santra, "Short-range radar-based gesture recognition system using 3D CNN with triplet loss," *IEEE Access*, vol. 7, pp. 125623-125633, 2019.

[11] Y. E. Acar, K. Ucar, I. Saritas, and E. Yaldiz, "Classification of human target movements behind walls using multi-channel range-doppler images," *Multimedia Tools and Applications*, pp. 1-18, 2023.

[12] X. Li, Y. He, and X. Jing, "A survey of deep learning-based human activity recognition in radar," *Remote Sensing*, vol. 11, no. 9, p. 1068, 2019.

[13]   H. T. Le, S. L. Phung, and A. Bouzerdoum, "Human gait recognition with micro-Doppler radar and deep autoencoder," *in 2018 24th International Conference on Pattern Recognition (ICPR), 2018*: IEEE, pp. 3347-3352.

[14]   Y. Shao, S. Guo, L. Sun, and W. Chen, "Human motion classification based on range information with deep convolutional neural network," *in 2017 4th International Conference on Information Science and Control Engineering (ICISCE), 2017: IEEE*, pp. 1519-1523.

[15]   P. van Dorp and F. Groen, "Feature-based human motion parameter estimation with radar*," IET Radar, Sonar & Navigation*, vol. 2, no. 2, pp. 135-145, 2008.

[16]   A. Sume et al., "Radar detection of moving targets behind corners," *IEEE Transactions on Geoscience and Remote Sensing*, vol. 49, no. 6, pp. 2259-2267, 2011.

[17]   X. Li, Z. Li, F. Fioranelli, S. Yang, O. Romain, and J. L. Kernec, "Hierarchical radar data analysis for activity and personnel recognition," *Remote Sensing*, vol. 12, no. 14, p. 2237, 2020.

[18]   J. Wang, Y. Chen, S. Hao, X. Peng, and L. Hu, "Deep learning for sensor-based activity recognition: A survey," *Pattern recognition letters*, vol. 119, pp. 3-11, 2019.

[19]   M. Zenaldin and R. M. Narayanan, "Radar micro-Doppler based human activity classification for indoor and outdoor environments," *in Radar Sensor Technology XX*, 2016, vol. 9829: SPIE, pp. 364-373.

[20]   F. Qi, H. Lv, F. Liang, Z. Li, X. Yu, and J. Wang, "MHHT-based method for analysis of micro-Doppler signatures for human finer-grained activity using through-wall SFCW radar," *Remote Sensing*, vol. 9, no. 3, p. 260, 2017.

[21]   M. He, Y. Nian, and Y. Gong, "Novel signal processing method for vital sign monitoring using FMCW radar," *Biomedical Signal Processing and Control*, vol. 33, pp. 335-345, 2017.

[22]   I. Seflek, Y. E. Acar, and E. Yaldiz, "Small motion detection and non-contact vital signs monitoring with continuous wave doppler radars," *Elektronika ir elektrotechnika*, vol. 26, no. 3, pp. 54-60, 2020.

[23]   G. Diraco, A. Leone, and P. Siciliano, "A radar-based smart sensor for unobtrusive elderly monitoring in ambient assisted living applications," *Biosensors*, vol. 7, no. 4, p. 55, 2017.

[24]   F. Fioranelli, J. Le Kernec, and S. A. Shah, "Radar for health care: Recognizing human activities and monitoring vital signs," *IEEE Potentials*, vol. 38, no. 4, pp. 16-23, 2019.

[25]   K. Hanifi and M. E. Karsligil, "Elderly fall detection with vital signs monitoring using CW Doppler radar," *IEEE Sensors Journal*, vol. 21, no. 15, pp. 16969-16978, 2021.

[26]   S. Z. Gurbuz and M. G. Amin, "Radar-based human-motion recognition with deep learning: Promising applications for indoor monitoring," *IEEE Signal Processing Magazine*, vol. 36, no. 4, pp. 16-28, 2019.

[27]   S. Nag, M. A. Barnes, T. Payment, and G. Holladay, "Ultrawideband through-wall radar for detecting the motion of people in real time," *in Radar Sensor Technology and Data Visualization*, 2002, vol. 4744: SPIE, pp. 48-57.

[28]   A. Krizhevsky and G. E. Hinton, "Using very deep autoencoders for content-based image retrieval," *in ESANN*, 2011, vol. 1: Citeseer, p. 2.

[29]   Z. Zhu, X. Wang, S. Bai, C. Yao, and X. Bai, "Deep learning representation using autoencoder for 3D shape retrieval," *Neurocomputing*, vol. 204, pp. 41-50, 2016.

[30] T. Liu, J. Wang, Q. Liu, S. Alibhai, T. Lu, and X. He, "High-ratio lossy compression: Exploring the autoencoder to compress scientific data," *IEEE Transactions on Big Data*, vol. 9, no. 1, pp. 22-36, 2021.

[31] Y. Jiang, H. Kim, H. Asnani, S. Kannan, S. Oh, and P. Viswanath, "Turbo autoencoder: Deep learning based channel codes for point-to-point communication channels," *Advances in neural information processing systems*, vol. 32, 2019.

[32] D. Bhatt et al., "CNN variants for computer vision: History, architecture, application, challenges and future scope," *Electronics*, vol. 10, no. 20, p. 2470, 2021.

[33] Y. E. Acar, I. Saritas, and E. Yaldiz, "An experimental study: Detecting the respiration rates of multiple stationary human targets by stepped frequency continuous wave radar," *Measurement*, vol. 167, p. 108268, 2021.

Bitlis Eren Üniversitesi Fen Bilimleri Dergisi

Thermal Power Plant Performance Analysis by Estimating Boiler Efficiency via Indirect Method: A Case Study

Pınar CELEN[1*], Hasan Hüseyin ERDEM[2]

[1]*Gümüşhane University, Gümüşhane Vocational School, Department of Electronics and Automation, Gümüşhane, Türkiye*
[2]*Yildiz Technical University, Faculty of Mechanical Engineering, Department of Mechanical Engineering, İstanbul, Türkiye*
(ORCID: 0000-0002-3369-143X) (ORCID: 0000-0002-3283-2229)

Abstract
In this paper, a coal (lignite) fired thermal power plant having capacity of 160 MW is taken into consideration and the impact of condenser pressure, moisture content of lignite, excess air coefficient, the efficiency of turbine pressure and heater numbers on power plant thermal efficiency is investigated. It is aimed to determine the performance losses of each equipment by means of thermodynamics and economic analysis. In this scope, it is expected that the power plant operator will be able to evaluate the reduction potential of equipment performance losses and ensure more effective use of the power plants by correctly planning the maintenance and rehabilitation needs and time. In the calculations, the boiler efficiency was determined with EN 12952-15 standard (indirect method) since this method has higher accuracy in coal-fired boilers. It is seen that the condenser pressure and excess air coefficient increments have no significant impact on power plant efficiency compared to moisture content of lignite, excess air coefficient, efficiency of turbine pressure and heater numbers. The significant effect is observed for fuel moisture content which rises from 22% to 47% and the power plant efficiency falls from 40% to 28%. The variation of the power plant thermal efficiency in case of failure of heaters is investigated and the power plant efficiency has decreased from 40.17% to 36.09% when the pre-heaters are no longer in to be in use because of any reason. In addition, revenue losses are estimated for each main equipment efficiency reduction for better use of power plant capacities and electricity lowering production costs.

1. Introduction

The energy needs of the world are increasing rapidly with the development of population and technology. One of these increasing needs can be stated as electrical energy and attention is directed to energy conversion plants. Among energy conversion plants, thermal power plants are commonly used to generate electricity all over the world and the energy produced in thermal power plants is related to the performance of the power plant. It is also known that about eighty percent of the world's power generation is provided by fossil fuels, with the other 20% depending on other types of energy sources such as nuclear energy or renewable energy sources, etc. [1],[2]. Since the

decrease in the performance of each equipment constituting the power plant affects the thermal efficiency and power generation, it increases the unit electricity production cost and causes a decrease in the revenues of the power plant [3]. Thus, many different parameters are used to determine the performance of thermal power plants. It is important to determine the parameters affecting the energetic performance of a power plant since it is directly related with generated electricity. The performance of power plants is very critical since it is directly related to operating and electricity production costs. Among the other different types of power plants, coal-fired ones have advantages such as reliability and low-cost fuel. There are several papers in the literature that

---

discuss the performances of coal-fired thermal power plants [4-16] and some of them are summarized as follows:

See and Coelli [9] investigated the technical efficiency levels of Malaysian thermal power plants and the extent to which various factors influence these plants' efficiency levels. Over eight years from 1998 to 2005, they used Stochastic Frontier Analysis (SFA) methods on plant-level data. Their empirical findings show that plant size and fuel type have a significant influence on technical efficiency levels, whereas plant age and peaking plant type have no statistically significant influence on Malaysian thermal power plant technical efficiencies.

Ahmadi and Toghraie [10] investigated the steam cycle of the Shahid Montazeri Power Plant in Isfahan, which has a capacity of 200 MW per unit. Analyses are carried out using EES (Engineering Equation Solver) software. The results of the energy analyses indicated that the condenser accounts for 69.8% of the total lost energy in the cycle, while exergy analysis identifies the boiler as the main equipment wasting exergy, accounting for 85.66% of the total exergy entering the cycle.

Oman et al. [11] investigated the effects of coal composition on the power plant in their study. In energy conversion, a significant heat loss occurs due to flue gas. In the study of electricity generating plants, they focused on the coal grinding and flue gas cleaning process. At 150°C flue gas temperature, when the excess air coefficient is increased by 10%, the total heat loss increases by 8% due to the heat dissipated by the flue gas, and an increase of 28% occurs when the excess air coefficient is increased by 50%. The findings of measurements and experiments on two power plant units were given in another study done by Oman et al. [11]. The processed coal is lignite, which has lower heating values between 9 and 10 MJ/kg, as well as ash and moisture concentrations of roughly 20% and 38%, respectively. The effect of lignite composition on heating value, boiler loss, boiler-specific steam generation, self-consumption of electricity, power consumption for coal grinding and flue gas desulphurization was explored.

Ganapathy et al. [12] calculated energy and exergy first law efficiency (energy efficiency) and the second law efficiency (exergy efficiency) of the 50MWe unit of lignite fired steam power plant at Thermal Power Station-I. The analyses show that 39% of the maximum energy losses occur in the condenser and 42.73% of the maximum exergy losses occur in the combustor.

Geete and Khandwawala [13],[14] presented a thermodynamic analysis to investigate the effect of back pressure and inlet temperature on the power and heat rate of the power plant. They considered a thermal power plant having capacity of 120 MW. They proposed power and heat rate correction curves for various condenser back pressures (in the range of 0.068-0.142 bar) and inlet temperatures (in the range of 507.78-567.78°C). They stated that the prediction of correction curves can be useful for thermal power plant design.

Vosough et al. [15] examined the energy and exergy analysis of the ideal preheated Rankine cycle and determined the largest energy losses in the cycle. After determining that the energy losses are predominantly in the condenser, they estimated the impact of condenser pressure on the performance of the cycle. It was observed that the maximum efficiency and output power decrease as the condenser pressure increases. In addition, they pointed out that the boiler is the primary source of irreversibility.

Huang et al. [16] researched the performance of a pressurized fluidized bed combustion power plant operated with ten different coal types. They aimed to investigate the effect of ash content, moisture content, sulfur content and calorific value of coal on overall efficiency. They concluded the ash content is the most effective parameter among them since the overall efficiency increased by 2.3% with the increment of ash content up to 40%.

The direct and indirect methods can be used in the calculation of boiler efficiency. While direct efficiency calculations do not provide any information about specific losses and their amounts, the indirect method allows to determine which equipment has low or high-capacity loss. In addition, the measurement errors do not have significant effect on efficiency in this method. In this study, Çan Thermal Power Plant, which is operated with lignite, was taken into consideration. The effect of condenser pressure, moisture content of lignite, excess air coefficient, efficiency of turbine pressure and heaters on power plant thermal efficiency and revenue loss were estimated by using Engineering Equation Solver Software [17]. For this purpose, the performance losses of each equipment were examined by means of thermodynamics and economic analysis. In the calculations, the boiler efficiency was determined with EN 12952-15 standard (indirect method) [18] since this method has higher accuracy in coal-fired boilers. The heat losses in the boiler (the losses due to flue gas, unburned CO, enthalpy and unburned combustibles in slag/flue dust and radiation /convection) were calculated according to this standard. In addition, the effect of these losses on the total efficiency of the power plant was calculated and the income loss caused by this in the power plant was

determined. It is expected that this research will be useful for the evaluation of the reduction potential of equipment performance losses and more effective use of the power plants.

2. Plant Description

Çan Thermal Power Plant, which is located in the town of Çan in Çanakkale, Türkiye, was considered in the current study. It is a coal (lignite) fired thermal power plant having capacity of 160 MW. The details of the thermal power plant's main equipment (such as boiler, generator, turbine, cooling system) are given in Table 1 [19]. The types, capacities and efficiencies of equipments can be seen in this table. Also, the schematic representation of Çan Thermal Power Plant is given in Figure 1. It can be classified as an ideal reheat–regenerative rankine cycle having one open feed water, six closed feed water heaters.

Steam enters the high pressure turbine at 17.2 MPa and 540°C and is condensed in the condenser at a pressure of 8.5 kPa. Some steam is extracted from the turbine at 4 MPa for the closed feedwater heater (K2) and the remaining steam is reheated at the same pressure to 540°C. There are 4 low pressure heaters, 2 high pressure heaters and one open feedwater heater to heat feedwater with extracted steam which is obtained from low, intermediate and high pressure turbines. The temperature of the steam is increased by passing through the preheaters and it enters the boiler at a temperature of 244.9 °C. The steam temperature, which was 330.5 °C at the exit from the high-pressure turbine, ix increased to 540 °C by applying the reheating process. The technical specification of Çan Thermal Power) are given in Table 2 [20].

The content of lignite used in the Çan Thermal Power Plant is given as follows: The percentages of ash, moisture, constant carbon, total sulfur and oxygen are 32%, 22%, 58%, 4.5% and 3%, respectively.

3. Calculation Method

Condenser pressure, boiler efficiency, turbine contamination and the use of preheaters significantly affect the efficiency of a thermal power plant. The performance of the thermal power plant considered in the study was evaluated with these parameters and the calculation procedure is given as follows:

Table 1. The details of the thermal power plant main equipment

Boiler	Coal	Turbine
Type Fluidized bed Lignite fired Capacity 128.6 kg/s vapour Efficiency 92%	Heating Value (Design) 2600± 10% kcal/kg (32% ash and 22% moisture) Heating Value (Revised) 2900± %10 kcal/kg (30% ash and 22% moisture) Stock Area Capacity 200.000 ton Capacity of Coal Belt Conveyors 166.7 kg/s	Type 3 Pressure stage Capacity 160 MW Rotation speed 3600 rpm Efficiency 45% General efficiency 42%
Generator	**Cooling System**	**Ash**
Type Synchronize Power 177 MVA Voltage 15 kV Cooling type Air cooling	Type Heller System Capacity 15800 m³/hour	Ash-slag amount 22.2 kg/s Ash Stock Area 800000 m²

The boiler efficiency is determined by using indirect method obtained from EN 12952-15 Standard (Water-tube boilers and auxiliary installations - Part 15: Acceptance tests) [18]. In this standard, the following equation is used for estimation of boiler efficiency as follows:

$$\eta_B = 1 - \frac{\dot{Q}_{L,tot}}{\dot{Q}_{Z,tot}} = 1 - \frac{\dot{Q}_{L,tot}}{\dot{Q}_Z + \dot{Q}_{ZF}} \tag{1}$$
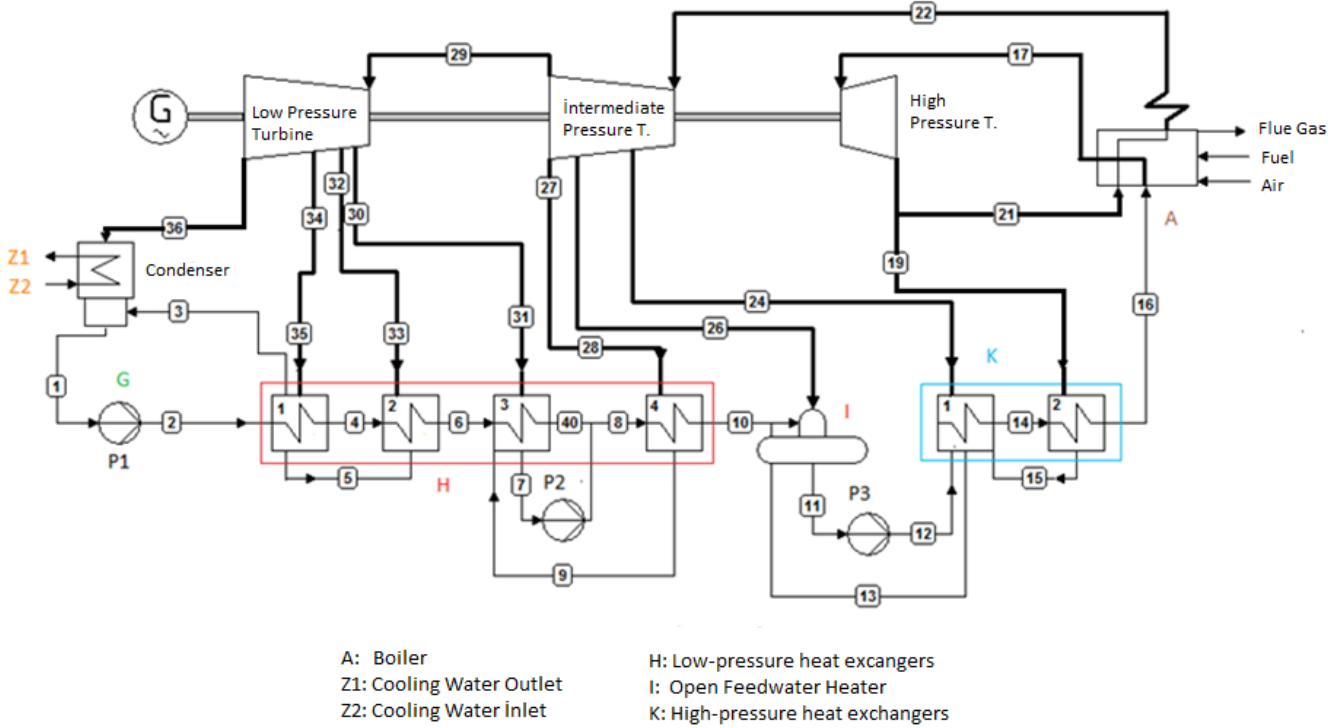
Figure 1. The schematic representation of Çan Thermal Power Plant [20]

The total heat input ($\dot{Q}_{Z,tot}$)is calculated as the sum of the heat credits ($\dot{Q}_Z$) and the heat input $\dot{Q}_{ZF}$), which is proportional to the flow rate of the burned fuel. The heat credit includes the amount of heat excluding chemical heat, coal mill power, circulating gas fan power, circulation pump power and powers of other drive motors. Moreover, if it is possible to measure atomizing steam flow the atomizing steam heat can be added to heat credits.

$$\dot{Q}_Z = P_M + P_{UG} + P + \dot{Q}_{SAE} + \dot{m}_{AS} h_{AS} \qquad (2)$$

$$\dot{Q}_{SAE} = \dot{m}_{SAE} (h_{SAE1} - h_{SAE2}) \qquad (3)$$

The heat input proportional to the burning fuel includes the heat obtained from fuel (chemical heat), the injected steam and in the combustion air and it is calculated as follows:

$$\dot{Q}_{ZF} = \dot{m}_F \left[\frac{H_{F,ref} + h_F}{1 - l_U} \right] + \mu_{AS}h_{AS} + J_A \qquad (4)$$

$$l_U = \frac{Y_{ash}\,(1-v)}{1 - Y_{ash} - Y_{H2O}} \frac{\dot{m}_{SL}\,u_{SL} + \dot{m}_{FA}\,u_{FA}}{\dot{m}_{SL}\,(1-u_{SL}) + \dot{m}_{FA}\,(1-u_{FA})} \qquad (5)$$

$$J_A = \dot{\mu}_A\, c_{pA}\, (T_A - T_r) \qquad (6)$$

Total heat loss in the boiler contains the losses due to flue gas ($\dot{Q}_G$), unburned CO ($\dot{Q}_{CO}$), enthalpy and unburned combustibles in slag ($\dot{Q}_{SL}$) and flue dust ($\dot{Q}_{FA}$) and radiation and convection ($\dot{Q}_{RC}$). The following equation is used to determine total heat loss as follows:

$$\dot{Q}_{L,tot} = \dot{Q}_G + \dot{Q}_{CO} + \dot{Q}_{SL} + \dot{Q}_{FA} + \dot{Q}_{RC} \qquad (7)$$

Flue gas losses can be determined by using the equation below if flue gas mass flow can be measured directly:

$$\dot{Q}_G = \dot{m}_G c_{p,G}(T_G - T_r) \qquad (8)$$

$$c_{p,G} = \frac{c_{p,TG}\,.\,T_G - c_{p,Tr}.\,T_r}{T_G - T_r} \qquad (9)$$

Unburned CO loss is estimated as follows:

$$\dot{Q}_{CO} = \dot{m}_F \dot{V}_{Gd} Y_{COd} H_{Con} \qquad (10)$$

$$V_{Gd} = V_{God} \frac{Y_{O2d}}{Y_{O2ad} - Y_{O2d}} \qquad (11)$$

$$V_{God} = -0.06018Y_F + 0.25437H^* \qquad (12)$$

$$H^* = H + 2.4425Y_{H2O} \qquad (13)$$

Slag and flue dusts are not taken into account if they contain very little unburned combustible materials.

$$\dot{Q}_{SL} = \dot{m}[\, c_{SL}\,(T_{SL} - T_r) + u_{SL}\,H_{UU}] \tag{14}$$
$$= \dot{m}_{SL}\,h_{SL}$$

$$\dot{Q}_{FA} = \dot{m}[\, c_{FA}\,(T_G - T_r) + u_{FA}\,H_{UU}] \tag{15}$$
$$= \dot{m}_{FA}\,h_{FA}$$

Since it is difficult to measure heat losses due to convection and radiation, empirical values are used for specification of them and it is calculated by using the following equation:

$$\dot{Q}_{RC} = C\,\dot{Q}_N^{0,7} \tag{16}$$

C value is equal to 0.0113, 0.0220 and 0.0315 for fuel-oil and natural gas boilers, hard coal boilers and lignite and fluidized bed boilers, respectively.

While calculating the useful heat output, the masses entering and leaving the boiler as in the TS EN 12952-15 standard are taken as basis. The useful heat output is estimated by using the following equation:

$$\begin{aligned}
\dot{Q}_N = \ & \dot{m}_{ST}(h_{ST} - h_{FW}) \\
& + \dot{m}_{SS}(h_{FW} - h_{SS}) \\
& + \dot{m}_{RHI1}(h_{RHI2} - h_{RHI1}) \\
& + \dot{m}_{SRI}(h_{RHI2} - h_{SRI}) \\
& + \dot{m}_{RHII1}(h_{RHII2} \\
& - h_{RHII1}) \\
& + \dot{m}_{SRII}(h_{RHII2} - h_{SRII}) \\
& + \dot{m}_{BD}(h_{BD} - h_{FW}) \\
& + \dot{m}_{SA}(h_{SA} - h)
\end{aligned} \tag{17}$$

In this study, the efficiency of thermal plant is estimated as follows:

$$\eta_{th} = \frac{\dot{w}_{net}}{\dot{q}_{in}} = 1 - \frac{\dot{q}_{out}}{\dot{q}_{in}} \tag{18}$$

One of the most effective parameters in calculating the cost of unit electricity production in thermal power plants is the fuel cost. Specific fuel consumption, which is defined as the amount of fuel required for a unit of energy, is calculated as follows:

$$b_e = \frac{3600}{\eta_t H_u} \tag{19}$$

Table 2. The technical specification of Çan Thermal Power [20]

Number	m (kg/s)	P (kPa)	T (C)	h (kJ/kg)
1	94.33	8.5	42.5	178
2	94.33	N/A	45.3	189.7
3	2.562	25.8	51.3	214.8
4	94.33	N/A	58.09	243.2
5	2.431	50.4	68.7	287.6
6	94.33	N/A	70.68	295.9
7	13.51	185.8	117.9	494.9
8	107.8	N/A	111.6	468.3
9	6.497	505.8	122.2	513.3
10	107.8	N/A	146.7	618.2
11	129.1	1008	176.4	747.5
12	129.1	20600	N/A	769.5
13	15.94	2098	191.8	816
14	129.1	N/A	N/A	908.3
15	9.45	3961	223.8	961.5
16	129.1	N/A	244.9	1061
17	129.5	17200	540	3397
18	129.5	4036	330.5	3043
20	9.45	3955	329.7	3041
21	120.1	4036	330.5	3041
22	120.1	3713	540	3540
24	6.488	2097	454.2	3366
26	5.313	1008	354.8	3167
27	6.497	521.4	269.7	3000
28	6.497	505.7	269.7	3001
29	100.4	521.4	267.6	2997
31	6.86	185.8	168.5	2807
33	2.139	52.56	84.6	2651
34	1.87	27.02	67	2621
35	1.87	25.9	65.8	2619
36	89.4	8.5	N/A	2399

Table 3. The work input of the pump, work output of turbines, heat inlet of the boiler and thermal efficiency of the power plant

$\dot{W}_{pump}$ (kW)	$\dot{W}_{LPT}$ (kW)	$\dot{W}_{MPT}$ (kW)	$\dot{W}_{HPT}$ (kW)	$\dot{W}_{T}$ (kW)	$\dot{Q}_{in}$ (kW)	η_{th}
4.302	56.495	61.885	45.781	164.161	362.368	0.401

The unit energy fuel cost is obtained by multiplying the specific fuel consumption and the fuel price as follows [21]:

$$c_f = Fb_e \qquad (20)$$

Revenue of the plant with unit power is determined as follows:

$$c_N = \dot{W}_{net}F_e \qquad (21)$$

Revenue losses in the power plant due to variable parameters are the difference between unit energy fuel cost and the income generated by the plant with unit power and it is estimated as follows:

$$RL = c_f - c_N \qquad (22)$$

4. Results and Discussion
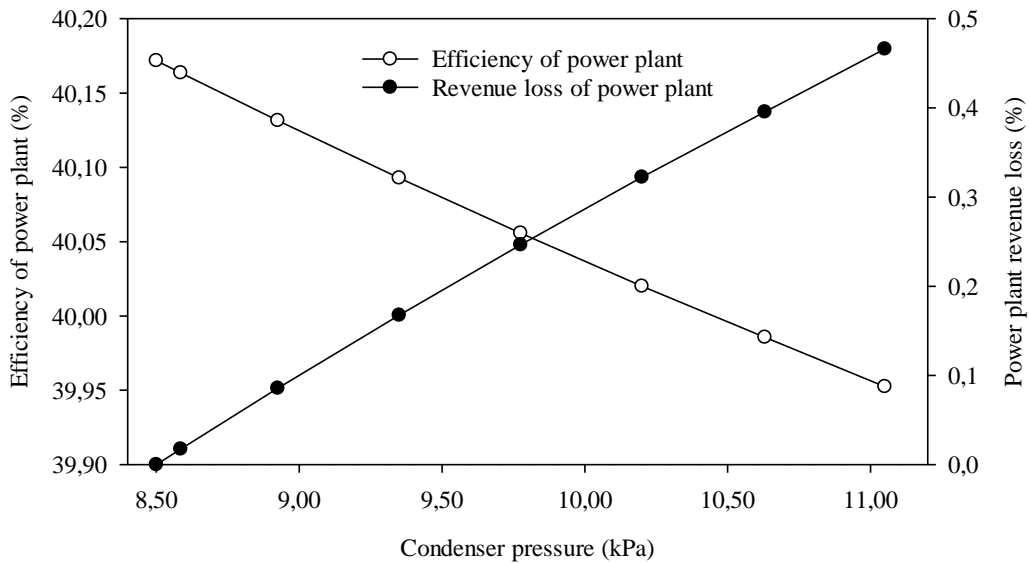
Figure 2. The effect of condenser pressure on power plant thermal efficiency and revenue loss

The thermodynamic analyses of the considered thermal power plant are determined by means of equations given in the previous section. Firstly, the thermal efficiency of the power plant was estimated for design operation conditions. Then, the thermal efficiency decrease due to the changing working conditions was determined in case of any failure in the equipment by keeping the heat entering the boiler constant. According to the determined efficiency results, the revenue losses in the power plant were calculated by considering unit electricity price (2.25 cents/kWh) and unit fuel cost (0.31 cent/kg) [21]. Table 3 shows the work input of the pump, work output of turbines, heat inlet of the boiler and thermal efficiency of the power plant.

Since the condenser pressure determines the output conditions of the low pressure turbine, it directly affects the power that can be produced from the turbine. Moreover, it is known that there is a decrease in efficiency with rising condenser pressure.
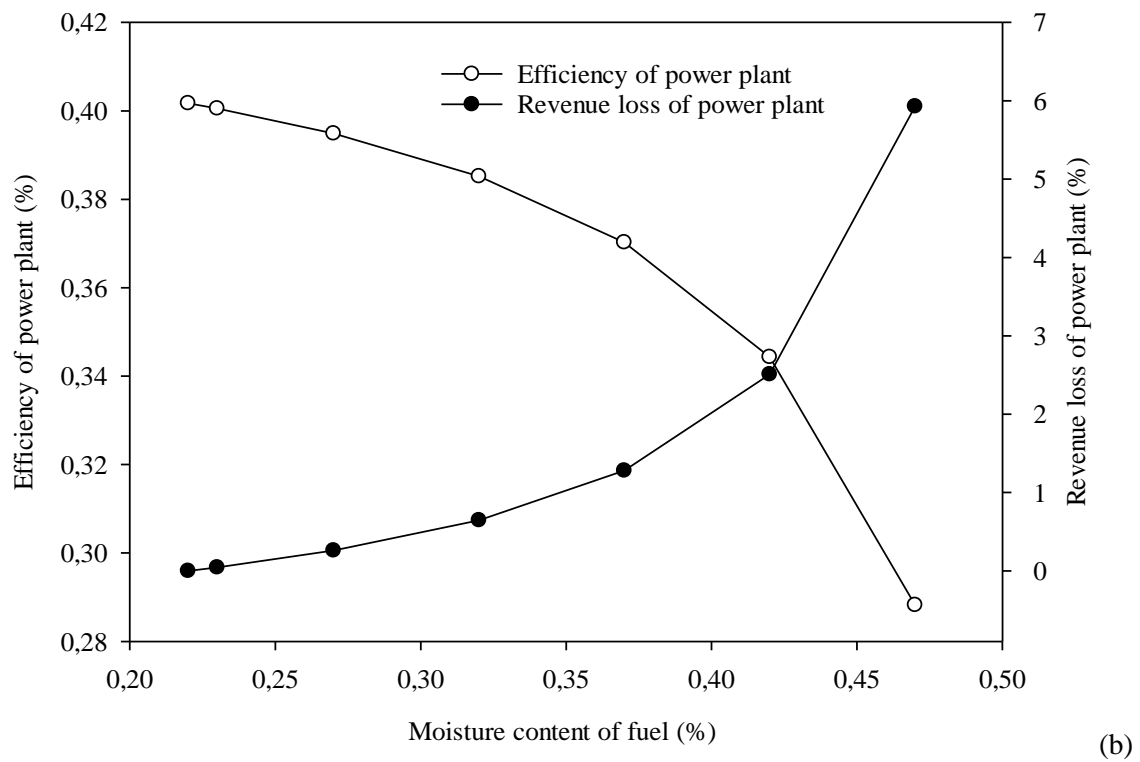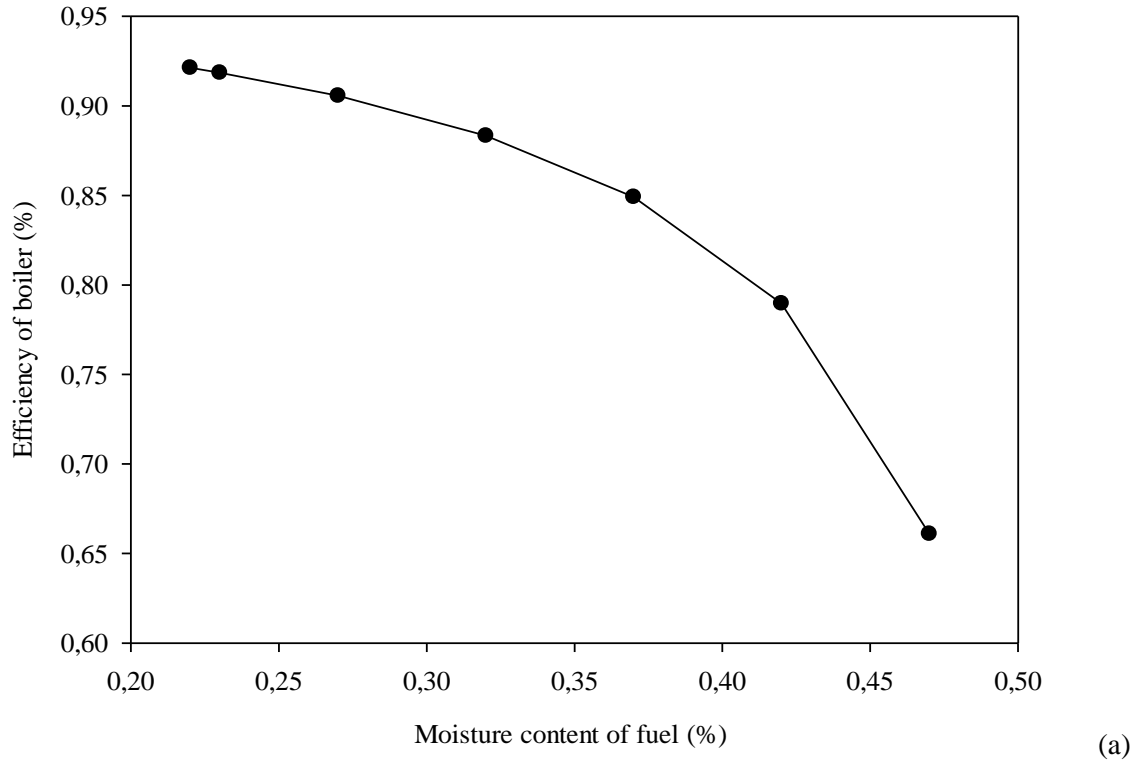
Figure 3. The impact of fuel moisture content increment on (a) the boiler efficiency (b) power plant thermal efficiency and revenue loss

(a)

(b)
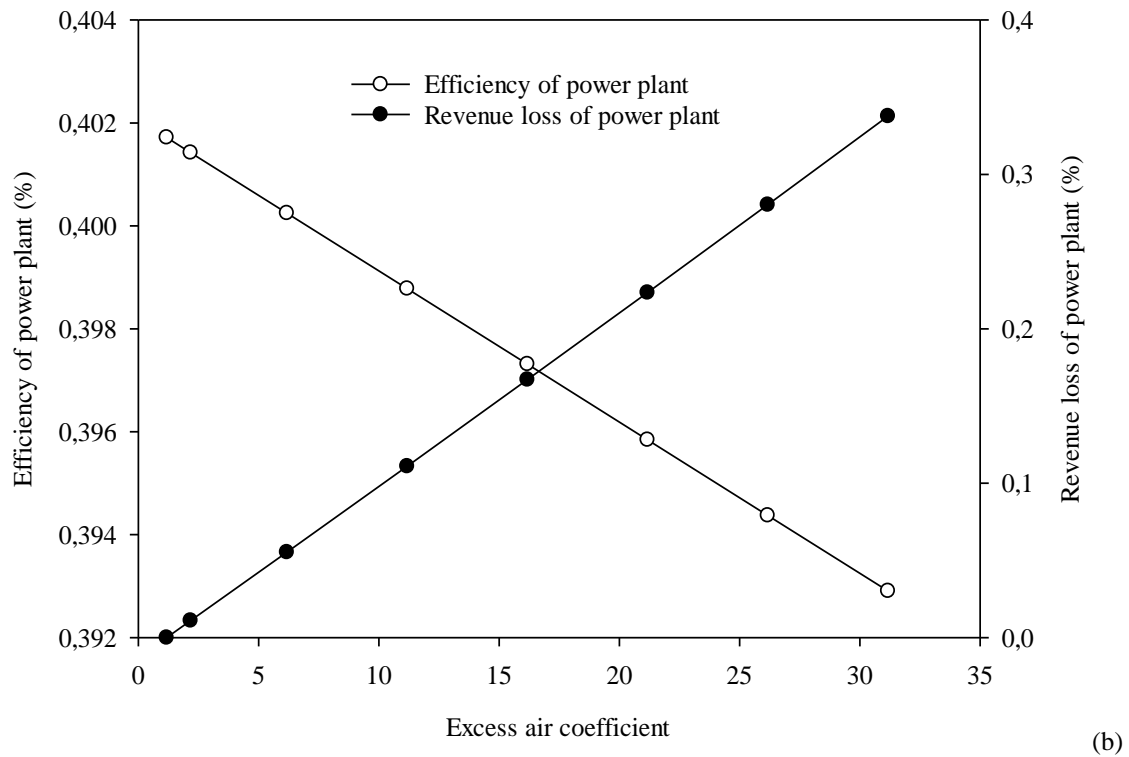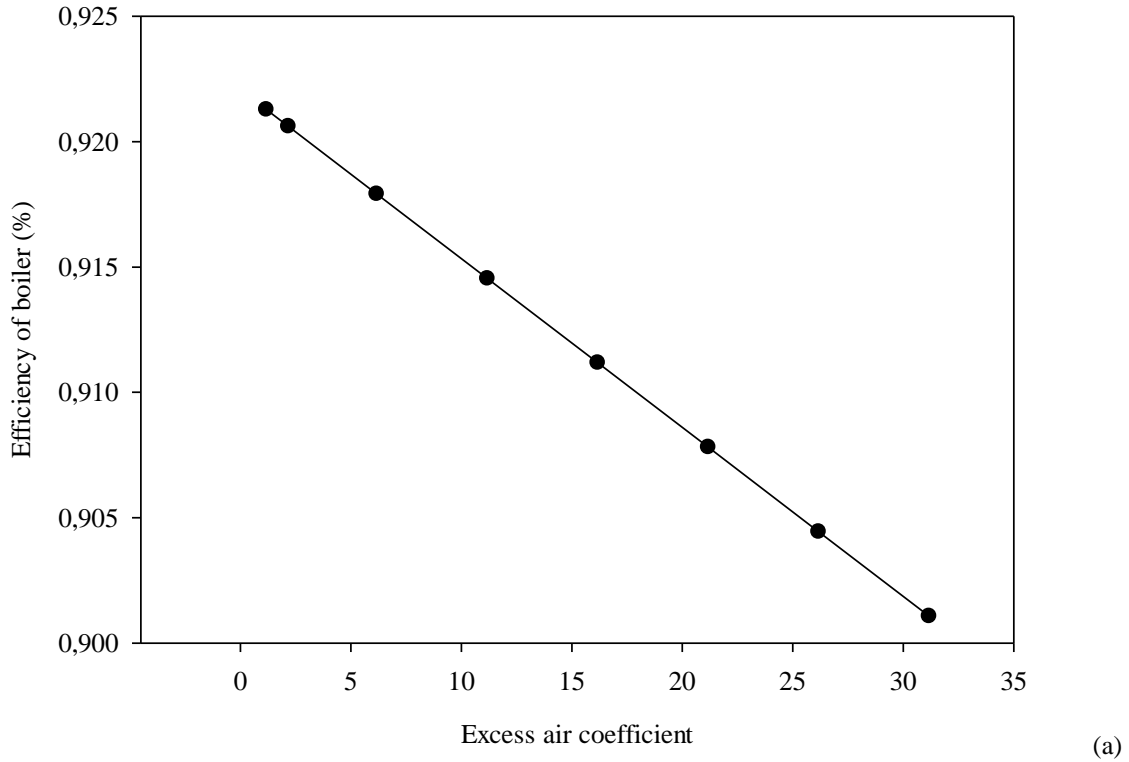
Figure 4. The effect of excess air coefficient increments on (a) the boiler efficiency (b) thermal efficiency and revenue

loss

The effect condenser pressure increment on the reduction of thermal efficiency and revenue loss variation were presented in Figure 2. It can be observed that the thermal efficiency reduces with the increment of condenser pressure as shown in Figure 2. The thermal efficiency of the power plant decreases from 40.17% to 39.95% for the condenser pressures of 8.5 kPa and 11.5 kPa, respectively. In other words,

the reduction in thermal efficiency was determined at 0.22% with the increment of condenser pressure to 30% since the amount of heat entering the boiler remained constant despite the decreasing turbine power when the condenser pressure increased. Also, Figure 2 depicts the variation of revenue loss with the increment of condenser pressure. The increment of condenser pressure up to 30% corresponds to 0.48% revenue loss. The cost of revenue lost is approximately equal to 126134 $/year.

In coal-fired thermal power plants, the boiler is designed according to coal with certain chemical and physical properties, and when the coal has these properties, it performs by the design values. In cases where coal properties change, the thermal efficiency and performance of the unit are directly affected. If the amount of water contained in the coal is higher than the design value, it will cause blockages in the system, plastering, excessive material wear and reduction in the boiler combustion chamber temperature, which will adversely affect the power plant load and efficiency. Figures 3(a) and 3(b) represent the impact of fuel moisture content increment on the boiler efficiency, thermal efficiency and revenue loss, respectively. In Figure 3(a), the fuel moisture content rises from 22% to 47%, the boiler efficiency falls from 92% to 66%, respectively. In Figure 3(b), when the fuel moisture content reaches 47%, the thermal efficiency of the power plant reduces to 28%. The reason of both them can be explained with the reduction in the heating value of fuel with elevated moisture content. The revenue loss is equal to 4.25% and the cost of revenue lost is approximately equal to 1095623 $/year.

The effect of excess air coefficient increment on the boiler efficiency, power plant thermal efficiency and revenue loss was shown in Figure 4(a) and Figure 4(b), respectively. It can be observed that both the boiler and power plant efficiencies diminish by 2% and 1% with the variation of excess air coefficient in the range between 1.17 and 31.17, respectively.
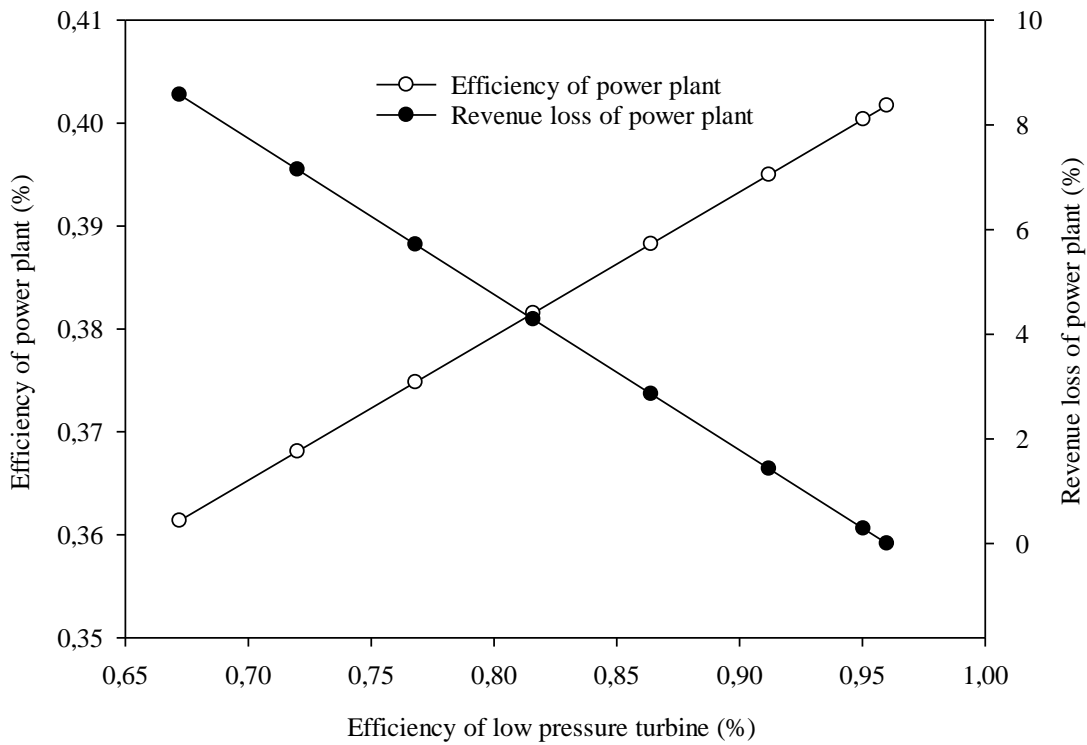
Figure 5. The effect of low pressure turbine efficiency reduction on the power plant thermal efficiency and revenue loss

It is known that the more excess air coefficient results in increased flue gas losses which clarifies the reduction in efficiencies. Moreover, the highest revenue loss was obtained as 62404 $/year for the highest excess air coefficient which is 31.17.

The performance loss of steam turbines is seen directly as a reduction in power generation. Wear and contamination and decrease the turbine isentropic efficiency. The effects of low pressure turbine contamination on the power plant's thermal efficiency and revenue loss were depicted in Figure 5. It should be noted that the reason for turbine efficiency decrement is contamination. It can be seen that these parameters increase as low pressure turbine

contamination increases. If the low pressure turbine efficiency decreases to 67% from 96%, the power plant efficiency reduction is 4%. The cost of revenue is approximately 2320292 $/year.

Figure 6 represents the variation in power plant efficiency with intermediate pressure turbine efficiency. By reducing the turbine efficiency by 30%, the power plant efficiency decreased from 40.17% to 40.08%. The revenue loss increased by 0.19% as seen in Figure 6 corresponding to 52515 $/year.

The change in power plant efficiency with different high pressure turbine efficiencies was given in Figure 7 and it can be seen that the power plant efficiency decreased from 40.17% to 36.71% where high pressure turbine efficiency reduced from 84% to 59%. Thus, the income of the power plant diminished

by 7.33% according to Figure 7 and it is equal to 1985386 $/year.

It is well known that a thermal power plant can encounter the failure of preheaters. In case of failure of them, the thermal power plant efficiency decreases. The variation of the power plant thermal efficiency and revenue loss were determined by considering that the feed water pre-heaters in the plant are out of service and the results were given in Table 4. It can be understood that the power plant's thermal efficiency reduces with the increment number of pre-heaters. According to the results, it is observed that the power plant efficiency has decreased from 40.17% to 36.09% when the pre-heaters are no longer in to be in use because of any reason. Plant revenue decreased by 9.4%, this loss corresponds to 2434661 $.
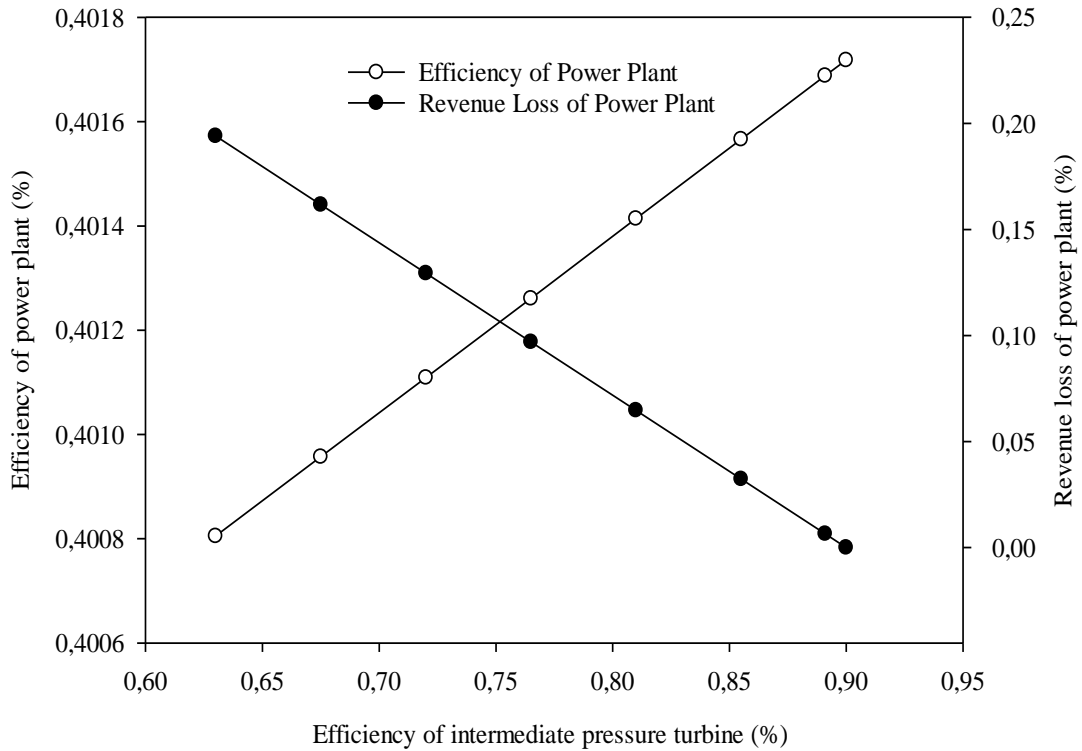
Figure 6. The effect of intermediate pressure turbine efficiency reduction on the power plant thermal efficiency and revenue loss
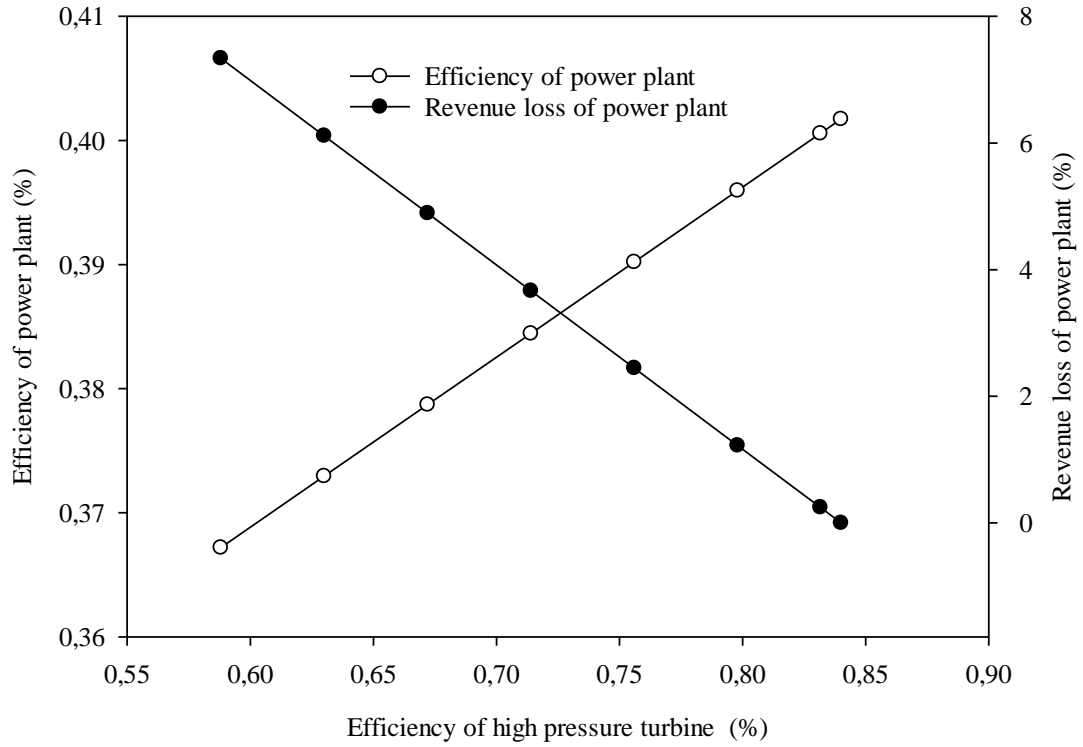
Figure 7. The effect of high pressure turbine efficiency reduction on the power plant thermal efficiency and revenue loss

Table 4. The variation of the power plant thermal efficiency and revenue loss in case of failure of heaters

	η_{th}	Annual Revenue Loss ($/year)	Annual Revenue Loss (%)
All pre-heaters are in use	0.402	0	0
Pre-heater (H1) is not in use	0.394	477637	1.9
Pre-heaters (H1) and (H2) are not in use	0.385	980542	3.8
Pre-heaters (H1), (H2) and (H3) are not in use	0.363	2277271	8.8
Pre-heaters (H1), (H2), (H3) and (H4) are not in use	0.355	2773364	10.8
Pre-heaters (H1), (H2), (H3), (H4) and (K1) are not in use	0.353	2903102	11.3
Pre-heaters (H1), (H2), (H3), (H4), (K1) and (K2) are not in use	0.360	2434661	9.4

5. Conclusion

In this study, the factors affecting performance in thermal power plants were determined by using thermodynamic analysis. Firstly, the boiler efficiency of the selected coal-fired thermal power plant was estimated using EN 12952-15 standard (indirect method) and power plant thermal efficiency was determined. Then, the parameters that reduce the efficiency of each equipment (condenser, boiler, turbines, and heaters) were determined and their impact on overall efficiency was researched for various operation conditions. In addition, the economic value of performance reduction was calculated. The main outputs of this research were given as follows:

•   When the condenser pressure, which is 8.5 kPa at nominal power, is increased up to 30% (11.5kPa), the power plant efficiency was slightly decreased. Revenue loss for this difference was determined as 126134 $.

•   According to EN 12952-15 standard, total heat input (the amount of heat excluding chemical heat, coal mill power, circulating gas fan power, circulation pump power and powers of other drive motors and chemical heat) and total heat loss (due to flue gas, unburned CO, enthalpy and unburned combustibles in slag and flue dust and radiation and convection) were estimated to get more accurate results boiler efficiency.

•   When the moisture content of the fuel was increased, the lower heating value of the fuel decreased so the boiler efficiency decreased. The fuel moisture content rises from 22% to 47%, the boiler efficiency falls from 92% to 66%, respectively. The revenue loss of the plant due to the decrease in efficiency was 1095623 $.

•   The increase of excess air coefficient increases the heat loss due to flue gas from the plant. Thus, both boiler and power plant efficiencies decreased by 2% and 1%, respectively. The revenue loss related to excess air coefficient was estimated 62404 $.

•   The efficiencies of the low, intermediate and high pressure turbines were reduced by 30% to investigate turbine contamination effect. Among these turbines, significant turbine efficiency losses were seen in the low and high pressure turbines compared to intermediate one. The highest revenue loss equals 2320292 $ for low pressure turbine.

•   When the feed water heaters were not in use, the boiler feed water inlet temperature gradually decreased. The power plant efficiency has decreased by approximately 4% when all pre-heaters are no longer in to be in use for any reason. Thus, the turbine power and the thermal efficiency of the power plant decreased and the annual income loss increased which is equal to 2434661 $/year.

Nomenclature

c_F	Specific heat of fuel, kJ/kgK
c_{SL}	Specific heat of slag, kJ/kgK
c_{pA}	Specific heat of combustion air, kJ/kgK
c_{PG}	Integral specific heat between T_G and T_r of flue gas, kJ/kgK
c_{FA}	Specific heat of flue dust, kJ/kgK
h_{FW}	Feed water enthalpy, kJ/kg
h_{ST}	Active vapour enthalpy, kJ/kg
h_{SS}	Atomizing water enthalpy at the system inlet, kJ/kg
h_{BD}	Blowdown water enthalpy, kJ/kg
h_{RHI1}, h_{RHII1}	Reheated steam enthalpy, kJ/kg
h_{SRI}, h_{SRII}	Atomizing water into reheated steam enthalpy, kJ/kg
h_{SA}	Air heater enthalpy, kJ/kg
h_{SAE1}	Air heater inlet enthalpy, kJ/kg
h_{SAE2}	Air heater condensate enthalpy, kJ/kg
h_{fuel}	Fuel enthalpy, kJ/kg
h_{AS}	Atomizing steam enthalpy (NCV calculation), kJ/kg
H_{UU}	NCV of unburned combustibles, kJ/kg
H_K	NCV of fuel at reference temperature, kJ/kg
H_{COn}	Calorific value per m^3 of CO in standard conditions), kJ/m^3
J_A	Combustion air enthalpy (NCV calculation), kJ/kg
l_U	The ratio of unburned to supplied fuel mass flow rates

$\dot{m}_{RHI1}, \dot{m}_{RHII1}$	Reheated steam mass flow rate, kg/s
$\dot{m}_{SS}$	Atomizing water mass flow rate for main steam cooler, kg/s
$\dot{m}_{SRI}, \dot{m}_{SRII}$	Atomizing water for reheated steam mass flow rate, kg/s
$\dot{m}_{BD}$	Blowdown water mass flow rate, kg/s
$\dot{m}_S$	The water flow rate of the atomizing steam, kg/s
$\dot{m}_{SA}$	Air heater mass flow rate, kg/s
$\dot{m}$	Hot water mass flow rate, kg/s
$\dot{m}_F$	Fuel mass flow rate, kg/s
$\dot{m}_{AS}$	Atomizing steam mass flow, kg/s
$\dot{m}_G$	Flue gas mass flow rate, kg/s
$\dot{m}_{FA}$	Flue dust mass flow rate, kg/s
$\dot{m}_{SL}$	Slag mass flow rate, kg/s
$\dot{\mu}_A$	Combustion air mass to fuel mass ratio
μ_{AS}	Atomizing steam mass flow rate, kg/s
P_M	Pulverizer power, kW
P_{UG}	Recirculating gas fan power, kW
P	Other electric power, kW
T_A	Air temperature at envelope boundary, °C
T_G	Flue gas temperature, °C
T_r	Reference temperature, °C
T_{SL}	Slag temperature, °C
u_{SL}	Unburned combustibles content of slag
u_{FA}	Unburned combustibles content of flue dust
V_{God}	Flue gas volume at standard pressure (1 bar) and temperature (0°C), m³/kg
V_{Gd}	Dry flue gas volume, m³
Y_{O2d}	Oxygen content of dry flue gas
Y_{O2ad}	Oxygen content of dry air (0.20938 m³/m³)
Y_{COd}	CO content by volume of dry flue gas
$\dot{Q}_G$	Flue gas losses, kW
$\dot{Q}_N$	Useful heat output, kW
$\dot{Q}_{L,tot}$	Total losses, kW
$\dot{Q}_{RC}$	Losses due to radiation and convection, kW
$\dot{Q}_{CO}$	Loss due to unburned CO, kW
$\dot{Q}_Z$	Heat credits, kW
$\dot{Q}_{ZF}$	Heat input proportional to fuel burned, kW
$\dot{Q}_{Z,tot}$	Total heat input, kW
η_B	Boiler efficiency
η_{th}	Overall power plant efficiency
γ_{H20}	Moisture content of fuel
γ_{Ash}	Ash content in fuel

Conflict of Interest Statement

There is no conflict of interest between the authors.

Statement of Research and Publication Ethics

The study is complied with research and publication ethics.

References

[1] H. H. Erdem et al., "Comparative energetic and exergetic performance analyses for coal-fired thermal power plants in Turkey," *Int. J. Therm. Sci.*, vol. 48, no. 11, pp. 2179–2186, 2009, doi: https://doi.org/10.1016/j.ijthermalsci.2009.03.007.

[2] M. H. Ahmadi *et al.*, "Thermodynamic and economic analysis of performance evaluation of all the thermal power plants: A review," *Energy Sci. Eng.*, vol. 7, no. 1, pp. 30–65, 2019, doi: https://doi.org/10.1002/ese3.223.

[3] S. C. Kaushik, V. S. Reddy, and S. K. Tyagi, "Energy and exergy analyses of thermal power plants: A review," *Renew. Sustain. Energy Rev.*, vol. 15, no. 4, pp. 1857–1872, 2011, doi: https://doi.org/10.1016/j.rser.2010.12.007.

[4] O. J. Khaleel, T. K. Ibrahim, F. B. Ismail, and A. T. Al-Sammarraie, "Developing an analytical model to predict the energy and exergy based performances of a coal-fired thermal power plant," *Case Stud. Therm. Eng.*, vol. 28, pp. 1-20, 2021, doi: https://doi.org/10.1016/j.csite.2021.101519

[5] S. Kumar, D. Kumar, R. A. Memon, M. A. Wassan, and S. A. Mir, "Energy and exergy analysis of a coal fired power plant," *Mehran Univ. Res. J. Eng. Technol.*, vol. 37, no. 4, pp. 611–624, 2018, doi: https://doi.org/10.22581/muet1982.1804.13

[6] M. N. Eke, D. C. Onyejekwe, O. C. Iloeje, C. I. Ezekwe, and P. U. Akpan, "Energy and exergy evaluation of a 220MW thermal power plant," *Niger. J. Technol.*, vol. 37, no. 1, p. 115, 2018, doi: https://doi.org/10.4314/njt.v37i1.15.

[7] P. Regulagadda, I. Dincer, and G. F. Naterer, "Exergy analysis of a thermal power plant with measured boiler and turbine losses," *Appl. Therm. Eng.*, vol. 30, no. 8–9, pp. 970–976, 2010, doi: https://doi.org/10.1016/j.applthermaleng.2010.01.008.

[8] M. Tontu, B. Sahin, and M. Bilgili, "Using energy and exergy analysis to compare different coal-fired power plants," *Energy Sources Recovery Util. Environ. Eff.*, pp. 1–16, 2019, doi: https://doi.org/10.1080/15567036.2019.1696429.

[9] K. F. See and T. Coelli, "An analysis of factors that influence the technical efficiency of Malaysian thermal power plants," *Energy Econ.*, vol. 34, no. 3, pp. 677–685, 2012, doi: https://doi.org/10.1016/j.eneco.2011.09.005.

[10] G. R. Ahmadi and D. Toghraie, "Energy and exergy analysis of Montazeri Steam Power Plant in Iran," *Renew. Sustain. Energy Rev.*, vol. 56, pp. 454–463, 2016, doi; https://doi.org/10.1016/j.rser.2015.11.074.

[11] J. Oman, A. Senegačnik, and B. Dejanovič, "Influence of lignite composition on thermal power plant performance," *Energy Convers. Manag.*, vol. 42, no. 3, pp. 251–263, 2001, doi; https://doi.org/10.1016/S0196-8904(00)00062-5.

[12] T. Ganapathy et al., "Exergy analysis of operating lignite fired thermal power plant," *J. Eng. Sci. Technol. Rev.*, vol. 2, no. 1, pp. 123–130, 2009, doi: https://doi.org/10.25103/jestr.021.23

[13] A. Geete and A. I. Khandwawala, "Thermodynamic analysis of 120MW thermal power plant with combined effect of constant inlet pressure (127.06 bar) and different condenser back pressures," *IUP J. Mech. Eng.*, vol. 7, no. 1, pp. 25-46, 2014.

[14] A. Geete and A. I. Khandwawala, "Thermodynamic analysis of 120MW thermal power plant with combined effect of constant inlet pressure (124.61 bar) and different inlet temperatures," *Case Stud. Therm. Eng.*, vol. 1, no. 1, pp. 17–25, 2013, doi; https://doi.org/10.1016/j.csite.2013.08.001.

[15] A. Vosough, A Falahat, and S. Vosough, "Improvement power plant efficiency with condenser pressure," *Int. J Multidiscip. Sci. Eng.*, vol. 2, no. 3, pp. 38–43, Jan. 2011.

[16] Y. Huang, J. T. McMullan, and B. C. Williams "Influences of coal type on the performance of a pressurised fluidised bed combustion power plant," *Fuel*, vol. 79, no. 13, pp. 1595–1601, 2000, doi; https://doi.org/10.1016/S0016-2361(00)00022-3.

[17] Engineering Equation Solver (EES), F-Chart Software, Middleton, WI, ABD.

[18] European Standards, EN 12952-1Water-tube boilers and auxiliary installations - Part 1: General (2001).

[19] T. C. Elektrik Üretim Anonim Şirketi (EÜAŞ), "18 Mart Çan Termik Santrali," [Çevrimiçi]. Erişilebilir: https://www.euas.gov.tr/santraller/18-mart-can. [Erişim: 20-May-2023].

[20] Z. Oktay, "Investigation of coal-fired power plants in Turkey and a case study: Can plant," *Appl. Therm. Eng.*, vol. 29, no. 2–3, pp. 550–557, 2009, doi; https://doi.org/10.1016/j.applthermaleng.2008.03.025.

[21] T. C. Elektrik Üretim Anonim Şirketi (EÜAŞ), Yıllık Rapor 2021, Türkiye.

Evaluation of Earthquake Performance of Reinforced Concrete Buildings with Fuzzy Logic Method

Mehmet Ali YILDIZ[1], Fırat KIPÇAK[2*], Barış ERDİL[3]

[1]Van Yüzüncü Yıl University, Civil Eng. Department, Master Student, Van, Türkiye
[2]Van Yüzüncü Yıl University, Department of Construction. Lecturer., Van, Türkiye
[3]Van Yüzüncü Yıl University, Civil Eng. Department, Assoc. Prof. Dr., Van, Türkiye
(ORCID: 0000-0003-3297-2982)[1] (ORCID: 0000-0003-3849-7545)[2] ,(ORCID: 0000-0001-5282-3568)[3]

Abstract

A reinforced concrete building is a type of building whose structural system consists of reinforced concrete columns, beams, shear walls, slabs, and foundations. It has been observed that reinforced concrete buildings have been severely damaged or collapsed even in moderate shaking. Evaluating buildings after earthquakes and their performances are quite important for the safety of life and property. In the literature, different methods have been developed for pre-earthquake evaluation of buildings, either low-cost and rapid or slow and high-cost and tool-demanding. In this study, in order to overcome the gap in the literature, the evaluation of the earthquake performance of buildings with the fuzzy logic method is discussed. In this context, the buildings' performance was evaluated by considering the concrete compressive strength, number of stories, ground floor area, area of column and shear walls, and architectural parameters. The data of 18, 28, and 146 buildings affected by the earthquakes in Afyon, Bingöl, and Van provinces in 2002, 2003, and 2011, respectively, were used in the study. Out of the 192 building data, 94 buildings were processed as data, and fuzzy logic rules available in Matlab were applied. The remaining 98 buildings were tested with this method. The buildings considered are light, moderate, and severely damaged or collapsed. The proposed method can be classified as rapid tier two (or level two) evaluation. According to the results, an 88% success rate was achieved which indicates the importance of the fuzzy logic method that can be utilized in determining the seismic performance of reinforced concrete buildings.

1. Introduction

Due to earthquakes, many lives have been lost in Türkiye until today. Damages to buildings also have caused great economic losses. Table 1 shows the significant earthquakes in Türkiye that occurred between 1990 and 2023 whose moment magnitude was greater than 6. The quick and reliable identification of the seismic performance of buildings before an earthquake gains importance after every earthquake. In particular, the February 6, 2023, Kahramanmaraş-Pazarcık (Mw=7.7) and Elbistan (Mw=7.6) earthquakes damaged many types of structures in 11 provinces. Rapid seismic performance assessment methods were also needed after these earthquakes [1, 2].

In recent years, studies on the earthquake performance of reinforced concrete buildings have increased in earthquake-prone countries. Considering that hundreds of buildings are damaged after earthquakes and pose a high risk, it becomes impossible to conduct detailed research because of its high cost and the great time it needs. In these methods, the final performance is obtained after performing linear or nonlinear analysis which needs geometric properties of the buildings and material tests of each

---

building [3]. Therefore, a long time and high cost are required for the implementation of detailed methods. Due to time and cost constraints, rapid evaluation methods have been developed. Those methods try to reach consistent results in a short time and at a low cost with simple analyses using less data. Although rapid assessment methods provide a lot of information about the building, they do not qualify as a final decision [4-6].

In the literature, for pre-earthquake damage assessments, 3-stage assessment (namely first, second, and third level) methods have been established requiring low to high amounts of data. The first level is called rapid visual screening, in which a building's seismic performance is to be determined by considering visual properties from outside and simple calculations without using the project or material data. In this method, geometric properties and material tests are not required. A score calculation is made with certain parameters and a risk score is given to the building. The main purpose here is to quickly group buildings according to their risk status. FEMA 154 (2002), ATC 21, Regulation on Determination of Risky Buildings (RYTEİE-2019), and Sucuoglu and Yazgan (2003) are examples of first-level assessment methods [7-10].

In the second level evaluation methods, unlike the first level, additional data such as the geometric properties of the building, size and location of structural elements, material properties, and architectural parameters may be used. This method aims to determine the risk status of the building quickly and with simple calculations. Methods proposed by Hassan and Sozen (1997), FEMA310 (1998), Otani (2000), Japan Building Disaster Prevention Association (JBDPA) (2001), Ozcebe et. al. (2003), Sucuoğlu and Yazgan (2003), Yakut (2004), Boduroğlu et. al. (2004, 2007), Temur (2006), Tezcan et. al. (2011), İlki et. al. (2014), Sucuoğlu et. al. (2015), ASCE 41-17 (2017), Kaplan et. al. (2018) Erdil and Ceylan (2019) are examples of second level assessment methods [3, 10-24].

The analysis of the structures with the help of programs developed according to the principles of the relevant regulations is handled in the third-level evaluation methods. At this stage, more detailed work is carried out. Many parameters such as material properties of the building, damaged elements, size and location of the structural elements, and information regarding the reinforcements are taken into consideration. Linear and nonlinear methods given in the Turkish Building Earthquake Code -2018 (TBEC-2018), can be given as an example for the third-level evaluation [25].

This study aims to evaluate the seismic performance of reinforced concrete buildings using the fuzzy logic method with a certain number of data to be an alternative method in second-level assessment. The fuzzy logic method and its place in civil engineering are mentioned under the title of material and method. Data from 146 buildings affected by the earthquakes that occurred in Van on October 23 and November 9, 2011, 18 buildings affected by the 2002 Afyon earthquake, and 28 buildings affected by the 2003 Bingöl earthquake were used in the study [3].

Table 1. Major earthquakes with a magnitude greater than 6 that occurred between 1990 and 2023 [26-28]

Earthquake Location	Date	Magnitude	Human Loss	Number of Damaged Buildings	Economic Loss, TL
Erzincan	13.03.1992	6.6	653	8057	750.000
Ceyhan (Adana)	28.06.1998	6.2	146	31463	550.000
Gölcük (Kocaeli)	17.08.1999	7.6	17480	73342	20.000.000
Düzce-Bolu	12.11.1999	7.2	763	35519	1.000.000
Çay-Sultandağı/ Bolvadin (Afyon)	03.02.2002	6.5	44	622	95.000
Merkez (Bingöl)	01.05.2003	6.4	176	6000	135.000
Merkez (Van)	23.10.2011	6.7	644	17005	1.500.000
Sivrice (Elâzığ)	24.01.2020	6.8	41	1815	
Ege Denizi (İzmir)	20.10.2020	6.6	117	475	
Pazarcık (Kahramanmaraş)	06.02.2023	7.7	50783	260000	104.000.000.000
Elbistan (Kahramanmaraş)	07.02.2023	7.6			

2. Material and Method

2.1. Fuzzy Logic Method and Its Use in Civil Engineering

The concept of Fuzzy Logic was introduced by Lotfi A. Zadeh in 1965 [29]. However, the first application was realized by Mamdani in 1973 [30]. Mamdani used this method to balance the steam pressure of a steam engine. In addition, Mamdani stated that the fuzzy logic approach that Zadeh created with linguistic rules can be easily processed in a computer environment [31]. Until today, the fuzzy logic method has shown quick development and has been used in many fields such as health, economy, education, and engineering. The concept of fuzzy logic can be perceived as the modeling of the ability to think, learn, and reason with this information that people perform in normal life in a computer environment. For the processing of this modeling, information can be given verbally, but the computer can process verbal data with numerical values and draw new conclusions [32]. The contribution of fuzzy logic to rapidly developing artificial intelligence studies and control systems is quite high. Studies in this field are progressing with fuzzy logic [33]. In the classical logic of mathematics, a proposition is either true or false. If a proposition is true, it is expressed numerically with 1, and if it is false with 0. However, in daily life, situations or events may not occur with precise information and uncertainties may arise between 1 and 0 [34]. Fuzzy logic comes into play at the point of uncertainty. According to Zadeh [22], an element in a fuzzy set can take a value between 1 and 0. The closer the membership degree of an element is to 1, the more it belongs to the set, and it is accepted that the degree of belonging increases. In addition, unlike classical logic, something can be both true and false in fuzzy logic. This varies according to the condition to which it is connected. In other words, for nested propositions, the truth of the proposition may change as the condition changes.

The fuzzy logic method has been used in many applications in civil engineering. Chao and Cheng (1998) [35] tried to determine crack control in reinforced concrete elements with a fuzzy pattern model. In the study, logical inference was made by considering time, depth, regularity, spacing, pattern, and location parameters for the crack. As a result, it is reported that a problem that is difficult to solve with mathematical solutions can be understood in a simple way. Aldawod et al. (2001) [36] investigated the behavior of a 306 m high, 76-floor building in Melbourne, Australia, under wind using the fuzzy logic method. In this building, a damping system was created with a special mass. The fuzzy logic method was used to control the damper and the building. According to the results obtained, it is stated that the fuzzy logic method gives more consistent results than the classical logic method. Kömür (2004) [37] investigated post-earthquake damage detection and earthquake safety of buildings with the fuzzy logic method. Relative floor drifts and concrete characteristic compressive strength was used in fuzzy logic for post-earthquake damage assessment. As a result, it was stated that more consistent and realistic results were found compared to classical logic. In Lin et al. (2004) [38], the early strength of concrete was evaluated according to fuzzy logic. Cement, water, and aggregate variables were processed in fuzzy logic. The results were compared with regression analysis, and it was stated that the results were acceptable. Tanyıldızı and Yazıcıoğlu (2006) [39] tried to determine the plastic collapse load value of steel beams using the fuzzy logic method. The collapse load value for the plastic moment generated in the steel beam was solved with fuzzy logic. In the study, for two beams, the fuzzy logic was used to input load and distance information and output rotation data. While the rule base is expert experience, the membership functions are selected according to the experience gained. Base values were found by trying many changes. As a result, it is stated that the fuzzy logic method gives consistent results. In Çakıroğlu et al. (2010) [40], the 7, 14, and 28-day compressive strength of concrete was predicted by fuzzy logic. For this purpose, 7, 14, and 28-day compressive tests of 9 standard cylinder and cube specimens were performed. The test results were processed with fuzzy logic and the results were compared. It was concluded that the fuzzy logic results were quite close and within acceptable limits. Doran et al. (2015) [41] investigated the structural behavior of FRP (Fiber Reinforced Polymer) reinforced columns using fuzzy logic. In the study, column width, length, compressive strength, thickness, and modulus of elasticity of FRP are input parameters while one output parameter is taken as output. According to the results, the structural behavior of FRP-reinforced columns was predicted and reliable results were found. Prieto et al. (2017) [42] tried to predict the service life of historical buildings with the fuzzy logic method. In the fuzzy logic method, vulnerabilities and risk variables that affect the performance of buildings are taken into account. In the study, five historical buildings in Spain were taken into consideration. In the study, building management and maintenance processes were taken as input parameters while service life was

taken as output. As a result, it is stated that the fuzzy logic method can be used in determining the service life of buildings.

2.2. Material

2.2.1. General features of the investigated buildings

In the study, data from 18, 28, and 146 buildings affected by the earthquakes in Afyon, Bingöl, and Van provinces in 2002, 2003, and 2011, respectively, were used. A total of 94 out of 192 buildings data were utilized for training in Matlab.

Details of the properties of the buildings were given in Erdil and Ceylan (2019) [3]. The number of lights, moderate and severely damaged buildings are 81, 17 and 58, respectively. The remaining 36 buildings were collapsed. In Erdil and Ceylan (2019), a number of stories, concrete compressive strength, ground floor area, and the ratio of the total vertical load-carrying member to the total floor area are stated to be the more important parameters that relate to the seismic performance of a building. Since similar parameters were mentioned in different studies [10, 11, 15-22, 43-45] parameters given in [3] were considered to be used directly in this study.

A number of stories is found to be more effective on the damage level. The damage level was found to increase with the increase in the number of stories [3, 10, 20, 21]. It is also observed that the mass of the building increases with the increase in the number of floors and the damage in the buildings with low earthquake resistance increases. It was stated that the percentage of moderate and severely damaged/collapsed buildings increased as the number of stories increased. It can be said that there is a significant relation between the number of stories and the level of damage. In the earthquakes experienced in Türkiye in 2023, it was stated that the damage rate increased with the increase in building weight as expected in high-rise buildings [46].

The other parameter used in the calculation is the concrete compressive strength. Since most of the buildings used in this study were constructed before 2000, i.e., before ready-mixed concrete, their concrete compressive strengths are much lower than the values required by the seismic codes. In TEC-1997 [55], it is mandatory to use concrete with a minimum strength of 20 Mpa (C20) in reinforced concrete buildings in 1st and 2nd degree earthquake zones and 16 Mpa (C16) in 3rd and 4th degree earthquake zones. In TEC-2007 [56], it is stated that the minimum concrete

compressive strength should be C20/25. According to TBEC-2018 [25], C25/30 for ready-mixed concrete and C30/37 for precast concrete elements are mandatory. After the earthquakes in Türkiye in 2023, it was determined that the concrete properties of most buildings were not in accordance with the regulations at the time of construction. Inappropriate aggregate distribution, aggregates with rounded surfaces, low cement ratio, and unplaced and unvibrated concrete were reported [47-50]. Only 8 buildings considered in this study met the code regulations. It was found that as the concrete strength increases, the number of buildings with low and moderate damage fluctuates while the number of buildings with severe damage decreases.

Another parameter affecting the building behavior and used in the calculation is the ground floor area. In the buildings considered in this study, it was determined that the building damage level increased as the ground floor area decreased [3]. After the earthquakes in Türkiye in 2023, it was stated that the size of the ground floor area directly affects the level of building damage [51, 52]. As the ground floor area of the building decreases from 800 m^2 to 200 m^2, the limited damaged building is replaced by a severely damaged or collapsed building.

Building a structural system is one of the main factors affecting earthquake behavior. In this study, this factor is taken into consideration as the ratio of the vertical structural elements (columns and shear walls) at the critical floor (mostly ground floor) to the total floor area above it. It was determined that the damage level increases as the ratio of vertical structural elements decreases. The importance of vertical structural elements was stated in the investigations made after the earthquakes in Türkiye in 2023 [46, 51, 53, 54].

Especially after the February 6, 2023, Kahramanmaraş-Pazarcık (Mw=7.7) and Elbistan (Mw=7.6) earthquakes, it was observed that structural irregularities played an important role in the behavior and negatively affected the damage level of the structure [57, 59]. According to TBEC-2018 [25], irregularities are divided into two categories irregularities in plan (Group A) and irregularities in vertical (Group B). In addition, short column, heavy overhang, and frame irregularity parameters, which are not included in this grouping but affect the behavior of the structure negatively, were also considered [57, 59]. It was stated that these irregularities were observed in many buildings in Türkiye after the earthquakes in 2023. It is stated that these irregularities cause serious problems due to

architectural and economic requirements and take a role in the collapse of the structure [51, 47, 46, 1, 2, 52, 58]. Irregularities related to weak and soft stories are the frequent irregularities observed in recent earthquakes [59]. The high impact of these irregularities was emphasized in different sources [47, 48, 50, 51]. Of the 192 buildings considered in this study, 86 of them have soft story irregularities. It was observed that 57% of these buildings were severely damaged or collapsed.

The other parameter considered in the calculation is heavy overhang. Heavy overhangs shift the center of mass of the building and increase the effect of earthquake forces acting on the building [59, 60]. Of the 192 buildings considered, 69 buildings have heavy overhangs. 62.3% of the buildings with heavy overhangs are severely damaged or collapsed.

Frame discontinuity is an irregularity that occurs due to design problems and adversely affects the earthquake behavior. This discontinuity is known to cause serious problems [61]. After the earthquakes in Türkiye in 2023, it was reported that frame discontinuity, stub beam, and eccentricity in column-beam joints caused damage to the structure [2, 46]. There are frame irregularities in 120 buildings considered in the study. It was observed that 52.5% of these buildings were severely damaged or collapsed.

The other parameter considered in the study is torsional irregularity. If the center of mass and rigidity of a building are far from each other, torsion occurs when the building rotates around its axis. In the case of torsional irregularity, additional shear forces occur in the structural system elements [64]. In the investigations conducted after the earthquakes in Türkiye in 2023, it was stated that many buildings were affected by torsion due to factors such as heavy overhang, vertical element irregularity, plan irregularity, serious damage, or collapse [47, 51].

2.3. Method

2.3.1. Zadeh's Principles of Fuzzy Logic

It can be stated that the principles of fuzzy logic became more evident with Lotfi A. Zadeh's work "Fuzzy Algorithms for Complex Systems and Decision Processes" in 1973 [29]. The fuzzy logic approach created by Zadeh with linguistic rules was stated by Mamdani that it can be easily processed in a computer environment [31]. The principles of this method found by Zadeh can be expressed as follows [66]:

- In the fuzzy logic method, approximate values are used instead of exact values.
- For fuzzy logic, information can be defined by data inputs that contain linguistic expressions such as a little, a lot, quite a little, and quite a lot.
- In fuzzy logic, values are represented by a membership degree in the range [0-1]. This means that increases and decreases can be calculated as a function.
- Any logical expression can be transformed into a fuzzy expression.
- Fuzzy logic is an ideal method for solutions when mathematical expressions are too complex and difficult.

2.3.2. Membership Functions and Gaussian Membership Function

The functions that show the degree of belonging of the elements in any set are called membership functions [67]. There is no specific rule in determining membership functions. Generally, the most appropriate function is selected for the data collected in the study for membership functions. Artificial neural networks and genetic algorithms can also be used in the selection of membership functions [67]. The membership functions developed to date and used in many fields are triangular, trapezoidal, Gaussian, S, and sigmoidal functions. Gaussian membership function is used in this study (Equation 1). In the equation, m is the center of the function and σ is the standard deviation of the function. The function lies between 0 and 1. As the standard deviation increases, the graph widens and as it decreases, the graph narrows. A graphical representation of a Gaussian membership function is given in Figure 1.

$$\mu_H(x; m, \sigma) = e^{\frac{-(x-m)^2}{2\sigma^2}} \qquad (1)$$
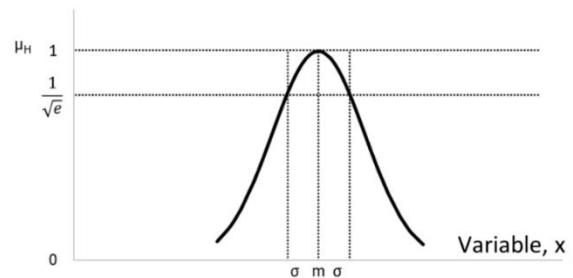
Figure 1. Gaussian Membership Function

2.3.3. Fuzzy Inference Systems

Fuzzy logic principles are established in a systematic way and fuzzy logic inference is performed with the given input information. The inference process against the given input information forms the basis of the method. The inference process is named fuzzy rule-based systems, fuzzy expert systems, fuzzy modeling, fuzzy associative memory, fuzzy logic controllers, and simple-variable fuzzy systems [65]. Inference systems have been used as an alternative to logic and probability theory. Unlike the classical set, instead of inferring that the elements belong or do not belong to the set, they can be expressed by a membership function that infers values between 0 and 1. The biggest feature that distinguishes fuzzy logic from other methods is that verbal terms are expressed in numerical terms [69]. Fuzzy inference systems combine fuzzy values using logical rules (if-then), binding operations (and, or, not), and mathematical operators (+, -, *, /, min, max) [70]. The most widely used fuzzy inference system is Mamdani fuzzy inference [30]. Figure 2 shows the rule base. The fuzzy inference system consists of subsystems and its schematic drawing is given in Figure 3 [71, 72, 77]. Inference is made in accordance with the subsystem order. These subsystems are given below.

• Defining if-then rules

• Defining the database

• Defining the membership functions of fuzzy sets

• Defining the inference unit for a given rules result

• Combining the given information with verbal variables and membership degrees, defining the fuzzification interface

• Defining a fuzzification interface for converting fuzzy results into precise outputs
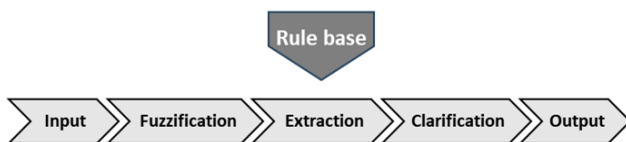
Figure 2. Gaussian Membership Function

2.3.4. Fuzzification and Rule Base

The transformation of the data to be processed with the rule base into symbolic values that are linguistic qualifiers is called fuzzification [31]. Input information is processed with the first fuzzification phase. In this unit, the input and output information are fuzzified by converting it to a certain value with the specified membership function [67]. Fuzzification is a step that connects the data with if-then rules [73]. The logical binding of input and output information forms the rule base of fuzzification [72]. In this context, input and output information are bound together. The rule base is available in all coding languages used nowadays.

2.3.5. Inference Unit and Mamdani Type Fuzzy Inference

A fuzzy inference unit is a collection of operations that collects and presents input and output information with a rule base [74]. It can also be considered as filtering the information with a rule base [75]. The most widely used inference rules in the literature are the Mamdani and Takagi and Sugeno inference approaches. The most widely used fuzzy inference is Mamdani type inference [30]. This method is widely used because it is easy to create and suitable for human behavior. It can be said that the Mamdani type is the basis of other inference methods [76]. A graphical representation of the Mamdani fuzzy inference method using minimum and maximum operators is given in Figure 3. The following rules can be given as examples of the use of minimum and maximum operators.

• Rule 1: If x = K1 and y = L1, then z = M1.
• Rule 2: If x = K2 and y = L2, then z = M2.

Here x and y are the digital input elements and z is the output element.
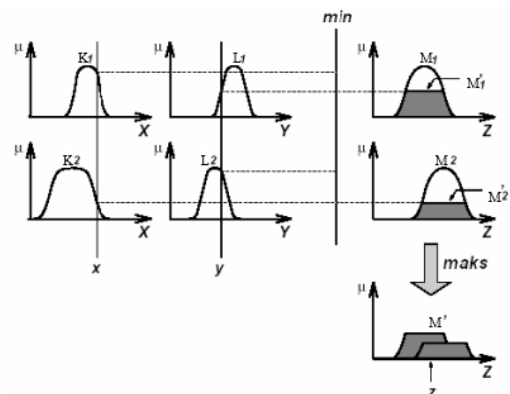
Figure 3. Mamdani fuzzy inference using fuzzy minimum and maximum operators [77].

2.3.6. Defuzzification and Center of Gravity Method

The last unit of the fuzzy inference method is defuzzification. In this unit, the verbal data from the inference unit is expressed numerically. There are

many different methods such as the average of the largest, center of gravity method, and maximum membership center method. Although all defuzzification methods (except for the smallest of the maximum and largest of the maximum) give similar results, for quantitative decisions like prioritization center of gravity method is recommended [73]. The most commonly used defuzzification method among these methods is the center of gravity method [70]. In this method, inference is obtained by finding the center of gravity of the combination of membership functions. The center of gravity method is given in Equation 2 and its graphical representation is given in Figure 4. Where k is the union of the fuzzy sets during the application of Mamdani and Larsen inference, z_i is the i'th element of the fuzzy union set, and z^* is the rationalized value [79].

$$z^* = \frac{\sum_{i=1}^{n} z_i \mu_k(z_i)}{\sum_{i=1}^{n} \mu_k(z_i)} \qquad (2)$$
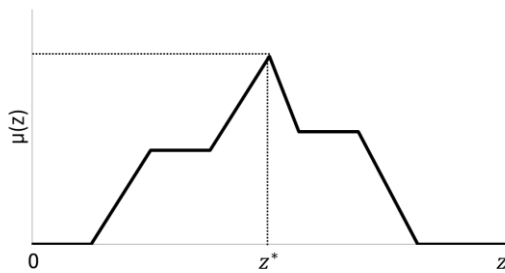
Figure 4. The center of gravity method

2.4. Fuzzy Logic Method for Determining Building Performance

The Matlab program was used to determine the seismic performance of the considered buildings. In the program, the effective parameters considered with the help of the toolbar are defined in the "Matlab Fuzzy Logic Toolbox". In the performance calculation, concrete strength (fc), ground floor area (Af), structural system element ratio ((Ac+Asw)/Aft), number of stories and irregularities (heavy overhang, short column, frame discontinuity, soft/weak floor, torsion) were defined as membership functions. Figure 5 shows the fuzzy logic method diagram and Figure 6 shows the membership functions of the parameters. A preliminary analysis was performed to find the range of the membership functions. Finally, it was seen that the best result was found with the Gaussian membership function.
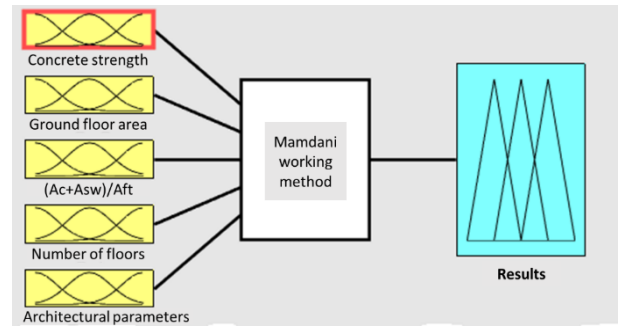
Figure 5. Fuzzy logic method used in the study

The membership function used for concrete compressive strength in the fuzzy logic method is given in Figure 6a. Concrete compressive strength was scored as too bad if between 0-5 MPa, bad if between 5-10 MPa, moderate if between 10-15 MPa, good if between 15-20 MPa, and very good if between 20-40 MPa. In the method, the ground floor area parameter was scored from small to large (Figure 6b). Scoring is given as too bad, bad, moderate, good, and very good. If the ground floor area of the building is smaller than 200 m², it is scored as too bad, if it is between 200-400 m² it is scored as bad, if it is between 400-600 m² it is scored as moderate, if it is between 600-800 m² it is scored as good and if it is larger than 800 m² it is scored as very good. The ratio of the total area of columns and shear walls on the ground floor to the total floor area was scored as too bad, bad, moderate, good, and very good (Figure 6c). This ratio is defined as too bad if it is less than 0.3%, bad if it is between 0.3-0.6%, moderate if it is between 0.6-0.9%, good if it is between 0.9-1.2%, and very good if it is greater than 1.2%. If the number of stories is 2 or less, it is scored as very good, 3 as good, 4 as moderate, 5 as bad, and 6 or more as too bad (Figure 6d). Since irregularities negatively affect the building behavior, they were scored with the membership function. Here, the scoring was changed according to whether the buildings had irregularities such as short columns, frame irregularities, torsion, heavy overhang, weak floor, and soft floor. Irregularities were calculated as negative and an initial score of +5 was given for irregularities. For each irregularity, 1 point was subtracted from the initial value. The remaining score gave the building a score for the irregularities. The scoring was determined as too bad, bad, moderate, good, very good. In this context, if the building has no irregularities or 1 irregularity, it is scored as very good, 2 irregularities as good, 3 irregularities as moderate, 4 irregularities as bad, and 5 irregularities as too bad (Figure 6e).

a) Concrete compressive strength membership function

b) Ground floor area membership function

c) Membership function for the ratio of total column and shear wall area to total floor area at the ground floor

d) Membership function for the number of floors

e) Membership function of architectural parameters
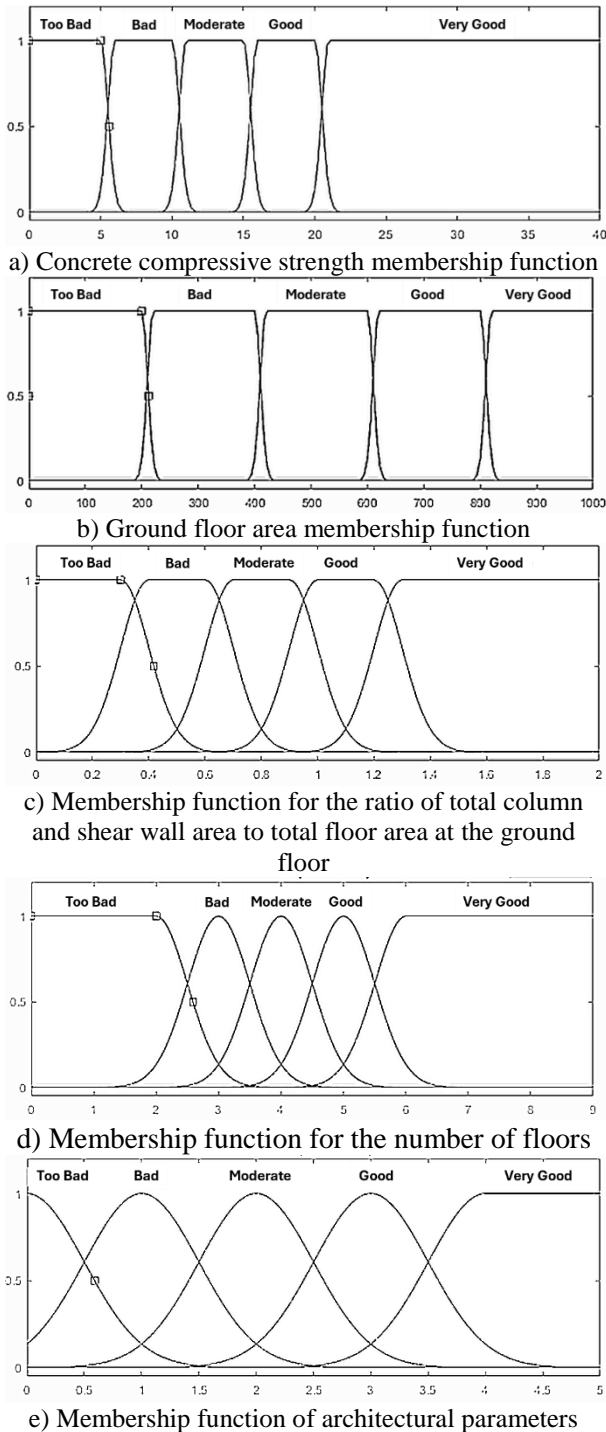
Figure 6. Membership functions

The membership functions are combined with the rule base to produce the final membership function (Figure 7). In the final membership function, a triangular membership function was used since the results should be accurate for building performance. For the results, it was determined that the most appropriate method for the rinsing unit was the center of gravity method. Considering TBEC-2018 and RYTEIE-2019, the resulting membership function was divided into 4 damage states (collapse, severe

damage, moderate damage, and limited damage) [9, 25]. If the resulting damage score from the building membership functions is in the range of 0-0.2, the building is collapsed, if it is in the range of 0.2-0.4, the building is in a severe damage state, if it is in the range of 0.4-0.6, it is in moderate damage state, and if it is in the range of 0.6-0.8, it is in limited damage state.
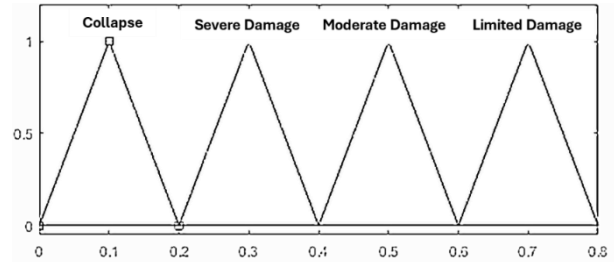
Figure 7. Result membership function

2.5. Training The Fuzzy Logic Rules

In the Matlab program "Fuzzy Logic Toolbox", membership functions were written according to if-then rules considering the actual building damage status. Mamdani inference method was used in these rules [30]. After the rules, the center of gravity method was used as a defuzzification method. 94 buildings' data were selected blindly and used in the training stage. Although several other building parameters affecting the vulnerability of a building (for example plastic hinge state was mentioned to be crucial) may be utilized in the training process [42], training can also be done with the limited data given in this study. The following 8 rules are given as examples:

• If (concrete strength is very good) and (ground floor area is very good) and ((Ac+Asw)/Aft is very good) and (number of stories is very good) and (no irregularities, i.e. irregularities are very good) then (result is limited damage)

• If (concrete strength is moderate) and (ground floor area is moderate) and ((Ac+Asw)/Aft is very good) and (number of stories is very good) and (irregularities are very good) then (result is limited damage)

• If (concrete strength is good) and (the ground floor area is too bad) and ((Ac+Asw)/Aft is bad) and (the number of stories is good) and (irregularities are very good) then (the result is moderate damage)

• If (concrete strength is good) and (ground floor area is bad) and ((Ac+Asw)/Aft is bad) and (the number of stories is good) and (irregularities are moderate) then (the result is moderate damage)

• If (concrete strength is good) and (the ground floor area is bad) ((Ac+Asw)/Aft is moderate) and (the number of stories is too bad) and (irregularities are good) then (the result is severe damage)

• If (concrete strength is moderate) and (the ground floor area is good) and ((Ac+Asw)/Aft is bad) and (the number of stories is bad) and (irregularities are bad) then (the result is severe damage)

• If (concrete strength is bad) and (ground floor area is bad) and ((Ac+Asw)/Aft is moderate) and (number of stories is moderate) and (irregularities are moderate) then (result is collapse)

• If (concrete strength is bad) and (the ground floor area is bad) and ((Ac+Asw)/Aft is bad) and (the number of stories is too bad) and (irregularities are very good) then (the result is collapse)

3. Results and Discussion

The seismic performance of a building depends on many parameters and in post-earthquake investigation reports, several reasons were mentioned related to the collapsed or severely damaged buildings [57, 59]. A building that collapsed for only one reason is rarely encountered. Therefore, determining the seismic performance of buildings with complex systems and many parameters requires time and cost. In this context, some studies in the literature have tried to predict the seismic performance of buildings by scoring with a limited number of parameters. Especially in the second-level evaluation methods, important parameters related to the seismic performance of buildings are required to calculate the performance score of the building to determine whether it will exhibit limited, moderate, or severe damage.

In this study, 192 buildings that experienced the Van, Afyon, and Bingöl earthquakes were processed with fuzzy logic method and compared with the second level evaluation methods proposed by Hassan and Sözen (1997), Otani (2000), JBDPA (2001), Yakut (2004), Tezcan et al. (2011) and Erdil and Ceylan (2019) [3, 11, 13, 14, 16, 20]. In order to make the comparison, the performance levels are basically divided into two: low damage risk and high damage risk. Two damage risk levels determine whether the building can be used after the earthquake or not. According to the studies where the results are compared, it is stated that undamaged buildings can be used immediately, limited damaged and moderately damaged buildings can be used after retrofitting or strengthening, but severely damaged and collapsed buildings cannot be used. Therefore, limited damaged and moderately damaged buildings are considered a low damage risk (LDR) while severely damaged or collapsed buildings are considered a high damage risk (HDR).

3.1. Evaluation of Existing Studies

In order to determine the reliability of the fuzzy logic method discussed in this study, 192 buildings should be tested with other existing studies. Hasan and Sözen method (1997) is quite simple to use. Building performance is estimated with 4 parameters of the building. This method, which aims to determine quickly and easily, has an important place in forming the basis of second-level evaluation methods. When these buildings were tested according to the Hassan and Sözen method (1997), 80.6% success was observed in the earthquake performance of buildings in the low damage risk (LDR) category and 53.2% in the high damage risk (HDR) category [3, 11]. In total, 67.2% success was achieved in determining the earthquake performance of buildings. When 192 buildings were tested with the Otani method and the results were compared, 97.9% success was obtained in the HDR category and 29.6% in the LDR category [3, 13]. The total correct prediction of this method in building performances was 63%. In Japan, where many earthquakes have been experienced and earthquake research has been conducted, the Japanese Seismic Index method (JBDPA-2001) was developed to determine building performances [14]. This method is based on the concept of equal energy and is a three-stage method. For performance prediction, 16 parameters of the building are used. As a result, while 100% of the buildings in the HDR category were successfully predicted correctly, 29.6% of the buildings in the LDR category were predicted correctly. In total, 64.1% of the earthquake performance of 192 buildings was predicted correctly. Since this method was developed according to the quality of buildings in Japan, it can be said that the limited values taken into account in the method are not valid for the buildings in Türkiye due to the difference in technical structure and structural system. Yakut method [16] made 91.5% successful prediction in the HDR category and 36.7% in the LDR category. Total success in all buildings was found to be 63.5%. According to the results of the P25 method [20], 79.8% of correct prediction was found in the HDR category and 71.4% in the LDR category. The total correct prediction was calculated as 75.5%. Erdil and Ceylan (2019) [3] tried to determine the seismic performance of the building with the MVP method developed in their study. From this method, 89.4% success in the HDR category and 88.8% success in the LDR category was achieved. Finally, 89.1% of the

investigated 192 buildings' seismic performance were predicted correctly.

3.2. Fuzzy Logic Method

As previously stated, 98 buildings'data were used for training and 94 buildings' data were utilized for testing. 10 parameters were considered in the study. Mamdani method was used as a fuzzy inference system. The membership function types and value ranges that make the study unique and reliable were determined through preliminary experiments as described in the following sections.

3.2.1. Selection of Membership Functions

Gauss, triangular, and trapezoidal membership functions were selected in preliminary tests to determine the membership function types. Not all buildings were tested since the success of the triangular membership function results was found to be low. In the calculations made with the trapezoidal membership function, among the 94 buildings tested, the correct prediction in the HDR category was 97.8%, while the correct prediction in the LDR category was 76.1%. In total, 86.9% of the buildings were correctly predicted. When the Gaussian membership function was used, the correct prediction in the HDR category was 97.8% while the correct prediction in the LDR category was 76.1%. Figure 8 shows the buildings and their damage levels. The results were the same for the two different membership functions. It was observed that the building damage scores changed with the membership functions, but since they were close to each other, they were in the same result range. Although the same results were obtained in a preliminary analysis, the Gaussian membership function was selected. Figures 8a and b show the building results according to the two membership functions. As can be seen from the figures the damage level of 0.4 is set as the boundary line, stating that the region above this line is called LDR and the region below this line is called HDR. The LDR region contains limited damage and moderate damage states of buildings, while the HDR region contains severe damage states and collapsed buildings. Comparing both figures, changes in the distribution of limited damaged buildings and moderately damaged buildings can be seen. Although there are changes in the scoring, the final assessment remains the same. For example, buildings between 0.4 and 0.6 were considered to be moderately damaged. Some error warnings were also received for some buildings which are because of the buildings with similar

characteristics that were identified in the collapsed area. In this case, even though such buildings were moderately damaged, they were perceived as collapsed buildings according to the method. This situation was mostly observed in buildings with a moderate damage state.
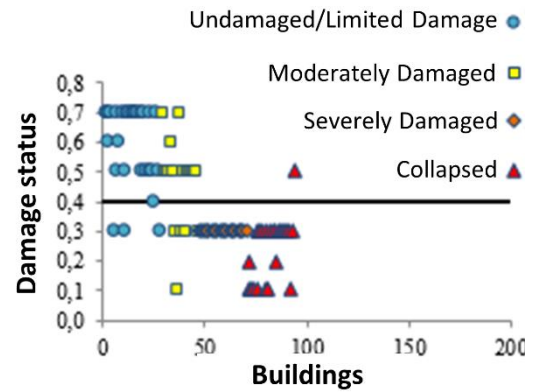
a) With the Gauss membership function
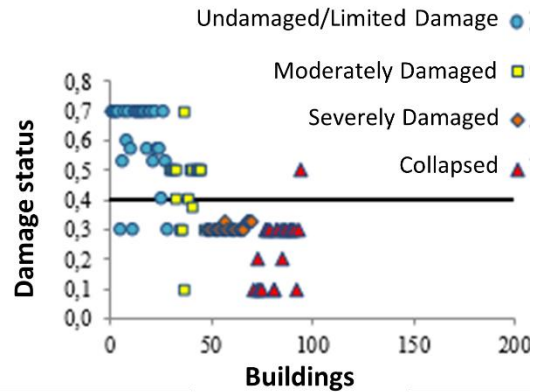
b) With Trapezoidal membership function
Figure 8. Buildings and damage states

3.2.2. Determination of Membership Function Ranges

The intervals for the selected Gauss membership function should be determined in a way that increases the percentage of success in damage state prediction. In this context, the best results for the seismic performance of buildings were determined by expanding and narrowing the ranges. Table 2 shows the ranges obtained by widening the membership function values. For example, concrete strength is assumed to be too bad up to 10 MPa and very good if it is more than 25 MPa. Except for the irregularities, other values were widened in the same way. As a result, 97.8% of the buildings in the HDR category were correctly predicted. However, the successful prediction of the buildings in the LDR category decreased to 52.2%. The damage status of all buildings was correctly estimated at 74.9%.

Table 2. Ranges in case of widening the membership function values

Concrete Compressive Strength		Ground Floor Area		Number of Stories	
$0<f_c\leq10$	Too bad	$A_f\leq300$	Too bad	≥7	Too bad
$10<f_c\leq15$	Bad	$300<A_f\leq500$	Bad	6	Bad
$15<f_c\leq20$	Moderate	$500<A_f\leq700$	Moderate	5	Moderate
$20<f_c\leq25$	Good	$700<A_f\leq900$	Good	4	Good
$25<f_c$	Very good	$900<A_f$	Very good	≤3	Very good
$(A_c+A_{sw})/A_{ft}$				Irregularities	
$(A_c+A_{sw})/A_{ft}\leq0.4$	Too bad			0-1	Too bad
$0.4<(A_c+A_{sw})/A_{ft}\leq0.7$	Bad			2	Bad
$0.7<(A_c+A_{sw})/A_{ft}\leq1.1$	Moderate			3	Moderate
$1.1<(A_c+A_{sw})/A_{ft}\leq1.3$	Good			4	Good
$1.3<(A_c+A_{sw})/A_{ft}$	Very good			5	Very good

The results obtained by increasing the membership function values are given in Figure 9. It is seen from the figure that almost half of the undamaged/limited damaged and moderately damaged buildings are in the HDR region. As can be seen from these ranges, when the critical ranges of the parameters were increased, most of the buildings fell into the HDR category. This may mean staying on the safe side, but it leads to a wrong estimate of the final prediction. Since the aim of this study is to estimate the existing damages, it was decided not to widen the ranges.

The opposite results were observed when the Gauss membership function ranges were narrowed. The values of the narrowed function ranges are given in Table 3 and the building results are given in Figure 10. The function ranges were narrowed, and it became difficult to determine the building damage level. For this reason, it was observed that the severely damaged and collapsed buildings were at the same level as the buildings with moderate and limited damage. As seen in Figure 12, the majority of the buildings remained in the LDR zone. The damage to all buildings in the LDR category was correctly estimated. However, a 4.2% correct prediction was made in the HDR category. As a result of narrowing the range, it is seen that the buildings will perform well, and the damage estimation will be far below reality. Overall correct estimate reached only 52.1%. Since this result is unrealistic, it was concluded that the membership function values should not be narrowed.

Figure 9. Building damages as a result of widening membership function ranges

Table 3. Ranges in case of narrowing membership function values

Concrete Compressive Strength		Ground Floor Area		Number of Stories	
$0<f_c\leq3$	Too bad	$A_f\leq100$	Too bad	≥5	Too bad
$3<f_c\leq8$	Bad	$100<A_f\leq300$	Bad	4	Bad
$8<f_c\leq13$	Moderate	$300<A_f\leq500$	Moderate	3	Moderate
$13<f_c\leq18$	Good	$500<A_f\leq700$	Good	2	Good
$18<f_c$	Very Good	$700<A_f$	Very Good	1	Very Good
$(A_c+A_{sw})/A_{ft}$				Irregularities	
$(A_c+A_{sw})/A_{ft}\leq0.2$	Too bad			0-1	Too bad
$0.2<(A_c+A_{sw})/A_{ft}\leq0.5$	Bad			2	Bad
$0.5<(A_c+A_{sw})/A_{ft}\leq0.8$	Moderate			3	Moderate
$0.8<(A_c+A_{sw})/A_{ft}\leq1.1$	Good			4	Good
$1.1<(A_c+A_{sw})/A_{ft}$	Very Good			5	Very Good
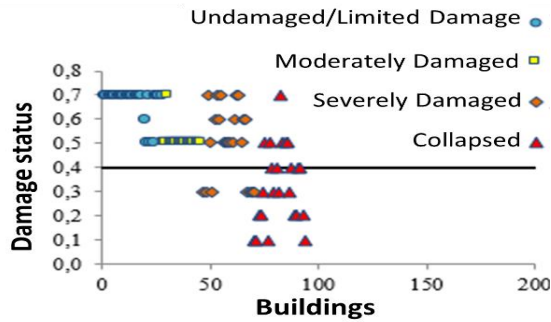
Figure 10. Building damages as a result of increasing membership function values

As a result, determining the value ranges directly affects the reliability of the study. For this reason, it was decided to use the ranges determined by Erdil and Ceylan (2019) [3] for the membership function ranges (Table 4). The study was reorganized for this value range. When the function ranges were averaged, it was seen that the results were closer to the actual performance of the building and were consistent.

Table 4. Function data ranges used in the study

Concrete Compressive Strength		Ground Floor Area		Number of Stories	
$0<f_c\leq5$	Too bad	$A_f\leq200$	Too bad	≥6	Too bad
$5<f_c\leq10$	Bad	$200<A_f\leq400$	Bad	5	Bad
$10<f_c\leq15$	Moderate	$400<A_f\leq600$	Moderate	4	Moderate
$15<f_c\leq20$	Good	$600<A_f\leq800$	Good	3	Good
$20<f_c$	VeryGood	$800<A_f$	Very Good	≤2	Very Good
$(A_c+A_{sw})/A_{ft}$				Irregularities	
$(A_c+A_{sw})/A_{ft}\leq0.3$	Too bad			0-1	Too bad
$0.3<(A_c+A_{sw})/A_{ft}\leq0.6$	Bad			2	Bad
$0.6<(A_c+A_{sw})/A_{ft}\leq0.9$	Moderate			3	Moderate
$0.9<(A_c+A_{sw})/A_{ft}\leq1.2$	Good			4	Good
$1.2<(A_c+A_{sw})/A_{ft}$	Very Good			5	Very Good

3.2.3. Determination of the Defuzzification Method

Preliminary evaluations showed that the center of gravity method is the most suitable method for the study. In addition, the bisector method was also tried for the defuzzification phase. Using the bisector method, 100% of the buildings in the HDR category and 72.91% in the LDR category were correctly predicted. Considering all predictions, the correct estimate reached to 86.45% of all buildings. Figure 11 shows the results obtained by using the area angle bisector method. Since the center of gravity method attained higher overall correct predictions, it was used for the defuzzification stage.
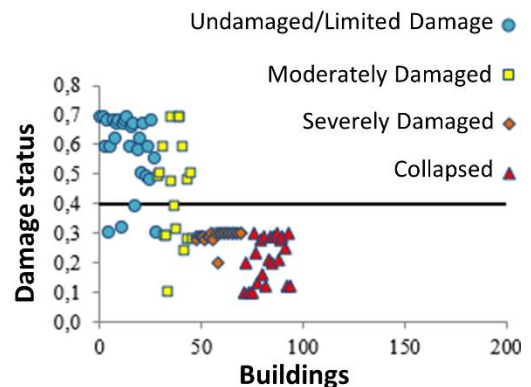
Figure 11. Results obtained by using the area angle bisector method

3.2.4. Proposed Fuzzy Logic Method

The fuzzy logic method as previously noted needs several assumptions related to the fuzzification and defuzzification stages. The reasonable assumptions increase the reliability of the results. Since the aim of this study is to utilize the fuzzy logic method to predict the seismic performance of reinforced concrete buildings, the rational assumptions associated with the building properties, range of the

properties, membership functions, and defuzzification methods were sought and the results were summarized in Table 5. As can be seen from the table, with the selected building parameters (concrete compressive strength, ground floor area, number of stories, ratio of the vertical load carrying members at the ground floor to the total floor area, irregularities) and selected ranges as proposed in [3] using Gaussian membership function for fuzzification and center of gravity method for defuzzification, higher correct estimate percentage can be attained.

Table 5. Correct estimate comparison related to fuzzy logic solution assumptions

Membership function	Range of the variables	Defuzzification method	Correct Estimate, %		
			Overall	HDR	LDR
Gauss	**Medium**	**Center of gravity**	**86.9**	**97.8**	**76.1**
Trapezoidal	Medium	Center of gravity	86.9	97.8	76.1
Gauss	Medium	Bisector	86.5	100.0	72.9
Gauss	Wide	Center of gravity	74.9	97.8	52.2
Gauss	Narrow	Center of gravity	52.1	4.2	100.0

3.3. General Comparison of The Methods

Table 5 presents the correct estimate percentages of different preliminary (level two) methods as well as the fuzzy logic method proposed herein. 97.8% of the buildings in the HDR category and 76.1% of the buildings in the LDR category were predicted correctly using the fuzzy logic proposed in this study. In addition, 86.9% of all buildings were predicted correctly. It was observed that the results of the fuzzy logic method reached the most accurate prediction after the MVP method. It can be said that this prediction value is quite high compared to other methods. The results were found to be close to the MVP method. However, since it is a simple and fast method, it can be said that it can be more efficient with additional training and testing building data.

Table 6. Comparison of existing studies and fuzzy logic method

Preliminary Methods	Correct Estimate, %		
	Overall	HDR	LDR
Proposed Fuzzy Logic	**86.9**	97.8	76.1
MVP Method [3]	**89.1**	89.4	88.8
P25 Method (2011) [20]	**75.5**	79.8	71.4
Hassan and Sözen (1997) [11]	**67.2**	53.2	80.6
JBDPA (2001) [14]	**64.1**	100.0	29.6
Yakut (2004) [16]	**63.5**	91.5	36.7
Otani (2000) [13]	**63.0**	97.9	29.6

4. Results

The fuzzy logic method is used to predict the seismic performance of 192 buildings covered in this study. For this purpose, 98 buildings' properties were processed as training data while 94 buildings were used for testing. The following conclusions were drawn from the study:

- Considering the building parameters such as concrete compressive strength, ground floor area, number of stories, the ratio of the vertical load carrying members at the ground floor to the total floor area, and irregularities only, the fuzzy logic method is found to be insensitive to the membership function. Either Gauss or trapezoidal membership functions reached the same correct estimate rate.
- The fuzzy logic method is highly sensitive to the data range of the building properties. If the data range is narrowed more buildings fall into low damage risk region indicating the false prediction of adequate seismic performances. On the contrary, when the data range is widened, then more buildings are placed in high damage risk indicating the inadequate seismic performance of most of the buildings. Although this result seems to be on the safe side, the estimates are not correct.
- Compared to other methods, the fuzzy logic method with the proposed parameters was found to be able to predict the damage state of the reinforced concrete buildings accurately with 86.9% and achieved better results than most of the preliminary methods available in the literature.

Since the fuzzy logic method is directly dependent on the selected functions and the value ranges of these functions, both functions and value ranges should be selected appropriately. The results were estimated with acceptable accuracy using less data than some of the second-stage assessment methods in the literature. In addition, since the fuzzy logic method uses a computer to process the building data, hand calculation errors are avoided, and fast analysis is possible. This can increase the speed of damage assessment studies and reduce the transaction cost. As a result, it can be concluded that the fuzzy logic method is simple, fast, and reliable. With this method, damage levels of buildings after an

earthquake can be determined quickly and early intervention can be provided.

Acknowledgment

This study was conducted within the scope of a master's thesis.

Contributions of the authors

Yıldız: conceptualization, data collection, formal analysis, visualization, software development, ınterpretation of results

Kıpçak: methodology, literature review, ınterpretation of results, writing-first draft, revision
Erdil: project administration, conceptualization, methodology, formal analysis, supervision, revision

Conflict of Interest Statement

There is no conflict of interest between the authors.

Statement of Research and Publication Ethics

The study complies with research and publication ethics

References

[1] S. K. Sezgin, G. B. Sakcalı, S. Özen, E. Yıldırım, E. Avcı, B. Bayhan, and N. Caglar, "Reconnaissance report on damage caused by the February 6, 2023, Kahramanmaraş earthquakes in reinforced-concrete structures," *Journal of Building Engineering*, vol. 89, p. 109200, 2024. doi: 10.1016/J.JOBE.2024.109200.

[2] A. I. Turan, A. Celik, A. Kumbasaroglu, and H. Yalciner, "Assessment of reinforced concrete building damages following the Kahramanmaraş earthquakes in Malatya, Turkey (February 6, 2023)," *Engineering Science and Technology, an International Journal*, vol. 54, p. 101718, 2024. doi: 10.1016/j.jestch.2024.101718.

[3] B. Erdil and H. Ceylan, "MVP interaction-based seismic vulnerability assessment of RC buildings," *Gradevinar*, vol. 71, no. 6, pp. 489-503, 2019.

[4] Ö. Özçelik, İ. S. Mısır, T. Baran, S. Kahraman, A. Saatçi, and S. C. Girgin, "Balçova ve Seferihisar İlçelerinde Gerçekleştirilen Yapı Stoğu Envanter ve Deprem Güvenliği Ön Değerlendirmesi Projesi Sonuçları," in *2. İzmir Kent Sempozyumu*, İzmir, 2013, pp. 12.

[5] E. Harirchian, S. E. A. Hosseini, K. Jadhav, V. Kumari, S. Rasulzade, E. Işık, and T. Lahmer, "A review on the application of soft computing techniques for the rapid visual safety evaluation and damage classification of existing buildings," *Journal of Building Engineering*, vol. 43, p. 102536, 2021.

[6] E. Işık, "Consistency of the rapid assessment method for reinforced concrete buildings," *Earthquakes and Structures*, vol. 11, no. 5, pp. 873-885, 2016.

[7] Federal Emergency Management Agency (FEMA), *Rapid Visual Screening of Buildings for Potential Seismic Hazards - A Handbook*, Washington, DC, USA, 2002.

[8] Applied Technology Council (ATC), *Rapid Visual Screening of Buildings for Potential Seismic Hazards - A Handbook (FEMA 154 Report), Second Edition*, ATC-21, California, USA, 2002.

[9] RYTEİE, "Riskli yapıların tespit edilmesine ilişkin esaslar," Turkey, 2019.

[10] H. Sucuoglu and U. Yazgan, "Simple survey procedures for seismic risk assessment in urban building stocks," in *Seismic Assessment and Rehabilitation of Existing Buildings*, Springer, Dordrecht, pp. 97-118, 2003.

[11] A. F. Hassan and M. A. Sozen, "Seismic vulnerability assessment of low-rise buildings in regions with infrequent earthquakes," *ACI Structural Journal*, vol. 94, no. 1, pp. 31-39, 1997.

[12] American Society of Civil Engineers (ASCE), *Handbook for the Seismic Evaluation of Buildings-A Prestandard*, Prepared for the Federal Emergency Management Agency, FEMA-310, Washington, D.C., USA, 1998.

[13] S. Otani, "Seismic vulnerability assessment methods for buildings in Japan," *Earthquake Engineering and Engineering Seismology*, vol. 2, no. 2, pp. 47-56, 2000.

[14] Japan Building Disaster Prevention Association (JBDPA), *Standard for Seismic Evaluation of Existing Reinforced Concrete Buildings (Version 2001)*, Japan, 2001.

[15] G. Özcebe, M. S. Yücemen, V. Aydoğan, and A. Yakut, "Preliminary seismic vulnerability assessment of existing reinforced concrete buildings in Turkey," in *Seismic Assessment and Rehabilitation of Existing Buildings*, pp. 29-42, 2003.

[16] A. Yakut, "Preliminary seismic assessment procedure for existing RC buildings," *Engineering Structures*, vol. 26, no. 10, pp. 1447-1461, 2004.

[17] H. Boduroglu, P. Ozdemir, A. Ilki, S. Sirin, C. Demir, and F. Baysan, "Towards a modified rapid screening method for existing medium-rise RC buildings in Turkey," in *13th World Conference on Earthquake Engineering*, 2004.

[18] M. H. Boduroğlu and P. Ö. Çağlayan, "Mevcut Yapıların Değerlendirmesinde Bir Tarama Yöntemi," in *Altıncı Ulusal Deprem Mühendisliği Konferansı*, 2007, pp. 16-20.

[19] R. Temur, "Hızlı Durum Tespit (DURTES) yöntemi ve bilgisayar programının geliştirilmesi," Master's thesis, Istanbul University, 2006.

[20] S. S. Tezcan, I. E. Bal, and F. G. Gulay, "P25 scoring method for the collapse vulnerability assessment of R/C buildings," *Journal of the Chinese Institute of Engineers*, vol. 34, no. 6, pp. 769-781, 2011.

[21] A. Ilki, M. Comert, C. Demir, K. Orakcal, D. Ulugtekin, M. Tapan, and N. Kumbasar, "Performance based rapid seismic assessment method (PERA) for reinforced concrete frame buildings," *Advances in Structural Engineering*, vol. 17, no. 3, pp. 439-459, 2014.

[22] H. Sucuoğlu, A. Yakut, A. Özmen, and J. Kubin, "Seismic risk prioritization and retrofit cost evaluation of code-deficient RC public buildings in Turkey," *Earthquake Spectra*, vol. 31, no. 1, pp. 601-614, 2015.

[23] American Society of Civil Engineers (ASCE), *Seismic Evaluation and Retrofit of Existing Buildings*, ASCE/SEI 41-13, Reston, VA, USA, 2014.

[24] O. Kaplan, Y. Guney, A. Topcu, and Y. Ozcelikors, "A rapid seismic safety assessment method for mid-rise reinforced concrete buildings," *Bulletin of Earthquake Engineering*, vol. 16, no. 2, pp. 889-915, 2018.

[25] Turkish Ministry of Public Works and Settlement, *Türkiye Bina Deprem Yönetmeliği 2018*, TBEC-2018, Ankara, Turkey, 2018.

[26] AFAD, "Deprem Kataloğu," 2023. [Online]. Available: https://deprem.afad.gov.tr/depremkatalogu. [Accessed: 14-Nov-2023].

[27] Kandilli Rasathanesi ve Deprem Araştırma Enstitüsü (KRDAE), "Büyük Depremler," 2018. [Online]. Available: http://www.koeri.boun.edu.tr/sismo/2/deprem-bilgileri/buyuk-depremler/. [Accessed: 14-May-2022].

[28] İ. Şahin and T. Kılınç, "Türkiye'de 1980-2014 Yılları Arasında Görülen Depremlerin Ekonomik Etkileri," *İktisadi Yenilik Dergisi*, vol. 4, no. 1, pp. 33-42, 2016.

[29] L. A. Zadeh, "Fuzzy sets," *Information and Control*, vol. 8, pp. 338-353, 1965.

[30] E. H. Mamdani, "Application of fuzzy algorithms for control of simple dynamic plant," in *Proceedings of the Institution of Electrical Engineers*, vol. 121, no. 12, pp. 1585-1588, 1974.

[31] A. E. Eğrisöğüt Tiryaki and R. Kazan, "Bulaşık makinesinin bulanık mantık ile modellenmesi," *Mühendis ve Makine*, vol. 48, no. 565, pp. 3-8, 2007.

[32] M. E. Tabar and Y. Şişman, "Bulanık Mantık ile Arsa Değerleme Modelinin Oluşturulması," *Türkiye Arazi Yönetimi Dergisi*, vol. 2, no. 1, pp. 18-24, 2020.

[33] Ş. Işıklı, "Bulanık mantık ve bulanık teknolojiler," *Ankara Üniversitesi Dil ve Tarih-Coğrafya Fakültesi Felsefe Bölümü Dergisi*, vol. 19, pp. 105-130, 2015.

[34] A. Özdemir, A. Alaybeyoğlu, and K. F. Balbal, "Bulanık mantığın eğitim alanındaki uygulamaları," *Bilim, Eğitim, Sanat ve Teknoloji Dergisi (BEST Dergi)*, vol. 3, no. 1, pp. 45-50, 2019.

[35] C. J. Chao and F. P. Cheng, "Fuzzy pattern recognition model for diagnosing cracks in RC structures," *Journal of Computing in Civil Engineering*, vol. 12, no. 2, pp. 111-119, 1998.

[36] M. Aldawod, B. Samali, F. Naghdy, and K. C. Kwok, "Active control of along wind response of tall building using a fuzzy controller," *Engineering Structures*, vol. 23, no. 11, pp. 1512-1522, 2001.

[37] M. Kömür, "Binaların deprem güvenliğinin belirlenmesinde bulanık mantık yaklaşımı," Doctoral dissertation, Fen Bilimleri Enstitüsü, 2004.

[38] M. Lin, C. Tsai, C. Cheng, and C. Chang, "Using Fuzzy QFD for Design of Low-End Digital Camera," *International Journal of Applied Science and Engineering*, vol. 2, no. 3, pp. 222-233, 2004.

[39] H. Tanyıldızı and S. Yazıcıoğlu, "Bulanık mantık metodu ile tekil yükler altında iki açıklıklı kirişlerin plastik göçme yük faktörü değerinin bulunması," *Teknik Dergi*, vol. 17, no. 84, pp. 3961-3971, 2006.

[40] M. A. Çakıroğlu, S. Terzi, S. Kasap, and M. G. Çakıroğlu, "Beton Basınç Dayanımının Bulanık Mantık Yöntemiyle Tahmin Edilmesi," *Yapı Teknolojileri Elektronik Dergisi*, vol. 6, no. 2, pp. 1-8, 2010.

[41] B. Doran, K. Yetilmezsoy, and S. Murtazaoglu, "Application of fuzzy logic approach in predicting the lateral confinement coefficient for RC columns wrapped with CFRP," *Engineering Structures*, vol. 88, pp. 74-91, 2015.

[42] A. J. Prieto, J. M. Macías-Bernal, M. J. Chávez, and F. J. Alejandre, "Fuzzy modeling of the functional service life of architectural heritage buildings," *Journal of Performance of Constructed Facilities*, vol. 31, no. 5, p. 04017041, 2017.

[43] E. Işık, F. Avcil, R. İzol, A. Büyüksaraç, H. Bilgin, E. Harirchian, and E. Arkan, "Field Reconnaissance and Earthquake Vulnerability of the RC Buildings in Adıyaman during 2023 Türkiye Earthquakes," *Applied Sciences*, vol. 14, no. 7, p. 2860, 2024.

[44] Ö. F. Nemutlu, A. Sari, and B. Balun, "A Novel approach to seismic vulnerability assessment of existing residential reinforced concrete buildings stock: a case study for Bingöl, Turkey," *Iranian Journal of Science and Technology, Transactions of Civil Engineering*, vol. 47, no. 6, pp. 3609-3625, 2023.

[45] E. Işık and F. Akat, "The Effect of Different Heavy Overhang on Structural Performance in Reinforced Concrete Structures," *Bitlis Eren Üniversitesi Fen Bilimleri Dergisi*, vol. 12, no. 1, pp. 261-271, 2023.

[46] O. İnce, "Structural damage assessment of reinforced concrete buildings in Adıyaman after Kahramanmaraş (Türkiye) Earthquakes on 6 February 2023," *Engineering Failure Analysis*, vol. 156, p. 107799, 2024. [Online]. Available: https://doi.org/10.1016/j.engfailanal.2023.107799.

[47] E. Altunsu, O. Güneş, S. Öztürk, S. Sorosh, A. Sarı, and S. T. Beeson, "Investigating the structural damage in Hatay province after Kahramanmaraş-Türkiye earthquake sequences," *Engineering Failure Analysis*, vol. 157, p. 107857, 2024. [Online]. Available: https://doi.org/10.1016/j.engfailanal.2023.107857.

[48] A. C. Altunışık, M. E. Arslan, V. Kahya, B. Aslan, T. Sezdirmez, G. Dok, and A. Baltaci, "Field observations and damage evaluation in reinforced concrete buildings after the February 6th, 2023 Kahramanmaraş-Türkiye earthquakes," *Journal of Earthquake and Tsunami*, vol. 17, p. 2350024, 2023. [Online]. Available: https://doi.org/10.1142/S1793431123500240.

[49] H. C. Mertol, G. Tunç, T. Akış, Y. Kantekin, and İ. C. Aydın, "Investigation of RC Buildings after 6 February 2023, Kahramanmaraş, Türkiye Earthquakes," *Buildings*, vol. 13, no. 7, p. 1789, 2023. [Online]. Available: https://doi.org/10.3390/buildings13071789.

[50] B. Zengin and F. Aydin, "The Effect of Material Quality on Buildings Moderately and Heavily Damaged by the Kahramanmaraş Earthquakes," *Applied Sciences*, vol. 13, no. 19, p. 10668, 2023. [Online]. Available: https://doi.org/10.3390/app131910668.

[51] A. Demir, E. Celebi, H. Ozturk, et al., "Destructive impact of successive high magnitude earthquakes occurred in Türkiye's Kahramanmaraş on February 6," *Bulletin of Earthquake Engineering*, 2023. [Online]. Available: https://doi.org/10.1007/s10518-024-01865-5.

[52] J. Yuzbasi, "Post-Earthquake Damage Assessment: Field Observations and Recent Developments with Recommendations from the Kahramanmaraş Earthquakes in Türkiye on February 6th, 2023 (Pazarcık M7.8 and Elbistan M7.6)," *Journal of Earthquake Engineering*, pp. 1-26, 2024. [Online]. Available: https://doi.org/10.1080/13632469.2024.2353864.

[53] F. Avcil, E. Işık, R. İzol, et al., "Effects of the February 6, 2023, Kahramanmaraş earthquake on structures in Kahramanmaraş city," *Natural Hazards*, vol. 120, pp. 2953–2991, 2024. [Online]. Available: https://doi.org/10.1007/s11069-023-06314-1.

[54] C. Tura, K. Orakcal, K. Kusunoki, and A. Ilki, "Seismic Response Simulation of a Reinforced Concrete Wall-Frame Building That Collapsed During the February 2023 Kahramanmaras Earthquake," *Journal of Earthquake Engineering*, pp. 1-25, 2024. [Online]. Available: https://doi.org/10.1080/13632469.2024.2372080.

[55] Turkish Earthquake Code 1997 (TEC-1997): *Specification for Structures to be Built in Disaster Areas*. Turkish Ministry of Public Works and Settlement, Ankara, Turkey, 1997.

[56] Turkish Earthquake Code 2007 (TEC-2007): *Specification for Buildings to be Built in Seismic Areas*. Turkish Ministry of Public Works and Settlement, Ankara, Turkey, 2007.

[57] K. Ö. Çetin, M. Ilgaç, G. Can, and E. Çakır, *6 Şubat 2023 Kahramanmaraş-Pazarcık Mw=7.7 ve Elbistan Mw=7.6 Depremleri Ön Değerlendirme Raporu*, Orta Doğu Teknik Üniversitesi, Ankara, 2023.

[58] F. Akar, E. Işık, F. Avcil, A. Büyüksaraç, E. Arkan, and R. İzol, "Geotechnical and Structural Damages Caused by the 2023 Kahramanmaraş Earthquakes in Gölbaşı (Adıyaman)," *Applied Sciences*, vol. 14, no. 5, p. 2165, 2024. [Online]. Available: https://doi.org/10.3390/app14052165.

[59] İstanbul Teknik Üniversitesi, *6 Şubat 2023 İTÜ Deprem Raporu: 04.17 Mw 7.8 Kahramanmaraş (Pazarcık, Türkoğlu), Hatay (Kırıkhan), 13.24 Mw 7.7 Kahramanmaraş (Elbistan/Nurhak-Çardak) Depremleri Ön İnceleme Raporu*, 2023.

[60] D. Ertürkmen and İ. H. Çağatay, "Dolgu Duvarlı Yapılarda Yumuşak Kat ve Zayıf Kat Düzensizliklerinin İncelenmesi," *Çukurova Üniversitesi Mühendislik-Mimarlık Fakültesi Dergisi*, vol. 31, no. 2, pp. 269-278, 2016.

[61] E. Meral, "Betonarme Binalarda Kısa Kolon Etkilerinin Araştırılması," *International Journal of Engineering Research and Development*, vol. 11, no. 2, pp. 515-527, 2019.

[62] H. Tokgöz and H. Bayraktar, "Düzce ili Kaynaşlı ilçesinde riskli binaların tespitinde sokak taraması yönteminin uygulanması," *Düzce Üniversitesi Bilim ve Teknoloji Dergisi*, vol. 3, no. 1, pp. 107-116, 2015.

[63] M. İnel, M. Bucaklı, and H. B. Özmen, "Betonarme binalarda çerçeve süreksizliğinin yapı performansı üzerindeki etkileri," in *Uluslararası Sakarya Deprem Sempozyumu*, Sakarya, 2009.

[64] H. Erdem, "Burulma düzensizliğinin betonarme kirişler ve kolonlar üzerine etkileri," *Niğde Ömer Halisdemir Üniversitesi Mühendislik Bilimleri Dergisi*, vol. 5, no. 2, pp. 148-156, 2016.

[65] C. Kubat, *Yapay Zekâ ve Mühendislik Uygulamaları*, İstanbul: Abaküs Kitap Yayın Dağıtım Hizmetleri, 2019.

[66] P. D. Ç. Elmas, *Yapay Zeka Uygulamaları*, Ankara: Seçkin Yayınevi, 2007.

[67] O. Doğan, "Uyarlamalı sinirsel bulanık çıkarım sisteminin (ANFIS) talep tahmini için kullanımı ve bir uygulama," *Dokuz Eylül Üniversitesi İktisadi İdari Bilimler Fakültesi Dergisi*, vol. 31, no. 1, pp. 257-288, 2016.

[68] İ. Uçal Sarı, *Yatırım Analizinde Bulanık Model Önerileri*, Ph.D. dissertation, İstanbul Teknik Üniversitesi, Fen Bilimleri Enstitüsü, 2012.

[69] A. C. A. R. Mustafa, M. Haberler-Weber, and T. Acar, "Bulanık çıkarım Sistemleri ile Heyelan Bloklarının Belirlenmesi Gürpınar Örneği," *Jeodezi ve Jeoinformasyon Dergisi*, no. 98, pp. 28-35, 2008.

[70] M. Özkan, "Bulanık Çıkarım Sistemi İle Bireysel Personel Performansının Değerlendirilmesinde Bir Uygulama," *C.Ü. İktisadi ve İdari Bilimler Dergisi*, vol. 19, no. 2, 2018.

[71] S. N. Sivanandam, S. Sumathi, and S. N. Deepa, *Introduction to Fuzzy Logic using MATLAB*. Springer, pp. 73-85, 2007.

[72] T. Uygunoğlu and Ü. N. A. L. Osman, "Seyitömer uçucu külünün betonun basınç dayanımına etkisi üzerine bulanık mantık yaklaşımı," *Yapı Teknolojileri Elektronik Dergisi*, vol. 1, no. 1, pp. 13-20, 2005.

[73] İ. Atacak and Ö. F. Bay, "Bulanık mantık denetimli seri aktif güç filtresi kullanarak harmonik gerilimlerin bastırılması," *Gazi Üniversitesi Mühendislik Mimarlık Fakültesi Dergisi*, vol. 19, no. 2, pp. 205-215, 2004.

[74] S. Subaşı, A. Beycioğlu, and M. Emiroğlu, "Genleştirilmiş kil agregalı hafif betonlarda bulanık mantık yöntemiyle yarmada çekme dayanımı tahmin modeli geliştirilmesi," *Eskişehir Osmangazi Üniversitesi Mühendislik ve Mimarlık Fakültesi Dergisi*, vol. 22, no. 3, pp. 157-166, 2009.

[75] K. M. Tay and C. P. Lim, "Fuzzy FMEA with a Guided Rules Reduction System for Prioritization of Failures," *International Journal of Quality and Reliability Management*, vol. 23, no. 8, pp. 1047-1066, 2006.

[76] M. Yılmaz and E. Arslan, "Bulanık Mantığın Jeodezik Problemlerin Çözümünde Kullanılması," presented at the *Harita ve Kadastro Mühendisleri Odası, Mühendislik 78 Ölçmeleri STB Komisyonu 2. Mühendislik Ölçmeleri Sempozyumu*, İstanbul Teknik Üniversitesi, İstanbul, Turkey, Nov. 23-25, 2005.

[77] G. Tanak Coşkun and Y. Y. A. Yılmaz, "Determining the best price with linear performance pricing and checking with fuzzy logic," *Computers & Industrial Engineering*, vol. 154, p. 107150, 2021. [Online]. Available: https://doi.org/10.1016/j.cie.2021.107150.

[78] S. Naaz, A. Alam, and R. Biswas, "Effect of different defuzzification methods in a fuzzy based load balancing application," *International Journal of Computer Science Issues (IJCSI)*, vol. 8, no. 5, p. 261, 2011.

[79] U. Karadavut and A. Akkaptan, "Bitkisel üretimde bulanık mantık uygulamaları," *Türk Bilimsel Derlemeler Dergisi*, vol. 5, no. 2, pp. 77-82, 20

Predictive Maintenance Planning Using a Hybrid ARIMA-ANN Model

Gamze KAYNAK[1], Bilal ERVURAL[1*]

[1]*Department of Industrial Engineering, Faculty of Engineering, Necmettin Erbakan University*

(ORCID: 0000-0003-0773-988X) (ORCID: 0000-0002-5206-7632)

Abstract
Predicting machine faults is crucial for maintaining operational efficiency in industrial settings, minimizing unplanned downtime, and ensuring customer satisfaction. Fault prediction helps identify faults and create maintenance schedules. Maintenance planning involves strategically scheduling activities to ensure the continuous operational efficiency of systems. This study focuses on reducing unplanned downtime in a food company by developing a predictive maintenance plan through machine fault prediction. Artificial Neural Networks (ANNs) are excellent in handling non-linear models, while the ARIMA model is adequate for linear models. However, real-world data often contains linear and non-linear elements, requiring hybrid models for improved accuracy. This study employs ARIMA, ANNs, and a Hybrid ARIMA-ANN model. The dataset is individually modeled using each approach. Using a 3-month machine fault dataset, predictive values for machine fault times are generated and statistically evaluated using metrics such as Mean Absolute Percentage Error (MAPE) and Root Mean Squared Error (RMSE). The findings indicate that the hybrid model outperforms both ARIMA and ANN models. The food company can significantly reduce unplanned downtime and ensure operational efficiency using a hybrid model. Predictive maintenance planning can help the food company save costs and maintain a competitive edge in the market.

1. Introduction

Predicting faults is crucial for industrial maintenance strategies to prevent system failures and minimize unplanned downtime. Accurate predictions of future failures are necessary for designing timely maintenance activities [1]. To remain competitive and satisfy customers, it is essential to eliminate system downtimes and unforeseen causes leading to them.

Many businesses perform breakdown maintenance randomly after the occurrence of a fault, resulting in significant time loss during repairs [2]. In several sectors, multiple machines work together in a cycle to produce final products. Therefore, the interdependency of operations is crucial to prevent system disruptions. Unplanned maintenance could cause damage to different machines or parts, leading to an imbalance in the system, accumulation of intermediate products, delays in work, and idle labor, resulting in waste. Poor planning damages a company's reputation and leads to financial losses due to untimely product deliveries.

Predicting faults and performing maintenance accordingly significantly mitigates hazardous situations, accidents, injuries, material damage, and extensive time loss. It also ensures that machines operate correctly, smoothly, and in a controlled manner [3]. Data processing, analyzing data, and generating meaningful insights for future predictions have become increasingly important [4]. Mathematical and statistical methods were initially used in prediction studies [5]–[8]. However, traditional methods have become inadequate with the increasing volume of data, variables, and uncertainties. Machine learning algorithms that can self-learn and adapt have been employed in prediction

studies [9]–[13]. Machine learning algorithms find applications in various fields, such as machine maintenance and repair planning, production and supply chain planning, financial calculations, and more in manufacturing.

Maintenance planning aims to calculate the occurrence time of a fault, take quick preventive measures before a fault occurs, and prevent unnecessary maintenance. Traditional maintenance planning methods are still used in businesses [14], [15]. Unnecessary maintenance can lead to the replacement of parts that could have lasted longer without a system failure, halting production for excessive maintenance and unnecessary labor and spare part usage. The goal is to optimize the duration of maintenance work, perform maintenance before faults occur, and prevent unnecessary maintenance.

Existing prediction studies in the literature use time series models and machine learning algorithms [16]–[18]. While predictions made using time series provide good results in linear models, predictions made using machine learning provide good results for non-linear models. A hybrid prediction model using the ARIMA-ANN method for fault prediction has yet to be found in the literature. Real-life data is a mix of linear and non-linear data, making it challenging to model and predict. Hence, it is predicted that the results of prediction studies using hybrid models will be better than those using linear and non-linear models.

The primary objective of this study is to eliminate unplanned downtimes and create a predictive maintenance plan to ensure that the system operates smoothly and is ready for production at any time. To achieve this, machine fault times were predicted by modeling the cumulative fault data obtained from a food production company's dryer, which causes the most interruptions in production, using ARIMA, ANN, and ARIMA-ANN hybrid models. The results obtained were compared using performance metrics such as Mean Absolute Percentage Error (MAPE) and Root Mean Square Error (RMSE).

The rest of the paper is organized as follows: Section 2 presents a comprehensive literature review. Section 3 provides information on maintenance planning. In Section 4, ARIMA, ANN, and the hybrid model are introduced, respectively. In Section 5, an experimental study is carried out to verify the forecasting performance of the proposed models. In the last section, conclusions and recommendations are presented.

2. Literature Review

Predictive maintenance is a crucial strategy in industrial settings. It aims to anticipate and prevent equipment failures before they occur. This approach helps minimize unplanned downtimes, improve operational efficiency, and reduce maintenance costs. The literature on predictive maintenance can be broadly categorized into three main approaches: statistical methods, machine learning techniques, and hybrid models.

Statistical methods, particularly time series analysis, have been extensively used in predictive maintenance. Time series models, such as ARIMA, effectively handle linear data and forecast future failures based on historical data trends. For instance, Aktaş and Aydın [19] employed time series analysis to predict production efficiency in machining operations, demonstrating the capability of these methods to provide accurate forecasts in linear systems. Similarly, ARIMA models have been utilized for error detection and predictive maintenance forecasts [6], [7]. However, compared to machine learning methods, ARIMA models are less flexible and often less accurate in capturing complex data patterns [20], [21].

With the continuing development of big data, AI, and IoT technologies, which are driving forces of Industry 4.0, machine learning techniques have gained prominence in predictive maintenance [22]. These techniques have been applied to various aspects, such as supervised classification, regression in high-dimensional data, reinforcement learning for system modeling, and unsupervised learning problems. Machine learning algorithms, such as ANN, have the ability to learn complex patterns and relationships within data, making them suitable for predicting equipment failures in non-linear systems. Zuo et al. [23] utilized a spiking neural network (SNN) for bearing fault diagnosis in manufacturing settings, highlighting the effectiveness of machine learning in detecting and predicting faults. Similarly, Sampaio et al. [24] applied ANN to predict motor failure times, further validating the robustness of these techniques in industrial applications. Ben Ali et al. [25] and Mahamad et al. [26] demonstrated the efficacy of ANN models in bearing fault diagnosis and remaining functional life prediction, respectively, showcasing significant improvements over traditional approaches.

Recent studies have also demonstrated the application of more advanced machine learning models. Zhang et al. [27] investigated the

development of models using temporally dependent sensor data for NASA's aircraft engine performance monitoring and useful life expectancy estimation. They employed a Long Short-Term Memory (LSTM) based model, which outperformed other machine learning techniques such as Support Vector Regression (SVR), Multilayer Perceptron (MLP), and Deep Convolutional Neural Networks (DCNN) in predicting useful life. Similarly, Lee et al. [28] used SVR and ANN models to predict spindle motor and cutting machine wear and malfunctions, achieving successful results. Hybrid models combine the strengths of statistical methods and machine learning techniques to address the limitations of each approach when used in isolation. These models are beneficial for handling real-life data that often exhibit both linear and non-linear characteristics. Paithankar and Chatterjee [29] proposed a hybrid data-driven method using a neural network and genetic algorithm to forecast failure time. Similarly, Yang et al. [30] developed a hybrid prediction model based on a state observer and a hidden Markov model (HMM) for control systems. Xu et al. [31] introduced a hybrid SARIMA-SVR model to predict statistical indicators in the aviation industry.

Predictive maintenance has been applied across various industrial sectors. In the manufacturing industry, predictive models are used to diagnose faults in critical components such as bearings and motors, ensuring continuous and efficient production processes. In the aviation industry, Çelikmıh et al. [32] utilized machine learning techniques to predict aircraft maintenance periods and fault counts, enhancing the reliability and safety of aircraft operations. Dindarloo et al. [33] applied SARIMA (Seasonal ARIMA) to predict the time between failures for heavy machinery, demonstrating the versatility of statistical models in different industrial contexts. The food industry presents unique maintenance and fault prediction challenges due to the high variability in production processes and the critical need to ensure product safety and quality. A few studies have explored the application of machine learning techniques in this sector to enhance predictive maintenance strategies. Liu [34] introduced a fault diagnosis approach for food machinery equipment based on neural networks. In another study, Setiawan et al. [35] performed multiple linear regression analysis to predict machine breakdowns in the food seasoning industry.

Given the advancements in production and technology, accurately estimating the remaining useful life (RUL) of machinery has become crucial for maintaining machine condition monitoring, enhancing productivity, ensuring reliability, and promoting safety [12], [36]. Various theoretical and practical methodologies have been proposed, including sophisticated deep learning models that consolidate multiple facets into a single application. The necessity for real-time processing of intricate data streams has been underscored across different application scenarios. Rivera et al. [37] investigated production system errors through the lens of anomaly detection, highlighting the pivotal role of data quality and expert knowledge in augmenting predictive accuracy.

The evolution of predictive maintenance has seen a transition from traditional statistical methods to advanced machine learning techniques and hybrid models. Each approach offers unique advantages and, when appropriately applied, can significantly enhance the reliability and efficiency of maintenance operations. Integrating these methods into a cohesive predictive maintenance strategy promises to improve industrial productivity further and reduce operational costs.

provides a summary of the reviewed studies in terms of focus, methodology, and field of application.

3. Maintenance Planning

Maintenance planning is a critical aspect of ensuring the smooth and efficient operation of industrial and service sectors. It encompasses the systematic arrangement of activities to maintain equipment functionality and minimize downtime. Effective maintenance planning is essential for businesses striving for uninterrupted production and service delivery [38]. Figure 1 illustrates various categories of maintenance planning [39].

Planned maintenance is the maintenance performed to prevent failures before they occur. It ensures that machines and equipment can operate smoothly at any given time. The objectives of planned maintenance include extending the life of machines and equipment, improving performance, reducing downtime and costs associated with breakdowns, keeping equipment ready for production at all times, minimizing damage in case of failures, reducing maintenance and repair expenses, decreasing the need for spare machines, creating a safe working environment for workers, and minimizing expenses arising from potential accidents [40]. Planned maintenance is often divided into preventive maintenance and corrective maintenance.
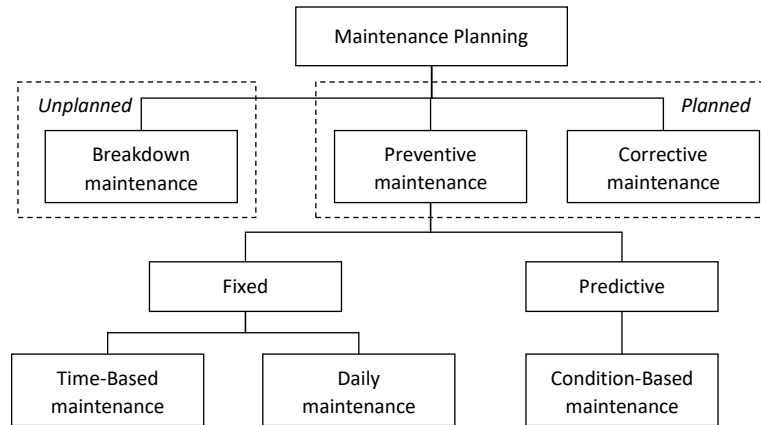
Figure 1. Types of maintenance

Table 1. A summary of the related literature

Study	Focus	Approach	Application Area
Zuo et al. [23]	Bearing fault diagnosis	SNN	Manufacturing
Çelikmıh et al. [32]	Prediction of aircraft maintenance periods and fault counts	Machine Learning	Aircraft
Sampaio et al. [24]	Motor failure time prediction	ANN	Engine
Aktaş and Aydın [19]	Production efficiency prediction	Time Series methods	Machining
Ben Ali et al. [25]	Bearing fault diagnosis	ANN	Manufacturing
Mahamad et al. [26]	Remaining useful life prediction of machines	ANN	Manufacturing
Baptista et al. [6]	Maintenance plan for an aircraft part	ARMA	Aircraft
Dindarloo [33]	The time between failure prediction	SARIMA	Heavy Machinery
Fernandes et al. [7]	Fault detection for predictive maintenance	ARIMA	Metallurgy
Medeiros et al. [41]	Failure prediction	Machine Learning Algorithms	Insulators
Kang et al. [42]	Anomaly perception and failure prediction	SVR	High-speed automatic train
Paithankar and Chatterjee [29]	Failure time prediction	Hybrid Neuro Genetic Algorithm	Mining machinery
Vargas et al. [36]	Fault prediction	Hybrid Machine Learning Algorithms	Automated teller machines (ATMs)

Preventive maintenance is a type of maintenance that businesses have recently begun to adopt. This method aims to prevent failures resulting from faults in machines and facilities. Serious research and development efforts are required for preventive maintenance. Preventive maintenance includes daily routine actions such as cleaning, refueling, inspection to prevent deterioration, periodic examination, and equipment diagnosis. These actions maintain the "health" of the equipment and prevent failures.

Predictive Maintenance predicts the life of a significant part through monitoring and diagnosis [43], [44]. Therefore, maintenance costs and breakdown losses are lower with this method compared to others. One type of predictive maintenance is Condition-Based Maintenance (CBM) [45]. This maintenance type uses condition diagnostic technology (CDT) to monitor the equipment's condition online.
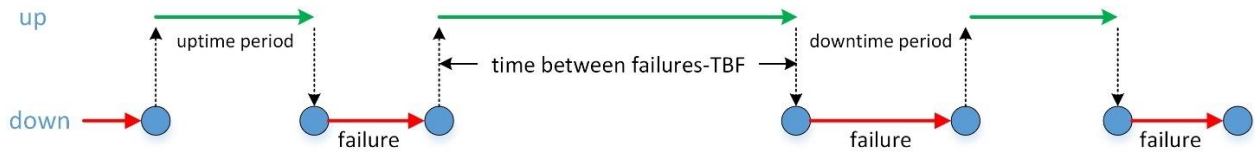
Figure 2. Measurement of time between failures [46]

In enterprise operations, thermal cameras, sensors, measurement devices, and similar technologies play a crucial role in monitoring specific areas of machinery and facilities at regular intervals [45], [47]. These observations are meticulously recorded to support proactive maintenance strategies, known as predictive maintenance. This approach focuses on swiftly detecting any deviations in system performance to intervene promptly and prevent potential malfunctions. Techniques employed in this maintenance paradigm include oil analysis, thermal imaging for temperature analysis, and other sensor-based assessments.

Predictive maintenance strategies typically involve three key stages. The first stage is detection, promptly identifying deviations in the machinery's operational conditions. Subsequently, the analysis and diagnosis phase examines the machine's characteristics to determine the underlying causes of the observed changes. Finally, the corrective phase involves implementing necessary repairs, maintenance, and replacements to rectify identified issues and ensure optimal operational efficiency. Predictive maintenance relies on accurate predictions of future failures to design timely maintenance activities. Approaches to failure prediction analyze current and past data representing system conditions, events, and operations [1]. A critical parameter in predicting failure time is the time between failures (TBF). Figure 2 illustrates how this duration is measured.

4. Methodology

4.1. The Autoregressive Integrated Moving Average

The autoregressive integrated moving average (ARIMA) model, introduced by Box and Jenkins [48], stands as a cornerstone in time series forecasting. ARIMA models capture the inherent relationships (autocorrelations) between past and present values within the data. A fundamental assumption of The ARIMA (p, d, q) model is that the underlying data series is stationary, meaning its statistical properties (mean, variance) remain constant over time and exhibit no specific trend.

The ARIMA model expresses the future value (Y_t) of a variable as a linear combination of two key elements: (i) past observations, represented by the terms $Y_{t-1}, Y_{t-2}, \ldots, Y_{t-p}$, where p signifies the order of auto-regression, (ii) past errors, captured by the terms $\varepsilon_{t-1}, \varepsilon_{t-2}, \ldots, \varepsilon_{t-q}$, where ε_t represents the error term at time t, and q denotes the order of moving average. This relationship can be mathematically expressed as:

$$Y_t = c + \phi_1 Y_{t-1} + \ldots + \phi_p Y_{t-p} + \varepsilon_t - \theta_1 \varepsilon_{t-1} - \ldots - \theta_q \varepsilon_{t-q} \qquad (1)$$

Y_t: Represents the value of the variable at time t.

c: Constant term.

ϕ_i: Coefficients associated with the autoregressive (AR) component, quantifying the influence of past observations (Y_{t-i}) on the future value.

ε_t: White noise error term at time t.

θ_i: Coefficients associated with the moving average (MA) component, reflecting the impact of past errors (ε_{t-i}) on the future value.

The ARIMA model leverages the power of past observations and error terms to provide a robust and data-driven approach to forecasting future trends in time series data.

4.2. Artificial Neural Network

ANNs are a class of machine learning models inspired by the neural networks in the human brain. They are designed to recognize patterns and make predictions based on input data. ANNs are composed of interconnected units called neurons, organized into layers. Each neuron calculates a weighted sum of its inputs and passes this sum through an activation function, introducing non-linearity to model complex relationships. The most common activation functions include the sigmoid, tanh, and rectified linear unit. There are many types of ANN, such as multilayer perceptron (MLP), radial basis function (RBF) networks, and recurrent neural networks (RNN) used by researchers in prediction studies [49]–[52].

Although MLP was initially developed to tackle complex classification problems, due to their

universal approximation capability, they were soon utilized for nonlinear regression models and subsequently for time series modeling and forecasting. However, the estimation and identification of these models involve sophisticated techniques, making it challenging to determine the correct architecture. These models are often overparametrized, the error functions to be minimized have numerous local minima, and their implementation is frequently difficult [53].

Nonlinear Autoregressive (NAR) Neural Network extends the basic principles of ANNs by incorporating temporal dependencies. NAR networks predict future values of a time series based on its past values. This autoregressive approach uses previous time points as part of its input to forecast future values. Unlike traditional ANNs, NAR networks have input, hidden, and output layers. However, the input layer takes lagged time series values, allowing the model to capture temporal dynamics.

The NAR model, depicted in Figure 3, can be mathematically expressed as:

$$y(t) = f\big(y(t-1), y(t-2), \ldots, y(t-d)\big) + \varepsilon(t) \quad (2)$$

where $y(t)$ is the value at time t, d is the time delay parameter, and the $\varepsilon(t)$ indicates the approximation error at time t.
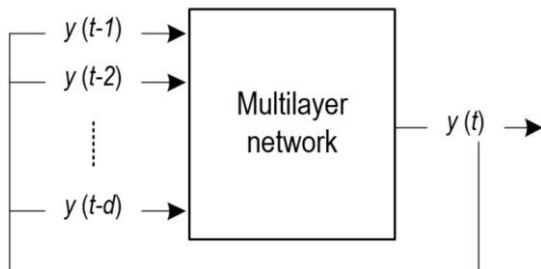
Figure 3. Non-linear autoregressive (NAR) network

4.3. ARIMA-ANN models

In recent years, in the field of time series analysis, hybrid models that use multiple models together have been introduced to improve modeling and forecasting performance. Especially with the advancement of machine learning, numerous hybrid models that combine classical statistical methods and machine learning techniques have been developed [54], [55].

One of the most important classes of hybrid models is the ARIMA-ANN hybrid model class. The strong performance of the ARIMA model for linear time series and the success of the ANN model for

nonlinear time series have led researchers to create hybrid models that incorporate both models. The fact that real-world time series often contain both linear and nonlinear characteristics is one of the main reasons for the high modeling and forecasting performance of ARIMA-ANN hybrid models [56]. In studies, time series is approached in various ways, such as the sum [18], product [57], or a nonlinear function of the values obtained from the linear series and the actual series [58] of linear and nonlinear series [56].

Zhang [18] introduced the first ARIMA-ANN model in the literature, considering the time series as the sum of linear and nonlinear series. In the model proposed by Khashei and Bijari [58], the series is not segmented into linear or nonlinear components. Instead, it is viewed as a nonlinear function of observations and errors. On the other hand, Babu and Reddy [59] separate the time series into linear and nonlinear series by passing it through a moving average filter.

4.4. Proposed Hybrid Model

The ARIMA-ANN model, first introduced by Zhang [18], is considered a highly effective tool for time series analysis. This model allows for the decomposition of time series into linear and nonlinear components, enabling separate modeling of each component.

$$Y_t = L_t + N_t \quad (3)$$

where, Y_t represents the actual observations of the time series, L_t denotes the linear trends captured by the ARIMA models. It uses autoregressive and moving average concepts based on past values to forecast future values. N_t represents the nonlinear trends and complexities of the series captured by ANNs. ANNs utilize their learning capability to model these trends. As shown in Figure 4, the proposed ARIMA-ANN hybrid model consists of four fundamental steps.

Step 1. The time series is modeled with ARIMA to obtain the initial forecast value. For this purpose, seasonality and trend analysis are conducted, and the stationarity of the series is checked. If it is non-stationary, it is transformed into a stationary form, and ACF-PACF plots are drawn. The most suitable ARIMA (p, d, q) model for the series is computed with the assistance of software, and the initial predicted value $\hat{x}(i)$ can be calculated.

Step 2. The residual values $y(i)$ are computed. Let the time series be denoted by $x(i)$, and the initial forecast

value be denoted by $\hat{x}(i)$. The residual value is calculated by taking the difference between the forecasted value and the actual data.

$$y(i) = \hat{x}(i) - x(i) \qquad (4)$$

Step 3. Raw data is utilized to train the ANN network. The architecture of the ANN model is determined. The number of hidden layers, neurons per layer, and activation functions can be adjusted within the chosen network type. The Levenberg-Marquardt algorithm or other available training functions optimize the network's weights and biases. The designed ANN architecture using the residual values is trained as the input data. This process continues until a specified number of epochs (iterations) is reached or until a certain error threshold is achieved.

Step 4. The final predicted value $x_t^*(i)$ of the combination model is obtained through the relationship between the new residuals $\hat{y}_t(i)$ and the initially predicted values $\hat{x}(i)$. The predicted values of the hybrid model are computed by taking the difference between the forecast value obtained with the ARIMA model and the forecast value obtained with the ANN model.

$$x_t^*(i) = \hat{x}(i) - \hat{y}_t(i) \qquad (5)$$
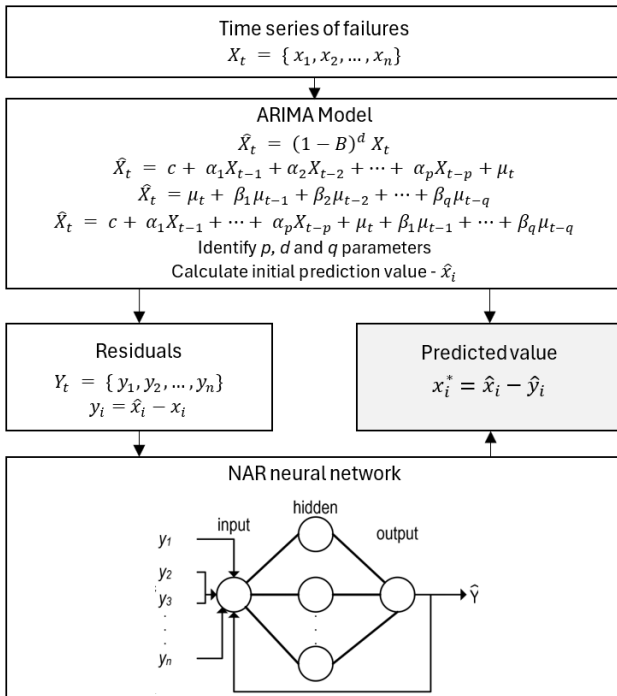
Figure 4. Flowchart of the ARIMA-ANN model

5. Case Study

In this study, predictions of machine failure time were derived utilizing the hybrid methodology described in the previous section. The linear component of the model was estimated using the ARIMA model, while the non-linear component was addressed by applying the NAR neural network method. The hybrid model was constructed by integrating these two models. Subsequently, the results of the hybrid model were compared with the prediction performances of the ARIMA and NAR neural network (NAR-NN) models. Time series plots of the predicted and actual values are presented in this section.

5.1. Background and Dataset

A case study was conducted at a facility engaged in pasta production to evaluate the proposed method. The facility operates three shifts per day. Data containing the day and time of malfunctions occurring on the production line were obtained from the company and utilized for prediction purposes. Upon examining the data, it was decided to focus on addressing malfunctions explicitly occurring in the drying machine, which constitutes a critical component causing significant disruptions to production and playing a vital role in daily operations. Should the drying line fail, the entire production process stops. Management aims to effectively anticipate the downtime of the machine, enabling the implementation of suitable maintenance scheduling activities to prevent malfunctions.

The times between failures and cumulative times for a total of 50 failures that occurred in the drying line are presented in Table A1 (see Appendix), along with a time series plot of the cumulative data shown in Figure 5. For prediction purposes, the cumulative downtime data were utilized, with the last 8 out of the 50 cumulative failure data points reserved as test data, while the remaining data points were used for training.
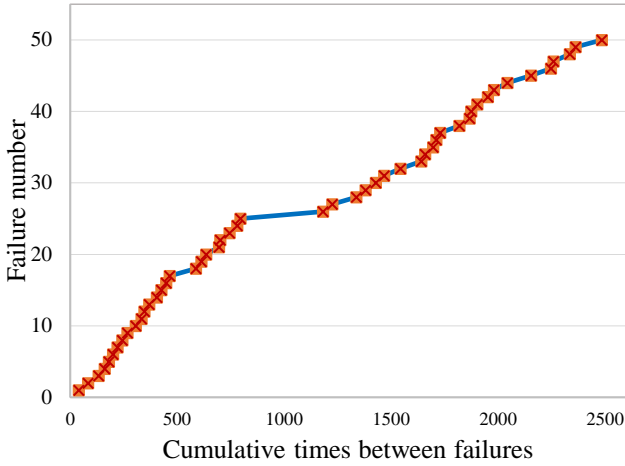
Figure 5. The time series of machine failure data

5.2. Performance Metrics

To quantitatively assess the deterministic predictions obtained from the ARIMA, ANN, and hybrid ARIMA-ANN models, three performance metrics were employed: Mean Absolute Percentage Error (MAPE), and Root Mean Squared Error (RMSE). The detailed mathematical expressions for these metrics are listed below:

$$MAPE = \frac{1}{n}\sum_{t=1}^{n}\left|\frac{y_t - \hat{y}_t}{y_t}\right| \qquad (6)$$

$$RMSE = \sqrt{\frac{\sum_{t=1}^{n}(y_t - \hat{y}_t)^2}{n}} \qquad (7)$$

where, y_t is the observed value, $\hat{y}_t$ is the predicted value, n is the total number of observations.

5.3. Analysis, Results and Discussions

In this section, the steps of the proposed model are applied to the data of the time between drying line failures. Then, a series of experimental studies are carried out to validate the effectiveness of the proposed model. The case study data is analyzed using ARIMA, NAR-NN, linear regression (LR), and Winters' methods and compared with the results of the hybrid model.

ACF and PACF graphs were used to assess the stationarity of the time series. The ACF graph indicated non-stationarity, as the autocorrelation values exceeded the boundary values. Therefore, differencing was considered necessary to achieve stationarity (Figure 5). The PACF graph revealed that the first lag had the highest partial autocorrelation value, suggesting that differencing of order 1 (d=1) should be applied to the series (Figure 6).
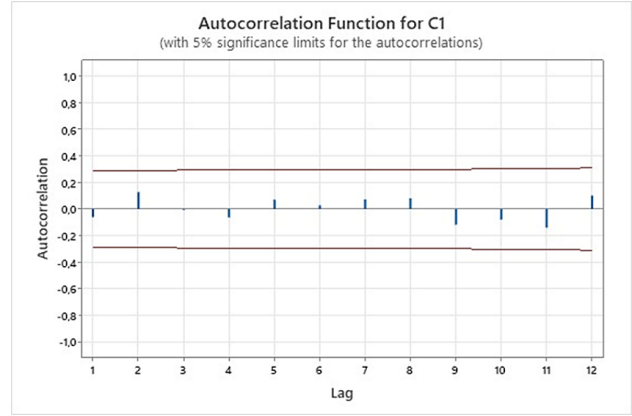
Figure 5. ACF graph of cumulative times between failures (TBFs) data
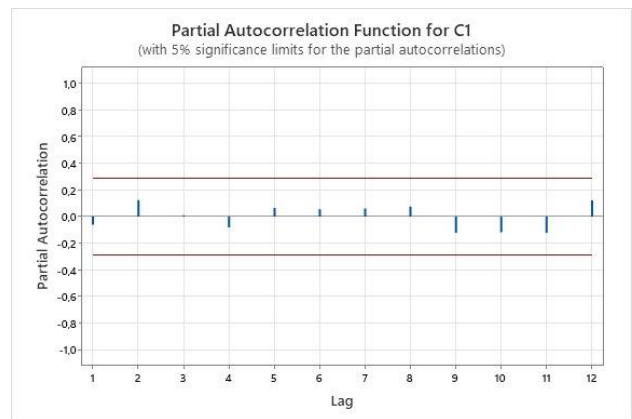
Figure 6. PACF graph of cumulative times between failures (TBFs) data

Since only the first lag was significant in the ACF graph, it was inferred that q=1. Therefore, the ARIMA model would contain a moving average component with q=1. Based on the analysis, the differencing of order 1 should be performed to achieve stationarity, and an ARIMA(0,1,1) model should be the most appropriate for the given data set. The predicted value of the ARIMA model for training data is plotted in Figure 7.
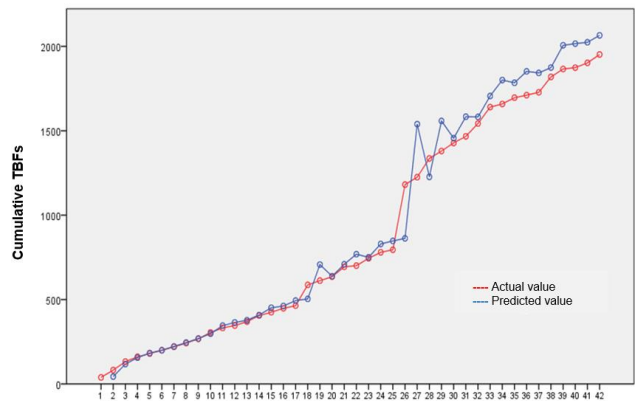
Figure 7. Failure prediction with ARIMA (0,1,1) model

In the case study, a multilayer NAR-NN was utilized for fault time prediction, characterized by its ability to model temporal dependencies through an autoregressive approach. This network, implemented in MATLAB, comprised one input layer, ten hidden layers, and one output layer. The choice of a lag of 1 allowed the network to use the immediate past value for making predictions. The hidden layers, numbering ten, were selected to provide sufficient depth for capturing complex patterns in the data, balancing model complexity with computational efficiency. Figure 8 shows the architecture of the NAR neural network.

The network employed the Levenberg-Marquardt algorithm for training, chosen for its speed and accuracy in converging to optimal solutions compared to other algorithms. The training was conducted over 1000 epochs to ensure thorough learning from the data, minimizing risks of underfitting. The network performance was evaluated using the Mean Squared Error (MSE), a standard metric for regression tasks that effectively quantifies prediction accuracy. The activation function used in the hidden layers was the hyperbolic tangent sigmoid (tansig), which was preferred for its strong gradients and reduced risk of neuron saturation, facilitating stable and effective learning. Combining these parameters and methods ensured a robust model capable of accurately predicting fault times.
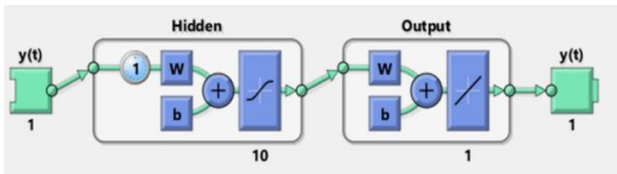
Figure 8. The architecture of the NAR-NN

The residual values, $y(i)$, are obtained by finding the difference between the ARIMA model's estimated value and the actual data using Eq. (4), and then they are used in the estimation process of the NAR-NN model. To build the neural network model, 42 instances of fault data were used from the dataset, while eight cases were kept aside for testing. Based on the dataset, the model accurately calculates the predicted values for eight residual values. The predicted residual, $\hat{y}_t(i)$, values for test data get presented in Table 2. To obtain the failure prediction results, $(x_t^*(i))$ for the hybrid approach, Eq. (5) is used. The failure prediction values of the hybrid model are also provided in Table 2.

Table 2. Validation of the hybrid method with test data

Failure no	Observed values $y_t(i)$	ARIMA $\hat{x}(i)$	Residual values $y(i)$	Predicted residual values $\hat{y}_t(i)$	Predicted values $x_t^*(i)$
43	1980	2125.5	145.5	120.1	2005.4
44	2043	2392.5	349.5	324.7	2067.8
45	2153	2693.1	540.1	522.0	2171.1
46	2246	3031.4	785.4	777.4	2254.0
47	2258	3412.2	1154.2	1163.3	2249.0
48	2335	3840.9	1505.9	1527.3	2313.6
49	2362	4323.4	1961.4	1978.7	2344.7
50	2485	4866.5	2381.5	2404.1	2462.4

Table 3 reveals the statistical results of the test data for the ARIMA, NAR-NN, and hybrid models. The ARIMA model has a MAPE value of 43.375, the NAR-NN model has a MAPE value of 5.117, and the hybrid model has a MAPE value of 0.832. Figure 9 shows the trend of the error rate of the prediction models over time. According to Lewis [60], the MAPE values are classified as follows:

- "Very good" for MAPE below 10%
- "Good" for MAPE between 10% and 20%
- "Acceptable" for MAPE between 20% and 50%
- "Incorrect and faulty" for MAPE above 50%

With this evaluation, we can confidently say that the hybrid and ANN models offer exceptional results, while the ARIMA model's results are unacceptable. Moreover, the hybrid model outperforms the ANN model with its lower MAPE value. Therefore, the hybrid model is the most reliable choice for accurate predictions.

Table 3. Comparison results of the test data

#	Observed values	ARIMA (0,1,1)		NAR-NN		Hybrid Model	
		Model value	Error %	Model value	Error %	Model value	Error %
Out-of-sample							
43	1980	2125.5	0.073	1980.0	0.000	2005.4	0.013
44	2043	2392.5	0.171	2107.4	0.032	2067.8	0.012
45	2153	2693.1	0.251	2159.0	0.003	2171.1	0.008
46	2246	3031.4	0.350	2159.0	0.039	2254.0	0.004
47	2258	3412.2	0.511	2159.0	0.044	2249.0	0.004
48	2335	3840.9	0.645	2159.0	0.075	2313.6	0.009
49	2362	4323.4	0.830	2159.0	0.086	2344.7	0.007
50	2485	4866.5	0.958	2159.0	0.131	2462.4	0.009
MAPE (%) (#43-50)		47.375		5.117		0.832	

Linear Regression and Winters' method are also applied for the machine failure data to verify the

proposed method's effectiveness. The results, as summarized in Table 4, demonstrate significant differences in accuracy and error across the methods. Linear regression performed the worst, with a high MAPE of 39.071% and an RMSE of 136.5, indicating poor prediction accuracy. Winters' method showed better performance with a MAPE of 7.829% and an RMSE of 93.30, but still fell short compared to more advanced models. ARIMA improved further, achieving a MAPE of 7.361% and an RMSE of 101.9, reflecting its capability to model time series data more effectively. The NAR-NN demonstrated a significant improvement, with a MAPE of 1.586% and an RMSE of 9.807, indicating its strong ability to capture nonlinear relationships and temporal dependencies. However, the proposed hybrid model outperformed all other methods, achieving the lowest MAPE of

0.384% and an RMSE of 2.167, showcasing the advantages of combining multiple techniques for superior accuracy and minimal prediction errors.

6. Conclusion and Suggestions

The primary objective of this research is to ensure the efficient functioning of a food production company's production line by foreseeing and preventing potential breakdowns through strategic maintenance planning. The focus lies in foreseeing unexpected downtime, conducting predictive studies on machine breakdowns, and scheduling maintenance at optimal intervals. The right timing for scheduling maintenance is crucial in averting unforeseen breakdowns, avoiding unnecessary disruptions in production, and reducing waste.
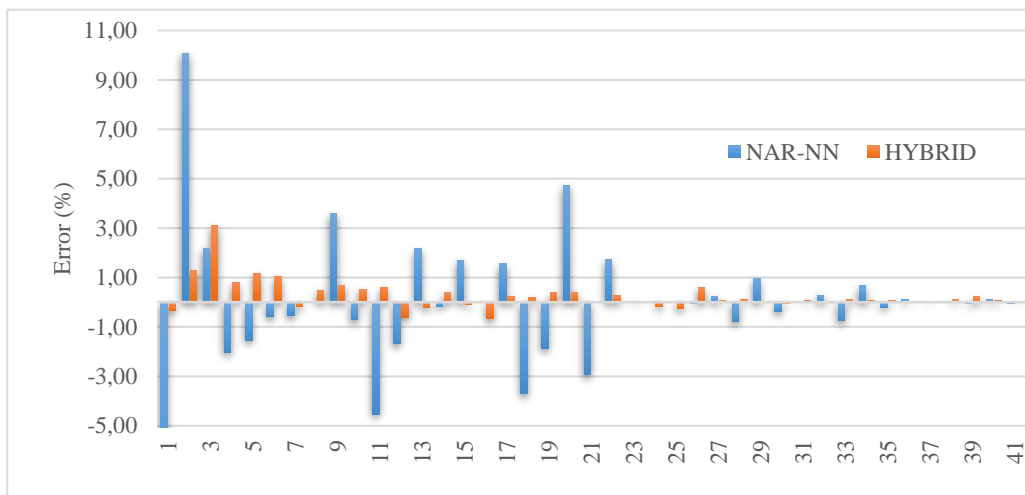
Figure 9. Trends of percentage of forecasting error

Table 4. Comparison of failure prediction results

Data	Methods	MAPE (%)	RMSE
machine failure data	Linear regression	39.071	136.5
	Winters'	7.829	93.30
	ARIMA	7.361	101.9
	NAR-NN	1.586	9.807
	Hybrid model	0.384	2.167

The study proposes a hybrid ARIMA-ANN method that combines time series and machine learning techniques. This hybrid model effectively integrates the strengths of linear and non-linear models to develop a preventive maintenance plan that can anticipate future potential breakdowns. This plan takes proactive measures to prevent breakdowns by scheduling maintenance at the appropriate times. The hybrid model outperforms traditional linear and non-

linear models. Below, we have itemized the discussions and findings into industrial gains.

- The proposed hybrid model accurately predicts machine faults, allowing for predictive maintenance planning. This reduces unplanned downtimes and improves overall production efficiency.
- By predicting faults and performing maintenance before failures occur, companies can avoid the high costs associated with emergency repairs, production stoppages, and idle labor.
- The model helps ensure that machinery operates smoothly and reliably, thereby extending the lifespan of equipment and reducing the frequency of maintenance interventions.
- Accurate fault predictions help streamline maintenance schedules, ensuring that maintenance activities are performed at optimal

times, minimizing disruptions to the production process.

This study contributes to the body of knowledge on predictive maintenance by demonstrating the effectiveness of a hybrid ARIMA-ANN model in a real-world industrial setting, specifically within the food industry. Integrating ARIMA and ANN models addresses linear and non-linear data patterns, offering a robust approach to fault prediction. This hybrid methodology can be adapted and applied to other industries and machinery types.

While this study focused on a food production company, the hybrid ARIMA-ANN model we developed for predictive maintenance is highly adaptable and applicable to various industries with similar maintenance challenges. The model combines the strengths of linear and non-linear prediction methods, making it suitable for industries such as manufacturing, automotive, aerospace, and energy sectors that require accurate maintenance planning. It relies on historical fault data and operational parameters, which are common across different industries, and its scalable methodology ensures consistent data collection, preprocessing, and model training for both large-scale production lines and smaller units. The model's parameters can be customized to meet specific maintenance requirements and operational conditions of various sectors.

While the hybrid ARIMA-ANN model showed promising results in predicting machine faults with the available data, it is essential to note that neural networks typically benefit from larger datasets. Increasing the volume of training data can enhance the model's reliability and generalization capabilities. Future studies should collect and utilize as much data as possible to improve prediction accuracy. To further validate the model, future research could implement it across different industries and compare performance metrics, benchmark it against existing industry-specific maintenance tools, and test it with diverse data types and machinery to ensure robustness and adaptability.

Contributions of the authors

Bilal Ervural: Conceptualization, Research Design, Editing, Supervision, Model Development, Manuscript Writing, Review, Final Approval. Gamze Kaynak: Literature Review, Data Collection, Data Analysis, Model Development.

Conflict of Interest Statement

There is no conflict of interest between the authors.

Statement of Research and Publication Ethics

The study complies with research and publication ethics.

References

[1]   J. Leukel, J. González, and M. Riekert, "Adoption of machine learning technology for failure prediction in industrial maintenance: A systematic review," *J. Manuf. Syst.*, vol. 61, no. September, pp. 87–96, 2021, doi: 10.1016/j.jmsy.2021.08.012.

[2]   D. M. Louit, R. Pascual, and A. K. S. Jardine, "A practical procedure for the selection of time-to-failure models based on the assessment of trends in maintenance data," *Reliab. Eng. Syst. Saf.*, vol. 94, no. 10, pp. 1618–1628, Oct. 2009, doi: 10.1016/J.RESS.2009.04.001.

[3]   M. Zufle, J. Agne, J. Grohmann, I. Dortoluk, and S. Kounev, "A Predictive Maintenance Methodology: Predicting the Time-to-Failure of Machines in Industry 4.0," in *2021 IEEE 19th International Conference on Industrial Informatics (INDIN)*, IEEE, Jul. 2021, pp. 1–8. doi: 10.1109/INDIN45523.2021.9557387.

[4]   E. F. Alsina, M. Chica, K. Trawiński, and A. Regattieri, "On the use of machine learning methods to predict component reliability from data-driven industrial case studies," *Int. J. Adv. Manuf. Technol.*, vol. 94, no. 5–8, pp. 2419–2433, Feb. 2018, doi: 10.1007/s00170-017-1039-x.

[5]   W. Zhao, T. Tao, and E. Zio, "System reliability prediction by support vector regression with analytic selection and genetic algorithm parameters selection," *Appl. Soft Comput.*, vol. 30, pp. 792–802, May 2015, doi: 10.1016/J.ASOC.2015.02.026.

[6]   M. Baptista, S. Sankararaman, I. P. de Medeiros, C. Nascimento, H. Prendinger, and E. M. P. Henriques, "Forecasting fault events for predictive maintenance using data-driven techniques and ARMA modeling," *Comput. Ind. Eng.*, vol. 115, no. September 2017, pp. 41–53, Jan. 2018, doi: 10.1016/j.cie.2017.10.033.

[7]   M. Fernandes, A. Canito, J. M. Corchado, and G. Marreiros, "Fault Detection Mechanism of a Predictive Maintenance System Based on Autoregressive Integrated Moving Average Models," in *Advances in Intelligent Systems and Computing*, vol. 1003, Springer International Publishing, 2020, pp. 171–180. doi: 10.1007/978-3-030-23887-2_20.

[8]   M. Ángel, N. Álvarez, J. Carpio Ibáñez, and C. Sancho De Mingo, "Reliability Assessment of Repairable Systems Using Simple Regression Models," *Int. J. Math. Eng. Manag. Sci.*, vol. 6, no. 1, pp. 180–192, 2021, doi: 10.33889/IJMEMS.2021.6.1.011.

[9]   H. İ. Ayaz and Z. Ozturk, Kamisli, "Shilling Attack Detection with One Class Support Vector Machines," *Necmettin Erbakan Üniversitesi Fen ve Mühendislik Bilim. Derg.*, vol. 5, no. 2, pp. 246–256, Dec. 2023, doi: 10.47112/neufmbd.2023.22.

[10] S. Fernandes, M. Antunes, A. R. Santiago, J. P. Barraca, D. Gomes, and R. L. Aguiar, "Forecasting Appliances Failures: A Machine-Learning Approach to Predictive Maintenance," *Information*, vol. 11, no. 4, p. 208, Apr. 2020, doi: 10.3390/info11040208.

[11] G. Makridis, D. Kyriazis, and S. Plitsos, "Predictive maintenance leveraging machine learning for time-series forecasting in the maritime industry," in *2020 IEEE 23rd International Conference on Intelligent Transportation Systems (ITSC)*, IEEE, Sep. 2020, pp. 1–8. doi: 10.1109/ITSC45102.2020.9294450.

[12] S. Ayvaz and K. Alpay, "Predictive maintenance system for production lines in manufacturing: A machine learning approach using IoT data in real-time," *Expert Syst. Appl.*, vol. 173, no. September 2020, p. 114598, Jul. 2021, doi: 10.1016/j.eswa.2021.114598.

[13] M. Bevilacqua, M. Braglia, M. Frosolini, and R. Montanari, "Failure rate prediction with artificial neural networks," *J. Qual. Maint. Eng.*, vol. 11, no. 3, pp. 279–294, Sep. 2005, doi: 10.1108/13552510510616487.

[14] P. Samaranayake and S. Kiridena, "Aircraft maintenance planning and scheduling: An integrated framework," *J. Qual. Maint. Eng.*, vol. 18, no. 4, pp. 432–453, Oct. 2012, doi: 10.1108/13552511211281598.

[15] C. Guedes Soares, Ed., *Safety and Reliability of Industrial Products, Systems and Structures*. CRC Press, 2010. doi: 10.1201/b10572.

[16] S. Kolidakis, G. Botzoris, V. Profillidis, and P. Lemonakis, "Road traffic forecasting — A hybrid approach combining Artificial Neural Network with Singular Spectrum Analysis," *Econ. Anal. Policy*, vol. 64, pp. 159–171, Dec. 2019, doi: 10.1016/J.EAP.2019.08.002.

[17] G. Aydin, I. Karakurt, and C. Hamzacebi, "Artificial neural network and regression models for performance prediction of abrasive waterjet in rock cutting," *Int. J. Adv. Manuf. Technol.*, vol. 75, no. 9–12, pp. 1321–1330, Dec. 2014, doi: 10.1007/s00170-014-6211-y.

[18] P. G. Zhang, "Time series forecasting using a hybrid ARIMA and neural network model," *Neurocomputing*, vol. 50, pp. 159–175, Jan. 2003, doi: 10.1016/S0925-2312(01)00702-0.

[19] A. Bahadır and C. Aydin, "Talaşlı İmalat Sektöründe Zaman Serileri Kullanarak Üretim Etkililiğinin Tahmini," *Bilişim Teknol. Derg.*, vol. 11, no. 4, pp. 407–416, Oct. 2018, doi: 10.17671/gazibtd.383339.

[20] A. Safari and M. Davallou, "Oil price forecasting using a hybrid model," *Energy*, vol. 148, pp. 49–58, Apr. 2018, doi: 10.1016/j.energy.2018.01.007.

[21] J.-J. Wang, J.-Z. Wang, Z.-G. Zhang, and S.-P. Guo, "Stock index forecasting based on a hybrid model," *Omega*, vol. 40, no. 6, pp. 758–766, Dec. 2012, doi: 10.1016/j.omega.2011.07.008.

[22] Z. Li, Y. Wang, and K.-S. Wang, "Intelligent predictive maintenance for fault diagnosis and prognosis in machine centers: Industry 4.0 scenario," *Adv. Manuf.*, vol. 5, no. 4, pp. 377–387, Dec. 2017, doi: 10.1007/s40436-017-0203-8.

[23] L. Zuo, L. Zhang, Z.-H. Zhang, X.-L. Luo, and Y. Liu, "A spiking neural network-based approach to bearing fault diagnosis," *J. Manuf. Syst.*, vol. 61, pp. 714–724, Oct. 2021, doi: 10.1016/j.jmsy.2020.07.003.

[24] G. Scalabrini Sampaio, A. R. de A. Vallim Filho, L. Santos da Silva, and L. Augusto da Silva, "Prediction of Motor Failure Time Using An Artificial Neural Network," *Sensors*, vol. 19, no. 19, p. 4342, Oct. 2019, doi: 10.3390/s19194342.

[25] J. Ben Ali, N. Fnaiech, L. Saidi, B. Chebel-Morello, and F. Fnaiech, "Application of empirical mode decomposition and artificial neural network for automatic bearing fault diagnosis based on vibration

signals," *Appl. Acoust.*, vol. 89, pp. 16–27, Mar. 2015, doi: 10.1016/J.APACOUST.2014.08.016.

[26] A. K. Mahamad, S. Saon, and T. Hiyama, "Predicting remaining useful life of rotating machinery based artificial neural network," *Comput. Math. with Appl.*, vol. 60, no. 4, pp. 1078–1087, Aug. 2010, doi: 10.1016/J.CAMWA.2010.03.065.

[27] J. Zhang, P. Wang, R. Yan, and R. X. Gao, "Deep Learning for Improved System Remaining Life Prediction," *Procedia CIRP*, vol. 72, pp. 1033–1038, Jan. 2018, doi: 10.1016/J.PROCIR.2018.03.262.

[28] W. J. Lee, H. Wu, H. Yun, H. Kim, M. B. G. Jun, and J. W. Sutherland, "Predictive Maintenance of Machine Tool Systems Using Artificial Intelligence Techniques Applied to Machine Condition Data," *Procedia CIRP*, vol. 80, pp. 506–511, Jan. 2019, doi: 10.1016/J.PROCIR.2018.12.019.

[29] A. Paithankar and S. Chatterjee, "Forecasting time-to-failure of machine using hybrid Neuro-genetic algorithm – a case study in mining machinery," *Int. J. Mining, Reclam. Environ.*, vol. 32, no. 3, pp. 182–195, Apr. 2018, doi: 10.1080/17480930.2016.1262499.

[30] D. Yang, X. Hai, Y. Ren, J. Cui, K. Li, and S. Zeng, "A hybrid fault prediction method for control systems based on extended state observer and hidden Markov model," *Asian J. Control*, vol. 25, no. 1, pp. 418–432, Jan. 2023, doi: 10.1002/ASJC.2802.

[31] S. Xu, H. K. Chan, and T. Zhang, "Forecasting the demand of the aviation industry using hybrid time series SARIMA-SVR approach," *Transp. Res. Part E Logist. Transp. Rev.*, vol. 122, pp. 169–180, Feb. 2019, doi: 10.1016/J.TRE.2018.12.005.

[32] K. Celikmih, O. Inan, and H. Uguz, "Failure Prediction of Aircraft Equipment Using Machine Learning with a Hybrid Data Preparation Method," *Sci. Program.*, vol. 2020, 2020, doi: 10.1155/2020/8616039.

[33] S. Dindarloo, "Reliability forecasting of a load-haul-dump machine: A comparative study of ARIMA and neural networks," *Qual. Reliab. Eng. Int.*, vol. 32, no. 4, pp. 1545–1552, Jun. 2016, doi: 10.1002/qre.1844.

[34] H. Liu, "Application of industrial Internet of things technology in fault diagnosis of food machinery equipment based on neural network," *Soft Comput.*, vol. 27, no. 13, pp. 9001–9018, Jul. 2023, doi: 10.1007/s00500-023-08412-5.

[35] I. Setiawan, A. Bahrudin, M. M. Arifin, W. I. Fipiana, and V. Lusia, "Analysis of Preventive Maintenance and Breakdown Maintenance on Production Achievement in the Food Seasoning Industry," *OPSI*, vol. 14, no. 2, pp. 253–261, Dec. 2021, doi: 10.31315/OPSI.V14I2.5540.

[36] V. M. Vargas, R. Rosati, C. Hervás-Martínez, A. Mancini, L. Romeo, and P. A. Gutiérrez, "A hybrid feature learning approach based on convolutional kernels for ATM fault prediction using event-log data," *Eng. Appl. Artif. Intell.*, vol. 123, p. 106463, Aug. 2023, doi: 10.1016/j.engappai.2023.106463.

[37] D. L. Rivera, M. R. Scholz, C. Bühl, M. Krauss, and K. Schilling, "Is Big Data About to Retire Expert Knowledge? A Predictive Maintenance Study," *IFAC-PapersOnLine*, vol. 52, no. 24, pp. 1–6, Jan. 2019, doi: 10.1016/j.ifacol.2019.12.364.

[38] N. Aktepe, "Toplam verimli bakım ve bir imalat işletmesinde uygulaması," Akdeniz Üniversitesi, 2007. Accessed: Mar. 31, 2024. [Online]. Available: http://acikerisim.akdeniz.edu.tr/xmlui/handle/123456789/5011

[39] M. A. Mansor, A. Ohsato, and S. Sulaiman, "Knowledge Management for Maintenance Activities in the Manufacturing Sector," *Int. J. Automot. Mech. Eng.*, vol. 5, no. 1, pp. 612–621, Jun. 2012, doi: 10.15282/ijame.5.2012.7.0048.

[40] R. Abbassi, J. Bhandari, F. Khan, V. Garaniya, and S. Chai, "Developing a Quantitative Risk-based Methodology for Maintenance Scheduling Using Bayesian Network," *Chem. Eng. Trans.*, vol. 48, pp. 235–240, Apr. 2016, doi: 10.3303/CET1648040.

[41] A. Medeiros, A. Sartori, S. F. Stefenon, L. H. Meyer, and A. Nied, "Comparison of artificial intelligence techniques to failure prediction in contaminated insulators based on leakage current," *J. Intell. Fuzzy Syst.*, vol. 42, no. 4, pp. 3285–3298, Mar. 2022, doi: 10.3233/JIFS-211126.

[42] R. Kang *et al.*, "A method of online anomaly perception and failure prediction for high-speed automatic train protection system," *Reliab. Eng. Syst. Saf.*, vol. 226, p. 108699, Oct. 2022, doi: 10.1016/j.ress.2022.108699.

[43] B. Soylu, H. Yiğiter, V. Sarıkaya, Z. Sandıkçı, and A. Utku, "Kestirimci bakim planlama için makine öğrenmesi temelli bir karar destek sistemi ve bir uygulama," *Veriml. Derg.*, vol. 0, no. Dijital Dönüşüm ve Verimlilik, pp. 48–66, Jan. 2022, doi: 10.51551/verimlilik.988104.

[44] S. PERÇİN and S. ÇAKIR, "Çok Kriterli Karar Verme Teknikleriyle Lojistik Firmalarında Performans Ölçümü," *Ege Akad. Bakis (Ege Acad. Rev.*, vol. 13, no. 4, pp. 449–449, 2013, doi: 10.21121/eab.2013418079.

[45] M. Cakir, M. A. Guvenc, and S. Mistikoglu, "The experimental application of popular machine learning algorithms on predictive maintenance and the design of IIoT based condition monitoring system," *Comput. Ind. Eng.*, vol. 151, p. 106948, Jan. 2021, doi: 10.1016/j.cie.2020.106948.

[46] A. Birolini, *Reliability Engineering*. Berlin, Heidelberg: Springer Berlin Heidelberg, 2004. doi: 10.1007/978-3-662-05409-3.

[47] S. Sajid, A. Haleem, S. Bahl, M. Javaid, T. Goyal, and M. Mittal, "Data science applications for predictive maintenance and materials science in context to Industry 4.0," *Mater. Today Proc.*, vol. 45, pp. 4898–4905, Jan. 2021, doi: 10.1016/J.MATPR.2021.01.357.

[48] G. E. P. Box, G. M. Jenkins, G. C. Reinsel, and G. M. Ljung, *Time series analysis: forecasting and control*. John Wiley & Sons, 2015.

[49] Q. Jiang, L. Zhu, C. Shu, and V. Sekar, "An efficient multilayer RBF neural network and its application to regression problems," *Neural Comput. Appl.*, vol. 34, no. 6, pp. 4133–4150, Mar. 2022, doi: 10.1007/s00521-021-06373-0.

[50] P. H. Borghi, O. Zakordonets, and J. P. Teixeira, "A COVID-19 time series forecasting model based on MLP ANN," *Procedia Comput. Sci.*, vol. 181, pp. 940–947, Jan. 2021, doi: 10.1016/J.PROCS.2021.01.250.

[51] A. Di Piazza, M. C. Di Piazza, G. La Tona, and M. Luna, "An artificial neural network-based forecasting model of energy-related time series for electrical grid management," *Math. Comput. Simul.*, vol. 184, pp. 294–305, Jun. 2021, doi: 10.1016/J.MATCOM.2020.05.010.

[52] T. Sarı, S. R. Şensoy, A. E. Nurbaki, and İ. A. Ağaç, "Yapay Sinir Ağları Yaklaşımı ile Talep Tahmini: Madeni Eşya İmalat Sektöründe Bir Uygulama," *Veriml. Derg.*, vol. 57, no. 4, pp. 701–718, Oct. 2023, doi: 10.51551/VERIMLILIK.1327524.

[53] L. Ruiz, M. Cuéllar, M. Calvo-Flores, and M. Jiménez, "An Application of Non-Linear Autoregressive Neural Networks to Predict Energy Consumption in Public Buildings," *Energies*, vol. 9, no. 9, p. 684, Aug. 2016, doi: 10.3390/en9090684.

[54] F. Çoban and L. Demir, "Yapay Sinir Ağları ve Destek Vektör Regresyonu ile Talep Tahmini: Gıda İşletmesinde Bir Uygulama," *Dokuz Eylül Üniversitesi Mühendislik Fakültesi Fen ve Mühendislik Derg.*, vol. 23, no. 67, pp. 327–338, Jan. 2021, doi: 10.21205/deufmd.2021236729.

[55] Ü. Ç. Büyükşahin and Ş. Ertekin, "Tek değişkenli zaman serileri tahmini için öznitelik tabanlı hibrit ARIMA-YSA modeli," *Gazi Üniversitesi Mühendislik Mimar. Fakültesi Derg.*, vol. 35, no. 1, pp. 467–478, 2020, doi: 10.17341/GAZIMMFD.508394.

[56] M. B. Erturan and F. Merdivenci, "Zaman serileri analizi için optimize ARIMA-YSA melez modeli," *Gazi Üniversitesi Mühendislik Mimar. Fakültesi Derg.*, vol. 37, no. 2, pp. 1019–1032, 2022, doi: 10.17341/GAZIMMFD.889513.

[57] L. Wang, H. Zou, J. Su, L. Li, and S. Chaudhry, "An ARIMA-ANN Hybrid Model for Time Series Forecasting," *Syst. Res. Behav. Sci.*, vol. 30, no. 3, pp. 244–259, May 2013, doi: 10.1002/SRES.2179.

[58] M. Khashei and M. Bijari, "A novel hybridization of artificial neural networks and ARIMA models for time series forecasting," *Appl. Soft Comput.*, vol. 11, no. 2, pp. 2664–2675, Mar. 2011, doi: 10.1016/J.ASOC.2010.10.015.

[59] C. N. Babu and B. E. Reddy, "A moving-average filter based hybrid ARIMA–ANN model for forecasting time series data," *Appl. Soft Comput.*, vol. 23, pp. 27–38, Oct. 2014, doi: 10.1016/j.asoc.2014.05.028.

[60] Colin D. Lewis, "Industrial and Business Forecasting Methods: A Practical Guide to Exponential Smoothing and Curve Fitting," *Butterworth Sci.*, no. June 1981, pp. 111–153, 1982.

Appendix

Table A1. Actual TBFs and cumulative data

Failure No	TBFs (hour)	Cumulative TBFs (hour)	Failure No	TBFs (hour)	Cumulative TBFs (hour)
1	39	39	26	386	1181
2	43	82	27	44	1225
3	50	132	28	111	1336
4	29	161	29	44	1380
5	19	180	30	48	1428
6	19	199	31	39	1467
7	21	220	32	76	1543
8	22	242	33	97	1640
9	25	267	34	19	1659
10	38	305	35	37	1696
11	27	332	36	15	1711
12	14	346	37	17	1728
13	23	369	38	91	1819
14	36	405	39	47	1866
15	20	425	40	8	1874
16	23	448	41	28	1902
17	16	464	42	50	1952
18	123	587	43	28	1980
19	25	612	44	63	2043
20	23	635	45	110	2153
21	59	694	46	93	2246
22	7	701	47	12	2258
23	43	744	48	77	2335
24	36	780	49	27	2362
25	15	795	50	123	2485

Buckling Analysis of FG Timoshenko Beam Based on Physical Neutral Surface Position

Pınar Aydan DEMİRHAN[1*]

[1]*Trakya University, Faculty of Engineering, Mechanical Engineering Department, Edirne, Türkiye*
(ORCID: 0000-0002-2618-4982)

Abstract
The paper investigates the buckling analysis of the functionally graded Timoshenko beams with arbitrary boundary conditions. The investigation focuses on the critical buckling loads, considering factors such as the slenderness ratio, boundary conditions, and the power-law index. The method involves defining the effective properties of the FG beam by rule of mixture, with physical neutral surface is assumed as a reference surface. Numerical results are presented, demonstrating the variation of the non-dimensional neutral surface position with the power law index for different material property ratios. The study concludes by discussing the influence of slenderness ratio, power law index value, and boundary conditions on critical buckling load of FG Timoshenko beams.

1. Introduction

In recent years, researchers have been focusing on composite materials as conventional materials are unable to meet the demands of high-end technological applications. Although laminated composites are used in a wide range of industrial applications, they have certain limitations due to stress concentrations occurring at their layer interfaces. However, functionally graded (FG) materials overcome these limitations by smoothly varying their properties. This is achieved by the smooth variation of material properties through the thickness direction to attain the desired function. These graded materials are ideal for various applications such as shells, plates, and beams, due to their advantageous features which eliminate sudden changes in properties.

The analysis of functionally graded sandwich plates is essential due to their wide use in aerospace, civil, and mechanical engineering. These plates, which have customized material properties, offer improved performance, including better strength-to-weight ratios and superior resistance to thermal and mechanical loads. Despite significant progress in understanding their behavior, there is still a need for further comprehensive studies to develop more

accurate and efficient models for predicting their responses. This study aims to address these gaps by providing an in-depth analysis of functionally graded sandwich plates using advanced theoretical and computational approaches.

Several studies have presented about the dynamic and the static behavior of the FG beams and plates. Zenkour[1] provided a comprehensive analysis of these plates, Li et al.[2] conducted a three-dimensional vibration analysis. Reddy [3] offered significant insights into the analysis of functionally graded plates. Vo et al.[4] developed a quasi-3D theory for vibration and buckling, and Thai and Choi[5] formulated a finite element approach for various shear deformation theories. Taskin and Demirhan [6] focused on the static analysis of simply supported porous sandwich plates. Demirhan and Taskin[7] investigated bending and free vibration using the state space approach. Vo et al. [8] developed a refined shear deformation theory for the finite element modeling of vibration and buckling. Nair and Pany [9] presented a comprehensive review on the static, buckling, and free vibration, thermo-mechanical analysis of FGM panel. Pany and Rao

presented studies on the fundamental frequency of a uniform cantilever beam undergoing large amplitude[10] and large amplitude fundamental frequency for a spring-hinged uniform beam[11]. Pany[12] presented a study to provide the large-amplitude first mode frequency for the non-prismatic (tapered beam) cantilever beam. Li and Batra [13] conducted a study on the critical buckling loads of FG Euler-Bernoulli and Timoshenko beams. Li et al. [14], [15] obtained analytical relations of the bending analysis of homogenous Euler-Bernoulli beams and FG Timoshenko beams. An analytical solution is developed by Nguyen et al. [16] for buckling, bending, and vibration of the functionally graded beam (FGB) utilizing the first-order shear deformation beam theory (FOSDT). Li et al. [17] compared functionally graded Levinson and Euler-Bernoulli beams in terms of the critical buckling loads.

Various theories have been used for analyzing functionally graded materials. Anisotropy of the material properties causes complexity for the solution; therefore, researchers investigate the new theories. Morimoto et al. [18] offered a suitably selected reference plane to eliminate coupled bending and stretching deformations. Abrate [19] indicated that choosing an appropriate reference plane enables in-plane and transverse deformations to be uncoupled. Zhang and Zhou [20] called this reference plane to the physical neutral surface (PNS) and emphasized that the stretching and bending deformations are uncoupled in constitutive equations of their theory. They presented a static and dynamic analysis of functionally graded thin plates based on the PNS. Since the calculation procedure of this theory is simpler than the other geometrical middle surface-based theories, it has been used by many researchers.

Concerning functionally graded plates, many research have conducted for static and dynamic analysis. Zhang [21] used PNS concept with high order shear deformation theory for investigation of nonlinear analysis of functionally graded plate (FGP). Fekrar et al. [22] developed a high order shear deformation plate theory for bending analysis of FGP, and used PNS to simplify the solution procedure. Zhang [23] presented a model for FGP resting on two-parameter elastic foundation based on PNS concept with high order shear deformation theory (HOSDT). Han et al. [24] contributed the dynamic instability analysis of Sigmoid FGP on elastic medium, used a four-variable refined plate theory with PNS concept. By utilizing neutral surface position, Bellifa et al. [25] proposed a novel FOSDT for functionally graded plate bending and dynamic analysis. Ebrahimi et al.

[26] investigated the analytical solution for free vibration of shear deformable porous smart plates considering neutral surface position. The four-variable refined theory with PNS concept was used by Nguyen et al. [27] to evaluate the static behavior of FGP resting on Winkler-Pasternak elastic foundation. For analyzing free vibration and mechanical buckling of FGP, Sadgui and Tati [28] established a novel HOSDT based on the precise neutral surface location.

There are limited number of papers dealing with dynamic and static analysis of FG beam using PNS position concept. Ma and Lee [29] offered an exact, closed-form solution for the nonlinear bending and thermal post buckling analysis of FG beam subjected to a uniform in-plane thermal loading using PNS concept. Larbi et al. [30] proposed an efficient beam theory considering shear deformation based on PNS position for free vibration and bending analysis of FGB. Zhang [31] investigated nonlinear vibration and the thermal post-buckling analysis of FGBs using HOSDT with PNS concept. Al-Basyouni et al. [32] presented a modified couple stress theory with neutral axis concept for vibration and bending analysis of FG micro-beams. Ebrahimi and Salari [33] developed a semi-analytical solution for free vibration and buckling of nano-FGBs based on the PNS position. Zoubida et al. [34] conducted the static and free vibration analysis of FGB using a new refined beam theory based on PNS position. Phuong et al. [35] presented the bending analysis of functionally graded porous beams using the PNS concept and Timoshenko beam theory. Derikvand [36] investigated the buckling behavior of a sandwich beam that had face layers made of functionally graded materials and a porous ceramic core. Van Vinh et al. [37] introduced a static bending analysis of the FGP by developing an improved first-order beam element that considers the PNS position.

While some previous studies investigated the buckling analysis of FGBs using the PNS position concept, these have primarily focused on thermal buckling and thermal post-buckling analysis [38] and [31]. To the best of the author's knowledge, no studies have yet presented a comprehensive investigation of arbitrary boundary conditions for critical buckling loads value of FGB using the neutral surface position concept. This gap in the literature emphasizes the need for further research. The current paper fills this gap by presenting a novel and comprehensive study on the buckling analysis of the FG Timoshenko beam with arbitrary boundary conditions, all based on the PNS position concept. The study investigates the variations of critical buckling load value of the FG Timoshenko beam in relation to the slenderness ratio,

value of the power law index, and boundary conditions.

2. Material and Method

In this study, we consider a FG beam of length L, width b, and thickness h.
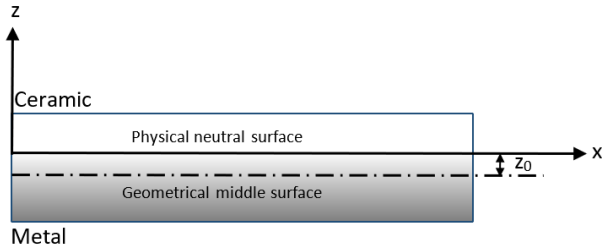
Figure 1. Position of the physical neutral surface.

The rule of mixture is utilized for defining effective properties of functionally graded beam.

$$E(z) = E_m + (E_c - E_m)\left(z + \frac{h}{2}\right)^k \quad (1)$$

$$\rho(z) = \rho_m + (\rho_c - \rho_m)\left(z + \frac{h}{2}\right)^k \quad (2)$$

where k is denotes for the power law index, E and ρ is the elasticity modulus and the density of functionally graded beam, respectively. Subscript c for ceramic and m for metal.

In this study reference surface of the FGB assume as the PNS (Fig.1) and the coordinates of axis is defined as follows [15]:

$$z_0 = \frac{\int_{-\frac{h}{2}}^{\frac{h}{2}} zE(z)}{\int_{-\frac{h}{2}}^{\frac{h}{2}} E(z)} = \frac{\int_{-\frac{h}{2}}^{\frac{h}{2}} z\left(E_m + (E_c - E_m)\left(z + \frac{h}{2}\right)^k\right)}{\int_{-\frac{h}{2}}^{\frac{h}{2}}\left(E_m + (E_c - E_m)\left(z + \frac{h}{2}\right)^k\right)} \quad (3)$$

The displacement field is defined for the functionally graded Timoshenko beam as follows:

$$u = u_0(x) - (z - z_0)\varphi_x(x) \quad (4)$$
$$w = w(x) \quad (5)$$

Strain-displacement relations are written as:

$$\varepsilon_x = \frac{\partial u_0}{\partial x} - (z - z_0)\frac{\partial \varphi}{\partial x} \quad (6)$$

$$\gamma_{xz} = \frac{dw_0}{dx} + \varphi \quad (7)$$

Constitutive relations can be derived as follows:

$$\sigma_x = Q_{11}(z)\varepsilon_x \quad (8)$$
$$\tau_{xz} = Q_{55}(z)\gamma_{xz} \quad (9)$$

where

$$Q_{11}(z) = E(z) \quad (10)$$
$$Q_{55}(z) = \frac{E(z)}{2(1+\upsilon)} \quad (11)$$

The strain energy of functionally graded beam can be given as:

$$U = \int_0^L \int_{-\frac{h}{2}}^{\frac{h}{2}} (\sigma_x\varepsilon_x + \tau_{xz}\gamma_{xz})\, dzdx = \int_0^L \left(A_{11}\left(\frac{\partial u}{\partial x}\right)^2 + 2B_{11}\frac{\partial \varphi}{\partial x}\frac{\partial u}{\partial x} + D_{11}\left(\frac{\partial \varphi}{\partial x}\right)^2 + A_{55}\varphi^2 + 2A_{55}\varphi\frac{\partial w}{\partial x} + A_{55}\left(\frac{\partial w}{\partial x}\right)^2\right) dx \quad (12)$$

Total potential energy due to the external axial load (P_0) can be written as follows:

$$V = \int_0^L \frac{1}{2}P_0\left(\frac{\partial w}{\partial x}\right)^2 \quad (13)$$

Total potential energy can be derived by:

$$\prod = U - V \quad (14)$$

$$\prod = \int_0^L \left(A_{11}\left(\frac{\partial u}{\partial x}\right)^2 + 2B_{11}\frac{\partial \varphi}{\partial x}\frac{\partial u}{\partial x} + D_{11}\left(\frac{\partial \varphi}{\partial x}\right)^2 + A_{55}\varphi^2 + 2A_{55}\varphi\frac{\partial w}{\partial x} + A_{55}\left(\frac{\partial w}{\partial x}\right)^2\right) dx - \int_0^L \frac{1}{2}P_0\left(\frac{\partial w}{\partial x}\right)^2 (15)$$

The rigidities are given as follows:

$$\{A_{11}, B_{11}, D_{11}\} = \int_{-\frac{h}{2}}^{\frac{h}{2}}\{1, (z - z_0), (z - z_0)^2\}Q_{11}dz \quad (16)$$

$$A_{55} = \int_{-\frac{h}{2}}^{\frac{h}{2}} K_s Q_{55}dz \quad (17)$$

Shear correction factor K_s is taken as 5/6.

For the solution of the governing equations Ritz method is employed. Displacement function u, w, φ is defined as follows:

$$u(x) = \sum_{i=1}^n c_i f_u \quad (18)$$

$$w(x) = \sum_{i=1}^n d_i f_w \quad (19)$$

$$\varphi(x) = \sum_{i=1}^n e_i f_\varphi \quad (20)$$

For boundary conditions (BC), trivial functions are chosen as the polynomial series (Table 1). F, C, and S denotes boundary conditions for the clamped, free, and simply supported, respectively (Fig.2).

Table 1. Trivial functions for boundary conditions

	S-S	C-C	C-S	C-F
f_u	x^i	$x^i(L-x)$	$x^i(L-x)$	x^i
f_w	$x^i(L-x)$	$x^i(L-x)$	$x^i(L-x)$	x^{i+1}
f_φ	x^{i-1}	$x^i(L-x)$	x^i	x^i

Simply supported – simply supported

Clamped – clamped

Clamped – simply supported

Clamped – free
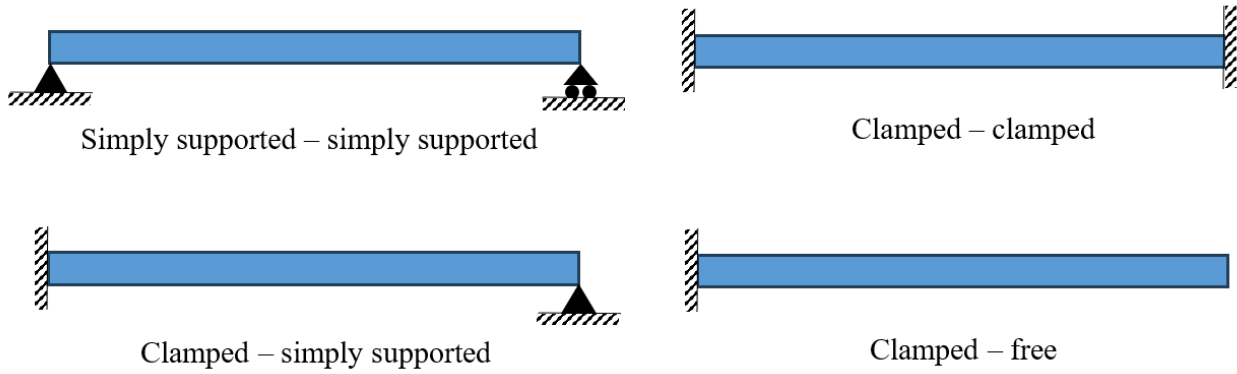
Figure 2. Boundary conditions of FG beam

For the buckling analysis, the governing equations can be obtained by substituting Eqs. (18-20) into Eq. (15) then minimizing the total energy function with respect to c_i, d_i, e_i

$$\frac{\partial \Pi}{\partial c_i} = 0 \tag{21}$$

$$\frac{\partial \Pi}{\partial d_i} = 0 \tag{22}$$

$$\frac{\partial \Pi}{\partial e_i} = 0 \tag{23}$$

The buckling behavior of functionally graded beam can be obtained by:

$$\left(\begin{bmatrix} [K_{11}] & 0 & [K_{13}] \\ 0 & [K_{22}] & [K_{32}] \\ [K_{13}] & [K_{23}] & [K_{33}] \end{bmatrix} - P_0 \begin{bmatrix} 0 & 0 & 0 \\ 0 & [K_G] & 0 \\ 0 & 0 & 0 \end{bmatrix} \right) \begin{Bmatrix} \{c\} \\ \{d\} \\ \{e\} \end{Bmatrix} = 0 \tag{24}$$

where $\{\{c\}, \{d\}, \{e\}\}^T$ is vector of unknown coefficients. Stiffness matrix $[K_{mn}]$ can be obtained as follows:

$$K_{11}(i,j) = \sum_{i=1}^{n} \sum_{j=1}^{n} \int_{-\frac{h}{2}}^{\frac{h}{2}} A_{11} \frac{df_{u_i}}{dx} \frac{df_{u_j}}{dx} dx \tag{25}$$

$$K_{13}(i,j) = -\sum_{i=1}^{n} \sum_{j=1}^{n} \int_{-\frac{h}{2}}^{\frac{h}{2}} B_{11} \frac{df_{u_i}}{dx} \frac{df_{\varphi_j}}{dx} dx \tag{26}$$

$$K_{22}(i,j) = \sum_{i=1}^{n} \sum_{j=1}^{n} \int_{-\frac{h}{2}}^{\frac{h}{2}} K_s A_{55} \frac{df_{w_i}}{dx} \frac{df_{w_j}}{dx} dx \tag{27}$$

$$K_{23}(i,j) = -\sum_{i=1}^{n} \sum_{j=1}^{n} \int_{-\frac{h}{2}}^{\frac{h}{2}} K_s A_{55} \frac{df_{w_i}}{dx} f_{\varphi_j} dx \tag{28}$$

$$K_{31}(i,j) = -\sum_{i=1}^{n} \sum_{j=1}^{n} \int_{-\frac{h}{2}}^{\frac{h}{2}} B_{11} \frac{df_{\varphi_j}}{dx} \frac{df_{u_j}}{dx} dx \tag{29}$$

$$K_{32}(i,j) = -\sum_{i=1}^{n} \sum_{j=1}^{n} \int_{-\frac{h}{2}}^{\frac{h}{2}} K_s A_{55} f_{\varphi_i} \frac{df_{w_j}}{dx} dx \tag{30}$$

$$K_{33}(i,j) = \sum_{i=1}^{n} \sum_{j=1}^{n} \int_{-\frac{h}{2}}^{\frac{h}{2}} D_{11} \frac{df_{\varphi_i}}{dx} \frac{df_{\varphi_j}}{dx} dx + \sum_{i=1}^{n} \sum_{j=1}^{n} \int_{-\frac{h}{2}}^{\frac{h}{2}} K_s A_{55} f_{\varphi_i} f_{\varphi_j} dx \tag{31}$$

$$K_G(i,j) = \sum_{i=1}^{n} \sum_{j=1}^{n} \int_{-\frac{h}{2}}^{\frac{h}{2}} \frac{df_{w_i}}{dx} \frac{df_{w_j}}{dx} dx \tag{32}$$

Critical buckling load can be found from the homogenous equation system as its lowest eigenvalue.

3. Results and Discussion

The investigation focused on analyzing the buckling behavior of functionally graded Timoshenko beams with arbitrary boundary conditions. The analysis centered on examining critical buckling loads in relation to factors such as slenderness ratio, boundary conditions, and the power-law index. This section presents the numerical results of the buckling analysis of the functionally graded Timoshenko beam. Effective properties of metal and ceramic are selected as E_m=70GPa, E_c=380GPa. Poisson's ratio is taken constant and is assumed as ν=0.3, unless specifically stated otherwise. For convenience, the non-dimensional parameter is used for the critical buckling load:

$$P_{cr} = P_0 \frac{12L^2}{E_m h^3}$$

Utilizing the rule of mixture, the effective properties of the FG beam were defined. Notably, the physical neutral surface was assumed as a reference surface, simplifying the analysis. The numerical results portrayed the variation of the non-dimensional neutral surface position with the power law index for different material property ratios. It was observed that as the power law index increased, the divergence of the neutral surface from the geometrical centroidal axis decreased, indicating a convergence towards isotropic behavior. Figure 3 shows the variation of the non-dimensional neutral surface position (NSP) concerning the power-law index for different elasticity modulus ratios. As known, the position of the neutral surface coincides with the geometrical centroidal axis for isotropic material. In functionally graded material, on the other hand, this position diverges from the geometrical centroidal axis as material properties become distinct. As shown in the figure, this divergence increases as the E_c/E_m ratio increases. The non-dimensional coordinates of the neutral surface increases with power law index (k) to specific values for each ratio. After passing this index value, z_0/h decreases as the power law index value increases. This is because the metallic properties increase as the k value increases in other words, the material properties of the beam approach isotropic.

Table 2 and Table 3 show the non-dimensional critical buckling load value of FG Timoshenko beam for arbitrary boundary conditions. To verify the solution, Table 2 compares the current results with those of [13] and [16] based on FOSDT, [8] based on refined shear deformation theory

(RSDT). Similarly, Table 3 compares current results with [17] based on Timoshenko (TB) and Levinson (LB) beams. The results are in good agreement with the reference results. Comparative analysis with existing literature showed consistency and alignment with prior research findings. The agreement between the current results and reference values validated the strength of the analytical approach used in this study. The results show that the closest values are obtained for the CF beam, while the values for the SS and CC beams are slightly different from the reference values. The reason for this might be the change in the shear effect with the boundary conditions. As power law index value increases, the non-dimensional critical buckling load value decreases due to the increase in the metallic properties of the functionally graded beam. As L/h ratio decreases, the critical buckling load value decreases as the flexibility of the beam decreases. The critical buckling load values were significantly influenced by the boundary conditions. Beams with clamped-free (CF) boundary conditions displayed the highest critical load values, while those with simply supported (SS) or clamped-clamped (CC) boundary conditions showed comparatively lower values. This difference can be attributed to the varying degrees of restraint imposed by different boundary conditions, which impact the overall stability of the beam.
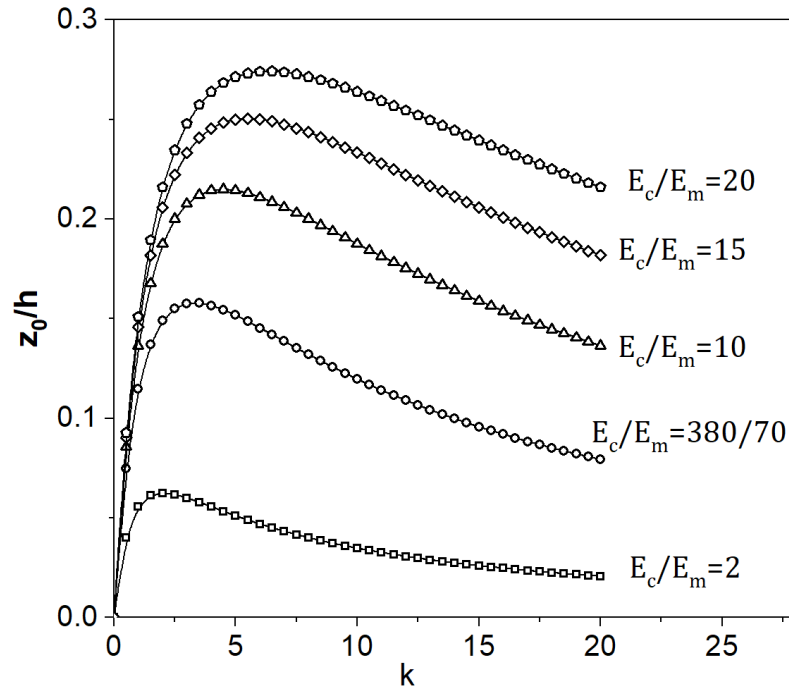
Figure 3. Variation of non-dimensional coordinates of neutral surface (z_0/h) with the power law index (k) for various E_c/Em ratios

Table 2. Non-dimensional critical buckling load of functionally graded beam

L/h	B.C.	Ref.	k=0	k=0.5	k=1	k=2	k=5	k=10
5	CC	[13]	154.3500	103.2200	80.4980	62.6140	50.3840	44.2670
		[8]	154.4150	103.2750	80.5480	62.6616	50.4207	44.2946
		Present	151.9319	102.7112	79.3843	61.7402	49.5793	43.4983
	SS	[13]	48.8350	31.9670	24.6870	19.2450	16.0240	14.4270
		[16]	48.8350	31.9610	24.6870	19.2450	16.0240	14.4270
		[8]	48.8372	31.9695	24.6898	19.2479	16.0263	14.4286
		Present	48.5904	31.8231	24.5844	19.1616	15.9417	14.3465
	CF	[13]	13.2130	8.5782	6.6002	5.1495	4.3445	3.9501
		[8]	13.0770	8.4992	6.5428	5.1042	4.2986	3.9031
		Present	13.0670	8.4900	6.5371	5.1000	4.2943	3.8979
	CS	Present	89.0643	58.9453	45.7487	35.6236	29.1454	25.9088
10	CC	[13]	195.3400	127.8700	98.7490	76.9800	64.0960	57.7080
		[8]	195.3730	127.9050	98.7923	77.0261	64.1324	57.7329
		Present	194.3623	127.2926	98.3263	76.6474	63.7669	57.3778
	SS	[13]	52.3090	33.9960	26.1710	20.4160	17.1920	15.6120
		[16]	52.3080	33.9890	26.1710	20.4160	17.1940	15.6120
		[8]	52.3085	33.9981	26.1728	20.4187	17.1959	15.6134
		Present	52.2857	33.9566	26.1429	20.3931	17.1771	15.5880
	CF	[13]	13.2130	8.5666	6.6570	5.1944	4.3903	3.9969
		[8]	13.3137	8.6363	6.6425	5.1830	4.3785	3.9850
		Present	13.3097	8.6337	6.6406	5.1823	4.3783	3.9840
	CS	Present	103.6303	67.5806	52.1023	40.6320	34.0357	30.7791
20	CC	Present	208.9496	135.8224	104.5632	81.5712	68.6805	62.3520
	SS	Present	53.2364	34.5342	26.5620	20.7264	17.5077	15.9383
	CF	Present	13.3731	8.6811	6.6675	5.2027	4.3984	4.0055
	CS	Present	108.0484	70.1508	53.9771	42.1128	35.5253	32.2977

Table 3. Critical buckling load of functionally graded beam (non-dimensional) (v=0.23)

h/L	BC	Ref.	0	0.1	0.5	1	2	5	10	100	10^10
1/5	CC	[17] LB	154.35	140.36	103.41	80.329	61.783	48.333	42.162	31.010	28.433
		[17] TB	154.35	140.16	103.22	80.497	62.614	50.384	44.267	31.231	28.433
		Present	154.35	140.16	103.22	80.497	62.614	50.384	44.267	31.231	28.434
	CS	[17] LB	89.523	81.172	59.317	45.905	35.473	28.477	25.183	18.146	16.491
		[17] TB	89.971	81.476	59.491	46.152	35.941	30.883	26.206	18.338	16.573
		Present	89.971	81.477	59.491	46.152	35.942	29.449	26.207	18.339	16.574
	SS	[17] LB	48.835	44.139	31.985	24.671	19.166	15.811	14.196	9.9975	8.9959
		[17] TB	48.835	44.118	31.967	24.687	19.245	16.024	14.427	10.020	8.9959
		Present	48.835	44.118	31.967	24.687	19.245	16.024	14.427	10.020	8.9959
1/10	CC	[17] LB	195.34	176.55	127.94	98.685	76.663	64.242	56.784	39.990	35.984
		[17] TB	195.34	176.47	127.87	98.748	76.980	64.096	57.708	40.081	35.984
		Present	195.34	176.47	27.870	98.748	76.980	64.096	57.708	40.082	35.985
	CS	[17] LB	103.93	93.719	67.712	52.161	40.590	33.814	30.531	21.324	19.122
		[17] TB	103.93	93.803	67.758	52.232	40.735	34.137	30.883	21.384	19.146
		Present	103.94	93.803	67.759	52.233	40.735	34.138	30.883	21.384	19.147
	SS	[17] LB	52.308	47.180	34.002	26.166	20.394	17.132	15.544	10.778	9.6357
		[17] TB	52.308	47.174	33.996	26.170	20.416	17.194	15.612	10.784	9.6357
		Present	52.308	47.174	33.996	26.171	20.416	17.194	15.612	10.784	9.6357
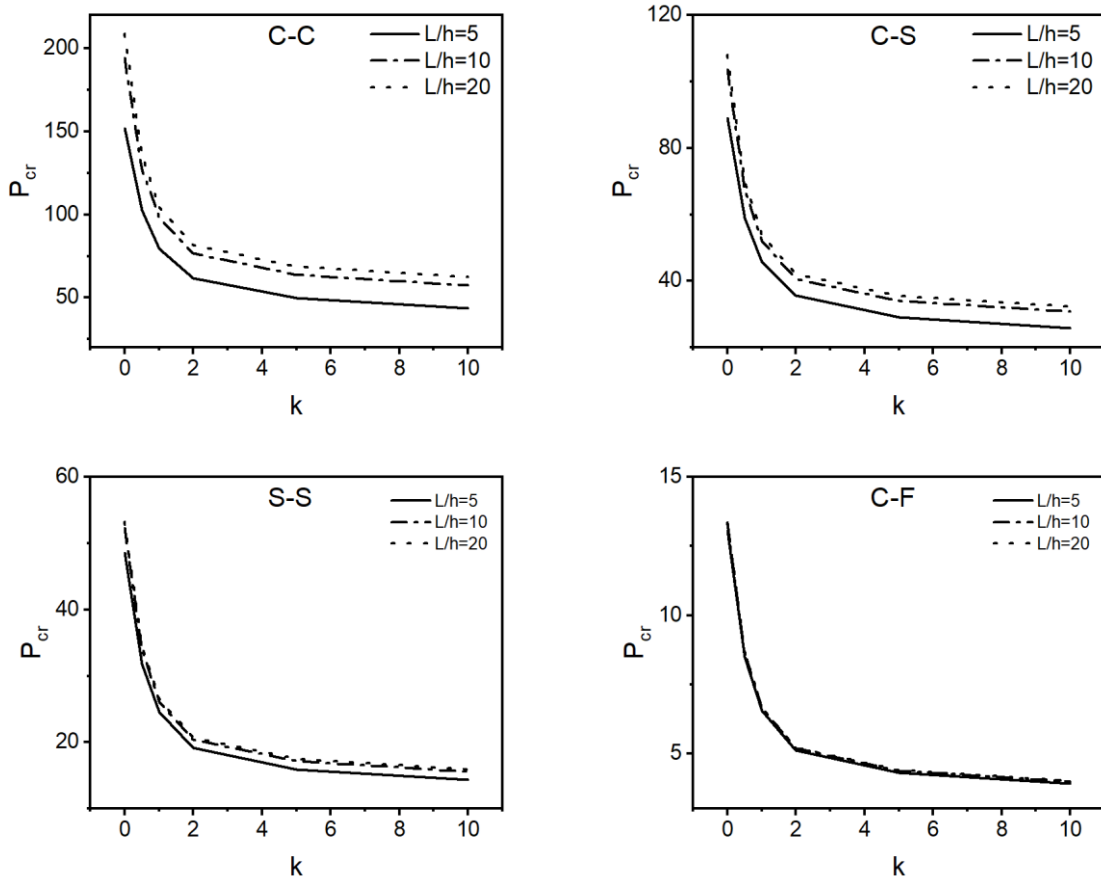
Figure 4. The non-dimensional critical buckling load for various slenderness ratio (L/h= 5, 10, 20)

Figure 4 illustrates the change in the critical buckling load of CC, CF, SS, and CS beams with power-law index value for various slenderness ratios (L/h=5, 10, and 20). As seen, the non-dimensional critical buckling load value increases with an increase in slenderness ratio, decreases with an increase in value of power law index for all presented boundary conditions. The analysis uncovered interesting findings about how the slenderness ratio and power law index affect the critical buckling load. As the

slenderness ratio goes up, the critical load decreases, showing that higher aspect ratios lead to reduced stability. Similarly, an increase in the power law index results in lower critical buckling loads, indicating that material gradient has a diminishing effect on beam stability.

Figure 5 illustrates the non-dimensional critical buckling loads of functionally graded beam (L/h=5, 10, and 20) with respect to power law index for CC, CS, SS, and CF boundary conditions. The critical load decrease with the increase in the value of power law index for all presented boundary conditions. As expected, the largest critical load values are obtained in CC beam followed by CS and SS beams, respectively. The smallest critical load values are observed in CF beam.

Figure 6 shows the non-dimensional critical buckling loads of the functionally graded beam concerning the slenderness ratio for SS, CC, CF, and

CS boundary-conditions. It is seen that the critical load value increase with the increase in slenderness ratio for all boundary conditions. The increment is more significant among the ratios 5 to 20, after passing this value, a small change is seen.

The findings highlight the complex interaction between material composition, boundary conditions, and geometric parameters in influencing the buckling behavior of functionally graded Timoshenko beams. It's important to understand these relationships for designing and optimizing structures in different engineering applications. The knowledge gained from this study offers valuable guidance for engineers and researchers aiming to improve the performance and reliability of functionally graded structures.
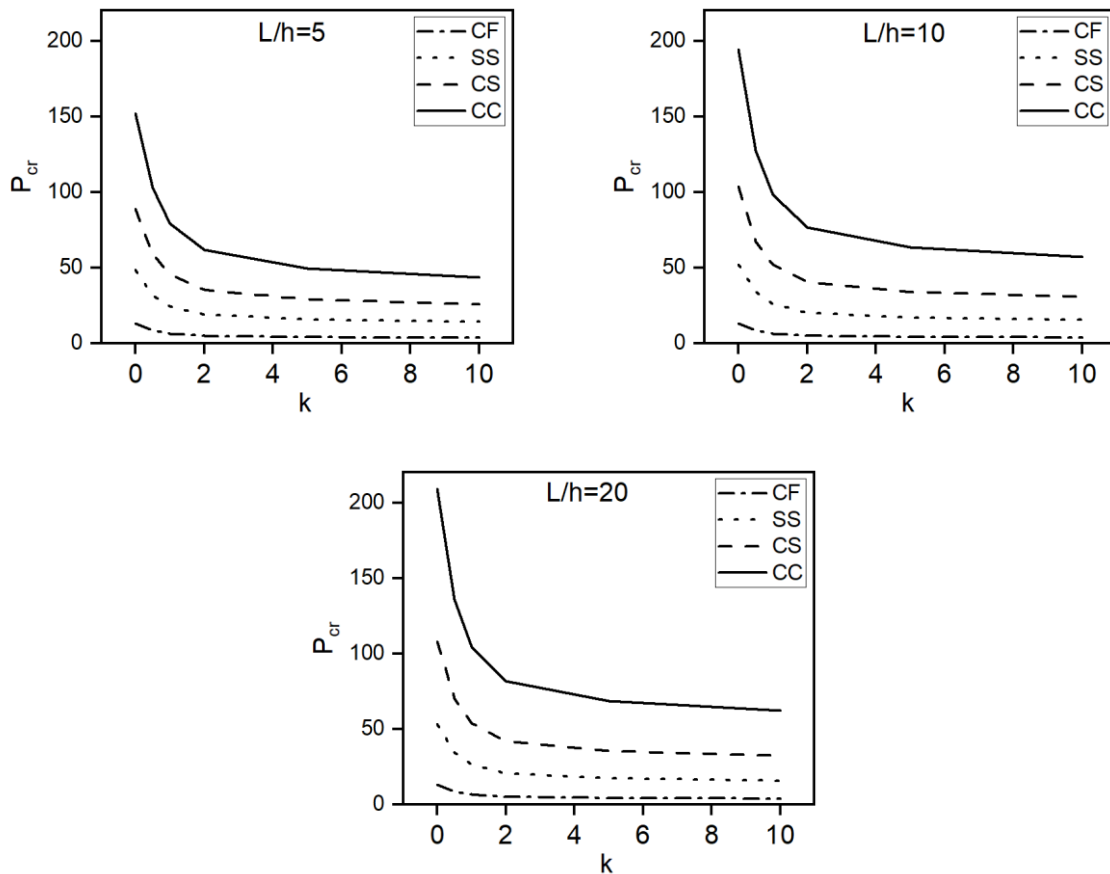
Figure 5. The non-dimensional critical buckling loads of functionally graded beam with respect to power law index for different boundary conditions
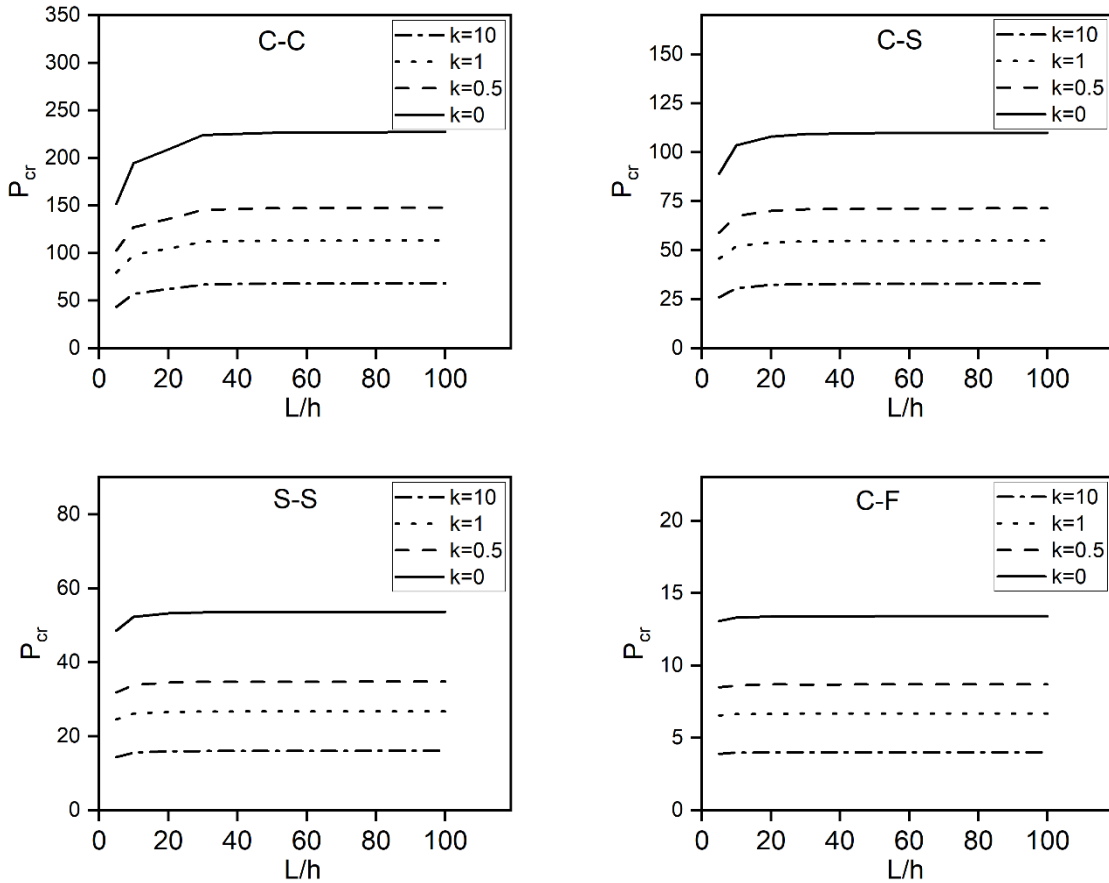
Figure 6. The non-dimensional critical buckling loads of functionally graded beam with respect to slenderness ratio for different boundary conditions

4. Conclusion and Suggestions

In this study, buckling analysis of FG Timoshenko beam is investigated. The reference surface of the FGB is assumed neutral surface then bending-stretching couplings vanished. This assumption leads to considerable simplification in the calculation. The governing equations of the FGB are derived from the principle of the minimum potential energy. The Ritz method is employed for obtaining the critical buckling load of the FGB with arbitrary boundary conditions. The current study examined the effect of boundary conditions, slenderness ratio, and power-law index value on the non-dimensional critical buckling load.

The present solution is in line with the results of previous study. The highest critical buckling load values occurred the beam with the CC boundary condition, as the CF has the lowest values. The slenderness ratio affects the critical load values adversely, the values decrease as the ratio increases. Similarly, the critical buckling loads decrease with an increase in the value of the power law index.

In conclusion, this study presents a refined understanding of the behavior of functionally graded sandwich panels and highlights the effectiveness of advanced theoretical and computational models in predicting their responses. In particular, a novel relationship between material composition and vibration characteristics have been identified, which provides insight into the design optimization of such structures for various engineering applications.

The study may have simplified the variation of material properties, assumed certain boundary conditions and made modeling assumptions that could affect the accuracy of the predictions. It may also lack comprehensive experimental validation and have a limited scope. Acknowledging these limitations is essential for understanding the study's scope and guiding future research. A future study may be conducted to include thermal effects in addition to the presented results.

Nomenclature of Symbols and Abbreviations

L	: length of beam
B	: width
$z0$	: Physical neutral surface position
ρ, ρ_m, ρ_c	: Density, density of metal, density of ceramic
E, E_m, E_c	: Elasticity modulus, Elasticity modulus of metal, Elasticity modulus of ceramic
x, y, z	: Coordinates
h	: Thickness of the beam
k	: power-law index
ν	: Poisson's ratio
u_0	: The in-plane displacements in the x direction
w_b , w_s	: Bending and shear components of the transverse displacement in the through-thickness direction
$f(z)$	: The shape function
$\varepsilon_x, \varepsilon_z \gamma_{xz}$	: Strain components
σ_x, τ_{xz}	: Stress components
Q_{ij}	: Rigidity matrix
U	: The strain energy
V	: Potential energy
P_0	: the external axial load
Ks	: Shear correction factor
$N_x, N_y N_{xy}$	: Force components
$A_{ij}, B_{ij}, B_{ij}^s, D_{ij}, D_{ij}^s, H_{ij}^s$	: Rigidity matrix components
$\{K\}$	: The column matrix derived from the boundary conditions of two edges parallel to the y-axis (x=0 and x=a)
u, w, φ	: Displacement function
f_u , f_w, f_φ	: Trivial functions for boundary conditions
$\{\{c\},\{d\},\{e\}\}^T$	: vector of unknown coefficients
$[K_{mn}]$	: Stiffness matrix
$\prod$	: the total energy function
FG	: functionally graded
FGB	: functionally graded beam
FOSDT	: the first-order shear deformation beam theory
PNS	: physical neutral surface
HOSDT	: high order shear deformation theory
FGP	: functionally graded plate
BC	: boundary conditions
NSP	: neutral surface position
TB, LB	: Timoshenko and Levinson beams
CF, SS, CC, CS	: clamped-free, fully simply supported, clamped-clamped and clamped-simply supported boundary conditions

Statement of Research and Publication Ethics

The study is complied with research and publication ethics.

References

[1] A. M. Zenkour, "A comprehensive analysis of functionally graded sandwich plates: Part 2-Buckling and free vibration," *Int J Solids Struct*, vol. 42, no. 18–19, pp. 5243–5258, Sep. 2005, doi: 10.1016/j.ijsolstr.2005.02.016.

[2] Q. Li, V. P. Iu, and K. P. Kou, "Three-dimensional vibration analysis of functionally graded material sandwich plates," *J Sound Vib*, vol. 311, no. 1–2, pp. 498–515, Mar. 2008, doi: 10.1016/j.jsv.2007.09.018.

[3] J. N. Reddy, *Analysis of functionally graded plates*, 2000.

[4] T. P. Vo, H. T. Thai, T. K. Nguyen, F. Inam, and J. Lee, "A quasi-3D theory for vibration and buckling of functionally graded sandwich beams," *Compos Struct*, vol. 119, pp. 1–12, Jan. 2015, doi: 10.1016/j.compstruct.2014.08.006.

[5] H. T. Thai and D. H. Choi, "Finite element formulation of various four unknown shear deformation theories for functionally graded plates," *Finite Elements in Analysis and Design*, vol. 75, pp. 50–61, 2013, doi: 10.1016/j.finel.2013.07.003.

[6] V. Taskin and P. A. Demirhan, "Static analysis of simply supported porous sandwich plates," *Structural Engineering and Mechanics*, vol. 77, no. 4, pp. 549–557, Feb. 2021, doi: 10.12989/sem.2021.77.4.549.

[7] P. A. Demirhan and V. Taskin, "Bending and free vibration analysis of Levy-type porous functionally graded plate using state space approach," *Compos B Eng*, vol. 160, pp. 661–676, Mar. 2019, doi: 10.1016/j.compositesb.2018.12.020.

[8] T. P. Vo, H. T. Thai, T. K. Nguyen, A. Maheri, and J. Lee, "Finite element model for vibration and buckling of functionally graded sandwich beams based on a refined shear deformation theory," *Eng Struct*, vol. 64, pp. 12–22, Apr. 2014, doi: 10.1016/j.engstruct.2014.01.029.

[9] C. P. Sreeju Nair S B, "Functionally Graded Panels: A Review," *International Journal for Modern Trends in Science and Technology*, no. 8, pp. 36–43, Aug. 2020, doi: 10.46501/ijmtst060808.

[10] C. Pany and G. V. Rao, "Calculation of non-linear fundamental frequency of a cantilever beam using non-linear stiffness," *Journal of Sound and Vibration*, vol. 256, no. 4. Academic Press, pp. 787–790, Sep. 26, 2002. doi: 10.1006/jsvi.2001.4224.

[11] C. Pany and G. V. Rao, "Large amplitude free vibrations of a uniform spring-hinged beam," *J Sound Vib*, vol. 271, no. 3–5, pp. 1163–1169, Apr. 2004, doi: 10.1016/S0022-460X(03)00572-8.

[12] C. Pany, "Large amplitude free vibrations analysis of prismatic and non-prismatic different tapered cantilever beams," *Pamukkale University Journal of Engineering Sciences*, vol. 29, no. 4, pp. 370–376, 2023, doi: 10.5505/pajes.2022.02489.

[13] S. R. Li and R. C. Batra, "Relations between buckling loads of functionally graded timoshenko and homogeneous euler-bernoulli beams," *Compos Struct*, vol. 95, pp. 5–9, Jan. 2013, doi: 10.1016/j.compstruct.2012.07.027.

[14] S. R. Li, D. F. Cao, and Z. Q. Wan, "Bending solutions of FGM Timoshenko beams from those of the homogenous Euler-Bernoulli beams," *Appl Math Model*, vol. 37, no. 10–11, pp. 7077–7085, Jun. 2013, doi: 10.1016/j.apm.2013.02.047.

[15] V. L. Nguyen, M. T. Tran, V. L. Nguyen, and Q. H. Le, "Static behaviour of functionally graded plates resting on elastic foundations using neutral surface concept," *Archive of Mechanical Engineering*, vol. 68, no. 1, pp. 5–22, 2021, doi: 10.24425/ame.2020.131706.

[16] T. K. Nguyen, T. P. Vo, and H. T. Thai, "Static and free vibration of axially loaded functionally graded beams based on the first-order shear deformation theory," *Compos B Eng*, vol. 55, pp. 147–157, 2013, doi: 10.1016/j.compositesb.2013.06.011.

[17] S. Li, X. Wang, and Z. Wan, "Classical and homogenized expressions for buckling solutions of functionally graded material Levinson beams," *Acta Mechanica Solida Sinica*, vol. 28, no. 5, pp. 592–604, Oct. 2015, doi: 10.1016/S0894-9166(15)30052-5.

[18] T. Morimoto, Y. Tanigawa, and R. Kawamura, "Thermal buckling of functionally graded rectangular plates subjected to partial heating," *Int J Mech Sci*, vol. 48, no. 9, pp. 926–937, Sep. 2006, doi: 10.1016/j.ijmecsci.2006.03.015.

[19] S. Abrate, "Functionally graded plates behave like homogeneous plates," *Compos B Eng*, vol. 39, no. 1, pp. 151–158, Jan. 2008, doi: 10.1016/j.compositesb.2007.02.026.

[20] D. G. Zhang and Y. H. Zhou, "A theoretical analysis of FGM thin plates based on physical neutral surface," *Comput Mater Sci*, vol. 44, no. 2, pp. 716–720, Dec. 2008, doi: 10.1016/j.commatsci.2008.05.016.

[21] D. G. Zhang, "Modeling and analysis of FGM rectangular plates based on physical neutral surface and high order shear deformation theory," *Int J Mech Sci*, vol. 68, pp. 92–104, Mar. 2013, doi: 10.1016/j.ijmecsci.2013.01.002.

[22] A. Fekrar, M. S. A. Houari, A. Tounsi, and S. R. Mahmoud, "A new five-unknown refined theory based on neutral surface position for bending analysis of exponential graded plates," *Meccanica*, vol. 49, no. 4, pp. 795–810, 2014, doi: 10.1007/s11012-013-9827-3.

[23] D. G. Zhang, "Nonlinear bending analysis of FGM rectangular plates with various supported boundaries resting on two-parameter elastic foundations," *Archive of Applied Mechanics*, vol. 84, no. 1, pp. 1–20, Jan. 2014, doi: 10.1007/s00419-013-0775-0.

[24] S. C. Han, W. T. Park, and W. Y. Jung, "A four-variable refined plate theory for dynamic stability analysis of S-FGM plates based on physical neutral surface," *Compos Struct*, vol. 131, pp. 1081–1089, Nov. 2015, doi: 10.1016/j.compstruct.2015.06.025.

[25] H. Bellifa, K. H. Benrahou, L. Hadji, M. S. A. Houari, and A. Tounsi, "Bending and free vibration analysis of functionally graded plates using a simple shear deformation theory and the concept the neutral surface position," *Journal of the Brazilian Society of Mechanical Sciences and Engineering*, vol. 38, no. 1, pp. 265–275, Jan. 2016, doi: 10.1007/s40430-015-0354-0.

[26] F. Ebrahimi, A. Jafari, and M. R. Barati, "Free Vibration Analysis of Smart Porous Plates Subjected to Various Physical Fields Considering Neutral Surface Position," *Arab J Sci Eng*, vol. 42, no. 5, pp. 1865–1881, May 2017, doi: 10.1007/s13369-016-2348-3.

[27] V. L. Nguyen, M. T. Tran, V. L. Nguyen, and Q. H. Le, "Static behaviour of functionally graded plates resting on elastic foundations using neutral surface concept," *Archive of Mechanical Engineering*, vol. 68, no. 1, pp. 5–22, 2021, doi: 10.24425/ame.2020.131706.

[28] A. Sadgui and A. Tati, "A novel trigonometric shear deformation theory for the buckling and free vibration analysis of functionally graded plates," *Mechanics of Advanced Materials and Structures*, vol. 29, no. 27 pp. 6648-6663, 2021, doi: 10.1080/15376494.2021.1983679.

[29] L. S. Ma and D. W. Lee, "Exact solutions for nonlinear static responses of a shear deformable FGM beam under an in-plane thermal loading," *European Journal of Mechanics*, A/Solids, vol. 31, no. 1, pp. 13–20, Jan. 2012, doi: 10.1016/j.euromechsol.2011.06.016.

[30] L. O. Larbi, A. Kaci, M. S. A. Houari, and A. Tounsi, "An efficient shear deformation beam theory based on neutral surface position for bending and free vibration of functionally graded beams," *Mechanics Based Design of Structures and Machines*, vol. 41, no. 4, pp. 421–433, Oct. 2013, doi: 10.1080/15397734.2013.763713.

[31] D. G. Zhang, "Thermal post-buckling and nonlinear vibration analysis of FGM beams based on physical neutral surface and high order shear deformation theory," *Meccanica*, vol. 49, no. 2, pp. 283–293, Feb. 2014, doi: 10.1007/s11012-013-9793-9.

[32] K. S. Al-Basyouni, A. Tounsi, and S. R. Mahmoud, "Size dependent bending and vibration analysis of functionally graded micro beams based on modified couple stress theory and neutral surface position," *Compos Struct*, vol. 125, pp. 621–630, Jul. 2015, doi: 10.1016/j.compstruct.2014.12.070.

[33] F. Ebrahimi and E. Salari, "A Semi-analytical Method for Vibrational and Buckling Analysis of Functionally Graded Nanobeams Considering the Physical Neutral Axis Position," 2015.

[34] K. Zoubida, T. H. Daouadji, L. Hadji, A. Tounsi, and A. B. el Abbes, "A New Higher Order Shear Deformation Model of Functionally Graded Beams Based on Neutral Surface Position," *Transactions of the Indian Institute of Metals*, vol. 69, no. 3, pp. 683–691, Apr. 2016, doi: 10.1007/s12666-015-0540-x.

[35] N. T. B. Phuong, T. M. Tu, H. T. Phuong, and N. van Long, "Bending analysis of functionally graded beam with porosities resting on elastic foundation based on neutral surface position," *Journal of Science and Technology in Civil Engineering (STCE) - NUCE*, vol. 13, no. 1, pp. 33–45, Jan. 2019, doi: 10.31814/stce.nuce2019-13(1)-04.

[36] M. Derikvand, F. Farhatnia, and D. H. Hodges, "Functionally graded thick sandwich beams with porous core: Buckling analysis via differential transform method," *Mechanics Based Design of Structures and Machines*, vol. 51, no. 7, pp. 3650-3677, 2021, doi: 10.1080/15397734.2021.1931309.

[37] P. Van Vinh, N. Q. Duoc, and N. D. Phuong, "A New Enhanced First-Order Beam Element Based on Neutral Surface Position for Bending Analysis of Functionally Graded Porous Beams*," Iranian Journal of Science and Technology - Transactions of Mechanical Engineering*, vol. 46, no. 4, pp. 1141–1156, Dec. 2022, doi: 10.1007/s40997-022-00485-1.

[38] Y. Liu, S. Su, H. Huang, and Y. Liang, "Thermal-mechanical coupling buckling analysis of porous functionally graded sandwich beams based on physical neutral plane," *Compos B Eng*, vol. 168, pp. 236–242, Jul. 2019, doi: 10.1016/j.compositesb.2018.12.063.

Determination of Cortisol Hormone from Sweat Samples and Interpretation with Microcontroller

Muhammed Ertuğrul ÇAPAN[1*], Ebru CİNGÖZ ÇAPAN[2], Hasan Uğur ÖNCEL[3],
Ercan ARICAN[4]

[1] Istanbul Gedik University, Faculty of Health Sciences, Department of Occupational Health and Safety, 34913, Istanbul, Turkey [1]
[2,4] İstanbul University, Faculty of Arts and Sciences, Department of Molecular Biology and Genetics, 34134, İstanbul, Turkey
[3] Istanbul Gedik University, Faculty of Health Sciences, Department of Nutrition and Dietetics, 34913, Istanbul, Turkey

(ORCID: 0000-0001-9398-7171)[2](ORCID: 0000-0002-5296-0009)
(ORCID: 0000-0002-6900-1955) (ORCID: 0000-0002-1676-5919)

Abstract

Cortisol, the body's stress hormone, regulates metabolism and the immune system. It also affects various body systems, such as the cardiovascular, respiratory, reproductive, and musculoskeletal systems. This study aims to quantitatively analyze cortisol hormone levels using colorimetric analysis with microcontrollers. The research focuses on detecting cortisol from artificial sweat samples utilizing microfluidic layers and microcontroller systems. This system employs an ESP 32 microcontroller within a closed environment, where the color changes on the microfluidic layer are photographed and quantified in terms of cortisol levels (ug/mL) based on RGB values obtained through basic image processing algorithms. The blue tetrazolium method used in the colorimetric analysis provides stable color changes and is preferred for its rapid reaction time (10 minutes). The system yields precise and reliable results with low detection limits (0.3 ug/mL), demonstrating high analytical performance. With the integration of the ESP 32 Cam module, the system can accurately measure cortisol levels across a wide concentration range (0.8 – 60 ug/mL). This technological approach leverages the advantages of wearable technologies in the field of biomedical engineering, enabling continuous monitoring of cortisol levels and facilitating the clinical assessment of these data.

1. Introduction

For organisms to perform vital functions and respond to internal or external changes, systems need to be in constant communication. This communication occurs through two pathways: the nervous system and the hormonal system. While the nervous system enables rapid information transmission, hormonal changes involve a slower process, including stages such as hormone production, secretion, and transportation.

Molecules produced by endocrine glands such as the pituitary gland, thyroid gland, parathyroid glands, adrenal glands, gonads (ovaries and testes), pancreas, and hypothalamus are defined as hormones. Hormones regulate metabolism, growth and development, the composition of body fluids, and reproductive systems. Endocrine refers to the release of products from various glands into the bloodstream in response to specific stimuli. Hormones entering the bloodstream are transported to target cells. Hormones can affect specific target cells as well as different cell types. This effect is defined by interactions with molecules located on or within the target cell, triggering biochemical processes that can alter the activity or function of the target cell. These processes are capable of changing the activity or function of the

---

target cell [1]. Hormone analysis holds significant importance, particularly in the fields of biology and medicine, for detecting syndromes, diseases, and emerging anomalies. Hormone analysis is frequently relied upon for identifying disorders and abnormalities. With advancing technology, various methods for hormone analysis have emerged, each with its own advantages and disadvantages. Not all hormones can be detected in the same manner, as the differences among hormones have led to the development of different detection methods [2]. Cortisol hormone is the primary glucocorticoid secreted from the adrenal cortex, influencing different functions in various systems of the body. Its secretion is regulated within the Hypothalamus-Pituitary-Adrenal axis, and potential dysregulation can lead to Cushing's syndrome or Addison's disease. Additionally, cortisol is considered a stress hormone in organisms, with effects on metabolism regulation, inflammatory response, immunity, respiration, and the reproductive system.

For these reasons, measuring and monitoring cortisol levels is highly important. Cortisol levels can be measured from body fluids such as blood, saliva, and sweat, and also from hair and nails. Human sweat and saliva fluids have comparable cortisol levels. While enzyme-linked immunosorbent assay (ELISA) testing is the gold standard for cortisol analysis, various successful methods for cortisol hormone measurement have been described in the literature.

The amount of cortisol hormone can be determined using chromatography, immunoassays, and electrochemical immuno-detection methods [3]. While commonly used methods allow for high-accuracy analysis, they often require large sample volumes, lengthy testing periods, specialized equipment, and experienced personnel, making many identified analyses unsuitable for general use. Microfluidics are analytical devices composed of cellulose-based papers, eliminating the need for extra fluid pumps, and consisting of absorbent papers/membranes. These layers enable analyses, especially on fluids, such as antigen-antibody detections and colorimetric analyses. Microfluidics devices are cost-effective, portable, flexible, lightweight, and can be integrated into different systems. The fundamental working principle involves the absorption of analysis reagents into the absorbent layer and the creation of channels for fluid transfer and transportation.

Wearable devices belong to the category of electronic devices that can be worn as accessories, embedded in clothing, implanted into the user's body, and even applied as tattoos. These devices, supported by microprocessors and equipped with data transmission and reception capabilities over the Internet, have practical applications [4].

These devices play a crucial role in personalized medicine as they can continuously collect data from the human body over time to detect meaningful changes in health status for preventive intervention purposes. A flexible electronic device typically includes several key components, including a substrate, an active layer, and an interface layer. In this context, detection methods with high mobility, flexibility, and adaptability provide a natural interaction between electronics and the human body, owing to their unique features [5].

Microcontrollers are embedded systems that control the actions and features of a device while it is in operation [6]-[7]. Most of the time, they control a specific task in the device rather than all functions of the device; they contain both software and hardware components [8]. Microcontrollers are commonly known today as single-board computers, popularly referred to as microcomputers [9]-[10].

However, microcontrollers should not be confused with microprocessors used for general-purpose computing; microcontrollers are designed for specific purposes [11]. The aim of this study is to contribute to biotechnology-based research by enabling the real-time detection of cortisol hormone using a practical, wearable device. Colorimetric detection methods are particularly prominent in biotechnological approaches and wearable technology due to their quick results, high accuracy, and low cost of production/utilization. Literature reviews indicate that wearable technology and colorimetric methods are often used together, but it has been observed that transporting color changes for analysis is not feasible. In this study, our primary goal was to create portable devices. Additionally, the lack of reusability in previously designed systems and the need for continuous bulk changes, including sensors, are also disadvantages. Making the wearable device reusable increases the usability of the system.

The developed system focuses on establishing a connection via the web between the wearable microfluidic-based device and a reading area, allowing measurements to be taken from the web. Furthermore, by storing the measurements taken from the wearable device within the web, the system aims to enable users to track changes in cortisol hormone levels. Thus, the system aims to contribute to the development of systems that enable low-cost, rapid detection, continuous monitoring of tested parameters, and analysis of results obtained at advanced stages.

In the conducted studies, the analysis of cortisol hormone was performed through colorimetric

color changes on a microfluidic layer. The resulting color changes were interpreted and quantitatively determined through a hardware-integrated system with a camera in the wearable device.

2. Material and Method

Hydrocortisone acetate (Sigma 5003-3), tetramethylammonium hydroxide (Sigma 7559-2), methanol (99% ACS grade), and blue tetrazolium (Sigma 1871223), No. 4 Whatman paper, No. 1 Whatmann Chromatography paper, Thin Layer Chromatography paper, Whatmann Glass Microfiber Filter paper, Coarse Filter Paper, Cotton-Based Sweat Absorbent Pad agar, glycerin, Tween 20, ESP 32 Cam, FTDI, Mini USB B cable, breadboard, jumper cable, 18*10*8 cm PVC box.

2.1. Preparation of Cortisol Stock Solution

Cortisol stock solutions were freshly prepared weekly using hydrocortisone acetate and ethanol.

2.2. Blue Tetrazolium Method

A 5% w/v tetramethylammonium hydroxide solution is prepared by diluting 5 mL of the aqueous solution in 45 mL of methanol. A second solution containing 100 mg of blue tetrazolium dissolved in 50 mL of methanol is prepared. Both solutions are mixed in equal proportions. Stored at room temperature.

2.3. Agar-Based Hydrophobization with Thermoplastic

In this method, the effect of hydrophobization by freezing the agar-based viscous liquid on paper was investigated, and described as thermoplastic in the literature. For this, 0.25 g of Agar agar was mixed with 10 mL of water and 1.5 mL of glycerin until boiling. Before reaching room temperature, 1 mL of Tween 20 was added and applied to the cut filter papers by melting. In this way, one surface of the microfluidic is hydrophobized.

2.4. Water Contact Angle

The water contact angle technique is used to determine the hydrophobicity or hydrophilicity of the surface. Water droplets tend to spread on hydrophilic surfaces, but on hydrophobic surfaces, droplets tend to form spherical shapes instead of spreading and being absorbed. A surface on which water is wetted (contact angle less than 90 degrees) is called a hydrophilic surface, while a surface not wetted by water (contact angle greater than 90 degrees) is called a hydrophobic surface. After the experiments, the water contact angles formed by liquids colored with food dye were determined on filter papers using various hydrophobization methods.

2.5. Sweat Absorbent Region Studies

The purpose of the sweat absorbent region is to collect sweat formed on the skin by creating a large surface and transferring it to the sample application area of the microfluidic layer. Therefore, liquid retention should be high. In the study, based on the absorbency capacities of the selected papers as the reaction zone, the amount of sample to be collected from the user needs to be taken into account to select the sweat absorbent region.

2.6. Artificial Sweat Sample Studies

Artificial sweat solutions were prepared to be both alkaline and acidic. For the alkaline artificial sweat solution, 0.05 g L-Histidine monohydrochloride and 0.5 g Disodium hydrogen phosphate were dissolved in 100 ml of distilled water. The pH was adjusted to 8 using NaOH.

The acidic artificial sweat solution was prepared by dissolving 0.05 g L-Histidine monohydrochloride, 0.5 g NaCl, and 0.22 g Sodium dihydrogen phosphate in 100 ml of distilled water. The pH was adjusted to 5.5 using NaOH. From the prepared sweat samples, 200 uL was transferred to separate Eppendorf tubes. Then, hydrocortisone solution (h:h) was added to each tube sequentially to achieve concentrations of 60, 40, 10, 5, 2, and 1 ug/mL.

2.7. Microcontroller Studies

In the study, it is possible to divide the setup and programming of technology-related components into 2 stages. Firstly, the connection of the Esp 32 Cam development board was made using the FTDI programming board, and it was programmed in C language using the Esp 32, ESPAsync Web, Async TCP libraries in the Arduino IDE. At the end of the study, the control of the board was provided via the web server. Thus, by using the buttons on the web interface, images were taken and transferred to the Firebase platform, which provides real-time database service. In the second stage, the Python programming language, Open Cv and NumPy libraries, and the firebase-admin package, which connects to the Python-Firebase platforms, were used. Numerical operations were performed on the image obtained

from Firebase, and the results were printed on the result screen.

2.7.1. Connection and Programming of Esp 32 Cam Development Board

Throughout the study, a Monster Abra A.5 V18.2 (Windows 10) model computer was used for all programming processes. The connection between the development board and the computer was made using the FTDI card, as shown in Figure.1. For the connection between the boards, a breadboard and male-to-male jumper cables were used. The Mini USB B cable attached to the FTDI card was connected to the computer (Figure 1).
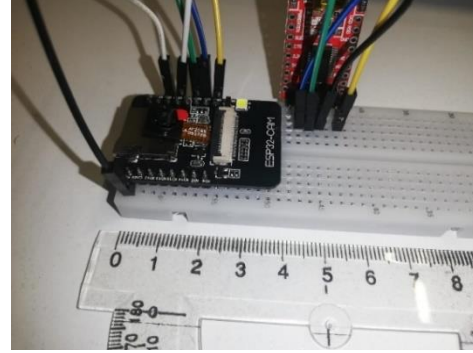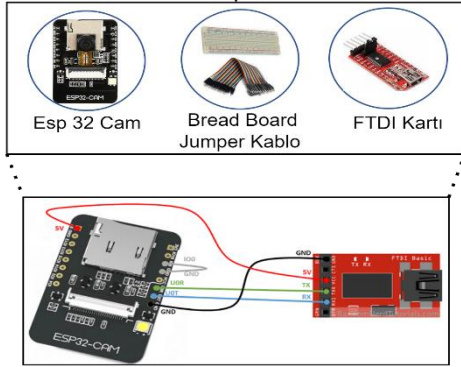
Figure 1. Schematic diagram showing the necessary components for the connection of the ESP 32 Cam development board.

Arduino IDE version 2.0.2 was downloaded from the website "https://www.arduino.cc/en/software". After the installation was completed, for the installation of the Esp 32 library, the "Preferences" menu was opened from the "File" menu at the top left of the Arduino IDE, and the link "Https://dl.espressif.com/dl/package_esp32_index.json" was added to the "Additional Board Manager URLs" section, and the "OK" button at the bottom right was clicked. After the installation of the board was completed, the "Tools" menu was selected again, and the "AI Thinker ESP32 CAM" board was selected from the "Board" section. The library installation is completed.

Initially, programming was carried out for taking photos with ESP 32. In the scope of the study, code sources shared by Rui Santos at https://randomnerdtutorials.com/ were used. For the transfer of the photo taken with the ESP 32 Cam development board to the Firebase database platform, code sources shared by Sara Santos at https://randomnerdtutorials.com/ were utilized.

2.7.2. Designing the Result Screen

In this stage of the study, obtaining the image from the Firebase platform, performing the operations, and conveying the result value to the user were realized. Firstly, the Scientific Python Development Environment Spyder (5.1.5) IDE was installed on the computer, and the work was started. Python version 3.11.0 was used.

Spyder IDE was used for Python programming. In the Python program, the connection of the application with the Firebase database was established. The region to be analyzed in the received image was cropped, and the average R, G, B channel intensities of the cropped region and the Z-Score value from these values were calculated.

Each image was acquired using the OpenCV library, ensuring consistent imaging conditions across all samples. A fixed region of interest (ROI) was selected from each image, and this area was consistently cropped for analysis. The coordinates defining the ROI (x1, y1, x2, y2) were kept constant for all images to ensure comparability. For each image, the designated ROI was cropped. This region, represented as a specific rectangular area within the image, allowed for a controlled analysis of color

changes. The chosen coordinates ensured that the same area was analyzed across all samples. The RGB values of each pixel within the cropped ROI were extracted, and the average RGB value for the entire region was then calculated using the following formula for each channel

$$(R, G, B): R_{avarage} = \frac{1}{N} \sum R i , \quad (1)$$

$$G_{avarage} = \frac{1}{N} \sum G i , \quad (2)$$

$$B_{avarage} = \frac{1}{N} \sum B i. \quad (3)$$

Here, N represents the total number of pixels within the ROI, while Ri, Gi and Bi denote the RGB values of each individual pixel.

The application of this method enabled the consistent tracking of color changes within the defined ROI across all images. The average RGB values provided a reliable metric for comparing different samples. By maintaining fixed imaging conditions (illumination source, light intensity, and distance), the applicability of the algorithm was validated, negating the need for alternative image processing methods.

The results obtained from 10 repetitions for each concentration were classified according to the result value to create label value ranges. Finally, control trials were conducted, and the study was completed.

2.7.3. Design of the Image Capture Box

To create stability in the photo to be taken, a shooting box was used to create a constant light intensity and a constant distance (Figure 2). It was determined that the development board captured the photo from a distance of 10 cm with the best clarity. Therefore, a box design was made with a distance of 10 cm between the board and the microfluidic. The dimensions of the image capture box are 18x10x8 cm.
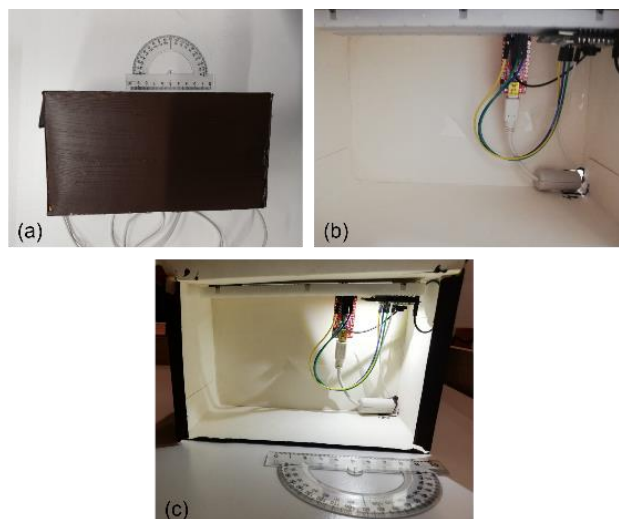
Figure 2. Shooting box, (a) External view of the image capture box, (b) Placement of the microcontroller/development board inside the box, (c) Diagram showing the microcontroller/development board in working condition.

3. Results

3.1. Methylene Blue Method

The relevant method was initially evaluated in Eppendorf tubes. At this stage, 100 μL of tetramethylammonium hydroxide and 100 μL of methylene blue solution were added to the tube and vortexed. Then, cortisol stock at appropriate concentrations was added and vortexed again. The reaction reached equilibrium after 10 minutes. The colors obtained from the reaction are shown in Figure 3.
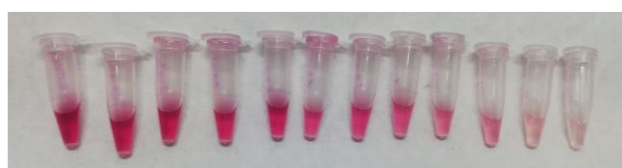
Figure 3. Color scale obtained after the reaction of stocks containing cortisol at concentrations of 60, 50, 40, 30, 20, 10, 5, 2, 1, 0.8, 0.4, and 0.2 uL/mL with the appropriate proportions of the color reagent.

3.2. Hydrophobization with Agar-Based Thermoplastic

Agar-based thermoplastic applied to cut filter papers rapidly solidified through the melting method. Colored water was applied to the agar-applied paper (Figure 4). This method enabled one-way hydrophobization.
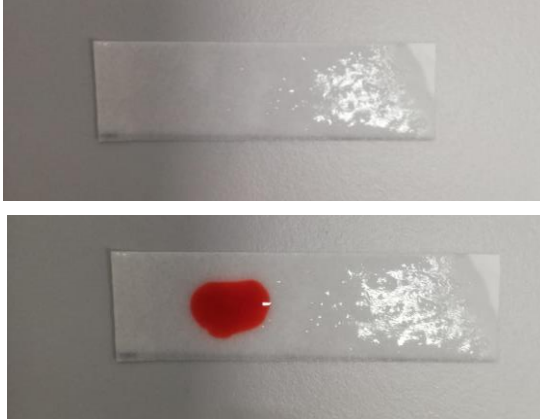
Figure 4. Figure showing the results of hydrophobization using the thermoplastic method.

3.3. Sweat Absorption Zone Studies

The liquid absorption capacities of the selected papers were calculated in the study. The results of the study are provided in Table 3.1.

Table 3.1: Table showing the liquid absorption capacities of the selected papers.

Absorbent Region	Capacity (μL)
No. 4 Whatman paper	40
No. 1 Whatman Chromatography paper	42
Thin Layer Chromatography paper	38
Whatman Glass Microfiber Filter paper	35
Coarse Filter Paper	30
Cotton-based Sweat Absorbent Pad	50

3.4. Microfluidic Arrangement

In the scope of the study, the cellulose-based microfluidic design included thick filter paper, No. 3 Whatman paper, No. 4 Whatman paper, and CHR 1 Whatman chromatography paper.

With the designed system, sweat samples collected from the user will be gathered via the wearable microfluidic layer. The microfluidic layer will be removed, immersed in the reactive solution contained in the created kit, and left to stand for 10 minutes. After the waiting period, discoloration will occur in the area where sweat samples are collected within the microfluidic, and the R (red), G (green), B (blue) channel density values will be analyzed with microcontrollers. Data will be shared with the user through a computer application created.

The created microfluidics were applied with 60 μL of solutions with different cortisol concentrations prepared with pure water to the sweat collection areas and left to stand for 15 minutes to ensure transfer to the sampling area. After 15 minutes, the microfluidics were immersed in the prepared liquid reagent in Eppendorf tubes and photographed after 10 minutes. The color change is shown in Figure 5.

Figure 5 The figure demonstrating the color reaction of the designed system with cortisol concentrations of 50, 40, 30, 20, 10, 5, 2, 1, 0.8, and 0.4 μg/mL, respectively.

3.5. Microcontroller Studies

The Esp32 development board was connected to the computer via USB cable through FTDI, and it was observed that the Esp32 development board was functioning properly from the serial port screen of the Arduino IDE.

During the program setup, the access address generated on the Serial Port Screen was entered into the web browser to run. The interface opened after this connection is completed is shown. When the "Capture Image" button is selected from the interface, the Esp32 development board inside the box captures the image, and the capture date, name, file format, and size of the image are stored in temporary memory. If no action is taken at this stage, the working page is closed, or a new image is captured, the saved image is deleted. If the "Show Image" button is selected, the image temporarily stored is shown to the user. If the user finds the

captured image suitable for use, they select the "Send" button, and the data stored in temporary memory is directed to the Firebase platform (Figure 6). The image and related information were sent to the Firebase platform.
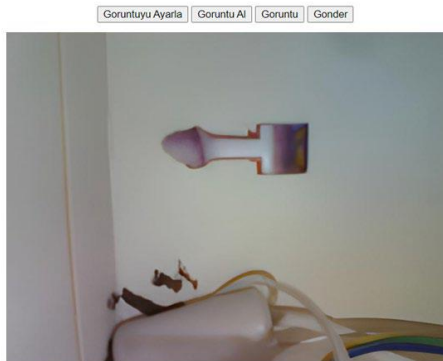
Figure 6 Interface allowing control of the Esp32 development board via the web server and the captured image.

Images captured from the Esp32 development board cannot be directly saved to the storage units on the computer but can be transferred either to a separate storage unit via an SD card or to a web server via the Wi-Fi connection port. For this reason, in this study, a Python program was used to save the captured image on the computer, select the regions to be analyzed, determine the intensity of the R, G, and B channels, and determine the z-score values. The regions for analysis from the raw image obtained from the Firebase platform are shown in Figure 7. The average channel intensity and z-score value in Roi1 are shown in Figure 7.
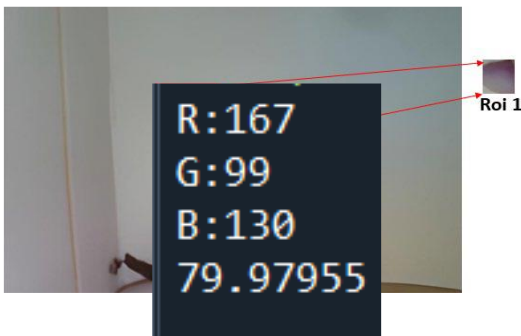
Figure 7 Image of the region of interest (ROI1) to be analyzed (a). Image showing the average RGB value and Z-score of Roi1 displayed on the Spyder console screen (b).

3.6. Validation Studies

The relevant system was tested in 10 repetitions, and the RGB values of the reaction regions were captured using a closed system and a microcontroller-based system established in a controlled light environment for validation studies. In the interpretation of RGB values, Z-score (standardization) was utilized. The Z-score value is calculated using the formula $z = (X - \mu) / \sigma$. The Z-score is a numerical measure that describes the relationship between a value and the mean of a group of values [18].

In essence, the Z-score indicates how many standard deviations a data point is from the mean. Z-scores are measured in terms of standard deviations from the mean. A Z-score of 0 means the data point has the same score as the mean. Using this method, a different coefficient was obtained for each concentration for the resulting color, and concentration differentiations were achieved based on the obtained coefficient values. The variation of Z-Score values by concentration is shown in Figure 8.
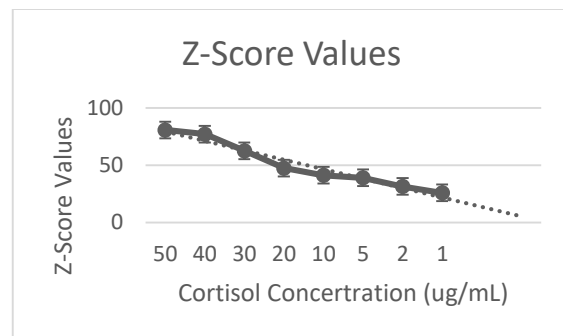
Figure 8 The graph showing the connection between cortisol concentrations and the Z-score coefficients resulting from validation studies.

The graph (Figure 8) illustrates the negative relationship between cortisol concentration ($\mu g/mL$) and Z-score values. As the cortisol concentration decreases from 50 $\mu g/mL$ to 1 $\mu g/mL$, the Z-score values correspondingly decrease from approximately 85 to 35. This inverse relationship indicates that higher cortisol concentrations result in higher Z-scores.

In this context, the Z-scores reflect the degree of color change detected by the microcontroller system. Higher cortisol concentrations induce more significant color changes, leading to higher Z-scores. Conversely, lower cortisol concentrations result in less intense color changes and lower Z-scores.

The error bars represent the standard deviation of the Z-score measurements for each cortisol concentration. Variability is higher at concentrations of 50 and 40 µg/mL, indicating some inconsistencies in measurements at these levels. In contrast, the error bars are smaller at lower across different concentrations highlight the system's potential for real-time monitoring of cortisol levels, which is essential for stress management and the diagnosis of related disorders.

The high analytical performance is evidenced by the low detection limit (0.3 µg/mL) and the system's ability to accurately measure cortisol concentrations within the range of 0.8 to 60 µg/mL. This graph substantiates the system's sensitivity and reliability.

The graph (Figure 8) effectively illustrates the quantitative relationship between cortisol concentration and Z-score values obtained through colorimetric analysis facilitated by the ESP 32 microcontroller system. The decreasing Z-score values with decreasing cortisol concentrations validate the system's sensitivity and reliability, confirming the potential of the developed wearable microfluidic device for continuous and accurate monitoring of cortisol levels in clinical and biomedical applications.

In validation studies, each sample was tested with 10 repetitions, and a standard cortisol curve was created (Figure 9).
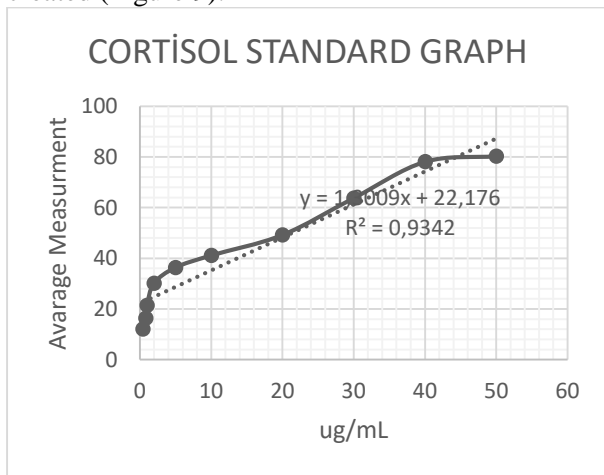
Figure 9 Standard graph showing cortisol concentration and label intervals.

The linear equation indicated on the graph (Figure 9), (y = 1.3009x + 22.176 \), shows that as cortisol concentration increases, the average measurement values also increase. This equation indicates that for each unit increase in cortisol, the average measurement increases by approximately

concentrations (5, 2, 1 µg/mL), suggesting more precise measurements at these levels.

The developed system demonstrates the capability to accurately measure cortisol levels across a wide range of concentrations. The consistency and predictability of Z-score values 1.3009 units, with a baseline measurement value of 22.176. The R^2 value of 0.9342, shown on the graph, indicates that the model fits the data well and has a strong explanatory power.

This graph (Figure 9) clearly demonstrates a linear relationship between cortisol concentration and average measurement values. The high R^2 value (0.9342) indicates that the linear model explains the data well and provides reliable results for measuring cortisol levels. This suggests that this standardization curve can be used for determining cortisol levels with high accuracy.

The ability to measure cortisol levels accurately and consistently is of great importance in both research and clinical applications. This graph (Figure 9) can serve as a reference for determining the cortisol concentrations in unknown samples, thereby enhancing the reliability of the results obtained. Consequently, this standard curve provides a valuable contribution to scientific studies and clinical applications by ensuring reliable and valid cortisol measurements.

In the scope of the study, slope, detection limit, and quantification limit values were calculated. The results are presented in Table 3.3.

Table 3.3: Table showing the validation results of cortisol RGB values.

Cortisol Validation Results	
Combined Standard Deviation	2,765629067
İnclination	212.332
Limit of Detection (LOD)	0,390749966
Limit of Quantification (LOQ)	1,172249898
Standard Curve Equation	y = 21.233x + 3.3922
R2 Value	$R^2 = 0.9439$

The determinable label range values are as shown in Table 3.4.

Table 3.4: The table showing the concentration values determinable by the created system.

Determined Label Intervals	
50	ug/mL
40	ug/mL
30	ug/mL
20	ug/mL
10	ug/mL
5	ug/mL
2	ug/mL
1	ug/mL
0,8	ug/mL

Table 3.5: Standard deviation, variance, relative standard deviation, and coefficient of variation values were examined for the correlation between samples for each ug/mL.
Validation results conducted for 50, 40, 30, 20, 10, 5, 2, 1, 0.8 ug/mL, n=10, respectively.

50 ug/mL	
Standard Deviation (s)	0,662748834
Variance (s^2)	0,439236017
Relative Standard Deviation (RSD)	1,508867234
Coefficient of Variation	150,8867234
Label Interval	79.45733-81.64688
40 ug/mL	
Standard Deviation (s)	1,287411716
Variance (s^2)	1,657428926
Relative Standard Deviation (RSD)	0,776752291
Coefficient of Variation	77,67522912
Label Interval	74.996944-79.847878
30 ug/mL	
Standard Deviation (s)	2,058650398
Variance (s^2)	4,238041462
Relative Standard Deviation (RSD)	0,485755134
Coefficient of Variation	20,8182106
Label Interval	54.623752-70.617808
20 ug/mL	
Standard Deviation (s)	2,799559391
Variance (s^2)	7,837532784
Relative Standard Deviation (RSD)	0,357199066
Coefficient of Variation	35,71990661
Label Interval	43.147088- 52.271786
10 ug/mL	

Standard Deviation (s)	1,203181454
Variance (s^2)	1,447645611
Relative Standard Deviation (RSD)	0,831129832
Coefficient of Variation	83,11298323
Label Interval	38.410248-42.870638
5 ug/mL	
Standard Deviation (s)	2,24180767
Variance (s^2)	5,02570163
Relative Standard Deviation (RSD)	0,446068596
Coefficient of Variation	44,6068596
Label Interval	32.907808-39.867084
2 ug/mL	
Standard Deviation (s)	1,752836372
Variance (s^2)	3,072435346
Relative Standard Deviation (RSD)	0,570503908
Coefficient of Variation	57,0503908
Label Interval	26.93363-33.44529
1 ug/mL	
Standard Deviation (s)	2,826891729
Variance (s^2)	7,991316845
Relative Standard Deviation (RSD)	0,353745419
Coefficient of Variation	35,37454194
Label Interval	17.394198-25.924386
0.8 ug/mL	
Standard Deviation (s)	2,007717889
Variance (s^2)	4,030931121
Relative Standard Deviation (RSD)	0,498077945
Coefficient of Variation	49,80779449
Label Interval	13.186178-20.536012

4. Discussion and Conclusion

The research conducted in this study is examined in four main stages. In the first stage, a colorimetric reaction was performed using the blue tetrazolium method, where the color intensity increased proportionally with the concentration, shifting from transparent to magenta. A color change was observed at a concentration of 0.8 ng/mL, which was found to be suitable for human sweat samples as reported by Ethan Tu et al. (8/142 ng/mL) [14]. The color intensity remained stable for up to one week as long as the Eppendorf tubes were not exposed to air. The blue tetrazolium method was repeated 10 times, and the colors obtained at specific cortisol concentrations were validated through RGB value readings.

In the second stage, various articles and designs aimed at the microfluidic layer were reviewed. Materials such as Whatman No. 4 paper and cotton-based absorbent pads, Whatman No. 1 chromatography paper, thin-layer chromatography paper, nitrocellulose membrane, and Whatman glass

microfiber filter paper were used. Studies were conducted to create the absorbent region, hydrophobization, and reaction area using these papers. Due to the different absorbency levels of each paper, varying amounts of reagent were applied to the reaction area. Cotton-based absorbent pads and Whatman glass microfiber filter paper were found to be more effective in reflecting color intensity. The difference in liquid retention between the two selected reaction areas affects the amount of sample collected and its transfer to the reaction region. Accordingly, a minimum of 50 µL sample was required to observe a visible color change in cotton-based absorbent pads, while 35 µL was determined for Whatman glass microfiber filter paper. These amounts were used in selecting the paper for the absorbent region and determining the flow in the microfluidic layer. The sizes of the Whatman No. 4 paper, cotton-based absorbent pads, Whatman No. 1 chromatography paper, thin-layer chromatography paper, Whatman glass microfiber filter paper, and coarse filter paper used were 1 cm². Accordingly, coarse filter paper had the lowest liquid absorption capacity at 30 µL, while cotton-based absorbent pads had the highest at 50 µL. It was concluded that using cotton-based absorbent pads with the highest liquid absorption capacity would be efficient in sample collection from the user and transfer to the reaction area.

In hydrophobization performed using the thermoplastic method, the water contact angle was determined to be 90±4°. Other hydrophobizing agents, such as paraffin, were not considered beneficial for wearable systems due to the potential for cracks during bending or stretching. Therefore, the use of the thermoplastic method for hydrophobization was deemed advantageous for the optimal use of the microfluidic layer. Despite being used in pharmaceutical coating and packaging and edible food packaging [15], no study was found in the literature regarding the hydrophobization of microfluidic layers using this method.

When the reaction areas were treated with solutions containing different concentrations of cortisol, the color intensity increased proportionally with the concentration. The study was repeated 10 times, and RGB intensities were determined by photographing with the ESP 32 CAM development board under constant light. Open-source software and hardware are crucial in the stages of scientific and commercial prototype development, being cost-effective and widely applicable. The ESP 32 CAM module, used in this study as one of the open-source development boards, although relatively new in image-based processes, is expected to become more widespread due to its potential. In a 2020 study by Mingdian Liu et al., the ESP 32 CAM module was actively used as a camera module with data transfer features over Wi-Fi and Bluetooth [16]. However, the major disadvantage of the ESP 32 CAM module used in this study is the low resolution of its built-in camera hardware. Additionally, the built-in Wi-Fi module on the board experiences a drop in connection quality as it moves away from internet access points, requiring extra modules to overcome this issue. Extra efforts are needed to address these technical problems. Although colorimetric detection at lower concentrations and intermediate values is possible, limitations in colorimetric detection were encountered due to the camera features of the ESP 32 CAM module.

The obtained RGB values were evaluated with the standard score/Z-score from the images of the microfluidic layer captured with the ESP 32 CAM module. The obtained values were compared with the population mean through Z-scores. The correlation between cortisol concentration and Z-score values was proportional, as shown in the Z-score graph (Figure 9). Similarly, the relationship between the increase in cortisol concentration and the average Z-score values calculated for each concentration was shown in the cortisol standard graph (Figure 8).

The criteria evaluated for validation were conducted according to the instructions of Harris's Quantitative Chemical Analysis [17]. The combined standard deviation (σ), an estimated value of the population standard deviation (σ), was calculated. This value is the weighted average of the sample values. The practical detection limit is generally determined by multiplying the standard deviation of the signal measured for at least ten repeated solutions by three. To determine the detection limit, this value was divided by the slope of the proposed standard graph after being multiplied by three. This value was calculated as three times the detection limit [17]. The combined standard deviation was determined to be 0.028%. It shows a high degree of similarity in terms of statistical significance. The slope of the regression line, which indicates how much Y_i changes when the X_i variable changes by one unit, was calculated as 21.23. The significance of the unit varies between the label ranges determined within the system, namely 50, 40, 30, 20, 10, 5, 2, 1, 0.8 µg/mL. In addition, the concentration and Z-score ranges were evaluated internally. The lowest standard deviation and variance were calculated as 0.66-0.44 at 50 µg/mL and 2.83-7.99 at 1 µg/mL, respectively. Therefore,

the confidence interval value was determined to be 50 µg/mL for the lowest concentration and 5 µg/mL for the highest concentration. When examining the label ranges, that is, the Z-score values, overlaps of 1.73 between 5 µg/mL and 10 µg/mL and 0.39 between 40 µg/mL and 50 µg/mL were observed.

This study has developed an innovative system enabling the rapid, accurate, and portable detection of cortisol using conventional image processing algorithms with the ESP 32 microcontroller and blue tetrazolium method. The system can accurately measure cortisol concentrations ranging from 0.8 to 60 µg/mL with a low detection limit of 0.3 µg/mL. Additionally, using thermoplastically hydrophobized microfluidic layers and cotton-based absorbent pads enhances the system's accuracy and reliability. This developed system offers a practical solution for non-invasive and real-time monitoring of cortisol levels, holding significant potential for clinical applications and personal health monitoring technologies.

The development of microfluidic layers in biotechnology studies and their use in health applications have become increasingly popular in recent years. One of the main reasons for this trend is the ability of technology applications to support minimal and more cost-effective systems that can replace large and high-cost devices. Our study aimed to create a system that strengthens this logic. Unlike high-cost systems like ELISA, which require long working hours and experienced personnel, our system is cost-effective, highly sensitive, and practical.

The potential of the developed system for real-time monitoring of cortisol levels provides significant insights for the diagnosis and management of stress-related disorders such as Cushing's syndrome and Addison's disease. The ability to non-invasively and continuously monitor cortisol levels offers a practical solution for both clinical and personal health applications.

This research paves the way for further development of wearable microfluidic devices capable of monitoring various biomarkers, thereby contributing to personalized healthcare. The presented methodology and technology can be adapted for detecting other clinically relevant analytes, thus expanding the scope and impact of this research in the field of biosensors and wearable health technology.

In summary, this study offers a robust and innovative solution for cortisol monitoring, demonstrating the practical application of microcontroller and microfluidic technologies in biomedical engineering. The integration of these technologies enhances the feasibility and accuracy of continuous health monitoring, providing significant potential for future research and clinical applications.

Acknowledgment

Conflict of Interest Statement

There is no conflict of interest between the authors.

Statement of Research and Publication Ethics

The study is complied with research and publication ethics

References

[1] S. Hiller-Sturmhöfel and A. Bartke, "The endocrine system: an overview," *Alcohol health and research world*, vol. 22, no. 3, pp. 153, 1998.

[2] N. E. Muda, M. A. A. Bakar, and B. Y. Majlis, "The Use of Electronic Sensor in Hormone Analysis," *The Malaysian journal of medical sciences: MJMS*, vol. 6, no. 2, pp. 12, 1999.

[3] S. Dalirirad and A. J. Steckl, "Aptamer-based lateral flow assay for point of care cortisol detection in sweat," *Sensors and Actuators B: Chemical*, vol. 283, pp. 79-86, 2019.

[4] L. Lu, J. Zhang, Y. Xie, F. Gao, S. Xu, X. Wu, and Z. Ye, "Wearable health devices in health care: Narrative systematic review," *JMIR mHealth and uHealth*, vol. 8, no. 11, pp. e18907, 2020.

[5] R. Royea, K. J. Buckman, M. Benardis, J. Holmes, R. L. Fletcher, E. Y. K. Ng, and J. D. Ellenhorn, "An introduction to the Cyrcadia Breast Monitor: A wearable breast health monitoring device," *Computer methods and programs in biomedicine*, vol. 197, pp. 105758, 2020.

[6]   M. Rafiquzzaman, *Microcontroller Theory and Applications with the PIC18F*. John Wiley & Sons, 2018.

[7]   W. A. Stapleton, "Development Of A Library For Teaching And Implementing Resource-Limited Embedded Systems," in *Proceedings of the International Conference on Embedded Systems, Cyber-physical Systems, and Applications (ESCS)*, The Steering Committee of The World Congress in Computer Science, Computer Engineering and Applied Computing (WorldComp), 2011, pp. 1.

[8]   G. Gridling and B. Weiss, *Introduction to microcontrollers*, Vienna University of Technology Institute of Computer Engineering Embedded Computing Systems Group, 2007.

[9]   Y. Güven, E. Coşgun, S. Kocaoğlu, H. Gezici, and E. Yılmazlar, "Understanding the concept of microcontroller based systems to choose the best hardware for applications," 2017.

[10] K. Hintz and D. Tabak, *Microcontrollers: architecture, implementation, and programming*. McGraw-Hill, Inc., 1992.

[11] H. K. Kondaveeti, N. K. Kumaravelu, S. D. Vanambathina, S. E. Mathe, and S. Vappangi, "Computer Science Review," 2021.

[12] R. Santos, "ESP32-CAM Take Photo and Display in Web Server," *randomnerdtutorials.com*, 2019. [Online]. Available: https://randomnerdtutorials.com/. [Accessed: 01-Jul-2022].

[13] S. Santos, "ESP32-CAM Save Picture in Firebase Storage," *randomnerdtutorials.com*, 2022. [Online]. Available: https://randomnerdtutorials.com/. [Accessed: 18-Jul-2022].

[14] E. Tu, P. Pearlmutter, M. Tiangco, G. Derose, L. Begdache, and A. Koh, "Comparison of colorimetric analyses to determine cortisol in human sweat," *ACS omega*, vol. 5, no. 14, pp. 8211-8218, 2020.

[15] S. Bandyopadhyay, T. Sáha, D. Sanétrník, N. Saha, and P. Sáha, "Thermo Compression of Thermoplastic Agar-Xanthan Gum-Carboxymethyl Cellulose Blend," *Polymers*, vol. 13, no. 20, pp. 3472, 2021.

[16] M. Liu, Y. Zhao, H. Monshat, Z. Tang, Z. Wu, Q. Zhang, and M. Lu, "An IoT-enabled paper sensor platform for real-time analysis of isothermal nucleic acid amplification tests," *Biosensors and Bioelectronics*, vol. 169, pp. 112651, 2020.

[17] D. C. Harris, *Quantitative Chemical Analysis*, W. H. Freeman, New York, 1995, pp. 750.

Moleculer Docking and Theoretical Analysis of the (E)-5-((Z)-4-methylbenzylidene)-2-(((E)-4-methylbenzylidene)hydrazineylidene)-3-phenylthiazolidin-4-one Molecule

Kenan GÖREN[1], Efdal ÇİMEN[2], Veysel TAHİROĞLU[3*], Ümit YILDIKO[4]

[1]Kafkas University, Department of Chemistry, Kars, Türkiye
[2]Kafkas University, Kars Vocational School, Chemistry and Chemical Processing Technologies, Kars, Türkiye
[3]Şırnak University, Health Sciences Faculty, Nursing Department, Şırnak
[4]Kafkas University, Department of Bioengineering,

(ORCID: 0000-0001-5068-1762) (ORCID: 0000-0003-2461-5870)
(ORCID: 0000-0003-3516-5561) (ORCID: 0000-0001-8627-9038)

Abstract
Theoretically ideal molecular structure of (E)-5-((Z)-4-methylbenzylidene)-2-(((E)-4-methylbenzylidene)hydrazineylidene)-3-phenylthiazolidin-4-one (EMPT) Gaussian 09 software was researched using. The theoretically ideal chemical structure of EMPT molecule has been examined. The B3LYP/SDD-B3LYP/6-311G bases and techniques were used to perform quantum chemical calculations. To find out how the molecule transfers charge, LUMO and HOMO analyses were done. The stability of the molecule was investigated as a function of charge dispersion and hyperconjugative interaction using NBO analysis. MEP was reported to be performed using a DFT technique. We observed the compatibility of HOMO-LUMO, MEPS, NLO, Mulliken Atomic Charges and optimized molecular geometry data in the two sets used. Molecular docking studies were performed using enzyme codes PDB: 5FGK and PDB: 5HBE to determine the binding affinity and possible fundamental interaction betwith the inhibitors and the target enzyme. Finally, in our study, ADME analysis of EMPT molecule was performed and many parameters were examined using virtual screening methods on small molecules, Molecular characteristics, cell permeability, HIA drug solubility S, medicament paralely point and polar surface area PSA are among them.

1. Introduction

Schiff bases are compounds generally represented by the formula R-CH=N-R'. In this formula, R and R' represent aryl or alkyl substituents. Schiff bases and some Schiff complexes are widely used in both synthesis and medical fields. These substances are very important due to the pharmacological effects of heterocycles [1]. Medicinal chemists utilize heterocyclic compounds with five and six members that are oxygen, sulfur, and nitrogen-containing. Diazoles or oxazole derivatives containing oxygen along with nitrogen as heteroatoms in the quintuple ring are very important due to their anti-inflammatory, antidepressant, analgesic, anti-cancer, antimicrobial, antidiabetic, and anti-obesity qualities. In other words, Schiff bases have also been studied because they are also used to form covalent organic frameworks [2]. These frameworks contain two- or three-size spongy crystal formation and utilize Schiff base interactions through covalent molecular assembly. Additionally, most Schiff bases exhibit remarkable coordination properties with metallic ions, forming corresponding complexes comprising actinide, lanthanide, transition metal, and main group elements [3]. When combined with a metal ion, its

---

characteristics are greatly enhanced. Its properties are significantly improved when coordinated with a metal ion. Schiff base ligands can be made quickly and combine with nearly all metal ions to form complexes [4]. Its antibacterial, antifungal, antioxidant, anticancer, anti-inflammatory, antimalarial, and antiviral properties have been utilized in biology. Moreover, they function as catalysts for a range of processes, such as the synthesis of bis(indomethacin) and polymerization, thionyl chloride reduction, oxidation of organic compounds, ketone reduction reaction, aldol reaction, Henry reaction, epoxidation of alkenes, and hydrosilylation of ketones. Additionally, there is evidence in the literature that it is used for the synthesis of hetero compounds or protecting groups in organic syntheses [5]. The development of contemporary computational simulation techniques has made it possible to compute orbital, optical, and structural properties with accuracy. Therefore, without conducting experimental research, it is feasible to predict the physical, chemical, and optical possessions of different nanomaterials, including molecules and alloys. The nonlinear visual (NLO) possessions of materials play a major role in signal processing, optical switches, and optical memory design in communications technology. The NLO properties of molecules arise from the movement of delocalized π-electrons around them. Increased conjugation and the addition of acceptor and donor groups to the molecule changes the NLO property [6]. Especially for such chemicals, which are difficult to examine in terms of analytical chemistry, preparation is required through data processing and statistical evaluation, optimization of experimental factors, time saving, calibration and theoretical calculations required for quantitative measurements [7]. Even in very large and complex systems, results can be obtained in a reasonable time. One of the fundamental principles of quantum chemical methods is approaches based on density functional theory (DFT) [8].

Since the DFT (B3LYP) method and 6-311G and SDD basis sets have been widely used in the literature, we preferred these methods in terms of docking interaction by making energy calculations, charge calculations and optimization of the potentially used molecule. Molecular modeling investigations of the chosen EMPT molecule compound were conducted in this work. to learn more about the compound's energy, electrical, and nonlinear optical properties, DFT investigations were conducted. Furthermore, ADME analysis was carried out to look into the compound's ADME characteristics. Ultimately, successful molecular docking done were do to ascertain whether the EMPT

molecule compound would be consistent with the drug design phenomena.

2. Material and Method

First, utilizing the Gaussian 09 software, EMPT molecule was drawn in ChemBioDraw for computations with DFT [9] and then reduced using the Chem3D program technique. In a similar manner, GaussView 6.0 was opened after the sketched molecules had been transformed to 3D MOL2 files in Chem3D. The B3LYP/SDD-B3LYP/6-311G bases and techniques were used to compute the DFT research. Each calculation's results, including HOMO and LUMO analysis, geometry optimization, Mulliken atomic charge and dipole moment, and MEP analysis, have been displayed. Schrödinger's Maestro Molecular Modeling platform (version 12.5) was utilized to accomplish molecular docking, which allowed for the precise identification of the binding mechanism and connecting site of ligand-protein interactions. For the ADME test, online servers like SwissADME (http://www.swissadme.ch/index.php) were utilized. The protein data bank's PDB: 5FGK and PDB: 5HBE enzyme codes were used for the docking analysis. The Discovery Studio 2016 client helped to conceptualize the molecular docking study.

3. Results and Discussion

3.1. Structure details and analysis

Using the GaussView 6.0 molecular imaging program, the approximate three-dimensional geometry of the EMPT molecule compound was drawn and the atomic positions were determined. All not practical compitation were made utilize the Gaussian 09W package aplication [9]. The structure of the examined molecule obtained from the literature [1] and the theoretically calculated geometric structure utilize the B3LYP/SDD-B3LYP/6-311G basis set and approaches are shown with atoms. B3LYP theory was used, which includes the Lee-Yang and Parr correlation functional [8]. Becke's hybrid energy functional approach with three parameters, and DFT coded in the Gaussian 09W program. The basis set used in the calculations is 6-311G(d,p); This set includes diffuse functions and polarized functions, which are added to model the situation where the electron density in excited ionic molecules is more dispersed than in the ground state of the molecule. To eliminate the polarization effect (when atoms are brought closer together, the electronic density is distorted by the influence of other nuclei). Bond lengths (Å) and bond angles (Å) for the

molecule are listed in Table 1 using approximations and the B3LYP/SDD-B3LYP/6-311G basis set.

Improved performance based on comparison of the EMPT molecule was investigated. The bond lengths and bond angles in the phenyl rings are within the standart reach. For the oxygen atom in the two phenyl rings, the C–O Nexus range for B3LYP are 1.20 Å and the C–C bond gap are 1.349–1.489 Å. The aromatic content in the C–H ring is 1.083–1.087 Å. Each angle C-C-C is 117° and its slope is 120.5°. N-

C-O 123°, C-C-H 120°, C-N-C 118°, C-S-C 91°, N-N-C 112°, C-N-C 118°, H-C-H 107° and C-O bond distances 1.21 Å, C-C bond distances 1.352-1.484 Å for B3LYP/6-311G. The aromatic content in the C–H ring is 1.086–1.089 Å. Each angle C-C-C is 117° and its slope is 120°. N-C-O is 123°, C-C-H is 120°, C-N-C is 118°, C-S-C is 92°, N-N-C is 111°, H-C-H is 107°. When we looked at a similar molecule in the literature, we observed similar bond length values when compared with experimental data [10].

Table 1. Theoretically determined some bond lengths (Å) and angles (º) of the EMPT molecule

Bond Lengths	B3LYP/ SDD	B3LYP/ 6-311G	Bond Lengths	B3LYP/ SDD	B3LYP/ 6-311G
C1-C2	1.39389	1.39427	C12-H36	1.08709	1.08949
C3-C4	1.39034	1.39145	C14-H37	1.08480	1.08712
C5-C6	1.39162	1.39163	C22-H41	1.08534	1.08761
C8-C9	1.48792	1.48474	C8-N7	1.41227	1.43783
C12-C13	1.45212	1.44997	C11-N7	1.39081	1.38840
C9-C12	1.34955	1.35205	C30-N20	1.28462	1.28847
C21-C30	1.45907	1.45625	C8-O29	1.20844	1.21363
Bond Angles	**B3LYP/ SDD**	**B3LYP/ 6-311G**	**Bond Angles**	**B3LYP/ SDD**	**B3LYP/ 6-311G**
C1-C2-C3	120.13201	120.17183	C1-C2-H32	120.17654	120.18659
C4-C5-C6	119.47092	119.41537	H45-C27-H46	107.88369	107.93864
C8-C9-C12	119.51263	119.25575	N7-C8-O29	123.29208	123.41517
C12-C13-C14	117.86380	117.80464	C9-S10-C11	91.10198	92.16928
C4-N7-C8	118.10449	118.05547	N19-N20-C30	112.23423	111.80088
Planar Bond Angles	**B3LYP/ SDD**	**B3LYP/ 6-311G**	**Planar Bond Angles**	**B3LYP/ SDD**	**B3LYP/ 6-311G**
C1-C2-C3-C4	-0.50573	-0.36664	C11-N19-N20-C30	179.93208	177.64062
C8-C9-C12-C13	-179.89223	-179.57650	C4-N7-C11-S10	179.58625	175.81861
C3-C4-N7-C11	92.80774	10218577	N7-C8-C9-C12	179.94703	179.64806
C4-N7-C8-O29	0.31301	3.22207	O29-C8-C9-12	-0.02363	-0.066774

3.2. Mulliken atomic charges

Unlike electron density, atomic charges cannot be calculated precisely using quantum mechanics. So there is some degree of randomness in every method developed to calculate this quantity. Despite some disadvantages, the Mulliken load distribution method is widely used [11]. The Mulliken charge distribution method is based on distributing wave functions between atoms and dividing equally the regions where two orbitals overlap. However, this distribution does not accurately represent the electronegativity of each element [12]. In some extreme cases, it may result in an orbital with a negative electron population or describe an orbital with more than two electrons. These are based heavily on the chosen base. Therefore

some qualitative estimates are made using Mulliken loadings instead [13].

In this study, Mulliken load values calculated with the Gaussian 09W program as a result of any optimization were evaluated for the purpose of calculating atomic loads. Table 2 shows the gas phase studied using the B3LYP/SDD-B3LYP/6-311G basis set and approximations. It was determined that the electronegative atoms (N7, N11, N19, N20 and O29) in the molecule had negative charge values. The calculated charge values of these atoms are -0.497, -0.253, -0.250 and -0.323 (a.u.). Figure 1 shows Structure Optimization using the DFT/B3LYP/6-311G basis set and approaches.

Table 2. Mulliken atomic charges of the EMPT molecule

ATOMS	B3LYP/ SDD	B3LYP/ 6-311G	ATOMS	B3LYP/ SDD	B3LYP/ 6-311G
C1	-0.093	-0.113	O29	-0.323	-0.485
C2	-0.101	-0.142	N7	-0.497	-0.641
C3	-0.008	-0.075	N19	-0.253	-0.355
C4	0.119	0.235	N20	-0.250	-0.325
C5	-0.008	-0.072	S10	0.252	0.299
C6	-0.101	-0.139	H31	0.097	0.124
C8	0.525	0.657	H32	0.099	0.129
C9	-0.419	-0.261	H33	0.090	0.137
C12	0.032	-0.150	H34	0.090	0.135
C13	-0.071	0.095	H35	0.099	0.129
C14	-0.059	-0.147	H36	0.125	0.165
C15	-0.075	-0.152	H37	0.093	0.129
C16	-0.091	0.101	H38	0.089	0.121
C17	-0.078	-0.155	H39	0.087	0.122
C18	-0.059	-0.141	H40	0.104	0.132
C21	-0.165	0.047	H41	0.089	0.122
C22	-0.052	-0.145	H42	0.085	0.116
C23	-0.076	-0.158	H43	0.083	0.116
C24	-0.088	0.103	H44	0.141	0.157
C25	-0.099	-0.154	H45	0.107	0.138
C26	-0.020	-0.123	H46	0.125	0.148
C27	-0.256	-0.448	H47	0.125	0.152
C28	-0.257	-0.448	H48	0.117	0.144
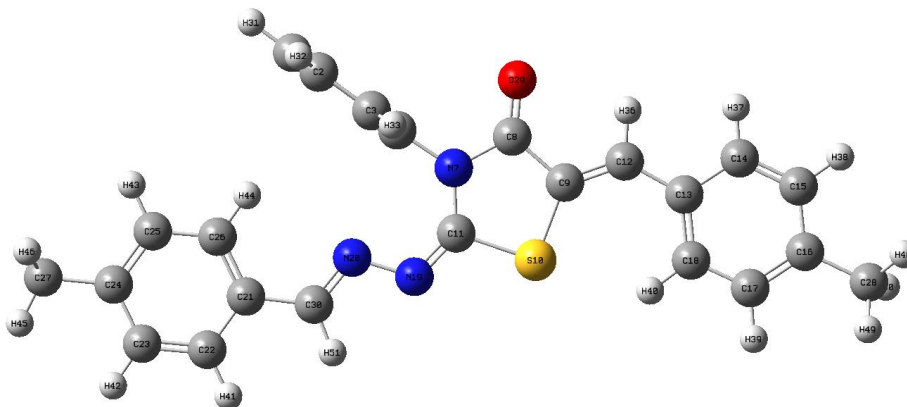
Figure 1. EMPT molecule with DFT/B3LYP/6-311G basis Structure Optimization

3.3. HOMO and LUMO analysis

Molecular orbital theory states that atoms combine to form molecules. When the atomic orbitals that make up the molecules approach each other by the required bond distance, they combine to create the molecule's orbitals. These orbitals can be thought of as places in the molecule where there is a maximum chance of finding an electron [14]. The lowest energy of unoccupied molecular orbitals (ELUMO) and the highest energy of occupied molecular orbitals (EHOMO) are found in the fundamental orbitals involved in chemical reactions [15]. The skill of a molecule to make a donation of electrons (π donor) is known as HOMO energy and the skill of a molecule to accept electrons (π acceptor) is known as LUMO energy.

The minimal unoccupied molecular orbital (LUMO) and the maximum occupied molecular

orbital (HOMO) are two crucial molecular orbitals. The bioactivity of a chemical is represented by its eigenvalues and hole energies for LUMO and HOMO. Shorter frontier orbital spaces cause a chemical to be more polarized, have less kinetic stability, and be more reactive toward chemicals [16]. Since the HOMO is the outer orbital that carries electrons and attempts to act as an electron donor, its energy has a direct impact on the ionization potential. However, LUMO has the potential to absorb electrons and its energy is involved to the electron proximity. The HOMO and LUMO chemicals' eigenvectors and energy gaps show the molecule's biological activity [17]. Figures 2 and 3 display the EMPT molecule's HOMO and LUMO energies, which were deternined using the B3LYP/SDD-B3LYP/6-311G basis set and methodologies. Two significant chemical orbitals for HOMO and LUMO energies were investigated, as shown in Figures 2 and 3. Table 3 displays the quantum chemical factor (in eV) determined for the nominal energy conformation of the EMPT molecule utilizing the DFT/B3LYP/6-311G and DFT/B3LYP/SDD techniques. When we examine two important chemical orbitals for HOMO and LUMO energies in Figures 2 and 3, the HOMO and LUMO electron clouds are completely located throughout the ligand, except for the aromatic ring (C1, C2, C3, C4, C5, C6). In addition, LUMO+1 electron clouds are completely localized throughout the ligand, except for the (C1, C2, C3, C4, C5, C6) aromatic ring, while HOMO-1 has been localized on the (C1, C2, C3, C4, C5, C6) aromatic ring and (E)-

3-methyl-2-(methylimino)thiazolidin-4-one. We observed that the localized regions were the same in both sets. The localized regions are the same in both sets, indicating that boundary molecular orbitals have important roles in chemical reactivity and stability.

The orbital energies of LUMO and HOMO can be used in the following formulas to calculate the electron proximity and ionization energy: $A = -E_{LUMO}$, $I = -E_{HOMO}$, $(\mu = -(I+A)/2)$ and $\eta = (I-A)/2$. An electrophilic system can store more electrons and resist the transfer of electrons to the environment than a non-electrophilic system [18]. It is a more accurate measure of total chemical reactivity because it contains information about both electron transfer (potential chemical) and durability (hardness). Chemical species are the affinity and ionization potential of electrons; Chemical potential and hardness (A) are calculated using the formulas $=(I-A)/2$ and $=(I+A)/2$, respectively [19].

The stable and negative chemical potential resulting from the negativity of this complex prevents the spontaneous dissolution of the components forming the title compound. An electron nebula's resistance to degradation caused by small perturbations during chemical processing is what gives it its hardness. Although it cannot be observed physically, both chemistry and physics make use of the notion of hardness. In contrast to soft systems, which can be highly and significantly polarized, hard systems are typically much smaller and less polarized.
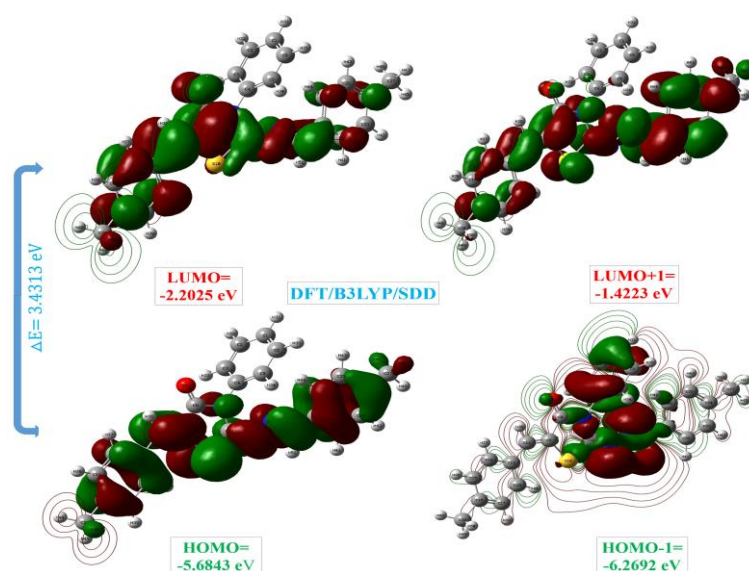
Figure 2. Boundary molecular orbitals of the EMPT molecule as per the DFT/B3LYP/SDD phase
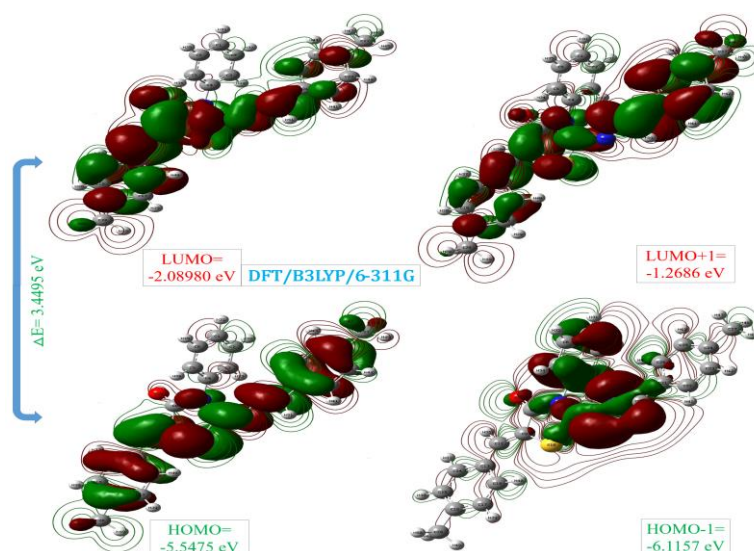
Figure 3. Boundary molecular orbitals of the EMPT molecule as per the DFT/B3LYP/6-311G level

Table 3. Quantum chemical parameters (in eV) of the EMPT molecule were calculated using the DFT/B3LYP/SDD-DFT/B3LYP/6-311G methods, leading to low energy compatibilities

Molecules Energy		DFT/B3LYP SDD	DFT/B3LYP 6-311G
E_{LUMO}		-2.2025	-2.0980
E_{HOMO}		-5.6849	-5.5475
E_{LUMO+1}		-1.4223	-1.2686
E_{HOMO-1}		-6.2692	-6.1157
Energy Gap	$(\Delta E) | E_{HOMO}-E_{LUMO}|$	3.4824	3.4495
Ionization Potential	$(I=-E_{HOMO})$	5.6849	5.5475
Electron Affinity	$(A=-E_{LUMO})$	2.2025	2.0980
Chemical hardness	$(\eta=(I-A)/2)$	1.7412	1.7248
Chemical softness	$(s=1/2\eta)$	0.8706	0.8624
Chemical Potential	$(\mu=-(I+A)/2)$	-3.9437	-3.8228
Electronegativity	$(\chi=(1+A)/2)$	1. 6013	1.549
Electrophilicity index	$(\omega=\mu^2/2\eta)$	13.5402	12.6029

3.4. Molecular electrostatic potential (MEP)

The predicted atomic charges are defined to calculate the atomic charges. The electrostatic potential (ESP) is determined by defining multiple points surrounding the molecule under study, provided that the atomic charges obtained from the least squares method correspond to the electrostatic potential [20]. These charges may vary slightly because the electrostatic potential calculation is based on estimating the locations of spatial points. Electronegativity and partial charges are related to ESP [21]. Together with the ESP potential surface, Figure 4 displays Molecular electrostatic potential field (MEP) mapped [22].

MEP can be used to identify hydrogen bond interactions in addition to electrophilic and nucleophilic activities. The relationship is with electron density (ED). The electrostatic potential V(r) is a useful tool for molecular characterization research procedures, such as studying the relationships between medications and receptors or between substrates and enzymes. Because these two types initially perceive each other through the lens of their prospective [23]. The electrophilic and nucleophilic moieties of the studied complex were divine utilize B3LYP/SDD-B3LYP/6-311G basis set using MEP in the optimal geometry. As shown in Figure 4, negative (yellow or red) regions of the MEP indicate electrophilic reaction, whereas favorable (blue) regions represent nucleophilic reactivity. As we expected, the negative regions were localized to the oxygen on the thiazolidine ring.
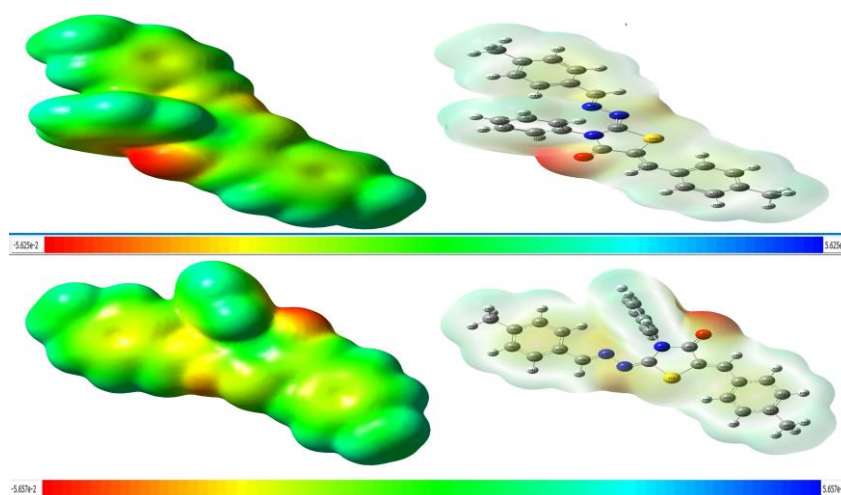
Figure 4. Molecular electrostatic potential field of EMPT molecule utilising B3LYP/SDD-B3LYP/6-311G methods and basis.

3.5. Non-Linear optical properties (NLO)

Polarizability (α) and hyperpolarizability (β) values are used to computationally predict nonlinear optical properties (NLO). Optical properties in organic matter-based materials are defined by their polarizability [24]. The performance of a material's

nonlinear optical properties is affected by its hyperpolarizability. A molecule needs to have a small HOMO-LUMO energy difference, a high dipole moment, polarizability, and hyperpolarizability in order to exhibit the NLO property [25]. Hyperpolarization (β), polarization (α), and electric dipole moment (μ) of EMPT molecule were measured using NLO activity, B3LYP/SDD(d,p) and B3LYP/6-311G method and basis set. Calculated NLO values are shown in Table 4.

Equations 1–4 gave the average polarizability (α), static dipole moment (μ), and total first static hyperpolarizability (β) values for the x, y, and z components. DFT/B3LYP/6-311G and DFT/B3LYP/SDD approaches gave total values of 3.47x10-30 esu and 3.54x10-30 esu for EMPT molecule, respectively.

$$\mu = (\mu_x^2 + \mu_z^2)^{1/2} \tag{1}$$

$$\alpha = 2^{-1/2}\left[(\alpha_{xx} - \alpha_{yy})^2 + (\alpha_{yy} - \alpha_{zz})^2 + (\alpha_{zz} - \alpha_{xx})^2 + 6\alpha_{xx}^2\right]^{1/2} \tag{2}$$

$$\beta_{Total} = (\beta^2 x + \beta^2 y + \beta^2 z)^{1/2} \tag{3}$$

$$= [(\beta xxx + \beta xyy + \beta xzz)^2 + (\beta yyy + \beta yxx + \beta yzz)^2 + (\beta zzz + \beta zxx + \beta zyy)^2]^{\frac{1}{2}} \tag{4}$$

Table 4. The dipole moments (Debye), polarizability (au), components, and total value of EMPT molecule are computed using the SDD and 6-311G basis s using the DFT/B3LYP technique

Parameters	B3LYP/ SDD	B3LYP/ 6-311G	Parameters	B3LYP/ SDD	B3LYP/ 6-311G
μ_x	0.4280	0.3405	β_{xxx}	-86.9694	-90.0332
μ_y	-0.9119	-0.8372	β_{YYY}	-47.3193	-44.5391
μ_z	0.0580	0.2335	β_{ZZZ}	0.9476	2.6570
$\mu_{(D)}$	1.0091	0.9335	β_{XYY}	35.0618	34.4839
α_{XX}	-128.8197	-123.5322	β_{XXY}	-32.3496	-33.6734
α_{YY}	-177.9241	-173.1954	β_{XXZ}	3.1931	3.2352
α_{ZZ}	-182.3465	-178.3604	β_{XZZ}	13.1104	13.5166
α_{XY}	8.7467	9.0193	β_{YZZ}	24.4836	23.6049
α_{XZ}	-0.3724	0.0065	β_{YYZ}	-0.3900	-0.6371
α_{YZ}	-0.1230	-1.2630	β_{XYZ}	0.7795	-1.1306
$\alpha_{(au)}$	-184.972	-184.7400	$\beta_{(esu)}$	3.47x10^{-30}	3.54x10^{-30}

3.6. NBO Analysis

To better understand the intermolecular interactions in EMPT molecule, NBO analysis was performed on the optimized structures [26]. The Gaussian 09W program package was used to make the NBO analysis. The percentages of individual bond electrons for σ and π bonds in various bonds using DFT(B3LYP) methods and the changes in the percentages of electrons in s, p, and d orbitals in each atom are shown in Table 5 comparisons. Hybridizations that occur to form bonds on atoms are also obtained from this pointIn this instance, π bonds by definition have to be made up of the p atomic orbitals of the C, O, and N atoms. Research has demonstrated how much the s orbital helps with hybridization at the C atom. Table 5 shows the changes in the percentages of electrons in s, p, and d orbitals in each atom, as well as the percentages of individual bond electrons and bonds in different bonds. A quadratic expression is used for EMPT molecule. Fock marix was used to estimate the relationship between the receiver (j) and the transmitter (i). The compensatory value associated with delocalization is estimated to be as in Equation 5 for each giver (i) and recipient (j) [27].

$$E(2) = \Delta E_{ij} = q_i \frac{(F_{i,j})^2}{(\varepsilon_i - \varepsilon_j)} \qquad (5)$$

The NBO element of the Fock matrix is F(i,j), the diagonal elements are i and j, and the donor orbital occupancy is qi. An increase in stabilization energy increases the probability of electrons moving to acceptor orbitals. For a few chosen donors and acceptors, Table 5 displays the electron volume, E(2), E(j)-E(i), and f(i,j) values along with the results of the NBO calculations. The relationship between electron delocalization from bonding (BD) to antibonding (BD*) orbitals, filled and unfilled NBO-type Lewis orbitals, and stabilization energy E(2) is characterized by NBO analysis. The interactions between bond (σ/π) and anti-bond (σ*/π*) also have a significant impact on structural stability. π(C16-C17) /π*(C13-C18) interaction has the maximum E value with 22. kcal/mol. (2), followed by π(C23-C24)/π*(C21-C22) interaction with 22.40 kcal/mol.

Table 5. Selected NBO results of EMPT molecule are computed using the DFT/B3LYP technique and the SDD basis

NBO(i)	Type	Occupancies	NBO(j)	Type	Occupancies	E(2)[a] (Kcal/mol)	E (j)-E(i)[b] (a.u.)	F (i, j)[c] (a.u)
C1-C6	π	1.66189	C4-C5	π *	1.66443	21.04	0.29	0.069
C1-H31	σ	1.97929	C2-C3	σ *	1.97429	3.88	1.10	0.058
C2-C3	σ	1.97429	C4-N7	σ*	1.97588	4.87	1.07	0.065
C3-C4	σ	1.97183	C4-C5	σ *	1.97182	4.67	1.28	0.069
C4-C5	π	1.66443	C2-C3	π*	1.97429	20.82	0.29	0.070
C5-C6	σ	1.97429	C4-N7	σ *	1.97588	4.87	1.07	0.065
C6-H35	σ	1.97932	C1-C2	σ*	1.97882	3.85	1.09	0.058
C8-C9	σ	1.96956	C12-C13	σ*	1.97275	5.96	1.18	0.068
C8-O29	π	1.98122	C9-C12	π*	1.84583	3.33	0.41	0.035
C9-C12	π	1.84583	C8-O29	π*	1.98122	20.07	0.30	0.072
S10-C11	σ	1.96241	N19-N20	σ *	1.96946	6.39	1.02	0.072
C11-N19	π	1.90607	N20-C30	π *	1.89638	11.41	0.37	0.059
C12-C13	σ	1.97275	C9-C12	σ*	1.97857	4.97	1.31	0.072
C12-H36	σ	1.95997	C9-S10	σ *	1.97510	1.15	0.70	0.079
C13-C18	π	1.61305	C14-C15	π*	1.67863	19.42	0.28	0.068
C14-C15	π	1.67863	C16-C17	π *	1.62397	21.37	0.29	0.071
C14-H37	σ	1.97943	C13-C18	σ*	1.97161	4.34	1.08	0.061
C15-H38	σ	1.97891	C16-C17	σ *	1.97352	4.36	1.09	0.062
C16-C17	π	1.62397	C13-C18	π*	1.61305	22.96	0.28	0.072
C17-H39	σ	1.97915	C15-C16	σ*	1.97335	4.39	1.09	0.062
N19-N20	σ	1.96946	S10-C11	σ*	1.96241	5.46	0.96	0.065
N20-C30	π	1.89638	C11-N19	π *	1.90607	13.58	0.32	0.062

C21-C22	π	1.63648	N20-C30	π *	1.89638	20.18	0.27	0.069
C22-H41	σ	1.97942	C21-C26	σ*	1.97115	4.46	1.08	0.062
C23-C24	π	1.64733	C21-C22	π *	1.62648	22.40	0.28	0.072
C25-C26	π	1.68248	C21-C22	π *	1.63648	18.52	0.28	0.066
C28-H50	σ	1.97391	C16-C17	σ *	1.62397	4.65	0.54	0.049

3.7. Molecular docking studies

The process of observing and analyzing interactions between a ligand and a protein sensor is called molecular docking [28]. A computer technique called "molecular docking" attempts to predict the noncovalent interaction between a small molecule (ligands) and a macromolecule (receptor). Automated docking has been extensively utilized in molecular design and structure/function analysis to forecast the configurations of bimolecular complexes [29]. Docking small molecule compounds into receptor binding sites and assessing the complex's binding affinity are two steps in the structure-based drug design process. The complexes of proteins of these enzymes have been discovered by investigating the online resource RSCB protein database for 5FGK and PDB: 5HBE. Enzyme codes PDB: 5FGK and PDB: 5HBE were used in molecular docking studies to ascertain the inhibitors' binding affinities and potential interactions with the target enzyme. The 5FGK and 5HBE proteins encoded by this gene are members of the cyclin-dependent protein kinase (CDK) family. CDK8 and cyclin C are associated with the mediator complex and regulate transcription by various mechanisms. CDK8 binds and/or phosphorylates a variety of transcription factors, which can have an activating or inhibitory effect on transcription factor function. CDK8 phosphorylates the Notch intracellular domain SREBP and STAT1 S727. CDK8 also inhibits transcriptional activation by affecting turnover of subunits in the tail module of the mediator complex. The molecular docking scores of PDB: 5FGK and PDB: 5HBE enzymes are shown in Table 6.

Table 6. Docking score of EMPT molecule for PDB: 5FGK, PDB: 5HBE enzyme and control

Compound	Docking Score (cal/mol)			
	PDB: 5FGK	Control 5FGK	PDB: 5HBE	Control 5HBE
EMPT Molecule	-7.10	-9.72	-6.11	-8.20

As a result of the docking study of EMPT molecule, Figure 5 shows their 2D and shows its interaction in 3D modes. As a result, in Table 6, the shift score with molecule (the (E)-5-((Z)-4-methylbenzylidene)-2-(((E)-4-methylbenzylidene)hydrazineylidene)-3-phenylthiazolidin-4-one)-PDB:5FGK was determined as -7.10 cal/mol and the shift score with PDB:5HBE was determined as -6.11 cal/mol. Here is the binding mechanism, Thiazolidin-4-one ARG-356 (4.47 Å), p-xylene pi-pi form HIS-106 (7.04 Å), benzene pi-alkyl LEU-158 (6.21 Å), VAL-35 (5.56 Å), ALA-50 (5.35 Å), benzene alkyl ALA-50 (5.02 Å), ILE-79 (4.34 Å), PHE-97 (3.80 Å), for van der Waals structures, other interactions with GLU-357, TYR- 99, ALA-155, ALA-172, ASP-173 are shown in Figure 6. Figure 6 shows a 3D view of the SAS surface on the receptor.
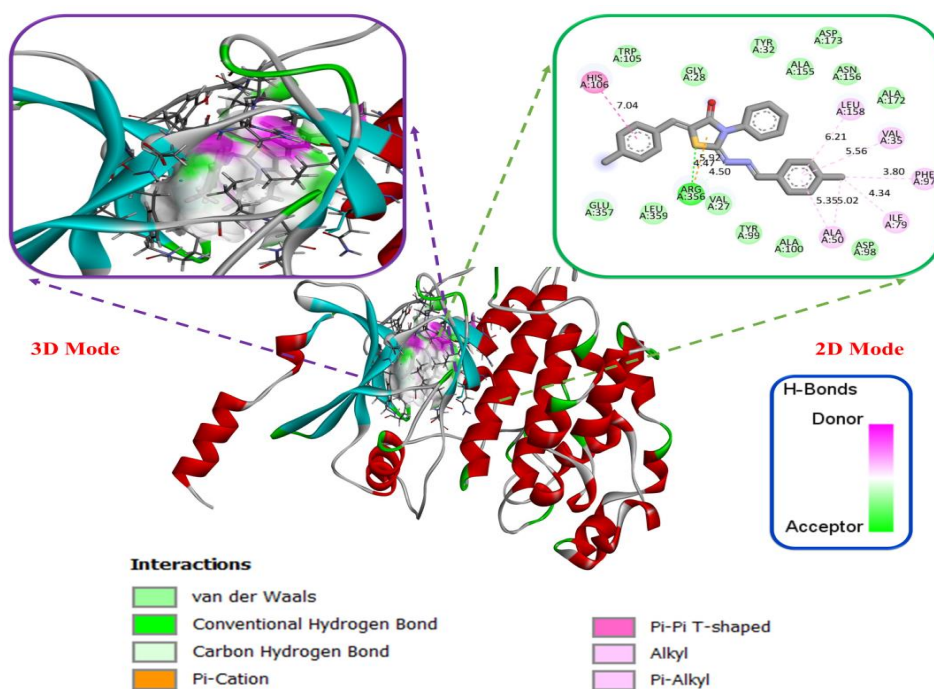
Figure 6. Ligand-5FGK mode of interaction with enzymes; 3D view of the donor/acceptor surface of hydrogen bonds on the receptor and 2D view of ligand enzyme interactions

As a result of the EMPT molecule 5HBE placement study, it is as shown in the 3D and 2D views in Figure 6. With PDB: 5HBE, the shift score was determined as -6.11 cal/mol. The binding mechanism is here, Thiazolidin-4-one TYR-32 (6.1 Å), benzene pi-alkyl LEU-158 (6.09 Å), VAL-35 (5.06 Å), ALA-100 (5.06 Å), benzene alkyl ALA-50 (4.59 Å), ILE-79 (4.61 Å), PHE-97 (5.48 Å), for van der Waals structures, TRP-105, TYR-32, ALA Other interactions with -155, ALA-172, ASP-173, ARG-356, VAL-27, HIS-106 are shown in Figure 7.
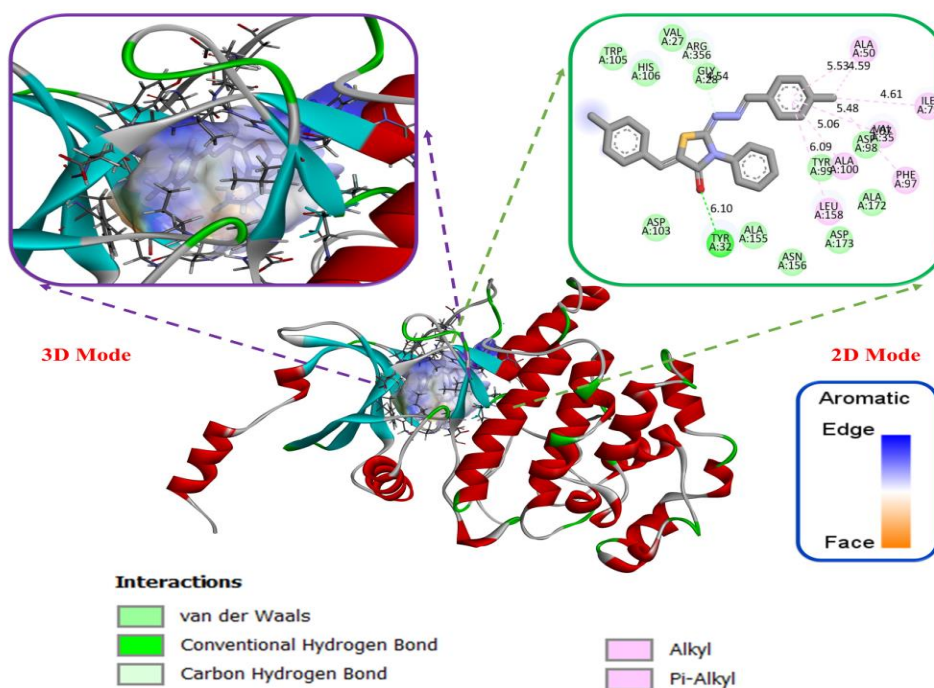
Figure 7. Molecule-5HBE mode of interaction with enzymes; a) 3D view of the donor/acceptor surface of aromatic bonds on the receptor b) 2D view of ligand enzyme interactions

Figure 8. Control Ligand-5FGK 2D Mode and control Ligand-5HBE 2D Mode view have been shown. When we look at the docking scores in Table 6, the binding scores for both proteins were found to be close to the binding scores of the natural ligand.

The compatibility difference was created during the optimization and creation of the logbox. However, binding in the pocket created here was achieved in sufficient amounts for enzyme inhibition.
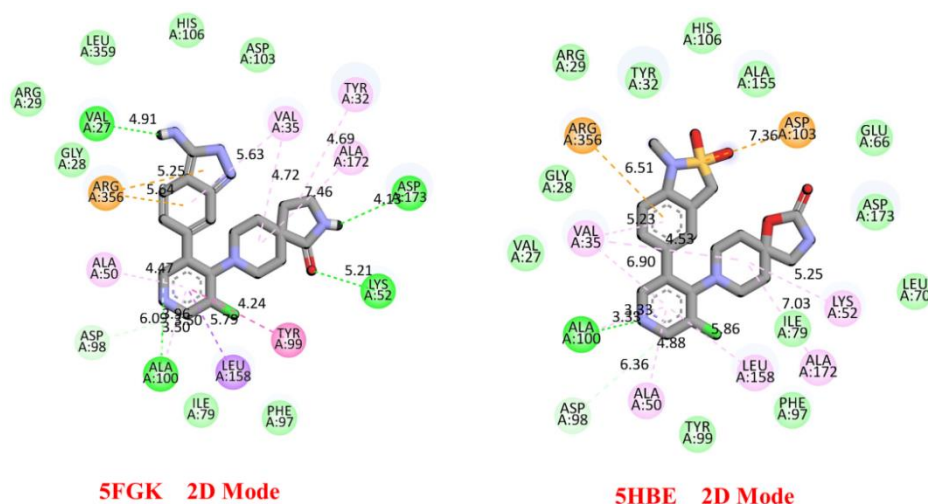
Figure 8. Control Ligand-5FGK 2D Mode and control Ligand-5HBE 2D Mode view

3.8. ADME analysis

Currently, the most promising compounds are selected through ADME studies in drug production in order to reduce the possibility of drug attrition in the final stage. These studies can be used as preliminary data to determine the balance between pharmacodynamic and pharmacokinetic properties [29]. Virtual screening methods have been applied to small molecules to investigate a variety of factors, like molecular quality, drug ability S, cell permeability, HIA, polar plane area PSA, and drug resemblance mark [30]. Bileşiklerin ilaca benzer bir yapıya sahip olup olmadığını ve canlı organizmalardaki aktivitesini tespit edebilmek için Lipinskinin beş kriteri, Veber ve Egan kriterleri gibi bazı kriterler vardır. Bu çalışmada başlıkta adı geçen bileşiğin ilaç benzerlik özellikleri Lipinski kriterleri kullanılarak araştırılmıştır. Lipinski's rule of five is a

method of analysis to calculate the drug similarity of the compound and also to determine whether a chemical compound with a certain pharmacological or biological activity can be used as an active and orally active drug in humans. According to the rule of five determined by Lipinski as a result of his studies, a molecule must meet these conditions (Molecular Weight (MW) ≤500 g/mol, lipophilicity coefficient LogP≤5, hydrogen bond donor ≤5, hydrogen bond acceptor ≤10, molar break values 4-130) in order to be a drug candidate [31]. A pharmaceutical product that is currently on the market that is chosen based on Lipinski's rule of five should have a molecular weight of no more than 500 and a logP of no more than 5, along with fewer than 10 hydrogen bond acceptors and fewer than 5 hydrogen bond donors [32]. Based on the data presented in Table 7, our compound complied with Lipinski's guidelines and produced satisfactory results for adme analysis.

Table 7. Physicochemical and lipophilicity of EMPT molecule

Code	Lipophilicity consensus log P	Physico-chemical properties								
EMPT Molecule		MW[a] g/mol	Heavy Atoms	Aromatic heavy atoms	Rot. bond	H-acceptor bond	H-donor bond	MR[b]	TPSA[c] (A^2)	% ABS[d]
	3.46	411.52	30	18	4	3	0	130.28	70.33	84.73

[a]**MW**, molecular weight; [c]**TPSA**, topological polar surface area; [b]**MR**, molar refractivity; [d]**ABS%:** absorption percent $ABS\% = 109 - [0.345 \times TPSA]$.

4. Conclusion

Important geometric data, including bond lengths and angles of the atoms in the structure, was obtained as a result of molecular optimization. Utilizing the B3LYP/6-31G and B3LYP//SDD techniques, the difference (E) between the HOMO and LUMO energy levels of the the EMPT compound was computed. Using the Mulliken charge distribution method, information was collected about the charge distribution of atoms and different properties of molecular structures. Additionally, DFT/B3LYP/6-31G and DFT/B3LYP//SDD basis of the compound were used to create the MEP map. The atoms surrounding the region were determined to be methyl and hydrogen atoms. These properties have given us information about the parts of the chemical where non-covalent interactions can occur. The grade and charge deploy of the optimized chemical construction were ascertained by means of NBO analysis. For the molecular compound (E), the highest stabilization energy value is 22, respectively 3-phenylthiazolidin, 5-((Z)-4-methylbenzylidene, 2-((E)-4-methylbenzylidene)hydrazineyilidene). The results were 22.96, and 22.40 Kcal/mol. The NLO study stated that the molecule had powerful optical characteristics in a range of orientations. By utilize the B3LYP/6 311G(d,p) method and the B3LYP/SDD method, the compound's isotropic polarizability was determined to be 3.54×10^{-30} esu and 3.47×10^{-30} esu, respectively. According to the molecular docking simulation of the molecule, it has a high capability to combine with PDB: 5FGK and PDB: 5HBE proteins. The study determined that the binding affinity shift scores for PDB: 5FGK and PDB: 5HBE were, respectively, -7.10 and -6.11 cal/mol. PDB: The 5FGK receptor binding score was found to be more effective. Furthermore, the phthalonitrile group's particular compounds and color regions were subjected to ADME analysis, which produced positive results for ADME analysis in accordance with Lipinski's guidelines.

Conflict of Interest Statement

There is no conflict of interest between the authors.

Statement of Research and Publication Ethics

The study is complied with research and publication ethics.

References

[1]   A.-R. L. H. Ismail, N. M. Ismael, and M. Abu-Dief, "Co (II) and Cd (II) complexes based on a tetradentate ONNO donor Schiff base ligand," *DFT calculations and biological studies of Mn (II), Fe (II)*, vol. 1134, pp. 851–862, 2017.

[2]   M. Salihović *et al.*, "Synthesis, characterization, antimicrobial activity and DFT study of some novel Schiff bases," *J. Mol. Struct.*, vol. 1241, no. 130670, p. 130670, 2021.

[3]   L. Touafri, A. Hellal, S. Chafaa, A. Khelifa, and A. Kadri, "Synthesis, characterisation and DFT studies of three Schiff bases derived from histamine," *J. Mol. Struct.*, vol. 1149, pp. 750–760, 2017.

[4]   E. Ermiş, "Synthesis, spectroscopic characterization and DFT calculations of novel Schiff base containing thiophene ring," *J. Mol. Struct.*, vol. 1156, pp. 91–104, 2018.

[5]   R. M. Issa, M. K. Awad, and F. M. Atlam, "DFT theoretical studies of antipyrine Schiff bases as corrosion inhibitors: Schiff bases as corrosion inhibitors," *Mater. Corros*, vol. 61, no. 8, pp. 709–714, 2010.

[6]   T. Bensafi, "Synthesis, characterization and DFT calculations of linear and NLO properties of novel (Z)-5-benzylidene-3-N (4-methylphenyl)-2-thioxothiazolidin-4-one," *Journal of Sulfur Chemistry*, vol. 42, no. 6, pp. 645–663, 2021.

[7]   M. Rashid, J. Yaqoob, N. Khalil, R. Jamil, M. U. Khan, and M. A. Gilani, "Nonlinear optical (NLO) response of boron phosphide nanosheet by alkali metals doping: A DFT study," *Mater. Sci. Semicond. Process.*, vol. 151, no. 107007, p. 107007, 2022.

[8]   M. Ishaq, R. A. Shehzad, M. Yaseen, S. Iqbal, K. Ayub, and J. Iqbal, "DFT study of superhalogen-doped borophene with enhanced nonlinear optical properties," *J. Mol. Model.*, vol. 27, no. 6, p. 188, 2021.

[9]   T. Michael, J. Frisch, G.W, Bernhard. Schlegel, Gustavo. Scuseria, 2016.

[10]   M. Bağlan, "Theoretical Investigation of 1H and 13C NMR Spectra of Diethanol Amine Dithiocarbamate RAFT Agent," *Journal of the Institute of Science and Technology*, vol. 12, no. 3, pp. 1677–1689, 2022.

[11]   A. Voityuk Institució Catalana de Recerca i Estudis Avançats (ICREA), Passeig de Lluís Companys, 23, 08010 Barcelona, Spain. alexander. voityuk@gmail. com, A. J. Stasyuk, and S. F. Vyboishchikov, "A simple model for calculating atomic charges in molecules," *Phys. Chem. Chem. Phys.*, vol. 20, no. 36, pp. 23328–23337, 2018.

[12]   P. Bultinck *et al.*, "The electronegativity equalization method II: Applicability of different atomic charge schemes," *J. Phys. Chem. A*, vol. 106, no. 34, pp. 7895–7901, 2002.

[13]   M. Bağlan, K. Gören, and Ü. Yildiko, "HOMO–LUMO, NBO, NLO, MEP analysis and molecular docking using DFT calculations in DFPA molecule," *Int. J. Chem. Technol.*, pp. 208–217, 2023.

[14]   V. Choudhary, A. Bhatt, D. Dash, and N. Sharma, "DFT calculations on molecular structures, HOMO-LUMO study, reactivity descriptors and spectral analyses of newly synthesized diorganotin (IV) 2-chloridophenylacetohydroxamate complexes," J. Comput. Chem., pp. 2354–2363, 2019.

[15]   F. Pereira, K. Xiao, D. A. R. S. Latino, C. Wu, Q. Zhang, and J. Aires-de-Sousa, "Machine learning methods to predict density functional theory B3LYP energies of HOMO and LUMO orbitals," *J. Chem. Inf. Model.*, vol. 57, no. 1, pp. 11–21, 2017.

[16]   E. S. Marinho and M. M. Marinho, "A DFT study of synthetic drug topiroxostat: MEP, HOMO, LUMO," *Int. J. Sci. Eng. Res*, vol. 7, no. 8, 2016.

[17]   S. Chandrasekar, V. Balachandran, and H.-S. Evans, "Synthesis, crystal structures HOMO-LUMO analysis and DFT calculation of new complexes of p-substituted dibenzyltin chlorides and 1, 10-phenanthroline," *Spectrochimica Acta Part A: Molecular and Biomolecular Spectroscopy*, vol. 143, pp. 136–146, 2015.

[18]   V. Balachandran, G. Mahalakshmi, A. Lakshmi, and A. Janaki, "DFT, FT-Raman, FT-IR, HOMO-LUMO and NBO studies of 4-Methylmorpholine," *Spectrochim. Acta A Mol. Biomol. Spectrosc.*, vol. 97, pp. 1101–1110, 2012.

[19]   Ü. Yildiko and G. K. Dft, "DFT Calculatıons and Molecular Dockıng Study ın 6-(2"-pyrrolıdınone-5"-Yl)-(," *Epıcatechın Molecule From Flavonoıds. Eskişehir Teknik Üniversitesi Bilim ve Teknoloji Dergisi B-Teorik Bilimler*, vol. 11, pp. 43–55, 2023.

[20]   S. Guidara and H. Feki, "Structural, vibrational, NLO, MEP, NBO analysis and DFT calculation of bis 2, 5-dimethylanilinium sulfate," *Journal of Molecular Structure*, vol. 1080, pp. 176–187, 2015.

[21]   B. K. Shukla, "DFT calculations on molecular structure, MEP and HOMO-LUMO study of 3-phenyl-1-(methyl-sulfonyl)-1H-pyrazolo pyrimidine-4-amine," *Materials Today: Proceedings*, vol. 49, pp. 3056–3060, 2022.

[22]   N. Uludağ, G. Serdaroğlu, Ir, and N. Uv-Vis, "An improved synthesis, spectroscopic (FT-IR, NMR) study and DFT computational analysis (IR, NMR, UV-Vis, MEP diagrams, NBO, NLO, FMO) of the 1, 5-methanoazocino indole core structure," *Journal of Molecular Structure*, vol. 1155, pp. 548–560, 2018.

[23]   S. Sevvanthi, "MEP) studies and molecular docking on benzodiazepine derivatives-heterocyclic organic arenes," *Chemical Data Collections*, vol. 30, 2020.

[24]   Ü. Yildiko, "Computational Investigation of 5.5'', 7''-trihydroxy-3, 7-dimethoxy-4'-4'''-O-biflavone from Flavonoids Using DFT Calculations and Molecular Docking," *Adıyaman University Journal of Science*, vol. 12, no. 2, pp. 283–298, 2022.

[25]   R. Saravanan, S. Seshadri, S. Gunasekaran, and R. Mendoza-Meroño, "Crystallographic, experimental (FT-IR and FT-RS) and theoretical (DFT) investigation, UV-Vis, MEP, HOMO-LUMO and NBO/NLMO of (E)-1-[1-(4-Chlorophenyl) ethylidene] thiosemicarbazide," *Spectrochimica Acta Part A: Molecular and Biomolecular Spectroscopy*, vol. 121, pp. 268–275, 2014.

[26]   K. Gören, "DFT Computations and Molecular Docking Studies of 3-(6-(3-aminophenyl) thiazolo [1, 2, 4] triazol-2-yl)-2H-chromen-2-one (ATTC) Molecule," *Hittite Journal of Science and Engineering*, vol. 10, no. 1, pp. 11–19, 2023.

[27]   S. Sundaram, V. N. Vijayakumar, and V. Balasubramanian, "Electronic and structure conformational analysis (HOMO-LUMO, MEP, NBO, ELF, LOL, AIM) of hydrogen bond binary liquid crystal mixture: DFT/TD-DFT approach," *Comput. Theor. Chem.*, vol. 1217, no. 113920, p. 113920, 2022.

[28]   M. Khattab and A. A. Al-Karmalawy, "Revisiting activity of some Nocodazole analogues as a potential anticancer drugs using molecular docking and DFT calculations," *Front. Chem.*, vol. 9, p. 628398, 2021.

[29]   N. A. Dlala, Y. Bouazizi, H. Ghalla, and N. Hamdi, "DFT calculations and molecular docking studies on a chromene derivative," *J. Chem.*, vol. 2021, pp. 1–17, 2021.

[30]   V. K. Singh *et al.*, "Docking, ADMET prediction, DFT analysis, synthesis, cytotoxicity, antibacterial screening and QSAR analysis of diarylpyrimidine derivatives," *J. Mol. Struct.*, vol. 1247, no. 131400, p. 131400, 2022.

[31]   C. A. Lipinski, "Lead-and drug-like compounds: the rule-of-five revolution," *Drug discovery today: Technologies*, vol. 1, no. 4, pp. 337–341, 2004.

[32]   A.-S. Badran and M. A. Ibrahim, "Synthesis, spectral characterization, DFT and in silico ADME studies of the novel pyrido[1,2-a]benzimidazoles and pyrazolo[3,4-b]pyridines," *J. Mol. Struct*., vol. 1274, no. 134454, p. 134454, 2023.

Combined Treatment with Tauroursodeoxycholic Acid and SCD Probiotics Reduces Oxidative Stress in Lung Tissue of Aged Rats

Burcu Baba[1*], Hüseyin Allahverdi [2]

[1]*Department of Medical Biochemistry, Faculty of Medicine, Yuksek Ihtisas University, Ankara, Turkey*
[2]*Department of Molecular Biology and Genetics, Muş Alpaslan University, Turkey*
(ORCID: 0000-0003-0994-3577) (ORCID: 0000-0001-9210-4787)

Abstract

Aging is associated with an increased level of oxidative stress, resulting from an elevated production of reactive oxygen species, which can lead to cellular and tissue damage, particularly in the lungs. In this study, it was aimed to evaluate the effects of tauroursodeoxycholic acid (TUDCA) and SCD Probiotics, both individually and in combination, on malondialdehyde (MDA), advanced oxidation protein products (AOPP), and myeloperoxidase (MPO) levels as oxidative stress markers in the lung tissue of aged Sprague-Dawley rats. The results showed that TUDCA significantly decreased MDA and AOPP levels, suggesting its antioxidant activity. SCD Probiotics also demonstrated a reduction in AOPP levels, highlighting their immunomodulatory and antioxidant effects. Furthermore, the combined treatment of TUDCA and SCD Probiotics resulted in a significant reduction in both MDA and AOPP levels, as well as a notable decrease in MPO activity. This suggests a synergistic interaction that enhances the antioxidative and anti-inflammatory properties of the individual treatments. These findings support the therapeutic potential of TUDCA and SCD Probiotics in mitigating oxidative damage in aging lung tissues, suggesting that their combined use may be a promising approach to combat age-related oxidative stress. Further research is needed to investigate these effects in various models and long-term applications.

1. Introduction

Aging is a biological process that involves a gradual decline in the functionality of cells and tissues, leading to an increased risk of age-related chronic diseases and mortality [1,2]. The aging process is influenced by numerous intricate and significant pathways associated with chronic oxidative stress resulting from excess levels of reactive oxygen species (ROS) [1]. ROS have been proposed as one of the contributing factors to aging due to their potential to induce oxidative damage to DNA, proteins, and lipids [3]. ROS are molecules derived from molecular oxygen that can have both beneficial and harmful effects. While ROS are byproducts of normal cellular metabolism and help maintain redox homeostasis, excessive ROS production leads to oxidative stress

[4]. ROS, previously believed to come only from mitochondrial metabolism, however, it is now known that ROS are also produced by other cellular sources such as NADPH oxidases, neutrophils, monocytes, xanthine oxidases, cytochrome P450 enzymes, lipoxygenases, nitric oxide synthases, and myeloperoxidase [5,6].

Myeloperoxidase (MPO) is a critical enzyme of neutrophils, responsible for producing potent oxidants, such as hypochlorous acid (HOCl), which act as a bactericidal system against invading organisms. However, the uncontrolled generation of oxidants leads to lipid peroxidation and protein oxidation, resulting in cellular and tissue damage [7]. Lipid peroxidation is a process that involves removing a hydrogen from a carbon and adding an oxygen molecule by attacking carbon-carbon double

bonds in lipids through reactive species. This process results in the generation of products such as malondialdehyde (MDA) and 4-hydroxynonenal [8]. Additionally, lipid peroxidation impacts proteins, causing structural changes that can impair their enzymatic functions [9]. Advanced oxidation protein products (AOPP), which are dityrosine-containing protein cross-linking products, serve as an indicator of oxidative stress and are correlated with the degree of monocyte activation, levels of dityrosine, advanced glycation end products, and inflammatory cytokines [10].

Age-related changes, such as telomere shortening, mitochondrial dysfunction, and increased oxidative stress, contributes to the inability of lung cells to maintain basic homeostasis [11]. Tauroursodeoxycholic acid (TUDCA) is a hydrophilic bile acid formed by the conjugation of the amino acid taurine with ursodeoxycholic acid [12]. It exhibits several properties, including antioxidation, anti-inflammation, anti-apoptosis, and neuroprotection [13]. The respiratory and gastrointestinal systems are closely interrelated with regard to their physiology and pathology [14]. In recent years, evidence has emerged on how probiotics and prebiotics, accepted as immunomodulators and gut health stimulators, could promote lung health [15]. The aim of the present study was to investigate the oxidative damage in aging lung by evaluating malondialdehyde, AOPP, and myeloperoxidase, and also the effect of probiotics and TUDCA on these oxidative damage markers.

2. Material and Method

2.1. Animals

Male Sprague-Dawley rats aged 24 months were enrolled in the study. The animals were divided into four groups. First group was the control group with no treatment, the second group received probiotics, the third group received TUDCA, and the fourth group received TUDCA in combination with SCD Probiotics supplementation (7 rats in each group). Each group received treatment for seven days. The rats were fed ad libitum with a standard rodent diet. TUDCA was administered intravenously at a dose of 300 mg/kg via the tail, while the probiotic supplement was given orally by gavage at a dose of 3 mL (1 x 108 CFU) per day [16]. The probiotic product used in the study, which contained 11 different strains including *Bacillus subtilis, Bifidobacterium bifidum, Bifidobacterium longum, Lactobacillus acidophilus, Lactobacillus bulgaricus, Lactobacillus casei,*

Lactobacillus fermentum, Lactobacillus plantarum, Lactococcus lactis, Saccharomyces cerevisiae, and Streptococcus thermophilus species, was marketed by SCD Probiotics company (Essential Probiotics XI - 500 ml H.S. Code: 2206.00.7000). After the treatment, the animals were euthanized one day later by ether treatment, and the lung tissues were extracted, immediately frozen on dry ice, and stored at 80°C until analysis. The animals were housed according to standard animal care protocols, and the study was approved by the Ethics Committee (approval number: 2022/03) of the Saki Yenilli Experimental Animal Production and Practice Laboratory.

2.2. Tissue Preparation

Lungs were taken out and rinsed with cold phosphate buffered saline (PBS). They were then homogenized in five volumes of cold 10 mM phosphate buffered saline (PBS, pH 7.4) containing protease inhibitor (PIC002, BioShop, Canada) and 0.5% Triton X-100 using a tissue homogenizer in an ice bath. Afterwards, the homogenates from the lung tissues were spun at 5,000xg for 10 minutes at 4°C. The supernatant was then collected and stored in aliquots at -80°C until analysis.

2.3. Protein Determination

The protein content in the supernatants was measured by the Bradford method using bovine serum albumin as standard [17].

2.4. Determination of Myeloperoxidase Activity

Measurement of myeloperoxidase (MPO) activity was carried out using a spectrophotometer. This was done by mixing the samples with 50 mM PBS, adjusted to pH 6.0, and containing o-dianisidine (0.167 mg/ml) and hydrogen peroxide (0.0005%). The absorbance was then measured at 460 nm for 5 minutes. The MPO activity was expressed in units per milligram of protein, as described by Bradley et al. (1982) [18].

2.5. Measurement of Malondialdehyde

Malondialdehyde, an indicator of lipid peroxidation was determined by monitoring thiobarbituric reactive substances (TBARS) formation. In brief, the samples were reacted with 20% trichloroacetic acid and 0.67% thiobarbituric acid, and then heated in a boiling water bath at 100°C. After cooling, the absorbance was

measured at 532 nm. The results were expressed as nmol/mg protein [19].

2.6. Measurement of Advanced Oxidation Protein Products

Advanced oxidation protein products, an indicator of oxidative damage to proteins, were assessed by measuring dityrosine-containing and cross-linking protein products. The AOPP levels were determined using the method developed by Witko-Sarsat and colleagues [20]. Specifically, the samples were diluted to a concentration of 20 mM with PBS (pH 7.4), followed by the addition of potassium iodide and acetic acid. The absorbance was then measured at 340 nm, and the values were expressed as nmol/mg protein.

2.7. Statistics

Statistical analyses and graph plotting of the results were performed using GraphPad Prism 9 (GraphPad, USA) to evaluate the experimental data. The data were analyzed using One-way ANOVA. Tukey's multiple comparisons test was performed for the difference between each pair of means. The statistical analyses were presented as mean ± standard error of the mean (SEM). The level of significance was indicated as $* p < 0.05$, $** p < 0.01$, $*** p < 0.001$, and $**** p < 0.0001$.

3. Results and Discussion

The current study focuses on investigating the dynamics of oxidative stress in aging lung tissue, and evaluating the potential of interventions such as TUDCA and SCD Probiotics to mitigate the detrimental effects of oxidative damage. With advancing age, there is a marked increase in the production of ROS, which significantly contribute to cellular and tissue dysfunction through complex pathways of oxidative damage [1,2]. This accumulation of ROS is closely linked to lipid peroxidation and protein oxidation, both of which are identified as pivotal factors in the aging process of cellular systems [3]. Recent studies have further validated these observations, demonstrating that enhanced oxidative stress is associated with a decline in mitochondrial function and an increase in cellular senescence, thereby exacerbating age-related pathologies [21,22]. Moreover, researchers elucidate how oxidative modifications to cellular proteins not only reduce their functional capacity but also trigger inflammatory responses that further deteriorate tissue

integrity [9,23,24,25]. The strategic use of TUDCA with antioxidant properties and the SCD Probiotics which balance gut microbiota, could play a crucial role in countering these oxidative processes and ameliorating the impacts of aging on lung tissues [16,26,27]. Since aging is a multifactorial and complex process, this combined treatment may offer a therapeutic approach to improve cellular resilience and overall lung health.

3.1. Effects of TUDCA, SCD Probiotics and Their Combined Treatment on Lung MDA Levels

The increase in lipid content with age may lead to higher lipid peroxidation. Additionally, increased ROS production has been reported with aging. Therefore, lipid peroxidation can be used as a marker for early and reversible tissue damage, as well as a reduction in antioxidant defenses. With aging, lipid peroxidation damage increased, and a notable decline in antioxidant defenses was reported in the previous studies [9,28,29]. Elevated MDA levels cause damage to macromolecules, leading to alterations in cellular structure and function. This damage worsens oxidative stress and inflammation, which further increases MDA generation. This process contributes to the progressive decline in physiological functions and the development of diseases. High plasma MDA levels increase the burden on the kidneys and promote a cyclical process of oxidative stress, which contributes to the decline in kidney function with age [30].

The findings of this study reveal a significant reduction in the MDA levels within lung tissue following treatments with TUDCA, SCD Probiotics, and their combined use, compared to the controls (p=0.03, p=0.012, p=0.007, respectively). This notable decrease in MDA levels underscores the potential of these agents in mitigating oxidative stress and protecting pulmonary tissue. In particular, the combined treatment group demonstrated a more pronounced reduction in MDA levels compared to treatments with either combined TUDCA or SCD Probiotics alone, potentially indicating a synergistic effect (Figure 1). Previous studies reported TUDCA treatment supports functional recovery by alleviating oxidative stress, inflammatory response and apoptosis in different experimental models [12,31,32]. In addition, growing evidence shows that probiotics provide beneficial antioxidative effects by scavenging ROS and activating specific enzyme activities [33,34,35]. Consistent with previous findings, our results suggest that the administration of TUDCA and

probiotics may help to reduce lipid peroxidation, thereby slowing cellular aging in the lungs.
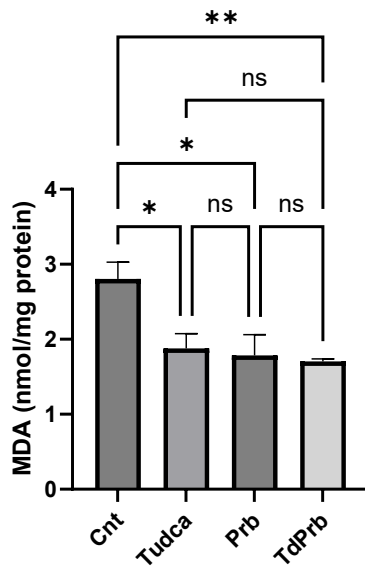
Figure 1. Effects of tauroursodeoxycholic acid, SCD Probiotics and combined treatment on lung malondialdehyde (MDA) levels. All data are shown as Mean ± SEM and the one-way ANOVA was used to compare the means of groups. Statistically significant differences are indicated in the following way: ns p > 0.05; * p < 0.05; ** p < 0.01. Cnt (control), Tauroursodeoxycholic acid (TUDCA), Prb (SCD Probiotics) and TdPrb (combined treatment)

3.2. Effects of TUDCA, SCD Probiotics and Their Combined Treatment on Lung AOPP Levels

In the study, it was found that TUDCA lowered the levels of AOPP in lung tissue due to its antioxidant properties (p=0.04) (Figure 2). TUDCA has been extensively documented for its potent antioxidative properties, particularly in stabilizing mitochondrial functions and inhibiting apoptotic pathways, which are essential for maintaining cellular integrity in aging tissues. It enhances mitochondrial biogenesis and reduces the release of cytochrome c, which is crucial in preventing cell death. TUDCA promotes tissue regeneration and enhanced functional recovery by decreasing oxidative stress, apoptosis, and inflammation in previous studies [12,13,36].

SCD Probiotics treatment resulted in lower AOPP levels, however, no statistically significant difference was found (Figure 2). Treatment with specific probiotics has been also associated with a decrease in AOPP levels, highlighting the crucial role of gut microbiota in modulating systemic oxidative stress and inflammation. This effect is thought to be mediated by the enhancement of gut barrier function and modulation of the gut-immune system interaction, leading to reduced systemic inflammatory markers and oxidative stress [37,38]. Lactic acid bacteria have been suggested as a promising source of antioxidants, offering potential benefits in alleviating the harmful effects of oxidative stress, a major contributor to the aging process [39]. Studies have demonstrated that lactic acid bacteria produce a range of antioxidants that help neutralize free radicals and diminish oxidative stress, which may enhance cellular health and support healthy aging [40,41]. In a randomized double-blind study, receiving of *Lactobacillus helveticus* resulted in a significant decrease in MDA and AOPP levels [42]. Furthermore, emerging studies emphasize the significance of gut microbial composition in influencing the host's antioxidant capacity, thereby providing a protective mechanism against oxidative damage [43]. In the combined treatment group, a reduction in AOPP levels was observed, emphasizing the synergistic interaction between TUDCA and SCD Probiotics (p=0.02) (Figure 2). It was concluded that the combined treatment is more effective than the application of either agent alone, suggesting that the concurrent use of these agents provides stronger protection against oxidative damage. In addition, these findings suggest that both TUDCA and probiotic treatments may be strategically used to mitigate the impacts of aging by enhancing antioxidative defenses and maintaining cellular and systemic homeostasis.

Figure 2. Effects of tauroursodeoxycholic acid, SCD Probiotics and combined treatment on lung advanced oxidation protein products (AOPP) levels. All

data are shown as Mean ± SEM and the one-way ANOVA was used to compare the means of groups. Statistically significant differences are indicated in the following way: ns p > 0.05; * p < 0.05. Cnt (control), Tauroursodeoxycholic acid (TUDCA), Prb (SCD Probiotics) and TdPrb (combined treatment)

3.3. Effects of TUDCA, SCD Probiotics and Their Combined Treatment on Lung Myeloperoxidase Activity

MPO plays a significant but complex role in the production of reactive oxygen species, specifically hypochlorous acid, which possesses strong bactericidal properties but can also contribute to cellular and tissue damage if not adequately controlled [7]. This dual nature of MPO underscores its importance in inflammatory and oxidative processes. Our study provides evidence that both TUDCA and SCD Probiotics effectively reduce MPO activity, which may act as a crucial protective mechanism against excessive oxidative stress within lung tissues (p=0.0002, p=0.0006, respectively) (Figure 3). This observation is consistent with recent findings that emphasize the anti-inflammatory and antioxidative properties of TUDCA, which has been shown to modulate inflammatory pathways and reduce oxidative stress in several models of disease [12,13,44]. The benefits of probiotics on systemic and localized inflammation are well documented [45,46,47,48]. Therefore, their potential may decrease MPO levels by modulating the gut-lung axis and thereby reducing pulmonary oxidative stress. These findings suggest that the targeted use of TUDCA and SCD Probiotics may offer therapeutic benefits in managing conditions characterized by elevated oxidative stress and inflammation. Further studies are needed to investigate these complex interactions between MPO activity, oxidative stress, and potential interventions.

One of the most significant findings of our research is the revelation of a synergistic effect when TUDCA and SCD Probiotics are administered together. This synergistic effect not only enhances the reduction of MDA and AOPP levels but also significantly decreases MPO activity (p<0.0001), suggesting that the combination of these treatments amplifies their individual antioxidative and anti-inflammatory effects. This finding is essential for developing therapeutic approaches that aim to minimize oxidative damage and promote cellular longevity in aging populations. Previous studies have reported the potential of probiotics in modulating systemic inflammation, which could contribute to

lower MPO levels through the modulation of the gut-lung axis, thus reducing pulmonary oxidative stress [26,27]. Moreover, the application of synbiotics has been demonstrated to effectively decrease inflammation in both healthy and diseased states, suggesting a broad therapeutic potential [49]. These observations support the idea that the systemic modulation of inflammation by gut microbiota interactions is a promising approach for decreasing inflammatory markers and oxidative stress across various conditions [50].
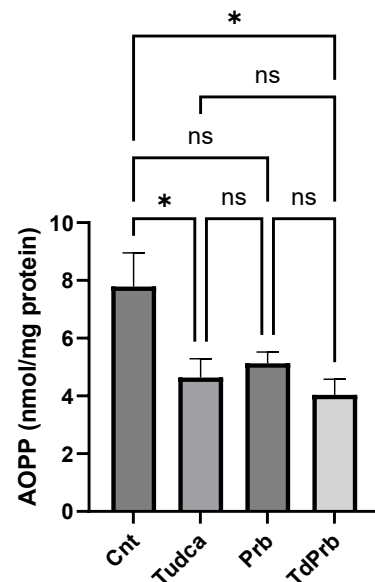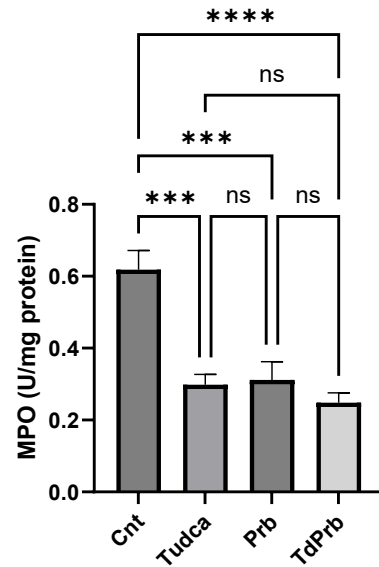

Figure 3. Effects of tauroursodeoxycholic acid, SCD Probiotics and combined treatment on lung myeloperoxidase (MPO). All data are shown as Mean ± SEM and the one-way ANOVA was used to compare the means of groups Statistically significant differences are indicated in the following way: ns p > 0.05; *** p < 0.001, **** p < 0.0001. Cnt (control), Tauroursodeoxycholic acid (TUDCA), Prb (SCD Probiotics) and TdPrb (combined treatment)

The study's outcomes reveal promising therapeutic pathways that warrant further exploration and optimization for the treatment or prevention of age-related degenerative diseases in lung tissue. Considering the complex nature of aging and the multifaceted roles of oxidative stress and inflammation, it is essential to conduct longitudinal studies to comprehensively understand the long-term consequences and potential side effects of these treatments. Furthermore, expanding the research to comprise various age groups and additional oxidative stress markers may provide deeper insights into the broader applicability of TUDCA and probiotics as preventive or therapeutic agents.

4. Conclusion and Suggestions

This study emphasizes the considerable potential of TUDCA and SCD Probiotics, both individually and collaboratively, to alleviate oxidative stress indicators in aging lung tissues. By reducing levels of malondialdehyde, advanced oxidation protein products, and myeloperoxidase activity, these treatments are effective in supporting cellular health and counteracting the detrimental effects of oxidative damage associated with aging. The synergistic effects observed with combined treatments particularly suggested that consolidated therapeutic approaches may offer improved protection against the progression of age-related pulmonary diseases. In the future, elucidating the mechanisms behind the effects of TUDCA and probiotics on the respiratory tract in diseased states will be crucial. Furthermore, this area of research is likely to become a key focus in pharmacology and clinical practice.

Contributions of the authors

All authors contributed to the design and implementation of the research, to the analysis of the results and to the writing of the manuscript.

Conflict of Interest Statement

There is no conflict of interest between the authors.

Statement of Research and Publication Ethics

The study is complied with research and publication ethics

References

[1]   J. Guo, X. Huang, L. Dou, et al., "Aging and aging-related diseases: from molecular mechanisms to interventions and treatments," *Signal Transduct. Target. Ther.*, vol. 7, p. 391, 2022.

[2]   J. L. Schneider, J. H. Rowe, C. Garcia-de-Alba, et al., "The aging lung: Physiology, disease, and immunity," *Cell*, vol. 184, pp. 1990–2019, 2021.

[3]   H. Cui, Y. Kong, H. Zhang, "Oxidative stress, mitochondrial dysfunction, and aging," *J. Signal Transduct.*, vol. 2012, p. 646354, 2012.

[4]   D. P. Rosanna, C. Salvatore. "Reactive oxygen species, inflammation, and lung diseases," *Curr Pharm Des.*, vol. 18, no. 26, pp. 3889-900, 2012.

[5]   S. K. Bardaweel, M. Gul, M. Alzweiri, A. Ishaqat, H. A. ALSalamat, R. M. Bashatwah. "Reactive oxygen species: the dual role in physiological and pathological conditions of the human body," *Eurasian J Med.*, vol. 50, no. 3, pp. 193-201, 2018.

[6]   I. Liguori, G. Russo, F. Curcio, G. Bulli, L. Aran, D. Della-Morte, G. Gargiulo, G. Testa, F. Cacciatore, D. Bonaduce, P. Abete. "Oxidative stress, aging, and diseases," *Clin Interv Aging.*, vol. 13, pp. 757-772, 2018.

[7]   T. G. Son, Y. Zou, B. P. Yu, et al., "Aging effect on myeloperoxidase in rat kidney and its modulation by calorie restriction," *Free Radic. Res.*, vol. 39, pp. 283–289, 2005.

[8]   J. Aguilar Diaz De Leon and C. R. Borges, "Evaluation of Oxidative Stress in Biological Samples Using the Thiobarbituric Acid Reactive Substances Assay," *J. Vis. Exp.*, vol. 12, no. 159, 2020.

[9]   Y. A. Hajam, R. Rani, S. Y. Ganie, T. A. Sheikh, D. Javaid, S. S. Qadri, S. Pramodh, A. Alsulimani, M. F. Alkhanani, S. Harakeh, A. Hussain, S. Haque, M. S. Reshi. "Oxidative stress in human pathology and aging: molecular mechanisms and perspectives," *Cells.*, vol. 11, no. 3, p. 552, 2022.

[10] G. Martínez-Sánchez, A. Giuliani, G. Pérez-Davison, et al., "Oxidized proteins and their contribution to redox homeostasis," *Redox Rep.*, vol. 10, pp. 175–185, 2005.

[11] S. J. Cho and H. W. Stout-Delgado, "Aging and Lung Disease," *Annu. Rev. Physiol.*, vol. 82, pp. 433–459, 2020.

[12] Y. Hou, J. Luan, T. Huang, et al., "Tauroursodeoxycholic acid alleviates secondary injury in spinal cord injury mice by reducing oxidative stress, apoptosis, and inflammatory response," *J. Neuroinflammation*, vol. 18, p. 216, 2021.

[13] J. Weng, L. Wang, K. Wang, et al., "Tauroursodeoxycholic Acid Inhibited Apoptosis and Oxidative Stress in H(2)O(2)-Induced BMSC Death via Modulating the Nrf-2 Signaling Pathway: the Therapeutic Implications in a Rat Model of Spinal Cord Injury," *Mol. Neurobiol.*, 2023, DOI: 10.1007/s12035-023-03754-5.

[14] E. Mortaz, I. M. Adcock, G. Folkerts, et al., "Probiotics in the management of lung diseases*," Mediators Inflamm.*, 2013, p. 751068.

[15] L. Keulers, A. Dehghani, L. Knippels, et al., "Probiotics, prebiotics, and synbiotics to prevent or combat air pollution consequences: The gut-lung axis," *Environ. Pollut.*, vol. 302, p. 119066, 2022.

[16] T. Ceylani, "Effect of SCD Probiotics supplemented with tauroursodeoksikolik asit (TUDCA) application on the aged rat gut microbiota composition," *J. Appl. Microbiol.*, 2023, DOI: 10.1093/jambio/lxad092.

[17] M. M. Bradford, "A rapid and sensitive method for the quantitation of microgram quantities of protein utilizing the principle of protein-dye binding," *Anal. Biochem.*, vol. 72, pp. 248–254, 1976.

[18] P. P. Bradley, D. A. Priebat, R. D. Christensen, et al., "Measurement of cutaneous inflammation: estimation of neutrophil content with an enzyme marker," *J. Invest. Dermatol.*, vol. 78, pp. 206–209, 1982.

[19] T. F. Slater and B. C. Sawyer, "The stimulatory effects of carbon tetrachloride and other halogenoalkanes on peroxidative reactions in rat liver fractions in vitro. General features of the systems used," *Biochem. J.*, vol. 123, pp. 805–814, 1971.

[20] V. Witko-Sarsat, M. Friedlander, C. Capeillère-Blandin, et al., "Advanced oxidation protein products as a novel marker of oxidative stress in uremia," *Kidney Int.*, vol. 49, pp. 1304–1313, 1996.

[21] J. A. Amorim, G. Coppotelli, A. P. Rolo, C. M. Palmeira, J. M. Ross, D. A. Sinclair. "Mitochondrial and metabolic dysfunction in ageing and age-related diseases," *Nat Rev Endocrinol.*, vol. 18, no. 4, pp. 243-258, 2022.

[22] Y. H. Lee, M. U. Kuk, M. K. So, E. S. Song, H. Lee, S. K. Ahn, H. W. Kwon, J. T. Park, S. C. Park. "Targeting mitochondrial oxidative stress as a strategy to treat aging and age-related diseases," *Antioxidants (Basel).*, vol. 12, no. 4, p. 934, 2023.

[23] M. Tosato, V. Zamboni, A. Ferrini, M. Cesari. "The aging process and potential interventions to extend life expectancy," *Clin Interv Aging.*, vol. 2, no. 3, pp. 401-12, 2007.

[24] Zgutka K, Tkacz M, Tomasiak P, Tarnowski M. "A role for advanced glycation end products in molecular ageing," *Int J Mol Sci.*, vol. 24, no. 12, p. 9881, 2023.

[25] J. Neves, P. Sousa-Victor. "Regulation of inflammation as an anti-aging intervention," *FEBS J.*, vol. 287, no. 1, pp. 43-52, 2020.

[26] H. T. Teker, T. Ceylani, S. Keskin, et al., "Supplementing probiotics during intermittent fasting proves more effective in restoring ileum and colon tissues in aged rats," *J. Cell. Mol. Med.*, vol. 28, pp. 1–13, 2024.

[27] H. T. Teker, T. Ceylani, S. Keskin, et al., "Reduced liver damage and fibrosis with combined SCD Probiotics and intermittent fasting in aged rat," *J. Cell. Mol. Med.*, pp. 1–11, 2023.

[28] R. S. Sohal, H. H. Ku, S. Agarwal, M. J. Forster, H. Lal. "Oxidative damage, mitochondrial oxidant generation and antioxidant defenses during aging and in response to food restriction in the mouse," *Mech Ageing Dev.*, vol. 74, no. 1-2, pp. 121-33, 1994.

[29] P. Arivazhagan, T. Thilakavathy, C. Panneerselvam. "Antioxidant lipoate and tissue antioxidants in aged rats," *J Nutr Biochem.*, vol. 11, no. 3, pp. 122-7, 2000.

[30] G. Li, Y. Chen, H. Hu, L. Liu, X. Hu, J. Wang, W. Shi, D. Yin. "Association between age-related decline of kidney function and plasma malondialdehyde," *Rejuvenation Res.*, vol. 15, no. 3, pp. 257-64, 2012.

[31] A. I. Rosa, I. Fonseca, M. J. Nunes, S. Moreira, E. Rodrigues, A. N. Carvalho, C. M. P. Rodrigues, M. J. Gama, M. Castro-Caldas. "Novel insights into the antioxidant role of tauroursodeoxycholic acid in experimental models of Parkinson's disease," *Biochim Biophys Acta Mol Basis Dis.*, vol. 1863, no. 9, pp. 2171-2181, 2017.

[32] R. H. Alhasani, M. Almarhoun, X. Zhou, J. Reilly, S. Patterson, Z. Zeng, X. Shu. "Tauroursodeoxycholic acid protects retinal pigment epithelial cells from oxidative injury and endoplasmic reticulum stress in vitro," *Biomedicines.*, vol. 8, no. 9, p. 367, 2020.

[33] V. Mishra, C. Shah, N. Mokashe, R. Chavan, H. Yadav, J. Prajapati. "Probiotics as potential antioxidants: a systematic review." *J Agric Food Chem.*, vol. 63, no. 14, pp. 3615–3626, 2015.

[34] Y. Wang, Y. Wu, Y. Wang, H. Xu, X. Mei, D. Yu, Y. Wang, W. Li. "Antioxidant properties of probiotic bacteria," *Nutrients*., vol. 9, no. 5, p. 521, 2017.

[35] J. Zhao, F. Tian, S. Yan, Q. Zhai, H. Zhang, W. Chen. "Lactobacillus plantarum CCFM10 alleviating oxidative stress and restoring the gut microbiota in D-galactose-induced oxidative stress model," *Food Funct*., vol. 9, no. 2, pp. 917-924, 2018.

[36] R. Soares, F. F. Ribeiro, S. Xapelli, T. Genebra, M. F. Ribeiro, A. M. Sebastião, C. M. P. Rodrigues, S. Solá. "Tauroursodeoxycholic acid enhances mitochondrial biogenesis, neural stem cell pool, and early neurogenesis in adult rats," *Mol Neurobiol*., vol. 55, no. 5, pp. 3725-3738, 2018.

[37] M. Lamprecht, S. Bogner, G. Schippinger, et al., "Probiotic supplementation affects markers of intestinal barrier, oxidation, and inflammation in trained men; a randomized, double-blinded, placebo-controlled trial," *J. Int. Soc. Sports Nutr*., vol. 9, p. 45, 2012.

[38] Y. Wu, R. Jha, A. Li, et al., "Probiotics (Lactobacillus plantarum HNU082) Supplementation Relieves Ulcerative Colitis by Affecting Intestinal Barrier Functions, Immunity-Related Gene Expression, Gut Microbiota, and Metabolic Pathways in Mice," *Microbiol. Spectr*., vol. 10, p. e0165122, 2022.

[39] R. Liu, B. Sun. "Lactic acid bacteria and aging: unraveling the interplay for healthy longevity," A*ging Dis*., vol. 15, no. 4, pp. 1487–98, 2023.

[40] W. Li, W. Huang, Y. Ma, I. Muhammad, A. Hanif, Z. Ding, et al. "Antioxidant properties of lactic acid bacteria isolated from traditional fermented yak milk and their probiotic effects on the oxidative senescence of Caenorhabditis elegans," *Food Funct*., vol. 13, pp. 3690–3703, 2022.

[41] H. Nakagawa, T. Miyazaki. "Beneficial effects of antioxidative lactic acid bacteria," *AIMS Microbiol*, vol. 3, p. 1, 2017.

[42] D. Michalickova, J. Kotur-Stevuljevic, M. Miljkovic, N. Dikic, M. Kostic-Vucicevic, M. Andjelkovic, V. Koricanac, B. Djordjevic. "Effects of probiotic supplementation on selected parameters of blood prooxidant-antioxidant balance in elite athletes: a double-blind randomized placebo-controlled study," *J Hum Kinet*., vol. 64, pp. 111-122, 2018.

[43] N. Aba, E. F. Koçpınar, T. Ceylani, "The Hepatic Antioxidant System Damage Induced with the Cafeteria (CAF) Diet Is Largely Counteracted Using SCD Probiotics during Development of Male Wistar Rats," *Nutrients*, vol. 15, 2023.

[44] M. O. Mendes, A. I. Rosa, A. N. Carvalho, et al. "Neurotoxic effects of MPTP on mouse cerebral cortex: Modulation of neuroinflammation as a neuroprotective strategy," *Mol Cell Neurosci*., vol. 96, pp. 1-9, 2019.

[45] R. P. Dickson and G. B. Huffnagle, "The Lung Microbiome: New Principles for Respiratory Bacteriology in Health and Disease," *PloS Pathog*., vol. 11, p. e1004923, 2015.

[46] M. A. K. Azad, M. Sarker, T. Li, J. Yin. "Probiotic Species in the Modulation of Gut Microbiota: An Overview", *Biomed Res Int*., 2018, 9478630, 2018.

[47] L. A. T. Cannarella, N. L. Mari, C. C. Alcântara, et al., "Mixture of probiotics reduces inflammatory biomarkers and improves the oxidative/nitrosative profile in people with rheumatoid arthritis," *Nutrition*, vol. 89, 2021.

[48] B. Weiss, Y. Bujanover, Y. Yahav, et al., "Probiotic supplementation affects pulmonary exacerbations in patients with cystic fibrosis: a pilot study," *Pediatr. Pulmonol*., vol. 45, pp. 536–540, 2010.

[49] A. Kazemi, S. Soltani, S. Ghorabi, A. Keshtkar, E. Daneshzad, F. Nasri, and S. M. Mazloomi, "Effect of probiotic and synbiotic supplementation on inflammatory markers in health and disease status: A systematic review and meta-analysis of clinical trials," *Clinical Nutrition (Edinburgh, Scotland)*, vol. 39, no. 3, pp. 789–819, 2020.

[50] T. P. Ivanovska, K. Mladenovska, Z. Zhivikj, M. J. Pavlova, I. Gjurovski, T. Ristoski, and L. Petrushevska-Tozi, "Synbiotic loaded chitosan-Ca-alginate microparticles reduces inflammation in the TNBS model of rat colitis," *International Journal of Pharmaceutics*, vol. 527, no. 1-2, pp. 126–134, 2017.

Bitlis Eren Üniversitesi Fen Bilimleri Dergisi

Evaluating the Effectiveness of Panoptic Segmentation Through Comparative Analysis

Cahide SARA[1*], İlhan DAŞDEMİR[2] , Sara ALTUN GÜVEN[1]

[1]Tarsus University, Faculty of Engineering, Department of Computer Engineering, Tarsus/TURKEY

[2] Tarsus University, Faculty of Engineering, Department of Electrical Electronics Engineering, Tarsus/TURKEY

(ORCID: 0009-0003-5432-3913) (ORCID: 0009-0004-4035-4425) (ORCID: 0000-0003-2877-7105)

Abstract

Image segmentation method is extensively used in the fields of computer vision, machine learning, and artificial intelligence. The task of segmentation is to distinguish objects in images either by their boundaries or as entire objects from the entire image. Image segmentation methods are implemented as instance, semantic, and panoptic segmentation. In this article, the panoptic segmentation method, seen as an advanced stage of instance and semantic segmentation, has been applied to three datasets and compared with the instance segmentation method. Experimental results are presented visually. Numerical results have been analyzed with the Panoptic Quality (PQ) and Semantic Quality (SQ) metrics. It has been observed that the segmentation outcome was best for the CityScapes dataset for panoptic segmentation.

1. Introduction

Computer Vision [1] is a subfield of computer science that enables computers to see and recognize objects or entities similarly to humans. In other words, it possesses the ability to perceive and interpret objects. Image segmentation techniques are frequently utilized in image and video analysis. These segmentation techniques are applied in various fields such as earth sciences [2],[3], smart cities [4]-[6], and healthcare services [7]-[9], and their applications are becoming increasingly widespread. There are three main approaches commonly used in image segmentation: semantic segmentation, instance segmentation, and panoptic segmentation.

Semantic segmentation is a computer vision task that divides an image into multiple segments corresponding to objects or areas of interest and assigns a class label to each pixel [10]. It is used in various fields, from self-driving cars to analyzing medical imagery, this capability enables the comprehension of image contents down to each individual pixel [11]. It is typically implemented with deep learning models, such as Convolutional Neural Networks (CNN) [12], and requires a large labeled dataset for training. Popular architectures include Fully Convolutional Networks [13], U-Net [14], and DeepLab [15], [16].

Instance Segmentation is a complex image segmentation task aimed at accurately identifying and delineating different objects within an image, making a distinction between multiple instances of the same object class. Unlike semantic segmentation, which groups pixels into categories, it enables the detailed pixel-level understanding of each distinct object instance. This means that each object instance is not only classified but also precisely outlined. Due to the necessity of distinguishing between overlapping or closely located objects of the same class, instance segmentation is often considered a more challenging

---

task than semantic segmentation. It finds applications in various fields such as autonomous driving, robotics, medical imaging, and object detection in complex scenes. Notable instance segmentation models include Mask R-CNN, Panoptic FPN, and YOLACT [17]-[19].

Panoptic Segmentation is an image segmentation task aimed at comprehensively understanding the image by assigning a category label to each pixel and facilitating the distinction between individual instances of objects. This task merges the benefits of semantic and instance segmentation, identifying the semantic category of every pixel in the image while also distinguishing between different instances of objects [20]. In panoptic segmentation, it is determined to which semantic category each pixel belongs. Objects belonging to the "object" category, such as people or cars, are identified individually, while areas belonging to non-object categories, such as the sky or road, are semantically labeled without specifying individual instances [20]. The goal of this task is to understand the entire scene and provide information at both the object and category levels. Panoptic segmentation is utilized in various fields including autonomous driving, robotics, scene understanding, and image editing [21].

Panoptic Segmentation models typically utilize a combination of CNNs [22] and specialized architectures that concurrently perform both Semantic Segmentation and Instance Segmentation tasks [23]. Leading Panoptic Segmentation frameworks include Panoptic FPN, UPSNet, and SOLO [24].

Many of the suggested panoptic segmentation techniques are applied to RGB images. For instance, in the study [25], A panoptic segmentation model called Panoptic-Fusion is introduced, serving as an online volumetric semantic mapping system designed to identify the class labels of background areas (items) and the individual segments of desired objects (things). For incoming RGB frames, it first predicts pixel-wise panoptic labels by combining traditional semantic and instance segmentation outputs. Similarly, in the study [26], Faraz et al. aimed to enhance the ability of networks to determine depth on a pixel-by-pixel basis from single RGB input images.. Various additional panoptic techniques have also been developed for the segmentation of RGB images[27]-[31]. For image segmentation using a panoptic approach, numerous frameworks have been initially suggested that employ both instance and semantic segmentation, subsequently merging the outcomes of each segment to produce the final panoptic segmentation results. To achieve this, Kirillov et al. [27] conduct instance and semantic segmentation independently before combining them.

Due to some limitations of instance segmentation, a panoptic architecture like Cell R-CNN has been proposed. In this case, the encoder part of the instance segmentation model is often used in learning global semantic features, in conjunction with a jointly trained semantic segmentation model [32]. Many other panoptic segmentation tools developed for segmenting medical images are widely used. For example, areas where these tools are frequently utilized include pathology image analysis [33], detection of prostate cancer [34], and segmentation of teeth in panoramic X-ray images [35].

The study [36] encompasses labeled LiDAR scans in various environments and car scenes. In [37], two fundamental approaches are employed for panoptic segmentation, combining semantic segmentation and 3D object detectors. Similarly, in [38], "The PointPillars object detection system is employed to determine bounding boxes and classify each object, while instance segmentation is executed for each category. The two principal networks undergo separate training and testing before their outcomes are merged in the final phase to achieve panoptic segmentation. An undisclosed test set is then utilized for the online assessment of LiDAR-driven panoptic segmentation.

In this article, the Mask R-CNN [17] method is used for instance segmentation. Mask R-CNN (Mask Region-Based Convolutional Neural Networks) is primarily based on Faster R-CNN, but it adds a segmentation mask for each detected object. It consists of three main components: a region proposal network (RPN), classification and bounding box regression, and segmentation mask prediction. Panoptic segmentation, on the other hand, uses the Panoptic-DeepLabmethod, which is based on the DeepLabv3+ model. It combines semantic segmentation and instance segmentation.

In this article, we focus on panoptic segmentation among image segmentation techniques (instance, semantic and panoptic segmentation), which are capable of distinguishing both the object and its boundaries within the image. The results of panoptic segmentation are visually compared and interpreted with those of instance segmentation. For image analyses, datasets such as COCO [39], CityScape [40], and an Industrial dataset have been utilized. Metric analysis employed includes Panoptic Quality (PQ) [27] and Semantic Quality (SQ) [27], which are used in panoptic segmentation methods. The results have been presented both in tabular and visual form.

The rest of the article is organized as follows. Section 2 covers the Materials and Methods. This section discusses the datasets used, the segmentation

methods employed, and the implementation settings. Section 3 contains the experimental results and discussion. The final section includes the conclusions of the article.

2. Material and Method

In this study, computer vision and image segmentation methods will be examined, with a focus on the most common image segmentation algorithms, particularly emphasizing the panoptic segmentation method. The processing of RGB images outputs as data types in panoptic segmentation will be explained. Results will be evaluated by processing three popular datasets with the panoptic segmentation algorithm.

2.1. Datasets

The datasets used for the panoptic segmentation task include the COCO dataset, the CityScapes dataset, and an Industrial dataset created in the structure of the COCO dataset with images captured in industrial settings.

The COCO dataset [39] is a large-scale data set for object detection, where objects are labeled according to their types. Based on this dataset, objects are categorized by type, and each category is assigned a color code. Accordingly, objects in the image are detected, and their category is determined based on the label. The primary uses of the COCO dataset include object detection, human detection in security systems, and background removal in object detection, among many others. Being an extensive dataset, it contains images of all kinds. Our preference, however, is for dense images where objects are more intertwined.

The CityScapes dataset [40] is another large-scale dataset created for the detection and labeling of objects. Again, objects are categorized, and these categories are assigned color codes. This dataset consists of images taken in various cities at different times of the year, in different seasons, and at different times of the day. Our preferred images are those from different cities that contain denser objects.

The Industrial dataset is organized following the logic of the COCO dataset, encompassing sequential images of environments populated with industrial objects. The objectives for utilizing the COCO dataset are similarly relevant here. The images selected for our study are prioritized for their clarity, as consecutive shots might compromise image quality, and those that feature a higher density of objects. Figure 1 in the manuscript showcases actual images alongside their corresponding panoptic masks for all discussed datasets.

Figure 1. Examples from the COCO, CityScapes, and Industrial datasets (1st Column: original images; 2nd Column: panoptic segmentation masks)

2.2. Methods

In this section, panoptic segmentation and instance segmentation are discussed in detail.

2.2.1. Panoptic segmentation

Panoptic segmentation is a machine learning method developed to understand and interpret images comprehensively. Beyond simple image segmentation, it determines which object each pixel belongs to, enabling a holistic understanding of objects and scenes. This method aims to classify and segment all objects in images both individually (instance segmentation) and as part of the background (semantic segmentation), determining not only to which object each pixel belongs but also what that object is. By merging object detection and semantic segmentation, this approach allows for richer and more detailed image analyses. Figure 2 presents various network structures used in the creation of panoptic segmentation.

In panoptic segmentation, there are two categories: items and objects. Items refers to innumerable areas such as the sky, sidewalks, and floors, while objects encompass all countable entities, including trees, cars and peoples. Items and objects are differentiated in the panoptic approach by assigning them distinct colors, which distinguishes them from one another, unlike object segmentation and semantic approaches where overlap between objects of the same type might occur. Panoptic segmentation provides a comprehensive view by recognizing each object and background separately, encompassing all these components. This method identifies and classifies each object individually while

also considering the relationship of these objects with the background. By enabling a detailed understanding of objects and areas in images, it allows for more complex image analysis and interpretations. Moreover, panoptic segmentation enables effective visualization of diverse components within a scene and can be described as a comprehensive approach that encompasses detection, localization, and classification of different scene elements. This outcome contributes to a clear and functional understanding of the scene.
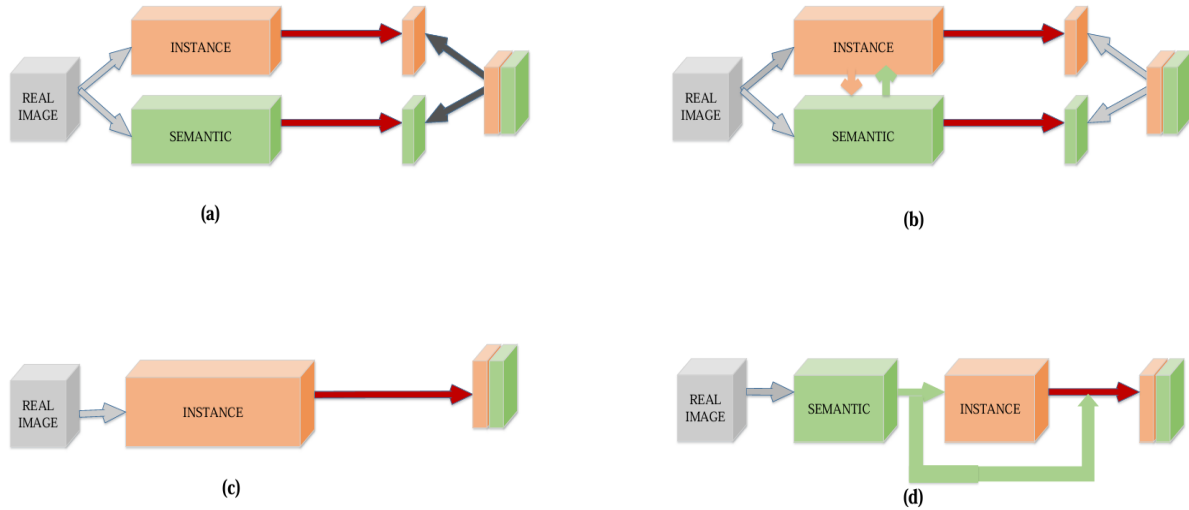
Figure 2. Network architectures for panoptic segmentation methods (a) Sharing image (b) Explicit coonection (c) One-shot Model (d) Cascade model

Panoptic segmentation, while merging instance and semantic segmentation, primarily uses architectures based on convolutional neural networks (CNN) [41]. This combination is shown in Equation 1.

$$P(x) = Combine(S(x), I(x)) \qquad (1)$$

Here, $P(x)$ represents the panoptic segmentation output, $S(x)$ represents the semantic segmentation output, and $I(x)$ represents the instance segmentation output. Panoptic segmentation combines these two segmentations to produce the final output.

These networks are designed to perform both object detection and pixel-based segmentation tasks. In the first phase, the classes and locations of objects are detected. In the second phase, semantic segmentation is applied to classify each pixel. During model training, special loss functions are usually used for both object detection and semantic segmentation. Model parameters are optimized using stochastic gradient descent (SGD) or similar algorithms.

Panoptic segmentation has a wide range of applications, such as detailed identification and understanding of vehicles, pedestrians, and other significant elements on roads. By identifying structures, roads, and other urban elements in cities, it provides valuable insights for urban planning and management processes. In distinguishing diseased tissues from normal ones, it contributes to diagnosis and treatment processes by enabling more detailed analysis of medical images. It is used in identifying and analyzing natural elements like vegetation and water resources, as well as man-made structures in satellite imagery.

2.1.2. Instance Segmentation

Instance segmentation is an advanced image analysis method developed through the combination of deep learning and computer vision techniques. It identifies the boundaries of each object in images at the pixel level, while also classifying objects into different categories. This method allows for detailed analysis on images by identifying each object individually and delineating their boundaries. This type of segmentation plays a crucial role in understanding the count, locations, shapes, and sizes of objects. In short, instance segmentation enables the determination of what the objects are (their class) and where they are (their location and shape at the pixel level).

Each pixel in the image is classified as belonging to a specific object. Even if they belong to the same class, different objects are identified separately, and a unique mask is generated for each. This method can precisely define the boundaries and shapes of objects, allowing even the subtle differences between them to be detected. Training the model requires a rich dataset labeled with the classes of objects and pixel-wise masks for each object.

Figure 3 features a block diagram of a one-stage instance segmentation process. It illustrates how an image can yield masks, classes, and bounding boxes outputs through instance segmentation.

Instance segmentation fundamentally employs CNN-based architectures. Architectures such as Mask R-CNN, YOLO, and Faster R-CNN are popular choices for instance segmentation. Among the architectures commonly used for object segmentation are Mask R-CNN [42], R-CNN [43, 44], Path Aggregation Network (PANet) [45], and YOLACT [46,47]. Mask R-CNN [42] is a method specifically developed for instance segmentation. It is based on Faster R-CNN and provides both classification and pixel-level mask output for each object. Different loss functions are used for object classification, localization (bounding box), and mask generation. To maximize the model's performance, optimization algorithms like Stochastic Gradient Descent (SGD) or similar are preferred. This method

offers valuable insights in various application areas, especially where the subtle differences between objects are significant. Instance segmentation is gaining increasing interest thanks to advancements in machine learning and artificial intelligence technologies, becoming a valuable tool across various industries.

2.3. Image Quality Metrics for Panoptic and Instance Segmentations

Panoptic segmentation merges object-based segmentation tasks (e.g., pedestrian, car) with scene segmentation tasks (e.g., road, sky). In this context, Panoptic Quality (PQ) [27] and Segmentation Quality (SQ) [27] are the most commonly used metrics.

Panoptic Quality (PQ) [27] evaluates both classification accuracy and segmentation quality simultaneously. PQ measures the agreement between predicted and true segments for each object, offering a single metric that combines both classification and segmentation performance. The formula for PQ is given in Equation 2. Segmentation Quality (SQ) [27] assesses only the accuracy of the segmentation, measuring how well the shapes and contours of the predicted segments match the true segments. SQ is typically calculated using the Intersection over Union (IoU) metric and is expressed as the average IoU for individual segments. The formula for SQ is given in Equation 3.
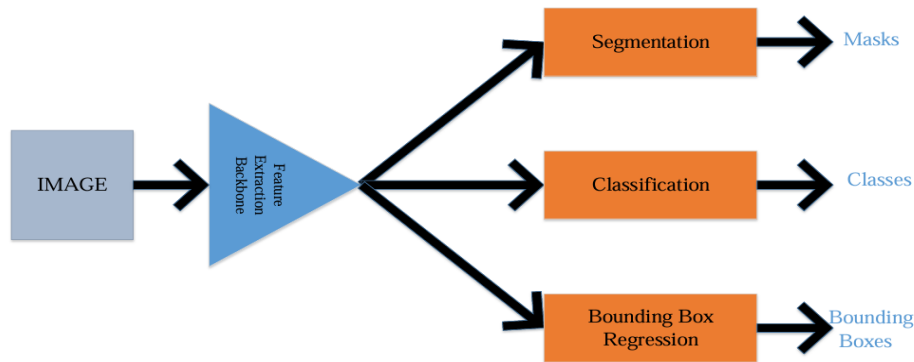
Figure 3: One-Stage instance segmentation process

PQ and SQ metrics are crucial for evaluating panoptic segmentation models. PQ comprehensively assesses a model's ability to correctly classify objects and accurately segment them, while SQ focuses on the quality of the segmentation. Understanding and utilizing these metrics play a significant role in the development and evaluation of panoptic segmentation models, leading to advancements in various

application areas such as object recognition and scene understanding.

$$PQ = \frac{\sum_{(p,g)\in TP} IoU(p,g)}{|TP| + 1/2|FP| + 1/2|FN|} \qquad (2)$$

$$SQ = \frac{1}{|TP|} \sum_{(p,g) \in TP} IoU(p,g) \qquad (3)$$

For the PQ equation; TP (True Positive) represents the number of correctly matched segment pairs, FP (False Positive) indicates the number of false positive predictions, and FN (False Negative) signifies the number of false negative predictions. $IoU(p,g)$ (Intersection over Union) expresses the ratio of the intersection to the union between the predicted segment p and the true segment g. For the SQ equation, TP again represents the correctly matched segment pairs, and $IoU(p,g)$ measures the ratio of the intersection to the union between the predicted and true segments.

Panoptic Quality (PQ) has been proposed for panoptic segmentation, but it is also used in instance segmentation. This metric measures both segmentation accuracy and detection accuracy. Segmentation Quality (SQ), on the other hand, measures the quality of segmentation masks. They are used as comparison metrics in instance segmentation methods.

3. Results and Discussion

This article aims to understand and interpret the results of instance segmentation and panoptic segmentation. Analyses were conducted on the COCO, CityScapes, and industrial datasets, with results presented visually. The analyses were based on the PQ and SQ metrics used for segmentation, from which conclusions were drawn and interpreted.

The figures show how the real images appear after instance segmentation and depict the boundaries of objects in images resulting from panoptic segmentation. Figure 4 presents the visual results of instance segmentation and panoptic segmentation for the COCO dataset.

Upon examining Figure 4, it's observed that instance segmentation focuses on objects, with the background not being given much importance. Objects are categorized into specific groups and labeled accordingly. In contrast, when looking at the panoptic segmentation results, both objects and the background are distinctly separated, with object labels being more clearly defined.

Figure 5 presents the visual outcomes of instance and panoptic segmentation for the CityScapes dataset.

Figure 4. Instance segmentation and panoptic segmentation results for the COCO dataset

When examining the instance segmentation results in Figure 5, it's noted that the objects are smaller and overlaid, with only the objects themselves being displayed. However, the types of objects are not clearly discernible. In the results of the panoptic segmentation, the entire environment appears to be color-coded with labels, illustrating a comprehensive labeling of both objects and the background.

Figure 6 features the visual outcomes of instance segmentation and panoptic segmentation for the Industrial dataset.

Figure 5. Instance segmentation and panoptic segmentation results for the CityScapes dataset
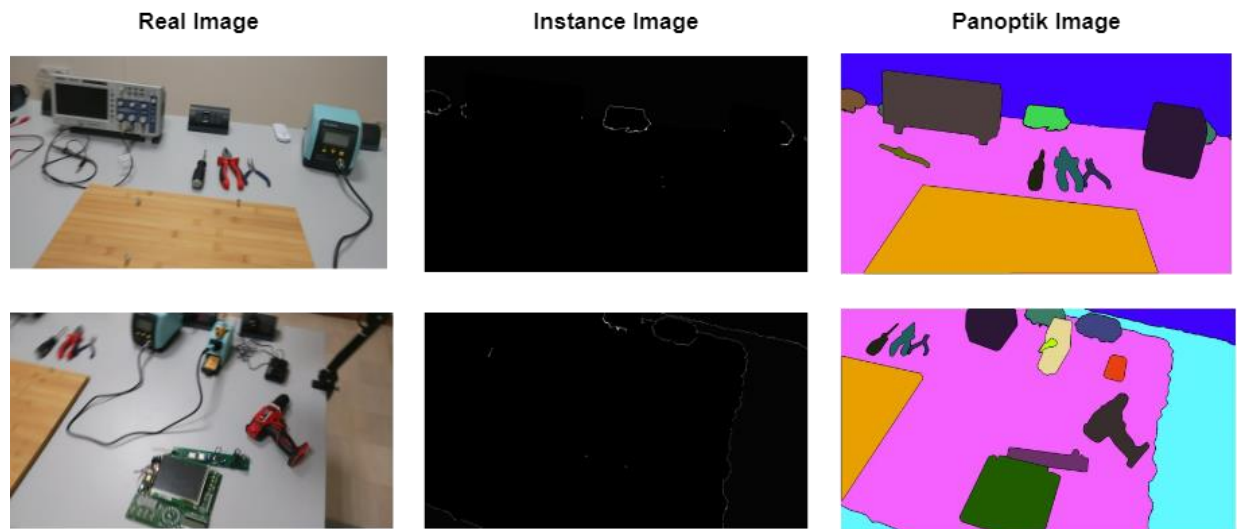
Figure 6. Instance segmentation and panoptic segmentation results for the Industrial dataset

In the real images depicted in Figure 6, due to the labels of objects not being distinctly clear, the outcome of instance segmentation shows that objects in the image are perceived similarly to the background and are not prominently displayed. However, in the results of panoptic segmentation, objects are displayed more distinctly.

Table 1 provides the metric results of PQ and SQ according to the datasets.

Table 1. PQ and SQ metric results for datasets used in panoptic segmentation

Datasets	PQ	SQ
COCO [39]	67.4	68.3
CityScapes [40]	**69.7**	**84.2**
Industrial	67.3	68.2

In Table 1, the PQ metric measures the quality of panoptic segmentation. It accounts for both correctly and incorrectly measured pixels, functioning by considering their ratio. The closer the ratio is to one hundred percent, the more accurate the results are. SQ, on the other hand, measures the quality of segmentation. Similarly, the closer the ratio is to one hundred percent, the more accurate the segmentation is deemed to be.

In the measurement of the PQ metric, a value of 69.7 and in the SQ metric, a value of 84.2 were observed, indicating that the Cityscape dataset showed the best performance for panoptic segmentation. The reason for the good results of the Cityscape dataset in panoptic segmentation is its ability to clearly distinguish objects and the background compared to other datasets. For example, when examining the panoptic segmentation visual

results of the COCO dataset, it is understood that objects are not fully distinguished. It can be observed that there might be confusion in distinguishing between a horse and a human. In tabular results, considering these reasons, the COCO dataset was observed to be less successful than the Cityscape dataset. The industrial dataset showed similar results to the COCO dataset.

Upon examining the values in the table, we observe that the CityScapes dataset provides better results in terms of ratios compared to the other datasets.

Table 2 provides the metric results of PQ and SQ according to the datasets for instance segmentation.

Table 2. PQ and SQ metric results for datasets used in instance segmentation

Datasets	PQ	SQ
COCO [39]	**0.0009**	**0.1764**
CityScapes [40]	0.0002	0.0317
Industrial	0.0008	0.0476

Table 2 presents the instance segmentation results according to the PQ and SQ metrics. With a value of 0.0009 for PQ and 0.1764 for SQ, the COCO dataset has shown better results. Since instance segmentation is a technique that individually identifies and masks each object instance in an image, the COCO dataset has been observed to be more successful in instance segmentation compared to other datasets.

In essence, the article illustrates the distinct outcomes of instance and panoptic segmentation processes on various datasets, using PQ and SQ metrics to evaluate the effectiveness of these segmentation methods. The visual presentation of segmentation results allows for a direct comparison between the original images and their segmented counterparts, highlighting the precision and capabilities of both instance and panoptic segmentation techniques in delineating object boundaries and classifying scene elements. This comparative analysis provides valuable insights into the strengths and limitations of each segmentation approach, contributing to the ongoing development and refinement of computer vision and image analysis technologies.

4. Conclusion and Suggestions

In conclusion, the analysis delineates a clear advantage of panoptic segmentation over instance segmentation in achieving higher precision and distinctiveness in object delineation and scene element classification. The deployment of PQ and SQ metrics furnishes a comprehensive method for evaluating the segmentation quality, where the CityScapes dataset emerges as a benchmark for superior segmentation performance. This distinction underscores the capability of panoptic segmentation to more accurately discern and categorize objects from the background, enhancing the overall clarity and effectiveness of image analysis. The juxtaposition of visual results from instance and panoptic segmentation not only underscores the enhanced accuracy and detail provided by panoptic segmentation but also illustrates its critical role in advancing computer vision technologies. Panoptic segmentation has been observed to work in conjunction with the ability to understand relationships between objects. This is an important feature for understanding how objects interact together, such as how a car progresses on a road or how a person holds an object. Instance segmentation has been observed to be able to identify and classify each object separately in images, ensuring that different objects are fully separated from each other. When compared, it is observed that instance segmentation exhibits a deficiency in distinguishing between objects compared to panoptic segmentation. Through meticulous comparison and evaluation, this study contributes significantly to our understanding of segmentation technologies, offering insights that propel the field towards more nuanced and effective image analysis methods. The findings advocate for further exploration and refinement of panoptic segmentation, promising improvements in various applications from autonomous driving to urban planning and beyond, thus marking a pivotal step in the evolution of image analysis and computer vision capabilities.

Contributions of the authors

Conception: Cahide SARA
Design:Cahide SARA
Supervision: Sara ALTUN GÜVEN
Materials: Cahide SARA
Literature review: İlhan DAŞDEMİR
Writer: Sara ALTUN GÜVEN
Critical review: İlhan DAŞDEMİR
Other: Sara ALTUN GÜVEN

Conflict of Interest Statement

There is no conflict of interest between the authors.

Statement of Research and Publication Ethics

There were no ethical objections to the publication

References

[1] K. Ikeuchi, Computer Vision: *A Reference Guide. Cham, Switzerland:* Springer International Publishing, 2021.

[2] T. Hoeser and C. Kuenzer, "Object detection and image segmentation with deep learning on Earth observation data: A review-part I: Evolution and recent trends," *Remote Sens. (Basel)*, vol. 12, no. 10, p. 1667, 2020.

[3] D. Galea, H.-Y. Ma, W.-Y. Wu, and D. Kobayashi, "Deep learning image segmentation for atmospheric rivers," *Artificial Intelligence for the Earth Systems*, 2023.

[4] X. Chen et al., "Efficient Decoder and Intermediate Domain for Semantic Segmentation in Adverse Conditions," *Smart Cities*, vol. 7, no. 1, pp. 254–276, 2024.

[5] J. Yuan, Z. Shi, and S. Chen, "Feature Fusion in Deep-Learning Semantic Image Segmentation: A Survey," *in International Summit Smart City 360°, Cham:* Springer International Publishing, 2021, pp. 284–292.

[6] P. Garg, A. S. Chakravarthy, M. Mandal, P. Narang, V. Chamola, and M. Guizani, "ISDNet: AI-enabled Instance Segmentation of aerial scenes for smart cities*," ACM Trans. Internet Technol*., vol. 21, no. 3, pp. 1–18, 2021.

[7] S. A. Güven and M. F. Talu, "Brain MRI high resolution image creation and segmentation with the new GAN method," *Biomedical Signal Processing and Control*, vol. 80, 2023.

[8] Y. Xu, S. Hou, X. Wang, D. Li, ve L. Lu, "A medical image segmentation method based on improved UNet 3+ network," *Diagnostics*, vol. 13, no. 3, 576, 2023.

[9] K. Huang, Y. Zhang, H.-D. Cheng, and P. Xing, "Trustworthy breast ultrasound image semantic segmentation based on fuzzy uncertainty reduction," *Healthcare (Basel)*, vol. 10, no. 12, p. 2480, 2022.

[10] B. Li, Y. Shi, Z. Qi, and Z. Chen, "A survey on semantic segmentation," *in 2018 IEEE International Conference on Data Mining Workshops (ICDMW)*, pp. 1233-1240, Nov. 2018.

[11] C. Kaymak and A. Ucar, "Semantic image segmentation for autonomous driving using fully convolutional networks," *in 2019 International Artificial Intelligence and Data Processing Symposium (IDAP)*, 2019.

[12] K. Fukushima, "Neocognitron: A self-organizing neural network model for a mechanism of pattern recognition unaffected by shift in position," *Biological Cybernetics*, vol. 36, no. 4, pp. 193-202, 1980.

[13] Y. Lecun, D. Touresky, G. Hinton, and T. Sejnowski, "A theoretical framework for back-propagation," *Proceedings of the 1988 connectionist models summer school*, vol. 1, pp. 21–28, 1988.

[14] O. Ronneberger, P. Fischer, ve T. Brox, "U-net: Convolutional networks for biomedical image segmentation," *in Medical Image Computing and Computer-Assisted Intervention–MICCAI 2015: 18th International Conference*, Munich, Germany, October 5-9, 2015, Proceedings, Part III, vol. 18, pp. 234-241, Springer International Publishing, 2015.

[15] L.-C. Chen, G. Papandreou, I. Kokkinos, K. Murphy, ve A. L. Yuille, "Semantic image segmentation with deep convolutional nets and fully connected crfs*," arXiv preprint arXiv:1412.7062*, 2014.

[16] İ. Kayadibi, U. Köse ve G. E. Güraksın, "Görüntü İşleme Teknikleri ve Evrişimsel Sinir Ağı Kullanılarak Bilgisayar Destekli Diş Segmentasyonu*," Pamukkale Üniversitesi Mühendislik Bilimleri Dergisi*, cilt 1000, no. 1000, ss. 0-0.

[17] W. He, X. Wang, L. Wang, Y. Huang, Z. Yang, X. Yao, ... Z. Ge, "Incremental learning for exudate and hemorrhage segmentation on fundus images," *in Information Fusion*, vol. 73, pp. 157-164, 2021.

[18] Y. Zhang, X. Sun, J. Dong, C. Chen, ve Q. Lv, "GPNet: gated pyramid network for semantic segmentation," *in Pattern Recognition*, vol. 115, 107940, 2021.

[19] Q. Sun, Z. Zhang, and P. Li, "Second-order encoding networks for semantic segmentation," *Neurocomputing*, 2021.

[20] W. Mao, J. Zhang, K. Yang, ve R. Stiefelhagen, "Panoptic lintention network: Towards efficient navigational perception for the visually impaired," *2021 IEEE International Conference on Real-time Computing and Robotics (RCAR)*, s. 857-862, July 2021.

[21] Liu, D., Zhang, D., Song, Y., Zhang, F., O'Donnell, L., Huang, H., ... & Cai, W. "Pdam: A panoptic-level feature alignment framework for unsupervised domain adaptive instance segmentation in microscopy images," *IEEE Transactions on Medical Imaging*, vol. 40, no. 1, pp.154-165, 2020.

[22] S. Albawi, T. A. Mohammed, and S. Al-Zawi, "Understanding of a convolutional neural network," *in 2017 International Conference on Engineering and Technology (ICET)*, pp. 1-6, Aug. 2017.

[23] J. Huang, D. Guan, A. Xiao, ve S. Lu, "Cross-view regularization for domain adaptive panoptic segmentation," *in Proceedings of the IEEE/CVF Conference on Computer Vision and Pattern Recognition*, pp. 10133-10144, 2021.

[24] Y. Chen, W. Chu, F. Wang, Y. Tai, R. Yi, Z. Gan, ... X. Li, "CFNet: Learning correlation functions for one-stage panoptic segmentation," *arXiv preprint arXiv:2201.04796*, 2022.

[25] G. Narita, T. Seno, T. Ishikawa, ve Y. Kaji, "PanopticFusion: Online volumetric semantic mapping at the level of stuff and things," *in 2019 IEEE/RSJ International Conference on Intelligent Robots and Systems (IROS)*, pp. 4205-4212, 2019.

[26] F. Saeedan and S. Roth, "Boosting monocular depth with panoptic segmentation maps," *in Proceedings of the IEEE/CVF Winter Conference on Applications of Computer Vision*, pp. 3853–3862, 2021.

[27] A. Kirillov, K. He, R. Girshick, C. Rother, ve P. Dollár, "Panoptic segmentation," *in Proceedings of the IEEE/CVF Conference on Computer Vision and Pattern Recognition*, pp. 9404-9413, 2019.

[28] S. Liu, L. Qi, H. Qin, J. Shi, ve J. Jia, "An End-to-End Network for Panoptic Segmentation," *in Proceedings of the IEEE/CVF Conference on Computer Vision and Pattern Recognition*, pp. 6172-6181, 2019.

[29] A. Nivaggioli, J.-F. Hullo, ve G. Thibault, "Using 3D models to generate labels for panoptic segmentation of industrial scenes," *ISPRS Annals of the Photogrammetry, Remote Sensing and Spatial Information Sciences*, vol. 4, pp. 61-68, 2019.

[30] W. Mao, J. Zhang, K. Yang, ve R. Stiefelhagen, "Can we cover navigational perception needs of the visually impaired by panoptic segmentation?," *arXiv preprint arXiv:2007.10202*, 2020.

[31] L. Shao, Y. Tian, ve J. Bohg, "ClusterNet: 3D instance segmentation in RGB-D images," *arXiv preprint arXiv:1807.08894*, 2018.

[32] D. Liu, D. Zhang, Y. Song, H. Huang, ve W. Cai, "Cell R-CNN v3: A novel panoptic paradigm for instance segmentation in biomedical images," *arXiv preprint arXiv:2002.06345*, 2020.

[33] D. Zhang, Y. Song, D. Liu, H. Jia, S. Liu, Y. Xia, ... W. Cai, "Panoptic segmentation with an end-to-end Cell R-CNN for pathology image analysis," *in Medical Image Computing and Computer Assisted Intervention–MICCAI 2018: 21st International Conference, Granada, Spain*, September 16-20, 2018, Proceedings, Part II, vol. 11, pp. 237-244, Springer International Publishing, 2018.

[34] X. Yu, B. Lou, D. Zhang, D. Winkel, N. Arrahmane, M. Diallo, ... A. Kamen, "Deep attentive panoptic model for prostate cancer detection using biparametric MRI scans," *in Medical Image Computing and Computer Assisted Intervention–MICCAI 2020: 23rd International Conference, Lima, Peru*, October 4–8, 2020, Proceedings, Part IV, vol. 23, pp. 594-604, Springer International Publishing, 2020.

[35] G. Jader, J. Fontineli, M. Ruiz, K. Abdalla, M. Pithon, ve L. Oliveira, "Deep instance segmentation of teeth in panoramic X-ray images," *in 2018 31st SIBGRAPI Conference on Graphics, Patterns and Images (SIBGRAPI)*, pp. 400-407, October 2018.

[36] J. Behley, M. Garbade, A. Milioto, J. Quenzel, S. Behnke, C. Stachniss, ve J. Gall, "SemanticKITTI: A dataset for semantic scene understanding of lidar sequences," *in Proceedings of the IEEE/CVF International Conference on Computer Vision*, pp. 9297-9307, 2019.

[37] J. Behley, A. Milioto, ve C. Stachniss, "A benchmark for LiDAR-based panoptic segmentation based on KITTI," *arXiv preprint arXiv:2003.02371*, 2020.

[38] A. H. Lang, S. Vora, H. Caesar, L. Zhou, J. Yang, ve O. Beijbom, "PointPillars: Fast encoders for object detection from point clouds," *in Proceedings of the IEEE/CVF Conference on Computer Vision and Pattern Recognition*, s. 12697-12705, 2019.

[39] T. Y. Lin, M. Maire, S. Belongie, J. Hays, P. Perona, D. Ramanan, ... C. L. Zitnick, "Microsoft COCO: Common Objects in Context*," in Computer Vision–ECCV 2014: 13th European Conference, Zurich, Switzerland, September 6-12, 2014, Proceedings, Part V*, vol. 13, pp. 740-755, Springer International Publishing, 2014.

[40] M. Cordts, M. Omran, S. Ramos, T. Rehfeld, M. Enzweiler, R. Benenson, ... B. Schiele, "The CityScapes dataset for semantic urban scene understanding," *in Proceedings of the IEEE Conference on Computer Vision and Pattern Recognition*, pp. 3213-3223, 2016.

[41] J. Huang, D. Guan, A. Xiao, ve S. Lu, "Cross-view regularization for domain adaptive panoptic segmentation," *arXiv preprint arXiv:2103.02584*, 2021.

[42] X. Liu, D. Zhao, W. Jia, W. Ji, C. Ruan, Y. Sun, "Cucumber fruits detection in greenhouses based on instance segmentation," *IEEE Access*, vol. 7, pp. 139635-139642, 2019.

[43] M.-C. Roh ve J.-y. Lee, "Refining faster-rcnn for accurate object detection," *in 2017 Fifteenth IAPR International Conference on Machine Vision Applications (MVA)*, IEEE, pp. 514-517, 2017.

[44] Y. Ren, C. Zhu, S. Xiao, "Object detection based on fast/faster rcnn employing fully convolutional architectures," *Mathematical Problems in Engineering*, vol. 2018, 2018.

[45] S. Liu, L. Qi, H. Qin, J. Shi, ve J. Jia, "Path aggregation network for instance segmentation," *in Proceedings of the IEEE Conference on Computer Vision and Pattern Recognition*, pp. 8759-8768, 2018.

[46] D. Bolya, C. Zhou, F. Xiao, ve Y. J. Lee, "YOLACT: Real-time instance segmentation," *in Proceedings of the IEEE/CVF International Conference on Computer Vision*, pp. 9157-9166, 2019.

[47] D. Bolya, C. Zhou, F. Xiao, ve Y. J. Lee, "YOLACT++: Better real-time instance segmentation," *in Proceedings of the IEEE/CVF International Conference on Computer Vision*, 2019.

Bitlis Eren Üniversitesi Fen Bilimleri Dergisi

Theoretical Investigation of The Properties of LiRuAs Semi-Heusler Alloy via Density Function Theory

Erol ALBAYRAK[1*]

[1]*Kırşehir Ahi Evran University, Faculty of Engineering and Architecturte,
Department of Metallurgy and Material Engineering, Kırşehir, Turkey*
ORCID: 0000-0001-9161-9068

Abstract
The structural, thermal, electronic and elastic properties of LiRuAS Semi Heusler alloy were investigated using a generalized gradient approximation (GGA) approach, which employs a density functional theory (DFT) to examine the alloy's optimized equilibrium lattice parameter. The optimized lattice parameter was found to be 5.601 Å. The results of the calculations indicate that the alloy was mechanically stable. Additionally, owing to the modulus and certain ratios, such as the bulk modulus Young's modulus the alloy was found to have low compressibility and a soft, ductile and anisotropic natüre. The Debye temperature of the alloy was calculated to be 281.186 K. We believe that the LiRuAs SH alloy may be particularly useful for magnetic field shielding applications due to its metallic conductive and nonmagnetic nature.

1. Introduction

Technology has become one of the almost indispensable facts in our lives in the 21st century. With the development of technology, people's quality and duration of life have increased. Materials science has played a major role in the development of technology. New applications of elements and materials composed of these elements, especially in the field of electronics, have enabled technology to advance step by step daily. As new generation smart materials, nanomaterials, semiconductors, and magnetic and nonmagnetic materials are examined, their previously unknown properties are determined, and new comfort areas are offered to humanity thanks to devices made using these properties.

In a 1903 study, it was observed that the alloys examined could have magnetic properties, although the elements that make up the alloys obtained were not magnetic [1]. This showed that some properties that are not present in the constituent elements of the alloys may be present in the alloys from which they are synthesized. Based on the abovementioned work, such alloys have been given the general name Heusler alloys, and these alloys

have been studied, especially for the production of new generation magnetoelectronic and spintronic devices. Heusler alloys generally consist of four nested face-centered cubic (FCC) cells, and their general formula was initially determined to be XY_2Z. Studies have shown that one of these FCC cells can be removed from alloys and that the properties of the new alloy formed in this way can change compared to those in the initial state. In this way, the alloys obtained by removing a subcell from the alloys in accordance with the general formula XY_2Z are called Semi-Heusler (SH) alloys. The general formula for preparing Semi-Heusler alloys is XYZ [2]. Heusler alloys are generally costly and time consuming to obtain. It is also possible that not all synthesized alloys are promising for various applications [3 -11]. Therefore, it is logical and scientific to determine promising materials by performing theoretical studies before the experimental study of alloys and to proceed to the device production stage by performing experimental studies after this stage.

In this study, the electronic, structural, elastic, thermal and physical properties of LiRuAs SH alloys were investigated with the help of the Quantum-

---

* Corresponding author:*erol_albayrak@hotmail.com*

ESPRESSO software package, which includes a density function theory (DFT) approach [12,13].

2. Material and Method

The state in which a material has minimum energy is called steady-state energy. The lattice constant of the material at this minimum energy is called the steady-state lattice constant. These constants are used to determine many properties of the material. To determine the steady-state lattice constants of materials, it is necessary to know the interactions between the electrons and atoms in the material. In this study, the DFT approach was used to theoretically calculate the steady-state optimized lattice constant and structural, electronic, and thermal properties of the material. To perform calculations with this approach, the ground-state electronic charge density expression proposed by Kohn and Sham in 1965 was used [14].

To perform calculations for the minimum-energy steady state, it is necessary to determine the exchange correlation potential of noninteracting electrons. This potential is determined by an approach called the local density approximation (LDA) [15]. To improve the success rate of the calculations, a group of scientists developed the Perdew-Burke-Ernzehof generalized gradient approximation (PBE-GGA) [16] The PBE-GYY approach was also used for the calculations performed in this study for the LiRuAs SH alloy. In addition to these approaches, it is necessary to solve the Schrödinger Equation in equation 1 to calculate the minimum energy of the alloy.

$$H\varphi = \varepsilon\varphi \qquad (1)$$

To solve this equation, potential contributions from the cor and valence electrons must be added to the equation. In the calculations, Rappe group potentials were selected from the potential pseudo potentials required for the LiRuAs SH alloy [17]. In the calculations, the plane wave shear energy was chosen as 40 Ry, the electronic charge density was chosen as 400 Ry, and the integration k-points in the Brilloin region were chosen as 8x8x8. The smearing parameter up to the Fermi surface was set as 0.02 Ry, and the Methfessel-Paxton smearing technique was used for the calculations [18]. Calculations for the thermodynamic and elastic properties of the alloy were performed with the Thermo_pw program using the Debye model [19].

3. Results and discussion

3.1. Structural features

The atoms of the LiRuAs SH alloy have an atomic arrangement belonging to the $F\bar{4}3$ m space group. Since the alloy has a SH structure, it has the general formula XYZ. Atomic positions of the unit cell of the alloy: (0, 0, 0, 0) for As atoms, (1/4, 1/4, 1/4, 1/4) for Li atoms and (3/4, 3/4, 3/4, 3/4) for Ru atoms. Figure 1 shows the unit cell structure of the $F\bar{4}3$ m crystalline LiRuAs SH alloy by using the Vesta programme.
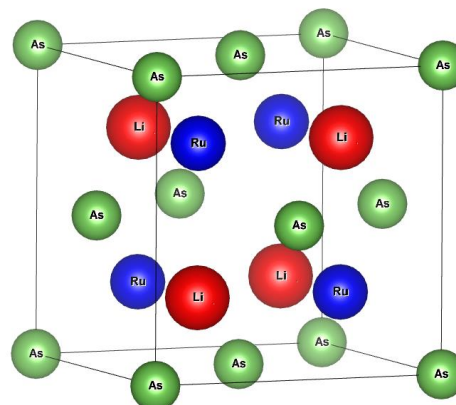
Figure 1. Unit cell structure of LiRuAs SH alloy with $F\bar{4}3$ m crystal arrangement.

A literature search on LiRuAs SH alloy revealed that there are no experimental studies on the alloy. To test the reliability of the results of the calculations for the alloy, models for the possible steady states of the alloy were created on the Open Quantum Materials Database [20] website. All three different atomic arrangements of the alloy are in the $F\bar{4}3$ m space group. Calculations were made for the alloy with these three different atomic arrangements, and it was determined that the lowest energy state could be the most stable state. All calculations were performed based on the unit cell structure of this alloy, as shown in Figure 1.

The optimized equilibrium state lattice constant was calculated with the Quantum Espresso program, where the total energy was a minimum of $a_0 = 5,601$ Å. This value is only 0.176% different from the lattice constant value reported on The Open Quantum Materials Database website, and the reliability of the calculations was confirmed by the agreement between the calculations and the values on the website.

3.2. Electronic specifications

To understand the electronic and magnetic properties of a material, elastic constants must be calculated, and

electronic band curves must be plotted along the spin-up and spin-down axes. In addition, density of states (DOS) plots are plotted to better understand the contribution of the atoms in the alloy to the conductivity. Figure 2 shows the electronic band curves obtained from calculations to understand the electronic and magnetic properties of the LiRuAs SH alloy.
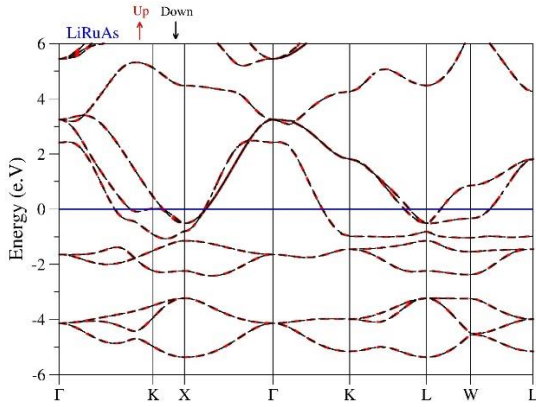
Figure 2. Electronic band graph of LiRuAs SH alloy.

According to the graph, the high symmetry axes in the valence and conduction bands overlap in the spin-up (↑) and spin-down (↓) directions, and the curves in the conduction band cross the Fermi energy level. The fact that the curves cross the Fermi energy level helps us to understand that there is no forbidden energy gap between the valence and conduction bands; therefore, electrons can be exchanged between both bands. This means that there is no forbidden energy gap near the Fermi energy level, and therefore, the alloy is a metallic conductor.

In addition, the fact that the curves coincide on the spin-up and spin-down high-symmetry axes allows us to understand that the alloy has a nonmagnetic character, that is, the magnetic moment is zero. Partial and total density of states (DOS) curves of the alloy were plotted, and the plotted curves are shown in Figure 3.
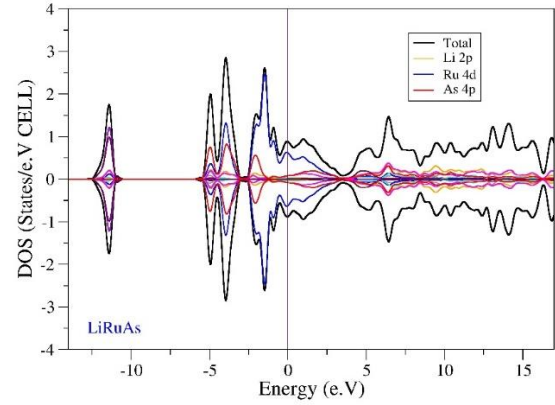
Figure 3. Density of state (DOS) plot of LiRuAs SH alloy.

According to the graph of the alloy, the most dominant contribution to the electrical conductivity in the spin-up and spin-down high symmetry orientations comes from the 4d, 2p and 4p orbitals of Ru, Li, As and Fe, respectively. The contributions of the other elements in the alloy to the electronic conductivity were found to be quite limited. The fact that the DOS curves are symmetric allows us to understand that the alloy does not have a magnetic moment [21].

3.3. Elastic properties

To understand the elastic properties of a material, several moduli and ratios, such as the bulk modulus (B), Young's modulus (E), shear modulus (G), and B/G ratio, should be calculated.

To make these calculations, it is necessary to calculate the values of C_{11}, C_{12} and C_{44}, which are called elastic constants. By using elastic constants, we can also understand whether the material is mechanically stable according to the Born criteria. For the material to be mechanically stable, the elastic constants must meet the Born stability criteria given in Equation 2 [22].

$$C_{44} > 0; \ C_{11} - C_{12} > 0; \ C_{11} + 2C_{12} > 0 \qquad (2)$$

Using the obtained elastic constants, the moduli and ratios are calculated to understand certain properties, such as the hardness, softness and brittleness of the material. Table 1 shows the elastic constants obtained from the calculations for the LiRuAs SH alloy.

Table 1. Calculated elastic constants for LiRuAs SH alloy (C_{11}, C_{12} and C_{44}; GPa)

Material	C_{11}	C_{12}	C_{44}
LiRuAs	148.425	96.515	30.187

The equations that allow us to calculate the moduli and ratios that help us understand some of the elastic and physical properties of the alloy are given below. All moduli and ratios given in Table 2 were obtained using these equations [23].

$$A = \frac{2C_{44}}{C_{11} - C_{12}} \tag{3}$$

$$\sigma = \frac{1}{2}(1 - \frac{E}{3B}) \tag{4}$$

$$B = \frac{2C_{12} + C_{11}}{3} \tag{5}$$

$$E = \frac{9BG}{3B + G} \tag{6}$$

$$G = \frac{5(C_{11} - 2C_{12})C_{44}}{3(C_{11} - 2C_{12}) + C_{44}} \tag{7}$$

Table 2. Bulk modulus (*B*; GPa), shear modulus (*G*; GPa), Young's modulus (*E*; GPa), *B/G* ratio, Poisson's ratio (σ), and anisotropy factor (*A*) were calculated for the LiRuAs SH alloy.

Material	*B*	*G*	*E*	*B/G*	σ	*A*
LiRuAs	113.8	28.4	78.7	4.01	0.385	1.16

The Alloy $C_{11} - C_{12}$ difference is positive. This difference between the elastic constants is called Cauchy Pressure. A positive Cauchy pressure allows us to understand that the bonds in the alloy are significantly ionic. In addition, a Poisson's ratio of approximately 0.25 indicates that the bonds in the alloy are significantly ionic [24]. The bulk moduli calculated for the alloys are given in Table 2 $C_{12} <$

$B < C_{11}$ and were calculated in the range of 100 GPa. A bulk modulus greater than 100 GPa indicates that the alloy has low compressibility. The larger the Young's modulus is, the greater the hardness of the material.

The Young's modulus calculated for the LiRuAs SH alloy is less than 100 GPa, and accordingly, the alloy is considered to be soft.

According to Pugh's criterion, the *B/G* ratio provides information about the ductile or brittle nature of materials. If the *B/G* ratio is greater than 1.75, the material is considered ductile, and if it is smaller, it is considered brittle. The calculated *B/G* ratio of 4.007 for the LiRuAs SH alloy allows us to understand that the alloy has a ductile nature [25].

Anisotropy can be explained as the directional dependence of some properties of a material during forming. The calculated anisotropy for the LiRuAs SH alloy is very slightly different from 1. Since the anisotropy factor is different from 1, we were able to infer that the alloy is anisotropic; that is, some physical properties of the alloy may change depending on the forming. Nevertheless, we believe that the fact that the anisotropy factor is very close to 1 may limit the effect of forming on the physical properties of the alloy during forming. The direction dependence of the Young's modulus, shear/shear modulus, Poisson's ratio and linear compressibility were calculated using ELATE codes, and their three-dimensional representations are given in Figures 4, 5 and 6 [26].
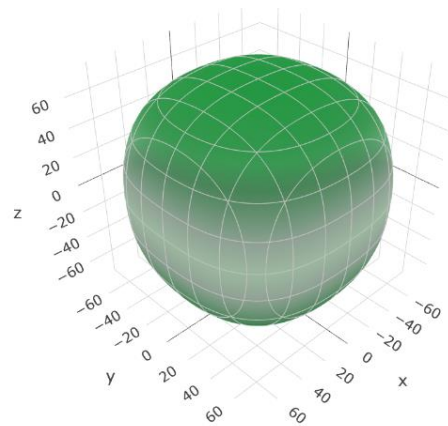
Figure 4. Three dimensional representation of the direction dependence of Young's modulus of LiRuAs SH alloy obtained with the help of Elate codes.
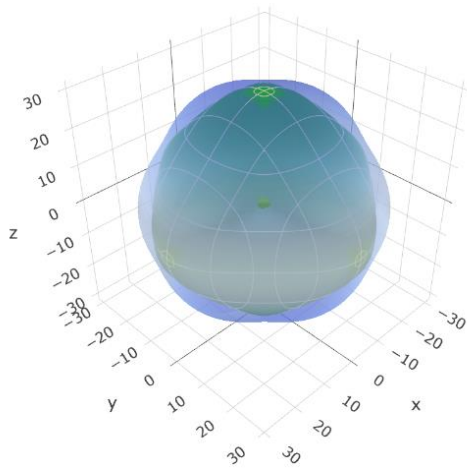
Figure 5. Three dimensional representation of the direction dependence of the shear modulus of LiRuAs SH alloy obtained with the help of Elate codes.
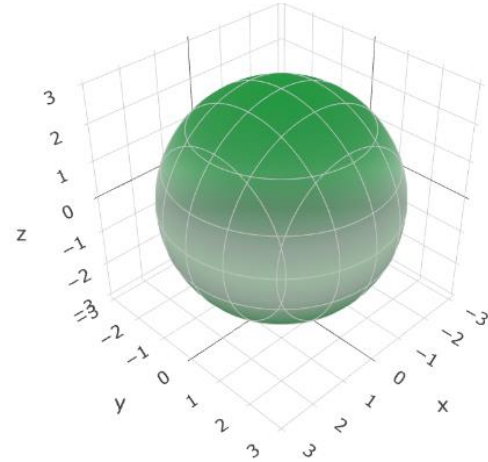
Figure 7. Three dimensional representation of the direction dependence of the linear compressibility of LiRuAs SH alloy obtained using Elate codes.
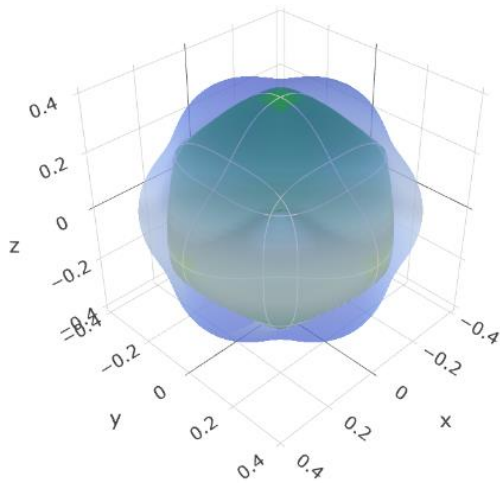
Figure 6. Three dimensional representation of the direction dependence of the Poisson's ratio of LiRuAs SH alloy obtained with Elate codes.

3.4. Thermal Properties

The thermal properties of the LiRuA SH alloy were investigated with the Thermo Pw program. The Thermo Pw program is based on the Debye model in its calculations. To understand the thermal properties of the alloy, the vibration energy-temperature, free vibration energy-temperature, heat capacity-temperature and entropy-temperature curves of the alloy were plotted. The plots are given in Figures 8, 9, 10 and 11.
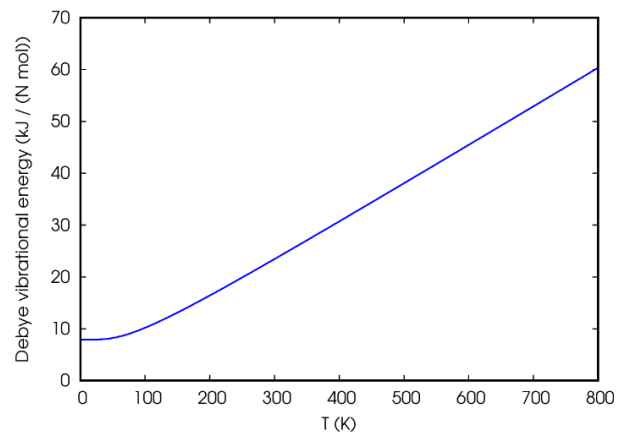
Figure 8. Vibration energy - Temperature plot of LiRuAs SH alloy

The internal energy of solid materials that receive heat increases. Increased internal energy is expected to increase the vibration of atoms in the material. In other words, the internal energy of a

material whose temperature increases; therefore, the vibration energy also increases. The correlation between temperature and vibration energy is shown in Figure 8. An increase in the temperature of a solid material leads to an increase in its internal energy, and an increase in internal energy leads to an increase in the vibration energy of the material. An increase in the vibrational energy of a material leads to a decrease in its free vibrational energy. Figure 9 shows the free vibration energy-temperature graph of the LiRuAs SH alloy. The graph shows that the free vibration energy decreases with temperature, as mentioned above.
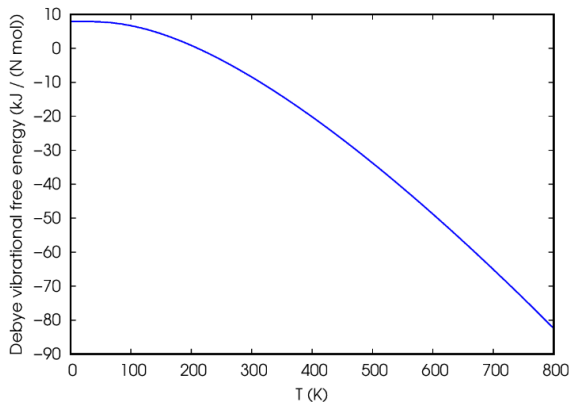
Figure 9. Free vibration energy - Temperature graph

The heat capacity-temperature graph in Figure 10 shows that the heat capacity of the alloy increases up to a certain temperature limit and then remains constant. This limit reached by the heat capacity of the LiRuA alloy is the Dulong-Petit limit [27]. The heat capacity of the alloy reached 3NR limit values with increasing temperature, confirming our expectation.
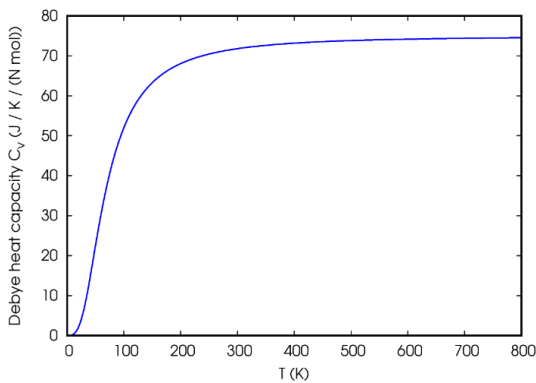
Figure 10. Heat capacity - temperature graph

As the temperature increases, the internal energy and atomic vibrations in the material also increase. This allows us to understand that the disorder in the material, i.e., the entropy, also increases with increasing temperature. Figure 11 shows the temperature-dependent graph of entropy. As expected, this graph shows that the disorder/entropy of a substance increases with temperature. The Debye temperature, which is a measure of the melting temperature of the alloy, was calculated to be 281.186 K.
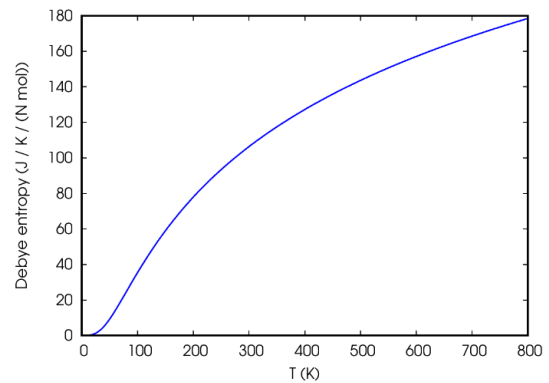
Figure 11. Entropy-temperature graph

4. Conclusion and Suggestions

In this study, several properties of LiRuAs SH alloys with $F\bar{4}3$ m space atomic arrangements were investigated theoretically using DFT. A literature search revealed that no experimental study of the alloy has been reported. Since Heusler alloys are both difficult and costly to obtain, it is important to determine theoretically the promising materials in areas such as spintronics and magnetoelectronic applications before experimental studies. The calculations for the alloy were performed with the Quantum Espresso program using the DFT approach.

The steady-state lattice constant of the alloy is $a_0 = 5,601$ Å. The value of 5,601 Å is in 99.824% agreement with the lattice constant calculated for the LiRuAs SH alloy on The Open Quantum Materials Database website. To understand the electronic properties of the alloy, electronic band curves and total and partial density of states (DOS) curves were plotted.

According to the information provided by these curves, the alloy has a net magnetic moment of zero and has a metallic conductive character. The calculation of the elastic constants of the alloy allowed us to make predictions about some of its

structural and physical properties. When the elastic constants were substituted for the Born stability criterion, we realized that the alloy was mechanically stable. Additionally, owing to the modulus and certain ratios, such as the bulk modulus Young's modulus the alloy was found to have low compressibility and a soft, ductile and anisotropic nature. The Poisson's ratio also showed that the atomic bonding in the alloy is largely ionic bonding.

To understand the thermal properties of the alloy, calculations were made in the Thermo Pw program using the Debye model, and the variations in the vibration energy, free vibration energy, heat capacity and entropy values of the alloy with temperature were examined. The Debye temperature of the alloy was calculated to be 281.186 K. We

believe that the LiRuAs SH alloy may be particularly useful for magnetic field shielding applications due to its metallic conductive and nonmagnetic nature. Although it is not desirable for the alloy to have zero magnetic moment for spintronic devices, it is thought that it can be used in applications that need magnetic isolation.

Conflict of Interest Statement

There is no conflict of interest between the authors.

Statement of Research and Publication Ethics

The study is complied with research and publication ethi

References

[1]   R. F. Heusler, "Über Magnetische Manganlegierungen," *J. Verhandlungen der Deutschen Physikalischen Gesellschaft*, vol. 5, p. 219, 1903.

[2]   G. Joseph Poon, "Chapter 2 Electronic and thermoelectric properties of Half-Heusler alloys," *Semiconductors and Semimetals*, vol. 70, pp. 37–75, 2001.

[3]   S. Berri, D. Maouche, M. Ibrir, B. Bakri, "Electronic structure and magnetic properties of the perovskite cerium manganese oxide from ab initio calculations," *Materials Science in Semiconductor Processing*, vol. 26, pp. 199-204, 2014.

[4]   F. Hosseinzadeh, A. Boochani, S.M. Elahi, Z. Ghorannevis, "GdPtBi Heuslerene: mechanical stability, half-metallic, magneto-optic, and thermoelectric properties by DFT", *Phil. Mag.*, vol. 102, p. 887–901, 2022.

[5]   Y. Sokolovskaya, O. Miroshkina, D. Baigutlin, V. Sokolovskiy, M. Zagrebin, V. Buchelnikov, A.T. Zayak, "A ternary map of Ni–Mn–Ga Heusler alloys from ab initio calculations", *J. Met.*, vol. 11, p. 973, 2021.

[6] M. Çanlı, E. Ilhan, N. Arıkan, "First-principles calculations to investigate the structural, electronic, elastic, vibrational and thermodynamic properties of the full Heusler alloys X2ScGa (X= Ir and Rh) ", *J. Mater. Today Commun.*, vol. 26, p. 101855, 2021.

[7]   J. Atulasimha, S. Bandyopadhyay, *Nanomagnetic and spintronic devices for energy-efficient memory and computing*, John Wiley & Sons. 2016.

[8]   A. Bsiesy, "Spin injection into semiconductors: towards a semiconductor-based spintronic device", *J. Comptes Rendus Physique,* vol. 6, pp. 1022–1026, 2005.

[9]   R.A.P. Ribeiro, A. Camilo, S.R. de Lazaro, "Electronic structure and magnetism of new ilmenite compounds for spintronic devices: FeBO3 (B= Ti, Hf, Zr, Si, Ge, Sn) ", *J. Magnet. Magnet. Mater.* Vol. 394 pp. 463–469, 2015.

[10]   Z. Chen, T. Li, T. Yang, H. Xu, R. Khenata, Y. Gao, X. Wang, " Palladium (III) fluoride bulk and PdF3/Ga2O3/PdF3 magnetic tunnel junction: multiple spin-gapless semiconducting, perfect spin filtering, and high tunnel magnetoresistance", *J. Nanomater.* Vol. 9, p. 1342, 2019.

[11]   J. M. Al-Issawe, I. Oreibi, " DFT Calculations of Trilayer Heterostructures from MoSe2, PtS2 Monolayers in Different Orders with Promising Optoelectronic Properties", *J.of the Turkish Chemical Society A*, vol. 11, pp. 405-414. 2024.

[12]   P. Gianozzi, S. Gironcoli, P. Pavone, S. Baroni, "Quantum Espresso: a modular and open-source software project for quantum simulations of materials," *Journal of Physics: Condensed Matter*, vol. 21, no. 39, p. 395502, 2009.

[13]   P. Giannozzi, O. Andreussi, T. Brumme, O. Bunau, M. B. Nardelli, M. Calandra, R. Car, C. Cavazzoni, D. Ceresoli, M. Cococcioni, N. Colonna, I. Carnimeo, A. D. Corso, S. de Gironcoli, P. Delugas, R. A. DiStasio Jr, A. Ferretti, A. Floris, G. Fratesi, G. Fugallo, R. Gebauer, U. Gerstmann, F. Giustino, T. Gorni, J. Jia, M. Kawamura, H-Y Ko, A. Kokalj, E. Küçükbenli, M. Lazzeri, M. Marsili, N. Marzari, F. Mauri, N. L. Nguyen, H-V Nguyen, A. Otero-de-la-Roza, L. Paulatto, S. Poncé, D. Rocca, R. Sabatini, B. Santra, M. Schlipf, A. P. Seitsonen, A. Smogunov, I. Timrov, T. Thonhauser, P. Umari, N. Vast, X. Wu and S. Baroni, "Advanced capabilities for materials modelling with QUANTUM ESPRESSO." *Journal of Physics: Condensed Matter,* vol 29, no 46, p. 465901, 2017.

[14]   L. J. Sham, W. Kohn, "Self-consistent equations including exchange and correlation effects," *Phys. Rev.*, vol. 140, p. A1133, 1965.

[15]   P. Gianozzi, P. Pavone, S. Baroni, "Ab initio calculation of phonon dispersions in semiconductors," *Phys. Rev. B*, vol. 43, no. 9, pp. 7231–7243, 1991.

[16]   J.P. Perdew, K Burke., M. Ernzerhof, "Generalized Gradient Approximation Made Simple," *Phys. Rev. Lett.*, vol. 77, no. 18, pp. 3865–3868, 1996.

[17]   G. P. Srivastava, *The physics of phonons*. Bristol.: Adam Hilger, 1990.

[17]   P. A. Methfessel M., "High-precision sampling for Brillouin- zone integration in metals," *Phys. Rev. B,* vol. 40, no. 6, p. 3616, 1989.

[19]   A. D. Corso, "Elastic constants of beryllium: a first-principles investigation," *J. Phys: Condens Matter*, vol. 28, no. 7, p. 075401, 2016.

[20]   "The Open Quantum Materials Database," *https://oqmd.org/.* [Online]. Available: https:// https://oqmd.org/materials/composition/LiRuAs

[21]   E. Albayrak., "XA yapıdaki Ti2RuSn ters-Heusler alaşımının yapısalı elektronik, elastik ve termodinamik özelliklerinin teorik olarak incelenmesi," *Journal of the Institute of Science and Technology*, vol. 12, no. 3, pp. 1496–1505, 2022.

[22]   K. Huang, M. Born, *Dynamical Teory of Crystal Lattices*. Oxford, England: Clarendon Press, 1965.

[23]   S. Al, N. Arikan, S. Demir and A. İyigor, "LatticeDynamic Properties of Rh2XAl (X= Fe and Y) Alloys," *Physica B: Condensed Matter*, vol. 531, pp. 16–20, 2018.

[24]   V.V. Bannikov, I.R. Shein, A.L. Ivanovskii, "Electronic structure, chemical bonding and elastic properties of the first thorium-containing nitride perovskite TaThN3," *Physica status solidi (RRL) – Rapid Res. Lett.*, vol. 1, no. 3, pp. 89–91, 2007

[25]   S. F. Pugh, *XCII. Relations between the elastic moduli and the plastic properties of polycrystalline pure metals*. London: The London, Edinburgh, and Dublin Philosophical Magazine and Journal of Science, 1954.

[26]   R. Gaillac, P. Pullumbi, FX Coudert, "ELATE: an open-source online application for analysis and visualization of elastic tensors," *J. Phys.:Condens. Matter*, vol. 28, no. 27, p. 275201, 2016.

[27]   P. Petit, "Recherches sur quelques points importants de la Théorie de la Chaleur," *Annales de Chimie et de Physique*, vol. 10395, p. 413, 1819.

Bitlis Eren Üniversitesi Fen Bilimleri Dergisi

Application of Deep Learning for Voice Command Classification in Turkish Language

Yusuf ÇELİK[1*]

[1]Department of Computer Engineering, Faculty of Engineering, Munzur University, Tunceli, Türkiye
(ORCID: 0000-0002-7859-7543)

Keywords: Deep Learning, Voice Command Recognition, Neural Network, Feature Extraction

Abstract

In this study, a deep learning model was developed for the recognition and classification of voice commands using the Turkish Speech Command Dataset. The division of training, validation, and test sets was carried out on an individual basis. This approach aims to prevent the model from memorizing and to enhance its generalization capability. The model was trained using Mel-Frequency Cepstral Coefficients features extracted from voice files, and its classification performance was evaluated in detail. The findings indicate that the model successfully classifies voice commands with a high accuracy rate, achieving an overall accuracy of 92.3% on the test set, highlighting the potential of deep learning approaches in voice recognition technologies

1. Introduction

Today, voice and speech recognition systems are gaining increasing importance in many areas such as smart assistants, automatic customer services, and biometric security systems. The foundation of these systems lies in the ability to extract meaningful features from raw voice signals and to make accurate classifications based on these features. This process requires the development of an effective machine learning model [1,2].

Deep learning is revolutionizing many fields today and is providing groundbreaking innovations across numerous sectors [3]. Deep learning techniques are being applied in areas including, but not limited to, image recognition and processing [4,5,21,23,24], natural language processing [6], and robotics [7], thereby expanding the boundaries of machine learning and artificial intelligence technologies.

Deep learning also plays a significant role in the field of voice recognition and processing. Applications such as speech recognition, voice assistants, emotion analysis, and speaker verification have shown significant development thanks to deep learning models [8,9,10]. The success in this field is fundamentally due to the ability to extract effective features from voice signals. In particular, feature extraction techniques like Mel-Frequency Cepstral Coefficients (MFCC) have achieved great success in capturing the characteristic features of voice signals. MFCC, which is based on the short-term spectral analysis of voice signals' frequency components, is widely used in speech recognition, voice classification, and similar tasks. This technique is crucial for training deep learning models, enabling them to interpret voice data and classify with high accuracy [11,12].

In the literature, MFCC have been frequently used. Deng et al. have proposed a new method for heart sound classification based on MFCC features and convolutional recurrent neural networks, processing heart sound signals entirely with MFCC in their study. This method allows for a detailed analysis of temporal changes in heart sounds, extracting features that, when applied to deep learning techniques, achieve high classification success rates in the early diagnosis of heart diseases [14].

Rejaibi et al. have presented a framework based on deep Recurrent Neural Networks (RNN) for detecting depression from speech and predicting the severity

---

level of depression. MFCC was used for the extraction of voice features [15].

Anjana et al. conducted a study on speech recognition across various local languages in India, utilizing MFCC and formant frequencies to distinguish between languages. Comparing two classification algorithms, LDA and SVM, their findings demonstrated that LDA outperformed SVM with a classification accuracy of 93.88% [20].

In the study conducted by Putra et al., an automatic door control system was developed using voice commands "buka" (open) and "tutup" (close). The research utilized MFCC and Convolutional Neural Networks (CNN) for feature extraction and classification of sound signals. The CNN model achieved a success rate of 89% in classifying these commands [22].

The number of existing studies on the classification of Turkish voice commands is limited. The aim of this study is to fill the existing gaps in the recognition and classification of Turkish voice commands and to provide a new contribution in this field. In this study, a voice recognition system was developed using the Turkish Speech Command Dataset with the MFCC feature extraction method followed by a deep learning-based classification model. The dataset comprises voice recordings from various speakers, categorized into different classes. The model's training, validation, and testing were conducted with the dataset divided into three parts: training, validation, and test. The deep learning model, created using various layers such as CNN and Long Short-Term Memory networks (LSTM), aims to successfully classify voice recordings from the dataset into relevant classes using the extracted MFCC features.

2. Material and Method

The study was conducted on the Turkish Speech Command Dataset. MFCC features were extracted from the voice files of this dataset, and these features were used to develop a deep learning model. The extracted MFCC features formed the basis for training the model, after which the model's classification performance was tested in detail. This study was carried out using the Python programming language in the Jupyter Notebook environment. The Keras library was utilized for coding the deep learning model, and the Librosa library was used for audio processing. The methodology of the study is shown in Figure 1.
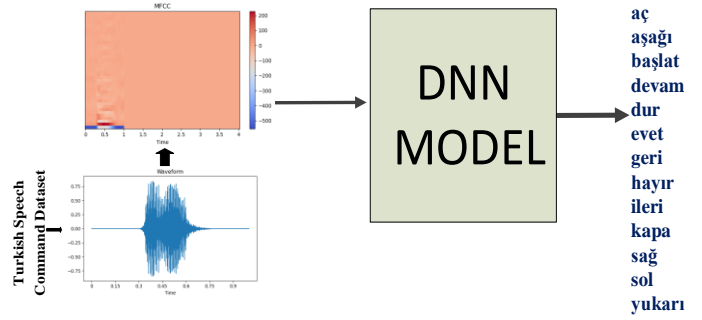
Figure 1. Overview of the Study Methodology

2.1. Dataset Description

The dataset considered in this study is specifically compiled for the recognition and processing of speech commands in Turkish. It has been published on the Kaggle platform by MURAT KURTKAYA under the name "Turkish Speech Command Dataset"[16].

The "Turkish Speech Command Dataset" consists of 14 different speech commands commonly used in daily life. These commands are as follows. The dataset contains a total of 26,484 voice recordings, each lasting 1 second and recorded at a sampling frequency of 16 kHz. The voice recordings are stored in wav format. Each voice recording is uniquely named in the format of "command-personID-specificID", which allows for the effective classification and processing of the recordings. The numerical distribution of the commands included in the dataset is shown in Figure 2.
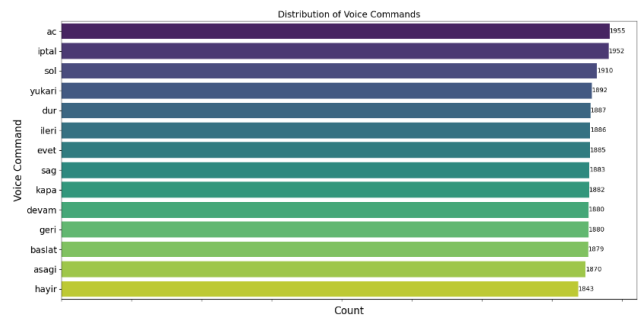
Figure 2. Number of Voice Commands in the Dataset

The "database.xlsx" file contains metadata for each sound recording, playing a crucial role in organizing the recordings by individuals and commands. This file comprises five columns: "id," "person," "type," "gender," "path." The "id" serves as a unique identifier for each sound file. The "person" column codes the identity of the individual who made the recording. "type" indicates the recorded sound command, while "gender" shows the gender of the recorder. "path" specifies the location of the sound

recording. The content of the "database.xlsx" file is detailed in Table 1.

Table 1. "database.xlsx" File Content

id	person	type	gender	path
ac_UXOD_BTMEAPU	UXOD	ac	ERKEK	dataBase\ac\
ac_UXOD_YJTEPUH	UXOD	ac	ERKEK	dataBase\ac\
ac_UXOD_CKTQBAP	UXOD	ac	ERKEK	dataBase\ac\
ac_UXOD_YCJKIMB	UXOD	ac	ERKEK	dataBase\ac\
ac_UXOD_YJKRCPO	UXOD	ac	ERKEK	dataBase\ac\
ac_UXOD_HJKNTRU	UXOD	ac	ERKEK	dataBase\ac\
ac_UXOD_XYGONEW	UXOD	ac	ERKEK	dataBase\ac\
ac_UXOD_HRWYZVK	UXOD	ac	ERKEK	dataBase\ac\
ac_UXOD_AQNLZBD	UXOD	ac	ERKEK	dataBase\ac\
asagi_UXOD_OQFUBAC	UXOD	asagi	ERKEK	dataBase\asagi\
asagi_UXOD_GSYOHNZ	UXOD	asagi	ERKEK	dataBase\asagi\
asagi_UXOD_QIUOVND	UXOD	asagi	ERKEK	dataBase\asagi\

The dataset uniquely consists of 257 individuals, among which 140 are identified as "ERKEK" and 117 as "KIZ".

2.2. Mel Frequency Cepstral Coefficients (Mfcc)

The Mel-Frequency Cepstral Coefficients (MFCC) method [13], introduced by Davis and Mermelstein, is a technique used to extract rich and meaningful features from audio signals, mimicking the logarithmic response of the human ear to sound frequencies. This method plays a critical role in speech and sound recognition systems by capturing the fundamental components of sound and their variations over time. MFCC are commonly used in speech processing and recognition applications because they model the sound spectrum in a way similar to human auditory perception [17]. The steps of MFCC are illustrated in Figure 3.
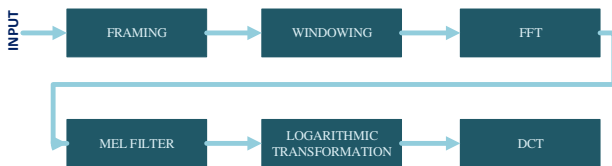
Figure 3. Steps of Mel Frequency Cepstral Coefficients (MFCC)

MFCC primarily consists of the following steps:
• Framing: The audio signal is divided into short time frames. This allows for the analysis of the audio signal in segments. Since the audio signal varies over time, analyzing a long audio recording directly is not practical. Instead, dividing the signal into short-term segments that can be considered quasi-stationary allows for a more detailed examination of each segment's characteristics.
• Windowing: Applying a window function to each frame mitigates spectral leakage that can occur at the edges of the frame (at the start and end points of the signal).
• FFT (Fast Fourier Transform): A fundamental step for analyzing the frequency content of the signal, FFT is used to identify the characteristic features of the audio signal, such as its pitch and harmonics.
• Mel Filter: Reflecting the human ear's greater sensitivity to lower frequencies and decreasing sensitivity towards higher frequencies, the Mel filter allows for a perceptually more relevant representation of the audio signal.
• Logarithmic Transformation: Since the perception of sound intensity by humans is logarithmic, this step ensures the audio signal is represented in a way that is closer to human perception.
• Cepstral Coefficients (DCT - Discrete Cosine Transform): Used to effectively capture the characteristic features of the audio signal, such as the voice tone of the speaker or the unique structure of spoken words [17,18].

2.2 Model Architecture

The model used in this study consists of a deep learning architecture designed for audio classification tasks. Initially, a convolutional layer (Conv1D) is employed to extract fundamental features from the audio signals. This layer is followed by batch normalization, which regulates the learning process and enhances stability. The max pooling (MaxPooling1D) operation reduces the size of the feature map, thus lowering the model's complexity and computational load. Additionally, dropout layers are incorporated to mitigate the risk of overfitting. An LSTM layer is added for processing time-dependent features, aiming to learn the temporal dynamics of the model. The model is trained using categorical cross-entropy loss and the Adam optimization algorithm. This approach allows the model to accurately distinguish between different classes. Further details on the model's architecture and layers are presented in Figure 4.
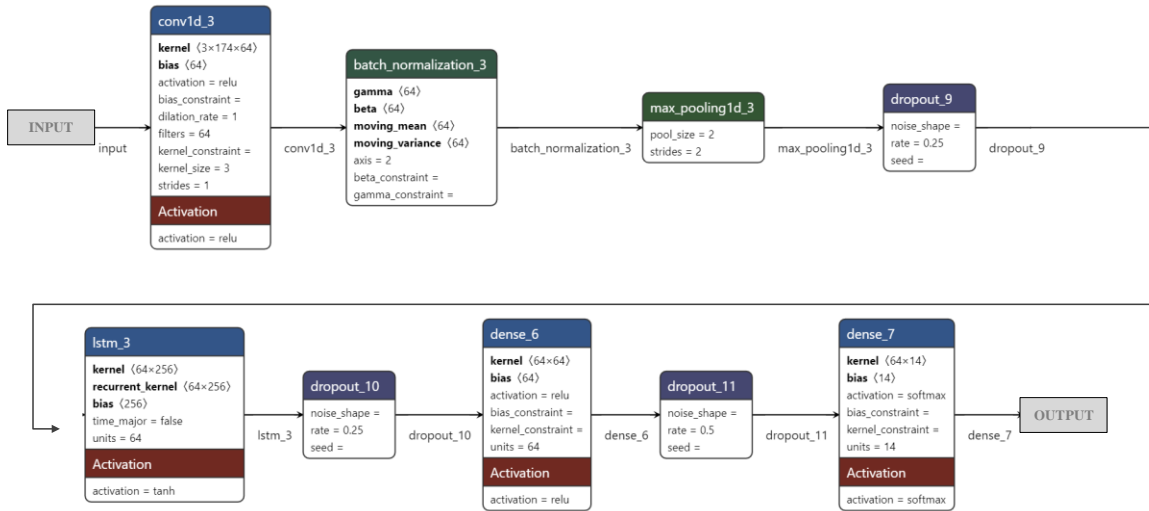
Figure 4. Convolutional Neural Network Model Used in the Study

3. Results and Discussion

To prevent overfitting on the data set, a strategy of separating the training, validation, and test sets on an individual basis has been adopted. Figure 5 illustrates how this distribution was implemented.
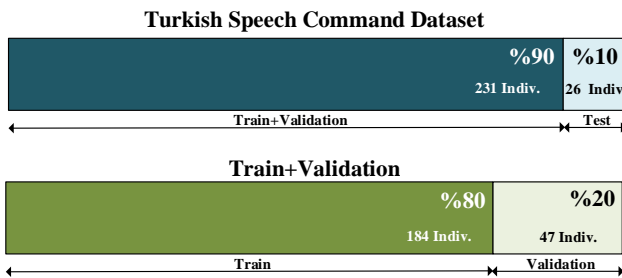
Figure 5. Distribution of the Dataset

Initially, the dataset, consisting of a total of 257 individuals, was divided into two main groups: a test set and a training set. During this division, 10% of the dataset was allocated for the test set, and the remaining 90% was used for the training set. Consequently, 26 individuals were designated for the test set and 231 for the training set.

The 231 individuals in the training set were further divided into training and validation sets. 80% of these individuals were allocated to the training set, and the remaining 20% to the validation set. Thus, the training set included 184 individuals, and the validation set included 47 individuals.

This person-based distribution resulted in 19,490 audio files for the training set, 4,410 for the validation set, and 2,548 for the test set. This methodology aimed to enhance the model's generalization ability and prevent it from memorizing person-specific characteristics. Alternatively, methods such as K-Fold Cross Validation can be used to evaluate the model's performance more reliably. This method measures the model's overall performance more accurately by training and testing it multiple times on different subsets of the dataset. However, in this study, a person-based split method was preferred because this approach aims to prevent the model from memorizing person-specific features and to enhance its generalization ability.

There are various versions of MFCC filter banks, each with different numbers of filters and their amplitudes. A commonly used filter bank, originally developed for speech analysis, consists of 40 filters in the Mel band-pass filter. This filter, like the human ear's perception of speech, aims to extract a non-linear representation of the speech signal. The conventional Mel filter bank is made up of 40 triangular filters. In this study, a Mel filter bank comprising 40 filters was used to extract meaningful features from the audio signals. These features were then used as inputs to the model.

3.1. Evaluation of the Model's Performance

The model was trained on a total of 19,490 training samples and validated with 4,410 validation samples. The validation and loss graphs related to the model are shown in Figure 6.
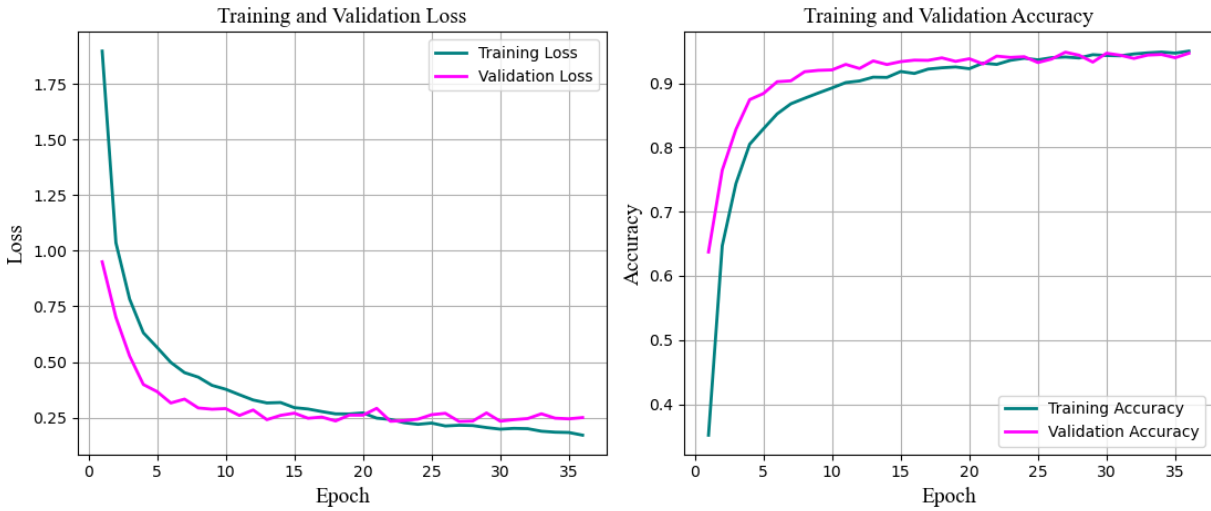
Figure 6. Validation and Loss Graphs of the Model

Training was planned for a total of 150 epochs, but due to the "early stopping" criteria, it was terminated at the 36th epoch. Early stopping halts the training process when the model's performance on the validation set does not improve over a certain period. Throughout the training process, both training and validation losses decreased while accuracy rates increased, indicating the effectiveness of the learning process and an improvement in the model's generalization capability.

The confusion matrix is a table used to evaluate the performance of classification algorithms. For each class, the model includes true positives (correct classification), false positives (misclassification of a sample as this class), false negatives (instances of this class being classified as another class), and true negatives (correctly identifying a non-member of this class) [19]. The classification confusion matrix of the model on the test data is shown in Figure 7.
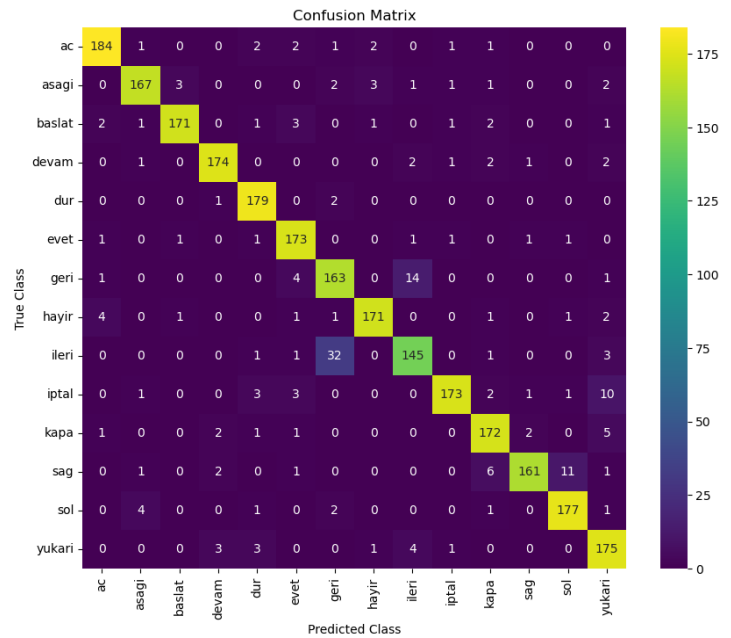
Figure 7. Classification Confusion Matrix on Test Data

The obtained confusion matrix meticulously highlights the performance of our deep learning-based voice command recognition model on the test dataset. The significant numbers along the main diagonal indicate the model's ability to recognize various voice commands with high accuracy, showcasing its robust training and generalization capabilities. Notably, the high classification accuracy rates for commands such as 'ac', baslat, 'devam', and 'dur' demonstrate the model's clear distinction and proper learning of these commands.

However, the low performance between the 'geri' and 'ileri' commands is due to their acoustic similarity. This makes it difficult for the model to distinguish between these two commands. To mitigate the impact

of this low performance on the model's overall success and to improve their performance, several strategies can be applied. Firstly, collecting more data for the 'geri' and 'ileri' commands can help the model learn these commands better. Additionally, using data augmentation techniques can increase the diversity of the existing dataset, thereby improving the model's generalization capability.

The model has demonstrated 92.30% accuracy across 2584 samples in the test set, indicating its capability to classify unseen data with a high accuracy rate. Table 2 includes metrics such as precision, recall, and F1-score for each class. These metrics illustrate how accurately the model predicts the classes and the balance of performance among them. The 'Precision' metric for each class denotes the rate at which the model accurately predicts that class; 'Recall' indicates the proportion of correctly predicted samples among all samples belonging to that class. The 'F1-Score', calculated as the harmonic mean of precision and recall, reflects the model's balanced performance across all classes. The 'Support' column shows the number of samples for each class, representing the sample size used in the calculation of these metrics.

Overall, the model maintains high precision and recall values for most classes. Although there might be performance variations among some classes, the model generally exhibits a balanced performance. The performance on both validation and test sets indicates a high generalization capability and successful avoidance of overfitting.

Table 2. Classification Performance Metrics by Voice Commands

Command	Precision(%)	Recall(%)	F1 Score(%)	Support
ac	95	95	95	194
asagi	95	93	94	180
baslat	97	93	95	183
devam	96	95	95	183
dur	93	98	96	182
evet	92	96	94	180
geri	80	89	84	183
hayir	96	94	95	182
ileri	87	79	83	183
iptal	97	89	93	194
kapa	91	93	92	184
sag	97	88	92	183
sol	93	95	94	186
yukari	86	94	90	187

When Table 2 is examined, it is observed that the model demonstrates impressive performance in classes such as 'ac', 'asagi', and 'baslat', with precision and recall values reaching up to 95%. However, in certain classes like 'geri' and 'ileri', these metrics are comparatively lower, indicating the challenges the model faces in distinguishing these commands. The recall value for the 'geri' class is 89%, while for 'ileri', this value is 79%, suggesting the model differentiates 'geri' more accurately than 'ileri'.

4. Conclusion and Suggestions

The deep learning model developed in this study possesses an effective ability to recognize and classify Turkish voice commands. The model has achieved a high overall accuracy rate of 92.30%. A methodological innovation of this study is the person-based separation process of the training, validation, and test sets, which has significantly contributed to enhancing the model's generalization capability. This approach has prevented the model from memorizing person-specific features, enabling it to exhibit a robust and generalizable classification performance. Although some classes like 'geri' and 'ileri' show lower performance, the model generally displays a balanced performance. This study proves the applicability and effectiveness of deep learning models in the development of voice recognition and classification systems. Future work is expected to further improve the model and test it on various voice datasets.

Statement of Research and Publication Ethics

The study is complied with research and publication ethics.

References

[1] R. M. Hanifa, K. Isa, and S. Mohamad, "A review on speaker recognition: Technology and challenges," *Computers & Electrical Engineering*, vol. 90, p. 107005, 2021.

[2] F. Afandi and R. Sarno, "Android application for advanced security system based on voice recognition, biometric authentication, and internet of things," *in 2020 International Conference on Smart Technology and Applications (ICoSTA)*, Feb. 2020, pp. 1-6.

[3] A. Esteva, K. Chou, S. Yeung, N. Naik, A. Madani, A. Mottaghi, and R. Socher, "Deep learning-enabled medical computer vision," *NPJ Digital Medicine*, vol. 4, no. 1, p. 5, 2021.

[4] C. Li, X. Li, M. Chen, and X. Sun, "Deep learning and image recognition," in *2023 IEEE 6th International Conference on Electronic Information and Communication Technology (ICEICT)*, July 2023, pp. 557-562.

[5] Y. Celik, M. Talo, O. Yildirim, M. Karabatak, and U. R. Acharya, "Automated invasive ductal carcinoma detection based using deep transfer learning with whole-slide images," *Pattern Recognition Letters* vol. 133, pp. 232-239, 2020.

[6] K. S. Tai, R. Socher, and C. D. Manning, "Improved semantic representations from tree-structured long short-term memory networks," arXiv preprint arXiv:1503.00075, 2015.

[7] M. Soori, B. Arezoo, and R. Dastres, "Artificial intelligence, machine learning and deep learning in advanced robotics, A review," Cognitive Robotics, 2023.

[8] Z. Bai and X. L. Zhang, "Speaker recognition based on deep learning: An overview," *Neural Networks*, vol. 140, pp. 65-99, 2021.

[9] S. Shon, S. Mun, W. Kim, and H. Ko, "Autoencoder based domain adaptation for speaker recognition under insufficient channel information," *arXiv preprint arXiv:1708.01227*, 2017.

[10] P. Dhakal, P. Damacharla, A. Y. Javaid, and V. Devabhaktuni, "A near real-time automatic speaker recognition architecture for voice-based user interface," *Machine Learning and Knowledge Extraction*, vol. 1, no. 1, pp. 504-520, 2019.

[11] M. D. Shakil, M. A. Rahman, M. M. Soliman, and M. A. Islam, "Automatic Isolated Speech Recognition System Using MFCC Analysis and Artificial Neural Network Classifier: Feasible For Diversity of Speech Applications," in *2020 IEEE Student Conference on Research and Development (SCOReD)*, Sept. 2020, pp. 300-305.

[12] H. Dolka, A. X. VM, and S. Juliet, "Speech emotion recognition using ANN on MFCC features," in *2021 3rd International Conference on Signal Processing and Communication (ICPSC)*, May 2021, pp. 431-435.

[13] S. Davis and P. Mermelstein, "Comparison of parametric representations for monosyllabic word recognition in continuously spoken sentences," *IEEE Transactions on Acoustics, Speech, and Signal Processing*, vol. 28, no. 4, pp. 357-366, 1980.

[14] M. Deng, T. Meng, J. Cao, S. Wang, J. Zhang, and H. Fan, "Heart sound classification based on improved MFCC features and convolutional recurrent neural networks," *Neural Networks*, vol. 130, pp. 22-32, 2020.

[15] E. Rejaibi, A. Komaty, F. Meriaudeau, S. Agrebi, and A. Othmani, "MFCC-based recurrent neural network for automatic clinical depression recognition and assessment from speech," *Biomedical Signal Processing and Control*, vol. 71, p. 103107, 2022.

[16] M. Kurtkaya, "Turkish Speech Command Dataset [Data set]," Kaggle, 2020. [Online]. Available: https://www.kaggle.com/murat-kurtkaya/turkish-speech-command-dataset

[17] Z. K. Abdul and A. K. Al-Talabani, "Mel Frequency Cepstral Coefficient and its applications: A Review," *IEEE Access*, 2022.

[18] T. Maka, "Change point determination in audio data using auditory features," *International Journal of Electronics and Telecommunications*, vol. 61, no. 2, pp. 185-190, 2015.

[19] M. Tripathi, "Analysis of convolutional neural network based image classification techniques," *Journal of Innovative Image Processing (JIIP)*, vol. 3, no. 02, pp. 100-117, 2021.

[20] Anjana, J. S., and Poorna, S. S., "Language identification from speech features using SVM and LDA," in *2018 International Conference on Wireless Communications, Signal Processing and Networking (WiSPNET)*, Mar. 2018, pp. 1-4.

[21]   C. Ozdemir and Y. Dogan, "Advancing brain tumor classification through MTAP model: an innovative approach in medical diagnostics," *Medical & Biological Engineering & Computing*, pp. 1-12, 2024.

[22]   B. S. P. Laksono, T. Syaifuddin, and F. Utaminingrum, "Voice Recognition to Classify 'Buka' and 'Tutup' Sound to Open and Closes Door Using Mel Frequency Cepstral Coefficients (MFCC) and Convolutional Neural Network (CNN)," *Journal of Information Technology and Computer Science*, vol. 9, no. 1, pp. 58-66, 2024.

[23]   C. Ozdemir, "Adapting transfer learning models to dataset through pruning and Avg-TopK pooling," *Neural Comput & Applic.*, vol. 36, pp. 6257–6270, 2024. https://doi.org/10.1007/s00521-024-09484-6

[24]   C. Ozdemir, "Classification of brain tumors from MR images using a new CNN architecture," *Traitement du Signal*, vol. 40, no. 2, pp. 611-618, 2023. https://doi.org/10.18280/ts.400219

Effect of Fly Ash and Metakaolin Substituted Forms on Structural Properties in Light Mortar with Pumice Aggregate

Fatime Zehra ÇİÇEK[1], Recep Kadir PEKGÖKGÖZ[1*], Sümeyye Büşra KAZANASMAZ[1], Ali SARIIŞIK[1], Fatih AVCİL[2]

[1]*Department of Civil Engineering, Harran University, Şanlıurfa, Türkiye*
[2]*Department of Civil Engineering, Bitlis Eren University, Bitlis, Türkiye*
(ORCID: 0000-0002-0599-410X) (ORCID: 0000-0002-3083-2241) (ORCID: 0009-0009-3255-8213)
(ORCID: 0000-0001-7698-6134) (ORCID: 0000-0001-6550-550X)

Abstract
In this study, experimental tests were conducted on composite mortars in different forms prepared using lime, pumice, fly ash, and metakaolin. This research aims to recycle fly ash produced as industrial waste and produce a building material that is durable, lightweight, and provides good insulation. In the composite structure mortar mixture designs prepared for the experiments, CEN standard sand was replaced with Nevşehir pumice (0.5-4 mm) at the rates of 10%, 20%, and 30%, respectively, and fly ash-metakaolin was replaced with the cement at the rates of 10%, 20%, and 30%, respectively. A total of 13 different mixtures were prepared. Unit volume mass test, Ultrasonic test, water absorption test, compressive strength test, flexural strength, thermal conductivity coefficient test, scanning electron microscope (SEM) analysis, and thermogravimetric - differential thermal (TGA/DTA) analysis were performed on the prepared samples. As a result of the research, it was determined that the mortar mixture obtained by substituting 30% pumice with standard sand and 30% fly ash and metakaolin with cement provided the highest compressive strength, lowest dry unit volume weight, and thermal conductivity coefficient compared to other mortar mixtures.

1. Introduction

In recent years, it has been observed that cement mortars in our country are insufficient to provide the required performance in construction applications in many respects. For this reason, the use of new-generation composite cement mortars is becoming widespread. Mortars used in the construction industry are generally normal-weight mortars prepared with cement, aggregate, water, and various chemical additives [1]. However, many R&D (Research and Development) studies are ongoing to improve the technical properties of new-generation composite mortars with lightweight aggregates with different characteristics and different binder uses [2]. Studies continue to improve the properties of plaster mortar by substituting alternative materials for both cement

and sand [3]. One of these alternative materials is pumice, a lightweight aggregate. Pumice aggregate is generally used in the construction industry in the world and in Türkiye. The main reason for this is its low unit volume weight, high heat and sound insulation, air-conditioning feature, excellent acoustic feature, elasticity against earthquake load and behavior, and being more economical than its alternatives. The use of lightweight aggregates in cementitious mortars is increasing significantly due to the energy savings they provide in production, transportation, heat, and sound insulation [4]. Since the earthquake forces affecting the structures vary in proportion to the weight of the structures, it is extremely important to use lightweight materials to reduce the loss of life and property, so that the structures are less affected by earthquakes. For this

---

reason, the importance of using lightweight aggregate in cementitious mortars is better understood. Particularly porous lightweight aggregates are an important raw material in the development of thermal insulating mortars [5]. In this study, pumice was substituted with CEN standard sand, and fly ash, and metakaolin were substituted with cement. The materials we produce are intended to be economical, provide heat and sound insulation, have high strength, and are lightweight. Rahman et al., in their study with pumice, showed that the samples produced had 9.8% higher compressive strength and 36% lower porosity than the control sample [4].

Lime was one of the most common building materials used as a binder in the production of mortar until the 1990s. It is known that lime was used as a binder in all historical buildings that have survived to the present day [7, 8]. It is known that Pozzolanas, which consist of natural and artificial substances that give hydraulic properties to mortars when mixed with lime, have been used in the construction of water-resistant structures in water and humid regions since ancient times [8]. In their study, Gülbe et al. examined the effect of white cement on the properties of lime mortars. They determined that the mechanical strength of the mortar increased significantly as the amount of cement in lime mortar mixtures increased [9]. Veiga et al. created separate mortar mixtures with air lime, natural hydraulic lime, white cement, silica fume, metakaolin, and natural pozzolana from the Cabo Verde region. They investigated the experimental application and performance evaluation of mortars with mortars with added additives. As a result, they observed the highest compressive strength in lime-white cement mortars in hardened mortar samples [10].

With the studies carried out in the academic world, due to environmental protection and sustainable construction requirements in the future; It has been shown that the use of by-products such as fly ash, granulated blast furnace slag, silica fume, rice husk ash and metakaolin in cement and concrete has gained great importance [11]. Turk et al. stated that generally the use of these mineral additives reduces and improves permeable voids through micro-filling effect, pozzolanic reaction, and densification of the cement paste-aggregate interface area [12]. Using fly ash instead of some cement also contributes to the protection of the environment by reducing the amount of natural raw materials used in cement production [13]. In this paper, fly ash and metakaolin waste materials were used as binders. Fly ash is the waste material formed by burning hard coal in thermal power plants built to produce energy and kept in chimneys with the help of filters. Fly ashes alone have little to no binding properties. For this reason, they are combined with slaked lime to create a chemical reaction and gain hydraulic binding properties. If fly ashes contain lime components in their structure, their strength increases as a result of their interaction with water, and they can gain durability. The increases in strength values that may occur very slowly in fly ashes form the basis of the pozzolanic properties of fly ashes [14]. Fly ashes, which have very high surface area values, do not conduct heat and electricity well because they are empty and spherical in micro dimensions. Therefore, fly ashes are known to be good insulators. Metakaolin is a substance obtained as a result of the calcination of clay and used in many areas of concrete production. [11]. Ahmed et al., stated in their study that metakaolin is an environmentally friendly alternative binder to Portland cement [15]. Various studies have proven that metakaolin contributes to the improvement of the properties of mortars by combining with calcium hydroxide, thanks to the high silica and alumina content it contains [15], [16].

2. Material and Method

In the research conducted, in the production of the control mortar series; CEM II A-LL 42.5 R Portland calcareous composite cement, lime, and CEN standard sand complying with TS EN 196-1 [17] were used. It is known that hydrated lime improves the workability and adhesion properties of mortars. Many studies have been conducted on how the use of hydrated lime affects the water requirement in mortars. It has been determined that in the mortars created by mixing a small amount of lime (0%~20%) with natural pozzolans, the lime particles fill the gaps between the natural pozzolan particles by acting as a filler. According to this evaluation, the water needs of lime-pozzolan mixtures are not higher than natural pozzolan mixtures. However, it is assumed that after the lime rate exceeds 20%, more water will be needed to wet the lime particles and fill the gaps between the particles [18]. For these reasons, the lime rate was kept constant at ~14% in this study. The basic characteristics of the lime used are given in Table 1.

Table 1. Basic characteristics of lime

Basic Characteristics	Performance
Grain Size Distribution	
0.009 mm	≤7
0.2 mm	≤2
Volume Constancy	≤2
Penetration/Water requirement	≥10 and ≤50
CaO+MgO	≥80
MgO	≤5
CO_2	≤7
SO_3	≤2
Free Lime	≥65

physical and chemical properties of the cement used are given in Table 2.

Table 2. Physical and mechanical properties of cement

Fineness (45 µm, above sieve, %)		5.7
Specific mass (g/cm^3)		3.00
Specific surface (cm^2/g)		3997
The initial setting of cement		2h-50 min
The final setting of cement		3h-30 min
Compressive strength (MPa)	Day 2	22.00
	Day 28	51.70

As shown in Figure 1, Nevşehir pumice (0.5-4 mm), fly ash, and metakaolin were used in the proportions of 10%, 20%, and 30% in the mortar mixture designs in the composite structure. The
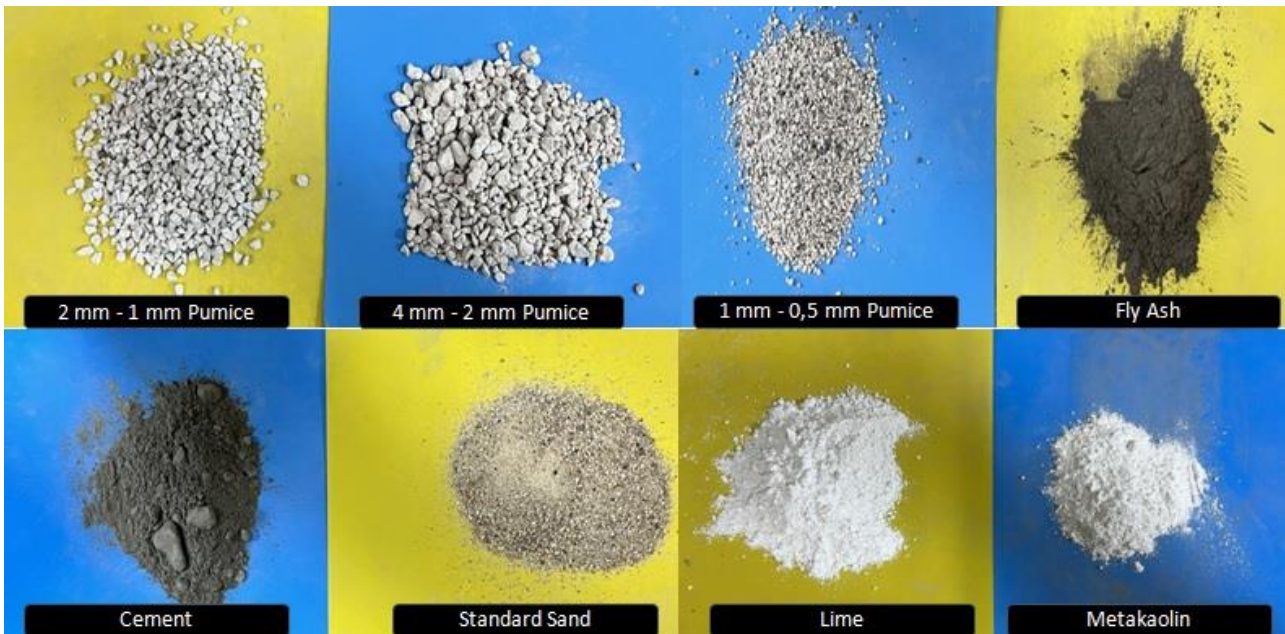
Figure 1. Materials used in mixtures

To provide lightness to the produced composite mortars, 3 different mixtures were prepared by substituting pumice at 10%, 20%, and 30% of the sand volume instead of standard sand. The Nevşehir pumice used is between 0.5 and 4 mm in size and the physical properties of each granulometry have been determined by experiments and are shown in Table 3. The sieving method of Nevşehir pumice was made in accordance with TS EN 933-1 [19] standard. TS EN 1097-3 [20] and TS EN 1097-6 [21] standards were used to determine the physical properties of aggregates. 9 different mixtures were

prepared by substituting fly ash, metakaolin, and fly ash-metakaolin as binders in the proportions of 10%, 20%, and 30% of the cement volume instead of cement. A total of 13 different composite mortar mixtures were produced.

Table 3. Physical Properties of Nevşehir Pumice

	Aggregate Size (mm)		
	1-0.5	2-1	4-2
Saturated unit volume mass (g/cm³)	1.13	1.08	1.00
Dry unit volume mass (g/cm³)	0.91	0.85	0.77
Water absorption (%)	23.59	26.35	30.11
Compact bulk density (g/cm³)	0.485	0.475	0.469
Loose bulk density (g/cm³)	0.422	0.448	0.451
Aggregate moisture content (%)	0.30	0.30	0.40

City tap water was used in all mixtures. The chemical properties of pumice, fly ash, and metakaolin used in the mixtures are given in Table 4, and their specific mass is given in Table 5.

Table 4. Chemical Properties of Pumice, Fly ash, and Metakaolin

Contents(%)	SiO_2	Al_2O_3	Fe_2O_3	CaO	MgO	P_2O_5	K_2O	SO_3	SrO	Na_2O	TiO_2	SiO_2	NiO	Loss of ignition
Metakaolin	53.0	43.1	0.7	0.5	0.1	0.1	0.1	0.0	0.0	0.1	2.0	0.0	-	0.2
Fly Ash	28.4	14.6	11.4	23.3	2.2	0.1	1.4	6.7	0.1	0.4	0.6	0.1	0.1	10.6
Pumice	73.2	12.3	1.1	0.7	0.1	-	4.2	0.0	-	3.6	0.1	0.0	-	4.5

2.1. Mixture Calculation

The water-solid ratio in the mixtures was kept constant at 0.20. In the mixtures, Nevşehir pumice 4-2 mm was used at a rate of 50%, 2-1 mm at a rate of 30%, and 1-0.5 mm at a rate of 20%. They are named "Control mortar "CS", Pumice "P10, P20, P30", Fly Ash "FA10, FA20, FA30", Metakaolin "MK10, MK20, MK30" and All (Pumice + Fly Ash + Metakaolin) "ALL10, ALL20, and ALL30".

Table 5. A specific mass of Fly ash, Metakaolin, and Lime

	FA	MK	Lime
Specific mass (g/cm³)	2.18	2.03	2.064

In mortar mixtures containing pumice (P10, P20, P30) and containing all components (ALL10, ALL20, ALL30), pumice was used as lightweight aggregate instead of sand by substituting 10%, 20%, and 30% of the sand volume, respectively. In mortar mixtures containing fly ash (FA10, FA20, FA30), metakaolin (MK10, MK20, MK30) and all components (ALL10, ALL20, ALL30), binders were used by substituting 10%, 20% and 30% of the cement volume. Thus, a total of 13 different mixtures (CS, P10, P20, P30, FA10, FA20, FA30, MK10, MK20, MK30, ALL10, ALL20, ALL30) were prepared. The materials used in the mortar mixture are given in Table 6.

For mortar mixtures in which only sand was used as aggregate, sand, lime, and binders were taken into the mixing bowl and mixed dry for 3 minutes. Then, 2/3 of the mixture water was added and mixed at high speed for 2 minutes. Finally, all the mixing water was added and mixed at high speed for 1 minute. In the mortar mixtures using sand and pumice as aggregates, sand and pumice aggregates of different sizes were taken into the mixing bowl, 1/3 of the mixture water was added and mixed for 3 minutes. Then, lime and binders (cement, fly ash, and metakaolin) were added and mixed at high speed for 2 minutes, using all the mixing water. For all mixtures, fresh mortar taken from the mixer was poured into 40x40x160 mm prism size and 50x50x50 mm cube molds according to TS EN 998-1 [22]. Mortar samples were compressed on the vibration table for 2 minutes and kept in the mold for 24 hours. It was then removed from the molds and left to cure in water for 7, 14, and 28 days. Unit volume mass analysis, compressive strength, flexural strength, thermal conductivity analysis, ultrasound test, water absorption test, SEM analysis, and TGA/DTA analysis were performed on the samples that completed the curing period following the standards.

Table 6. Materials Used in 1 m³ Mortar

Code	Standard sand (kg)	Lime (kg)	Cement (kg)	Water (kg)	Pumice (kg)	Metakaolin (kg)	Fly ash (kg)
CS	1000	280	400	340			
P10	900	280	400	340	100		
P20	800	280	400	340	200		
P30	700	280	400	340	300		
MK10	1000	280	360	340		40	
MK20	1000	280	320	340		80	
MK30	1000	280	280	340		120	
FA10	1000	280	360	340			40
FA20	1000	280	320	340			80
FA30	1000	280	280	340			120
ALL10	900	280	360	340	100	20	20
ALL20	800	280	320	340	200	40	40
ALL30	700	280	280	340	300	60	60

3. Results and Discussion

3.1. Compressive Strength Analysis

For each of the 13 different composite mortar mixtures prepared, the compressive strength tests of 3 cube samples of 50x50x50 mm dimensions after 7, 14, and 28 days of curing were carried out following the TS EN 1015-11 [23] standard. In these tests, the crushing operations were carried out perpendicular to the mortar casting direction in accordance with the relevant standards. In the study, the 7, 14, and 28-day compressive strength of the samples was calculated according to Equation 1. The arithmetic average of the obtained values was taken as shown in Figure 2.

$$f_c = \frac{F}{A_c} \tag{1}$$

In the statement given above; f_c is the compressive strength (MPa), F is the maximum load reached at the moment of fracture (N) and A_c is the cross-sectional area (mm²) where the pressure load is applied on the sample.
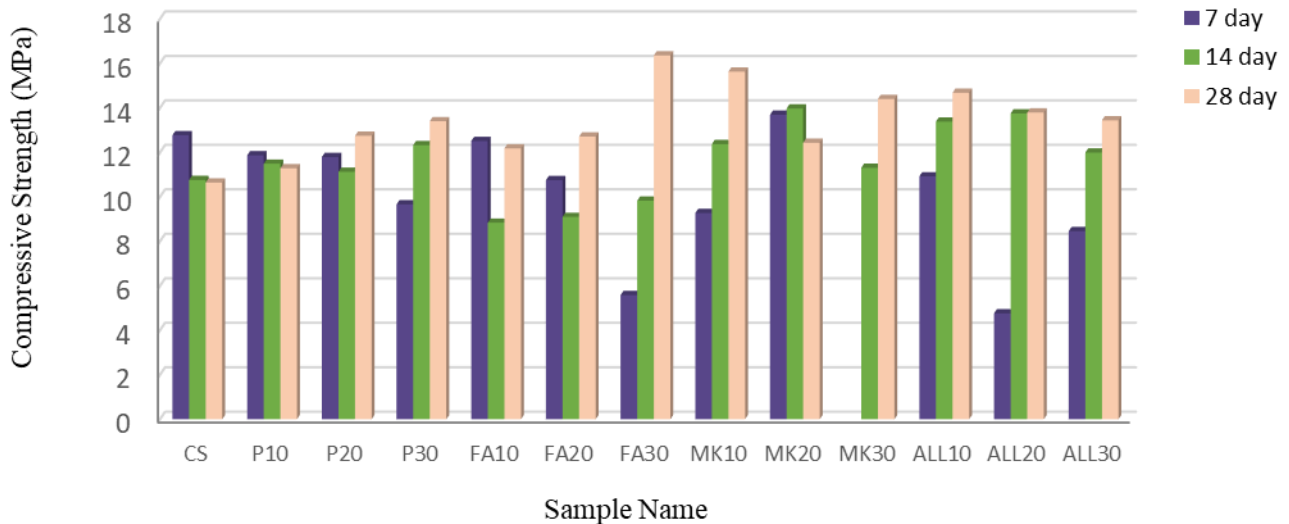
Figure 2. Compressive strength of the samples

In the TS EN 998-1 standard, four separate strength classes are prescribed for the 28-day compressive strength values of mortar groups (CS I - CS IV). The strength limits in these classes are given in Table 7:

Table 7. 28-day compressive strength values of mortar groups [1]

The strength class	28-day mortar strength range (MPa)
CS I	0.4 – 2.5
CS II	1.5 – 5.0
CS III	3.5 – 7.5
CS IV	≥ 6

When Figure 2 is examined, the highest compressive strength result of the 7-day samples belongs to the MK20 mortar mixture, and it is seen that the metakaolin used increases the compressive strength. When the results of 14-day samples were examined, the compressive strength value of the MK20 mortar mixture gave the best result with 13.97 MPa. However, the results for ALL10 and ALL20 mortar mixtures were 13.38 MPa and 13.75 MPa, respectively, and a lighter and higher compressive strength building material was obtained. When previous studies were examined, it was observed that the compressive strength increased in samples produced by substituting 10-20% metakaolin with cement in mortar production [24], [25]. However, when replacing metakaolin with cement, it has been observed that the compressive strength decreases above 30% MK [26]. Among the samples, the highest compressive strength was obtained with 16.36 MPa in the FA30 mortar mixture in the 28-day curing results. Many studies have shown that the use of fly ash deteriorates the early-age concrete strength, but generally increases the strength and durability of composites over time, as it consumes the $Ca(OH)_2$ produced during the hydration of cement and forms secondary hydrates such as CSH [27, 28, 29]. It was also observed that it had a positive effect on the 28-day compressive strength of the samples in which fly ash was used instead of cement. When the evaluation of lightweight aggregates for the production of composite mortar is analyzed, it is envisaged in the TS EN 998-1 standard that mortars with low unit volume mass values will be included in the CS I and CS II classes in terms of 28-day compressive strength class [2]. When the 7, 14, and 28-day compressive strength values of the ALL20 mortar mixture, in which pumice was used as lightweight aggregate,

were examined, it was seen that they were 4.76 MPa, 13.75 MPa, and 13.79 MPa, respectively. When this situation was evaluated, it was determined that all of the mortars we produced were included in the CS IV mortar strength class.

3.2. Flexural Strength Analysis

In the study, beam samples of 40x40x160 mm were prepared from composite mortar mixtures for flexural strength tests. When the samples completed their 14-day cure in the curing pool, flexural strength analysis was performed following TS EN 1015-11 [23] standard. The longitudinal axis of the sample was placed perpendicular to the longitudinal axis of the lower and upper loading cylinders and was placed exactly centered as shown in Figure 3. Flexural strength was calculated using Equation 2.

$$f = \frac{3 \times F \times L}{2bh^2} \qquad (2)$$

Figure 3. Three-point flexural test

In this expression; f is the flexural strength (N/mm^2), F is the ultimate load (N), L is the distance between the support cylinders (mm), b is the beam width (mm) and h is given as the beam height (mm).

In the study, the test results of the composite mortar mixtures that completed their 14-day cure are shown in Figure 4. Flexural strength is an important mechanical property in exterior plaster applications. When Figure 4 is examined, the highest flexural strength of the 14-day-old samples was obtained in the P30-coded samples. It was concluded that as the ratio of pumice used as lightweight aggregate in the mixtures increased, the flexural strength improved. When looking at the mortar mixtures using metakaolin, it was observed that their flexural strengths were lower compared to other mortar mixtures.

Figure 4. Flexural strength of the composite mortar mixtures

3.3. Water Absorption Analysis

In the water absorption test, the prepared composite mortar samples with dimensions of 50x50x50 mm were kept in the oven at 105°C for 24 hours. The composite mortar samples taken out of the oven were left to cool at room temperature. After the cooled samples were weighed and their weights were recorded, they were left to cure in 20°C water for 24 hours. The samples were removed from the water after 24 hours and placed on a dry towel to remove moisture. The samples were then weighed, and their saturated weights were recorded. The weight water absorption percentages of the samples were calculated using Equation 3.

$$\delta_k = \frac{G_d - G_k}{G_k} \times 100 \tag{3}$$

In this equation, δ_k denotes the water absorption percentage by weight (%), G_d denotes the water-saturated sample weight, and G_k denotes the oven-dry sample weight.

In the study, experiments were carried out on three cube samples each to obtain the 14 and 28-day water absorption test results of the samples. These results were then averaged and shown in Figure 5.

When the graphs in Figure 5 showing the test results are examined, according to the water absorption percentage, the highest water absorption value in the 14-day samples was obtained in the ALL30 mixture at 19.77%. It has been observed that this value is related to the dry unit volume mass value of the 14-day T30 mixture. It was observed that the water absorption value increased as the dry unit volume mass decreased. It can be said that the reason for this is that lightweight materials are more porous. Similar results were also observed in 28-day samples.

When the 14-day results of the water absorption test are examined, the water absorption amount increases by 20% in the ALL30 sample compared to the control samples, and it has the highest water absorption amount. The P10 sample gave the lowest value, measuring 6.7% less water absorption than the control sample. When evaluated regarding control samples for 28-day results, the FA30 sample gave the highest water absorption amount with a 20% increase, while the P10 sample gave the lowest value with a 3.8% decrease.
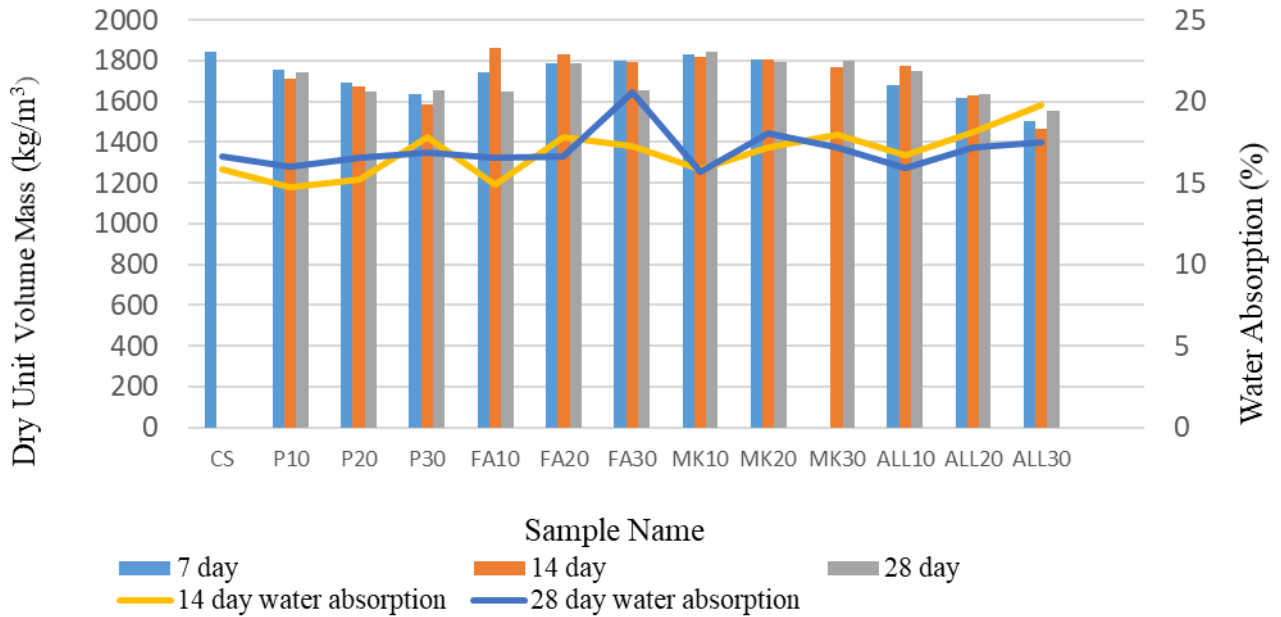
Figure 5. Water absorption test results

3.4. Dry Unit Volume Mass Analysis

In this experiment, which was carried out following the TS EN 1015-10 [30] standard, cube samples of 50x50x50 mm were left in the oven at 105 °C for 24 hours, then removed from the oven and allowed to cool at room temperature. The oven-dry weights of the cooled samples were weighed on a scale and the readings were recorded. The dry unit volume mass of the samples was calculated using Equation 5.

In this expression, ρ is the unit volume mass of the sample (kg/m³), M_{dry} is the oven-dry mass of the sample at the end of 24 hours (kg), and V is the volume of the cube samples of 50×50×50 mm size (m³).

$$\rho = \frac{M_{dry}}{V} \tag{5}$$

When the results of the unit volume mass values of the control mortar samples after 7, 14, and 28 days of curing, determined according to TS EN 12390-7, were examined, the unit volume mass value of the control sample (CS) was higher because it did not contain light aggregate. It can be seen in the graph in Figure 5 that the unit volume mass value decreases in the ALL-mixture series in which pumice, fly ash, metakaolin, and all materials are used. This is a result of reducing the amount of cement and sand in the mixtures by substituting less dense fly ash and metakaolin with cement, and standard sand with

pumice. It has been observed that the use of pumice provides lightness to a certain extent in mortar series. Binici, [31] in his study, showed the positive effect of using pumice in composite mortars on unit volume mass results. Today, both sustainability and economy will be achieved by choosing light aggregate mortars instead of traditional mortars in the interior and exterior spaces of buildings.

3.5. Thermal Conductivity Analysis

The thermal conductivity test was carried out following the ISO 22007-2 standard [32]. In this experiment, 50x50x50 mm cube samples, which were kept in the curing pool for 28 days, were kept in the laboratory until they reached the appropriate temperature before starting the experiment. The sensor was contacted to the flat and smooth surface of the 50x50x50 mm sample placed on the 3 cm diameter sensitive sensor of the Hot Disk brand device called TPS 500 S, and the temperature between the sensor and the sample was balanced and the heat conduction value (k) was obtained in W/mK. Analysis results are given in Figure 6.

Sample Name	P10	P20	P30	FA10	FA20	FA30	MK10	MK20	MK30	ALL10	ALL20	ALL30
28-day	1,122	0,909	0,828	1,097	1,135	1,093	1,154	1,120	1,065	1,065	0,904	0,759
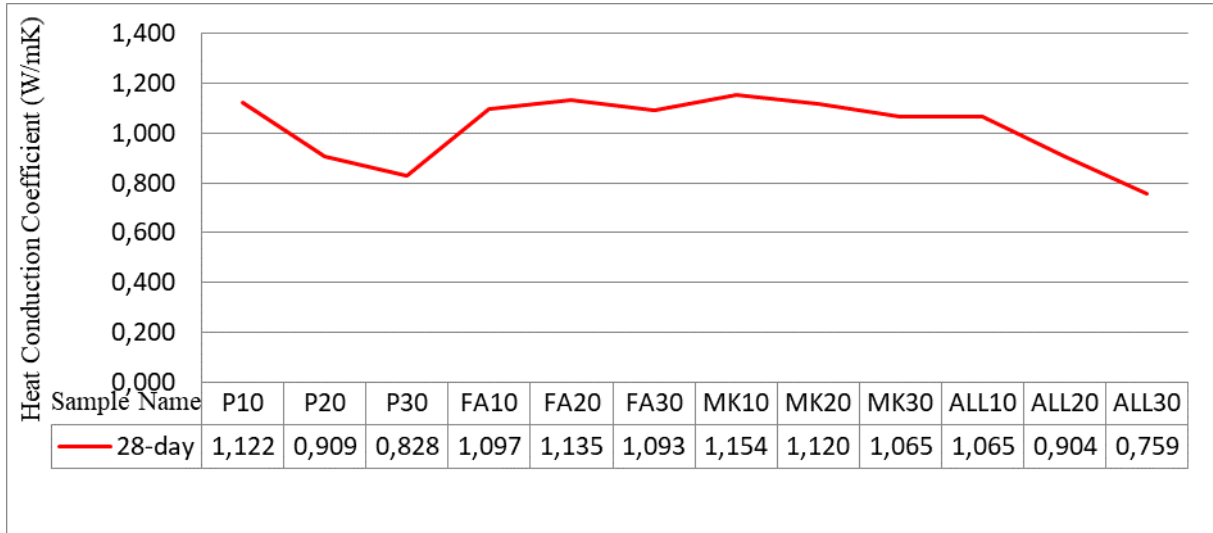
Figure 6. Thermal conductivity coefficient test results

When the results were examined, it was observed that the thermal conductivity coefficients of the samples using pumice aggregate were lower than the other samples. The lowest thermal conductivity coefficient was observed in the sample coded ALL30, and the positive effect of pumice aggregate was observed. It was understood that the reason why the thermal conductivity coefficient of the samples using pumice was lower than the other samples without pumice was due to the porosity of the pumice aggregate.

3.6. Ultrasonic Test

Ultrasound tests were carried out on the produced samples after 7, 14, and 28 days of curing, according to the TS EN 12504-4 [33] standard. First of all, the sample is placed between the probes of the UPV device, with the casting surface of the sample to be tested on top. At this location, the sound velocities of the samples were measured. In order to make the measurement results more precise, measurements were made on three cube samples of 50x50x50 mm from two different directions, and the average value was taken. Sound transmission speed was calculated by dividing the sample length by the transition speed time according to Equation 6.

$$v = \frac{l}{t} \tag{6}$$

In this expression, v is expressed in terms of sound speed (m/s), l is expressed in sample size (m) and t is expressed in transition speed time (s). The results are summarized in Figure 7.
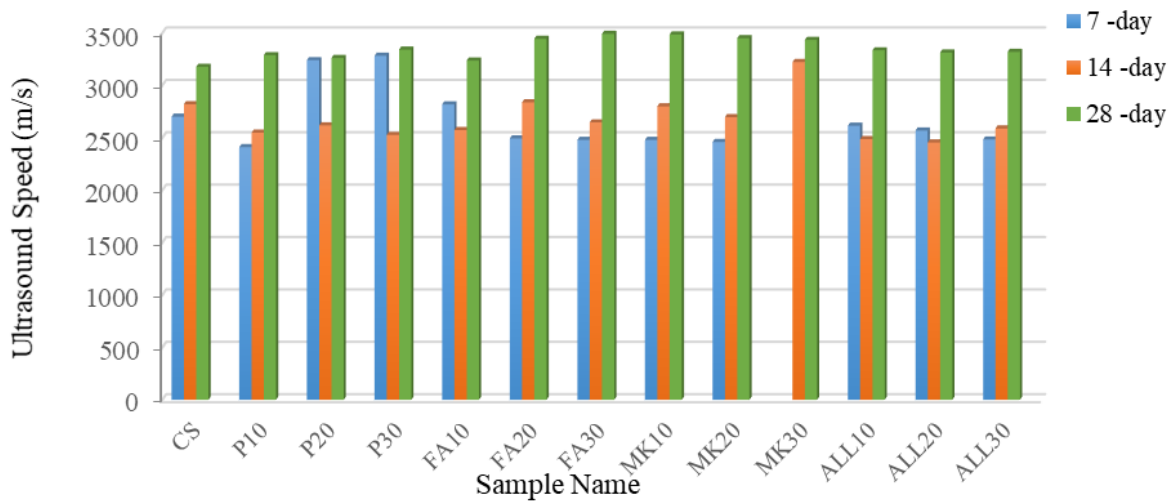
Figure 7. Ultrasound speed test results

Ultrasound testing is a method that gives an idea about the strength of materials in terms of existing voids and cracks [34]. When the ultrasound transmission rate results were examined, it was observed that the 14-day cure result was lowest in the ALL20 mortar mixture. It has been observed that the porous structure of pumice as an aggregate positively affects the sound insulation properties of the mortar. When the results of the ultrasound test are examined, taking the control samples as reference, the MK20 sample gave the lowest value with a 9% decrease for the 7-day results, while the P30 sample gave the highest value with a 17.7% increase. For 14-day results, the ALL20 sample gave the lowest value with a 13% decrease, while the MK30 sample gave the highest value with a 12.5% increase. Although there was no significant difference between the 28-day results of the samples compared to CS, the most significant increase was 9% in the FA30 sample.

In general, from the graph given in Figure 7, it can be seen that the ultrasound transmission rate values of the 28-day-old samples are higher than the 7- and 14-day-old samples. This shows that after 28 days of curing, the samples have largely completed their hydration, and their compressive strength has increased.

3.7. SEM Analysis

The morphological features of the samples were characterized using a scanning electron microscope (ZEISS EVO50 SEM) on a Secondary Electron (SE) detector at a distance of approximately 4-11 Work Distance (WD) at an acceleration voltage of 7 kV. After the test samples were subjected to the pressure test, the sample samples taken from the broken surface were carefully taken and packaged in ziplock bags, and then the samples were made conductive at a thickness of 5 ηm in a gold plating device (electron microscope system) for electron microscope imaging. Images of the test samples were taken from regions where the materials used (pumice, fly ash, metakaolin, lime, standard sand, and cement) were dense and where they contacted each other and formed interfaces. Analyzes were carried out at Harran University Science and Technology Application and Research Center (HUBTAM). The magnification ratio was chosen as 5.00KX and 10.00KX, and the cross-sectional images have a magnification ratio of 250X.

When looking at the SEM analysis in Figure 8 (a), the porous structure of the pumice draws attention to the mixture containing 10% pumice, while lime and cement grains stuck to the pores on the surface of the pumice were observed in the second image. In Figure 8 (b), samples with 10%, 20%, and 30% fly ash added, it was observed that the ashes were shaped in a spherical shape and the pores were completely covered with ashes. As the amount of fly ash increases, it is seen in the SEM images that it covers the surface of the cement in a spherical manner.
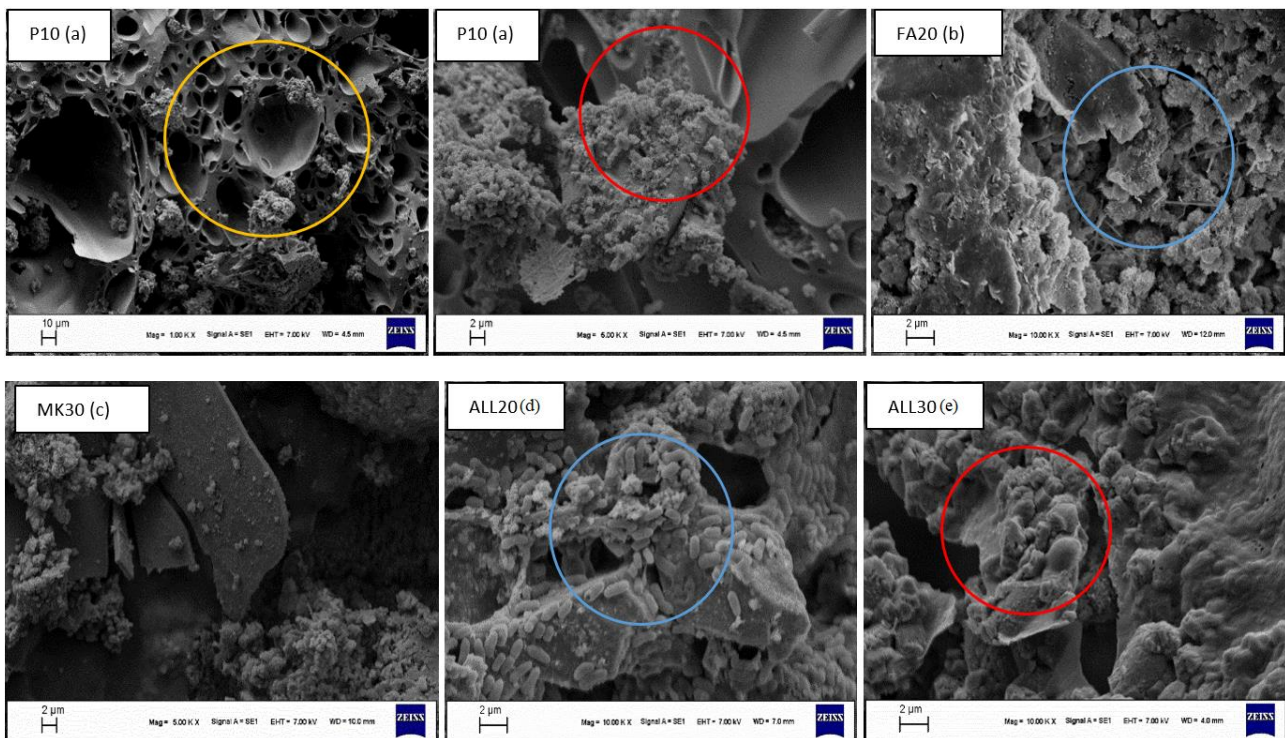
Figure 8. SEM Analysis of the samples coded P10 (a), FA20 (b), MK30 (c), ALL20 (d), and ALL30 (e)

Since pumice aggregate is a light material with a rough and porous structure, it is possible to adhere to the aggregate in the paste phase. This situation caused the interface region to not be clearly understood in the SEM images of pumice-added samples, as in some previous studies [34], [35], [36].

In the SEM images of the MK30 sample in Figure 8 (c), as the amount of metakaolin increased, metakaolin deposits were seen in the sample, and the interface that emerged when the metakaolin material seen in this mass was combined with cement was photographed. The difference in clarity in the photographs is due to the difference in elevation on the surface of the sample. Due to the presence of pumice, fly ash, and metakaolin in ALL20 and ALL30 mixtures, together with the spherical structure of fly ash and the thick and short structure of metakaolin, porosity increases were observed in the SEM images in Figure 8 (d-e) as the ratio of pumice increased.

3.8. TGA/DTA Analysis

TGA/DTA Analysis is performed to determine the changes that occur within the material as the temperature increases. The TGA experiment was conducted at Harran University Science and Technology Application and Research Center (HÜBTAM). For this analysis, samples that completed their 28-day cure in the cure pool were exposed to pressure testing. Then, the pieces taken from these samples were ground into powder. The powder pieces that were ready for testing were placed in thermo balance, the temperature was increased by 20°C per minute, and the mass losses (TGA) and energy losses (DTA) occurring in their structures were monitored for 1 hour as shown in Figure 9.
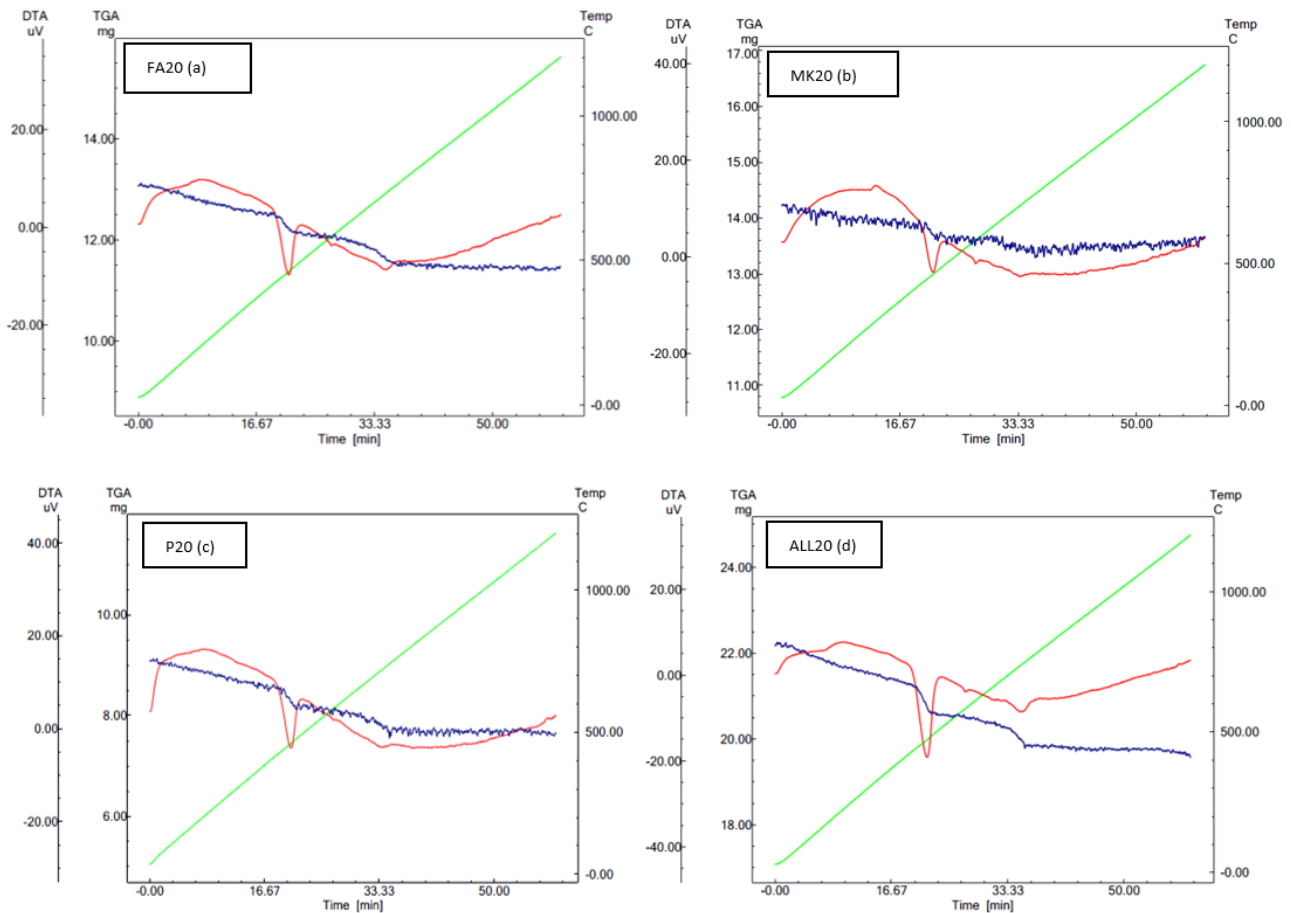
Figure 9. TGA/DTA analyzes samples coded FA20 (a), MK20 (b), P20 (c), and ALL20 (d)

With TGA/DTA analysis, endothermic and exothermic reactions of the sample against the heat it is exposed to in the experiment are determined. The red line seen in the graphs is the DTA (energy loss) line, the blue line is the TGA (mass loss) line, and the green lines are the temperature change line.

When the TGA analysis of the FA20 coded sample was examined, as seen in Figure 9(a), it was understood that there was a mass decrease in the temperature range of 680-485 °C, and in a similar case, in the MK20 coded sample, in the temperature range of 700-520 °C, as shown in Figure 9(b).

When the TGA analysis was examined, as seen in Figure 9 (c), in the P20-coded sample, a mass decrease was observed in the temperature range of 650-560°C, and a two-stage mass loss was observed in the ALL20-coded sample, as in Figure 9 (d). In the first stage, there was a mass decrease in the temperature range of 650-550°C. In the second stage, the mass decrease occurred in the temperature range of 550-430°C.

In TGA analyses, the highest mass loss occurred in the P10-coded sample and the least mass loss occurred in the MK20-coded sample. It was observed that pumice-added samples had more mass loss compared to other composite mortar samples. It is thought that the behavior of pumice aggregate against temperature is effective in this result.

According to the DTA analysis results of composite mortars, it is seen that there is an endothermic peak between 400°C and 500 °C and an exothermic peak between 750°C and 1000 °C. This peak arises from the free moisture in the system and the loss of water in the C–S–H structure. These peaks correspond to the removal of water molecules bound or free to structural compounds. When temperatures exceed 300 °C, chemically bound water begins to move away [36].

4. Conclusion and Suggestions

Within the scope of this study, Nevşehir pumice (0.5-4 mm) was replaced with CEN standard sand at the rates of 10%, 20%, and 30%, respectively, and fly ash-metakaolin was replaced with cement at the rates of 10%, 20%, and 30%, respectively. Thus, a total of 13 different mixtures (CS, P10, P20, P30, FA10, FA20, FA30, MK10, MK20, MK30, ALL10, ALL20, ALL30) were prepared. The results of the experiments are summarized below.

When the results of 28-day-old samples were evaluated according to their dry unit volume mass, as the amount of pumice increased, the dry unit volume mass decreased, while as the amount of metakaolin increased, the dry unit volume mass increased.

When the compressive strength results were evaluated, it was observed that as the ratio of pumice, fly ash, and metakaolin increased, the compressive strength increased, according to the 7, 14, and 28-day results. ALL30 sample provides the required compressive strength according to mortar strength classes and is the lightest composite mortar material.

According to flexural strength test results, P30 showed the highest flexural strength value in the beam samples, and the ALL30 sample showed the lowest value. It has been understood that pumice material increases flexural strength, while metakaolin decreases it.

It was observed that the water absorption value increased as the dry unit volume weight decreased. This is because lightweight materials are more porous.

According to the thermal conductivity coefficient results, the high thermal conductivity coefficient of the samples containing only metakaolin caused low thermal insulation, while the samples containing pumice and fly ash had a low thermal conductivity coefficient and provided high thermal insulation. Therefore, the ALL30 sample provided the best thermal insulation value.

Ultrasound transmission rate results show that the samples that completed their 28-day cure are higher than the samples that completed their 7 and 14-day cure. This shows that after 28 days of curing, the samples have largely completed their hydration, and their compressive strength has increased.

When the SEM images were examined, it was observed that there were minerals and light aggregates with a porous glassy structure, and hydrated phases such as portlandite, ettringite, and C-S-H. In the mixtures, the spherical structure of fly ash, the thick and short threadlike structure of metakaolin, and the porous structure of pumice were observed.

According to the TGA-DTA analysis results of composite mortars, the samples deteriorated in more than one stage with the use of pumice, fly ash, and metakaolin.

In light of these evaluations, it was determined that the ALL30 composite mortar mixture has high compressive strength, low dry unit volume mass, and the lowest thermal conductivity coefficient (highest thermal insulation value). Therefore, considering these features, it is thought that it can be used in the supply of mortar for the construction industry.

Conflict of Interest Statement

There is no conflict of interest between the authors.

Statement of Research and Publication Ethics

The study complies with research and publication ethics

References

[1]   O. Uğurer, Ş. O. Kalkan, and L. Gündüz, "Poli vinilalkol (PVA) lif boyutunun çimento esaslı hafif harcın özelliklerine etkisi üzerine bir inceleme", *BAUN Fen. Bil. Enst. Dergisi*, vol. 25, no. 2, pp. 543–563, 2023, doi: 10.25092/baunfbed.1126102.

[2]   E. Çapun and N. Şapcı, "Vermikülit Agreganın Kompozit Yapılı Hafif Harç Üretiminde Kullanımı Üzerine Teknik Bir Analiz", *DÜFED*, vol. 11, no. 2, pp. 307–323, 2022, doi: 10.55007/dufed.1096993.

[3]   Y. T. Altuncı and C. Öcal, "Pamuk Küspesinin Sıva Harcı İçerisinde Agrega Olarak Kullanılabilirliğinin Araştırılması", *SDÜ Fen Bil Enst. Der.*, vol. 25, no. 3, pp. 558–563, 2021, doi: 10.19113/sdufenbed.880877.

[4]   L. Gündüz, and Ş. O. Kalkan. "Pirinç Kabuğu Külünün Çimentolu Hafif Kompozit Harçlarda Dayanım Arttırıcı Katkı Olarak Kullanılması Üzerine Teknik Bir İnceleme", *Beton 2017 Kongresi Bildirileri, 13-14 Nisan, 2017, İstanbul, Türkiye*: Türkiye Hazır Beton Biriliği, 2017. pp. 575-585

[5]   N. Şapcı, & M. Sivri, "Isı Yalıtımlı Harç Üretiminde Bazı Etken Parametrelerin SPSS Yöntemi İle İncelenmesi", *KSÜ, Müh. Bil. Dergisi*, vol. 27, no. 1, pp. 1-15, 2024, doi: 10.17780/ksujes.1269727.

[6]   F. Rahman, W. Adil, M. Raheel, M. Saberian, J. Li and T. Maqsood, "Experimental investigation of high replacement of cement by pumice in cement mortar: a mechanical, durability and microstructural study" *J. Build. Eng*. 49, 104037, 2022, doi: 10.1016/j.jobe.2022.104037

[7]   H. Y. Aruntaş, M. Şahinöz, ve M. Dayı, "Çimento hamur ve harçlarında kireç kullanımının incelenmesi", *Politeknik Dergisi*, vol. 24, no. 3, pp. 1045-1054, 2021, doi: 10.2339/politeknik.801346.

[8]   T. Uğur and A. Güleç, "Harç, Sıva ve Diğer Kompozit Malzemelerde Kullanılan Bağlayıcılar ve Özellikleri", *Restorasyon ve Konservasyon Çalışmaları Dergisi*, no. 17, pp. 77–91, December 2016.

[9]   L. Gulbe, I. Vitina, and J. Setina, "The influence of cement on properties of lime mortars", *Procedia Engineering*, vol. *172*, pp 325-332, 2017, doi: 10.1016/j.proeng.2017.02.030

[10]   M. R. Veiga, A. Velosa, A. Magalhães, "Experimental applications of mortars with pozzolanic additions: characterization and performance evaluation", *Construction and Building Materials*, vol. 23, no. 1, pp 318-327, 2009, doi: 10.1016/j.conbuildmat.2007.12.003

[11]   R. Siddique and J. Klaus, J. "Influence of metakaolin on the properties of mortar and concrete: A review" *Appl. Clay Sci.*, vol. 43, no. 3–4, pp. 392-400, 2009, doi: 10.1016/j.clay.2008.11.007

[12]   K. Turk, C. Kina, M.L. Nehdi, "Durability of Engineered Cementitious Composites Incorporating High-Volume Fly Ash and Limestone Powder", *Sustainability* vol. 14, 10388. 2022, doi: 10.3390/su141610388

[13]   P. Turgut, F. Demir, and K. Türk, "Kendiliğinden Yerleşen Yüksek Dayanımlı Portland Çimentosuz Briket Malzemesi Üretimi", *Dokuz Eylül Üniversitesi Mühendislik Fakültesi Fen ve Mühendislik Dergisi*, vol. 24 no. 72, pp. 703-716, 2022, doi: 10.21205/deufmd.2022247202

[14]   M. Çetin, *Uçucu kül ve cam atıklarından üretilen seramiklerin özelliklerine ZnO katkısının etkisinin incelenmesi*, Yüksek lisans tezi, Sakarya Üniversitesi, 50, 2019.

[15]   A Ahmed, S. I. Bajahry, I. Garba, J. Abubakar, A. Lawan, A. Ocholi, and J. M. Kaura, "Strength Optimization of Metakaolin-Based Geopolymer Concrete Modified with Metabentonite Using Response Surface Method". *International Journal of Research Findings in Engineering, Science and Technology* vol. 5, pp. 21-36, 2023, doi: 10.48028/iiprds/ijrfest.v5.i1.03.

[16]   D. Gür, *Tarihi yapıların onarımında kullanılmak üzere puzolan katkılı hidrolik kireç esaslı onarım harcı üretilme olanaklarının araştırılması*, Yüksek lisans tezi, İstanbul Teknik Üniversitesi, 51, 2021.

[17]   TS EN 196-1, "Çimento Deney Metotları - Bölüm 1: Dayanım Tayini", Türk Standartları Enstitüsü, Ankara, Türkiye, 2016.

[18] C. Shi, "Studies on Several Factors Affecting Hydration and Properties of Lime-Pozzolan Cements" *Journal of Materials in Civil Engineering*, vol.13 no. 6, pp. 444-445, 2001, doi:10.1061/(asce)0899-1561(2001)13:6(441)

[19] TS EN 933-1, "Agregaların geometrik özellikleri için deneyler bölüm 1: Tane büyüklüğü dağılımı tayini- Eleme metodu", Türk Standartları Enstitüsü, Ankara, 2012.

[20] TS EN 1097-3, "Agregaların fiziksel ve mekanik özellikleri için deneyler bölüm 3: Gevşek yığın yoğunluğunun ve boşluk hacminin tayini", Türk Standartları Enstitüsü, Ankara, 1999.

[21] TS EN 1097-6, "Agregaların mekanik ve fiziksel özellikleri için deneyler - Bölüm 6: Tane yoğunluğunun ve su emme oranının tayini", Türk Standartları Enstitüsü, Ankara, 2022.

[22] TS EN 998-1, "Kâgir harcı - Bölüm 1: Kaba ve ince sıva harcı", Türk Standartları Enstitüsü, Ankara, 2017.

[23] TS EN 1015-11, "Kagir harcı- Deney yöntemleri Bölüm 11: Sertleşmiş harcın eğilmede çekme ve basınç dayanımının tayini", Türk Standartları Enstitüsü, Ankara, 2020.

[24] E. Güneyisi, M. Gesoğlu and K. Mermerdaş, "Improving strength, drying shrinkage, and pore structure of concrete using metakaolin", *Mater Struct,* vol. 41, pp. 937–949, 2008, doi: 10.1617/s11527-007-9296-z

[25] G. Görhan and G. Kürklü. "Farklı Sınıf Çimento Harcı Üretiminde Metakaolin Katkısı Kullanımının Araştırılması", *IJERAD,* vol. 7, no. 3, pp. 7–14, 2015.

[26] J. M. Khatib, E.M. Negim and E. Gjonbalaj, "High volume metakaolin as cement replacement in mortar", World J. Chem, vol. 7, no. 1, pp. 7–10, 2012.

[27] G. Li, C. Zhou, W. Ahmad, K. I. Usanova, M. Karelina, A. M. Mohamed and R. Khallaf, "Fly Ash Application as Supplementary Cementitious Material: A Review" Mater, vol. 15, no. 7, pp. 2664, 2022, doi:10.3390/ma15072664

[28] A. B. Harwalkar and S.S. Awanti, "Laboratory and field investigations on high-volume fly ash concrete for rigid pavement", *Transp. Res. Rec*, vol. 2441, no. 1, pp. 121–127, 2014.

[29] U. A. Khan, H. M. Jahanzaib, M. Khan, M. Ali, "Improving the Tensile Energy Absorption of High Strength Natural Fiber Reinforced Concrete with Fly-Ash for Bridge Girders" *KEM*. vol. 765, pp. 335-342, 2018, doi: 10.4028/www.scientific.net/kem.765.335

[30] TS EN 1015-10 "Kâgir harcı-Deney metotları- Bölüm 10: Sertleşmiş harcın boşluklu kuru birim hacim kütlesinin tayini", Türk Standartları Enstitüsü, Ankara, 2001

[31] H. Binici, "Atık Mukavva, Alçı, Pomza, Perlit, Vermikülit ve Zeolit ile Yapılan Kompozitlerin Yangın Direncinin Araştırılması", *cukurovaummfd,* vol. 31, no. 1, pp. 1–10, 2016, doi: 10.21605/cukurovaummfd.317714.

[32] ISO 22007-2 Plastics- Determination Of Thermal Conductivity and Thermal Diffusivity- Part 2: Transient Plane Heat Source (Hot Disc) Method, 2015.

[33] TS EN 12504-4. Yapılarda beton deneyleri-Bölüm 4: Ultrasonik atımlı dalga hızının tayini. Türk Standartları Enstitüsü, Ankara, Türkiye, 2021

[34] Ş. Ekmen, *Uçucukül esaslı hafif geopolymer harçların taze ve sertleşmiş özelliklerinin incelenmesi, modellenmesi ve optimizasyonu*, Doktora tezi, Harran Üniversitesi, 129, 2021.

[35] İ. B. Topçu, and T. Uygunoğlu, "Properties of autoclaved lightweight aggregate concrete", *Built and Environ.*, vol. 42 no. 12, pp. 4108-4116, 2007, doi: 10.1016/j.buildenv.2006.11.024

[36] Nergis, D. D. B., Abdullah, M. M. A. B., Sandu, A. V., &Vizureanu, P. "XRD and TG-DTA study of new alkali activated materials based on fly ash with sand and glass powder," *Mater*, vol. 13, no. 2, pp. 343, 2020 doi: 10.3390/ma13020343

Phenylsulfonylpiperazines as α-Glucosidase Enzyme Inhibitors: Design, Synthesis, DFT Calculations, Docking and ADME Studies

Kerem BURAN [1*], Yiğit İNAN [2], Gülşah Selin AKYÜZ [3], Celile DERVİŞOĞLU[5] ÖZDEMİR [4,5], Fatih KOCABAŞ [6]

[1] Department of Pharmaceutical Chemistry, Hamidiye Faculty of Pharmacy, University of Health Sciences, 34668 İstanbul, Türkiye.
[2] Department of Pharmacognosy, Hamidiye Faculty of Pharmacy, University of Health Sciences, 34668, İstanbul, Türkiye.
[3] Department of Pharmacognosy, School of Pharmacy, Bahçeşehir University, İstanbul, Türkiye.
[4] Department of Chemistry, Institute of Science, Marmara University, 34720 Goztepe, İstanbul, Türkiye.
[5] Department of Analytical Chemistry, Faculty of Pharmacy, Istanbul Health and Technology University, 34445, Beyoglu, İstanbul, Türkiye.
[6] Department of Genetics and Bioengineering, Faculty of Engineering, Yeditepe University, Istanbul, Türkiye.

(ORCID: 0000-0002-7783-7533) (ORCID: 0000-0002-3253-0124) (ORCID: 0000-0002-8455-8970)
(ORCID: 0000-0001-8603-3820) (ORCID: 0000-0001-8096-6056)

Abstract

Diabetes mellitus (DM) is one of the most common diseases affecting people all over the world. An important treatment for DM is the inhibition of the α-glucosidase enzyme. A wide range of biological activities of piperazine and sulfonamide moieties are known. In this study, five phenylsulfonyl piperazine derivatives were synthesized. Their inhibitory capacities were evaluated. The analogues (**1-5**) showed a good degree of inhibition of α-glucosidase enzyme. Compound **1** has the highest inhibition potential for the α-glucosidase enzyme. Its inhibition percentages (83.52±0.41) were higher than the reference molecule quercetin (81.41±0.02). *In silico* molecular docking studies were performed for the most potent compound **1** for α-glucosidase enzyme to determine possible protein-ligand interactions. Furthermore, a DFT study was carried out for the evaluation of the quantum mechanical and electronic properties. Finally, ADME profiles of the compounds were theoretically analyzed.

1. Introduction

Diabetes mellitus (DM) is one of the most common metabolic diseases in the world. DM is characterized by low insulin levels and high blood glucose levels. In the case of damage to pancreatic cells, abnormalities in insulin secretion occur and this phenomenon is called hyperglycemia. Hyperglycemia causes significant health problems in vital organs such as, blood vessels, kidneys, eyes, brain, and heart [1]. DM is mainly categorized into two subtypes which are Type 1 (T1DM) and Type 2 (T2DM) DM.

The low level of insulin is the major reason for these subtypes of DM [2]. There are some factors that cause high levels of glucose in the human body such as high activity of α-amylase and α-glucosidase enzymes. α-amylase (E.C. 3.2.1.) is an enzyme that breaks down carbohydrates like starch to monosaccharides in the human body. Further degradation is continued to glucose by the α-glucosidase enzymes. Because of their important role in carbohydrate digestion process, inhibition of these enzymes can decrease degradation of carbohydrate, postpone glucose consumption, and decrease blood glucose level [3]. Therefore,

inhibition of these enzymes has become an important strategy to treat T2DM. Acarbose, Voglibose and Miglitol have been discovered and used as drug for treatment of T2DM. Although there are some side-effects such as flatulence and diarrhea. Acarbose is used for treatment of T2DM worldwide [4].

The piperazine heterocycle is one of the most important moieties for drug molecules. It can be used as a main scaffold or be moiety for molecular hybridization. Vitaku *et al*. investigated that drugs which were approved by U.S. Food and Drug Administration (FDA) [5] . According to this study, piperazine heterocycle is the third most common nitrogen heterocycles which participated in the FDA approved drugs. Additionally, piperazine derivatives have different pharmacological activities such as anticancer [6], anticonvulsant [7], antianginal [8], anti-inflammatory [9], carbonic anhydrase enzyme inhibitor [10]. Another important functional structure with various biological activities is sulfonyl structures. The sulfonyl group either contributes to the biological activities of the molecules to which they are attached, or the derivatives have biological activities. These biological activities are anti-inflammatory activity [11], anticancer [12] and antidiabetic [13].

In this study, it was investigated that inhibition potential of sulfonyl-piperazine molecules against α-glucosidase enzyme. Docking studies and Density Functional Theory (DFT) calculations were done for correlating biological activity and molecular properties. Additionally, for investigation of ADME properties of compounds bioavailability radar charts were calculated. While Xiao *et al*. [14] synthesized two phenylsulfonyl piperazine derivatives without probing their biological activities, and Abbasi *et al*. [15] synthesized and reviewed similar compounds without focusing on their α-glucosidase inhibition, this study bridges these gaps. Emphasis is placed on compound 2, which earlier reports have not evaluated for α-glucosidase enzyme activity or through Density Functional Theory (DFT) calculations. Our comprehensive approach includes docking studies and DFT calculations to correlate biological activities with molecular properties, as well as ADME analysis via bioavailability radar charts to predict pharmacokinetic behavior. This research could pave the way for improved treatments of T2DM with optimized therapeutic profiles and reduced side effects.

2. Material and Method

2.1. Chemicals

2.1.1. Materials and reagents

All the chemicals were purchased from Fluka Chemie AG Buchs and Sigma Aldrich and used without further purification. Reactions were monitored by thin-layer chromatography (TLC) on silica gel 60 F254 aluminium sheets. The mobile phase was ethyl acetate: *n*-Hexane (1:1), and detection was made using UV light. ^{1}H NMR and ^{13}C NMR spectra were registered in CDCl$_3$ on Agilent 400/54 (400 MHz) NMR. The mass spectra were obtained on Agilent 6530 Accurate Mass Q-TOF LC/MS.

2.1.2. General procedure for the synthesis of compounds 1-5

Triethylamine (3.0 eq) was added slowly to a solution of piperazine derivatives (1.0 eq) CH$_2$Cl$_2$ at 0 °C, then to this was added benzene sulfonyl chloride (1.0 eq) and stirred for 2 hours. The completion of the reaction was checked with TLC (*n*-hexane and ethyl acetate (1:3)). After the reaction was finished, the solution was quenched with water and extracted with CH$_2$Cl$_2$. The combined organic layer was dried over anhydrous Na$_2$SO$_4$ and evaporated to give compounds **1-5** [13].

1-Ethyl-4-(phenylsulfonyl)piperazine (1)
Yield: 90%, grey solid. ^{1}H NMR (400 MHz, CDCl$_3$) δ 7.72 (d, *J* = 7.4 Hz, 2H), 7.52 (dt, *J* = 14.1, 6.8 Hz, 3H), 3.01 (s, 4H), 2.48 (s, 4H), 2.36 (dd, *J* = 14.2, 7.1 Hz, 2H), 0.99 (t, *J* = 7.1 Hz, 3H); ^{13}C NMR (400 MHz, CDCl$_3$) δ 135.1, 132.7, 128.9, 127.8, 76.7, 51.8, 46.0, 11.8; HRMS (ESI) calcd for C$_{12}$H$_{18}$N$_2$O$_2$S [M + H]$^+$ m/z: 255.1189, found 255.1161.

1-Phenyl-4-(phenylsulfonyl)piperazine (2)
Yield: 78%, white solid. ^{1}H NMR (400 MHz, CDCl$_3$) δ 7.77 (d, *J* = 7.2 Hz, 2H), 7.57 (dt, *J* = 25.8, 7.2 Hz, 3H), 7.27 − 7.19 (m, 2H), 6.84 (d, *J* = 7.9 Hz, 3H), 3.18 (dd, *J* = 21.2, 4.4 Hz, 8H). ^{13}C NMR (400 MHz, CDCl$_3$) δ 150.5, 135.2, 133.0, 129.1, 127.7, 125.9, 120.7, 116.8, 49.1, 46.0. HRMS (ESI) calcd for C$_{16}$H$_{18}$N$_2$O$_2$S [M+H]$^+$ m/z: 302.1089, found 302.8967.

1-(3-Fluorophenyl)-4-(phenylsulfonyl)piperazine (3)
Yield: 78%, light pink. ^{1}H NMR (400 MHz, CDCl$_3$) δ 7.78 (d, *J* = 7.4 Hz, 2H), 7.58 (dt, *J* = 28.2, 7.3 Hz, 3H), 7.42 − 7.29 (m, 1H), 6.85 − 6.57 (m, 3H), 3.28 (d, *J* = 12.4 Hz, 8H), 1.34 (t, *J* = 7.3 Hz, 1H); ^{13}C NMR (400 MHz, CDCl$_3$) δ 164.7, 162.3, 135.3, 133.2, 130.7, 129.2, 128.2, 127.7, 125.8, 49.6, 46.1,

45.3; HRMS (ESI) calcd for $C_{16}H_{17}N_2O_2FN_2S$ [M+H]$^+$ m/z: 321.0995 found 321.0329.

1-(4-Methoxyphenyl)-4-(phenylsulfonyl) piperazine (4)

Yield: 63%, light pink solid. ^{1}H NMR (400 MHz, CDCl$_3$) δ 7.79 (d, J = 7.2 Hz, 2H), 7.58 (m, 3H), 6.84 (m, 4H), 3.74 (s, 2H), 3.17 (d, J = 25.3 Hz, 8H); ^{13}C NMR (400 MHz, CDCl$_3$) δ 135.3, 133.0, 129.1, 127.7, 125.8, 119.3, 114.5, 55.5, 50.8, 46.0; HRMS (ESI) calcd for $C_{16}H_{17}FN_2O_2S$ [M+H]$^+$ m/z: 332.1195 found 332.0596.

4-(Phenylsulfonyl)piperazine-1-carbaldehyde (5)

Yield: 84%, white solid. ^{1}H NMR (400 MHz, CDCl$_3$) δ 7.92 (s, 1H), 7.70 (d, J = 7.5 Hz, 2H), 7.59 (t, J = 7.3 Hz, 1H), 7.51 (t, J = 7.5 Hz, 2H), 3.59 (t, J = 4.9 Hz ,2H), 3.43 (t, J = 4.9 Hz, 2H), 3.00 (t, J = 4.7 Hz, 2H), 2.95 (t, J = 4.8 Hz, 2H). ^{13}C NMR (400 MHz, CDCl$_3$) δ 160.6, 135.2, 133.3, 129.2, 127.5, 46.5, 45.4, 44.8, 39.2. HRMS (ESI) calcd for $C_{11}H_{14}N_2O_3S$ [M+H]$^+$ m/z: 255.0788 found 255.0796.

2.2. Pharmacological/biological assay

α-Glucosidase inhibitory activity of samples obtained was measured according to the method also explained by Balan *et al*. [16]. Firstly, proper amounts of monosodium phosphate and disodium phosphate were mixed with procuring 100 mM phosphate buffer (pH 7). Then, α-glucosidase enzyme was dissolved in phosphate buffer to obtain α-glucosidase solution (0.2 U/mL). Later, 170 μL of phosphate buffer, 20 μL of

α-glucosidase solution and 20 μL of sample solutions were mixed and incubated in 37 °C oven for 15 min. After that, 20 μL of 2.5 mM p-nitrophenyl-α-D-glucopyranoside solution in 100 mM potassium phosphate buffer (pH 7.0) was added to the mixture, and another incubation period was executed at 37 °C for 15 min. Then, 80 μL of 0.2 M sodium carbonate solution was appended to the mixture to terminate the reaction. Absorbance was measured at 405 nm. Quercetin was used as a reference solution at 31.25, 62.5, 125, 250, 500 and 1000 μg/mL concentrations. Results were estimated as the percentage of inhibitory activity in 1 mg/mL concentrations of samples.

2.3. Molecular docking

Method details. Ligand Preparation: SDF files of ligands were generated using Data Warrier. Briefly, SMILES codes are used to generate conformers with setting as following: Random, Low Energy Bias, Torsions based on crystallographic database, energy minimization based on MMFF94s+ Forcefield. SD file version 3 with 3D atom coordinates has been used. Docking Parameters and Protein Preparation: PDB ID: 5NN5 Alpha-glucosidase (Homo sapiens) in complex with 1-deoxynojirimycin has been used to for docking studies. Briefly, crystal structure of protein was downloaded in pdb format from https://www.rcsb.org. PDB ID: 5NN5 structure was optimized for docking by removing of water molecules, 1-deoxynojirimycin, chloride ions, 1,2-ethanediols, sulfate ions and other chains (B-F). A grid box with 26Åx26Åx26Å and coordinates of x=-15.43, y=-37.864, z=93.588 and spacing of 1Å around the 1-deoxynojirimycin binding pocket (for PDB ID: 5NN5) has been generated using AutoDockTools 1.5.6. Automated docking of ligands was performed with PaDelADV. To investigate the interaction of molecules and enzymes' amino acids BIOVIA Discovery studio was used.

3. Results and Discussion
3.1. Chemistry

Compounds **1**-**5** were synthesized according to refence [13] with some modifications. Briefly, piperazine was dissolved in CH$_2$Cl$_2$ (DCM) derivatives (1.0 eq) and triethylamine (3.0 eq) was added to solution slowly at 0 °C. Then this mixture was added to benzene sulfonyl chloride (1.0 eq) and stirred for 2 hours at room temperature. The completion of the reaction was checked with TLC. After the reaction was finished, water was added, and extraction was done with DCM. The combined organic layer was dried over anhydrous Na$_2$SO$_4$ and evaporated to give compounds **1**-**5** (**Figure 1**). Compounds were characterized with ^{1}H-NMR, ^{13}C-NMR and HRMS. In ^{1}H-NMR spectrum, basic peaks of aromatic hydrogens of compounds were observed at 7.70 – 7.50 ppm. Aliphatic hydrogens of the piperazine ring were found 3.50 – 2.0 ppm. The peaks of these hydrogens were designated in two different manners. Some of them had only one peak and others had two peaks according to the substituent on piperazine ring.
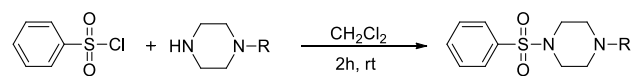
Figure 1. Synthesis pathway of compounds **1**-**5**

3.2. Enzyme inhibition

Five piperazine sulfonamide derivatives (**1-5**) were synthesized and investigated for α-glucosidase enzyme inhibition activity. Quercetin was used as a reference molecule, because of its well-known α-glucosidase inhibitory potential. According to the results of study, all compounds have good inhibitory activities (63.45 ± 0.14 – 83.52 ± 0.41) against α-glucosidase enzyme (**Table 1**). Compound **1** has higher inhibition values than quercetin and the most active compound against α-glucosidase enzyme in this series. The phenyl group that was attached to the piperazine which is substituted with EDG group like methoxy as in compound **4** showed the lowest inhibition value. This result cannot be only correlated with the EDG, but this can be explained by the different binding states of the substituents to the enzyme. Lastly, compound **5** has reasonable inhibition value. It can be resulted from EWG on the phenyl group. According to this result, different types of substituents have high α-glucosidase enzyme inhibition activity in this series.
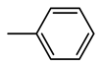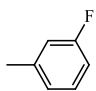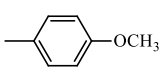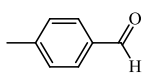
3.3. Molecular docking

Molecular docking is an important tool for elucidating the structural properties of ligands that have biological activity for target enzymes. In this part, the most active compound was investigated based on their molecular interactions and binding energies for α-glucosidase enzymes. A molecular docking study was done for the most potent compound **1**. The binding energy of compound **1** was calculated and found to be -5.3 kcal/mol. For compound **1**, the phenyl group has two different types of interaction: π-anion interaction between ASP518 and π-π stacks with PHE649 and TRP376. Moreover, sulfonamide group has π-sulfur interaction with TRP481 and hydrogen bond formation between ARG600. In addition, carbon hydrogen bond interaction between ASP616 (**Figure 2**).
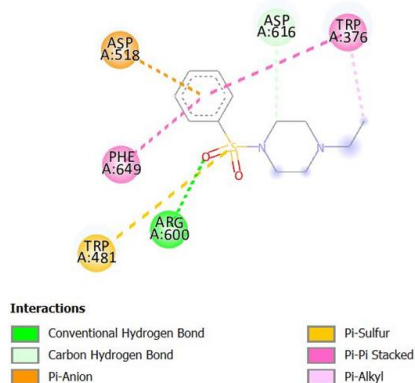
Figure 2. Docking result of the compound **1** for α-glucosidase enzyme

Table 1. α-Glucosidase enzyme inhibition results of compounds **1-5**

Compounds	R	α-Glucosidase enzyme inhibition (%)
1	-CH$_2$CH$_3$	82.48 ± 0.21
2	(phenyl)	77.45 ± 0.13
3	(fluorophenyl, F)	75.68 ± 0.23
4	(methoxyphenyl, OCH$_3$)	63.45 ± 0.14
5	(benzaldehyde, CHO)	77.35 ± 0.45
Quercetin		81.41 ± 0.02

[a]Results were presented as α-glucosidase enzyme inhibition experiments were performed independently three different times.
[b]Standard deviation was symbolized with ±.

3.4. ADME profiling

ADME (absorption, distribution, metabolism, and excretion) is an important factor for the development of biologically active oral drug candidates. ADME parameters of compounds were investigated using the freely accessible silico SwissADME web tool (http://www.swissadme.ch). This tool provides bioavailability radar and boiled-egg charts. Bioavailability radar charts contain physicochemical properties that are used to explore physicochemical characteristics and drug-likeness properties of molecules. The physicochemical properties of compounds **1-5** were predicted with SwissADME free web tool [17]. The bioavailability radar indicates rapid pre-assessment of drug-likeness. In this chart six main physicochemical properties are investigated, these are lipophilicity, polarity, size, solubility, saturation, and flexibility (**Figure 3**). The part within the pink area is the border drawn for the physicochemical properties of the molecules to be a drug-likeness. When the red frame of the molecules is in the pink area, it shows that the physicochemical values of the molecule remain within the desired limits. Calculated physicochemical properties of compounds (**1** – **5**) are in desired limits and in pink area. These charts indicate that lipophilicity, oral

bioavailability, and solubility of compounds are suitable for drug-likeness properties.
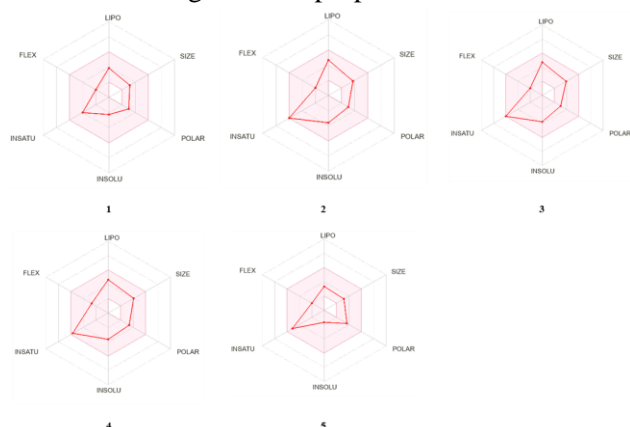
Figure 3. Bioavailability radar chart of compounds **1**-**5**

3.5. Quantum mechanical calculations

3.5.1. Computational DFT method

Density functional theory (DFT) with the Gaussian 09 were used to optimize geometry. At the B3LYP/6-31+G level of theory [18], [19] DFT approaches were utilized to refine the geometry of a promising molecule. The lowest unoccupied molecular orbital (LUMO), and highest occupied molecular orbital (HOMO) localization energies of promising molecules were investigated. Data from DFT analyses revealed that the five molecules were ordered by their chemical reactivity as follows: molecules **2**, **4**, **3**, **1**, and **5** respectively. The primary step in computing quantum chemicals for a molecular system is geometry optimization. Finding the conditions under which the molecule is most stable, or where the energy is lowest, is the aim of geometry optimization. The entire quantum chemical calculations have been performed at DFT (B3LYP) methods 6-31+G basis set using the Gaussian 09W software package [20]. **Table 2** displays both the geometrical parameters derived from optimized geometry data and the optimized molecular structure of molecules **1** - **5** as determined by DFT calculations at the B3LYP level using a 6-31+G basis set. The bond length, bond angles and torsional angles of optimized molecule **2** are shown in **Table 3**. Frontier molecular orbitals were employed to assess the electrical properties and electron transport potential of the compounds under investigation. These orbitals determine the molecular characteristics and biological activity of the substances. The LUMO, which represents the electron-deficient orbital, is associated with the ability to accept electron density and electron affinity. On the other hand, the HOMO, representing the electron-rich orbital, is proportional to the ionization potential.

Table 2. Gaussian-based calculations of frontier molecular orbital energies of molecules **1-5**

Compounds	HOMO (eV)	LUMO (eV)	Energy Gap- ΔE (eV)
1	-0.20843	-0.06621	0.14222
2	-0.20197	-0.07080	0.13117
3	-0.21012	-0.07827	0.13185
4	-0.19923	-0.06765	0.13158
5	-0.26323	-0.07662	0.18661

The energies of the LUMO and HOMO govern the molecule's interactions with other species and contribute to its chemical reactivity and kinetic stability. A small difference between the LUMO and HOMO energies indicates a low band energy gap (ΔE), suggesting a compound's higher reactivity with a receptor. A smaller energy gap signifies greater reactivity since the LUMO and HOMO are responsible for charge exchange during chemical reactions [21], [22]. The reactivity order among the ten molecules was found to be **2 > 4 > 3 >1 > 5**, with compound molecule **2** exhibiting the smallest band energy gap, indicating its highest reactivity compared to the others. In molecule **2**, the HOMO is localized on the piperazine moiety, while the LUMOs are localized on the benzenesulfonyl and some portion of the piperazine scaffold. The highly delocalized HOMO suggests that electrons can move more freely within the molecule, leading to improved intramolecular charge transfer (**Figure 4**).
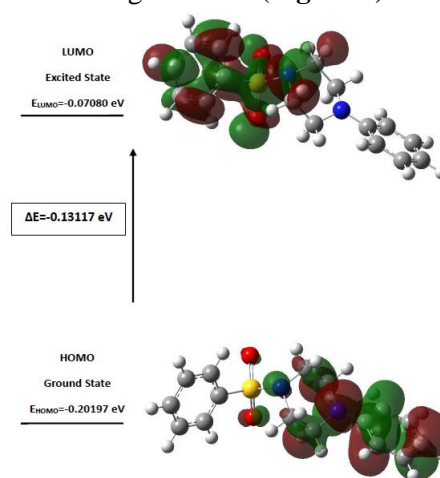
Figure 4. HOMO, LUMO energy of the compound molecule **2**.

Table 3. B3LYP/6-31+G level of basis set's computed optimum geometrical parameters for molecule **2**.

Bond lengths (Å)		Bond angle (°)		Torsional angle (°)		
C1-C2: 1.40062	C25-C27: 1.41473	C6-C1-C2: 120.12889	H39-C16-N23: 104.76470	C26-C28-C32: 120.87460	C1-C2-C3-C4: 0.62773	O14-S12-N23-C16: -36.50082	N24-C25-C27-H31: -0.69937
C1-C6: 1.40363	C26-C28: 1.40110	H7-C1-C6: 120.25198	H39-C16-C19: 109.84204	C26-C28-C32: 119.05799	C2-C3-C3-S12: 178.79721	C15-C17-N24-C19: -58.35667	N24-C25-C27-C28: 177.94183
C1-H7: 1.08498	C26-H29: 1.08347	H7-C1-C2: 119.61849	C15-C17-N24: 110.25336	H33-C28-C32: 120.06155	C1-C6-C5-H10: - 179.42996	C15-N23-C16: 45.03652	N24-C25-C27-C30: -178.58698
C2-C3: 1.39215	C27-C30: 1.39630	C1-C2-C3: 117.80224	H21-C17-H37: 107.98579	C27-C30-C32: 120.77630	C2-C3-C4-C5: 0.62267	C15-N23-C16: 154.02944	C25-C26-C28-C32: 0.73283
C2-H8: 1.08381	C27-H31: 1.08484	H8-C2-C1: 121.49330	H21-C17-C15: 109.48725	H34-C30-C32: 119.9945	C2-C3-C4-H9: 178.43062	C15-N23-C16: 169.13079	C25-C27-C30-C32: 0.51527
C3-C4: 1.39109	C28-C32: 1.39897	H8-C2-C3: 120.70311	H21-C17-H24: 110.33388	H34-C30-C27: 119.21736	C2-C3-S12-O13: -174.53970	H39: -75.32334	C25-C27-C30-H34: 179.85327
C3-S12: 1.87148	C28-H33: 1.08629	C2-C3-C4: 123.66214	H37-C17-C15: 109.06070	C28-C32-C30: 118.79517	C2-C3-S12-O14: -43.39410	C16-C19-N24-C17: 57.57380	C25-C27-C30-H34: 179.56022
C4-C5: 1.40289	C30-C32: 1.40317	S12-C3-C2: 118.42090	H37-C17-N24: 109.67615	C28-C32-C30: 120.55976	C2-C1-C6-H11: 179.82806	C16-N23-C15: -45.44815	C26-C28-C32: -0.27875
C4-H9: 1.08457	C30-H34: 1.08630	S12-C3-C4: 117.89274	C16-C19-N24: 110.18807	H35-C32: 120.64507	C3-C4-C5-C6: 0.17980	C16-N23-C15: 74.97009	C26-C28-C32: -0.06606
C5-C6: 1.40155	C32-C35: 1.08513	C3-C4-C5: 117.79537	H22-C19-H38: 107.91906		C3-C4-C5-H10: 179.83731	C16-N23-C15: -169.68266	C26-C25-N24-C19: -11.33074
C5-H10: 1.08501		H9-C4-C3: 120.03339	H22-C19-C16: 107.97814		C3-S12-N23-:	C16-N23-S12-:	C26-C25-N24-:
C6-H11: 1.08537		H9-C4-C5: 122.16416	H22-C19-N24: 109.07734		C16: -150.50221	C25: -154.99164	C31: 177.82155
S12-O13: 1.50103		C4-C5-C6: 120.10095	H38-C19-C16: 109.90970		C4-C5-C6-C1: 0.22496	H22: 175.94165	C26-C28-C32: 179.71158
S12-O14: 1.50103		H10-C5-C6: 120.32319	H38-C19-N24: 111.66519		C4-C5-C6-H11: 179.83293	H38: -64.87002	C27-C25-C26: -0.55045
C15-C17: 1.53349		H10-C5-C4: 119.57497	C15-N23-C16: 113.50443		C4-C3-C2-H8: 178.95736	H21: 62.70456	C28-C30-C32: -0.34113
C15-H18: 1.09793		C1-C6-C5: 120.50718	S12-N23-C16: 112.08208		C4-C3-S12-O13: 3.73648	C19-N24-C17: 178.46389	C27-C25-N24: -47.59573
C15-N23: 1.48464		H11-C6-C5: 119.77744	S12-N23-C15: 112.71052		C4-C3-S12-O14: 134.88208	N23-C16-C19: 96.17470	C27-C25-N24: 119.16771
C15-H36: 1.09436		H11-C6-C1: 119.71422	C17-N24-C19: 112.47201		C5-C6-C1-C2: 0.21984	N24: 51.51380	C27-C25-C26: 167.12989
C16-C19: 1.53564		O13-S12-O14: 119.72057	C25-N24-C17: 119.17263		C5-C6-C1-H7: 179.49073	N23-C15-C17: -70.05152	H29: 178.08067
C16-N23: 1.48464		C17-C15-N23: 113.76871	C25-N24-C19: 119.67221		C5-C4-C3-S12: 178.80115	H37: 171.99138	C30-C32-C30: 179.66853
C16-H20: 1.09324		H18-C15-C17: 110.10835	C26-C25-C27: 117.95607		C6-C1-C2-C3: 0.18978	H22: -169.57294	H34: -179.37864
C16-H39: 1.09762		H18-C15-N23: 104.93945	N24-C25-C27: 121.92734		C6-C1-C2-H8: 179.39184	N23-C16-C19: 72.93938	C30-C32-C28: -179.39041
C17-H21: 1.10206		H18-C15-H36: 107.86922	N24-C25-C27: 120.09940		S12-N23-C15: H18: -156.24326	N23-C16-C19: 72.93938	C32-C30-C27: -179.39041
C17-N24: 1.47933		H36-C15-N23: 109.04865	C25-C26-C28: 120.71204		S12-N23-C15: H36: -40.89601	N23-S12-C3-C4: -115.26063	H31: -177.38460
C19-H22: 1.09351		H36-C15-C17: 110.80128	C25-C27-C30: 120.88104		S12-N23-C16: H20: 40.02372	N24-C17-C15: H18: -65.95160	

4. Conclusion and Suggestions

In this study, five phenylsulfonyl piperazine derivatives were synthesized. Their inhibitory potentials against α-glucosidase enzyme were evaluated. Compound **1** has a higher inhibition value than the reference molecule quercetin in the α-glucosidase enzyme assay. The other molecules had valuable α-glucosidase enzyme inhibition values. Bioavailability radar chart was used to study the physicochemical properties and compliance with the Lipinski rule of five molecules. Acceptable drug-like

and pharmacokinetic properties were expected from the synthesized molecules according to the results. In addition, docking studies and DFT calculations have been carried out. Molecular docking studies were performed to identify the significant interactions between molecules and enzymes. These promising results were confirmed by their binding energy of compound **1** was -5.3 kcal/mol for the α-glucosidase enzyme. The enzyme inhibition results were in good agreement with the docking studies. Although, DFT calculations showed that compound **2** had the lowest energy gap (ΔE (eV): 0.13117), that may be the most active compound, but it was the second the most potent α-glucosidase enzyme inhibitor. Consequently, all these results suggest these molecules, especially compound **1**, as potential leads for further optimization of antidiabetic molecules.

Acknowledgment

Contributions of the authors

Plan and design of the study: KB; Data collection: Yİ, GSA, CDÖ; Data analysis and interpretation: KB, CDÖ, FK; Writing-critical evaluation: KB, FK.

Conflict of Interest Statement

There is no conflict of interest between the authors.

Statement of Research and Publication Ethics

The study is complied with research and publication ethics.

References

[1] M. J. Fowler, "Microvascular and Macrovascular Complications of Diabetes," *Clinical Diabetes*, vol. 26, no. 2, pp. 77–82, Apr. 2008.

[2] M. Dehghan *et al.*, "Progress toward molecular therapy for diabetes mellitus: A focus on targeting inflammatory factors," *Diabetes Res Clin Pract*, vol. 189, p. 109945, Jul. 2022.

[3] A. S. Alqahtani *et al.*, "Alpha-amylase and alpha-glucosidase enzyme inhibition and antioxidant potential of 3-oxolupenal and katononic acid isolated from Nuxia oppositifolia," *Biomolecules*, vol. 10, no. 1, 2020.

[4] M. D. P. T. Gunawan-Puteri, E. Kato, and J. Kawabata, "α-Amylase inhibitors from an Indonesian medicinal herb, Phyllanthus urinaria," *J Sci Food Agric*, vol. 92, no. 3, pp. 606–609, Feb. 2012.

[5] E. Vitaku, D. T. Smith, and J. T. Njardarson, "Analysis of the Structural Diversity, Substitution Patterns, and Frequency of Nitrogen Heterocycles among U.S. FDA Approved Pharmaceuticals," *J Med Chem*, vol. 57, no. 24, pp. 10257–10274, Dec. 2014.

[6] M. K. Akkoç, M. Y. Yüksel, I. Durmaz, and R. E. Atalay, "Design, synthesis, and biological evaluation of indole-based 1,4-disubstituted piperazines as cytotoxic agents," *Turk J Chem*, vol. 36, no. 4, pp. 515–525, 2012.

[7] D. Mukherjee, A. Mukhopadhyay, K. S. Bhat, A. M. Shridhara, and K. S. Rao, "Synthesis, characterization and anticonvulsant activity of substituted 4- chloro-2-(4-piperazin-1-YL) quinazolines," *Int J Pharm Pharm Sci*, vol. 6, no. 5, pp. 567–571, 2014.

[8] T. Kálai, M. Khan, M. Balog, V. K. Kutala, P. Kuppusamy, and K. Hideg, "Structure-activity studies on the protection of Trimetazidine derivatives modified with nitroxides and their precursors from myocardial ischemia-reperfusion injury," *Bioorg Med Chem*, vol. 14, no. 16, pp. 5510–5516, 2006.

[9] K. Buran, R. Reis, H. Sipahi, and F. E. Önen Bayram, "Piperazine and piperidine-substituted 7-hydroxy coumarins for the development of anti-inflammatory agents," *Arch Pharm (Weinheim)*, vol. 354, no. 7, p. e2000354, 2021.

[10] K. Buran, S. Bua, G. Poli, F. E. Ö. Bayram, T. Tuccinardi, and C. T. Supuran, "Novel 8-substituted coumarins that selectively inhibit human carbonic anhydrase IX and XII," *Int J Mol Sci*, vol. 20, no. 5, 2019.

[11] A. Ignat, V. Zaharia, C. Mogoşan, N. Palibroda, C. Cristea, and L. Silaghi-Dumitrescu, "Heterocycles 25. Microwave assisted synthesis of some p-toluensulfonyl- hydrazinothiazoles with analgesic and anti-inflammatory activity," *Farmacia*, vol. 58, no. 3, pp. 290–302, 2010.

[12] R. A. Finch, K. Shyam, P. G. Penketh, and A. C. Sartorelli, "1,2-Bis(methylsulfonyl)-1-(2-chloroethyl)-2-(methylamino)carbonylhydrazine (101M): A novel sulfonylhydrazine prodrug with bbroad-spectrum antineoplastic activity," *Cancer Res*, vol. 61, no. 7, pp. 3033–3038, 2001.

[13] M. Taha *et al.*, "Synthesis of piperazine sulfonamide analogs as diabetic-II inhibitors and their molecular docking study," *Eur J Med Chem*, vol. 141, pp. 530–537, 2017.

[14] J. L. Xiao, R. S. Luo, Y. Shi, Q. Guo, Z. X. Zhou, and C. S. Zhao, "Synthesis, crystal structure and dft study of benzenesulfonamide compounds 1-ethyl-4-(phenylsulfonyl)piperazine and 1-((3-bromophenyi)sulfonyl)-4-methyipiperazine," *Molecular Crystals and Liquid Crystals*, vol. 755, no. 1, pp. 80–90, 2023.

[15] M. A. Abbasi *et al.*, "Synthesis, enzyme inhibition and molecular docking studies of 1- arylsulfonyl-4-Phenylpiperazine derivatives," *Pak J Pharm Sci*, vol. 30, no. 5, pp. 1715–1724, 2017.

[16] K. Balan, P. Ratha, G. Prakash, P. Viswanathamurthi, S. Adisakwattana, and T. Palvannan, "Evaluation of invitro α-amylase and α-glucosidase inhibitory potential of N2O2 schiff base Zn complex," *Arabian Journal of Chemistry*, vol. 10, no. 5, pp. 732–738, 2017.

[17] A. Daina, O. Michielin, and V. Zoete, "SwissADME: A free web tool to evaluate pharmacokinetics, drug-likeness and medicinal chemistry friendliness of small molecules," *Sci Rep*, vol. 7, no. October 2016, pp. 1–13, 2017.

[18] C. W. Bauschlicher Jr. and H. Partridge, "A modification of the Gaussian-2 approach using density functional theory," *J Chem Phys*, vol. 103, no. 5, pp. 1788–1791, Aug. 1995.

[19] A. M. Toth, M. D. Liptak, D. L. Phillips, and G. C. Shields, "Accurate relative pKa calculations for carboxylic acids using complete basis set and Gaussian-n models combined with continuum solvation methods," *J Chem Phys*, vol. 114, no. 10, pp. 4595–4606, Mar. 2001.

[20] M. J. Frisch *et al.*, "Gaussian 09, Revision A.02." Gaussian, Inc., Wallingford CT, 2016.

[21] M. Govindarajan and M. Karabacak, "Spectroscopic properties, NLO, HOMO–LUMO and NBO analysis of 2,5-Lutidine," *Spectrochim Acta A Mol Biomol Spectrosc*, vol. 96, pp. 421–435, Oct. 2012.

[22] M. A. Mumit, T. K. Pal, M. A. Alam, M. A. A. A. A. Islam, S. Paul, and M. C. Sheikh, "DFT studies on vibrational and electronic spectra, HOMO–LUMO, MEP, HOMA, NBO and molecular docking analysis of benzyl-3-N-(2,4,5-trimethoxyphenylmethylene)hydrazinecarbodithioate," *J Mol Struct*, vol. 1220, p. 128715, Nov. 2020.

Hybrid Optimal Time Series Modeling for Cryptocurrency Price Prediction: Feature Selection, Structure and Hyperparameter Optimization

Mehmet Akif BÜLBÜL[1*]

[1]*Kayseri University, Faculty of Engineering, Architecture and Design, Software Engineering, Kayseri, Turkey*
(ORCID: 0000-0003-4165-0512)

Abstract

The prime aim of the research is to forecast the future value of Bitcoin which is commonly known as a pioneer of the Cryptocurrency market by constructing a hybrid structure over the time series. In this perspective, two separate hybrid structures were created by using Artificial Neural Network (ANN) together with Genetic Algorithm (GA) and Particle Swarm Optimization Algorithm (PSO). By using the hybrid structures created, both the network model and the hyperparameters in the network structure, together with the time intervals of the daily closing prices and how much data should be taken retrospectively, were optimized. Employing the created GA-ANN (DCP1) and PSO-ANN (DCP2) hybrid structures and the 721-day Bitcoin series, the goal of accurately predicting the values that Bitcoin will receive has been achieved. According to the comparative results obtained in line with the stated objectives and targets, it has been determined that the structure obtained with the DCP1 hybrid model has a success rate of 99% and 97.54% in training and validation, respectively. It should also, be underlined that the DCP1 model showed 47% better results than the DCP2 hybrid model. With the proposed hybrid structure, the network parameters and network model that should be used in the ANN network structure are optimized in order to obtain more efficient results in cryptocurrency price forecasting, while optimizing which input data should be used in terms of frequency and closing price to be chosen.

1. Introduction

Digital financial assets are becoming increasingly important in today's digital economy [1]. Cryptocurrencies are particularly notable for their short-term volatility and price fluctuations. Therefore, it is crucial to develop accurate and reliable forecasting approaches [2]. It is possible to express cryptocurrencies, which are one of the last rings of globalization and which have started to appear in the financial context, in the form of digitally encrypted number sequences [3]. In other words, cryptocurrencies are digital or virtual currencies that use cryptography for security. Because of this cryptography feature, a cryptocurrency is difficult to fake [4]. In addition,

cryptocurrencies have the feature of being a distributed system because they are not dependent on a central authority [5]. The crypto market is becoming increasingly in demand as investors adopt it to diversify their portfolios.

The cryptocurrency market has evolved through various market cycles and bull-bear runs, public interest, technological advancements in Blockchain, speculation and adoption phases, among other natural processes. As market phases evolve, pricing factors that influenced one phase of the market no longer apply to the next phase, creating anxiety among investors looking to buy on dips or sell at a profit [6]. It is therefore difficult to predict cryptocurrency prices due to price fluctuations and instability. This gap in the field is

filled by comparing various machine learning models to predict the market movements of Bitcoin, the most relevant cryptocurrency [6].

The terms Artificial Intelligence (AI), Machine Learning, and Deep Learning have become common and popular concepts in almost every industry [7] [8] [9]. The financial sector, as expected, is playing a leading role in integrating AI technologies into its operations. In recent years, more and more research and studies have been published on machine learning models for time series forecasting. Most of these studies point out that newer machine-learning models outperform traditional time series forecasting methods [10]. When we look at the studies on cryptocurrency price prediction in the literature: Zhou et al. [11] performed a multi-source data-driven cryptocurrency price prediction in their study. Support Vector Machines and global minimum variance models were used in the study. The findings show that the proposed model produces successful results in cryptocurrency price prediction.

Rashid and Ismail [12] used linear regression methods with the Minimum Akaike Information Criterion, quadratic trend and exponential trend for forecasting cryptocurrency prices. The study examined the trend of prices with deterministic methods by drawing graphs based on residual trend and diagnostic statistics control. The results showed that the methods used were successful in predicting cryptocurrency prices.

Mariappan et al. [13] used reinforcement learning for cryptocurrency price forecasting. Multi-Layer Perception (MLP) and The Long Short-Term Memory (LSTM) are used in the forecasting process over time series. In light of the findings, the proposed method is more successful than the comparative results with different technology strategies.

Murray et al. [14], presented an approach with Deep Learning for the prediction of cryptocurrency prices. In this study, five popular cryptocurrency prices were predicted with LSTM and successful results were obtained.

Nayak et al. [15] used Random Vector Functional Link Networks (RVFLN) for cryptocurrency price forecasting. They proposed an elitist artificial electric field algorithm (eAEFA) for RVFLN training. In the study where eAEFA + RVFLN model was proposed, ML methods such as MLP, SVM, LSTM were applied and comparative results were obtained with the proposed model. The results show that the proposed hybrid method produces more successful results than other ML methods.

Shang et al. [2] proposed a reconstructed dynamic-bound Levenberg-Marquardt neural network approach for cryptocurrency price forecasting. ML methods such as LM-Neural Networks, Artificial Neural Networks (ANN), LSTM, and CNN were also used in the study. The results show that the proposed method produces more successful results than other ML methods.

Hawi et al. [16] used three different ML methods, namely K-Nearest Neighbor, SVM, and Light Gradient Augmented Machine (LGBM), to predict cryptocurrencies. In the experimental studies conducted in two stages, successful results were obtained with KNN in the first stage and SVM in the second stage.

Ateeq et al. [17] used the LSTM model for bitcoin price prediction. In this study, minute, hourly, daily, weekly, weekly and monthly models were extracted. In the forecasting process in these different time periods, which are put forward as different models, there is no differentiation as a model other than the temporal difference. In the study where only input variables were differentiated, successful results were obtained in Bitcoin price prediction with LSTM.

Alarab and Prakoonwit [18] develop a classification model that combines long short-term memory with a GCN, called temporal-GCN, that classifies illegal transactions of elliptical data using only the characteristics of the transaction, in an active learning framework applied to a large-scale Bitcoin transaction graph dataset. As a result, it is claimed that the temporal-GCN model achieves significant success compared to previous studies with the same experimental settings on the same dataset.

Aziz et al. [19] created a model based on the Light Gradient Boosting Machine (LGBM) approach in this article in order to precisely detect fraudulent transactions. The Euclidean distance structured estimation technique is used by the modified LGBM model to optimize the Light GBM parameters. In a restricted manner, it also looks into the effectiveness of some well-known models, including ADAboost, k-Nearest Neighbors (KNN), Random Forest (RF), Multilayer Perceptron (MLP), Logistic Regression, XGBoost, and Support Vector Classification (SVC).

Li [20] focuses on utilizing CNN, LightGBM, and LSTM models to forecast the real volatility of stocks using a Kaggle data set. A thorough examination of the performance

comparison between the three models is provided by the research. Following experiments with the chosen dataset, it is discovered that LGBM performs better when it comes to short-term stock volatility predictions.

Kazeminia et al. [21] employed a novel hybrid 2D-CNNLSTM model with OPTUNA hyperparameter adjustment to forecast the closing price of Bitcoin based on historical data. In terms of R2 and MAPE, the suggested model performs better than other popular algorithms like CNN, LSTM, and GRU.

ML methods contain different hyperparameters. The differences in these hyperparameters directly affect the performance of the models used. In structures with the same hyperparameters, different input parameters produce different results. In the literature on cryptocurrency price prediction, models and studies on both feature selection and optimization of hyperparameters according to these features are very insufficient

ML methods involve different hyperparameters. Differences in these hyperparameters directly affect the performance of the models used. Different input parameters produce different results in structures with the same hyperparameters. In the literature on cryptocurrency price prediction, models and studies on both feature selection and optimization of hyperparameters according to these features are quite insufficient [22]. In the proposed study, unlike the studies in the literature, all parameters and architectural structures in the architecture targeted to be used for bitcoin price prediction are optimized with different optimization algorithms. This feature enables the model to create more complex architectures. In this context, the aim of this paper is:

- To achieve a high rate of success in bitcoin price prediction.
- To optimize both the hyperparameters and the architecture of the proposed ML method and to determine the appropriate input parameters of the structure with these optimized hyperparameters and architecture.
- To take advantage of the capabilities of both ANN and optimization algorithms.

For this purpose:

- A dataset was prepared with bitcoin price information between January 21, 2019 and January 20, 2021.
- Using the Genetic Algorithm and Particle Swarm Optimization Algorithm, 2 different

hybrid models were created to optimize the input values of the model to be created, as well as to optimize all the parameters and architectural structure of the ANN structure based on time series prediction.

- The results of the experimental studies on the dataset are presented in a controversial manner.

The study's plan is outlined as follows: The next section will provide an explanation of the methods employed in the study. Subsequently, the experimental studies will be detailed, and the results will be discussed in the following section. The final section will summarize the results and delve into the discussion of future work.

2. Material Methods

In this part of the study, ANN, GA, and Particle Swarm Optimization methods, which are used for the purpose of predicting Bitcoin price movements, are mentioned in detail.

2.1. Artificial Neural Network

ANN represents a mathematical model of the events that occur in nerve cells in the brain of living things [23]. In these neural networks formed by the combination of neurons, each neuron is modeled as shown in Figure 1.
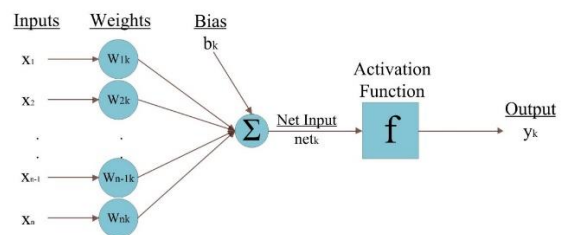
Figure 1. A single-neuron cell structure

In the single-neuron cell structure presented in Figure 1, the information that comes to the neuron as input data is multiplied by the weights and sent to the addition function. After the obtained values are combined with each other, these data collected with the bias value, which is determined by the network structure and provides the translation of the activation function used in the neuron, constitutes the net input for the neuron cell. The resulting net input value is passed through the activation function in the neuron, and the net output

value for that neuron cell is obtained from the input data.

An ANN network structure consists of many neuron cells coming together. These networks formed by neurons can be divided into different groups in terms of sequence and functioning [24]. One of the network models frequently used in the literature is feedforward and backpropagation networks [25]. A multilayer feedforward and backpropagation ANN structure is shown in Figure 2.
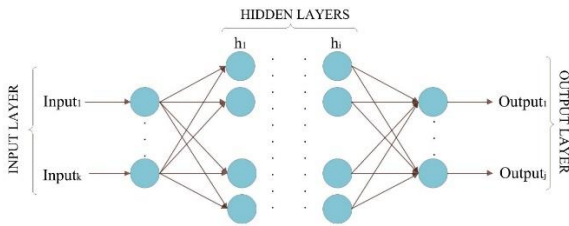
Figure 2. Structure of a simple feedforward backpropagation ANN

In Figure 2, the input information given to the network from the input layer is transmitted forward along the network by each neuron cell. ANN is capable of learning relationships by training data and predicting new data [26]. In this process, error detection is performed for each neuron cell in the last step. Weight information contained in neurons is changed during backpropagation. Hidden layer errors are determined and these errors are returned to neuron cells. Thus, the performance of the network is tried to be improved.

2.2. Genetic Algorithm

GA is an optimization method [27] that uses population-based and heuristics search to replicate the natural evolutionary process of humans. When we compare the GA with the traditional optimization algorithms, it is seen that better optimization results can usually be obtained faster [28]. The steps of GA are as follows [29]:

1. Initialize algorithms parameters.
2. s_sel selection probability, r_cross crossover rate, r_mut mutation, t_iter number of iterations, n_pop number of individuals in a population.
3. Initialize population with random values in accepted range.
4. Calculate the fitness value of individuals.
5. Selection.
6. Crossover.

7. Mutation.
8. Repeat(4.) t_iter.

The GA uses an initial population to find a quality solution within the solution space. Within the solution space formed by the values to be optimized, random solutions are first generated. These solutions form the population in the algorithm. Each solution in the population is called an individual. The algorithm applies different strategies to produce more resilient individuals from these individuals. The probability of individuals surviving to the next generation increases according to the quality of the fitness values set for the problem. Individuals are selected with different strategies according to the quality of their fitness values. Crossover and mutation processes are carried out on the selected individuals. With these processes, the individual is directed to better regions in the search space. Each individual is passed on to the next generation [30].

2.3. Particle Swarm Optimization Algorithm

PSO first emerged in a study by Reeves in 1983, using the particle system, and was introduced as an algorithm by Kennedy and Eberhart in 1995 [31]. PSO uses principles of social behavior within its population of particles [32]. The steps of the PSO are described below [31].

1. Initialize the algorithm parameters.
2. n_pop number of individuals in a population, t_iter is the number of iterations.
3. Position particles with random values within the accepted range.
4. Calculate the fitness value of the particles.
5. Determine the best position of the particles (pbest) and the best position of the population (gbest)
6. Calculate the velocity value of each particle and change their position.
7. Update particles best position (pbest) and population best position.
8. Repeat (4.) t_iter.

In PSO, the position of each particle in the population represents a solution for the problem to be optimized. Particles are in motion along the solution space based on the experience of neighboring particles. The best positions (pbest) of the particles placed in random positions in each iteration and the position (gbest) of the particle belonging to the best position in the population are

determined according to their fitness values [31]. The velocity of the particles in each iteration is calculated according to Equation 1.

$V_{kl}(t+1)=WV_{kl}(t)+c_1rand(1)(pbest_{kl}(t)-X_{kl}(t))+c_2rand(1)(gbest_{kl}(t)-X_{kl}(t))$ (1)

In Equation 1, the W value represents the momentum coefficient. The value of $V_{kl}(t+1)$ represents the speed of particle k in dimension l in iteration t. The value of $pbest_{kl}(t)$ shows the best position of particle k in dimension l in iteration t. Also, the value of $X_{kl}(t)$ represents the position of particle k in dimension l in iteration t. The $gbest_{kl}(t)$ value indicates the best position in the l dimension in the t iteration. The constants c1 and c2 are the learning parameters used to find the best solution. That is, while the c1 constant provides cognitive learning, the c2 constant provides social learning skills [33]. rand(1) takes a random number between 0 and 1 [34]. The positions of the particles in each iteration are provided according to Equation 2. On the other hand, the initial velocity of each particle in the population is determined randomly.

$$X_{kl}(t+1) = X_{kl}(t) + V_{kl}(t+1)$$ (2)

2.4. Success Assessment Metrics

To measure the success of the models to be developed for cryptocurrency price prediction, metrics that measure the success of machine learning methods in the literature will be used [35]. These metrics are Mean Squared Error, Root Mean Squared Error, Mean Absolute Error, R2, and the mathematical formulas of these values are shown in Equations 3-6.

$$MAE = \frac{1}{n}\sum_{i=1}^{N}|yi^r - yi^p|$$ (3)

$$MSE = \frac{1}{n}\sum_{i=1}^{N}(yi^r - yi^p)^2$$ (4)

$$RMSE = \sqrt{\frac{1}{n}\sum_{i=1}^{N}(yi^r - yi^p)^2}$$ (5)

$$R^2 = 1 - \frac{\sum_{i=1}^{N}(yi^r - yi^p)^2}{\sum_{i=1}^{N}(yi^r - yi^m)^2}$$ (6)

In Equation 3-6, y^r represents the predicted values of the actual values, y^p represents the predicted values and y^m represents the average of the predicted values. These evaluation metrics are used in machine learning to measure the accuracy of predicted values.

3. Models and Results

In this part of the study, hybrid structures of an ANN model that will predict cryptocurrencies (Bitcoin) over time series are created separately with GA and PSO. The number and selection of input values in ANN network structures, the hidden layer used and the number of neurons in these layers, the activation functions used in all neurons in the network and the learning function of the network directly affect the prediction success of the network [36]. It is almost impossible to select the most appropriate parameter values within certain limits with classical methods [37]. Among the networks that can be established, the parameter values that should be used to establish a network that is the most successful or close to the most successful network can only be possible with hybrid structures to be established with optimization algorithms [22].

The models created will optimize the hyperparameters and architecture within the ANN, as well as the number of inputs required for the architecture and the frequency at which data should be received retrospectively. GA and PSO were preferred in this study due to their frequent use in the literature, ease of coding, and successful results [22].

In order to create an ANN network structure with the best performance in cryptocurrency prediction and the most suitable backward input data for this network structure, a hybrid Detection Crypto Price (DCP1) model was created with GA-ANN. The flow chart of the created hybrid structure is shown in Figure 3.
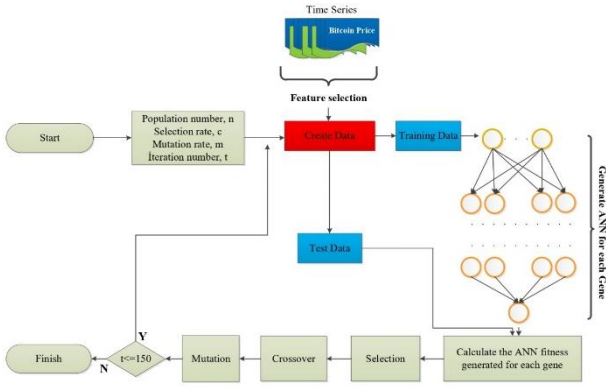
Figure 3. DCP1 hybrid model flowchart

The structure presented in Figure 3 is coded in the MATLAB programming language. The Bitcoin data that is used for training and validation data for the ANN network structure with optimum parameters to the hybrid structure are obtained from January 21, 2019 to January 20,2021 [38]. These data are shown in Figure 4.
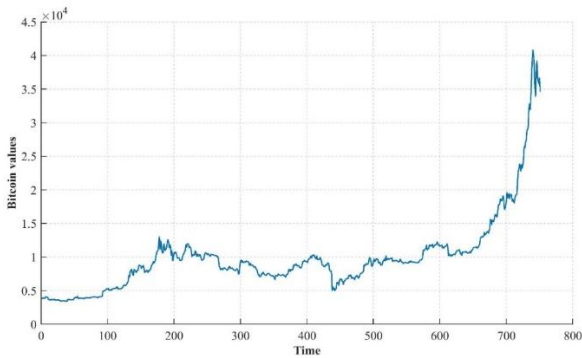
Figure 4. Bitcoin values

Figure 4 shows the graphical representation of the closing value of 756 bitcoins at the daily frequency.

In Figure 3, the initial parameters for GA were determined as shown in Table 1. Parameters presented in Table 1 were obtained as a result of experimental studies.

Table 1. DCP1 hybrid model GA parameters

Genetics Algorithm Parameters	Values
Population number (n)	25
Solution Space (D)	6
Selection Rate (c)	0.8
Mutation Rate (m)	0.25
Iteration Number (T)	50

Each individual in the GA will create an ANN within itself. All parameters necessary for each individual to form a network structure constitute

the gene sequence. The gene sequence of each individual in the population is shown in Figure 5.
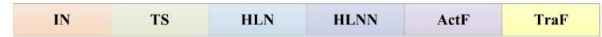
Figure 5. Gene sequencing of the DCP1 hybrid model

In the gene sequence shown in Figure 5, IN denotes the valid number of entries in the ANN to be generated for each individual. TS specifies the time series for the number of entries to be received in a given number of times. Specifies the number of hidden layers in the HLN network structure. HLNN indicates the number of neurons in each hidden layer. ActF refers to the activation function used in each neuron cell. TraF specifies the learning function of the network.

The first step of the presented DCP1 hybrid construct is to generate a random initial population. While creating the population, the parameters included in each gene (G) were determined randomly and limited to the functions presented in Equation 7 - 10.

$$G_i IN_j(x) = \begin{cases} 1, & x < 1 \\ x, & 1 \le x \le 10 \\ 10, & x > 10 \end{cases} \quad (7)$$

$$G_i TS_j(y) = \begin{cases} 1, & y < 1 \\ y, & 1 \le y \le 10 \\ 10, & y > 10 \end{cases} \quad (8)$$

$$G_i HLN_j(k) = \begin{cases} 1, & k < 1 \\ k, & 1 \le k \le 10 \\ 10, & k > 20 \end{cases} \quad (9)$$

$$G_i HLNN_j(s) = \begin{cases} 1, & s < 1 \\ s, & 1 \le s \le 10 \\ 10, & s > 20 \end{cases} \quad (10)$$

Given in Equation 7, $G_i IN_j(x)$ is the restriction function used to determine the IN value of gene i in j iteration. Given in Equation 8, $G_i TS_j(y)$ is the restriction function used to determine the TS value of gene i in j iteration . Given in Equation 9 is the $G_i HLN_j(k)$ restriction function used to determine the HLN value of gene i in j iteration . Given in Equation 10 $G_i HLNN_j(s)$, it is the limitation function used to determine the number of neurons in the hidden layers in the j iteration of the i gene. ActF value in each gene sequence is determined randomly from Equation 11 and TraF value from Equation 12.

$$ActF = \begin{Bmatrix} \text{ttrainbfg, trainbr, traincgb,} \\ \text{traincgf, traincgp, traingd,} \\ \text{traingda, traingdm, traingdx,} \\ \text{trainoss, trainrp, trainscg,} \\ \text{trainb, trainc, trainr} \end{Bmatrix} \quad (11)$$

$$TraF = \begin{Bmatrix} \text{tansig, logsig, hardlim,} \\ \text{hardlims, radbas, purelin} \end{Bmatrix} \quad (12)$$

Equations 7 to 10 are used both for population generation for GA and for mutation operations applied to genes. The next step in the created DCP1 hybrid structure is the input and output values to be created for each gene. Bitcoin in Gen In order to make an estimation of the future value , how many data will be taken before the estimation and how often these data will be taken are in the chromosomes of each gene. Within the framework of the restriction functions, since these values in each gene in the randomly determined population differ, the test and validation data for the ANN network structure created by each gene differ. At this point, input and output values are obtained for each gene according to IN and TS values.

In the population generation step, random chromosomes are generated according to the given constraint functions. Each chromosome contains a unique ANN structure and hyperparameters specific to this structure. In addition, input selection specific to the generated structure is also performed. The number of inputs and the backward time coefficient for each chromosome differ. Thanks to this feature, the model can access many regions of the multidimensional solution space.

In the next step of the proposed DCP1 hybrid construct, the quality of the fitness values of each gene will be determined. The quality of fitness values of each gene in the presented DCP1 model was determined as shown in Equation 13.

$$f(G_i) = MSE(ANN_i) \quad (13)$$

In Equation 13, $f(G_i)$ represents the fitness value of the i gene and the $MSE(ANN_i)$ value calculated according to the test values of the ANN construct created for the ANN_i i gene. The fitness values calculated for each G will be used for the probability of survival in the next generation.

In the network structure created for each G, there are parameters that are not included in the gene and concern the training and testing stages of the network structure. These parameters were determined as shown in Table 2.

Table 2. Parameters in ANN network structure

Other parameters in ANN for each gene	Values
trainParam.epochs	500
trainParam.show	5
trainParam.goal	1e -5
trainParam.lr	0.3
trainParam.mc	0.7
trainparam.min_grad	1e -10

The next step in the DCP1 hybrid structure created is the selection process. There are different strategies in the literature as a selection operator [39]. Since it produces successful results in gene selection, the roulette wheel was chosen as the selection operator in the hybrid structure created with DCP1. In the roulette wheel method, the success of each gene in the fitness function directly affects the survival probability of that gene. The fitness value of each G is calculated as presented in Equation 13. The fitness values of all individuals in the population were cumulatively summed and placed in the roulette wheel in percentages. After this process, a random roulette value between 1-100 was generated and the individual corresponding to the generated value was selected and passed to the next generation.

The next step in the DCP1 hybrid structure created is the crossover process. The genes of the two selected parents are combined to produce new offspring in the crossover process [40]. In this context, a random point was determined on the individuals in the crossover process in DCP1, and crossover was performed over this point.

After this stage, the next step in the DCP1 hybrid structure is the mutation process. The mutation rate given in Table 1 and the restriction functions given in Equation 7 to 10 were taken into account while performing the mutation operation on the genes in the population. With the mutation process, the diversity of genes in the population increases

The generated DCP1 hybrid construct was run for 150 generations as presented in Table 1.

In order to create an ANN network structure with the best performance in estimating cryptocurrencies, a hybrid structure was created with DCP2 secondly. The flow chart of the created hybrid structure is shown in Figure 6.
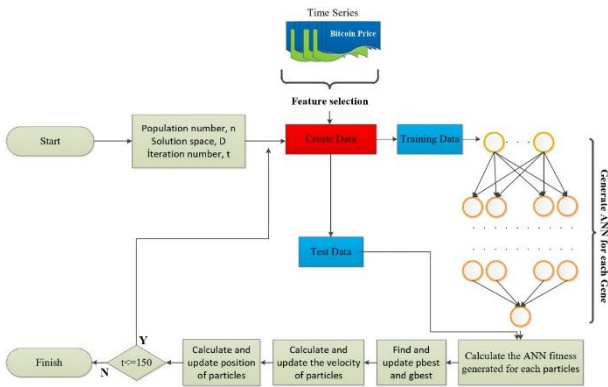
Figure 6. DCP2 hybrid model flowchart

In the flow chart of the DCP2 hybrid structure shown in Figure 6, firstly, the initial parameters for PSO were determined to be able to compare with GA, and this information is presented in Table 3.

Table 3. DCP2 hybrid model PSO parameters

PSO Algorithm parameters	Values
population number (n)	25
Solution Space (D)	6
Iteration Number (T)	50

Each particle in the PSO constitutes an ANN in itself. The network parameter values presented in Figure 5 are included in the structure of each particle.

Initially, a random initial population is created in the created DCP2 hybrid structure, and each particle is determined by the restriction functions used from Equations 7 to 10. In the following stage, pbest and gbest values were calculated in DCP2. The fitness function given in Equation 13 was used to calculate the pbest and gbest values. Since each particle in the population creates an ANN mesh structure in itself and allows a fair comparison with ANN-GA, other parameters in the ANN mesh structure were determined as presented in Table 2.

In the next step of DCP2, the velocity values of each particle and accordingly their positions were updated according to Equation 1 and Equation 2, respectively. The W value used in Equation 1 causes changes in the velocity expression. If the value of the W constant is greater than 1, the speed increases with time and the herd diverges in the algorithm. In the case of small values, the global search capability of the algorithm weakens [27]. For this reason, W value is taken as

1. The constants c1 and c2 were randomly determined to add up to about 4 [31]. Finally, the generated DCP2 hybrid construct was run for 150 generations as presented in Table 3.

The parameter values of the most successful gene and the most successful particle obtained as a result of the DCP1 and DCP2 hybrid models created by the experimental studies are shown in Table 4.

When the network structures created by the hybrid models are examined in Table 4, it has been determined that the parameter changes in the network structures differ in order to reach correct results on the same type of data. ANN network structures created by the DCP1 and DCP2 hybrid models presented in Table 4 and the performance analyzes of these network structures are presented in Figure 7.

Table 4. The most successful population members of the DCP1 and DCP2 hybrid models

Hybrid Models	OF	TS	HLN	HLNN	ActF	TraF	MSE
HCP1	6	2	1	7	purelin _ purelin	trainoss	123.405,80
HCP2	7	4	1	5	purelin _ purelin	trainscg	135.417,05
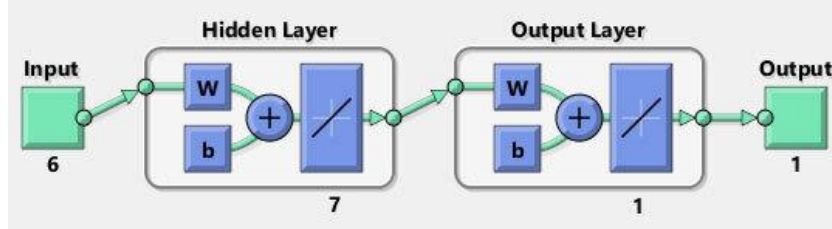
a) DCP1 ANN structures
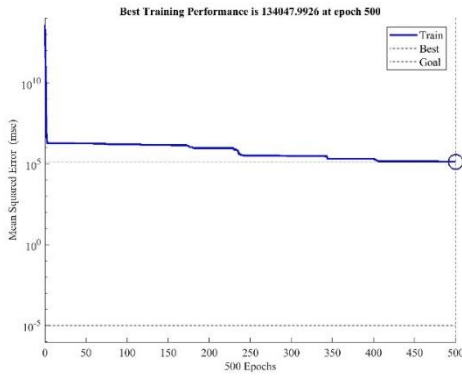
b) DCP1 ANN Performance
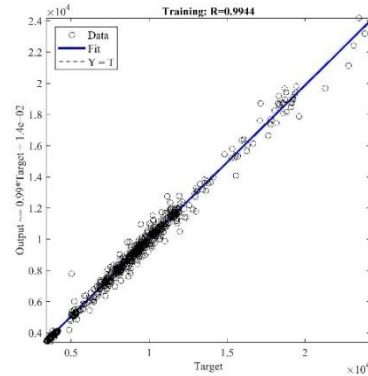
c) DCP1 ANN Regression
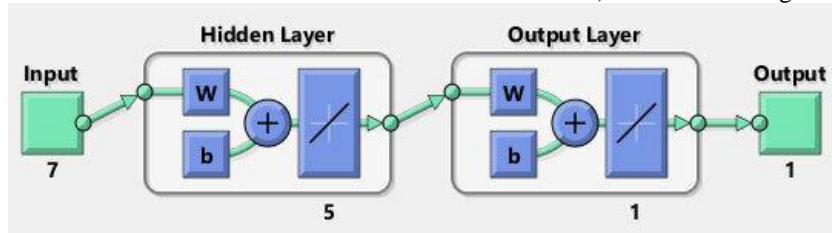
d) DCP2 ANN structures
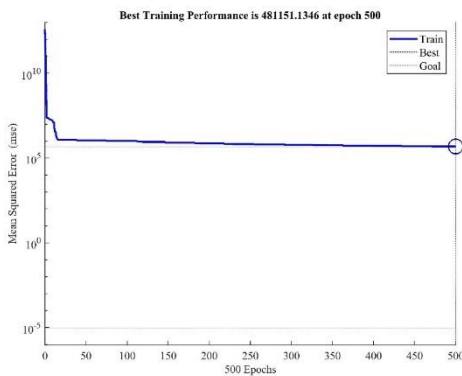
e) DCP2 ANN Performance
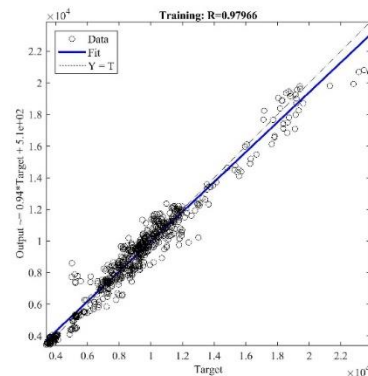
f) DCP2 ANN Regression

Figure 7. The most successful ANN network structures and performances obtained with hybrid models

In the ANN model determined by DCP1 presented in Figure 7(a), the number of entries to be given to the network is 6 data with an interval of 2 days. In this model, 1 hidden layer is determined and the

number of neurons in this hidden layer is 4. The activation functions used in this model and the learning function of the network are presented in Table 4. In the performance graph of the ANN

model determined by DCP1 presented in Figure 7(b), it is observed that the network has learned from the zeroth iteration to the 203rd iteration. In the regression graph of the ANN model determined by DCP1 presented in Figure 7(c), it is seen that the target line and the fit line overlap. In addition, the fact that the data are concentrated in this region shows that the estimation rate in the education process is high. In the ANN model determined by DCP2 presented in Figure 7(d), the number of entries to be given to the network is 7 data with an interval of 4 days. In this model, 1 hidden layer is determined and the number of neurons in this hidden layer is 5. The activation functions used in this model and the learning function of the network are presented in Table 4. In the performance graph of the ANN model determined by DCP1 presented in Figure 7(e), it is observed that the network has learned from the zeroth iteration to the 50th iteration. In the regression graph of the ANN model determined by DCP1 presented in Figure 7(f), it is seen that the target line and the fit line overlap. In addition, the fact that the data are concentrated in this region shows that the estimation rate in the education process is high.

The cryptocurrency predictions of the ANN structures created by the most successful gene of the DCP1 hybrid model and the particle belonging to the best position in the DCP2 hybrid model are shown in Figure 8.
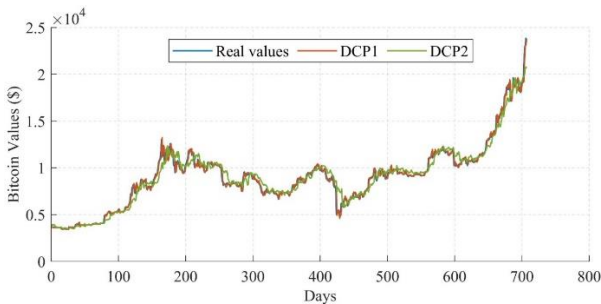
Figure 8. Bitcoin values obtained with hybrid models

Within the scope of a fair comparison, the first estimated data is ensured to be the same, considering the inputs related to the time series determined by the hybrid models. For this reason, the retrospective data used as input has been removed. Thus, the estimated data numbers were equalized and determined as 707. The performance of the models in cryptocurrency forecasting according to the prediction values presented in Figure 8 and the success evaluation metrics presented in Equations 3-6 are presented in Table 5.

Table 5. Cryptocurrency price prediction success of the models

Models	MAE	MSE	RMSE	R^2
DCP1	227,62	136.400,7	369,32	0,99
DCP2	481,33	481.105,68	693,62	0,96

The MAE, MSE, and RMSE values in Table 5, commonly employed in the literature to assess the performance of machine learning methods, are anticipated to be low, while the R^2 value is expected to approach 1. Table 5 reveals that the MAE, MSE, and RMSE values for the DCP1 model are lower than those for the DCP2 model. Furthermore, the R^2 value closely approaches 1. Considering the success of the models presented in Table 5, it is observed that the architecture of the hybrid model with GA and ANN produces more successful results than the architecture of the hybrid model with PSO and ANN. The 707-day standard deviation graph for both models is shown in Figure 9.

a) DCP1 standard deviation   b) DCP2 standard deviation
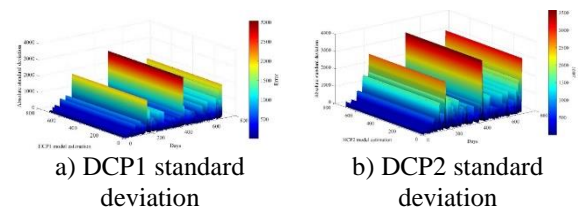
Figure 9. Standard deviation performance of the most successful ANN networks obtained with hybrid models

According to Table 5 and Figure 8, it is seen that the ANN network parameters determined with the DCP1 hybrid model produce more successful results in cryptocurrency prediction. According to Figure 9, the ANN network model created with the DCP1 model produced correct results with an average absolute error of 2.46%, while the ANN model created with the DCP2 model produced correct results with an average absolute error of 5.34%. It is noteworthy that DCP1 model produces 47.29% more successful results than DCP2 model.

4. Conclusion and Discuss

In recent years, in parallel with the development of Blockchain technology, the use of crypto assets has become increasingly widespread. Cryptocurrencies, which can be expressed as digitally encrypted sequences of numbers, are carefully followed and used by all segments of

society. As with all financial instruments or investment instruments, the sole purpose of market participants is primarily to try to predict price movements. In this context, many different technical or fundamental analysis methods have been applied. The use of artificial intelligence, which penetrates all areas of life with the developing technology, has also found its use in financial circles. Although it is claimed that it is impossible to predict price movements according to the Efficient Markets Hypothesis put forward by Fama, the existence of predictable trends or price movements is manifested in many studies as an 'anomaly'. In this perspective, there is no doubt that predicting the future positions of cryptocurrencies, as in other financial assets, is of great importance and priority. In this context, in the content of the study, it is aimed to predict the future value of Bitcoin, as the pioneer of crypto money markets, with a hybrid structure constructed over the time series. From the perspective of this purpose, two separate hybrid structures were created using ANN, GA, and PSO. With the two hybrid structures created, the time series coefficient, number of inputs and hyperparameters in the feedforward backpropagation ANN network structure to be used for prediction were optimized. The best mesh structures revealed by the proposed DCP1 and DCP2 models were arguably compared, and more successful results were obtained with the DCP1 model. In addition to revealing the optimum values of the parameters to be used in the ANN model with the hybrid models presented, the number of inputs to be used in such a problem and the time intervals that should be collected retrospectively were determined by optimization.

Ultimately, it can be claimed that the hybrid structure offered is easily usable and applicable not only for Bitcoin but also for other cryptocurrencies thanks to its flexible structure.

Conflict of Interest Statement
There is no conflict of interest between the authors.

Statement of Research and Publication Ethics

The study is complied with research and publication ethics

References

[1] K. Meng and K. Khan, "Is cryptocurrency Efficient? A High-Frequency Asymmetric Multifractality Analysis," *Comput. Econ.*, pp. 1-22, 2023, doi: 10.1007/s10614-023-10402-6.

[2] D. Shang, Z. Yan, L. Zhang, and Z. Cui, "Digital financial asset price fluctuation forecasting in digital economy era using blockchain information: A reconstructed dynamic-bound Levenberg–Marquardt neural-network approach," *Expert Syst. Appl.*, vol. 228, 2023, doi: 10.1016/j.eswa.2023.120329.

[3] M. Campbell-Verduyn, "Bitcoin, crypto-coins, and global anti-money laundering governance," *Crime, Law Soc. Chang.*, vol. 69, pp. 283-305, 2018, doi: 10.1007/s10611-017-9756-5.

[4] J. Bhosale and S. Mavale, "Volatility of select Crypto-currencies: A comparison of Bitcoin, Ethereum and Litecoin," *Annu. Res. J. SCMS, Pune*, vol.6, no.1, pp. 132-141, 2018.

[5] U. Rahardja, I. Handayani, and A. A. Ningrum, "Pemanfaatan Sistem iMe Berbasis WordPress sebagai Official Site RCEP pada Perguruan Tinggi," *Creat. Inf. Technol. J.*, vol. 4, no. 3, pp. 207, 2018, doi: 10.24076/citec.2017v4i3.111.

[6] B. Tripathi and R. K. Sharma, "Modeling Bitcoin Prices using Signal Processing Methods, Bayesian Optimization, and Deep Neural Networks," *Comput. Econ.*, vol. 62, no. 4, pp. 1919-1945, 2023, doi: 10.1007/s10614-022-10325-8.

[7] E. Işık, N. Ademović, E. Harirchian, F. Avcil, A. Büyüksaraç, M. Hadzima-Nyarko, … and B. Antep, "Determination of Natural Fundamental Period of Minarets by Using Artificial Neural Network and Assess the Impact of Different Materials on Their Seismic Vulnerability," *Appl. Sci.*, vol. 13, no. 2, pp. 809, 2023, doi: 10.3390/app13020809.

[8] I. Ayus, N. Natarajan, and D. Gupta, "Prediction of Water Level Using Machine Learning and Deep Learning Techniques," *Iran. J. Sci. Technol. - Trans. Civ. Eng.*, vol. 47, no. 4, pp. 2437–2447, 2023, doi: 10.1007/s40996-023-01053-6.

[9] J. V. Tembhurne, N. Hebbar, H. Y. Patil, and T. Diwan, "Skin cancer detection using ensemble of machine learning and deep learning techniques," *Multimed. Tools Appl.*, vol. 82, no. 18, pp. 27501-27524, 2023, doi: 10.1007/s11042-023-14697-3.

[10] S. Goutte, H. V. Le, F. Liu, and H. J. von Mettenheim, "Deep learning and technical analysis in

cryptocurrency market," *Financ. Res. Lett.*, vol. 54, pp. 103809, 2023, doi: 10.1016/j.frl.2023.103809.

[11] Z. Zhou, Z. Song, H. Xiao, and T. Ren, "Multi-source data driven cryptocurrency price movement prediction and portfolio optimization," *Expert Syst. Appl.*, vol. 219, pp. 119600, 2023, doi: 10.1016/j.eswa.2023.119600.

[12] N. A. Rashid and M. T. Ismail, "Modelling and Forecasting the Trend in Cryptocurrency Prices," *J. Inf. Commun. Technol.*, vol. 22, no. 3, pp. 449–501, 2023, doi: 10.32890/jict2023.22.3.6.

[13] L. T. Mariappan, J. A. Pandian, V. D. Kumar, O. Geman, I. Chiuchisan, and C. Năstase, "A Forecasting Approach to Cryptocurrency Price Index Using Reinforcement Learning," *Appl. Sci.*, vol. 13, no.4, pp.2692, 2023, doi: 10.3390/app13042692.

[14] K. Murray, A. Rossi, D. Carraro, and A. Visentin, "On Forecasting Cryptocurrency Prices: A Comparison of Machine Learning, Deep Learning, and Ensembles," *Forecasting*, vol. 5, no. 1, pp. 196–209, 2023, doi: 10.3390/forecast5010010.

[15] S. C. Nayak, S. Das, S. Dehuri, and S. B. Cho, "An Elitist Artificial Electric Field Algorithm Based Random Vector Functional Link Network for Cryptocurrency Prices Forecasting" *IEEE Access*, 2023, doi: 10.1109/ACCESS.2023.3283571.

[16] L. Al Hawi, S. Sharqawi, Q. A. Al-Haija, and A. Qusef, "Empirical Evaluation of Machine Learning Performance in Forecasting Cryptocurrencies," *J. Adv. Inf. Technol.*, vol. 14, no. 4, pp. 639–647, 2023, doi: 10.12720/jait.14.4.639-647.

[17] K. Ateeq, A. A. Al Zarooni, A. Rehman, and M. A. Khan, "A Mechanism for Bitcoin Price Forecasting using Deep Learning," *Int. J. Adv. Comput. Sci. Appl.*, vol. 14, no. 8, 2023, doi: 10.14569/IJACSA.2023.0140849.

[18] I. Alarab and S. Prakoonwit, "Graph-Based LSTM for Anti-money Laundering: Experimenting Temporal Graph Convolutional Network with Bitcoin Data," *Neural Process. Lett.*, vol. 55, no. 1, pp. 689-707, 2023, doi: 10.1007/s11063-022-10904-8.

[19] R. M. Aziz, M. F. Baluch, S. Patel, and P. Kumar, "A Machine Learning Based Approach to Detect the Ethereum Fraud Transactions with Limited Attributes," *Karbala Int. J. Mod. Sci.*, vol. 8, no. 2, pp. 139-151, 2022, doi: 10.33640/2405-609X.3229.

[20] J. Li, "The comparison of lstm, lgbm, and cnn in stock volatility prediction," *In: 2022 7th International Conference on Financial Innovation and Economic Development (ICFIED 2022)*, pp. 905–909 2022. Atlantis Press. doi: 10.2991/aebmr.k.220307.147.

[21] S. Kazeminia, H. Sajedi, and M. Arjmand, "Real-time bitcoin price prediction using hybrid 2d-cnn lstm model," *In: 2023 9th International Conference on Web Research (ICWR)*, pp. 173–178, 2023. IEEE. doi: 10.1109/ICWR57742.2023.10139275.

[22] M. A. Bülbül and C. Öztürk, "Optimization, Modeling and Implementation of Plant Water Consumption Control Using Genetic Algorithm and Artificial Neural Network in a Hybrid Structure," *Arab. J. Sci. Eng.*, vol. 47, no. 2, pp. 2329-2343, 2022, doi: 10.1007/s13369-021-06168-4.

[23] P. Matić, O. Bego, and M. Maleš, "Complex Hydrological System Inflow Prediction using Artificial Neural Network," *Teh. Vjesn.*, vol. 29, no. 1, pp. 172-177, 2022, doi: 10.17559/TV-20200721133924.

[24] D. Nahavandi, R. Alizadehsani, A. Khosravi, and U. R. Acharya, "Application of artificial intelligence in wearable devices: Opportunities and challenges," *Computer Methods and Programs in Biomedicine*. vol. 213, pp. 106541, 2022. doi: 10.1016/j.cmpb.2021.106541.

[25] S. S. Ul Hasan, A. Ghani, I. U. Din, A. Almogren, and A. Altameem, "IoT devices authentication using artificial neural network," *Comput. Mater. Contin.*, vol. 70, pp. 3701-3716, 2022, doi: 10.32604/cmc.2022.020624.

[26] D. P. Soman, P. Kalaichelvi, and T. K. Radhakrishnan, "Density modelling and apparent molar volume of ionic liquid 1-butyl-3-methylimidazolium bromide in water," *J. Brazilian Soc. Mech. Sci. Eng.*, vol. 44, no. 3, pp. 1–14, 2022, doi: 10.1007/s40430-021-03248-2.

[27] M. A. Bülbül, "Optimization of artificial neural network structure and hyperparameters in hybrid model by genetic algorithm: iOS–android application for breast cancer diagnosis/prediction," *J. Supercomput.*, vol. 80, no. 4, pp. 4533-4553, 2023, doi: 10.1007/s11227-023-05635-z.

[28] B. Sun and Y. Zhou, "Bayesian network structure learning with improved genetic algorithm," *Int. J. Intell. Syst.*, vol. 37, no. 9, pp. 6023-6047, 2022, doi: 10.1002/int.22833.

[29] A. Taha and O. Barukab, "Android Malware Classification Using Optimized Ensemble Learning Based on Genetic Algorithms," *Sustain.*, vol. 14, no. 21, pp. 14406, 2022, doi: 10.3390/su142114406.

[30] X. Liu, D. Jiang, B. Tao, G. Jiang, Y. Sun, J. Kong, X. Tong, G. Zhao and B. Chen, "Genetic Algorithm-Based Trajectory Optimization for Digital Twin Robots," *Front. Bioeng. Biotechnol.*, vol. 9, pp. 7937822, 022, doi: 10.3389/fbioe.2021.793782.

[31] M. A. Bülbül, C. Öztürk, and M. F. Işık, "Optimization of Climatic Conditions Affecting Determination of the Amount of Water Needed by Plants in Relation to Their Life Cycle with Particle Swarm Optimization, and Determining the Optimum Irrigation Schedule," *Comput. J.*, vol. 65, no. 10, pp. 2654-2663, 2022, doi: 10.1093/comjnl/bxab097.

[32] R. P. de Gusmão and F. de A. T. de Carvalho, "Clustering of multi-view relational data based on particle swarm optimization," *Expert Syst. Appl.*, vol. 123, pp. 34-53, 2019, doi: 10.1016/j.eswa.2018.12.053.

[33] S. Papadakis and M. Markaki, "An in depth economic restructuring framework by using particle swarm optimization," *J. Clean. Prod.*, vol. 215, pp. 329–342, 2019, doi: 10.1016/j.jclepro.2019.01.041.

[34] J. Zhu, J. Liu, Y. Chen, X. Xue, and S. Sun, "Binary Restructuring Particle Swarm Optimization and Its Application," *Biomimetics*, vol. 8, no. 2, pp. 266, 2023, doi: 10.3390/biomimetics8020266.

[35] S. Xu , X. Yang, S. Zhang, X. Zheng, F. Zheng, Y. Liu, H. Zhang, Q. Ye and L. Li, "Machine learning models for orthokeratology lens fitting and axial length prediction," *Ophthalmic Physiol. Opt.*, vol. 43, no. 6, pp. 1462-1468, 2023, doi: 10.1111/opo.13212.

[36] M. A. Bülbül, E. Harirchian, M. F. Işık, S. E. Aghakouchaki Hosseini, and E. Işık, "A Hybrid ANN-GA Model for an Automated Rapid Vulnerability Assessment of Existing RC Buildings," *Appl. Sci.*, vol. 12, no. 10, 2022, doi: 10.3390/app12105138.

[37] M. F. Işık, F. Avcil, E. Harirchian, M. A. Bülbül, M. Hadzima-Nyarko, E. Işık, R. İzol and D. Radu, "A Hybrid Artificial Neural Network—Particle Swarm Optimization Algorithm Model for the Determination of Target Displacements in Mid-Rise Regular Reinforced-Concrete Buildings," *Sustainability*, vol. 15, no. 12, pp. 9715, 2023, doi: 10.3390/su15129715.

[38] coinmarketcap.com: Bitcoin price today. https://coinmarketcap.com/currencies/ bitcoin/historical-data/. [Date of access: September 2022]

[39] N. M. Razali, J. Geraghty, "Genetic algorithm performance with different selection strategies in solving tsp," *In: Proceedings of the World Congress on Engineering*, vol. 2, pp. 1–6, 2011. International Association of Engineers Hong Kong, China.

[40] I. Jannoud, Y. Jaradat, M. Z. Masoud, A. Manasrah, and M. Alia, "The role of genetic algorithm selection operators in extending wsn stability period: A comparative study," *Electron.*, vol. 11, no. 1, pp.28, 2022, doi: 10.3390/electronics11010028.

Bitlis Eren Üniversitesi Fen Bilimleri Dergisi

Approximation Solution for Initial Value Problem of Singularly Perturbed Integro-Differential Equation

Derya ARSLAN[1*]

Department of Mathematics, Faculty of Arts and Sciences, Bitlis Eren University, Bitlis, TR
(ORCID: 0000-0001-6138-0607)

Keywords: ADM, Singularly perturbed equation, Volterra-Fredholm integro-differential equation, Approximate solution.

Abstract
Adomian Decomposition Method (ADM) is used to approximately solve the initial value problem of the singularly perturbed Volterra-Fredholm differential equation. With this method, the desired accurate results are obtained in only a few terms. The approach is simple and effective. An example application is made to demonstrate the effectiveness of ADM. The result obtained is compared with the exact solution. Convergence analysis of the method is performed.

1. Introduction

Volterra-Fredholm integro-differential equations are involved in many different fields of science and engineering: Oceanography, fluid mechanics, electromagnetic theory, finance mathematics, plasma physics, population dynamics, artificial neural networks and biological processes are among these fields [1], [2], [28]. It is quite difficult to solve analytically the Volterra-Fredholm integro-differential equations needed in such fields. Therefore, strong numerical methods must be used. Some of them are Adomian decomposition method, spectral collocation method, Legendre wavelet method, 2D block-pulse functions method, finite difference method, Legendre collocation method, Bernstein polynomials method, homotopy perturbation method [3]-[8]. Existence and uniqueness investigations of the solutions of integro-differential equations have also been done [9], [10].

Singularly perturbed problems are characterized by the fact that the coefficient of the highest-order term in the equation is a very small parameter ε. Their approximate solutions have been studied in many articles and books. The mathematical models seen here are population dynamics, fluid dynamics, heat transport problem, nanofluid, neurobiology, mathematical biology, viscoelasticity

and simultaneous control systems etc. They can be listed in many applications in fields [11]-[16]. The perturbation parameter ε in the equation produces unlimited derivatives in the solution. Appropriate numerical methods should be preferred to eliminate this situation [14]-[18]. The fact that the problem examined in this study has both singular perturbation and integro-differential equation properties makes it difficult to obtain an analytical solution. Therefore, the Adomian decomposition method was used in the study to overcome these two difficulties. In the literature, there are studies in which different techniques are applied on singularly perturbed Volterra-Fredholm integro-differential equations: Using the Richardson extrapolation, the convergence of the singularly perturbed Volterra integro-differential equations was obtained in [24]. Durmaz and et al., Fredholm created a finite difference scheme for the integro-differential equation [17]. In recent years, many authors have applied different methods such as homotopy analysis method, modified variational iteration method, Adomian decomposition method, modified homotopy perturbation method to obtain approximate analytical solutions for Volterra, Fredholm, Volterra-Fredholm equations and fuzzy Volterra-Fredholm integro-differential equations [17]-[20].

In the study, the following singularly perturbed Volterra-Fredholm integro-differential equation with an initial condition are examined [17]:

$$\varepsilon y' + b(x)y + \int_0^x M(x,s)y(s)ds +$$
$$\mu \int_0^1 N(x,s)y(s)ds = H(x), \qquad (1)$$

$$y(0) = A, \qquad (2)$$

where $0 < \varepsilon \ll 1$ is a very small perturbation constant, μ and A are real constants, $(x,s) \in (0,1] \times [0,1]$. We assume that $b > 0$; M, H and N are the sufficiently smooth functions.

2. Material and Method

2.1. ADM and Its Convergence Analysis

George Adomian introduced ADM to solve nonlinear functional equations in the 1980s. These solutions are in the form of infinite power series obtained by a simple formula [21]-[23]. Additionally, Cherruault and Adomian [24], [25], [27] obtained convergence analysis of ADM. Al-Kalla [26] offered a different view on the error analysis of ADM.

It is defined as ADM [21]-[23]: Let F be an ordinary or partial differential operator, which is itself nonlinear, containing linear and nonlinear terms, and let the given function be g: The method should be given in detail and clearly in terms of reproducibility of the study. The methods used should be supported by previously published references. In the study, the changes that will contribute to the method should be explained in detail [3], [4].

$$Fy(t) = g(t). \qquad (3)$$

Let's take the equation (3). If this equation is written in decomposed form, the following equation is formed:

$$Ly + Ry + Ny = g, \qquad (4)$$

L is the highest order derivative of the given differential equation and its inverse is a linear operator that is easily taken. R is the remaining linear part from the linear operator; N is the nonlinear term in the given differential equation.

If the integral operator L^{-1} is applied from the left side to both sides of equation (4), we have

$$L^{-1}Ly + L^{-1}Ry + L^{-1}Ny = L^{-1}g,$$

$$\boldsymbol{L^{-1}Ly = L^{-1}g - L^{-1}Ry}$$
$$\boldsymbol{- L^{-1}Ny}. \qquad (5)$$

If the differential equation is $\boldsymbol{nth}$-order, linear differential operator for ordinary differential equations is as

$$L(.) = \frac{d^n}{dt^n}(.),$$

the integral operator is as given below:

$$L^{-1}(.) = \int_0^t (.)\, dt,$$

$$L^{-1}(.) = \int_0^t \int_0^t (.)dtdt,$$
$$L^{-1}(.) = \int_0^t \int_0^t \ldots \int_0^t (.)\, dtdt \ldots dt.$$

The nonlinear Ny terms in equation (5) are defines as

$$Ny = \sum_{n=0}^{\infty} A_n,$$

where A_n is Adomian polynomials.

$$y = y(0) + L^{-1}g - L^{-1}Ry - L^{-1}Ny. \qquad (6)$$

The decomposed series solution function (6) is obtained by using some calculations in equation (5) and the derivative and integral operators above.

The first term y_0 of the series solution function (6) is obtained using the given initial value and integrating of g as following:

$$y_0 = y(0) + L^{-1}g,$$

$$y_{n+1} = -L^{-1}R\ y_n - L^{-1}A_n, \ n = 0,1,2,3, \ldots \qquad (7)$$

Then, the terms $y_1, y_2, y_3, \ldots$ are obtained with the help of the above recurrence relation (7) with the initial function y_0,

$$y_1 = -L^{-1}R\ y_0 - L^{-1}A_0,$$

$$y_2 = -L^{-1}R\ y_1 - L^{-1}A_1.$$

Finally, it has been obtained the following approximate series solution with the ADM

$$y(t) = \sum_{n=0}^{\infty} y_n = y_0 + y_1 + y_2 + y_3$$
$$+ \cdots \qquad (8)$$

Convergence analysis of ADM is done with the definition given below:

Definition 2.1.

$\forall i \in N$,

$$\alpha_i = \begin{cases} \frac{\|y_{i+1}\|}{\|y_i\|}, & \|y_i\| \neq 0 \\ 0, & \|y_i\| = 0, \end{cases} \qquad (9)$$

is defined [25].

Corollary 2.1. The approximate series solution converges to the exact solution y for as [25]:

$$0 \leq \alpha_i < 1, \qquad \sum_{n=0}^{\infty} y_i.$$

2.2. Application of the ADM

In this section, firstly, the equation (1) is written in operator form with the help of a linear differential operator. Adomian polynomials A_n are used to linearize the nonlinear terms. Then, recurrence relation is obtained. The $y_0, y_1, y_2, \ldots$ are written in the sum (8) and the series solution is found.

Application 1:

$$\varepsilon y' + y + \int_0^x xy(s)ds + \frac{1}{10}\int_0^1 y(s)ds$$
$$= \frac{-\varepsilon}{(x+1)^2} + \frac{1}{x+1} + x\varepsilon\left(1 - e^{\frac{-x}{\varepsilon}}\right) + xln(x+1) +$$
$$\frac{1}{10}\left(1 - e^{\frac{-1}{\varepsilon}} + ln(2)\right) \qquad (10)$$

$$y(0) = 2, \qquad (11)$$

This problem (10)-(11) has the following exact solution:

$$y(x) = e^{\frac{-x}{\varepsilon}} + \frac{1}{x+1}.$$

$$L(.) = \frac{d}{dt}(.), \qquad L^{-1}(.) = \int_0^x (.) \, dx.$$

Now let's write the equation (10) in the operator form using the above differential operator

$$Ly = -y - \int_0^x xy(s)ds - \frac{1}{10}\int_0^1 y(s)ds - \frac{\varepsilon}{(x+1)^2}$$
$$+ \frac{1}{x+1} + x\varepsilon\left(1 - e^{\frac{-x}{\varepsilon}}\right)$$
$$+ xln(x+1) + \frac{1}{10}\left(1 - e^{\frac{-1}{\varepsilon}} + ln(2)\right)$$

Let's apply the left-hand integrate operator to both sides of the above equation.

$$L^{-1}Ly = -L^{-1}y$$
$$- L^{-1}\left(\int_0^x xy(s)ds - \frac{1}{10}\int_0^1 y(s)ds\right)$$
$$- L^{-1}\left(\frac{\varepsilon}{(x+1)^2}\right) + L^{-1}\left(\frac{1}{x+1}\right)$$
$$+ L^{-1}\left(x\varepsilon\left(1 - e^{\frac{-x}{\varepsilon}}\right) + xln(x+1)\right)$$
$$+ L^{-1}\left(\frac{1}{10} - \frac{e^{\frac{-1}{\varepsilon}} + ln(2)}{10}\right), \qquad (12)$$

if we find the value of the $L^{-1}Ly$ here and substitute it, we get the following equation:

$$L^{-1}Ly = \int_0^t y'(x)dx = \varepsilon y(x) - 2\varepsilon. \qquad (13)$$

When the equation (13) is written in equation (12), the following decomposition series solution function is obtained.

If the y_n terms of the decomposition series obtained from the reduction relation are substituted in the series solution function, we have series solution as:

$$y(x) = 2.000000000$$
$$+ \frac{1}{x+1}(1.8.10^{-29}(-6.127188770$$

$\times 10^{28} x e^{1.111111111x} - 4.5.\,10^{28} e^{1.111111111x}$
$+ 1.234567901 \times 10^{28} x^3 e^{1.111111111x}$
$+ 3.086419752 \times 10^{28} \ln(x+1)\, e^{1.111111111x})$
$+ \cdots + 4.500000000 \times 10^{28} + \cdots$ $\quad (14)$

Table 1. The values of the exact solution, approximate solution and error for $\varepsilon = 0.9$

Exact solution	Approximate solution	Error
2.0000000000	2.0000000000	0.00000000
1.8039302260	1.8021043650	0.00182584
1.6340707360	1.6314713230	0.00259941
1.4857620800	1.4844007420	0.00136131
1.3554661030	1.3576017060	0.00213552
1.2404200880	1.2478274050	0.00740736
1.1384171190	1.1515967820	0.01317965
1.0476611180	1.0649416730	0.01728048
0.9666678461	0.9831551520	0.01648714
0.8941952300	0.9005210400	0.00632573
0.8291929878	0.8100025118	0.01919066
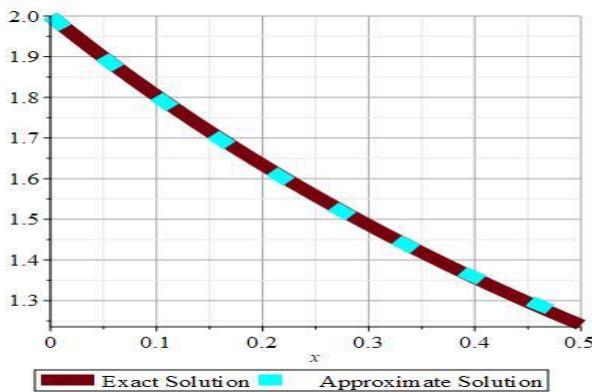
Figure 1. The curves of approximate and exact solution for ε=0.9

An algorithm is built to solve this example using ADM for ε=0.9. This algorithm is solved with a suitable mathematical program. Numerical results were obtained with only 3 iterations. Figure 1 shows that the exact and approximate solution curves overlap. That is, the convergence has achieved. In Table 1, the values of the exact, approximate solution and error are given. Here, it has seen that the error increases as the x values approach towards 1.

To investigate the convergence of Example 1, Definition 2.1 and Corollary 2.1 have been used and this convergence has been showed as follows:

$\alpha_0 = 0.9831550086 < 1,$

$\alpha_1 = 0.9005209752 < 1,$

$\alpha_2 = 0.8100025048 < 1.$
…

These convergence results are great proof for the accuracy of the approximate solution. This proof shows that ADM is a powerful and well-chosen method in paper.

3. Conclusion and Suggestions

The initial value problem of the Volterra-Fredholm integro-differential equation with singularly perturbed was quickly solved using only three iterations with ADM. Approximate, exact solution and error values are compared in the Table 1 and Figure 1. Convergence analysis was performed. So, the values of $\alpha_i,\ i = 0,1,2,...$ were found to be less than 1. According to all these results, the method is stable, reliable and useful. In order to contribute to the literature, it can be said that ADM can also be applied to the delayed, fuzzy and fractional types of integral equations.

Conflict of Interest Statement

There is no conflict of interest between the authors.

References

[1] O. Diekmann, "Thresholds and travelling waves for the geographical spread of infection," *J. Math. Biol.*, vol. 6, pp. 109-130, 1978.
[2] E.H. Ouda, S. Shihab and M. Rasheed, "Boubaker wavelet functions for solving higher order integro-differential equations," *J. Southwest Jiaotong Univ.*, vol. 55, pp. 1-12, 2020.

[3]   M.K. Kadalbajoo and V. Gupta, "A brief survey on numerical methods for solving singularly perturbed problems," *Appl. Math. Comput.*, vol. 217, pp. 3641-3716, 2010.

[4]   M.E. Durmaz, Ö. Yapman, M. Kudu and G. M. Amiraliyev, "An efficient numerical method for a singularly perturbed Volterra-Fredholm integro-differential equation," *Hacettepe Journal of Mathematics & Statistics*, vol. 52, pp. 326 – 339, 2023.

[5]   L.A. Dawood, A.A. Hamoud and N.M. Mohammed, "Laplace discrete decomposition method for solving nonlinear Volterra-Fredholm integro-differential equations," *J. Math. Computer Sci.*, vol. 21, pp. 158-163, 2020.

[6]   N.A. Mbroh, S.C. Oukouomi Noutchie and R.Y. M'pika Massoukou, "A second order finite difference scheme for singularly perturbed Volterra integro-differential equation," *Alex. Eng. J.*, vol. 59, pp. 2441-2447, 2020.

[7]   M.S.B. Issa, A.A. Hamoud and K.P. Ghadle, "Numerical solutions of fuzzy integro-differential equations of the second kind," *J. Math. Computer Sci.*, vol. 23, pp. 67-74, 2021.

[8]   G. Adomian, "A review of the decomposition method and some recent results for nonlinear equation," *Math. Comput. Model.*, vol. 13, pp. 17, 1992.

[9]   G. Adomian and R. Rach, "Analytic solution of nonlinear boundary-value problems in several dimensions by decomposition," *Journal of Mathematical Analysis and Applications*, vol.174, pp. 118-137, 1993.

[10]   G. Adomian, *Solving Frontier problems of physics: The decomposition method*. Kluwer Academic Publishers, Boston: 1994.

[11]   Y. Cherruault and G. Adomian, "Decomposition methods a new proof of convergence," *Mathematical and Computer modelling*, vol. 18, pp. 103- 106, 1993.

[12]   Y. Cherruault, "Convergence of Adomian's method," *Kybernetes*, vol. 18, pp. 31–38, 1989.

[13]   I. El-Kalla, Error analysis of Adomian series solution to a class of non-linear differential equations, *Appl. Math E-Notes,* vol. 7, pp. 214-221, 2007.

[14]   M. Cakir and D. Arslan, "The Adomian decomposition method and the differential transform method for numerical solution of multi-pantograph delay differential equations," *Applied Mathematics*, vol. 6, pp. 1332-1343, 2015.

[15]   E. Banifatemi, M. Razzaghi and S. Youse, "Two-dimensional Legendre wavelets method for the mixed Volterra-Fredholm integral equations," *J. Vib. Control*, vol.13, pp. 1667-1675, 2007.

[16]   H. Brunner, "Numerical analysis and computational solution of integro-differential equations." *Contemporary Computational Mathematics*-A Celebration of the 80th Birthday of Ian Sloan, 205-231, 2018.

[17]   M. Gülsu, Y. Öztürk and M. Sezer, "A new collocation method for solution of mixed linear integro-differential-difference equations," *Appl. Math. Comput.*, vol. 216, pp. 2183- 2198, 2010.

[18]   D.A. Maturi and E.A.M. Simbawa, "The modified decomposition method for solving Volterra Fredholm integro-differential equations using Maple", *Int. J. GEOMATE*, vol. 18, pp. 84-89, 2020.

[19]   B. Raftari, "Numerical solutions of the linear Volterra integro-differential equations: Homotopy perturbation method and finite difference method," *World Appl. Sci. J.*, vol. 9, pp. 7-12, 2010.

[20]   A. M. Dalal, "Adomian decomposition method for solving of Fredholm integral equation of the second kind using matlab," *International Journal of GEOMATE*, vol. 11, pp. 2830-2833, 2016.

[21]   A.A. Hamoud and K.P. Ghadle, "Existence and uniqueness of the solution for Volterra-Fredholm integro-differential equations," *J. Sib. Fed. Univ. - Math. Phys.*, vol. 11, pp. 692-701, 2018.

[22]   A.H. Mahmood and L.H. Sadoon, "Existence of a solution of a certain Volterra-Fredholm integro differential equations," *J. Educ. Sci.*, vol. 25, pp. 62-67, 2012.

[23]   H.G. Roos, M. Stynes and L. Tobiska, *Robust Numerical Methods for Singularly Perturbed Differential Equations*. Springer-Verlag, Berlin Heidelberg: 2008.

[24]   E.R. Doolan, J. J. H. Miller, and W. H. A. Schilders, *Uniform numerical methods for problems with initial and boundary layers*. Dublin: Boole Press, 1980.

[25]   G.M. Amiraliyev and I. Amirali, *Nümerik Analiz Teori ve Uygulamalarla*. Ankara: Seçkin Yayıncılık, 2018.

[26]   P.A. Farrell, A.F. Hegarty, J.J.H. Miller, E. O'Riordan and G.I. Shishkin, *Robust Computational Techniques for Boundary Layers*. New York: Chapman Hall/CRC, 2000.

[27] R.O. O'Malley, *Singular Perturbations Methods for Ordinary Differential Equations*. New York: Springer-Verlag, 1991.

[28] V. Lakshmikantham, *Theory of Integro-differential Equations*. CRC press, 1995.

Bitlis Eren Üniversitesi Fen Bilimleri Dergisi

Numerical Investigation of the Effects of Impactor Geometry on Impact Behavior of Sandwich Structures

Ilyas BOZKURT[1*]

[1]Department of Mechanical Engineering, Architecture and Engineering Faculty, Muş Alparslan
 University, Muş, Türkiye.
(ORCID: 0000-0001-7850-2308)

Abstract
The aim of this study is to examine the impact performance and damage behavior of sandwich composite structures with a core material of aluminum and a facesheet of glass fiber composites using the finite element method. In the study, the effects of impactor shape, impact velocity and number of core layers on peak force, absorbed energy efficiency, maximum displacement and damage deformation were examined. For low velocity impact simulation, *progressive damage analysis* was performed based on the *Hashin damage criterion* using the *MAT 54* material model in the *LS DYNA* finite element program. While providing the connection between the core structure and its surfaces, a *Cohesive Zone Model (CZM)* based on the *bilinear traction-separation law* was created and examined. At the end of the study, it was determined that the shape of the impactor had a significant effect on impact resistance. Energy absorption efficiency may vary as impact energy changes. However, as the impact energy increases, the energy absorption efficiency increases. It was determined that the largest and dominant damage type for all three impactors was matrix damage.

1. Introduction

Composite structures are used effectively in many sectors, especially in the defense industry, due to their high strength/weight ratios [1]. Especially recently, with the technological developments and the development of production machines and production methods, it has started to be used in many areas in our daily lives, from mobile phone cases to car steering wheels. In addition, the use of composite structures, which are widely used in the aviation and space industry, especially in large passenger aircraft, and which carry life and property, is increasing day by day. However, their performance decreases due to the loads they are exposed to in application areas and during service [2]. Especially under impact load, major damage may occur over time due to delamination that occur in the material structure and are sometimes invisible to the eye. To prevent this, the impact performance and damage behavior of these structures must be known very well. In addition, since the shape or size of the object causing the impact is not known precisely, the reaction of the material and structure against it is unknown [3]. Therefore, when engineers or researchers design a new structure, they need to review all these possibilities and realize the optimum design within these possibilities.

Determining the behavior of composite structures under load is more difficult than metal materials [4]. Because metal structures have linearity, material reactions and behaviors under load can be predicted. However, it was more difficult to determine this behavior in composite structures. Because after impact is applied to composite structures, different types of damage (such as matrix damage, fiber damage, delamination) occur to absorb this energy. These damages gradually occur to absorb the incoming energy, and then the damage to the structure is completed. In addition, the complex micromechanical structure of composite structures

---

*Corresponding author: *ilyasbozkurt02@gmail.com*

makes it difficult for researchers to determine this material behavior. Because there may be composites with very different numbers of fiber bundles, very different types of matrix materials and produced at very different temperatures [5]. The mechanical behavior of these structures is different from each other. Therefore, it is essential to further determine the impact performance and damage behavior of these structures and develop them further.

Many studies have been conducted on the impact performance of composite structures [6-12]. However, there are many studies examining the impact behavior of sandwich composite structures, which have a very high impact absorption potential [13-23]. Manes et al. [24-25] examined the impact performances of foam-based sandwich composites with different densities. Albayrak et al. [26-27] investigated the low velocity impact behavior of curved glass sandwich composites with rubber interlayers. They examined impact performances for different orientation angles and curvature shapes. They carried out numerical simulations using the *LS DYNA MAT 162* material model. Bozkurt et al. [15, 28] examined the effects of structural differences of carbon sandwich composites with different core structures on the impact performance. They successfully applied numerical simulations with the *LS DYNA* finite element model. Xue et al. [29] experimentally and numerically examined the impact behavior of specimens produced using honeycomb core carbon/glass fiber hybrid composite facesheets. Yellur et al. [30] experimentally and numerically examined the effects of upper and lower facesheet thicknesses on impact behavior in polypropylene honeycomb sandwich structures. They used the *LS-DYNA* finite element model for numerical analysis. Susainathan et al. [31] numerically investigated the impact behavior of innovative wood-based sandwich structures with plywood cores and coatings made of aluminum or fiber-reinforced polymer (carbon, glass or flax composite coatings). Numerical models were created with ls dyna. Shirbhate et al. [32] examined the explosion response of a hexagonal honeycomb sandwich structure with holes along the cell height of the core compared to conventional honeycomb cores. They performed detailed numerical analysis to accurately reproduce the deformation process by finite element analysis using the open *LS-DYNA* software. Yalkın et al. [33] numerically investigated the low-speed impact properties of E-glass fiber/epoxy and PVC foam core sandwich composite configurations. Numerical simulations were carried out using material models of hard impact, foam core and composite material models of *LS-DYNA* software. Damghani et al. [34] simulated the impact behavior of

aluminum foam core sandwich structures with *LS-DYNA* software. They investigated the effects of foam density on impact performance.

In this study, the impact performance and damage behavior of sandwich composite structures, whose core material is aluminum and facesheet material is glass fiber composite, were examined using the finite element method. In the study, unlike the literature, the effects of impactor shape (cylinder, cone and sphere) impact velocity (10 J, 30 J and 60 J), and number of core layers (1 layer, 2 layers and 3 layers) on peak force, absorbed energy efficiency, maximum displacement and damage deformation were investigated. The energy absorption efficiency values obtained at the end of the study were compared with similar studies in the literature.

2. Material and Method

The dimensions details of sandwich composite specimens with aluminum core and glass fiber composite facesheets are given in Figure 1 and the tests to be performed are given in Table 1. Low velocity impact test will be applied to the specimens whose dimensions are given. The dimensions and shapes of the impactors used in the study are given in Figure 2. The upper and lower holders are fixed to ensure the same boundary conditions as the standard experimental testing mechanism. The impactor was limited to displacements in the x and y directions and could only move in the impactors direction (z-axis).

An eight-node solid element (*ELFORM1*) was used in the modeling. There are many element types in the finite element model. Generally, eight-node solid element types are used in the studies. There are many reasons why this is preferred. First of all, as the number of nodes increases, the processing time increases significantly. Especially in studies where the number of elements is high, the processing time becomes very long. Eight-node solid element types can be intervened more effectively in the calibration process. In addition, the damage criteria coefficients that allow this in the *LS DYNA MAT 54* material model make this process easier. This element type is used in most of the *LS DYNA* applications in the literature. 30197 nodes and 26750 solid elements were used. The lower and upper holders were modeled with 7740 nodes and 5500 solid elements. The CONTACT ERODING SURFACE TO SURFACE contact card was used to model the contact force between the sandwich composite and the impactor. The CONTACT AUTOMATIC SURFACE TO SURFACE contact card was used to prevent the specimen between the holders from moving during impact and to keep it fixed by the

holder. The static and dynamic friction coefficients here are entered as 0.2 and 0.3, respectively [28].
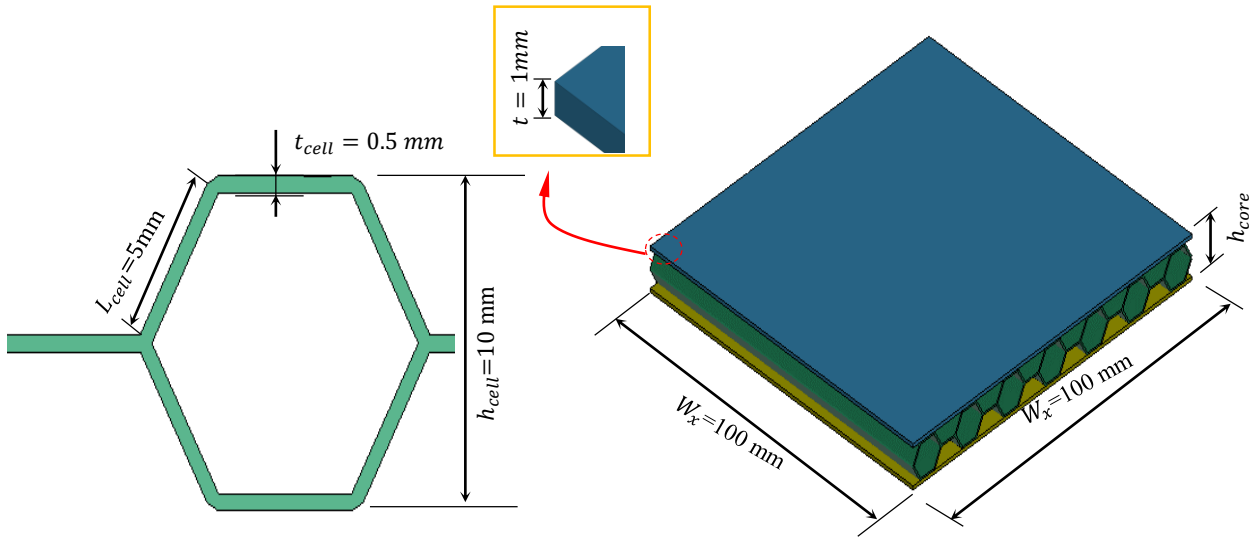
Figure 1. Specimen dimensions.
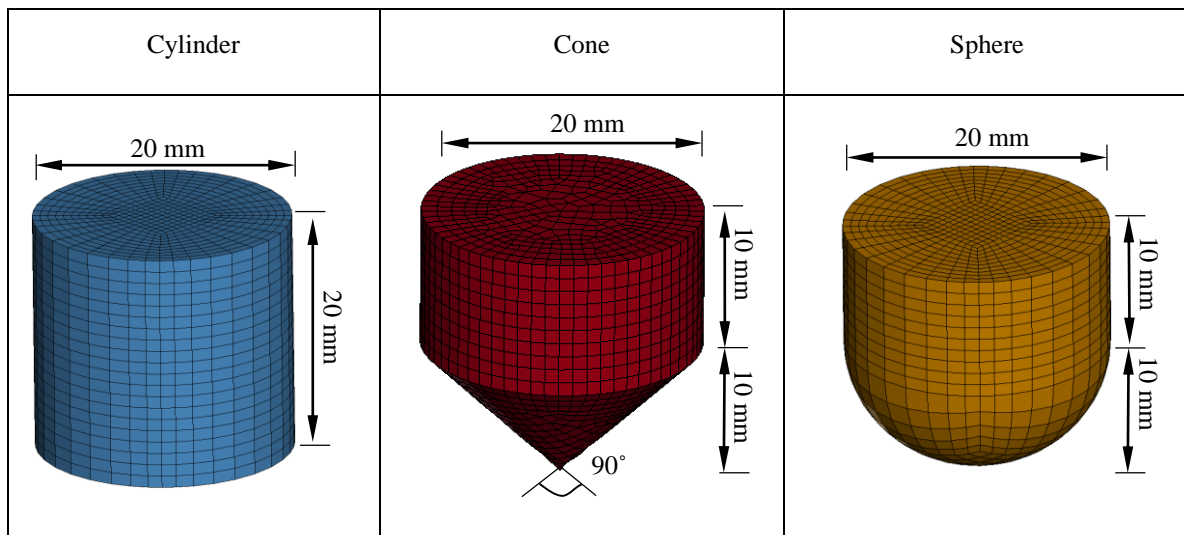
Figure 2. Impactor's dimensions.

The program's solution methodology includes material cards that provide damage models based on the *continuous damage mechanism* (CDM). It allows progressive visualization of structural damage using models based on CDM. Impact tests with dimensions of 100x100 mm were carried out numerically for all specimens used in this research. The mesh size is taken as 2x2 mm. The sandwich composite plate and the upper and lower holders are modeled as shown in Figure 3. As indicated in Figure 4, the impact test was applied to the center of all specimens.

Table 1. Parameters examined for sandwich panels in impact testing.

No	Impactor shape	Core number, n	Impact Energy, E [J]
1	Sphere	1-2-3	10-30-60
2	Cylinder	1-2-3	10-30-60
3	Cone	1-2-3	10-30-60
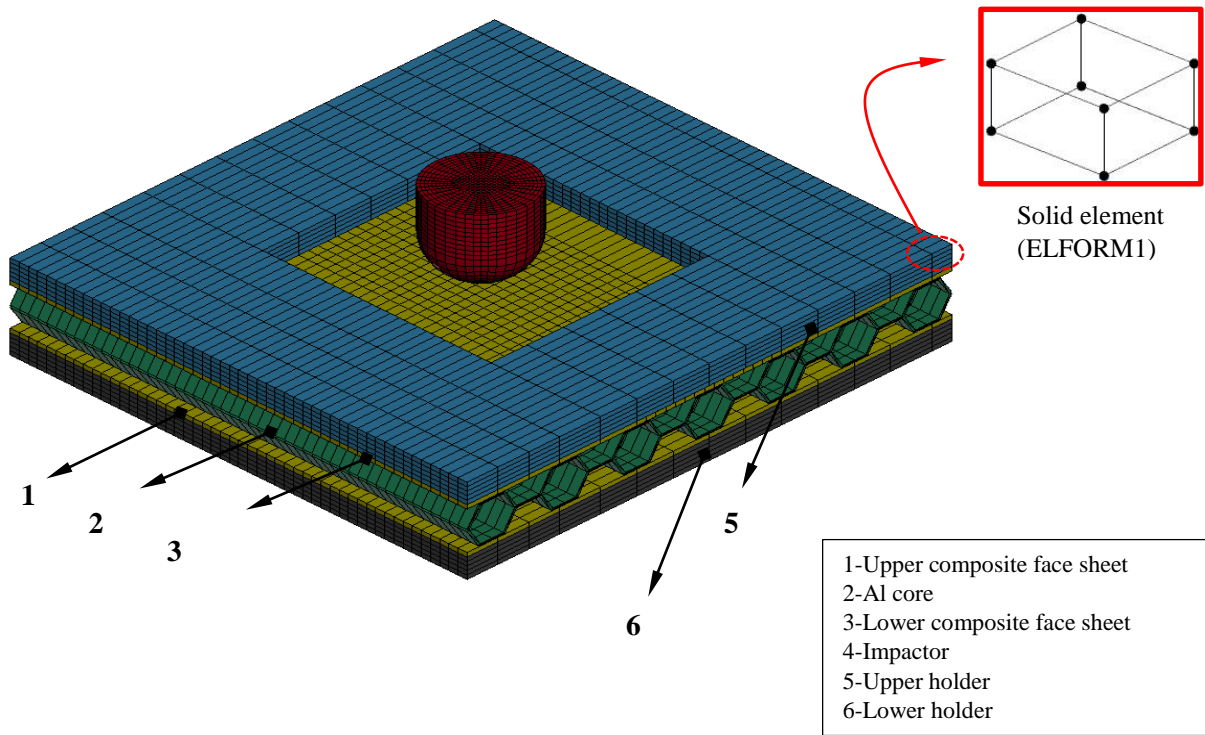
Figure 3. Finite element model of low velocity impact test.
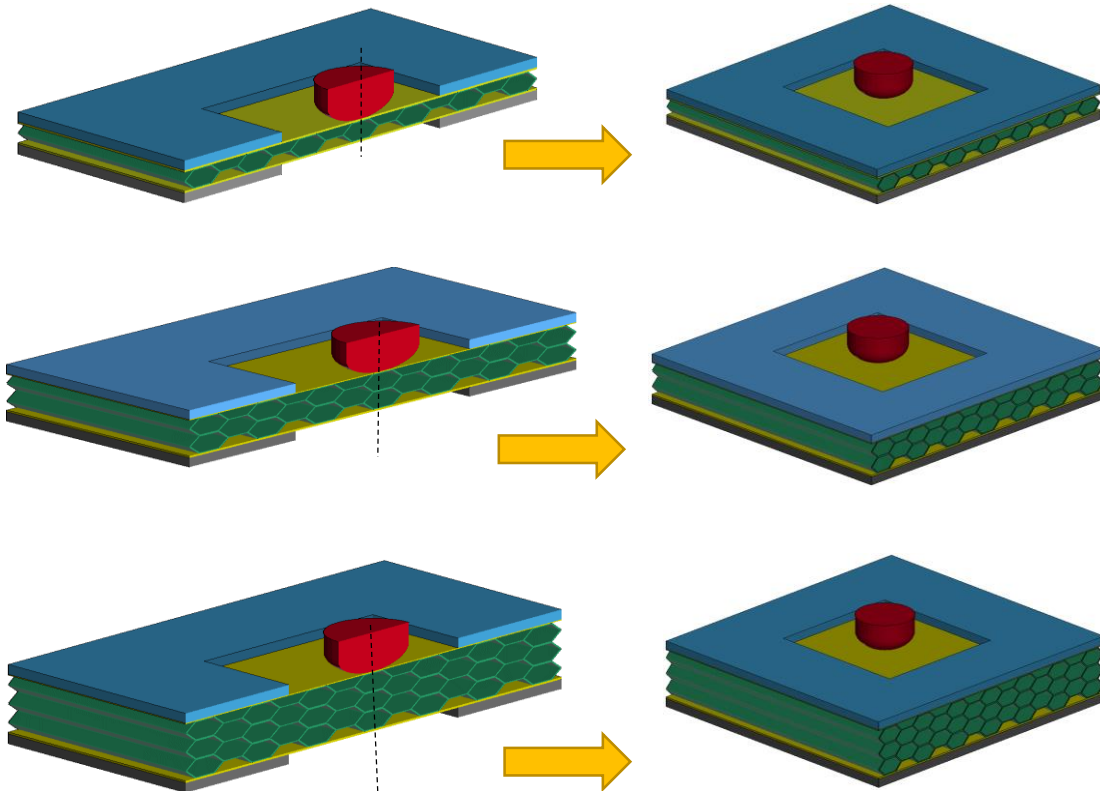
Figure 4. Impact point for sandwich composites with different layer numbers.

Many finite element programs have been developed to determine the impact behavior of aluminum honeycomb glass sandwich specimens. Among these, *LS-DYNA*, a commercial finite element software program, was preferred due to its wide material library, ease of use of interfaces and the ability to develop complex numerical models [35].

In low velocity impact tests, many graphs and data about the mechanical performance of the material are obtained. In these graphics and outputs, it is decided whether the material is suitable for the component or location to be used or not by comparing it with the standards. In the low velocity impact experimental test setup, these data are obtained by reading from the impactor shape. Displacement graphs are derived from the impactor's position along with changes in kinetic energy and velocity. Equations (1)-(4) were used to obtain the changes in velocity, displacement, and energy based on the impactor's impact timing. Data regarding the contact force, displacement and absorbed energy obtained from the impactor were evaluated.

$$v(t) = v_i + gt - \int_0^t \frac{F(t)}{m} d(t) \qquad (1)$$

Here, t is the time of the first contact of the impactor to the specimen, which is $t = 0$; $v(t)$ is the velocity of the impactor at time t; v_i is the velocity of the impactor at time $t = 0$; and $F(t)$ is the impact contact force measured at time t.

$$\delta(t) = \delta_i + v_i t + \frac{gt^2}{2} - \int_0^t \left(\int_0^t \frac{F(t)}{m} dt \right) dt \qquad (2)$$

δ is the displacement of the impactor at time t, while δ_i is the displacement of the impactor from the reference point at time $t = 0$.

$$E_a(t) = \frac{m(v_i^2 - (v(t))^2)}{2} + mh\delta(t) \qquad (3)$$

Here, $E_a(t)$ is the absorbed energy at time t, m is the weight impact, and g is the gravitational acceleration. To evaluate the weight efficiency of the energy absorption of a structure, the specific energy absorption (SEA) is generally used.

$$SEA = \frac{E_a}{m} \qquad (4)$$

Here, m is the mass of the crash structure. Higher SEA values indicate better energy-absorbing efficiency of the structures.

2.1. Modeling of Adhesive Layer

Sandwich composite structures are formed by combining the upper and lower facesheets and the core structure between these surfaces. Different applications and methods are used to join these two elements. But this bonding is mostly achieved by using different adhesive types. Determining the mechanical behavior of this structure at the time of impact is very important from an engineering perspective. To model the adhesive behavior between these two elements, a CZM model with a bilinear traction-separation relationship was developed. The basis of this law lies in the application of three independent parameters. The traction between the layers when the force is applied is t_0, the separation distance that occurs when the damage begins is δ_0 and the remaining under this curve is G_C. After the impact occurs, separation between layers occurs according to this principle (Figure 5)

Adhesion here can be achieved in two ways. This can be achieved by first defining a thin interface material between the top facesheets and the core in the middle. Or, this adhesion can be achieved by using the adhesion surface that performs the same function. Dogan et al. [36] determined that this method is effective instead of using intermediate materials. In this study, The CONTACT_AUTOMATIC SURFACE TO SURFACE TIEBREAK contact card was used to adhere the upper and lower facesheets to the core material in between. While the adhesion here is achieved, as shown in Figure 5, separations occur based on the *bilinear traction-separation law*. With this contact card, the nodes making contact in the beginning connect with each other according to the following criterion.
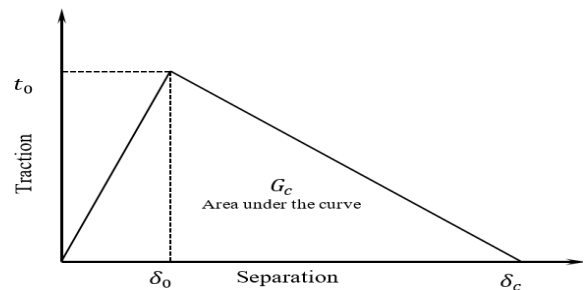
Figure 5. Bilinear traction-separation law.

$$\left(\frac{|\sigma_n|}{NFLS}\right)^2 + \left(\frac{|\sigma_s|}{SFLS}\right)^2 \geq 1 \tag{5}$$

Here, while σ_n and σ_s are the current normal and shear stresses, $NFLS$ and $SFLS$ are respectively the interface and shear strength. When the condition of Equation (5) is met, interface node stress is decreased to zero and the connection between the nodes is released. The contact parameters for *Araldite 2015*, which was used as the adhesive material in this research, are provided in Table 2.

Table 2. Cohesive parameters of delamination between core and face sheets interfaces [15].

Contact Tiebreak Variable	Value	Units
NFLS	21.63x10^9	Pa
SFLS	17.9x10^9	Pa
PARAM	1	-
ERATEN	430	N/m
ERATES	4700	N/m
CT2CN	1	-
CN	8080	Pa/m

2.3. MAT_54-55: Enhanced Composite Damage Model

The mechanical properties of the GFRP material used in the study are given in Table 3-4 and the mechanical properties of the Al 6061-T6 core material are given in Table 5. The most used model in the analysis of composite structures is the *MAT_54-55* material model. If there is no damage in the material model, the material is assumed to be orthotropic and linear elastic. In this model, *MAT 54* damage criterion was proposed by Chang and *MAT 55* damage criterion was proposed by *Tsai-Wu*. Although the working logic of this material model and the *MAT 22* model is the same, it additionally includes the compression damage mode. The Chang–Chang criterion (*MAT_54*) is given below; Tensile fibre ($\sigma_{11} > 0$).

$$\left(\frac{\sigma_{11}}{S_1}\right)^2 + \bar{\tau} = 1 \tag{6}$$

All moduli and Poisson's ratios are set to zero when the tensile fibre failure criteria are met, that is $E_1 = E_2 = G_{12} = \upsilon_{12} = \upsilon_{21} = 0$ All the stresses in the elements are reduced to zero, and the element layer has failed.

Failure mode for compressive fibre ($\sigma_{11} > 0$),

$$\left(\frac{\sigma_{11}}{S_{12}}\right)^2 = 1 \tag{7}$$

Failure mode for tensile matrix ($\sigma_{11} > 0$),

$$\left(\frac{\sigma_{22}}{S_2}\right)^2 + \bar{\tau} = 1 \tag{8}$$

Failure mode for compressive matrix

$$\left(\frac{\sigma_{22}}{2S_{12}}\right)^2 + \left[\left(\frac{C_2}{2S_{12}}\right) - 1\right]\frac{\sigma_{22}}{C_2} + \bar{\tau} = 1 \tag{9}$$

Where E_1 and E_2 are the longitudinal and transverse elastic moduli, respectively, G_{12} is the shear modulus, υ_{12} and υ_{21} are the in-plane Poisson's ratios.

Table 3. Mechanical parameters of the GFRP composite [37].

Symbol	Value	Unit
ρ	1500	kg/m^3
E_a, E_b	19	GPa
E_c	6	GPa
υ_{ab}	0.162	-
υ_{bc}	0.162	-
υ_{ca}	0.162	-
G_{ab}	3.786	GPa
G_{bc}	1.709	GPa
G_{ca}	1.709	GPa
S_{aT}	0.459	GPa
S_{aC}	0.2238	GPa
S_{bT}	0.459	GPa
S_{bC}	0.2238	GPa
S_{ab}	0.0828	GPa

Table 4. Failure parameters of the GFRP composite [37].

Symbol	Unit
DFAILM	0.0
DFAILS	0.0
DFAILT	0.0
DFAILC	0.0
TFAIL	0.16
Alpha	0.0
Soft	0.7
FBRT	1
YCFAC	3
EFS	0.90

Table 5. Mechanical properties of Al 6061-T6.

Density (kg/m^3)	E (GPa)	Poisson ratio	Yield stress (MPa)	Failure strain
2850	72	0.33	252	0.4

3. Results and Discussion

Impact simulations were carried out in the *LS DYNA* finite element program to determine the impact behavior of sandwich composite specimens with Aluminum T6061 core and GFRP facesheets. Impact testing results in three different scenarios. The impactor may bounce back from the specimen's surface. It loses some of its energy but then continues with a certain energy. This is called rebounding. The impactor may get stuck in the specimen and its velocity will decrease to zero. Here, the specimen absorbed all the energy of the impactor. This is called penetration. If the impactor pierces the specimens and comes out from the back surface, it is called perforation [15]. The name of an impact test may change depending on the velocity of the impactor. If the impactor's velocity is less than 10 m/s, it is called a low velocity impact. If it is between 10-50 m/s, it is called medium velocity impact, and if the impactor's velocity is more than 50 m/s, it is called high velocity impact [21]. These studies are mostly used for ballistic research. Three different impactor types were used in this study. These are Sphere, Cylinder and Cone. The width and height of these impactors are the same, but their volumes are different. Therefore, in order to perform an impact test with the same energy values, it is necessary to have different velocities. Impact tests were carried out at three different energies: 10 J, 30 J and 60 J. The specimens used in the study include 1-layer core specimen, 2-layers core

specimen and 3-layers core specimen. Separate situations have been evaluated for these.

In Figure 6, variation of contact force-time, energy-time, contact force-displacement and velocity-time graphs with impactor geometry are given for 10 J. When the contact force-time graph is examined in Figure 6a, the contact force for the cylinder impactor reached a maximum point of 11.43 kN and then returned to the zero point. The impactor rebounded from the specimen surface. This impact phenomenon is called rebounding. It has been determined that there are no sharp oscillations on the graph. It was observed that the impact process was completed without damaging the layers. When the graph for the sphere impactor is examined, the contact force reaches a peak of 4.58 kN and a sharp decrease in force occurs. Here it is understood that the upper surface is damaged. In the cone impactor, it has been observed that the force decreases sharply after a shorter period of time compared to other impactor types. The reason for this is that the impactor shape is sharper than the others. When the energy-time graph in Figure 6b is examined, an impact simulation was applied with an impact energy of 10 J for all three impactors. However, the remaining energies at the end of the impact are different from each other. While the initial energy for the sphere impactor is 10 J, the energy after the impact is 1.32 J. When the energy in the final state is subtracted from the energy in the initial state and divided by the initial energy, the absorbed energy efficiency value is obtained. This value was determined as 0.86 for sphere impactor, 0.79 for cylinder impactor and 0.97 for cone impactor. When the contact force-displacement graph is examined in Figure 6c, the maximum displacement occurred as 2.96 mm in case of impact with the cylinder impactor. It is observed for all specimens that after the impactor contacts the specimen, the displacement increases with the force, and then the force and displacement reach zero values. In Figure 6d, it was determined that changes occurred in the velocity-time graph in parallel with the energy-time graph. More detailed results of these graphs will be given in the next section.
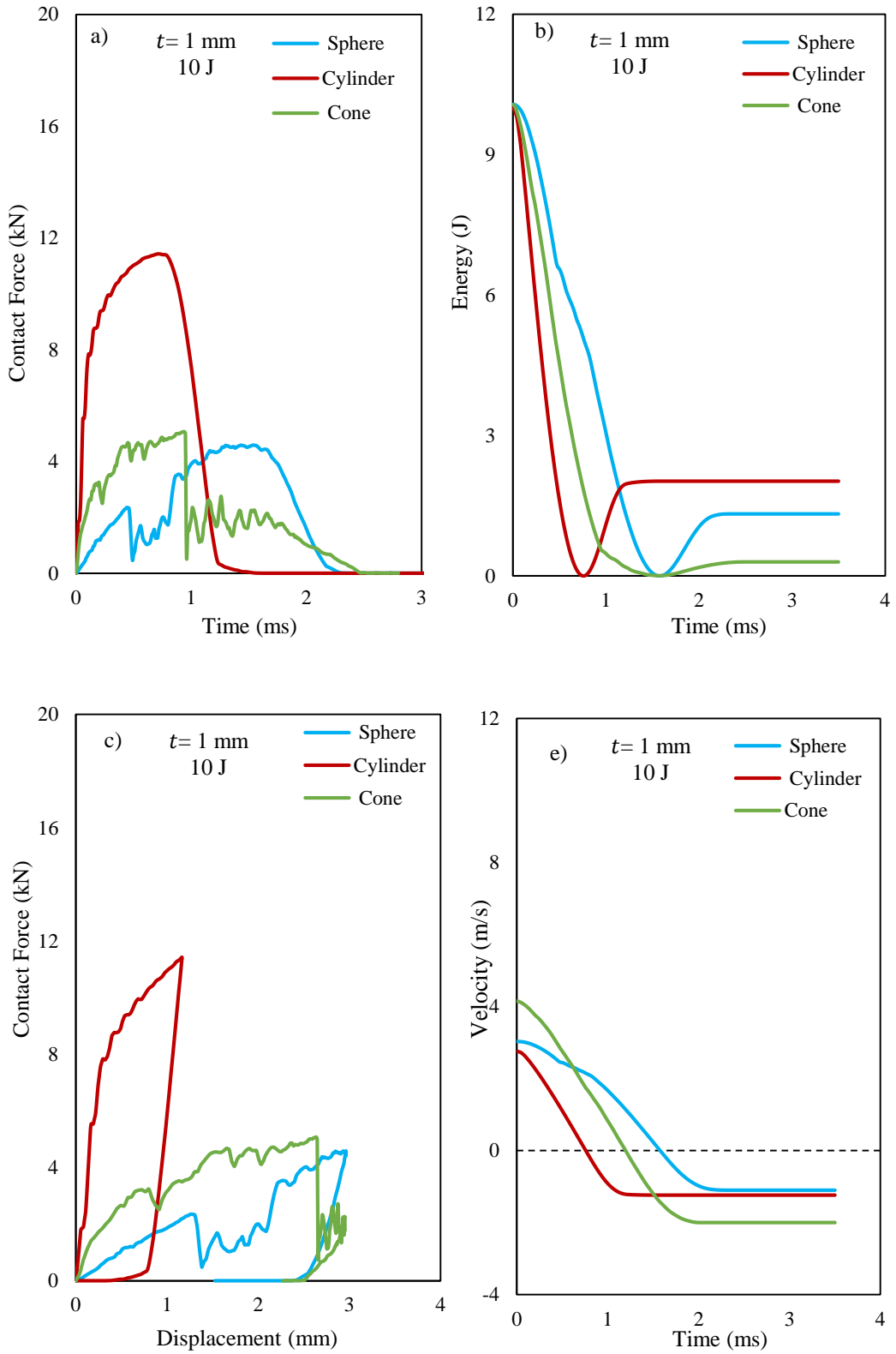
Figure 6. Variation of a) Contact force-Time, b) Energy-Time, c) Contact force-Displacement and d) Velocity-Time graphs with impactor geometry (10 J).
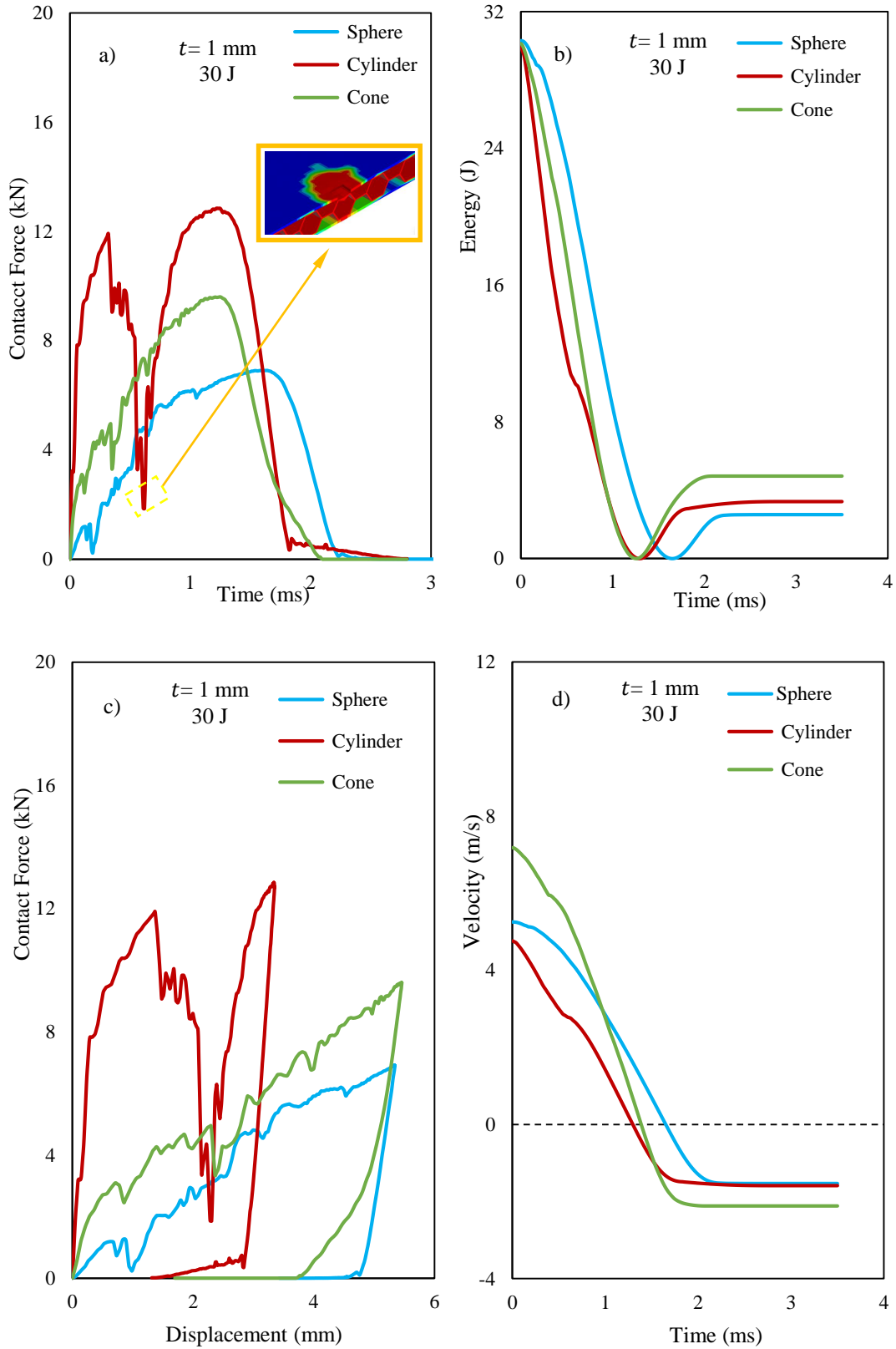
Figure 7. Variation of a) Contact force-Time, b) Energy-Time, c) Contact force-Displacement and d) Velocity-Time graphs with impactor geometry (30 J).
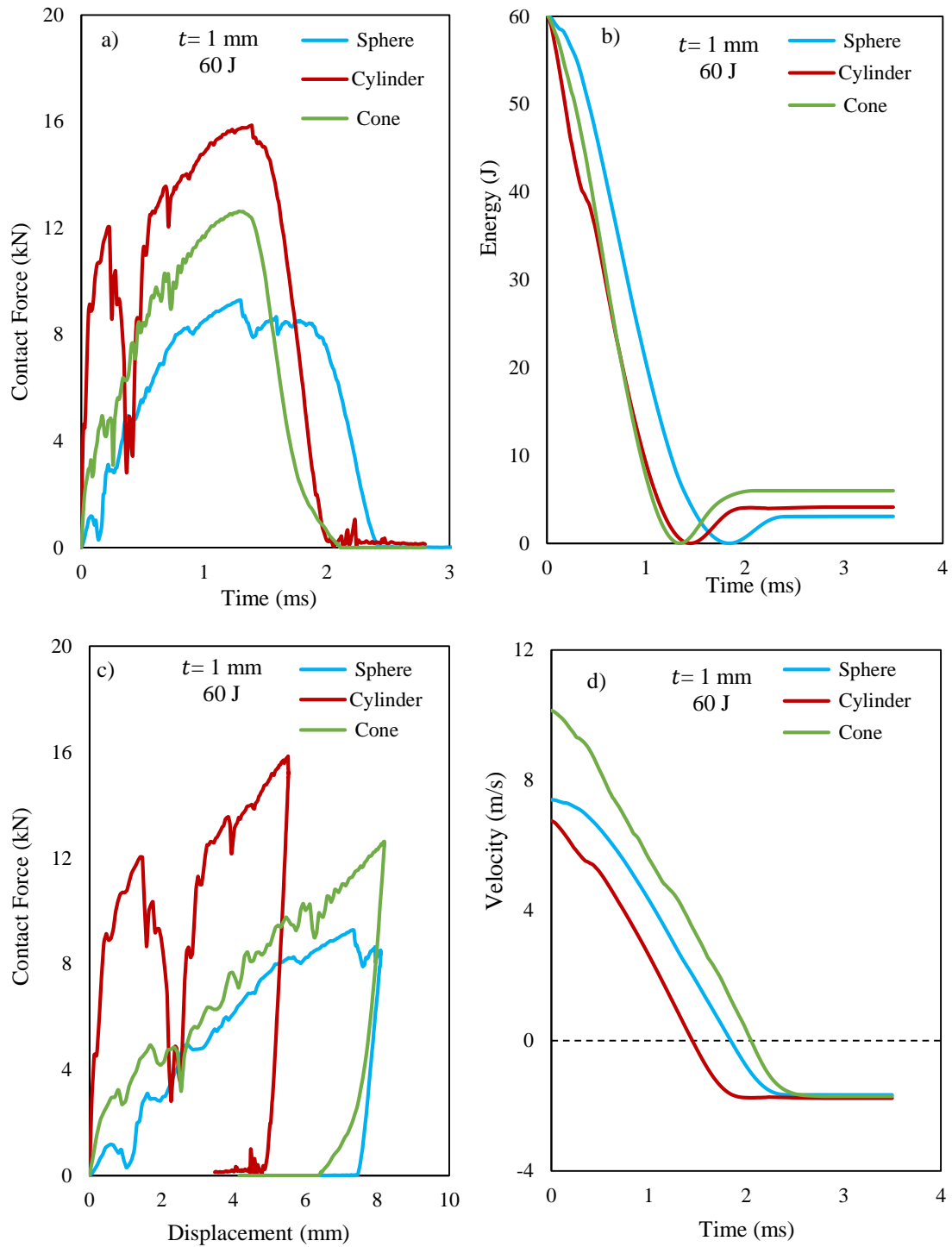
Figure 8. Variation of a) Contact force-Time, b) Energy-Time, c) Contact force-Displacement and d) Velocity-Time graphs with impactor geometry (60 J).

Variation of contact force-time, energy-time, contact force-displacement and velocity-time graphs with impactor geometry are given in Figure 7 for 30 J and in Figure 8 for 60 J. The general evaluation of these graphs will be made through Figure 9. In Figure 9, peak force, energy absorption efficiency and maximum displacement values of impactor types for 10 J, 30 J and 60 J are compared using 1-layer core specimen. In Figure 9a, peak force values for cylinder, cone and sphere were obtained as 11.42 kN, 5.07 kN and 4.58 kN, respectively, at 10 J impact energy. It was determined that the highest contact

force was obtained with the cylinder impactor if all three specimens were impacted with equal impact energy. The reason for this is that as the contact surface area increases, the time for damage to the material becomes longer. Therefore, the contact time continues to increase until the energy runs out [26]. When looking at the energy absorption efficiency value, it was determined as 0.79, 0.97 and 0.86 for cylinder, cone and sphere, respectively. The maximum displacement values were 2.96 mm in the test performed with the sphere impactor. When the impact energy increased from 10 J to 30 J, it was determined in Figure 9b that the contact force and maximum displacement value increased for all three specimens. Energy absorption efficiency value varies. In other words, while this value decreases for the cone impactor, it increases for the cylinder and sphere impactor. It was determined that when the impact energy was 60 J, the contact force and maximum displacement value increased in parallel. When energy absorption efficiency values are compared between 10 J and 60 J for cylinder, cone and sphere, changes occurred as 16.2%, -7.26% and 9.27%, respectively. In general, as the impact energy increased for the cylinder and sphere impactor, the energy absorption efficiency value of the specimens also increased. In cone impactor, the absorption rate varies because material damage occurs in the specimen structure caused by the impactor. In Figure 10, peak force, energy absorption efficiency and maximum displacement values of impactor types for 10 J, 30 J and 60 J are compared using a 2-layer core specimen. When the number of layers increased from 1 to 2, the peak force value for the cylinder impactor at 10 J decreased by 39%, while the peak force values for the cone and sphere impactor increased by 21.9% and 38.8%, respectively. In Figure 11, peak force, energy absorption efficiency and maximum displacement values of impactor types for 10 J, 30 J and 60 J are compared using a 3-layer core specimen. As the impact energy increases, the peak force value also increases in parallel. The maximum displacement value increases for the same impact energy as the number of layers increases.

In Table 6, the damage deformations occurring on the specimen for cylinder, cone and sphere for 10 J are given. The *LS DYNA MAT-54* material model and the ability to see different damages offered to users were used here [38]. Tensile fiber mode, Compressive fiber mode, Tensile matrix mode and Compressive matrix damage modes occurring in the specimen were shown separately.

The areas shown here in red indicate the damage to the structure. The areas shown in blue represent areas where damage has not occurred yet. The colors between these two color scales can be determined from here whether damage is close at the fringe level. Total stress values are calculated for the initiation of damage in an element. When these stress values reach the yield strength of this element, that is, 1, damage occurs here and the element at this point is deleted in the finite elements [15]. The force then passes to the other element. When the impact results with different impactors are examined in Table 6, it was determined that the biggest damage type for all three impactors was matrix damage. While damage occurred on the specimen surfaces with all three impact impacts, no damage occurred on the back surface of the specimen for the Tensile fiber mode and Compressive fiber mode [15]. The greatest matrix damage on the front surface occurred in the impact simulation made with the cone impactor. Since the shape of the cone impactor is more pointed than the others, it leaves large deformations on the element it contacts. Therefore, even though the area it contacts is small, it can cause great damage because it leaves a devastating effect [3]. However, the damage area it causes on the back surface is less. Table 7 shows the damages for impact energy of 30 J. It is seen that as the impact energy increases, the damage areas also increase. It is seen that destructive damage increases when the impact energy is 60J [39]. Especially in the test performed with the cone impactor, the upper cover and core structure were severely damaged.
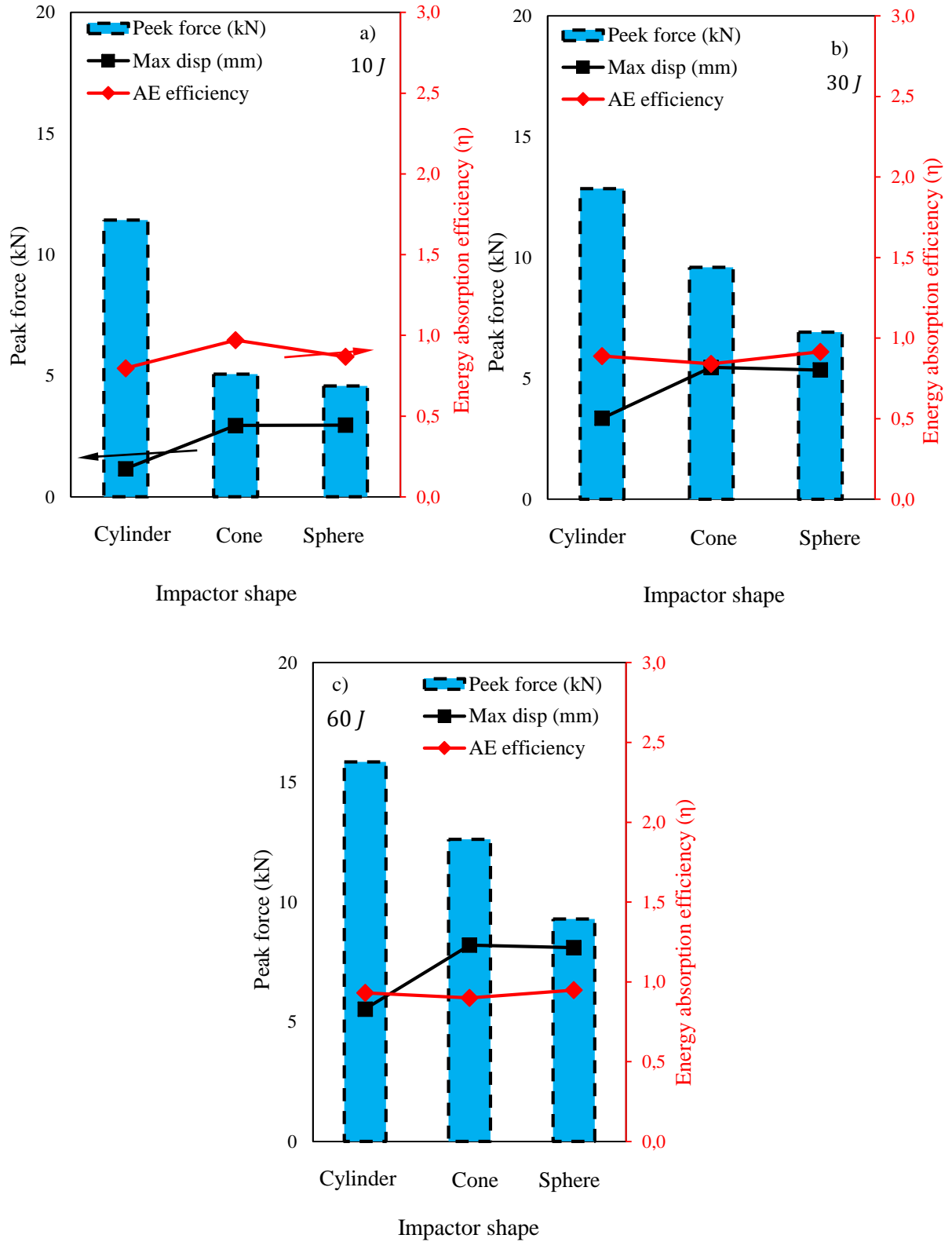
Figure 9. Variation of Contact force, Absorbed energy efficiency, maximum displacement values for a) 10 J, b) 30 J and c) 60 J (1-layer core specimens).
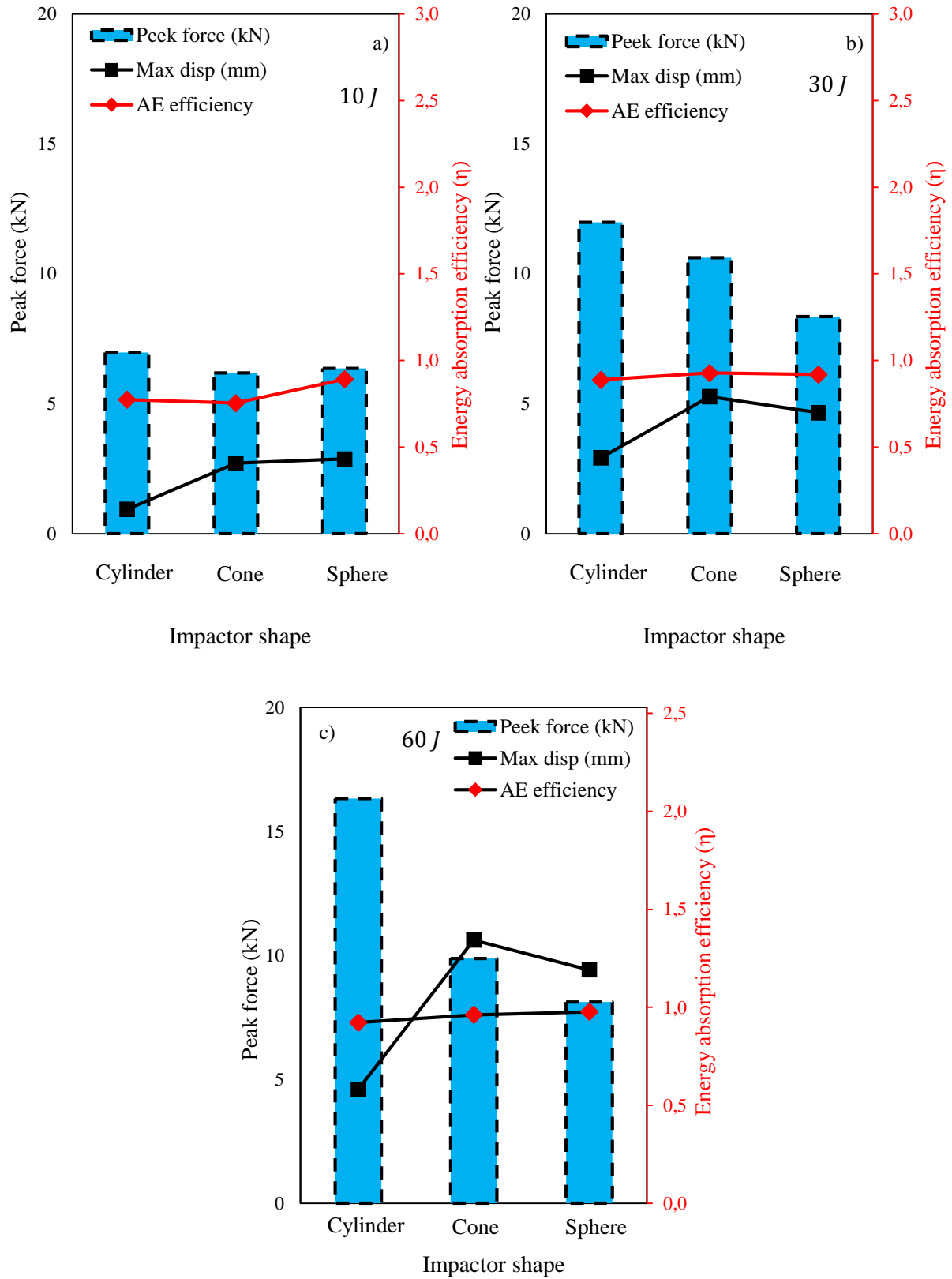
Figure 10. Variation of Contact force, Absorbed energy efficiency, maximum displacement values for a) 10 J, b) 30 J and c) 60 J (2-layer cores specimens).
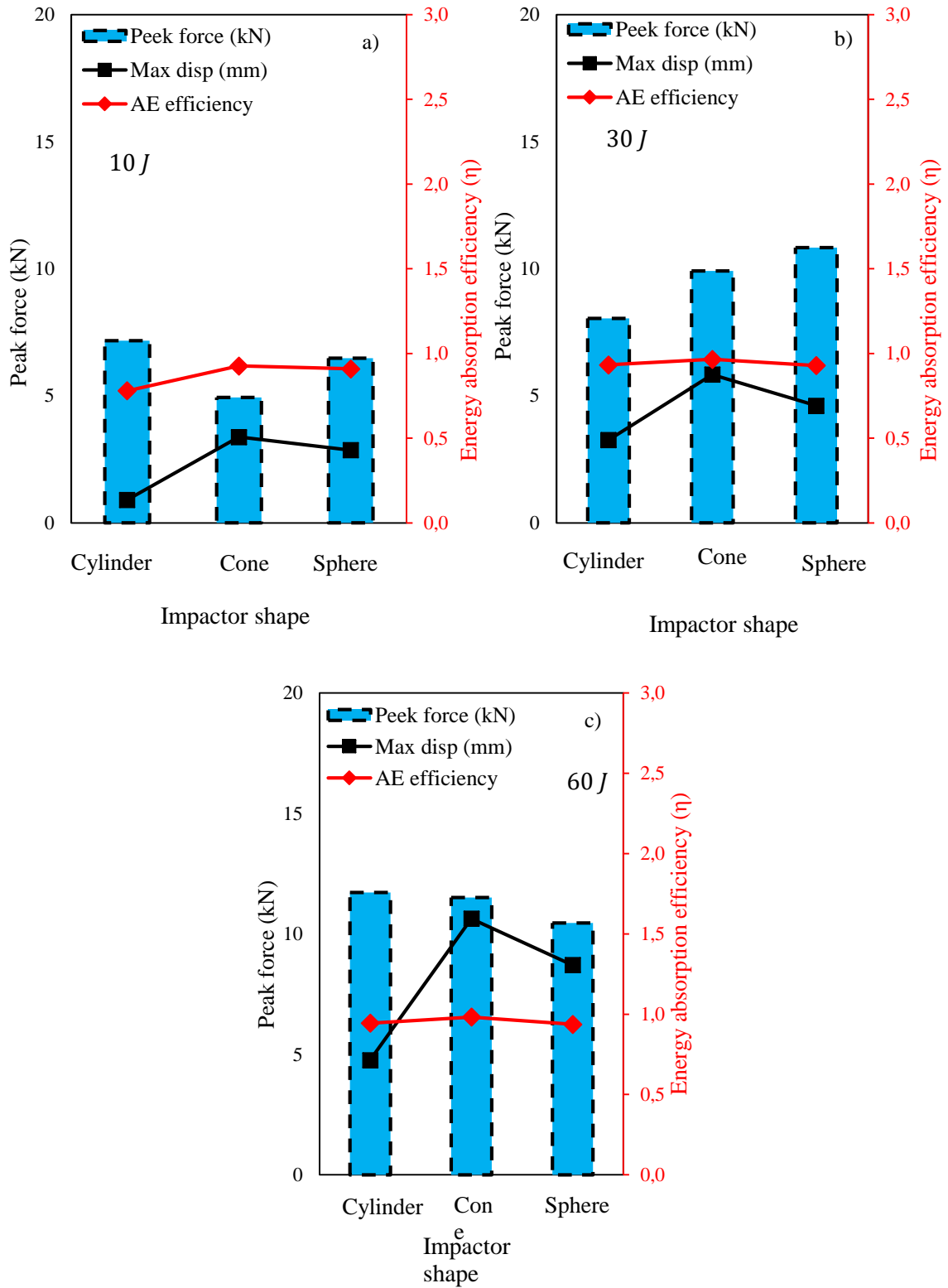
Figure 11. Variation of Contact force, Absorbed energy efficiency, maximum displacement values for a) 10 J, b) 30 J and c) 60 J (3-layer cores specimens).

Table 6. Deformation images under different impactor force [10 J].

E [J]		Tensile fiber mode	Compressive fiber mode	Tensile matrix mode	Compressive matrix mode	Fringe levels
Cylinder, 10 J	Top face					
	Back face					
	Section view					
Cone 10 J	Top face					
	Back face					
	Isometric					
Sphere, 10 J	Top face					
	Back face					
	Isometric					

Table 7. Deformation images under different impactor force [30 J].

Table 8. Deformation images under different impactor force [60 J].
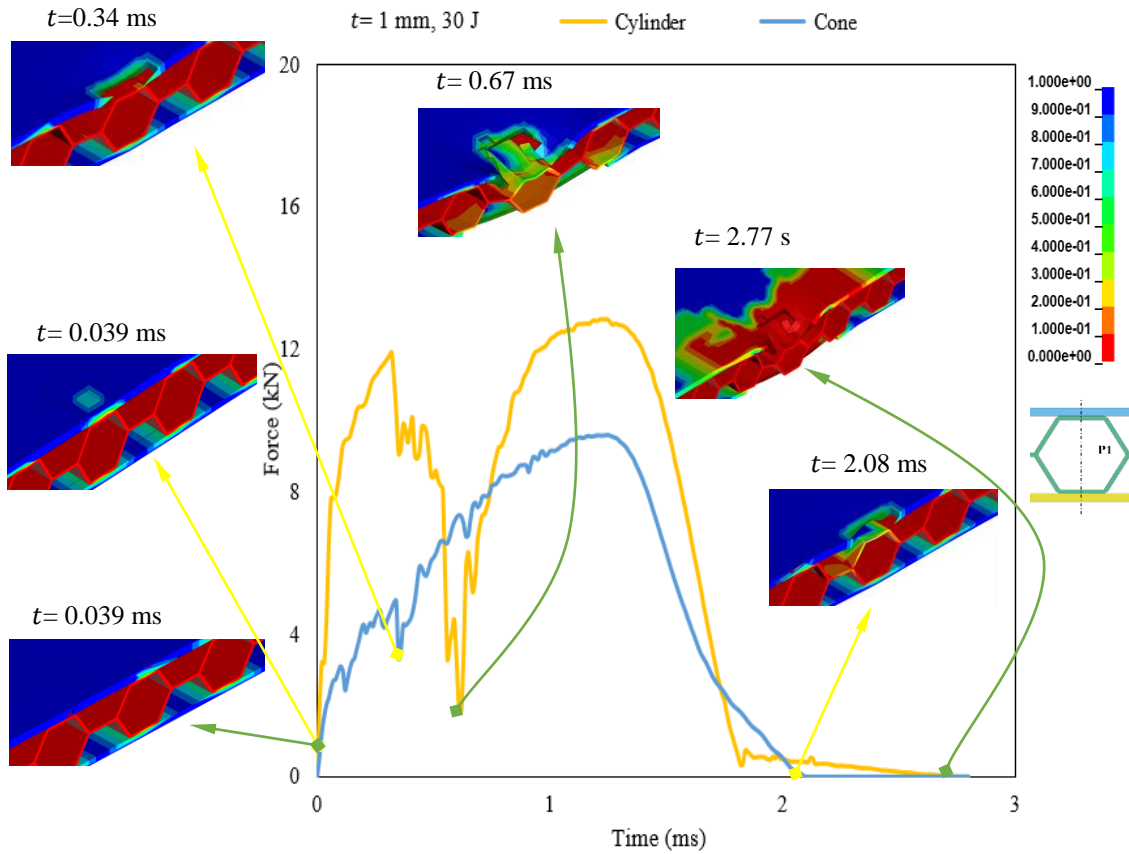
Figure 12. Matrix damage progress graph for cylinder and cone impactor.

When the impactor applies an impact to the specimen surface at a certain velocity, the stress value increases at the point of contact and damage occurs to the elements at this point due to high stresses [26]. This process occurs in a very short time. It is very difficult to follow this damage progression in experimental studies. With developing technology, this damage process can be monitored, at least partially, with high-pixel cameras. Nevertheless, it is difficult to see the damage that occurs in the internal structure of the material during impact. However, the finite element method provides convenience for researchers at this point [5]. The types of damage occurring in the specimen can be seen at any time during the impact. Figure 12 shows the peak force-time graph of impact simulations with cylinder and cone impactors. Here the sphere graph is not included because it is too close to the cone shape and the graph is too complex. When adding matrix damage images, only the images at the critical point were added. Immediately after the impactor contacted the specimen, the stress values in the specimen increased

at $t = 0.039$ ms. It is seen for both specimens that the stress values increase, especially at the point where the impactor contacts and on the back surface just below. In the simulation with the cone impactor, damage occurred on the upper surface at $t=0.039$ ms and the force value decreased accordingly. In the simulation with the cylinder impactor, damage occurred to the upper facesheet at $t = 0.067$ ms, but there was a larger decrease in force. Here, it was determined that damage occurred to the core structure along with the upper cover. In the cone impactor, since the impactor shape is sharp, the facesheets elements at the point of contact are deleted [27]. Therefore, the force decrease occurred to be smaller. At the end of the impact test, in the simulation with the cylinder impactor, the impact test ended at $t = 2.77$ ms and the damage to the facesheet and core structure was caused at the point of contact. In the simulation made with the cone impactor, the impact test ended at $t = 2.08$ ms and damage pictures are shown.
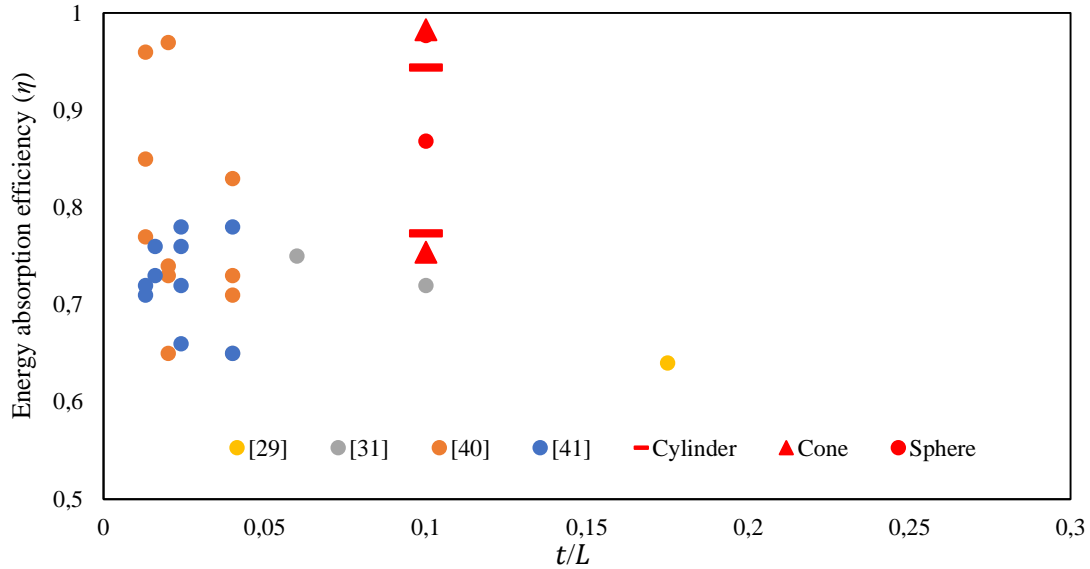
Figure 13. Comparisons of energy absorption efficiencies.

In order to increase the energy absorption efficiency of sandwich composite structures, tests and analyzes have been carried out by making many structural changes. At the end of these tests and analyzes, energy absorption efficiency values are obtained and evaluated to compare their efficiency. The minimum and maximum absorption efficiency values of the sandwich structures used in the current study for different impactors are compared with other studies in the literature [29, 31, 40, 41] with different features and different structures (Figure 13). In the present study, the highest energy efficiency value obtained in the simulation with the cone impactor was found to be 3% higher than the study by He et al [40] and 42.4% higher than the study by Xue et al [29]. What is important here is to determine the optimum dimensions of the sandwich composite structure in terms of engineering by knowing the area of use and the load it will be exposed to. The focus of all these researches is to make the most suitable design for different impactors that the system will be exposed to within the limits of minimum cost and maximum safety.

4. Conclusion and Suggestions

In this study, the impact performance and damage behavior of sandwich composite structures with a core material of aluminum and a facesheet of glass fiber composites were examined using the finite element method. In the study, the effects of impactor shape, impact velocity and number of core layers on peak force, absorbed energy efficiency, maximum displacement and damage deformation were investigated. For low velocity impact simulation, progressive damage analysis was performed based on the Hashin damage criterion using the *MAT 54* material model in the *LS DYNA* finite element program. The results obtained at the end of the study can be listed as follows;

- The peak force value obtained with the cylinder impactor is higher than other specimens. This is due to the large contact area of the impactor with the specimen.
- In the impact test performed with the cone impactor, the damage time to the specimen is shorter than in the others. Because its impactor shape is sharper, its destructive effect is greater.
- The largest displacement as a result of the impact occurred with the sphere impactor.
- Energy absorption efficiency varies as impact energy changes. But as the impact energy increases, the energy absorption efficiency also increases.
- As the number of layers of the core structure increases, the peak force for the cylinder impactor decreases while the peak force for the sphere and cone impactor increases.
- It was determined that the largest and dominant damage type for all three hitters was matrix damage.

Statement of Research and Publication Ethics

The study is complied with research and
publication ethics.

References

[1] V. Crupi, E. Kara, G. Epasto, E. Guglielmino, and H. Aykul, "Prediction model for the impact response of glass fibre reinforced aluminium foam sandwiches," *Int J Impact Eng*, vol. 77, pp. 97–107, 2015, doi: 10.1016/j.ijimpeng.2014.11.012.

[2] R. Mohmmed, F. Zhang, B. Sun, and B. Gu, "Finite element analyses of low-velocity impact damage of foam sandwiched composites with different ply angles face sheets," *Mater Des*, vol. 47, pp. 189–199, 2013, doi: 10.1016/j.matdes.2012.12.016.

[3] J. Liu, W. He, D. Xie, and B. Tao, "The effect of impactor shape on the low-velocity impact behavior of hybrid corrugated core sandwich structures," *Compos B Eng*, vol. 111, pp. 315–331, 2017, doi: 10.1016/j.compositesb.2016.11.060.

[4] İ. Bozkurt, M. Kaman, and M. Albayrak, "LS-DYNA MAT162 Finding Material Inputs and Investigation of Impact Damage in Carbon Composite Plates. XVI. international research conference 2022.," pp. 3–7, 2022.

[5] M. Albayrak, M. O. Kaman, and I. Bozkurt, "Determination of LS-DYNA MAT162 Material Input Parameters for Low Velocity Impact Analysis of Layered Composites," pp. 39–43, 2022.

[6] L. Ballère, P. Viot, J. L. Lataillade, L. Guillaumat, and S. Cloutet, "Damage tolerance of impacted curved panels," *Int J Impact Eng*, vol. 36, no. 2, pp. 243–253, Feb. 2009, doi: 10.1016/J.IJIMPENG.2008.03.004.

[7] R. F. Alshahrani, N. Merah, S. M. A. Khan, and Y. Al-Nassar, "On the impact-induced damage in glass fiber reinforced epoxy pipes," *Int J Impact Eng*, vol. 97, pp. 57–65, Nov. 2016, doi: 10.1016/j.ijimpeng.2016.06.002.

[8] M. N. Saleh, H. M. El-Dessouky, M. Saeedifar, S. T. De Freitas, R. J. Scaife, and D. Zarouchas, "Compression after multiple low velocity impacts of NCF, 2D and 3D woven composites," *Compos Part A Appl Sci Manuf*, vol. 125, Oct. 2019, doi: 10.1016/j.compositesa.2019.105576.

[9] J. Krollmann, T. Schreyer, M. Veidt, and K. Drechsler, "Impact and post-impact properties of hybrid-matrix laminates based on carbon fiber-reinforced epoxy and elastomer subjected to low-velocity impacts," *Compos Struct*, vol. 208, no. August 2018, pp. 535–545, 2019, doi: 10.1016/j.compstruct.2018.09.087.

[10] A. P. Christoforou and A. S. Yigit, "Scaling of low-velocity impact response in composite structures," *Compos Struct*, vol. 91, no. 3, pp. 358–365, Dec. 2009, doi: 10.1016/J.COMPSTRUCT.2009.06.002.

[11] A. Khodadadi *et al.*, "Numerical and experimental study of impact on hyperelastic rubber panels," *Iranian Polymer Journal (English Edition)*, vol. 28, no. 2, pp. 113–122, Feb. 2019, doi: 10.1007/s13726-018-0682-x.

[12] Y. Li, F. Wang, X. Shi, L. Guo, and C. Huang, "Impact Response of 3D Orthogonal Woven Composites with Different Fiber Types," *Applied Composite Materials*, 2023, doi: 10.1007/s10443-023-10150-8.

[13] B. Kazemianfar, M. Esmaeeli, and M. R. Nami, "Response of 3D woven composites under low velocity impact with different impactor geometries," *Aerosp Sci Technol*, vol. 102, Jul. 2020, doi: 10.1016/j.ast.2020.105849.

[14] M. Y. Solmaz and T. Topkaya, "The flexural fatigue behavior of honeycomb sandwich composites following low velocity impacts," *Applied Sciences (Switzerland)*, vol. 10, no. 20, pp. 1–14, 2020, doi: 10.3390/app10207262.

[15] I. Bozkurt, M. O. Kaman, and M. Albayrak, "Experimental and numerical impact behavior of fully carbon fiber sandwiches for different core types," *Journal of the Brazilian Society of Mechanical Sciences and Engineering*, vol. 46, no. 5, p. 318, May 2024, doi: 10.1007/s40430-024-04865-3.

[16] W. He, S. Lu, K. Yi, S. Wang, G. Sun, and Z. Hu, "Residual flexural properties of CFRP sandwich structures with aluminum honeycomb cores after low-velocity impact," *Int J Mech Sci*, vol. 161–162, no. July, p. 105026, 2019, doi: 10.1016/j.ijmecsci.2019.105026.

[17] W. He, J. Liu, B. Tao, D. Xie, J. Liu, and M. Zhang, "Experimental and numerical research on the low velocity impact behavior of hybrid corrugated core sandwich structures," *Compos Struct*, vol. 158, pp. 30–43, 2016, doi: 10.1016/j.compstruct.2016.09.009.

[18] Y. Chen, K. Fu, S. Hou, X. Han, and L. Ye, "Multi-objective optimization for designing a composite sandwich structure under normal and 45° impact loadings," *Compos B Eng*, vol. 142, no. December 2016, pp. 159–170, 2018, doi: 10.1016/j.compositesb.2018.01.020.

[19] X. Zhang, F. Xu, Y. Zang, and W. Feng, "Experimental and numerical investigation on damage behavior of honeycomb sandwich panel subjected to low-velocity impact," *Compos Struct*, vol. 236, no. January, p. 111882, 2020, doi: 10.1016/j.compstruct.2020.111882.

[20] W. He, J. Liu, S. Wang, and D. Xie, "Low-velocity impact behavior of X-Frame core sandwich structures – Experimental and numerical investigation," *Thin-Walled Structures*, vol. 131, no. July, pp. 718–735, 2018, doi: 10.1016/j.tws.2018.07.042.

[21] T. K. Demircioğlu, F. Balıkoğlu, O. İnal, N. Arslan, Ay, and A. Ataş, "Experimental investigation on low-velocity impact response of wood skinned sandwich composites with different core configurations," *Mater Today Commun*, vol. 17, no. May, pp. 31–39, 2018, doi: 10.1016/j.mtcomm.2018.08.003.

[22] J. Wang, A. M. Waas, and H. Wang, "Experimental and numerical study on the low-velocity impact behavior of foam-core sandwich panels," *Compos Struct*, vol. 96, pp. 298–311, 2013, doi: 10.1016/j.compstruct.2012.09.002.

[23] Y. Rong, J. Liu, W. Luo, and W. He, "Effects of geometric configurations of corrugated cores on the local impact and planar compression of sandwich panels," *Compos B Eng*, vol. 152, no. August, pp. 324–335, 2018, doi: 10.1016/j.compositesb.2018.08.130.

[24] J. Zhou, M. Z. Hassan, Z. Guan, and W. J. Cantwell, "The low velocity impact response of foam-based sandwich panels," *Compos Sci Technol*, vol. 72, no. 14, pp. 1781–1790, 2012, doi: 10.1016/j.compscitech.2012.07.006.

[25] A. Manes, A. Gilioli, C. Sbarufatti, and M. Giglio, "Experimental and numerical investigations of low velocity impact on sandwich panels," *Compos Struct*, vol. 99, pp. 8–18, 2013, doi: 10.1016/j.compstruct.2012.11.031.

[26] M. Albayrak, M. O. Kaman, and I. Bozkurt, "Experimental and Numerical Investigation of the Geometrical Effect on Low Velocity Impact Behavior for Curved Composites with a Rubber Interlayer," *Applied Composite Materials*, vol. 30, no. 2, pp. 507–538, 2023, doi: 10.1007/s10443-022-10094-5.

[27] M. Albayrak, M. O. Kaman, and I. Bozkurt, "The effect of lamina configuration on low-velocity impact behaviour for glass fiber/rubber curved composites," *J Compos Mater*, vol. 57, no. 11, pp. 1875–1908, 2023, doi: 10.1177/00219983231164950.

[28] I. Bozkurt, M. O. Kaman, and M. Albayrak, "Low-velocity impact behaviours of sandwiches manufactured from fully carbon fiber composite for different cell types and compression behaviours for different core types," *Materialpruefung/Materials Testing*, vol. 65, no. 9, pp. 1349–1372, 2023, doi: 10.1515/mt-2023-0024.

[29] X. Xue, C. Zhang, W. Chen, M. Wu, and J. Zhao, "Study on the impact resistance of honeycomb sandwich structures under low-velocity/heavy mass," *Compos Struct*, vol. 226, no. May, p. 111223, 2019, doi: 10.1016/j.compstruct.2019.111223.

[30] M. R. Yellur, H. Seidlitz, F. Kuke, K. Wartig, and N. Tsombanis, "A low velocity impact study on press formed thermoplastic honeycomb sandwich panels," *Compos Struct*, vol. 225, no. November 2018, p. 111061, 2019, doi: 10.1016/j.compstruct.2019.111061.

[31] J. Susainathan, F. Eyma, E. DE Luycker, A. Cantarel, and B. Castanie, "Numerical modeling of impact on wood-based sandwich structures," *Mechanics of Advanced Materials and Structures*, vol. 27, no. 18, pp. 1583–1598, Sep. 2020, doi: 10.1080/15376494.2018.1519619.

[32] P. A. Shirbhate and M. D. Goel, "Investigation of effect of perforations in honeycomb sandwich structure for enhanced blast load mitigation," *Mechanics of Advanced Materials and Structures*, vol. 30, no. 17, pp. 3463–3478, 2023, doi: 10.1080/15376494.2022.2076958.

[33] H. E. Yalkın, R. Karakuzu, and T. Alpyıldız, "Low-velocity impact behaviors of sandwich composites with different structural configurations of foam core: numerical study and experimental validation," *Phys Scr*, vol. 98, no. 11, Nov. 2023, doi: 10.1088/1402-4896/ad008f.

[34] M. Nouri Damghani and A. Mohammadzadeh Gonabadi, "Numerical study of energy absorption in aluminum foam sandwich panel structures using drop hammer test," *Journal of Sandwich Structures and Materials*, vol. 21, no. 1, pp. 3–18, Jan. 2019, doi: 10.1177/1099636216685315.

[35] H. JO., *LS-DYNA Keyword User's Manual Volume II Material Models, Version 971. Livermore Software Technology Corporation; . [24].* 2017.

[36] F. Dogan, H. Hadavinia, T. Donchev, and P. S. Bhonge, "Delamination of impacted composite structures by cohesive zone interface elements and tiebreak contact," *Central European Journal of Engineering*, vol. 2, no. 4, pp. 612–626, 2012, doi: 10.2478/S13531-012-0018-0.

[37] M. Albayrak and M. O. Kaman, "Production of Curved Surface Composites Reinforced With Rubber Layer," *European Journal of Technic*, vol. 11, no. 1, pp. 19–22, 2021, doi: 10.36222/ejt.824761.

[38] A. M. Bozkurt İ, Kaman MO, "LS-DYNA MAT162 Finding Material Inputs and Investigation of Impact Damage in Carbon Composite Plates. XVI. international research conference 2022.," 2022.

[39] K. Malekzadeh Fard, S. M. R. Khalili, S. H. Forooghy, and M. Hosseini, "Low velocity transverse impact response of a composite sandwich plate subjected to a rigid blunted cylindrical impactor," *Compos B Eng*, vol. 63, pp. 111–122, 2014, doi: 10.1016/j.compositesb.2014.03.011.

[40] W. He, L. Yao, X. Meng, G. Sun, D. Xie, and J. Liu, "Effect of structural parameters on low-velocity impact behavior of aluminum honeycomb sandwich structures with CFRP face sheets," *Thin-Walled Structures*, vol. 137, no. August 2018, pp. 411–432, 2019, doi: 10.1016/j.tws.2019.01.022.

[41] Y. Duan, Z. Cui, X. Xie, Y. Tie, T. Zou, and T. Wang, "Mechanical characteristics of composite honeycomb sandwich structures under oblique impact," *Theoretical and Applied Mechanics Letters*, vol. 12, no. 5, p. 100379, Sep. 2022, doi: 10.1016/J.TAML.2022.100379.

Printable Hollow Concrete Beams by 3D Concrete Printer

Osman HANSU[1], Furkan Boran AKKOYUN[2*], Nildem TAYŞİ[2]

[1]Gaziantep Islam Science and Technology University, Faculty of Engineering and Natural Science, Department of Civil Engineering, 27010 Gaziantep, TÜRKİYE
[2]Gaziantep University, Faculty of Engineering, Department of Civil Engineering, 27310 Gaziantep, TÜRKİYE
(ORCID: 0000-0003-1638-4304) (ORCID: 0000-0002-9932-937X) (ORCID: 0000-0003-0947-5662)

Keywords: 3d concrete printing, Hollow concrete beams, Additive manufacturing.

Abstract

3D printers are constantly developing and have a wide range of uses. Today, it is actively used in many fields, from the production of implants and prostheses to the production of jewelry. This technology, which is widely used in civil engineering in areas such as building element production, sustainability, and building construction offers several advantages over conventional concrete pouring and processing methods. Decreasing material waste, decreasing labor costs, freedom and originality in design, and saving time are among these advantages. In this context, 3DCP compared to traditional methods, it reduces the use of materials and makes the construction process more efficient since it is designed with different internal patterns and hollows. This study focuses on the printing process of hollow concrete beam designs in 3 different patterns with 2 different mixtures. Crushing between the layers of beams printed with 3D concrete printing, layer height, and printability and fresh state tests of the mixtures were examined.

1. Introduction

In a rapidly changing world, technology also advances and develops at the same pace. With these developments, new automation process that will make people's lives easier are also emerging. 3D printers, which are a type of additive manufacturing, operate successfully in the construction industry as well as many areas. This technology, which reduces material waste and labor cost, has shown the same benefits in the construction industry as in other sectors, with the gain in production time [1].

Each stage in the traditional application of concrete, one of the most used materials in the construction industry, requires high costs, labor and time. High dependence on labor can lead to loss of time, poor quality production, and material waste. Another problem with traditional methods is the limitation of design freedom. Since the use of formworks in reinforced concrete structures is not used in 3D Concrete Printing (3DCP) technology, designs with complex geometries can be produced

easily, It has become clear that there is a problem in this regard, as it constitutes approximately 80% of those involved in the waste generated in the construction industry [2]. This is one of the reasons for increase in waste in the construction industry, as formworks are eventually thrown away.

On the other hand, working in construction sites and manufacturing areas has conditions that pose risks to employee health. The fact that construction sites are messy, large and generally outdoors poses many risks in the sector. Due to these conditions, the working area is exposed to many effects and dangers and is also highly affected by weather conditions [3].

Considering what 3DCP technology offers; Advantages such as reducing the cost because no formwork is used, saving time by working continuously at a constant level, contributing to sustainability by reducing construction waste, adding freedom and originality to the design, contributing to the protection of workers' health by reducing risky work, may play an important role in solving the mentioned problems [4]. In the literature, studies on

---

recycling to reduce cost or CO_2 emissions [5]-[19], it is thought that it is important for both engineering and sustainable production to evaluate the mechanical and durability properties of concrete or mortar content together in pavement design in future studies such as these.

The first 3D concrete printing technique, which Khoshnevis calls Contour Crafting (CC), is an additive manufacturing method with significant potential in the automatic production of small-scale structures [20]. Contour Crafting has been an important development in the transition to automation for the construction industry, which lags behind in automation compared to other sectors.

The Concrete Printing method promises to reduce construction costs due to the possibility of not using formworks. This technology, which enables production in complex geometries, cannot produce a smooth surface compared to Contour Crafting. This method, which requires a manual process for a smooth surface, is against automation and has a disadvantages compared to Contour Crafting [21].

In the additive manufacturing technique called D-Shape, unlike other methods, production is made with powder and adhesive layers instead of a paste-like cement-like material. Following a programmed route, the nozzle sprays a liquid that adheres to the bed. The extruded material reacts and begins solidify, and in the continuation of the process, this movement is repeated, and accumulation is ensured.

Studies on 3DCP technology are continued by different teams in many points of the world. The 3DCP facility established by a group of researchers at Eindhoven University makes a mixture of traditional components used in concrete and printing in layers. The printer's head is independent of its axis, while the X, Y, Z axes also make movement possible. While all the parameters required for the movement are under control, designs in the originality and freedom emerge [22].

Significant studies have been carried out and contributed to literature about design freedom and optimized printable elements, which are major promises of this technology. In the study conducted by Gosselin et al., a "multifunctional wall" consisting of 139 layers was designed. Fiber reinforced Ultra High-Performance Concrete (UHPC) is used in this building element. The production of the element with a dimensions of 1360 mm x 1500 mm x 170 mm lasted approximately 12 hours [23].

In Asprone et al. [24] study, designed a prefabricated beam in different geometry. Due to the low tensile strength of concrete this prefabricated beam is strengthened by steel reinforcement from the outer surface. Designed for long spans, such elements must pass different tests with loading.

Wang et al. [25] designed five different concrete mixtures using ceramcite sand and silica sand. The optimized mixture was selected to work in harmony with the printing process. Four different types of hollow cubic and beam elements were printed with selected mixture. The internal pattern of the elements was planned as lattice, cellular, triangle and, truss. As a result of the tests, the rectangular lattice hollow cubic sample has the best mechanical resistance against compression, and the truss-shaped prism structure shows the best flexural strength.

In one of the studies that contribute to the literature about the structural elements in different geometries, Dey et al. [26] printed the beams in 3D, while they examined the beams through the computer with Finite Elements (FE) method. They reported that the best resistance against bending deformation belongs to the triangular pattern in this study, which they think will benefit in designing large scale structures.

2. Material and Method

Concrete required to work compatible with a 3D printer must meet certain requirements. It distinguishes this concrete from conventional concrete in that it can withstand its own weight because it is printed layer by layer, has a flowable consistency for exiting the nozzle, and the workability of the concrete in the printer maintains while the printing process continues. There is no standard yet for mixtures to be used in 3D printing. However significant studies in the literature have made some determinations for printable mixtures as a result of their traditional tests.

2.1. Extrudability

In a mixture where extrusion is successfully achieved, it is expected that the nozzle maintains its shape after the concrete leaves the nozzle, it does not block the nozzle at all, the flow is not interrupted during exit, and the process proceeds repeatedly [27]. In this study, fine aggregate was used to avoid blockage since the nozzle diameter was 15 mm. The fine sand used also helped create the required spreading. Low flowability was avoided because extrudability was stated to be related to flowability [28]. Visual observations were used to determine whether extrusion was achieved.

2.2. Workability

The Slump Test (a) Figure 1. which is a simple and useful test for the workability of concrete, is widely used to determine consistency. In this experiment that correlates with shear strength, Özalp et al. it states that mixtures with 200 mm slump value can be printed in only 3 layers, but mixtures with 190 mm slump value can be printed easily [29]. As a result of the Slump Test ASTM C143 [30] conducted in this study, it was observed that 2 mixtures obtained with slump values of Mix-2 185 mm and Mix-1 190 mm could be printed. In order to add workability to the mixture, methods are being tried to reduce the shear strength by increasing the water/cement ratio of the mixture and adding superplasticizer to the mixture, and if there is amount of superplasticizer, increasing it percentage compared to the cement [29]. Another test evaluated to get an idea about workability is the ASTM C1437-20 [31] Flow Table Test (b) and (c) Figure 1. Tay et al. [32] defined the printable region as a diameter value of 15-19 cm. they stated that mixtures with this diameter value are workable and also allow for higher buildability. Mixtures with a diameter below 15 cm almost block the nozzle and have difficulty in being extruded (a) Figure 2. It was observed that the layers of the mixtures with diameter above 19 cm spread after extrusion and the layers interpenetrate with each other, and the mixture could not be printed successfully (b) Figure 2. Successful extrusion in (c) Figure 2. Mix-1 has a diameter value of Flow Table 16,6 cm and Mix-2 has a diameter value of Flow Table 16 cm.

2.3. Buildability

Layers printed on top of each other support each other's weight and maintain their shape, indicating buildability. Some studies determined buildability as the maximum number of layers that could be printed without important deformation [33], while other studies determined it by measuring the vertical settlement of printed layers [34]. According to Austin [35] buildability in 3D printable concrete is defined as the number of layers without significant deformation of the lower layers. In this study, the total layer height of the beams printed in 10 layers was measured as 110 mm in the measurement made immediately after printing, and when the total layer height of the hardened state was measured, it was found that this value decreased between 105-108 mm.

Figure 1. Slump Test (a) and Flow Table Test (b), (c)
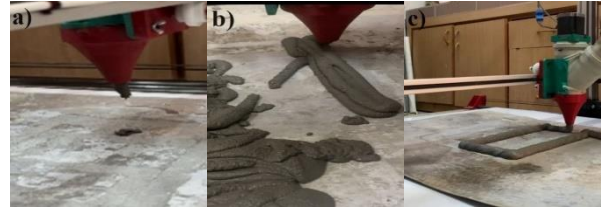
Figure 2. a) Flow Table Diameter Value Below 15 cm
b) Flow Table Diameter Value Above 19 cm
c) Flow Table Diameter Value Between 15-19 cm

2.4. Process of Printing Concrete

In this study, studies in the literature were examined and based on the reference mix designs, sand, cement, silica fume, fly ash, superplasticizer, and water were used to produce printable concrete as a result of preliminary trials. Two mix designs were created by using these materials in different proportions. Coarse aggregates were not preferred to avoid blockage of the 15 mm nozzle diameter, which is the exit point of the printer. In order not to increase the w/b ratio too much while maintaining workability, the amount of superplasticizer was increased in a mixture and fly ash was used in the mix due to its ability to reduce the need for water. The cement type used in the mixtures is CEM-I 42.5R. MasterGlenium51, which increases the workability time was chosen as the superplasticizer. Before adding water and superplasticizer to the mixture, the dry materials were mixed in a drum type mixer for 2 minutes. Then 50% of the mixture water was added and the mixture was mix for 1 minute. Superplasticizer was added to the remaining mixing water as recommended [36] and the mixer was stopped. After the mixer was scraped with a trowel, the remaining mixing water and superplasticizer were added while the mixing process continued. Finally, the mixture was mixed for 1 more minute and then the resulting concrete was taken from the mixer. Beams with 10 layers and dimensions of 600 mm x 200 mm x 110 mm were produced. Three different internal patterns were selected to be printed with a 3D printer. These internal patterns are called wave shape (a), rectangular shape (b), parallelogram shape (c) in Figure 3. The volume occupancy rates of the internal patterns of these shapes are wave shape has 25%, rectangular shape has 28%, parallelogram

shape has 50%. Elements that failed in preliminary attempts during the printing process are shown in Figure 4. The mix designs created are included in Table 1 and Table 2.

Table 1. Mix Design-1 (kg/m³), w/b ratio: 0,40

Material	Amount
Sand	1220
Cement	630
Silica Fume	74,8
Fly Ash	19,7
Superplasticizer	3,95
Water	291

Table 2. Mix Design-2 (kg/m³), w/b ratio: 0,37

Material	Amount
Sand	1200
Cement	640
Silica Fume	76
Fly Ash	24
Superplasticizer	5
Water	280
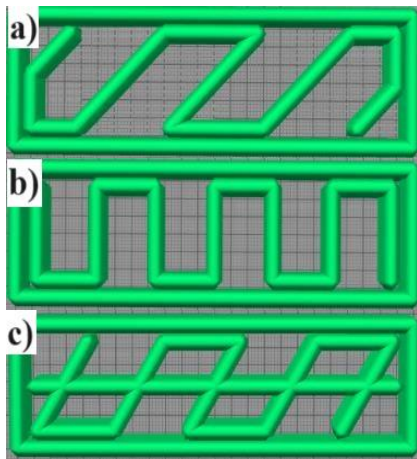
Figure 3. Different internal patterns
a)Wave shape
b)Rectangular shape
c)Parallelogram shape
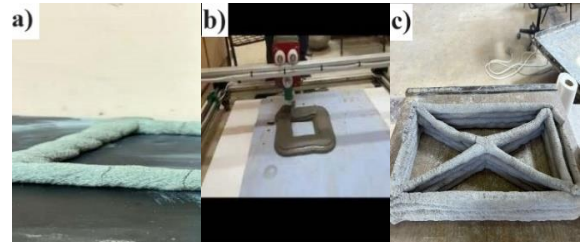
Figure 4. a) Shrinkage crack
b) High flowability because of high amount of superplasticizer
c) Thin layers because of low w/b ratio

3. Results

Mix designs that work compatible with the printer after extrusion process have yielded successful results. A total of 6 samples in 3 different patterns with 2 different mix designs were successfully produced with a 3D concrete printer. Hollow concrete beams with internal patters of wave shape, rectangular shape, and parallelogram shape have reached a height of 110 mm in 10 layers. From the beginning to the end of the printing process, there were no problems such as blockage in the nozzle, deformation of the hollow concrete beams, or interpenetration of layers. Situation such as loss of function, loss of flowability, segregation, and heterogeneity were not observed in either of the two mix designs created to work compatible with the 3D printer. Immediately after the printing process, the crushing between the layers of the hollow concrete beams was examined and the total height was measured. This measurement was made again after the hollow concrete beams had dried. In the dry state measurement made on the hollow concrete beams print with Mix Design-1, it was observed that the height of the parallelogram shape among all the hollow concrete beams, which was initially 110 m, decreased to 105 mm, and the rectangular shape and wave shape decreased to 106 mm. In the dry state measurement made on the hollow concrete beams print with Mix Design-2, it was observed that the height of the parallelogram shape among all the hollow beams, which was initially 110 mm, decreased to 107 mm, and the height of the rectangular shape and wave shape decreased to 108 mm. During these height decreases, the layers were examined one by one, and it was determined that there was no significant visible deformation in any layer.

Figure 5. 3D Printed Hollow Concrete Beams

Figure 6. Fresh State Height Measurement

Figure 7. Hardened State Height Measurement

4. Conclusion

Considering the investigations, experiments and observations made in this study, it is possible to make some inferences about the effect of mix designs, w/b ratio, concrete printing process, and volumetric filling ratio of internal patterns. During the printing process, printing begins by assuming that the layers will be at the same height, but looking at the results, as the layers accumulate on top, there may be a slight loss in the layers below due to weight.

•   When the volumetric filling ratio is examined, it is seen that the parallelogram shape, whose internal pattern is 50% filled, is the shape that suffers the most height loss for both mix designs. A 4.5% height loss in Mix-1 of the parallelogram shape;

It was observed that there was a 2.7% height loss in Mix-2. It is thought that the reason why this shape experiences different levels of loss in the 2 mixes is that Mix-1 has a higher w/b ratio and contains more water. When the rectangular shape with a volumetric filling rate of 28% and the wave shape with a volumetric filling rate of 25% are examined, the measured height loss for Mix-1 is 3.6%; It was observed that the measured height loss for Mix-2 was 1.81%.

•   When approaching the study in terms of extrudability, as stated and shown in the photographs, it is pointed out that there are no issues with extrusion. Mix-1 and Mix-2 do not cause blockage in the nozzle for a 3D concrete printer under laboratory conditions, the nozzle shape is maintained after the concrete exit, and the flows are not interrupted.

•   When the issue of workability is considered, Mix-1 and Mix-2 have a Flow Table diameter of 15-19 cm, which is called the printable region in the literature, and Slump Test values are 190 mm and 185 mm. The fact that Mix-1 and Mix-2 are easily printed in a flowable manner without losing their homogeneity indicates that there is no issue in terms of workability about these 2 mixes.

•   Visible deformation of the layers, which is an important visual data in buildability, was not experienced in the samples presented in this study. It was determined that there was a maximum loss of 4.5% in samples with final height values in the range of 105-108 mm. This paper focuses on the printability of 3 hollow concrete beams with different internal pattern with 2 different mix and was conducted with the aim of expanding experimental studies in the future to print elements of complex geometry with different mix designs in a laboratory environment with a laboratory-scale 3D concrete printer.

Conflict of Interest Statement

There is no conflict of interest between the authors.

Statement of Research and Publication Ethics

The study is complied with research and publication ethics.

References

[1] A. E. Çerçevik, Y. C. Toklu, S. Y. Kandemir, and M. Özgür, '3B Beton Üretimi İçin Mermer Tozu Ve Seramik Artıklarının Kullanılmasının Araştırılması', vol. 10, no. 2, 2018.

[2] C. Llatas, 'A model for quantifying construction waste in projects according to the European waste list', *Waste Management*, vol. 31, no. 6, pp. 1261–1276, Jun. 2011, doi: 10.1016/j.wasman.2011.01.023.

[3] A. Ercan, 'Türkiye'de Yapı Sektöründe İşçi Sağlığı ve Güvenliğinin Değerlendirilmesi,' *Politeknik Dergisi*, vol. 13, no. 1, pp. 49-53, 2010.

[4] B. Nematollahi, M. Xia, and J. Sanjayan, 'Current Progress of 3D Concrete Printing Technologies', presented at the 34th International Symposium on Automation and Robotics in Construction, Taipei, Taiwan, Jul. 2017. doi: 10.22260/ISARC2017/0035.

[5] S. Etli, 'Evaluatıon Of Curing Time For Micro Concrete Mixes Containing Silica Fume, Nano-Silica and Fly Ash', *İstanbul Ticaret Üniversitesi Fen Bilimleri Dergisi*, vol. 21, no. 42, pp. 304–316, Dec. 2022, doi: 10.55071/ticaretfbd.1093891.

[6] S. Etli, 'Investigation of the Effect of Glass Sand Used in SCC on the Behavior of the SCC Stress- Strain Relationship', *International Journal of Innovative Engineering Applications*, vol. 6, no. 2, pp. 237–244, Dec. 2022, doi: 10.46460/ijiea.1108476.

[7] S. Lakusic, Ed., 'Effect of glass sand used as aggregate on micro-concrete properties', *JCE*, vol. 75, no. 01, pp. 39–51, Feb. 2023, doi: 10.14256/JCE.3538.2022.

[8] S. Etli, 'Evaluation of the effect of silica fume on the fresh, mechanical and durability properties of self-compacting concrete produced by using waste rubber as fine aggregate', *Journal of Cleaner Production*, vol. 384, p. 135590, Jan. 2023, doi: 10.1016/j.jclepro.2022.135590.

[9] 'Effect of Partial Inclusion of Tiles and Brick Waste as Binders in SCM Elements on Fresh State and Early Age Mechanical Properties', in *International Conference on Innovative Academic Studies*, All Sciences Academy, 2023. doi: 10.59287/icias.1616.

[10] S. Etli and S. CemalgiL, 'Effects of Specimen Size on The Compressive Strength of Rubber Modified Self-Compacting Concrete', *International Journal of Pure and Applied Sciences*, vol. 6, no. 2, pp. 118–129, Dec. 2020, doi: 10.29132/ijpas.789480.

[11] O. Hansu and S. Etli, 'Beton ile Üretilen Suda Yüzebilen Kano Tasarımı Üzerine Bir Araştırma', *European Journal of Science and Technology*, Jan. 2022, doi: 10.31590/ejosat.1052105.

[12] S. Etli, T. Yılmaz, and O. Hansu, 'Effect of White-Portland cement containing micro and nano silica on the mechanical and freeze-thaw properties of self compacting mortars', *Engineering Science and Technology, an International Journal*, vol. 50, p. 101614, Feb. 2024, doi: 10.1016/j.jestch.2023.101614.

[13] M. Akgül, O. Dogan, and S. Etli, 'Investigation of Mechanical Properties of Granulated Waste Rubber Aggregates Substituted Self-Compacting Concrete Mortar Produced with Different Cement', *Uluslararası Muhendislik Arastirma ve Gelistirme Dergisi*, vol. 12, no. 2, pp. 787–798, Jun. 2020, doi: 10.29137/umagd.734614.

[14] S. Etli, S. Cemalgil, and O. Onat, 'Mid-Temperature Thermal Effects on Properties of Mortar Produced with Waste Rubber as Fine Aggregate', *International Journal of Pure and Applied Sciences*, vol. 4, no. 1, pp. 10–22, Jul. 2018, doi: 10.29132/ijpas.341413.

[15] S. Cemalgil, S. Etli, and O. Onat, 'Curing effect on mortar properties produced with styrene-butadiene rubber', *Computers and Concrete*, vol. 21, no. 6, pp. 705–715, Jun. 2018, doi: 10.12989/CAC.2018.21.6.705.

[16] S. Cemalgil, O. Onat, M. K. Tanaydın, and S. Etli, 'Effect of waste textile dye adsorbed almond shell on self compacting mortar', *Construction and Building Materials*, vol. 300, p. 123978, Sep. 2021, doi: 10.1016/j.conbuildmat.2021.123978.

[17] S. Etli, S. Cemalgil, and O. Onat, 'Effect of pumice powder and artificial lightweight fine aggregate on self-compacting mortar', *Computers and Concrete*, vol. 27, no. 3, pp. 241–252, Mar. 2021, doi: 10.12989/CAC.2021.27.3.241.

[18] M. Gesoglu, E. Güneyisi, O. Hansu, S. Etli, and M. Alhassan, 'Mechanical and fracture characteristics of self-compacting concretes containing different percentage of plastic waste powder', *Construction and Building Materials*, vol. 140, pp. 562–569, Jun. 2017, doi: 10.1016/j.conbuildmat.2017.02.139.

[19] M. Akgül and S. Etli, 'Investigation of the variation of mechanical and durability properties of elements manufactured with rubber substituted SCMs with element height', *Construction and Building Materials*, vol. 428, p. 136300, May 2024, doi: 10.1016/j.conbuildmat.2024.136300.

[20] B. Khoshnevis, 'Automated construction by contour crafting—related robotics and information technologies', *Automation in Construction*, vol. 13, no. 1, pp. 5–19, Jan. 2004, doi: 10.1016/j.autcon.2003.08.012.

[21] S. Lim, R. A. Buswell, T. T. Le, S. A. Austin, A. G. F. Gibb, and T. Thorpe, 'Developments in construction-scale additive manufacturing processes', *Automation in Construction*, vol. 21, pp. 262–268, Jan. 2012, doi: 10.1016/j.autcon.2011.06.010.

[22] F. Bos, R. Wolfs, Z. Ahmed, and T. Salet, 'Additive manufacturing of concrete in construction: potentials and challenges of 3D concrete printing', *Virtual and Physical Prototyping*, vol. 11, no. 3, pp. 209–225, Jul. 2016, doi: 10.1080/17452759.2016.1209867.

[23] C. Gosselin, R. Duballet, Ph. Roux, N. Gaudillière, J. Dirrenberger, and Ph. Morel, 'Large-scale 3D printing of ultra-high performance concrete – a new processing route for architects and builders', *Materials & Design*, vol. 100, pp. 102–109, Jun. 2016, doi: 10.1016/j.matdes.2016.03.097.

[24] D. Asprone, F. Auricchio, C. Menna, and V. Mercuri, '3D printing of reinforced concrete elements: Technology and design approach', *Construction and Building Materials*, vol. 165, pp. 218–231, Mar. 2018, doi: 10.1016/j.conbuildmat.2018.01.018.

[25] L. Wang, H. Jiang, Z. Li, and G. Ma, 'Mechanical behaviors of 3D printed lightweight concrete structure with hollow section', *Archiv.Civ.Mech.Eng*, vol. 20, no. 1, p. 16, Mar. 2020, doi: 10.1007/s43452-020-00017-1.

[26] D. Dey, V. N. Van, H. N. Xuan, D. Srinivas, B. Panda, and P. Tran, 'Flexural performance of 3D printed concrete structure with lattice infills', *Developments in the Built Environment*, vol. 16, p. 100297, Dec. 2023, doi: 10.1016/j.dibe.2023.100297.

[27] S. Ahmed and S. Yehia, 'Evaluation of Workability and Structuration Rate of Locally Developed 3D Printing Concrete Using Conventional Methods', *Materials*, vol. 15, no. 3, p. 1243, Feb. 2022, doi: 10.3390/ma15031243.

[28] B. Panda and M. J. Tan, 'Experimental study on mix proportion and fresh properties of fly ash based geopolymer for 3D concrete printing', *Ceramics International*, vol. 44, no. 9, pp. 10258–10265, Jun. 2018, doi: 10.1016/j.ceramint.2018.03.031.

[29] F. Özalp, H. D. Yılmaz, and Ş. Yaşar, '3D Yazıcı Teknolojisine Uygun Sürdürülebilir Ve Yenilikçi Betonların Geliştirilmesi'.

[30] 'Standard Test Method for Slump of Hydraulic-Cement Concrete'. Accessed: Jul. 18, 2024. [Online]. Available: https://www.astm.org/c0143_c0143m-12.html

[31] 'Standard Test Method for Flow of Hydraulic Cement Mortar'. Accessed: Jul. 18, 2024. [Online]. Available: https://www.astm.org/c1437-20.html

[32] Y. W. D. Tay, Y. Qian, and M. J. Tan, 'Printability region for 3D concrete printing using slump and slump flow test', *Composites Part B: Engineering*, vol. 174, p. 106968, Oct. 2019, doi: 10.1016/j.compositesb.2019.106968.

[33] T. T. Le, S. A. Austin, S. Lim, R. A. Buswell, A. G. F. Gibb, and T. Thorpe, 'Mix design and fresh properties for high-performance printing concrete', *Mater Struct*, vol. 45, no. 8, pp. 1221–1232, Aug. 2012, doi: 10.1617/s11527-012-9828-z.

[34] Y. Zhang, Y. Zhang, G. Liu, Y. Yang, M. Wu, and B. Pang, 'Fresh properties of a novel 3D printing concrete ink', *Construction and Building Materials*, vol. 174, pp. 263–271, Jun. 2018, doi: 10.1016/j.conbuildmat.2018.04.115.

[35] S. A. Austin, 'Low-volume wet-process sprayed concrete: pumping and spraying', *Mater. Struct.*, vol. 38, no. 276, pp. 229–237, Jan. 2005, doi: 10.1617/14025.

[36] 'Master Builders Solutions | MasterGlenium 51', Türkiye. Accessed: Apr. 14, 2024. [Online]. Available: https://mbcc.sika.com/tr-tr/products/masterglenium/masterglenium-51

Study on Strength Properties of Woven Fabrics Including Recycled Cotton Yarns

Mihriban KALKANCI[1*]

[1] Pamukkale University, Denizli Vocational School of Technical Sciences, Denizli, TR
(ORCID: 0000-0003-3287-1428)

Abstract

In this study, yarn was produced by mixing pre-consumer cotton yarn waste and original cotton fibers in certain proportions and plain sheet fabrics were woven using these yarns. Within the scope of the study, yarns with cotton/recycled cotton fiber ratios of 100-0%, 90-10%, 80%-20%, 70-30%, 60-40% were used. All fabrics were subjected to finishing processes respectively under the same conditions. Breaking strength and tear strength tests were carried out to understand the effect of the recycling rate on the strength loss in fabrics. It was determined that there was a decrease of nearly 45% in the tear strength of fabrics obtained by mixing 40% recycled fiber. Additionally, the loss in tensile strength was less than the loss in tear strength.

1. Introduction

Recycling processes have become more important due to the increasingly depleting natural resources and environmental problems in the world. The textile industry is one of the sectors that harms nature the most. Whereas, many products in the textile industry are recyclable. On condition that the textile waste is systematically collected and utilized, textile recycling can be a viable and sustainable industry [1]. The most important solution to prevent environmental damage both in the production phase and end use is recycling [2]. In other words, it is the reuse of the fibers of old textile products [3]. It is very crucial to evaluate the recycling issue in textile products under a single heading, since the machinery, energy types, costs and raw materials used during production, environmental interactions occurring in the processes and the recycling potential of the products are not the same [4].

Textile production processes consume large amounts of natural resources (water, oil, soil), toxic chemicals are used, and this releases carbon dioxide. In addition, millions of tons of textiles are thrown away every year. Many studies are being carried out in the textile sector on minimizing and recycling this waste. A single cotton t-shirt requires 2,700 liters of water. The World Wildlife Fund argues that 20,000 liters of water are required to produce 1 kilogram of cotton, that current production methods are unsustainable, and that by using cotton obtained from discarded clothing, the need for virgin cotton can be reduced and billions of gallons of water can be saved with post-consumer recycled products [37].

It is seen that approximately one million tons of textile waste is generated in Turkey every year. These wastes are recyclable. If this recovery can be fully realized, the amount of recycled cotton to be obtained will meet 17% of the country's seed cotton production. 766,390 hectares of land, corresponding to 17% of Turkey's cultivated area for cotton production, can be used for another agricultural product. 29% of pesticides used in Turkey are used in cotton production. This situation causes significant losses in wildlife in regions where cotton production is intense, such as Çukurova. Recycling of these wastes will also prevent the amount of pesticides that would be used for the same amount of cotton production [8]. Recycled cotton yarn is a valuable alternative to cotton resources, and by using recycled cotton yarn, agricultural land and water will be saved, and CO_2 emissions will be reduced.

---

*Corresponding author: mkalkanci@pau.edu.tr

To recover fibers from textile wastes and use them in conventional textile processes in the future, the wastes must be opened and separated into fibers [5]. Depending on the end use of the yarn, the fibers may remain combined. Then, through the carding process, the fibers are cleaned and mixed and made ready for spinning for subsequent weaving or knitting processes [6].

Recycling takes place largely in spinning, and recycled fibers are mostly used, especially in the open-end rotor spinning system, where shorter fibers are used compared to the ring spinning system [7].

The wastes that arise during the ready-made garment phase are fabric pieces at the beginning and end of the fabric roll (approximately 15% of the total fabric), scraps and faulty fabric pieces during marker cutting [4]. The amount of waste generated during the carded yarn production phase in a ring mill is approximately 5.5-10.5%, in combed yarn production it is approximately 12%, and in the fabric production and ready-made garment stages, this rate rises up to 23% [8]. When the wastes during garment and yarn production are evaluated, a serious raw material can be gained.

Reusing the residues generated during cotton yarn production is an important recycling step. Cotton recycling is the process of converting cotton fabric into cotton fibers that can be used in textiles over again. Recycled cotton is sometimes also called regenerated cotton, reclaimed cotton, or poor-quality cotton. Recycled content includes parts that are used, refurbished, or rebuilt from scratch. Most recycled cotton products are made from pre-consumer trash, such as cutting residues. Post-consumer trash is more difficult to sort because it comes in many different colors and fabrics and generally requires more work [9].

Wastes are classified as pre-consumer waste and post-consumer waste according to their production stages. Pre-consumer wastes are the industrial wastes generated in fibrous products' manufacturing processes. Post-consumer waste refers to materials and products scrapped after their service life is over [10, 24]. A study was carried out on the production of products that create added value by utilizing textile waste. It has been shown that functional textile materials with high thermophysiological comfort and odor masking properties can be produced by converting waste into biochar and applying it to textile fabrics [11].

There are studies in the literature on the physical, mechanical and structural properties of recycled fabrics. It has been emphasized in many studies that the addition of recycled fibers negatively affects yarn strength and yarn unevenness [26]. It has also been observed that the air permeability values of fabrics obtained from recycled yarns and the effective clothing insulation of garments decrease, but the thermal resistance values increase [28,36]. The effects of waste fiber ratio and number of recycling transitions on yarn properties have been estimated with a mathematical approach [29]. One of the most important difficulties in recycled fabrics is the decrease in the mechanical properties of the produced fabric. For this purpose, optimization studies are being carried out on which fiber blend ratios or which techniques should be used for the production [30]. The effect of waste ratio on the properties of rotor yarns produced from raw cotton has been investigated and it has been stated that the waste ratio can be up to 25% [31]. The effects of production parameters such as rotor diameter, rotor speed, nozzle type, opening roller speed and yarn count on the use of recycled fiber in open-end spinning have been investigated [32, 33]. Dimensional and physical properties of socks produced from recycled yarns have been investigated [34]. The properties of raw and waste cotton blended yarns have been investigated using the parameters of recycling blend ratio, blend technique, drum speed and rotor speed [35]. Again, in the study on the use of waste in rotor yarns, it has been determined that the use of pneumophilic waste between 5-25% has a positive effect on the strength, elongation, irregularity and breakage numbers of yarns [41]. In some studies, only recycling and blends of weft yarns were used to reduce the loss of strength in woven fabrics. Especially if cotton is to be recycled, polyester fiber is used in the warp or as a blend to ensure fabric strength. [12,13]. Studies have also been conducted on the surface properties of recycled fabrics and woven fabric defects and decreases in fabric surface quality were observed [14].

It is possible to use 100% polyester fiber in recycled fabrics. There are studies in the literature on recycled polyester fabrics and yarn quality [15-19]. However, it has not yet been possible to produce durable fabric using 100% recycled cotton fiber. The biggest problem in this regard is that sufficient strength value cannot be provided [20,21].

There are very few studies in the literature on woven fabrics using recycled yarns in both weft and warp yarns. In studies conducted on denim fabrics, the air permeability, bending strength and dimensional change after washing of denim fabrics recycled after consumer use were determined according to standards and according to the results obtained, it was determined that this recycling process could be used

effectively in denim production. As a result of the tests, it was evaluated that the recycled fiber added to the blend caused a decrease of approximately 15% in the warp and 10% in the weft in fabric strength, but this was within acceptable limits [38-40].

In this study, bed sheet fabrics were woven using recycled yarns in different ratios in both weft and warp directions and their strength values were examined. As it is known, bed sheet fabric is produced with low fabric weight and thin yarns. Therefore, the strength loss that will occur in thin fabric is more important than fabrics with higher fabric weight and woven with thicker yarns. Therefore, in this study, it was aimed to determine the highest recycling mixture ratio that can be used in bed sheet fabric and to obtain the mixture ratio that remains within the quality standards. For this purpose, the recycling ratio was increased in 10% increments and the changes in the strength properties were examined.

2. Material and Method

The study was conducted in an integrated textile factory producing home textiles, including yarn production, woven fabric production, finishing processes and testing processes. In order to examine the effect of cotton yarn recycling rate on fabric strength loss in fabrics produced with recycled yarns, 5 different yarns were used in both warp and weft directions.

In the mechanical recycling process, no chemicals are used and textile products are converted back into fiber without wet processing. Textile pre-consumer waste was converted into recycled cotton by mechanical method. In this study, 100% cotton waste, namely yarn spinning waste, generated in the winding section of the spinning mill of the factory was evaluated. Table 1 provides the properties of cotton and recycled cotton fibers. The properties of these fibers were measured using Uster AFIS Pro 2 with five specimens. used should be supported by previously published references. Changes that contribute to the method in the study should be described in detail [3], [4].

Table 1. Parameters of cotton and recycled cotton fibers

Parameters	Length (mm)	Short Fiber Content (uniformity) (%)	Fineness (micronare)	Strength (cN/tex)	Fiber Quality Index (FQI)
Cotton	28,78	8,6	3,93	29,5	216
Recycled cotton	20,7	19,5	4,13	27,7	139

FQI have been related fiber strength, mean length and fineness and defined by the following relationship [29, 42]:

$$\text{Fiber Quality Idex (FQI)} = (L \times S) / f \qquad (1)$$

where L = fiber length(mm), S = the fiber strength cN/tex, f = fiber fineness (mic).

The fiber, which is cotton waste in yarn production, was mixed with original cotton in four different mixing ratios. The proportions of recycled cotton and cotton blends are shown in Table 2. In order to determine the highest recycled fiber blend ratio and the best strength value in compliance with the standards, the recycled fiber blend ratio in the yarns was increased by 10 percent. These blends are 100-0%, 90-10%, 80%-20%, 70-30%, 60-40% cotton-recycled cotton. The yarns were produced in the open-end yarn department of the textile factory.

For Ne 30 yarns, the twist coefficient is 4.16 in weft yarns and 4.79 in warp yarns.

Table 2. In yarns cotton / recycled cotton blend ratio

Fabric code		Material %
	F1	100% cotton
	F2	90% cotton -10% recycled cotton
Weft Yarns	F3	80% cotton -20% recycled cotton
	F4	70% cotton -30% recycled cotton
	F5	60% cotton -40% recycled cotton
	F1	100% cotton
	F2	90% cotton -10% recycled cotton
Warp Yarns	F3	80% cotton -20% recycled cotton
	F4	70% cotton -30% recycled cotton
	F5	60% cotton -40% recycled cotton

The properties of the produced woven fabrics are given in Table 3. Weft and warp yarns in all fabrics are Ne 30. In woven fabrics, both weft and warp yarns affect the physical and mechanical properties of the fabric. All fabrics are woven in the same density and plain pattern. All fabrics were subjected to finishing processes under the same

conditions: burning+cold bleaching / drying / equalize / printing / fixation / finishing / sanforizing. Care has been taken to ensure that yarn production, weaving and finishing processes are carried out under the same conditions for all fabrics.

Table 3. Fabric production details

Parameter	Explanation
Yarn (Warp)	Ne 30, OE-Rotor
Yarn (Weft)	Ne 30, OE-Rotor
Weaving machine	Dornier HTV Jacquard Loom
Width of fabric	280 cm
Fabric structure	Plain 1/1
Weft density	27 ends/cm
Warp density	33 ends/cm
Mass per unit area (g/m2)	~120

After weaving and finishing processes, fabric unit weights (g/m^2) were measured to make comparisons for sheeting fabrics. Fabric unit area weight directly affects fabric properties. For this purpose, all fabrics were produced under the same conditions. In order to make reliable comparisons, it was aimed to ensure that the differences between fabric weights were insignificant. In order to see the mechanical behavior of the fabric against different effects, breaking force (warp/weft) and tearing strength (warp/weft) were measured. Unit fabric weight determination was performed according to TS 251 EN ISO 3801. Tensile strength tests were made according to TS EN ISO 13934-1 with the strip method using the commercial TINIUS OLSEN tensile testing device. The test length is 200 mm, the test speed is 100 mm/min and the width of the fabric samples is 50 mm. Since the fabric weight is less than 200 g/m², the pre-tension is 2 N. Tear strength tests were also carried out with test samples in the same device according to TS EN ISO 13937-2 (single tear test method). Tear strength tests were also applied in both warp and weft directions. Five samples were tested in weft and warp directions for each fabric type in terms of tensile properties of the fabrics.

The results obtained from these measurements were evaluated statistically by ANOVA and correlation analysis. The analysis was performed according to the 95% confidence level. Therefore, if the p value is less than 0.05, it means that the difference is statistically significant. The measurement results obtained from the tests carried out to determine the effects of recycled yarns used in weft and warp on the breaking and tearing strength of bed sheet fabrics were analyzed and evaluated. Additionally, the relationships between the blending ratio of fibers and fabric results were analyzed using correlation analysis.

3. Results and Discussion

3.1. Fabric Weight Results

Mean values of mass of fabrics per unit area are shown in Figure 1. As expected, there are very slight differences in fabric weights in terms of unit area mass of the fabrics.

The fabric weight planned before production is 120 gr/m², deviations are insignificant. Since the production and finishing stages are applied to each fabric under the same conditions, the fabric weights are very close to each other.
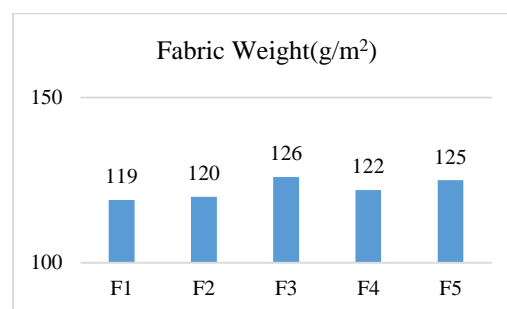
Figure 1. Fabric weight results

3.2. Breaking Strength Results

Mean values of breaking strength (warp/weft) are shown in Table 4. In order to determine the effect of recycled cotton ratio on the strength properties of the fabrics, breaking strength tests were conducted in the warp and weft directions of woven fabrics. It was determined that the breaking strength values of all fabrics, especially in the weft direction, were above 250 N and showed similar behavior. In the warp direction, a decrease in the breaking strength value was observed with a 10% increase in the recycling rate. When the effect of recycled fiber ratio on the breaking strength of the fabrics was evaluated, it was seen that the breaking strength values in both the warp and weft directions in fabrics obtained from recycled cotton fiber decreased compared to 100% cotton yarn. However, this decrease is lower than the values in the warp direction.

The fabric with the highest value for breaking strength is 100% cotton (F1). When F2 fabrics consisting of 90% cotton-10% recycled cotton fiber and F3 fabrics consisting of 80% cotton-20% recycled cotton fiber were evaluated in terms of breaking strength, a decrease in warp direction was observed. For F4 and F5 fabrics, this decrease continued in the warp direction by increasing the recycled cotton fiber ratio to 30% and 40%. While the breaking strength value in the warp direction in 100% cotton yarn was

measured as 426 N, with the increase of the 10 percent recycled cotton rate, the warp breaking strength

values were 397 N for F2, 367 N for F3, 355 N for F4, and 310.5 for F5.

Table 4. Fabric breaking strength and tear strength results (N) / breaking and tear strength loss results (%)

Fabric Code	Breaking Strength (N)		Tear Strength (N)		Breaking Strength Loss%		Tear Strength Loss %	
	warp	weft	warp	weft	warp	weft	warp	weft
F1	426	312	0	0	0	0	7,8	7,5
F2	397	308	-6,8	-1,3	-18,5	-24,1	6,36	5,69
F3	367	303,5	-13,8	-2,7	-29,5	-32	5,5	5,1
F4	355	286	-16,7	-8,3	-38,7	-42,7	4,78	4,3
F5	310,5	249,5	-27,1	-20	-39	-45,3	4,76	4,1

When the breaking strength values of fabrics in the weft direction were examined, it was seen that the breaking strength values in the weft direction decreased in fabrics obtained from recycled cotton fiber compared to 100% cotton yarn. However, this decrease is lower than the values in the warp direction. When evaluated for breaking strength, a decrease in weft was observed in F2 fabrics consisting of 90% cotton-10% recycled cotton fiber and F3 fabrics consisting of 80% cotton-20% recycled cotton fiber. However, there are no significant differences between the reduction rates. In F4 and F5 fabrics, this decrease continued with small differences in the warp direction in the breaking strength values by increasing the recycled cotton fiber ratio to 30% and 40%. While the breaking strength value in the weft direction in the fabric produced from 100% cotton yarn is measured as 312 N, with the increase of the 10 percent recycled cotton rate, the weft breaking strength values are 308 N for F2, 303.5 N for F3, 286 N for F4, 249 N for F5. While the weft breaking strength of F2, F3 and F4 fabrics was close to the F1 fabric, the lowest weft strength value was observed in 60% cotton-40% recycled cotton (F5), as expected.

The strength of yarns produced from cotton and recycled cotton blends decreases proportionally with the increase in the percentage of recycled fibers in the yarn content. Previously recycled cotton fibers contained a high percentage of short fibers due to the shredding process. While the short fiber content of the fibers used in yarn and fabric production was 8.6% for cotton, the short fiber content in recycled cotton was 19.5%. In addition, the Fiber Quality Index was calculated as 216 and 139 for cotton and recycled cotton fiber according to Formula 1. Globally, the quality of recycled fiber can be determined by the Fiber Quality Index (FQI). The high value of this value means that the fiber quality is also high. The results of the study also show that the quality of recycled fiber decreases compared to the quality of

raw cotton [43]. During the draft loading performed while obtaining the yarn, the short fibers in the yarn are more prone to slipping instead of resisting the applied load and as a result, the yarn strength decreases. Therefore, the fabric strength woven with lower strength yarns is also low [24].

The warp and weft strength loss rates in fabrics woven using recycled cotton fiber at 10% increasing rates compared to the F1 fabric in which 100% cotton yarn is used in the warp and weft are given in Table 4. As the recycled fiber ratio increased, the strength values decreased inversely.

When the warp and weft directions were compared, it is seen that the warp breaking strength is higher than the weft breaking strength. Since woven fabrics have more threads in the warp direction, they are stronger in the warp direction, and generally more twist is given to the warp threads to provide the more strength they need during weaving. For this reason, in fabrics produced with the same yarn count and the same texture, warp breaking strength values were higher than weft breaking strength values.

TS 2994 Standard [25] has been produced by weaving or knitting, bed linen, bedsheet, quilt, duvet cover and pillowcase with those products occurs brought bedding for directions, classification and properties, sampling, involves the way supply the market with. The weft and warp breaking strength values of bed sheet fabrics produced according to this standard are expected to be greater than >178 N. Considering this standard value, it can be seen that the warp and weft breaking strengths of all samples are above the lower limit.

The loss in breaking strength values is higher in the warp direction than in the weft direction. As seen in Figure 2, when the graphic lines are examined, the decrease in the strength in the warp direction is greater than the decrease in strength in the weft direction.

The breaking strength loss rates in the warp direction compared to F1 fabric, which is 100% cotton in both warp and weft directions, are shown in Figure 2. Accordingly, the strength loss in the warp direction of F2, obtained by adding 10% recycled cotton compared to F1, was 6.8%. Warp strength loss was 13.8% at 20% recycled cotton, 16.7% at 30% recycled cotton, and 27.1% at 40% recycled cotton.

Compared to F1, the breaking strength loss in the weft direction of F2, obtained with the addition of 10% recycled cotton, was 1.3%. Weft strength loss was 2.7% for 20% recycled cotton, 8.3% for 30% recycled cotton, and 20% for 40% recycled cotton.

Figure 2. Breaking strength loss (%) of woven fabrics for warp and weft direction

The "p-significance level" results of the breaking strength ANOVA test in warp and weft directions are given in Table 6. The breaking strength values in the warp direction in all fabrics were found to be statistically significant at the 5% level (Table 5). However, although there was a decrease in the breaking strength values in the weft direction, the breaking strength values in the weft direction were found to be statistically insignificant at the 5% level in all fabrics (Table 5). ANOVA statistical analysis results show that the recycled cotton fiber ratio significantly affects the tensile strength value in the warp direction. According to statistical evaluation, the differences between the breaking strength values in the warp direction in fabrics woven with warp yarns with gradually increasing recycled cotton ratio were statistically significant ($p=0.008<0.05$).

Table 5. ANOVA test results of fabric breaking strength values for warp and weft direction

Parameters	Warp		Weft	
	Significant (p)	R^2	Significant (p)	R^2
Fabric Recycled Rate	0,008*	0,977	0,068	0,822
*: p < 0.05 it is significant				

However, the recycled cotton fiber ratio does not have a significant effect on the breaking strength in the weft direction. The difference between the breaking strength values in the weft direction in the fabrics woven with weft yarns with a gradually increased recycled cotton ratio was not statistically significant ($p=0.068>0.05$).

3.3. Tear Strength Results

Mean values of tear strength (warp/weft) are shown in Table 4. In order to determine the effect of the recycled cotton ratio on the mechanical properties of the fabrics, the tear strength of woven fabrics was tested in warp and weft directions. A decrease in tear strength values in warp and weft directions was observed with a 10 percent increase in the recycling rate in all fabrics. The warp tear strength values were measured as 7.8 N for 100% cotton yarn (F1), 6.36 N for F2, 5.5 N for F3, 4.76 N for F4 and 4.78 N for F5. The weft tear strength values measured as 7.5 N for 100% cotton yarn (F1), 5.69 N for F2, 5.1 N for F3, 4.3 N for F4 and 4.1 N for F5. Consistent with previous studies [44], the lowest tear strength was observed in F5 fabric with increasing recycled fiber ratio.

The tear strength loss rates of the fabrics having recycled cotton yarns in both warp and weft directions are shown in Figure 3 by comparing to F1 fabric, which is 100% cotton. Accordingly, the tear strength losses in the warp direction were calculated as 18.5% for F2, 29.5% for F3, 38.7% for F4, and 39% for F5 fabrics. The tear strength losses in the weft direction were also calculated as 24.1% for F2, 32% for F3, 42.7% for F4, and 45.3% for F5 fabrics.
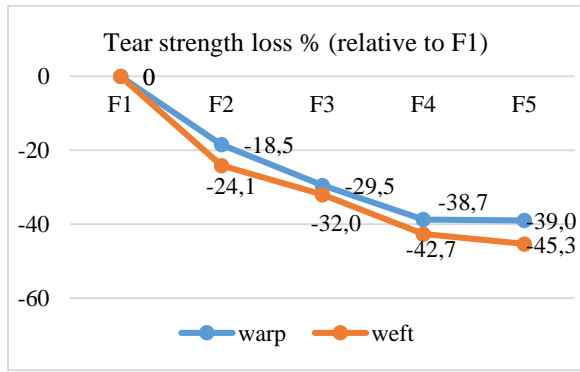
Figure 3. Tear strength loss (%) of woven fabrics for warp and weft direction

When the effect of fabrics produced using different proportions of recycled cotton fibers on the tear strength was examined, different tear strength values were determined for fabrics obtained from original cotton and recycled cotton fibers. The p-significance level results of the tear strength ANOVA test in warp (p=0.035<0.05) and weft (p=0.036>0.05) directions are given in Table 6 and were found to be statistically significant at the 5% level in all fabrics. The results show that the ratio of recycled cotton fiber significantly affects the tear strength value in both directions.

Table 6. ANOVA test results of fabric tear strength values for warp and weft direction

Parameters	Warp Significant (p)	R^2	Weft Significant (p)	R^2
Fabric recycled rate	0,035*	0,900	0,036*	0,899

*: $p < 0.05$ it is significant

Since tear strength is measured by tearing the yarns one by one, and breaking strength is based on tearing all the yarns within 5 cm together, it is expected that the tear and breaking strength results will be directly proportional to each other.

4. Conclusion and Suggestions

The results of the study can be evaluated as follows:

-Recycled fabric productions in the literature contain research information involving recycled fibers in either the weft or warp direction. However, in this study, the same proportions of recycled fiber were used in both weft and warp directions. In this case, as a result of using recycled fiber in the same blending ratios in both weft and warp directions, strength decreases in both warp and weft directions occurred in the same fabric.

-When blended fabrics containing recycled cotton fibers and fabrics woven from 100% cotton were compared, they showed lower tensile strength and tear strength values with a proportional increase in the percentage of recycled fibers. Especially in 60% cotton-40% cotton recycled fabric, strength losses of up to 45% occurred.

- In terms of fabric strength, blend yarn containing up to 40% pre-consumer recycled fiber was found to be suitable to produce woven fabric. Despite the decrease in strength, recycled fabric containing up to 40% pre-consumer recycled fiber was found to be within tolerances according to the relevant standard in bed linen and home textile production. However, if post-consumer waste is used as recycling, it is thought that the strength values will decrease even more.

-It is necessary to work on the proportions in which strength-increasing fibers can be mixed in linen and home textile fabrics at a level that does not adversely affect the touch and comfort properties, and solutions that can increase the quality of fabric obtained from recycled fibers.

- The lifespan of the bed sheet fabrics produced may be shortened due to the lower yarn strength caused by the addition of recycled fiber. However, today consumers consciously prefer to buy environmentally friendly recycled products and are aware of the problems that may occur.

-In this study, it was investigated to what extent recycled cotton fibers could be included within the quality limits that would not cause problems in the home textile industry. It is recommended to identify the quality differences and problems of the recycled products produced and to complete the missing information of our companies regarding the problems to be encountered.

Acknowledgment

Conflict of Interest Statement

There is no conflict of interest between the authors.

References

[1] J.M.Hawley, *''Economic Impact of Textile Recycling''*, http://krex.kstate.edu/dspace/bitstream/2097/1228/1/EconImpactHawley2008.pdf (Accessed April 14, 2024), 2008.

[2] H. Chen and L.D. Burns, "Environmental analysis of textile products", *Clothing and Textile Research Journal*, 24, 3, pp 248-26, 2006.

[3] T. Bayraktar, "Tekstil ve konfeksiyon sektöründe ekoloji ve ekolojik etiketler", *İTKİB AR&GE ve Mevzuat Şubesi*, 2005.

[4] A. Güngör, S. Palamutçu and Y. İkiz,, "Pamuklu tekstiller ve çevre: bir bornozun yaşam döngü değerlendirmesi", *Tekstil ve Konfeksiyon*, vol 3, pp 197-205, 2009.

[5] J.J. Lu and H. Hamouda, "Current status of fiber waste recycling and its future", *Advanced Materials Research*, vol. 878, no.28, pp 122-131, 2014.

[6] S.H. Eryuruk, "Greening of the textile and clothing industry", *Fibres & Textiles in Eastern Europe*, vol.95, no. 6, pp 22-27, 2012.

[7] A.A. Merati and M. Okamura, "Producing medium count yarns from recycled fibers with friction spinning". *Textile Research Journal.,* vol 74, no.7, pp 640-645, 2004.

[8] Ş. Altun, "Prediction of textile waste profile and recycling opportunities in Turkey", *Fibres & Textiles in Eastern Europe*, vol. 20, pp.16–20, 2012.

[9] R. Guru, J. Rani, P. Yadav and U. Saini, "Basic application for fibre & fabric recycling to sustainability products." *UGC Approved Journal*, vol. 14, no. 8.1, ISSN : 0976-6650, August 2023.

[10] H. Wang, H. Memon, R. Abro and A. Shah, "Sustainable approach for mélange yarn manufacturers by recycling dyed fibre waste", *Fibres & Textiles in Eastern Europe*, vol 3, pp 18–22, 2020.

[11] A. Çay, J. Yanık, Ç. Akduman, G. Duman and H. Ertaş, "Application of textile waste derived biochars onto cotton fabric for improved performance and functional properties", *Journal of Cleaner Production,* vol 251, no. 14, pp 119664, 2020.

[12] T, Vadicherla and D. Saravanan "Effect of blend ratio on the quality characteristics of recycled polyester/cotton blended ring spun yarn", *Fibres & Textiles in Eastern Europe*, vol 25, no. 2, pp 48-52, 2017.

[13] M. Kalkanci, "Qualitative classification of woven fabrics produced from recycles threads of cotton and blends.", *Industria Textila,* vol 71, no. 2, pp 118-123, 2020.

[14] M. Kalkanci, "Investigation of surface defects and apparel manufacturing efficiency of fabrics woven from recycled cotton and blends", *Industria Textila*, vol 71 no 3, pp 266-274, 2020.

[15] A. E. Tayyar and S. Ustun,"Usage of recycled pet", *Pamukkale University Journal of Engineering Sciences*, vol. 16, no. 1, pp 53–62, 2010.

[16] A. Telli, and N. Ozdil, "Properties of the yarns produced from r-pet fibers and their blends", *Textile & Clothing*, vol. 23, no. 1, pp 3–10, 2013.

[17] A. Telli, and N. Ozdil, "Effect of recycled PET fibers on the performance properties of knitted fabrics", *Journal of Engineered Fibers and Fabrics*, vol. 10, no. 2, pp 47–60, 2015.

[18] A. Telli, N. Ozdil and O. Babaarslan, "PET bottle wastes in textile industry and contribution to sustainability", *Journal of Textiles & Engineer*, vol.19, no. 86, pp 49–55, 2012.

[19] S. Uyanık, "The bursting strength properties of knitted fabrics containing recycled polyester fiber", *The Journal of The Textile Institute*, vol 112, no.2, pp 1998-2003, 2020.

[20] D. Yilmaz, S. Yelkovan, Y. Tirak, "Comparison of the effects of different cotton fibre wastes on different yarn types", *Fibres & Textiles in Eastern Europe*, vol. 25, no.124, pp 19-30, 2017.

[21] B. Ütebay, P. Celik and A. Çay, "Effects of cotton textile waste properties on recycled fibre quality", *Journal of Cleaner Production*, vol 222, pp 29-35, 2019.

[22] TS EN ISO 13934-1:2013. Textiles—tensile properties of fabrics— part 1: Determination of maximum force and elongation at maximum force using the strip method.

[23] TSE EN ISO 13937-2. Textiles - Tear properties of fabrics - Part 2: Determination of tear force of trouser-shaped test specimens (Single tear method).

[24] Y. Arafat and A.J. Uddin, "Recycled fibers from pre-and post-consumer textile waste as blend constituents in manufacturing 100% cotton yarns in ring spinning: A sustainable and eco-friendly approach", *Heliyon*, vol. 8, no. 11, 2022.

[25] TS 2994 – 2015. Textiles - Woven and knitted - Sheet, quilt case and pillowcase.

[26] J.T. Bolaji, and P.I. Dolez, "Mechanical properties of woven fabrics containing elastane fibers". *Fibers*, vol. 12, no. 30, pp 3-16, 2024.

[27] A. Aypar and E. Öner , "Quality properties of recycled yarns obtained by recycling fabrics produced from virgin yarns", *Revista Matéria*, vol.29, no.2, 2024.

[28] Ö. Necef, et al., "Investigating the effect of recycled cotton included fabrics on the thermal behaviour by using a female thermal manikin", *AUTEX Research Journal*, vol. 23, no 3, 2023.

[29] W. Béchir, A. Béchir and B.H. Mohamed, "Industrial cotton waste: Recycling, Reclaimed fiber behavior and quality prediction of its blend", *Tekstil ve Konfeksiyon*, vol. 28, no. 1, pp 14-20, 2018.

[30] A. Telli and O. Babaarslan, "Usage of recycled cotton and polyester fibers for sustainable staple yarn technology", Textile and Apparel, vol 27, no. 3, pp. 224–233, 2017.

[31] M.T. Halimi, M.B. Hassen and B. Azzouz,, "Influence of spinning parameters and recovered fibers from cotton waste on the uniformity and hairiness of rotor spun yarn", *Journal of Engineered Fibers and Fabrics*, vol 4, no. 3, pp. 36–44, 2009.

[32] H. Hasani, D. Semnani and S. Tabatabaei,, "Determining the optimum spinning conditions to produce the rotor yarns from cotton wastes", *Industria Textila*, vol 61, no. 6, pp. 59–64, 2010.

[33] H. Hasani and S.A. Tabatabaei, "Optimizing spinning variables to reduce the hairiness of rotor yarns produced from waste fibers collected from the ginning process", *Fibres & Textiles In Eastern Europe*, vol. 19, no. 86, pp. 21–25, 2011.

[34] A. G. Demiroz , H.N. Akturk, A. M. Sevkan and G. Alan, "Dimensional and physical properties of socks made from reclaimed fibre", *The Journal of the Textile Institute*, vol 105 no.10, pp 1108-1117, 2014.

[35] R.K., Khan, M.M., Hossain and R.C., Sarker, "Statistical analyses and predicting the properties of cotton/waste blended open-end rotor yarn using taguchi oa design", *International Journal of Textile Science*, vol. 4, no. 2, pp 27-35, 2015.

[36] J.L. Schmitt and L.F. Folle, "Analysis of the thermophysiological comfort and tensile strength in fabric woven with recycled cotton and filaments obtained from post-consumer waste pet bottle recycling", *Revista Matéria*, vol. 26, no .1, 2021.

[37] M. M. Mekonnen, and A. Y.Hoekstra, "The green, blue and grey water footprint of crops and derived crop products", *Hydrol. Earth Syst. Sci.*, vol. 15, pp 1577–1600, 2011.

[38] F. Doba Kadem, and Ş. Özdemir, "Denimde Geri Dönüşüm Uygulamaları-Tüketici Sonrası Geri Dönüşüm (Post-Consumer Re-Cycle)", *Ulusal Çukurova Tekstil KongresiUÇTEK'2019*, 26-27 Eylül 2019, pp 501-508, Adana.

[39] F.Doba Kadem, and Ş. Özdemir, "Tüketici Sonrası Geri Dönüştürülen Denim Kumaşların Seçilmiş Konfor Özellikleri Üzerine Bir Çalışma". *Çukurova Üniversitesi Mühendislik Mimarlık Fakültesi Dergisi*, vol 35, no. 2, pp. 379-388, 2020.

[40] F.Doba Kadem, "Sürdürülebilir Bir Yaklaşım: Denim Sektöründe Pamuk Atıklarının Geri Dönüşümü Üzerine Bir Çalışma", *12. Ulusal Kimya Mühendisliği Kongresi (UKMK 2016)*, 23-26 Ağustos 2016, İzmir.

[41] R.K., Khan and H. Rahman, "Study of Effect of Rotor Speed, Combing-Roll Speed and Type of Recycled Waste on Rotor Yarn Quality Using Response Surface Methodology", *IOSR Journal of Polymer and Textile Engineering*, vol 2, no. 1, pp 47-55, 2015.

[42] M.L Regar , C. R Meena, and S. Hada, "In Textile Calculation Fibre to Finished Garment, Fiber Testing", *Woodhead Publishing*, Sawston, UK; pp. 301–324, 2023.

[43] A, Majundar, P. K, Majundar and B. Sarkar, "Determination of The Technological Value of Cotton Fibre: A Comparative Study of The Traditional and Multiple-Criteria Decision-Making Approaches. *AUTEX Research Journal.;*vol. 5, no. 2, pp.71–80, 2005.

[44] A. Telli and O. Babaarslan, "The effect of Recycled Fibers on the Washing Performance of Denim fabrics", *The Journal of The Textile Institute*, vol. 108, no. 5, pp 812-820, 2017.

Coulomb Stress Analysis in Nemrut Caldera (Eastern Anatolia, Türkiye)

Hamdi ALKAN[1*], Özcan BEKTAŞ[2], Aydın BÜYÜKSARAÇ[3]

[1]Engineering Faculty, Department of Geophysics, Van Yüzüncü Yıl University, Van, TR
[2]Engineering Faculty, Department of Geophysics, Sivas Cumhuriyet University, Sivas, TR
[3]Çan Vocational School, Çanakkale Onsekiz Mart University, Çanakkale, TR
(ORCID: 0000-0003-3912-7503) (ORCID: 0000-0001-5232-4654) (ORCID: 0000-0002-4279-4158)

Abstract

In volcanic areas, seismic events with low energy occur before earthquake activity or due to the movement observed in the magma. These earthquakes, which are caused by the expansion-contraction movement that has been revealed in different studies and is mostly observed in the magma chamber, can be recorded with continuous observations. On the other hand, it is not easy to distinguish between tectonic and volcanic origins of earthquakes occurring in volcanic areas. In this study, Coulomb stress analysis was carried out using earthquakes in the Nemrut Stratovolcano, which is located in eastern Anatolia and is at the westernmost end of a volcano arc. The results demonstrate a very good correlation between positive Coulomb stress changes and earthquake hypocentre depths. It was concluded that the stress is related to the Nemrut Caldera, therefore the positive stress caused by the expansion of the magma chamber of the Nemrut Volcano creates tremors.

1. Introduction

Eastern Anatolia region is mostly represented by volcanic rocks, mainly due to the large Quaternary volcanic centers such as Nemrut, Süphan, Tendürek, and Ağrı Mountains (Figure 1a). Nemrut Stratovolcano is one of the important volcanoes in the Eastern Anatolia located at its westernmost tip and is on the western shore of the Lake Van called the largest lake in Türkiye. Nemrut Stratovolcano started volcanic activity about 1 million years ago and was last active in 1692 [1-4]. Nemrut Stratovolcano is one of the few volcanic mountains in Türkiye that has no activity however is defined as a dormant volcano. The caldera apex of the volcano is ~2948 m in elevation, and its base is about 17 km in diameter [5]. Nemrut Caldera, the largest of which covers an area of 12.5 km² and has a freshwater lake with a depth of around 135 m and four lakes of different sizes, is the largest caldera in Türkiye [1]. The region where the Nemrut Caldera is located is also very close to the area where the Arabian Plate thrusts the Anatolian Plate, and it is a very important region in terms of tectonism. Depending on the closure of the Tethys between the

Eurasian and Arabian Plates, a thrust towards Anatolia started along the Bitlis-Zagros Suture Belt (BZSB) from the Middle Miocene, and Eastern Anatolia rose with a mean elevation of ~2 km and took the form of a plateau [5, 6]. Therefore, this system is at the source of the volcanism in Eastern Anatolia. The volcanic material started to rise along the opening cracks that started in the N-S direction and led to the development of Plio-Quaternary volcanoes [7, 8].

It was observed continuously between 2003 and 2005 with three seismometers placed around the Nemrut Caldera and the volcanic tremors recorded. These volcanic earthquakes were caused by magma activity mostly occurring at a depth of 4-5 km [1]. The depths of the crystallized and solidified deep rock masses were determined by the inversion and normalized full gradient (NFG) techniques from the air magnetic anomalies of the region where the Nemrut Caldera was located at a depth of 4-5 km. It was suggested that a magma chamber may be found at this depth [4]. The power spectrum analysis performed to estimate the deeper magnetic sources affected by hydrothermal fluids and Fe-rich rocks

described almost the same depths. This depth range was also associated with volcanogenic earthquakes occurring at 4-5 km depth [4].

The volcanic products that form on the volcanic basement are classified into pre-caldera, syn-caldera, and post-caldera phases in the region. The basaltic trachyandesitic lava flows and peripheral silicic domes were observed in the pre-caldera activity of the Nemrut Stratovolcano. During the syn-caldera stage, explosive eruptions occurred and produced pyroclastic deposits. On the contrary, the basaltic-rhyolitic effusive activity appeared in the post-caldera activity. The post-caldera stage produced

peralkaline-type rocks, ash eruptions, and rift activities with basalt- and rhyolite-type lava flows. The last activities of Nemrut Mountain were recorded in 1441, 1597, and 1692 [5-9]. These activities refer to shallower magma chambers around a depth of 4-5 km [1, 2]. Nemrut Stratovolcano has hosted various rock groups from the Paleozoic to the present. Especially Quaternary volcanics cover a large area around the volcano. On the other hand, while Neogene units in the north and Paleogene units in the south are present, Triassic volcanics are situated to the west. On the other hand, Holocene and Quaternary faults are observed to the north and northwest of the Nemrut volcano (Figure 1b).
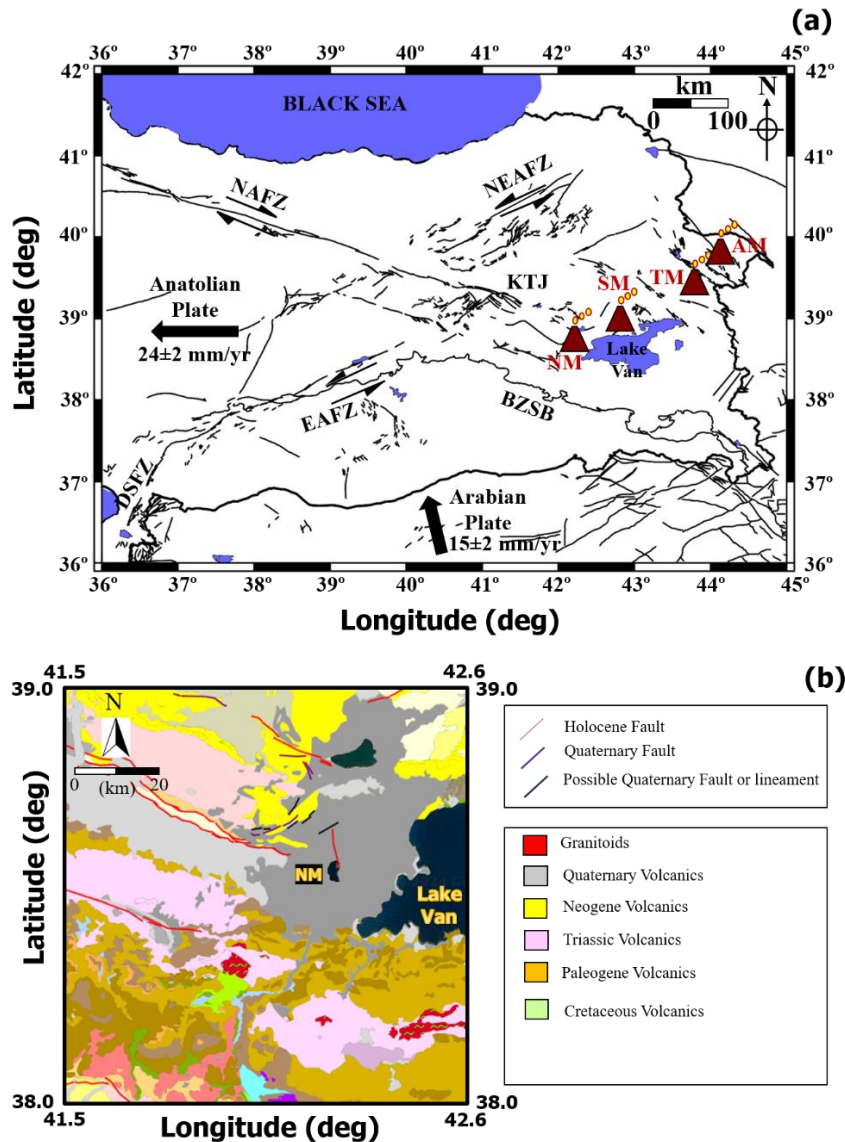
Figure 1. (a) Main tectonic elements of Eastern Anatolia (modified from [6, 24, 25]). Claret red triangles depict Quaternary volcanic centers. Black arrows show plate motions (taken from [26]). The solid black lines represent the active faults modified by [27, 28]. Abbreviations; AM: Ağrı Mountain, BZSB: Bitlis-Zagros Suture Belt, DSFZ: Dead Sea Fault Zone, KTJ: Karlıova Triple Junction, NAFZ: North Anatolian Fault Zone, NEAFZ: North East Anatolian Fault Zone, NM: Nemrut Mountain, SM: Süphan Mountain, TM: Tendürek Mountain. (b) The geological map of Nemrut Mountain and its surroundings [27, 29]

In literature, many studies have investigated the relationship between volcanic activity and local seismicity [10-18]. Recently, [19] used seismic data from 2003 to 2017 to describe subsurface fault structures related to volcanism and crustal tectonics in the Aleut volcanic arc near Tanaga Island. They concluded that all four volcanic centers on the island exhibited volcanic seismic activity since the observations began in 2003. Volcán de Fuego in Guatemala created a violent eruption with little warning on June 3, 2018. It created pyroclastic density currents affecting nearby settlements. This resulted in 169 deaths, 256 disappearances and approximately 13,000 people permanently displaced from their homes. It was observed with an extensive network of seismic and infrared sensors [20]. Using both seismic and infrasound data, [21] and [22] quantitatively modeled the source properties of seismo-acoustic signals associated with eruptions at Mount Cleveland in the United States and Mount Santiaguito in Guatemala, respectively.

Seismicity in volcanic regions is mainly caused by the dynamic interaction of molten rock and hydrothermal fluids with solid host rock, the fracturing and disintegration of the magma itself, and tectonic processes interacting with the volcano. [23] examined the relationships between the circulation of hydrothermal fluids, travertine precipitation, and tectonic activity. They particularly revealed the role of faults in controlling the uplift of fluids, the location of thermal sources, and the accumulation of travertine masses. Within the scope of this study, recent micro-earthquakes that occurred near the Nemrut Caldera were examined, and whether these earthquakes could be due to the pressure effects in the magma chamber or not, depending on the Coulomb stress changes.

2. Seismicity of Nemrut Caldera

In volcanic regions, it is necessary to discriminate between seismic activity created by tectonic processes and triggered by fluid dispersal. A full-time history analysis of the seismicity preceding and accompanying volcanic eruptions is required to understand the interaction between tectonic and magmatic processes [30]. Although the current activity of Nemrut Caldera is revealed as hot springs, fumaroles, and a small, hot lake [8], there are significant Holocene/Quaternary active fault systems around the Nemrut stratovolcano (Figure 2) [4]. In the region, the Nemrut extensional fissure is associated with the normal fault mechanism and is considered an active structural feature causing Quaternary volcanic activities in the region [28]. In addition to this, the Nazik Gölü Fault is located in the west of the Nemrut stratovolcano and has a right-lateral strike-slip mechanism. In the west of the Nemrut Stratovolcano, the Muş Fault Zone is accompanied by a thrust-reverse character [28]. In the east of Nemrut Stratovolcano, the Southern Boundary Fault and Northern Boundary Fault are located on Lake Van.

To model the local seismicity around the Nemrut Stratovolcano, the Coulomb failure stress changes in bars should be calculated for the best-oriented focal mechanism solutions. Since the focal mechanism parameters (strike/dip/rake) of the local earthquakes around the Nemrut Caldera cannot be reached, we overcome this problem by obtaining the numerical 3-component data recorded at the Disaster and Emergency Management Authority (AFAD) broadband stations. Detailed information on permanent broadband seismic stations is shown in Table 1. Also, the locations of the broadband seismic stations employed by the AFAD are demonstrated in Figure 2. For fault plane solutions, we perform the Seisan software package [31], which is composed of different programs such as FPFIT [32] and PINV [33]. FPFIT uses first-motion polarities for selected earthquakes based on the double-couple fault-plane solution and is the weighted sum of first-motion polarity discrepancies. It automatically finds a solution in the least squares sense, which means that it is not a correct solution however it corresponds to the best solution. FPFIT estimates the uncertainty in the model parameters (strike, dip, rake). Finally, FPFIT calculates a uniformly distributed set of solutions within the range of estimated uncertainty [32]. Besides, PINV makes an inversion with the first arrivals of all P phases selected from earthquakes and gives the best focal mechanism solution depending on P-phase polarities [32-34]. Considering the general characteristics of active fault systems around Nemrut Caldera, we state that the focal mechanism solutions of 9 local earthquakes with low magnitudes ($1.1 \leq M_L \leq 2.9$) are compatible with local tectonic structures. Focal mechanism solutions calculated in this study depict generally reverse/normal fault mechanisms, consistent with the Nemrut Rift Zone in the region [5, 9]. Figure 2b and Table 2 show the selected earthquakes' locations and focal mechanisms.

Table 1. The broadband stations of the AFAD (TU) with detailed information in the study region were used to calculate the focal mechanism solutions

Station Code	Latitude (°)	Longitude (°)	Elevation (m)	Opening Date
MUSM	38.724	41.511	1357	2013/03/21
TVAN	38.524	43.403	1970	2001/10/20
BLIS	38.414	42.115	1608	2013/03/21
ADCV	38.808	42.724	1774	2011/10/28
GEVA	38.312	43.058	1672	2008/11/02
PERV	37.946	42.541	1377	2014/11/28
SRTM	37.991	41.922	1145	2011/10/29
TUTA	39.401	42.813	2154	2006/09/15
DORK	39.387	42.780	1714	2017/11/09
TATV	38.580	42.267	1831	2006/10/21
BNGL	38.952	41.149	1968	2005/07/13
BTMN	37.891	41.269	962	2010/11/25

Table 2. The fault plane solutions of the selected earthquakes based on the FPFIT and PINV Methods [33] to calculate Coulomb failure stress changes in the study region

No	Date (day/month/year) (hh:mm:ss)	Latitude (°)	Longitude (°)	Depth (km)	Local Magnitude (M_L)	Dip (°), Strike (°), Rake (°)	Focal Mechanism Type
1	01/01/2023 12:26:57	38.657	42.210	4.4	1.4	71,38,-121	Normal
2	17/11/2022 06:10:57	38.624	42.266	4.6	2.0	13,77,-161	Strike-slip
3	28-03-2021 23:02:41	38.606	42.242	4.6	1.1	33,45,-89	Normal
4	30/05/2020 06:32:56	38.595	42.249	4.5	2.0	84,88,25	Strike-slip
5	21/05/2020 20:28:52	38.607	42.271	5.0	1.9	15,90,0	Strike-slip
6	05/03/2018 18:43:44	38.604	42.239	4.6	1.8	29,90,0	Strike-slip
7	19/01/2018 17:41:41	38.775	42.280	3.9	2.1	38,18,38	Reverse
8	24/04/2015 10:13:54	38.598	42.261	7.5	2.5	234,88,-69	Strike-slip
9	03/12/2010 11:29:34	38.606	42.281	4.6	2.9	14,28,38	Reverse
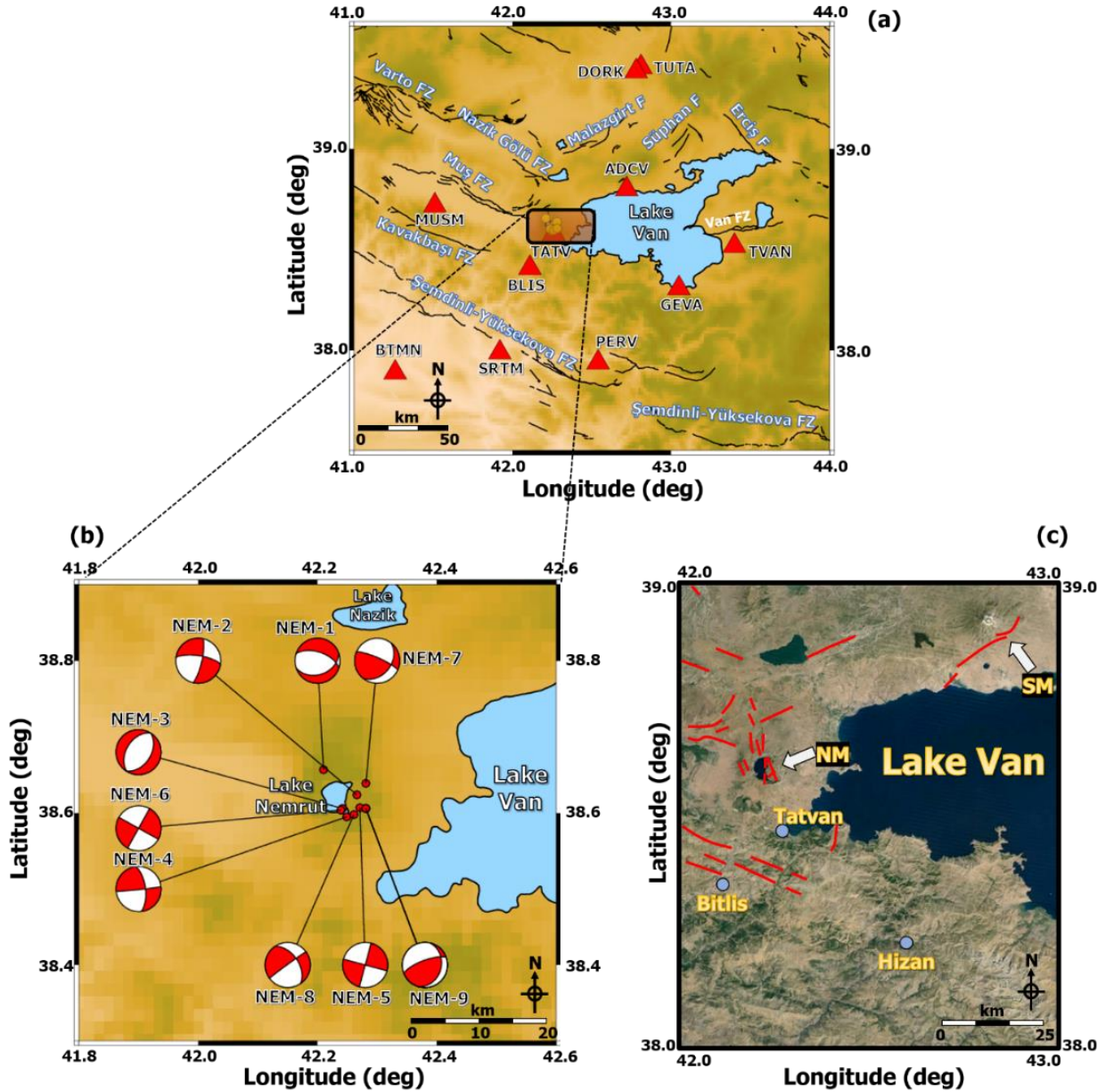
Figure 2. (a) Location of broadband seismic stations (red triangles). The active faults are shown with thick black lines with their names (white color) taken from [28]. The black rectangular area represents the study region. (b) The fault plane solutions and locations of the selected earthquakes (in detail please see Table 2). (c) The thick red lines depict the active faults in and around Nemrut Volcano. Blue circles represent the cities. NM: Nemrut Mountain, SM: Süphan Mountain (modified from [4])

3. Method of Coulomb Failure Stress Changes

Coulomb Failure stress changes (*ΔCFS*) are computed for several sources of different depths and geometry. Modeling of stress change associated with the faults slip in the tectonic regions is widely used and given information about the seismicity mechanisms [11]. In volcanic regions or non-tectonic sources such as the Nemrut Stratovolcano, it is necessary to distinguish between seismic activity generated by tectonic processes and fluid propagation.

The dip of the fault, crust rheology, the magma reservoir depth, amplitude of the pressure variation, and the nearby fault strongly influences the location of the areas of positive and negative values of Coulomb failure stress [30]. Failure occurs when the change in stress exceeds a threshold value [35, 36, 37]. *ΔCFS* can be defined as

$$\Delta CFS = \Delta\tau + \mu(\Delta\sigma\eta + \Delta P) \qquad (1)$$

where *Δτ* and *Δση* represent the shear stress and normal stress, respectively. *ΔP* is the pore pressure

change and μ is the frictional coefficient. According to [30], the frictional coefficient is assumed to be 0.75 associated with the viscoelastic elements of a volcano [38]. Coulomb stress changes are computed on the best-oriented fault mechanism parameters given in Table 2. Total stress change is related to the

background regional tectonic loading and the stress change resulting from the local overpressure [13]. The algorithm diagram of Seisan software and Coulomb 3.3 software is shown in Figure 3.

Stress Change Calculation Procedure
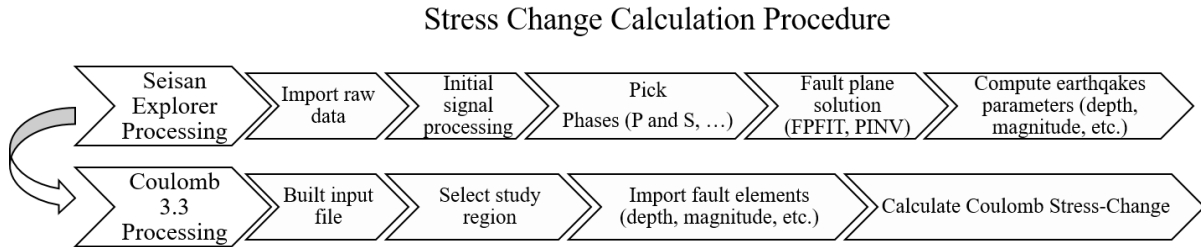
Figure 3. Algorithm diagram of Seisan software package [31] and Coulomb 3.3 software [37]
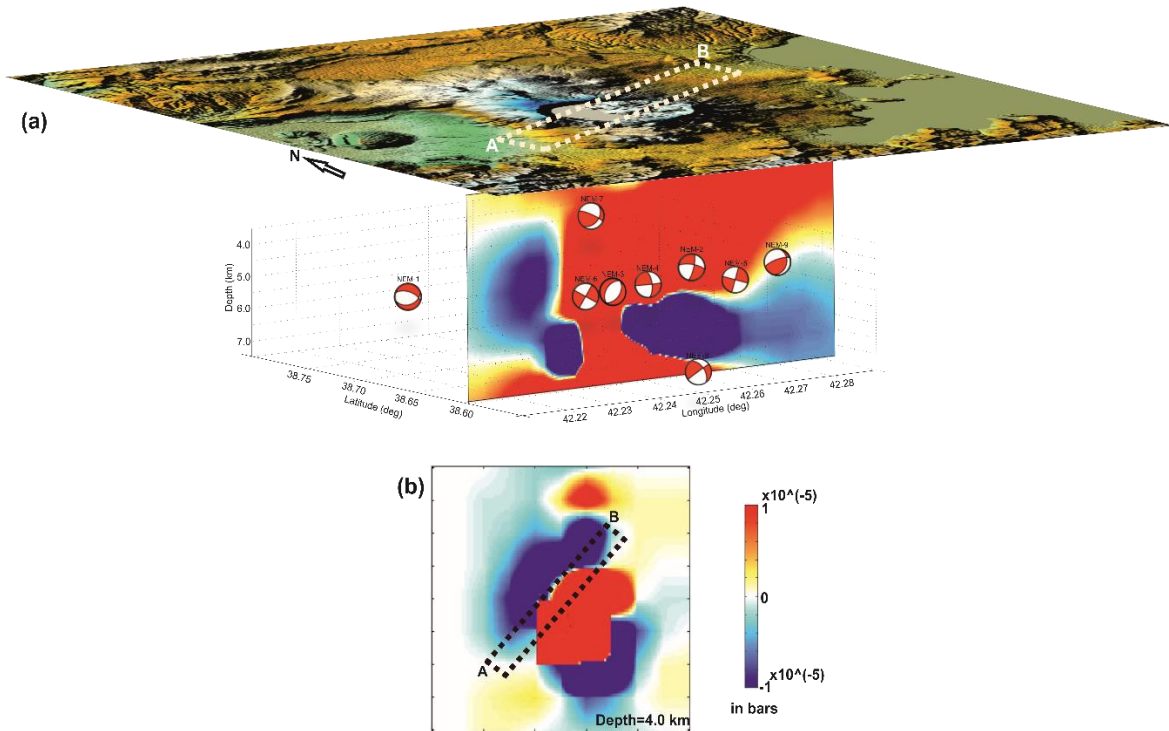
Figure 4. (a) 3D Topographic map around the Nemrut stratovolcano with a vertical cross-section of Coulomb failure stress (ΔCFS) in bars. The white dashed rectangle (line A-B) restricts the vertical cross-section with a dip angle of 70°. The fault friction coefficient is used as $\mu = 0.75$. The red beach balls belong to the focal mechanism solutions of the earthquakes given in Table 1. (b) The map of Coulomb failure stress (ΔCFS) at the depth of 4 km associated with all earthquakes. The black dashed rectangle depicts line A-B. The stress values are linear in the range -1×10^{-5} to $+1 \times 10^{-5}$. Blue areas show relaxed regions, while red areas demonstrate loading regions

4. Results and Discussion

This study aims to investigate the source of stress transfer and seismicity under the volcano caldera by utilizing the focal mechanism solutions of local and small earthquakes occurring around Nemrut Mountain. In Figure 4, a profile is created to cut

through the volcano caldera. According to profile A-B, both the cross-section going down to 7.5 km and the Coulomb stress change map at 4 km depth are shown. Since the deepest earthquakes with focal mechanism solutions are 7.5 km (Table 2), the cross-section is taken up to this depth. The average hypocentral depths of earthquakes are observed at a

depth of 4-5 km and these depth intervals coincide with magma chamber depth (~4 km) [4].

When we look at the cross-section, positive stress is observed in the upside and downward direction, while negative stress strikes approximately the west and east directions. At the same time, regions with positive stresses correspond to the hypocentral points of earthquakes. When the focal mechanism solutions of earthquakes are examined, it is striking that they are in the structure of strike-slip, normal faults, and oblique faults. This confirms the upward-downward stress variation. On the other hand, when the stress change at 4 km depth is examined, it can be observed that there is a similar upward positive stress. On the other hand, [39] found a Curie Point depth of approximately 17 km around the Nemrut Caldera. In the steady-state geothermal evaluation calculated using the method proposed by [40], it was predicted that a temperature of 150 °C could exist around 5 km. This corresponded to a heat flow value of approximately 90 mW/m^2. However, [41] expressed the existence of an average temperature of around 1000°C. This high-temperature value was naturally associated with the pressure increase due to expansion in the caldera. Therefore, we can state that the origin of the earthquakes with irregular activity observed in the Nemrut Caldera corresponds to the expansion effects in the Caldera.

In recent years, different seismotectonic parameters such as b-value, Dc-value, and Coulomb stress variation have been used by earth scientists to forecast the future seismicity for the Eastern Anatolia region. [42] investigated the seismic quiescence in the eastern part of Turkey. They identified clear quiescence anomalies at several seismogenic sources. These anomalies appeared in the Erzurum, Tunceli, Elazığ, Bingöl provinces, and Van Lake region. For these regions, they calculated the duration of quiescence before the occurrence of an earthquake as 5.0 ± 1.5 years. [43] performed a statistical analysis to find out the current earthquake potential in the Eastern Anatolia region. For this purpose, he used some seismotectonic parameters called seismic b-value, seismic quiescence Z-value, cumulative moment, and annual probability and recurrence time of earthquakes. The results showed a significant decrease in b-value and clear quiescence anomalies in Z-value at the beginning of 2015 in the Central Anatolia Fault Zone, Malatya, and Ovacık faults, the southeastern part of the EAFZ, north of Lake Van, and Malazgirt Fault. These results may supply significant clues to reveal the seismic potential and trigger stress increases in the region. [44] made a similar and enhanced study for the Eastern Anatolia region based on the seismotectonic b-value, fractal dimension Dc-value, and precursory seismic quiescence Z-value. According to the results of [44], small b-values and large Dc-values were observed in the Çaldıran Fault, around the Genç Fault, Pülümür and Karakoçan Faults, and the Sancak-Uzunpınar Fault Zone. Moderate b-values changing between 1.0 and 1.1 and Dc-values changing between 2.1 and 2.2 were calculated around the Nemrut Volcano and the southern area of the BZTZ, EAFZ, and eastern area of the NAFZ. [45] made an analysis of the spatial and temporal changes of b-value and Coulomb stress change around the Lake Van region. For this purpose, they used a homogeneous earthquake catalog for b-value distribution and focal mechanism solutions of 83 local earthquakes for Coulomb stress change. They observed a decreasing trend in the b-values and positive Coulomb stress changes around the eastern part of Lake Van covering the Van Fault Zone, Yeniköşk Fault, Çaldıran, Başkale and Yüksekova-Şemdinli Fault Zones. On the contrary, their analysis presented the Süphan and Nemrut volcanoes did not show any significant stress change. [46] made a seismic hazard analysis of the multiple parameters in and around the Lake Van region covering the Nemrut Volcano. They used some important seismotectonic parameters such as b-value, Z-value, relative intensity (RI) and pattern informatics (PI), and Coulomb stress changes. Especially RI-PI algorithm in first assessed in the region. They stated that smaller b-values, higher Z-values, positive-Coulomb stress changes, and the locations of earthquake hotspots for 2022-2032 corresponded with Muradiye, Çaldıran, Özalp, Erçek, Van and Gevaş, Erciş, Malazgirt and Saray provinces. For the Nemrut Volcano and its surroundings, they calculated a higher b-value and positive seismic quiescence anomaly. These values generally indicated a great number of small-magnitude earthquakes. On the contrary, negative/moderate Coulomb stress values were calculated around the Nemrut Volcano. These negative Coulomb stress values and higher b-values indicated that tectonic earthquakes were less likely to occur in volcanic regions.

In the case of an increase in pressure of the magma reservoir or the reservoir inflation, changes in Coulomb failure stress indicate that the positive variations are most marked above and beneath the magma chamber. Therefore, seismicity and cracks may be expected to develop in this region [12]. When the pressure decreases (the reservoir deflation), the seismicity should occur laterally offset from the extent of the magma reservoir and at the same depth [30]. [13] modeled the Coulomb stress changes of Campi Flegrei Caldera due to the magma chamber overpressure and associated them with shallow

earthquake locations (≤ 4 km) during magma reservoir inflation. The stress changes associated with overpressure in the shallow magma chamber were then likely to be the primary cause of local seismicity. The seismicity can be interpreted in terms of Coulomb stress changes produced by a source of overpressure, in the presence of ring faults bordering the caldera, and with a background, regional stress.

5. Conclusions

This study models Coulomb stress variations caused by the local seismic activity beneath the Nemrut Caldera. Coulomb stress changes have been calculated for the best-oriented focal mechanism solutions demonstrating a perfect correlation to active fault mechanisms located in the region. Results indicate that positive stress changes are oriented upward and downward striking due to the possible magma chamber and hypocenter areas. The focal mechanism depths of the earthquakes calculated in this study are compatible with the possible magma chamber depth. The magnitudes of earthquakes agree with the magnitudes of energy released during volcanic tremors. On the contrary, negative stress changes strike roughly the E-W directions. Also, the findings of this study suggest that the magma chamber beneath the Caldera plays a more relevant ole in increased stress changes. As a consequence, the activation of volcanic sources such as overpressure in the magma chambers or magma movement except tectonic seismicity may cause low-magnitude volcano-tectonic seismicity.

Contributions of the authors
The authors' contributions to the paper are equal.

Conflict of Interest Statement
There is no conflict of interest between the authors.

Statement of Research and Publication Ethics
The study is complied with research and publication ethics

References

[1] İ. Ulusoy, *Etude volcano-structurale du volcan Nemrut (Anatolie de l'Est Turquie) et risques naturels associes*, PhD. Thesis, University of Clermont-Ferrand II, France & Hacettepe University, Turkey, 2008.

[2] İ. Ulusoy, H. E. Çubukçu, E. Aydar, P. Labazuy, O. Ersoy, E. Şen, and A. Gourgaud, "Volcanological evolution and caldera forming eruptions of Mt. Nemrut (Eastern Turkey)", *Journal of Volcanology and Geothermal Research*, vol. 245-246, pp. 21-39, 2012.

[3] H. E. Çubukçu, İ. Ulusoy, O. Ersoy, E. Aydar, E. Şen, A. Gourgaud, and H. Guillou, "Mt Nemrut Volcano (Eastern Turkey): Temporal petrological evolution", *Journal of Volcanology and Geothermal Research*, vol. 209-210, pp. 33-60, 2012.

[4] Y.L. Ekinci, A. Büyüksaraç, Ö. Bektaş, and C. Ertekin, "Geophysical investigation of Mount Nemrut stratovolcano (Bitlis, Eastern Turkey) through aeromagnetic anomaly analyses", *Pure and Applied Geophysics*, vol. 177, pp. 3243-3264, 2020.

[5] C. Ertekin, Y.L. Ekinci, A. Büyüksaraç, and R. Ekinci, " Geoheritage in a mythical and volcanic terrain: an inventory and assessment study for geopark and geotourism, Nemrut Volcano (Bitlis, Eastern Turkey)", *Geoheritage*, vol. 13, no. 3, p. 73, 2021.

[6] F. Şaroğlu, and Y. Güner, "Doğu Anadolu'nun Jeomorfolojik Gelişimine Etki Eden Ögeler: Jeomorfoloji, Tektonik, Volkanizma İlişkileri", *Türkiye Jeoloji Kurumu Bülteni*, vol. 24, no. 2, pp. 39-50, 1981.

[7] A. Koçyiğit, A. Yılmaz, S. Adamia, and S. Kuloshvili, "Neotectonics of East Anatolian Plateau (Turkey) and Lesser Caucasus: implication for transition from thrusting to strike-slip faulting", *Geodin Acta*, vol.14 pp. 177–195, 2001.

[8] İ. Ulusoy, P. Labazuy, E. Aydar, O. Ersoy, Çubukçu E., "Structure of the Nemrut caldera (Eastern Anatolia, Turkey) and associated hydrothermal fluid circulation", *J. Volcanol. Geotherm. Res.*, vol. 74 pp. 269-283, 2008.

[9] E. Işık, M.C. Aydın, A. Bakış, and M.H. Özlük, "Bitlis ve civarındaki faylar ve bölgenin depremselliği", *Bitlis Eren Üniversitesi Fen Bilimleri Dergisi*, vol. 1, no. 2, pp.153-169, 2012.

[10] R. I. Tilling, and J. J., Dvorak, "Anatomy of a basaltic volcano", *Nature*, vol. 363, pp. 125-132, 1993.

[11] C. Troise, "Stress changes associated with volcanic sources: constraints on Kilauea rift dynamics", *J. Volcanol. Geoth. Res.*, vol. 109, pp.191-203, 2001.

[12] S. Toda, R. Stein, and T. Sagiya, "Evidence from the AD 2000 Izu islands earthquake swarm that stressing rate governs seismicity", *Nature,* vol. 419, pp. 58-61, 2002.

[13] C. Troise, F. Pingue, and G. De Natale, "Coulomb stress changes at calderas: Modeling the seismicity of Campi Flegrei (southern Italy)", *Journal of Geophysical Research: Solid Earth*, vol. 108, no. B6, 2003.

[14] T. R. Walter, and F. Amelung, "Influence of volcanic activity at Mauna Loa, Hawaii, on earthquake occurrence in the Kaoiki seismic zone", *Geophys. Res. Lett.*, vol. 31, no. 7, 2004.

[15] C. Doubre, *Structure et mecanique des segments de rift volcano-tectoniques: application aux rift anciens (Ecosse, Islande) et actifs (Asal-Ghoubbet)*, Doctoral dissertation, Universite´ du Maine, Le Mans, France, 2004.

[16] G. R. Foulger, B. R. Julian, D. P. Hill, A. M. Pitt, P. E. Marlin, and E. Shalev, "Non-double-couple microearthquakes at Long Valley caldera, California, provide evidence for hydraulic fracturing", *J. Volcanol. Geoth. Res.*, vol. 132, pp. 45-71, 2004.

[17] G. R. Foulger, J. H. Natland, and D. L. Anderson, "Genesis of the Iceland melt anomaly by plate tectonic processes. In: Plates, Plumes and Paradigms (G.R. Foulger, J.H. Natland, D.C. Presnall and D.L. Anderson, eds)", *Geological Society of America*, Boulder, vol. 388, pp.595-626, 2005.

[18] J. Gargani, L. Geoffroy, S. Gac, and S. Cravoisier, "Fault slip and Coulomb stress variations around a pressured magma reservoir: consequences on seismicity and magma intrusion", *Terra Nova*, vol. 18, no.6, pp. 403-411, 2006.

[19] K. F. Lally, J. Caplan-Auerbach, and J. A. Power, "Volcanic and tectonic sources of seismicity near the Tanaga volcanic cluster, Alaska", *Geochemistry, Geophysics, Geosystems*, vol. 24, no. 6, 2023.

[20] A. Diaz-Moreno, A. Roca, A. Lamur, B. H. Munkli, T. Ilanko, T. D. Pering, A. Pineda, and S. De Angelis, "Characterization of Acoustic Infrasound Signals at Volcán de Fuego, Guatemala: A Baseline for Volcano Monitoring", *Front. Earth Sci.*, vol. 8, 2020.

[21] A. M. Iezzi, D. Fee, M. M. Haney, and J. J. Lyons, "Seismo-Acoustic Characterization of Mount Cleveland Volcano Explosions", *Front. Earth Sci.*, vol. 8, 2020.

[22] A. Rohnacher, A. Rietbrock, E. Gottschämmer, W. Carter, Y. Lavallée, S. De Angelis, J. E. Kendrick, and G. Chigna, "Source Mechanism of Seismic Explosion Signals at Santiaguito Volcano, Guatemala: New Insights From Seismic Analysis and Numerical Modeling", *Frontiers in Earth Science*, vol. 8, 2021.

[23] A. Brogi, C. Alçiçek, C. Ç. Yalciner, E. Capezzuoli, D. Liotta, M. Meccheri, V. Rimondi, G. Ruggieri, A. Gandin, A. Büyüksaraç, H. Alçiçek, A. Bülbül, C. C. Shen, M. O. Baykara, and C. Boschi, "Hydrothermal fluids circulation and travertine deposition in an active tectonic setting: insights from the Kamara geothermal area (western Anatolia, Turkey)", *Tectonophysics*, vol. 680, pp. 211-232, 2016.

[24] F. Şaroğlu, O. Emre, and O. Kuşcu, "Active fault map of Turkey", *General Directorate of Mineral Research and Exploration, Ankara, Turkey*, 1992.

[25] E. Bozkurt, E. " Neotectonics of Turkey-a synthesis", *Geodinamica Acta*, vol. 14, no. 1-3, pp. 3-30, 2001.

[26] R. Reilinger, S. McClusky, P. Vernant, S. Lawrence, S. Ergintav, and R. Cakmak, "GPS constraints on continental deformation in the Africa-Arabia-Eurasia continental collision zone and implications for the dynamics of plate interactions", *Journal of Geophysical Research*, vol. 111, no. B05411 pp. 1-26, 2006.

[27] O. Emre, T. Y. Duman, S. Ozalp, H. Elmaci, S. Olgun, and F. Saroglu, "1/1.125.000 scale Active Fault Map of Turkey, General Directorate of Mineral Research and Explorations Special Publications Series", Ankara-Turkey, 2013.

[28] Ö. Emre, T. Y. Duman, S. Özalp, F. Şaroğlu, Ş. Olgun, H. Elmacı, and T. Çan, "Active fault database of Turkey", *Bulletin of Earthquake Engineering*, vol. 16, no. 8, pp.3229-3275, 2018.

[29] B. Akbaş, N. Akdeniz, A. Aksay, İ. E. Altun, V. Balcı, E. Bilginer, T. Bilgiç, M. Duru, T. Ercan, İ. Gedik, Y. Günay, İ. H. Güven, H. Y. Hakyemez, N. Konak, İ. Papak, Ş. Pehlivan, M. Sevin, M. Şenel, N. Tarhan, N. Turhan, A. Türkecan, Ü. Ulu, M. F. Uğuz, A. Yurtsever, and et al., "1:1.250.000 ölçekli Türkiye Jeoloji Haritası", *Maden Tetkik ve Arama Genel Müdürlüğü Yayını*, Ankara-Türkiye, 2011.

[30] J. Gargani, L. Geoffroy, S. Gac, and S. Cravoisier, "Fault slip and Coulomb stress variations around a pressured magma reservoir: consequences on seismicity and magma intrusion", *Terra Nova*, vol. 18, no. 6 pp. 403-411, 2006.

[31] L. Ottemöller, P. H. Voss, and J. Havskov, *SEISAN Earthquake Analysis Software for Windows, Solaris, Linux and Macosx*, University of Bergen, Version 12.0., 607, 2021.

[32] P. Reasenberg, and D. Oppenheimer, "Fpt, fpplot, and fppage: Fortran computer programs for calculating and displaying earthquake fault plane solutions", *Technical report*, U.S. Geol. Survey, 1985.

[33] D. Suetsugu, "Practice on source mechanism", iisee lecture note, *Technical report*, Tsukuba, Japan, 1998.

[34] H. Alkan, S. Öztürk, and İ. Akkaya, " Analysis of Coulomb stress transfer and earthquake hazard in the Çaldıran Fault Zone and its adjacent region", *Mühendislik Bilimleri ve Tasarım Dergisi*, vol. 11, no. 2, pp. 519-534, 2023.

[35] G. C. King, R. S. Stein, and J. Lin, "Static stress changes and the triggering of earthquakes", *Bulletin of the Seismological Society of America*, vol. 84, no. 3, pp. 935-953, 1994.

[36] R. Stein, "The role of stress transfer in earthquake occurrence", *Nature,* vol. 402, pp. 605-609, 1999.

[37] S. Toda, R. S. Stein, and J. Lin, "Widespread seismicity excitation throughout central Japan following the 2011 M=9.0 Tohoku earthquake and its interpretation by Coulomb stress transfer", *Geophysical Research Letters*, vol. 38, no. 7, 2011.

[38] T. Parsons, "Post-1906 stress recovery of the San Andreas fault system calculated from three-dimensional finite element analysis", *J. Geophys. Res.,* vol. 107, 2002.

[39] Ö. Bektaş, D. Ravat, A. Büyüksaraç, F. Bilim, and A. Ateş, "Regional Geothermal Characterisation of East Anatolia from Aeromagnetic, Heat Flow and Gravity Data", *Pure appl. geophys.*, vol. 164, pp. 975-998, 2007.

[40] J. H. Sass, and A. H. Lachenbruch, "Heat flow and conduction-dominated thermal regimes, Assessment of Geothermal Resources of the United States", *United States Geological Survey Circular*, vol. 790, pp. 8-11, 1978.

[41] I. S. Peretyazhko, E. A. Savina, and N. S. Karmanov, "Comendites and pantellerites of Nemrut volcano, eastern Turkey: Genesis and relations between the trachyte-comenditic, comenditic, and pantelleritic melts", *Petrology*, vol. 23, pp. 576-622, 2015.

[42] S. Öztürk, and Y. Bayrak, " Spatial variations of precursory seismic quiescence observed in recent years in the eastern part of Turkey", *Acta Geophys.*,vol. 60, pp. 92-118, 2012.

[43] S. Öztürk, "Space-time assessing of the earthquake potential in recent years in the eastern Anatolia region of Turkey", *Earth Sciences Research Journal*, vol. 21, no. 2, pp. 67-75, 2017.

[44] S. Öztürk, "Earthquake hazard potential in the Eastern Anatolian Region of Turkey: seismotectonic b and Dc-values and precursory quiescence Z-value", *Front. Earth Sci.*, vol. 12, pp. 215-236, 2018.

[45] H. Alkan, and E. Bayrak, "Coulomb stress changes and magnitude-frequency distribution for Lake Van region", *Bulletin of the Mineral Research and Exploration*, vol. 168, no.168, pp. 141-156, 2022.

[46] S. Öztürk, and H. Alkan, " Multiple parameter analysis for assessing and forecasting earthquake hazards in the Lake Van region, Turkey", *Baltica*, vol. 36, no.2, pp. 133-154, 2023.

[47] P. Wessel, J. F. Luis, L. Uieda, R. Scharroo, F. Wobbe, W. H. F. Smith, and D. Tian, "The Generic Mapping Tools version 6", *Geochemistry Geophysics Geosystems*, vol. 20, pp. 5556-5564, 2019.

A Nonstandard Finite Difference Scheme for a Mathematical Model Presenting the Climate Change on the Oxygen-plankton System

Zahraa Makki Farhan ALJAMMALI [1], İlkem TURHAN ÇETİNKAYA [2*]

[1]*Kütahya Dumlupınar University, Graduate Education Institute, Department of Mathematics, Kutahya, Turkey.*

[2]*Kütahya Dumlupınar University, Science and Art Faculty, Department of Mathematics, Kutahya, Turkey.*

(ORCID: 0009-0000-8077-4118) (ORCID: 0000-0002-5520-310X)

Abstract

This paper presents a mathematical model describing climate change in the oxygen-plankton system. The model consists of a system of non-linear ordinary differential equations. The Nonstandard Finite Difference (NSFD) method is applied to discretize the non-linear system. The stability of the continuous and discrete model is presented for the given parameters in the literature. Similar results for stability are obtained in both continuous and discrete models. The model is solved by the Runge–Kutta–Fehlberg (RKF45) method, and the numerical results are compared in graphical forms. Moreover, the comparison of numerical results obtained by the NSFD method, the Euler method and the fourth order Runge-Kutta (RK4) method is presented in tabular form. Furthermore, the efficiency of the NSFD method compared to classical methods such as the Euler method and the RK4 method for the bigger step sizes is shown in tabular forms.

1. Introduction

Climate change and global warming are serious threats to ecological life. One of the results of climate change and global warming is the increasing of the sea surface temperature in the oceans. Therefore, the photosynthetic production rate of phytoplankton changes. Mathematical models describing climate change are developed. Some of them can be summarized as follows. Sekerci and Petrovskii [1] consider a model of coupled plankton-oxygen dynamics under climate change. The stability of the steady states is analyzed and detailed numerical simulations are presented in [1]. Moreover, they analyze both analytically and numerically a model of the oxygen-phytoplankton-zooplankton dynamics in [2]. The climate models are presented by Priyadarshini and Veeresha [3]. The stability analysis is presented, and the Adams Predictor-Corrector method is applied to obtain the numerical results in [3]. Mondal et al. [4] give a detailed analysis of the

dynamics of the oxygen-plankton model with a modified Holling type II functional response. Furthermore, the continuous model given in [1] is reconsidered in the fractional cases in [5-7]. A new delayed plankton–oxygen dynamical model is presented by Xu et al. [8]. They explore bifurcation and stability. Gökçe [9] analyzes the stability of a mathematical model of oxygen–phytoplankton interactions. Chowdhury et al. [10] consider a coupled model presenting plankton-oxygen dynamics and investigate the model using analytical techniques and numerical simulations.

Remarkable mathematical methods can be encountered in solving mathematical models. In this study, we prefer the Nonstandard Finite Difference (NSFD) method developed by Mickens [11-15] considering the advantages over the classical and standard finite difference methods. The NSFD method can be considered as a generalization of the usual discrete models of differential equations. In many cases, it removes the numerical instabilities

---

encountered in usual finite difference schemes. The method can be applied to both ordinary and partial differential equations. Moreover, the NSFD method preserves dynamic consistency. By virtue of the advantages of NSFD schemes, many researchers have been studying NSFD schemes for solving mathematical models. The detailed studies presented about the NSFD schemes can be found in [16, 17]. Moreover, there have been numerous studies of the NSFD schemes in the literature, recently. For example, Khan et al. [18] consider a nonlinear mathematical model of COVID-19. The NSFD schemes are constructed, local and global stability are studied in [18]. Zhang et al. [19] examine an epidemic model for waterborne disease, where the NSFD method is applied, and stability analysis is presented. Yang et al. [20] construct an NSFD scheme for a diffusive within-host virus dynamics model. Globally asymptotically stability of the model under the effect of virus-to-cell and cell-to-cell transmissions is studied in [20]. Kocabıyık et al. [21] and Dang and Hoang [22] consider computer virus models in the view of NSFD schemes. Moreover, Hoang et al. [23] construct the NSFD schemes for a modified epidemiological model of computer viruses. More studies about NSFD schemes can be found in [24-37]. This study constructing an NSFD scheme for an ecological model consists of five sections. The study begins with a brief introduction section. The second section presents a mathematical model of the oxygen-plankton system. The third section gives the method used in the study. The fourth section gives the stability of the model and numerical simulation. Lastly, the final section belongs to the conclusion and suggestions section.

2. Definition of the Model

In this paper, a simplified mathematical model of the climate change on the oxygen-plankton system given in [1,2,5] is considered. The continuous model is defined as

$$\frac{df}{dt} = T\left(1 - \frac{f(t)}{f(t)+1}\right)g(t) - \frac{\delta g(t)f(t)}{f(t)+f_2}$$
$$- \frac{vf(t)s(t)}{f(t)+f_3} - f(t) \qquad (1a)$$

$$\frac{dg}{dt} = \left(\frac{Gf(t)}{f(t)+f_1} - g(t)\right)g(t) - \frac{g(t)s(t)}{g(t)+\tilde{h}}, \qquad (1b)$$
$$- \sigma g(t)$$

$$\frac{ds}{dt} = \left(\frac{\eta f^2(t)}{f^2(t)+f_4^2}\right)\left(\frac{g(t)s(t)}{g(t)+\tilde{h}}\right) - \xi s(t) \qquad (1c)$$

subject to initial conditions

$$f(0) = f_0, \ g(0) = g_0, \ s(0) = s_0. \qquad (2)$$

The unknowns of the system of non-linear ordinary differential equations (1a)-(1c) presented by $f(t)$, $g(t)$, and $s(t)$ denote the oxygen concentration, phytoplankton density, and zooplankton density, respectively. The parameters T, δ, v, G, σ, η, and ξ denote the rate of oxygen production by phytoplankton, phytoplankton respiration coefficient, zooplankton respiration coefficient, rate of phytoplankton maximum growth, phytoplankton natural mortality rate, zooplankton feeding efficiency, and zooplankton natural mortality, respectively. Moreover, the parameters $\tilde{h}$, f_1, f_2, f_3, and f_4 denote the half saturation values of the phytoplankton predation, phytoplankton growth, respiration by phytoplankton, respiration by zooplankton, and zooplankton feeding efficiency, respectively.

3. Material and Method

This section presents the discrete model of Eqs. (1a)-(1c) with the help of the NSFD method which has many advantages compared to classical methods. The NSFD method leads to determining a convenient denominator function that can be chosen instead of step size. Therefore, unlike classical methods, the convergent schemes that satisfy positivity conditions can be constructed by the NSFD method for bigger step sizes. Moreover, while numerical instabilities may be encountered in standard finite difference methods, the NSFD method removes the numerical instabilities. Detailed explanations about the rules of the NSFD method, determining denominator functions, and the benefits of the methods take place in [11-15].

The continuous model (1a)-(1c) can be discretized using the discretizing procedure of the NSFD method given in [11-15]. Thus, the following substitutions i)-iii) are employed to discrete the continuous model (1a)-(1c), respectively:

i)　$g(t) \rightarrow g(n)$,　$\dfrac{f(t)g(t)}{f(t)+1} \rightarrow \dfrac{f(n+1)g(n)}{f(n)+1}$,

$$\frac{g(t)f(t)}{f(t)+f_2} \rightarrow \frac{g(n)f(n+1)}{f(n)+f_2},$$

$$\frac{f(t)s(t)}{f(t)+f_3} \to \frac{f(n+1)s(n)}{f(n)+f_3} \text{ and } f(t) \to f(n+1).$$

ii) $\dfrac{f(t)g(t)}{f(t)+f_1} \to \dfrac{f(n)g(n)}{f(n)+f_1}$, $g^2(t) \to g(n+1)g(n)$,

$$\frac{g(t)s(t)}{g(t)+\tilde{h}} \to \frac{g(n+1)s(n)}{g(n)+\tilde{h}} \text{ and } g(t) \to g(n+1).$$

iii)

$$\frac{f^2(t)g(t)s(t)}{\left(f^2(t)+f_4^2\right)\left(g(t)+\tilde{h}\right)} \to \frac{f^2(n)g(n)s(n)}{\left(f^2(n)+f_4^2\right)\left(g(n)+\tilde{h}\right)}$$

and $s(t) \to s(n+1)$.

Therefore, the following discrete model preserving positivity condition is obtained for the mathematical model describing climate change in the oxygen-plankton system:

$$f(n+1) = \frac{f(n)+\varphi_1 Tg(n)}{1+\varphi_1\left(1+\dfrac{Tg(n)}{f(n)+1}+\dfrac{\delta g(n)}{f(n)+f_2}+\dfrac{vs(n)}{f(n)+f_3}\right)}, \quad (3a)$$

$$g(n+1) = \frac{g(n)\left(1+\dfrac{\varphi_2 Gf(n)}{f(n)+f_1}\right)}{1+\varphi_2\left(g(n)+\dfrac{s(n)}{g(n)+\tilde{h}}+\sigma\right)}, \quad (3b)$$

$$s(n+1) = \frac{s(n)\left(1+\dfrac{\varphi_3\eta f^2(n)g(n)}{\left(f^2(n)+f_4^2\right)\left(g(n)+\tilde{h}\right)}\right)}{1+\xi\varphi_3}, \quad (3c)$$

where φ_1, φ_2 and φ_3 denote the denominator functions constructed as

$\varphi_1 = e^h - 1$,

$\varphi_2 = \dfrac{e^{\sigma h}-1}{\sigma}$,

and

$\varphi_3 = \dfrac{e^{\xi h}-1}{\xi}$.

The following lemma can be given for the positivity condition of the discrete system (3a)-(3c):

Lemma 3.1. All solutions of discrete system (3a)-(3c) satisfy the positivity condition under the assumption of positive initial conditions f_0, g_0, s_0, and positive parameters T, δ, v, G, σ, η, ξ, $\tilde{h}$, f_1, f_2, f_3, f_4 and h.

Proof. Assume that the initial conditions f_0, g_0, s_0 and the parameters T, δ, v, G, σ, η, ξ, $\tilde{h}$, f_1, f_2, f_3, f_4, and h are positive. Then, it is obvious

from the discrete system (3a)-(3c) and their corresponding denominator functions that, all solutions of discrete system (3a)-(3c) are positive.

3.1. Stability Analysis

In this section, some theorems used during the stability analysis of the continuous model (1a)-(1c) and the discrete model (3a)-(3c) are given.

For an autonomous differential equation defined as

$$\dot{x} = f(x), \qquad x \in \Box^n, \tag{4}$$

the linearized system can be determined for an equilibrium point E as

$$\frac{dy}{dt} = J(E)y,$$

where $J(E)$ is the Jacobian matrix of the system (4) at the equilibrium point E.

Theorem 3.1 gives a condition for the stability of a continuous system.

Theorem 3.1. [38] Assume that all eigenvalues of the Jacobian matrix of the system (4) have negative reel parts. Then the equilibrium point E is asymptotically stable.

Theorem 3.2 (The Schur-Cohn Criterion, n=3).

Let us consider the discrete system defined by

$x(k+1) = Ax(k)$.

Assume that the characteristic polynomial of the matrix A is

$$p(\lambda) = \lambda^3 + a_1\lambda^2 + a_2\lambda + a_3, \tag{5}$$

where a_1, a_2 and a_3 are constants. The zeros of the characteristic polynomial (5) lie inside the unit disk if and only if the following conditions hold [39]:

    i) $1 + a_1 + a_2 + a_3 > 0$.

    ii) $1 - a_1 + a_2 - a_3 > 0$.

    iii) $|a_1 + a_3| < 1 + a_2$ and $|a_2 - a_1 a_3| < 1 - a_3^2$.

Thus, it can be deduced that if the conditions i)-iii) of Schur-Cohn criterion are satisfied then the discrete system (3a)-(3c) is locally asymptotically stable at the equilibrium point.

4. Results and Discussion

This section is devoted to showing the stability analysis of the model and numerical results for the following parameters [5]:

$\sigma = 0.1$, $f_1 = 0.7$, $f_2 = 1$, $f_3 = 1$, $f_4 = 1$, $G = 1.8$,

$\delta = 1$, $v = 0.01$, $\eta = 0.7$, $\tilde{h} = 0.1$, $\xi = 0.1$. $\qquad (6)$

Firstly, the stability of the continuous model (1a)-(1c) will be examined for the parameter $T = 1.8$ in addition to the parameters (6). Eleven equilibrium points are obtained for the continuous model (1a)-(1c). Considering Theorem 3.1, it can be concluded that only the trivial equilibrium and the equilibrium point obtained as

$$
\begin{aligned}
E &= E(f, g, h) \\
&= \begin{pmatrix} 0.455479762381921, 0.493302878184821 \\ , 0.0689661098622050 \end{pmatrix}
\end{aligned} \quad (7)
$$

are asymptotically stable.

Here, only the stability of the non-trivial equilibrium point E defined by Eq. (7) will be shown.
The Jacobian matrix of the continuous system (1a)-(1c) at the equilibrium point (7) is obtained as

$$
J(E) = \begin{bmatrix} -1.65234318346793 & 0.923764295710813 & -0.00312941322960424 \\ 0.465542685604508 & -0.396654077620652 & -0.831452022774700 \\ 0.0250797518364091 & 0.0023563816122754 & 0 \end{bmatrix}.
$$

Corresponding eigenvalues of the Jacobian matrix $J(E)$ determined as

$\lambda_1 = -1.93764307516937$,

$\lambda_{2,3} = -0.0556770929596066 \mp 0.0923582563050207i$

have negative real parts. Thus, it can be deduced from Theorem 3.1 that the equilibrium point (7) of the continuous model (1a)-(1c) is asymptotically stable.
From now on, the stability of the discrete model (3a)-(3c) will be examined. In addition to parameters (6), the step size is considered as $h = 0.001$. The continuous model (1a)-(1c) and the discrete model (3a)-(3c) possess the same equilibrium points. Thus, considering Theorem 3.2, the equilibrium point (7) and the trivial equilibrium point of the discrete model are asymptotically stable.
Now, we will show the stability of the model at the equilibrium point (7):
The Jacobian matrix of the discrete system (3a)-(3c) is determined as

$$
J(E) = \begin{bmatrix} 0.998350048513008 & 0.000922427186186707 & -0.00000312488353706965 \\ 0.000465235841788792 & 0.999603607361028 & -0.000830904004474441 \\ 0.0000250784978914492 & 0.0000023562637972002 & 1 \end{bmatrix}. \quad (8)
$$

The characteristic polynomial of the Jacobian matrix (8) is as

$$
p(\lambda) = \lambda^3 + a_1 \lambda^2 + a_2 \lambda + a_3, \quad (9)
$$

where the constants of characteristic polynomial (9) are as

$a_1 = -2.99795365587404$,

$a_2 = 2.99590753866671$,

$a_3 = -0.997953882770182$.

Next, we check the conditions of Theorem 3.2.

i. $1 + a_1 + a_2 + a_3 = 2.2488 \times 10^{-11} > 0$.

ii. $1 - a_1 + a_2 - a_3 = 7.99181507731093 > 0$.

iii. Since $|a_1 + a_3| = 3.99590753864422$ and $1 + a_2 = 3.99590753866671$, the condition $|a_1 + a_3| < 1 + a_2$ is satisfied. Similarly, since $1 - a_3^2 = 0.004088047863918$ and $|a_2 - a_3 a_1| = 0.00408804742215$, the condition $1 - a_3^2 > |a_2 - a_3 a_1|$ is satisfied, too.

Thus, it can be deduced from the Schur-Cohn criterion (Theorem 3.2), the discrete system (3a)-(3c) is locally asymptotically stable.

Hereinafter, the numerical results obtained by the NSFD and the RKF45 methods are presented in graphical forms. In addition to the parameters (6), the step size is chosen as $h = 0.01$, and the positive initial conditions are considered as $f_0 = 0.4$, $g_0 = 0.36$, $s_0 = 0.12$. The parameter defining the rate of oxygen production by phytoplankton T is chosen as $T = 1.8$, $T = 2$, and $T = 2.2$ to be able to compare the obtained numerical results with the studies in the literature. Moreover, the numerical results obtained by the Euler, RK4, and NSFD methods are given in tabular forms and the effectiveness of the NSFD method is presented.

Figure 1 presents the variation in oxygen concentration $f(t)$, phytoplankton density $g(t)$, and zooplankton density $s(t)$ for $T = 1.8$. It can be concluded from Figure 1 that the system approaches the extinction state rapidly. Thereby, the plankton-oxygen system is not sustainable for $T = 1.8$.
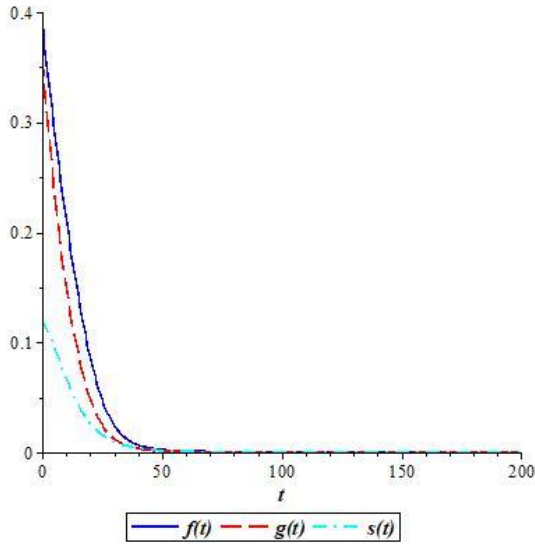
Figure 1. NSFD solution for oxygen concentration $f(t)$, phytoplankton density $g(t)$, and zooplankton density $s(t)$ for $T = 1.8$.

Figure 2 presents the variation in oxygen concentration $f(t)$, phytoplankton density $g(t)$, and zooplankton density $s(t)$ for $T = 2$. It can be concluded from Figure 2 that the system approaches the coexistence state for $T = 2$.
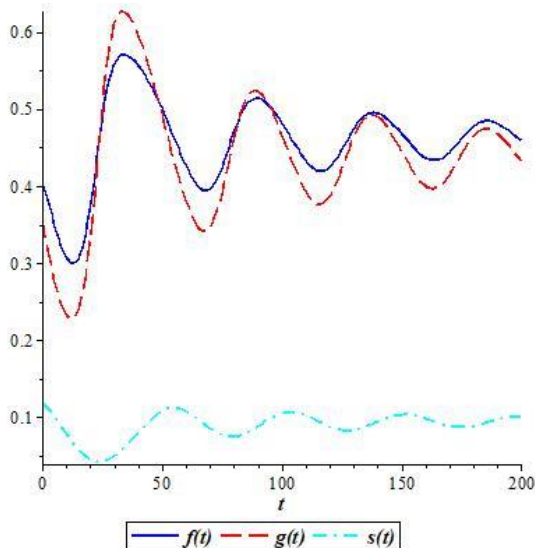
Figure 2. NSFD solution of oxygen concentration $f(t)$, phytoplankton density $g(t)$, and zooplankton density $s(t)$ for $T = 2$.

Figure 3 presents the variation in oxygen concentration $f(t)$, phytoplankton density $g(t)$, and zooplankton density $s(t)$ for $T = 2.2$. It can be concluded from Figure 3 that the system shows a few oscillations before approaching the extinction state for $T = 2.2$.
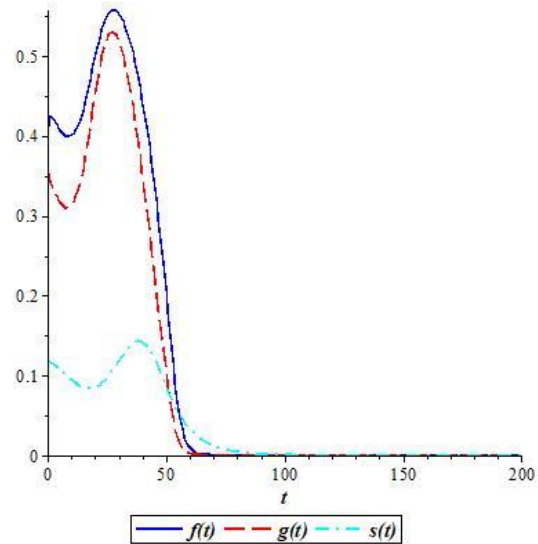
Figure 3. NSFD solution of oxygen concentration $f(t)$, phytoplankton density $g(t)$, and zooplankton density $s(t)$ for $T = 2.2$.

The model (1a)-(1c) has been solved numerically by using the Adams predictor-collector method in [3]. One can see that Figures 1-3 are the same as Figure 8, Figure 9, and Figure 11 provided in [3], respectively. Moreover, the model (1a)-(1c) takes into account the effect of global warming through the parameter T [3]. Thus, detailed interpretations of the effects of global warming can be found in [1, 3, 5, 40].

Figure 4 presents the numerical comparison of the NSFD method with the RKF45 method for the parameters (6) and $T = 1.8$. It can be concluded from Figure 4 that the numerical results for the NSFD method are in good agreement with the RKF45 method.
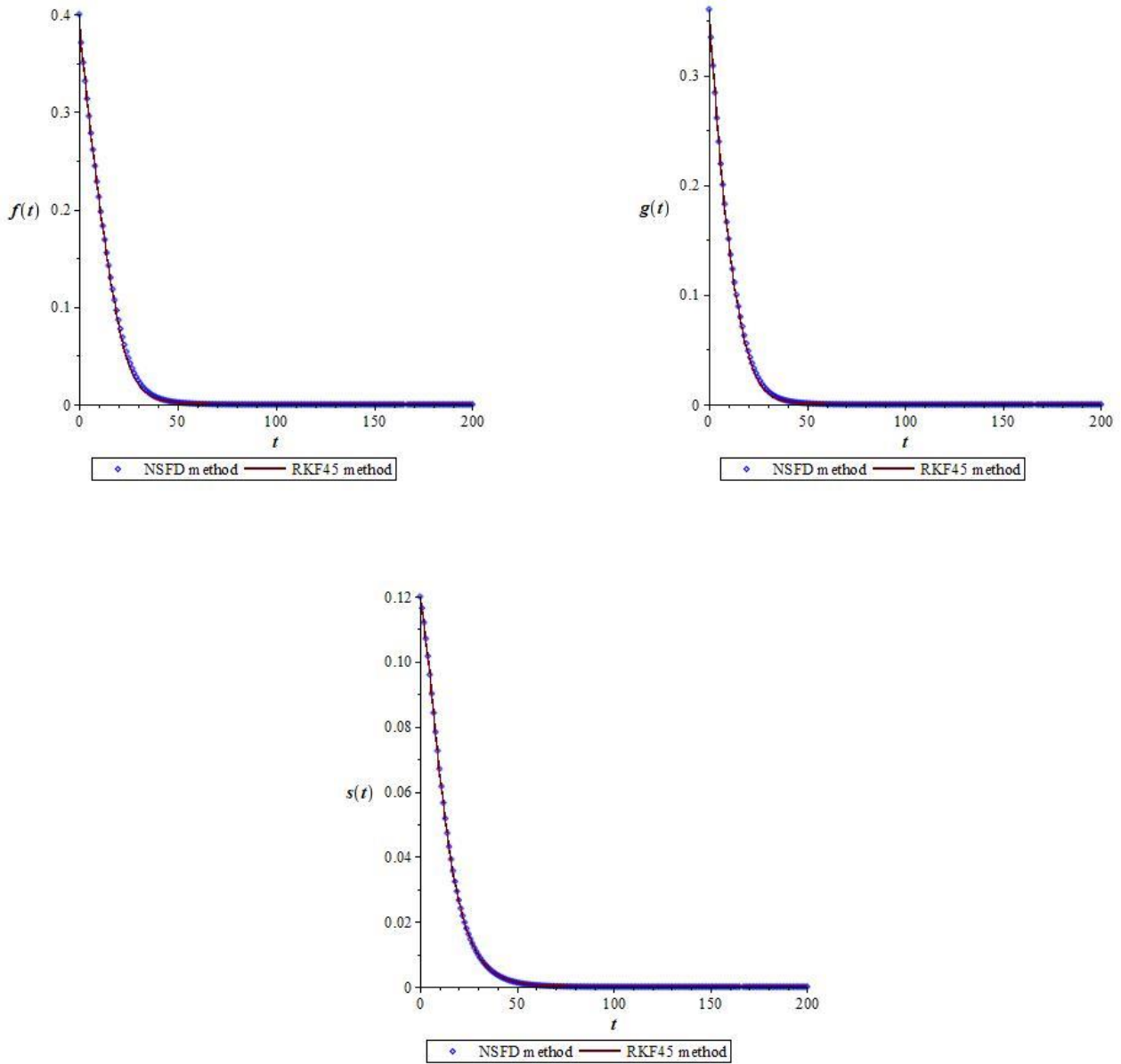
Figure 4. Numerical comparison of NSFD method with RKF45 method. ($T = 1.8$)

Moreover, the numerical comparison of the NSFD method with the Euler and RK4 methods is given in Table 1 for the step size $h = 0.001$ and the parameter $T = 2.2$. Thus, the accuracy of the numerical results obtained by the NSFD method is verified.

Table 1. Numerical comparison of the NSFD, Euler, and RK4 methods for the step size $h = 0.001$

($T = 2.2$).

	Euler			RK4			NSFD		
t	$f(t)$	$g(t)$	$s(t)$	$f(t)$	$g(t)$	$s(t)$	$f(t)$	$g(t)$	$s(t)$
0	0.4	0.36	0.12	0.4	0.36	0.12	0.4	0.36	0.12
1	0.42490	0.34497	0.1177	0.42489	0.34497	0.1177	0.42489	0.34498	0.1177
5	0.40838	0.31779	0.10864	0.40838	0.31779	0.10864	0.40840	0.31781	0.10864
10	0.40011	0.31291	0.09521	0.40012	0.31292	0.09522	0.40015	0.31294	0.09522
50	0.20067	0.10209	0.08609	0.20077	0.10218	0.08608	0.20132	0.10259	0.08621
100	0.000004	0.00001	0.00059	0.000004	0.000001	0.00059	0.000004	0.000001	0.00059

Table 2 presents the numerical results at $t = 700$ obtained by the Euler, RK4, and NSFD methods for different step sizes ($T = 2.2$). Thus, the system approaches the extinction state for the bigger step sizes by the NSFD method. Table 2 confirms the advantage of the NSFD method over the Euler and RK4 methods.

Table 2. Numerical results at $t = 700$ obtained by the Euler, RK4, and NSFD methods for different step sizes (

$T = 2.2$).

	Euler			RK4			NSFD		
h	$f(t)$	$g(t)$	$s(t)$	$f(t)$	$g(t)$	$s(t)$	$f(t)$	$g(t)$	$s(t)$
0.01	3.4×10^{-32}	1.3×10^{-32}	5×10^{-30}	3.7×10^{-32}	1.5×10^{-32}	5.2×10^{-30}	3.9×10^{-32}	1.5×10^{-32}	5.2×10^{-30}
0.1	1.5×10^{-32}	6.3×10^{-33}	3.7×10^{-30}	3.7×10^{-32}	1.5×10^{-32}	5.2×10^{-30}	6.1×10^{-32}	2.5×10^{-32}	6.1×10^{-30}
1	3.6×10^{-37}	1.4×10^{-37}	1.7×10^{-31}	3.6×10^{-32}	1.4×10^{-32}	5.2×10^{-30}	10^{-30}	7.5×10^{-31}	2.6×10^{-29}
5	Float (undefined)	Float (undefined)	Float (undefined)	Float (undefined)	Float (undefined)	Float (undefined)	4.2×10^{-27}	10^{-27}	6.3×10^{-27}
10	Float (undefined)	Float (undefined)	Float (undefined)	Float (undefined)	Float (undefined)	Float (undefined)	10^{-23}	2.2×10^{-24}	4×10^{-24}

Similarly, Table 3 presents the comparison of three methods for the stability of the equilibrium point E for different step sizes. The NSFD method is the most appropriate for the bigger step sizes compared with the Euler and RK4 methods.

Table 3. Comparison of stability of the equilibrium point E for different step sizes. ($T = 2$)

h	Euler	RK4	NSFD
0.01	Convergence	Convergence	Convergence
0.1	Convergence	Convergence	Convergence
1	Convergence	Convergence	Convergence
5	Divergence	Divergence	Convergence
10	Divergence	Divergence	Convergence
100	Divergence	Divergence	Convergence

5. Conclusion and Suggestions

The study aims to present an NSFD scheme for the model describing climate change in the oxygen-plankton system. The continuous model is discretized through the NSFD schemes and solved numerically. The numerical results are compared by the RKF45 method to present the accuracy of the NSFD method. Moreover, the numerical result obtained by the Euler, and the RK4 methods are presented to compare with the NSFD method. The effectiveness of the considered method for the bigger step sizes is presented in Table 2 and Table 3.

It can be concluded from Figures 1-3 that when the parameter defining the rate of oxygen production by phytoplankton is $T = 1.8$, $T = 2$ and $T = 2.2$, the plankton-oxygen system is not sustainable, the system approaches the coexistence state, and the system shows a few oscillations before approaching the extinction state, respectively.

This study implies that the NSFD method is easy to apply to the system of nonlinear ordinary differential equations. It preserves positivity conditions and is efficient even for bigger step sizes. In future studies, the NSFD schemes can be applied to the other versions of oxygen-plankton models.

Contributions of the authors

The authors' contributions to the paper are equal.

Conflict of Interest Statement

There is no conflict of interest between the authors.

Statement of Research and Publication Ethics

The study is complied with research and publication ethics.

References

[1]   Y. Sekerci, and S. Petrovskii, "Mathematical modeling of plankton–oxygen dynamics under the climate change," *Bulletin of Mathematical Biology*, vol. 77, pp. 2325-2353, 2015.

[2]   Y. Sekerci, and S. Petrovskii, "Mathematical modelling of spatiotemporal dynamics of oxygen in a plankton system," *Mathematical Modelling of Natural Phenomena*, vol. 20, no.2, pp. 96-114, 2015.

[3]   P. Priyadarshini, and P. Veeresha, "Analysis of models describing thermocline depth-ocean temperature and dissolved oxygen concentration in the ocean-plankton community," *Waves in Random and Complex Media*, pp. 1-25, 2023.

[4]   S. Mondal, G. Samanta, and M. De la Sen, "Dynamics of oxygen-plankton model with variable zooplankton search rate in deterministic and fluctuating environments," *Mathematics*, vol. 10, no. 10, 1641, 2022.

[5]   Y. Sekerci, and R. Ozarslan, "Marine system dynamical response to a changing climate in frame of power law, exponential decay, and Mittag-Leffler kernel," *Mathematical Methods in the Applied Sciences*, vol. 43, no.8, pp. 5480-5506, 2020.

[6]   Y. Sekerci, and R. Ozarslan, "Oxygen-plankton model under the effect of global warming with nonsingular fractional order," *Chaos, Solitons & Fractals*, vol. 132, 109532,2020

[7]   Y. Sekerci, and R. Ozarslan, "Fractional order oxygen–plankton system under climate change," *Chaos: An Interdisciplinary Journal of Nonlinear Science*, vol. 30, no. 3, 2020.

[8]   C. Xu, Y. Zhao, J. Lin, Y. Pang, Z. Liu, J. Shen,..., and S. Ahmad, "Mathematical exploration on control of bifurcation for a plankton–oxygen dynamical model owning delay, "*Journal of Mathematical Chemistry*, pp. 1-31, 2023.

[9]   A. Gökçe, "A mathematical study for chaotic dynamics of dissolved oxygen-phytoplankton interactions under environmental driving factors and time lag." *Chaos, Solitons & Fractals*, vol. 151, 111268, 2021.

[10]   P. R. Chowdhury, M. Banerjee, and S. Petrovskii, "A two-timescale model of plankton-oxygen dynamics predicts formation of Oxygen Minimum Zones and global anoxia." *arXiv preprint arXiv:2309.15447.*,2023

[11]   R. E. Mickens, *Difference Equations Theory and Applications*, Atlanta, Ga, USA: Chapman & Hall, 1990.

[12]   R. E. Mickens, *Nonstandard finite difference models of differential equations*, World Scientific Publishing Co., Inc., River Edge, NJ, 1994.

[13]   R. E. Mickens, "Nonstandard Finite Difference Schemes for Differential Equations," *Journal of Difference Equations and Applications,* vol. 8, no. 9, pp. 823-847, 2002.

[14]   R. E. Mickens, *Advances in the applications of Nonstandard Finite Difference Schemes*, Singapore: Wiley-Interscience, 2005.

[15]   R. E. Mickens, "Calculation of denominator functions for nonstandard finite difference schemes for differential equations satisfying a positivity condition," *Numerical Methods for Partial Differential Equations*, vol. 23, no. 3, pp. 672-691, 2006

[16]   K. C. Patidar, "On the use of nonstandard finite difference methods," *Journal of Difference Equations and Applications*, vol. 11, no. 8, pp. 735-758. 2005.

[17]   K. C. Patidar, "Nonstandard finite difference methods: recent trends and further developments," *Journal of Difference Equations and Applications*, vol. 22, no. 6, pp. 817-849, 2016.

[18]   I. U. Khan, A. Hussain, S. Li, and A. Shokri, "Modeling the transmission dynamics of coronavirus using nonstandard finite difference scheme," *Fractal and Fractional*, vol. 7, no. 6, p. 451, 2023.

[19]   I. Zhang, S. Gao, and Q. Zou, "A non-standard finite difference scheme of a multiple infected compartments model for waterborne disease," *Differential Equations and Dynamical Systems*, vol. 28, no. 1, pp. 59-73, 2020.

[20]   Y. Yang, J. Zhou, X. Ma, and T. Zhang, "Nonstandard finite difference scheme for a diffusive within-host virus dynamics model with both virus-to-cell and cell-to-cell transmissions," *Computers & Mathematics with Applications*, vol. 72, no. 4, pp. 1013-1020, 2016.

[21]   M. Kocabıyık, N. Özdoğan, and M. Y. Ongun, " Nonstandard Finite Difference Scheme for a Computer Virus Model," *Journal of Innovative Science and Engineering*, vol. 4, no. 2, pp. 96-108, 2020.

[22]   Q. A. Dang, and M. T. Hoang, "Numerical dynamics of nonstandard finite difference schemes for a computer virus propagation model," *International Journal of Dynamics and Control*, vol. 8, no. 3, pp. 772-778, 2020.

[23]   T. M. Hoang, A. Q. Dang, L. Q. Dang, "Nonstandard finite difference schemes for solving a modified epidemiological model for computer viruses," *Journal of Computer Science and Cybernetics*, vol. 34, no. 2, pp. 171-185, 2018.

[24]   M. Yakıt Ongun, and İ. Turhan, "A numerical comparison for a discrete HIV infection of CD4+ T-Cell model derived from nonstandard numerical scheme," *Journal of Applied Mathematics*, vol. 2013, 2013.

[25]   İ. T. Çetinkaya, M. Kocabıyık, and M.Y. Ongun, "Stability analysis of discretized model of glucose–insulin homeostasis," *Celal Bayar University Journal of Science*, vol. 17, no. 4, pp. 369-377, 2021.

[26] İ. T. Çetinkaya, "An Application of Nonstandard Finite Difference Method to a Model Describing Diabetes Mellitus and Its Complications," *Journal of New Theory*, vol. 45, pp. 105-119, 2023.

[27]   M. Kocabıyık, M. Y. Ongun, "Discretization and Stability Analysis for a Generalized Type Nonlinear Pharmacokinetic Models," *Gazi University Journal of Science*, vol. 36, no. 4, pp.1675-1691, 2023.

[28]   N. Özdoğan, M. Y. Ongun, "Dynamical Behaviours of a discretized model with Michaelis-Menten Harvesting Rate," *Journal of Universal Mathematics*, vol. 5, no. 2, pp. 159-176, 2022.

[29]   S. Li, I. Bukhsh, I. U. Khan, M. I. Asjad, S. M. Eldin, M. Abd El-Rahman, and D. Baleanu, "The impact of standard and nonstandard finite difference schemes on HIV nonlinear dynamical model," *Chaos, Solitons & Fractals*, vol. 173, 113755, 2023.

[30]   J. Calatayud, and M. Jornet, "An improvement of two nonstandard finite difference schemes for two population mathematical models," *Journal of Difference Equations and Applications*, vol. 27, no. 3, pp. 422-430, 2021.

[31]   M. Z. Ndii, N. Anggriani, and A. K. Supriatna, "Comparison of the differential transformation method and non standard finite difference scheme for solving plant disease mathematical model," *Communication in Biomathematical sciences*, vol. 1, no. 2, 2018.

[32]   M. Mehdizadeh Khalsaraei, A. Shokri, S. Noeiaghdam, and M. Molayi, "Nonstandard finite difference schemes for an SIR epidemic model," *Mathematics*, vol. 9, no. 23, 3082, 2021.

[33]   A. Zeb, and A. Alzahrani, "Non-standard finite difference scheme and analysis of smoking model with reversion class," *Results in Physics*, *21*, 103785, 2021.

[34]   M. T. Hoang, and O. F. Egbelowo, "Nonstandard finite difference schemes for solving an SIS epidemic model with standard incidence," *Rendiconti del Circolo Matematico di Palermo Series 2*, vol. 69, pp. 753-769, 2020.

[35]   M. T. Hoang, and J. C. Valverde, "A generalized model for the population dynamics of a two stage species with recruitment and capture using a nonstandard finite difference scheme," *Computational and Applied Mathematics*, vol. 43, no. 1, pp. 1-27, 2024.

[36]   X. L. Liu, C. C. Zhu, "A non-standard finite difference scheme for a diffusive HIV-1 infection model with immune response and intracellular delay," *Axioms*, vol. 11, no. 3, 129, 2022.

[37]   K. Nonlaopon, M. Mehdizadeh Khalsaraei, A. Shokri, and M. Molayi, " Approximate solutions for a class of predator–prey systems with nonstandard finite difference schemes," *Symmetry*, vol. 14, no. 8, 1660, 2022.

[38]   S. Wiggins, *Introduction to Applied Nonlinear Dynamical Systems and Chaos*, second edition, Springer, New York.

[39]   S. Elaydi, *An Introduction to Difference Equations*, third edition, Springer, New York, 2005.

[40] R. Ozarslan, and Y. Sekerci, "Fractional order oxygen–plankton system under climate change," *Chaos: An Interdisciplinary Journal of Nonlinear Science*, vol. 30, no. 3, 2020.

An Innovative Approach for Mission Sharing and Route Planning of Swarm Unmanned Aerial Vehicles in Disaster Management

Ilhan AYDIN[1*], Çağrı KARAKAŞ[1], Gökhan ALTUN[1], Mehmet Umut SALUR[2]

[1]Department of Computer Engineering Firat University, Elazig, Turkiye
[2] Department of Computer Engineering, Faculty of Engineering and Natural Sciences,
Gaziantep Islamic University of Science and Technology, Gaziantep, Türkiye
(ORCID: 0000-0001-6880-4935) (ORCID: 0009-0001-9196-4387) (ORCID: 0000-0002-8039-5764)
(ORCID: 0000-0003-0296-6266)

Keywords: UAV, Mission Sharing, Route Planning, Disaster management, optimization, simulation.

Abstract

Fast and effective response in disaster situations is critical for the success of rescue operations. In this context, swarm Unmanned Aerial Vehicles (UAVs) play an important role in disaster response by rapidly scanning large areas and performing situation assessments. In this paper, we propose an innovative method for task allocation and route planning for swarm UAVs. By combining Genetic Algorithm (GA) and Ant Colony Optimization (ACO) techniques, this method aims to ensure the most efficient routing of UAVs. First, clusters are created using GA to determine the regions of the disaster area that need to be scanned. At this stage, factors such as the capacities of the UAVs, their flight times, and the breadth of their mission areas are taken into account. Each UAV is optimized to scan a specific area assigned to it. Once the clusters are formed, the routes of the UAVs within each cluster are determined by the Ant Colony Algorithm (ACA). The route planning is tested both on Google Maps and in a Gazebo simulation environment. Google Maps is used to evaluate the accuracy and feasibility of route planning based on real-world conditions, while the simulation environment provides the opportunity to test the behavior of the UAVs and the effectiveness of the routes in a virtual setting. With real-time data integration, the UAVs' route planning can be updated instantly and quickly adapted to emergency situations.

1. Introduction

In Fast response in disaster situations is critical to saving lives and mitigating damage. Making timely and well-informed decisions during natural disasters, fires, earthquakes, and other emergencies directly affects the success of rescue operations. After these disasters, terrestrial cellular networks are often disrupted due to damage to base station infrastructure [1-2]. In this context, swarm UAVs can quickly and efficiently scan large areas to assess the status of disaster zones and provide vital information to emergency responders [3]. Swarm UAVs are particularly effective in complex and large terrain areas, facilitating the work of search and rescue teams. By communicating with each other, swarm UAVs can work in a coordinated manner, enabling them to quickly scan extensive areas. Thanks to these features, the process of locating and rescuing missing people and those trapped in disaster areas is significantly accelerated [4].

The most significant limitations of UAVs are their low payload capacity, limited battery power, and short flight durations [5]. To overcome these challenges, the use of swarm UAVs is becoming increasingly common. Swarm UAVs distribute the area to be scanned and the tasks to be performed among individual UAVs according to the principle of task sharing for a specific purpose. This allows for the scanning of large disaster areas with multiple UAVs

that have short flight durations. The initial response time is critical for search and rescue operations. Swarm UAVs play a crucial role in these operations, as they can quickly and effectively search large areas. With their high-resolution cameras and other sensors, they can provide detailed observations of the surroundings, offering a significant advantage in locating missing or distressed individuals. Additionally, by working in a swarm, they facilitate the coordination and direction of operations, thereby having the potential to guide rescue teams.

In this study, a new clustering approach is presented that divides the area to be scanned into clusters, allowing for the determination of the optimal path for each UAV to obtain disaster images in the fastest and most effective way after a disaster. To achieve this, a novel method is proposed to determine the optimal flight routes for UAVs to acquire images from the disaster area. The system is designed to enable UAVs to reach disaster areas from a specific starting point as quickly as possible, collect images, and return, first by using the proposed clustering method and then by planning the optimal route to be followed. The proposed method was tested in a simulation environment for different regions, varying numbers of UAVs, and different starting points. After the tests, the effectiveness of the proposed method was verified. The main contributions of the proposed approach are as follows:
• Introduction of a novel GA-based clustering approach for routing multiple UAVs,
• Enabling UAVs to collect data from different regions with minimal distance cost,
• Testing the method in both a two-dimensional environment on real maps and in the Gazebo simulation environment.

Especially the test performed in the Gazebo simulation environment has not been applied in the literature to the best of our knowledge. The studies in the literature mostly apply tests by applying two-dimensional or three-dimensional obstacles on a graph. This study allows for easy point determination and route planning with an interface to be written for a UAV with GPS.

2. Literature Review

Disaster management is a critical area that enables societies to recover quickly and effectively after natural or man-made disasters. Satellite imagery and unmanned aerial vehicles (UAVs) are used in disaster management and damage assessment. High-resolution satellite imaging systems have limitations such as image acquisition time, satellite connectivity, weather conditions, and delays in data delivery [6]. In contrast, UAVs are preferred in disaster management because they are fast, safe and flexible [7]. The video and still images captured by UAVs provide more detail than satellite images, making it easier to quickly identify and respond to damaged infrastructure [8-9]. In addition, the data collected enables emergency teams to make fast and effective decisions. UAVs can easily access areas that are difficult to reach with traditional methods. UAVs can be used for reconnaissance, detection, search and rescue support and coordination activities in disasters such as earthquakes and landslides, as well as for the detection and rescue of people under rubble [10]. UAVs have been used to provide communication and coordination by creating a communication infrastructure after disasters [11]. The advantages of UAVs such as rapid response, accessibility and cost-effectiveness make this technology an indispensable tool in disaster management, and the wider and more effective use of UAVs in disaster management will help minimize the negative effects of disasters by increasing social resilience. When UAVs are used in disaster situations, they are organized in multiples. A single UAV cannot complete complex missions on its own due to limitations such as flight time and computational capacity. Therefore, the swarm UAV system is used to accomplish a variety of challenging missions. Swarm UAVs have an important mission allocation problem that needs to be solved before they can accomplish the missions [12-13]. One of the most important issues for UAVs is route planning algorithms. An efficient route planning not only allows UAVs to perform their missions more efficiently and safely, but also saves energy and time. Optimal routes minimize unnecessary flights, shorten mission duration and extend battery life. The control and communication structure in swarm UAVs is used to improve route planning operations [14-15].

In the literature, some studies have been conducted for different purposes such as coordination of swarm UAVs for search and rescue activities, reaching the target as soon as possible, and target identification. Zahng et al. [16] proposed a mathematical optimization framework for communication of UAVs in post-disaster affected areas. Aydin and Altun [17] compared differential evolution and particle swarm optimization for route planning of UAVs in an environment with multiple obstacles. The comparison proved that differential evolution is more successful in terms of both the number of steps and the path traveled. Wang et al. [18] presented an approach combining linear programming and PDA for the multi-point vehicle routing problem for post-disaster relief delivery. The proposed approach is tested on standard benchmark

datasets. Zahng et al. [19] proposed a modified differential evolution algorithm for disaster emergency routing. The proposed approach considers two parameters to be optimized. These are risk and vehicle angle. To solve the problem with a constrained optimization, a differential evolution algorithm based on exponential selection is proposed and the B-spline method is used for route generation. The proposed approach is tested in both two-dimensional and three-dimensional environments in the presence of obstacles. Wan et al. [20] proposed a multi-objective swarm intelligence algorithm for three-dimensional route planning. The method transforms the path planning task into a multi-objective optimization task with multiple constraints and simultaneously optimizes the objectives based on the total flight path length and terrain threat degree. Scherer et al. [21] proposed an architecture for building an autonomous system of small-scale UAVs for search and rescue missions. The proposed architecture allows the use of swarm UAVs with different autonomy levels. The proposed architecture supports the addition or removal of a new UAV at a scalable level. Silvagni et al. [22] designed an unmanned aerial vehicle with special capabilities for mountaineering activities. The proposed UAV is equipped with capabilities customized for mountain operations, such as flying at high altitude, flying in rainy and snowy weather conditions, and flying day and night. Arnold et al. [23] investigated the effect of UAV role on first response time by using multi-role swarm UAVs in a simulation environment for search and rescue operations. They were successful in finding more than 90% of the survivors in less than 40 minutes in their tests with 10 to 50 UAVs in the simulation. Karaköse [24] used GA to optimize the task allocation of UAVs. The number of UAVs to be assigned for each target point and the optimum path and number of UAVs were determined according to the obstacles on the route. Gladence et al. [25], organized a flood disaster in a simulation environment and detected people trapped in the flood. In the developed simulation, swarm UAVs were used and each UAV was given a route. The images collected by the UAVs were processed on the server and people trapped in the flood were detected in each region. Alawad et al. [26] proposed a swarm optimization algorithm based disaster and crisis management control system for disaster and crisis management in smart cities. The proposed swarm optimization method enables UAVs to find the optimal path and consume less energy. Bakirci and Ozer [27] used k-means clustering algorithm and hierarchical virtual communication ring strategy for subtasks such as task allocation of swarm UAVs,

communication between UAVs, and determination of unsafe routes. They also developed recommendations for UAVs not to collide during take-off and not to communicate securely among themselves. Masroor et al. [28] proposed a linear optimization-based approach to reach more disaster victims with minimum UAVs in an emergency. The main objective is to enable users to communicate with the UAV. Wang et al.[29] modeled the 3D UAV deployment problem as a Markov process involving role assignment and role switching for each UAV. In this study, reward and cost functions are defined to minimize energy consumption. Ashraf et al. [30] presented an approach that optimizes the order of places to visit and the speed of the IHA to minimize the task time in IHAs. For this purpose, they treated the problem as a nonlinear integer problem and presented two algorithms that combine the optimal radius of trajectories and circular trajectories. Mahajan et al. [31] proposed a multi-objective Markov decision process based route management. The proposed approach utilizes Markov decision process and Q learning approach. For routing performance, they compared energy minimum remaining node ratio, delay and power to distance ratio. Li et al. [32] proposed an adaptive full coverage algorithm for data collection with UAVs in a disaster situation. The proposed approach provides an approach to optimize the path planning of UAVs in which optimal paths intersect less and routes are minimized. In the proposed approach, two different algorithms are developed for node distribution density and optimal path planning on the generated nodes. Wan et al. [33] proposed an attention-based deep reinforcement learning approach for the routing problem with multiple IHAs. Service time and route selection at each node are analyzed. For the collected potential disaster data, the interaction between UAV arrival time and service time is analyzed and an approach is developed to speed up the process.

Despite the growing body of research on the use of swarm UAVs for disaster management and search and rescue operations, several significant gaps persist in the literature. Firstly, most existing studies are heavily reliant on theoretical implementation and lack real-world implementation and validation. This discrepancy raises concerns about the practical applicability and robustness of the proposed methods under actual disaster conditions. In addition, most of the studies consist of placing obstacles and running algorithms in a two-dimensional environment. Simulation environments such as Gazebo give very accurate results in terms of modeling real life. There is no study in the literature on the use of swarm UAVs in such an environment in case of a disaster.

3. Proposed Approach for Route Planning

In the proposed study, a system has been designed to enable UAVs to reach disaster areas from a specific starting point as quickly as possible, collect images, and return. This system first distributes tasks using a proposed clustering method and then plans the optimal routes for the UAVs to follow. The system is coded in the Python programming language. In the designed system, calculations can be made using either the Cartesian or Geographical Coordinate System, and the results can be displayed and tested in a simulation environment. The general scheme of the system is shown in Figure 1.
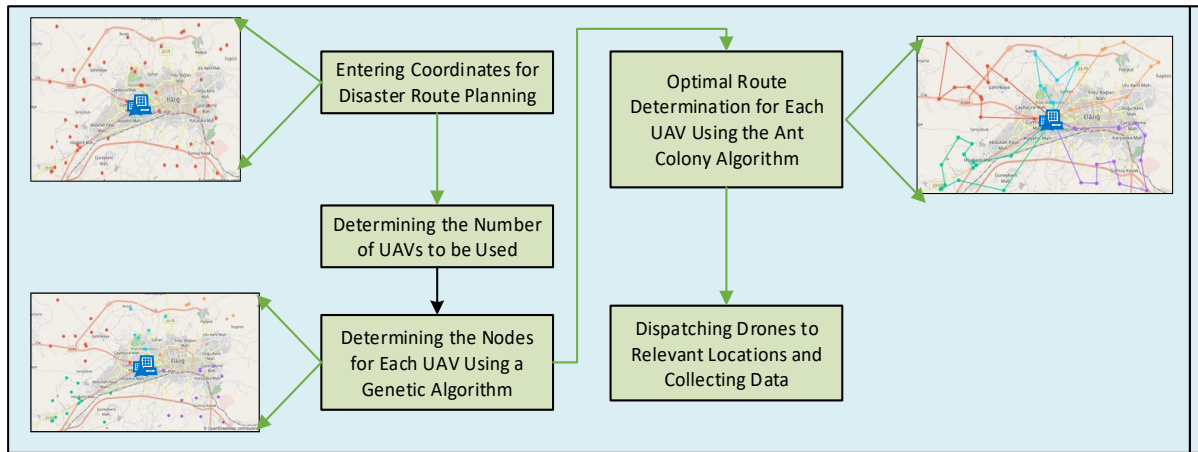
Figure 1. Workflow diagram of the system designed for route planning

In this study, a Genetic Algorithm (GA) is used to allocate the coordinates to be reached by a large number of UAVs departing from a selected starting point. The UAVs at the starting point are positioned to reach the coordinates closest to them. This 360-degree positioning ensures that the UAVs can fulfill their missions in the fastest and easiest way. As the number of UAVs and coordinates increases, this becomes a very long computation process, which is optimized using GA in this study. First, the coordinates to be accessed during the image collection process must be defined in the system. To exemplify this process, random coordinates are used in the study. Examples of 100 random coordinates for the Cartesian Coordinate Plane and 50 random coordinates for the map representation can be seen in Figure 2.
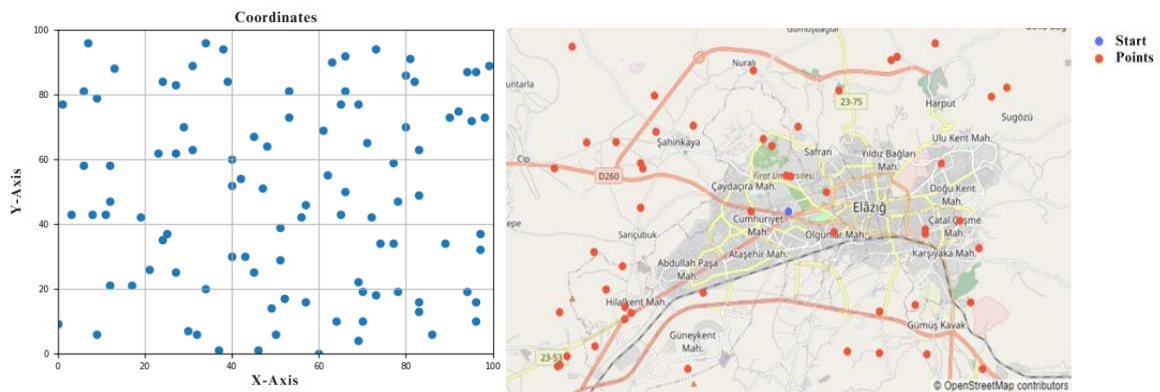
Figure 2. Cartesian Coordinate Plane and map representation of randomly determined points

In the study, the matplotlib library was used for visualizations on the cartesian coordinate plane, and the plotly library was used for map visualizations. The determined coordinates need to be allocated according to the number of available UAVs and a selected starting point for the UAVs to begin their movement. In this study, a clustering method is proposed to enable the system to perform this task allocation. Although this process can be done with known clustering methods, those methods are

inefficient since the clustering process is independent of the starting point. In the proposed method, the coordinates are allocated so that the UAVs closest to the starting point are in the same cluster. The position of each UAV is determined by placing it at an optimal location on a circle with a small radius around the origin. GA is used to calculate the positions of the UAVs on the circle [34]. According to an angle value between 0 and 360 degrees determined for each UAV, its position on the circle is found using Equation 1. This process is performed with an objective function that minimizes the intra-cluster Euclidean distance using GA. Figure 3 shows the proposed GA clustering approach.

$$Location_X = \cos\left(\frac{2 \times \pi \times a\varsigma\iota}{360}\right), Location_Y = \sin\left(\frac{2 \times \pi \times a\varsigma\iota}{360}\right) \tag{1}$$

```
function clusters=Genetic_clustering(#uavs, x, y, points)
#uavs: Number of UAVs to be deployed
x: Point x where UAVs will start flying
y: Point y where UAVs will start flying
points: Points where UAVs will fly1.          Chromosome coding
a.         Create as multiple angle values as the number of UAVs for each chromosome on the circle as K=[a₁,a₂,…aₙ].
b.         Determine the UAV positions from the angles created according to Equation (1)
2.         Create the initial population
3.         while(number of iteration)
4.            for each chromosome in population do
                  a. Determine the position of UAVs
                  b. Find the clusters of each of the locations to visit according to the closest UAV
                  c. Find the average distance to the center for each cluster and take the highest distance as the objective
function
5.         endfor
6.         Crossover
7.         Mutation
8.         Rulet Selection based selection
9.         endwhile
```

Figure 3. Determining the clusters to be flown for each UAV with the genetic algorithm

As a result, the optimal clustering positions for the UAVs are calculated, as shown in Figure 3. In the circle formed by centering on the initial position of the UAVs, they are placed at positions determined by angle values between 0 and 360 degrees. The UAV positions are derived from these angle values. Clusters are then formed based on the proximity of the UAVs to the points they will fly to. The average distance of the points to the cluster centers is calculated, and the cluster center with the highest average distance is minimized. The algorithm prevents UAVs from hovering at the same points by ensuring the formation of disjoint clusters. The UAVs are placed at the starting point designated for image collection. They must reach the targeted coordinates to collect the images and return. With appropriate route calculation, it is important for the UAVs to accomplish this task in the shortest distance possible, in terms of time and fuel savings. In this study, the Route Determination Algorithm (RDA) was used for route calculation. For each UAV, the shortest route that allows them to reach their designated coordinates from the starting point and return is calculated using RDA [35]. The initial pheromone values ($\tau\_ij,$), attractiveness (η), number of ants (n), importance of the pheromone trail (α), importance of attractiveness (β), and pheromone evaporation rate (ρ) are determined for each UAV for route planning. As a first step, the probabilistic path selection from point i to point j is calculated as follows.

$$P_{ij}(t) = \frac{|\tau_{ij}(t)|^{\alpha}|\eta_{ij}|^{\beta}}{\sum_{k \in N_i} |\tau_{ik}(t)|^{\alpha}|\eta_{ik}|^{\beta}} \tag{2}$$

In Equation (2), $P_{ij}(t)$ represents the probability that an ant moves from point i to point j. In equation (2), $\tau_{ij}(t)$ is the pheromone density between point i and j, and η_{ij} is the attractiveness between point i and j. Ni in the equation represents the set of points that can be traveled to. At the end of each tour, the pheromone trails on the paths that the ants have traveled are updated. The pheromone update is done according to equation (3).

$$\tau_{ij}(t + 1) = (1 - \rho).\tau_{ij}(t) + \Delta\tau_{ij}(t) \tag{3}$$

In the equation, the pheromone value is multiplied by (1-ρ) for the evaporation of the existing pheromone trail. In this equation, ρ is chosen between 0 and 1. The $\Delta\tau_{ij}(t)$ in the equation is used for the ants to leave a new pheromone trail. The new pheromone trail left by the ants depends on the length of the path taken by the ant. This is usually expressed as in equation (4).

$$\Delta\tau_{ij}(t) = \sum_{k=1}^{m} \Delta\tau_{ij}^{k}(t) \qquad (4)$$

In route planning with ACO, possible routes are selected using pheromone trails and attractiveness. The ants then complete their routes according to the determined probabilities. After the tours are completed, the pheromone trails are updated, and the process is repeated for a given number of iterations until the best solution is found. The proposed approach was also tested in a simulation environment using multiple UAVs. For this purpose, ROS software and the Gazebo simulation environment were used. ROS, which stands for Robot Operating System, is a software framework based on FreeBSD, an open-source operating system by Berkeley Software Distribution [36]. It is not a traditional operating system but a meta-operating system that provides services expected from an operating system, including hardware abstraction, low-level device control, implementation of commonly used functions, message passing between processes, and package management [37]. ROS promotes flexibility and modularity in a system, represented as nodes in a network, allowing robot components to communicate through an anonymous and asynchronous publish/subscribe mechanism [38]. The simulation environment used is Gazebo, a 3D dynamic simulator capable of accurately and efficiently simulating robot populations in complex indoor and outdoor environments. Unlike game engines, Gazebo offers physics simulation with a high degree of accuracy, along with a range of sensors and interfaces for both users and programs [39]. Gazebo is built on two different executable file structures: gzserver and gzclient. The gzserver executable runs the physics update loop and generates sensor data, while the gzclient executable provides the user interface. Typical uses of Gazebo include testing robotics algorithms, designing robots, and implementing realistic scenarios [40]. An experimental study was conducted on the deployment of multiple UAVs to capture simultaneous images from multiple points in a real-world setting. The study was carried out using Gazebo, a 3D simulation program. Within the scope of the study, a 20,000 m² experimental area consisting of 50 target points was designed in the Gazebo simulation environment. The geometric objects representing the target points were modeled as square prisms with a side length of 1 meter. A 3D view of the simulation environment is shown in Figure 4.
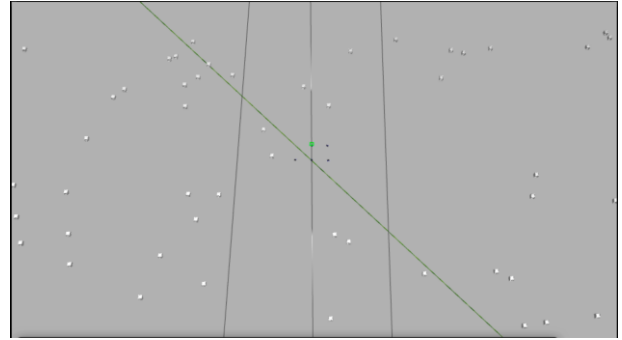
Figure 4. Representation of points in Gazebo Simulation environment

Four UAVs controlled by Ardupilot flight controllers were added to the 3D working environment. The UAV model with Ardupilot flight controller is given in Figure 5.
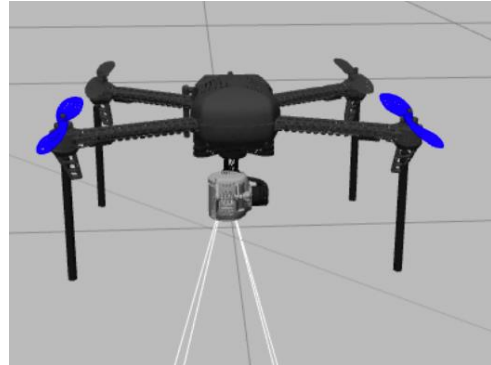
Figure 5. Gazebo UAV

MAVProxy ground station software was used to control the UAVs. A ground station software was run for each UAV and a connection was established with the UAVs. Instant command sending and data retrieval operations were performed with UAVKit, a Python library that enables application development for UAVs connected in a 3D simulation environment.

4. Application Results

The implementation of the proposed approach consists of three stages. In the first stage, cluster points are determined using a Genetic Algorithm (GA) for the given coordinates. In addition to GA, the K-means clustering algorithm was also used to determine the cluster centers. According to the

number of UAVs and the starting point where the UAVs will take off, GA determines the points each UAV will fly to. The parameters of the GA are provided in Table 1.

Table 1. The parameters of genetic algorithm

Parameter	Value
Number of iteration	500
Population size	100
Mutation rate	0.01
Crossover rate	0.7

In this study, we also compare the proposed method with one of the known clustering methods, K-Means. Figure 5 shows examples of clustering with both algorithms. In the study, for each UAV, the shortest path will be taken between the points determined by ACO, starting from the starting point, traveling through all the points in the relevant cluster with the shortest path and returning back to the starting point. Table 2 shows the ACO parameters.

Table 2. The parameters of ACO

Parameter	Value
Number of ants for each coordinate	4
Size of colony	100
Pheromone amount	1
Evaporation rate (ρ)	0.1
Relative importance of pheromone (α)	1
The importance of attractiveness (β)	5

The UAVs, which are placed at the starting point determined to collect the images, need to reach the targeted coordinates in sequence, take the images and return back. With an appropriate route calculation, it is important for the UAVs to perform this process on the coordinates from the shortest distance in terms of time and battery savings. In this study, ACO was used for route calculation. For each UAV, the shortest route that allows them to reach their own coordinates starting from the starting point and return to the starting point was calculated with ACO. Figure 6 shows the clusters generated by GA and K-means and the routes generated by ACO for 5 UAVs in two-dimensional space.
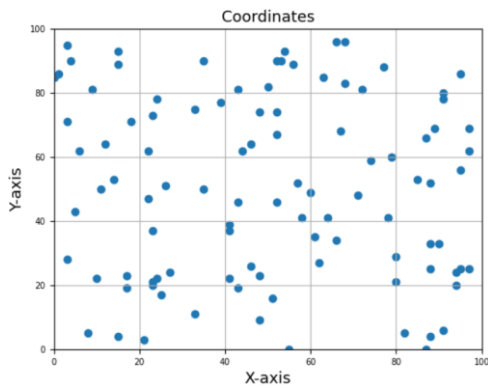
(a) Points generated in the coordinate system
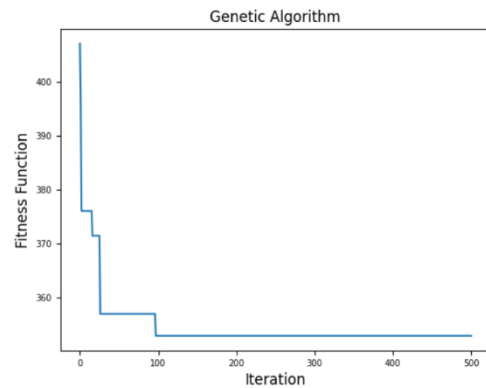
(b) Genetic algorithm objective function change
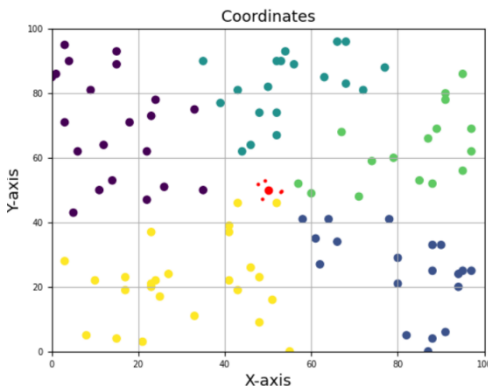
(c) Clusters generated by genetic algorithm

(d) Routes generated for genetic clusters
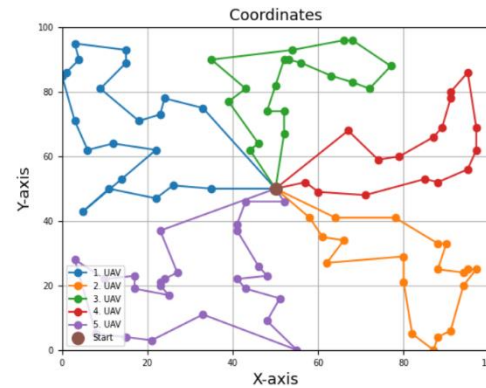
(e) Clusters generated with K-means   **(f)** Routes generated for K-means clusters
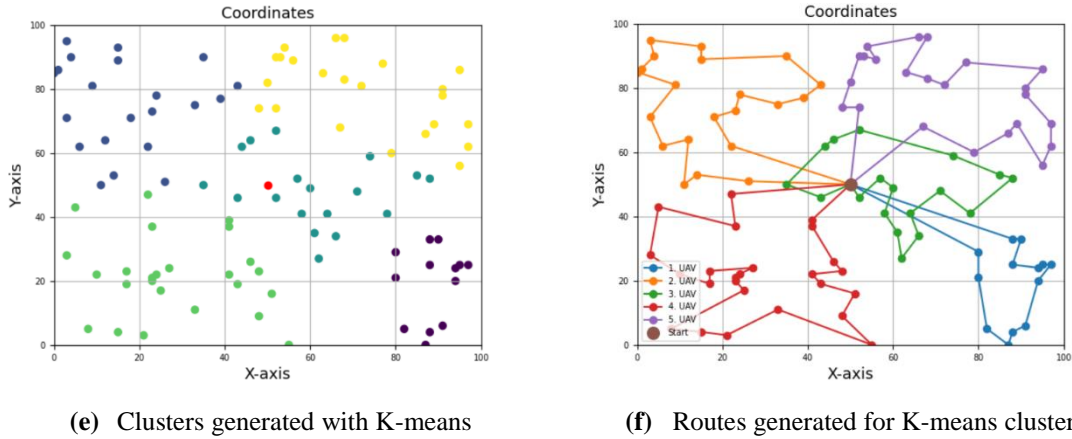
Figure 6. Clusters created in two-dimensional space and route planning

In Figure 6, the starting point of the UAVs in the coordinate system is given as coordinate (50,50). With GA, the initial angles of the UAVs on the unit circle were found as [90, 163, 217, 318, 343]. These points are shown in Figure 6(c). It is seen that the routes of the UAVs in the clusters created with k-means intersect more than the clusters created with genetics. We also compared the distances traveled by the UAVs for each case. The comparison result is given in Figure 7.
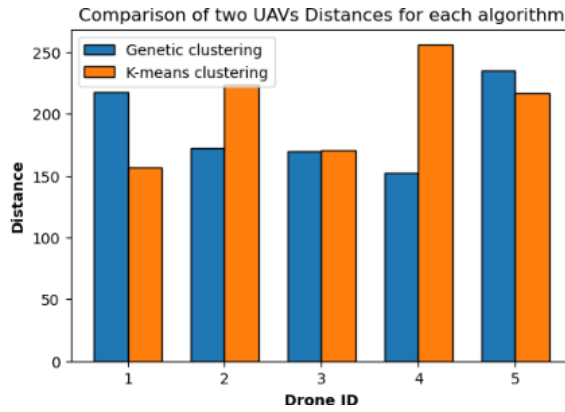
Figure 7. Total route length in each clustering for five UAVs

Figure 7 shows that the genetic clustering model finds shorter routes for many UAVs and shortens the total flight time. In addition, the total distance traveled is 945 units in genetic clustering and 1023 units in k-means clustering. Another advantage of genetic clustering is that UAVs are less likely to collide with each other. Because the routes do not intersect. In the second scenario, 3 UAVs were used on a map. The application results are shown in Figure 8.
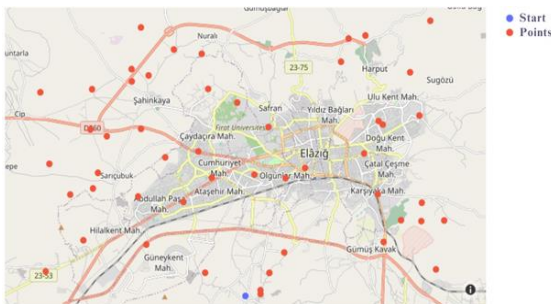
(a) Points generated on the map   **(b)** Genetic algorithm objective function change

(c) Clusters generated by genetic algorithm

(d) Routes generated for genetic clusters

(e) Clusters generated by K-means

(f) Routed generated for K-means clusters
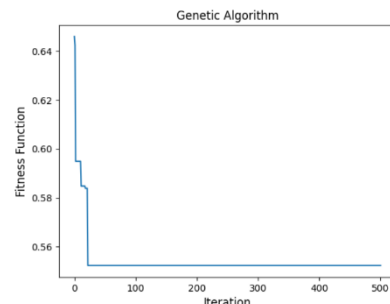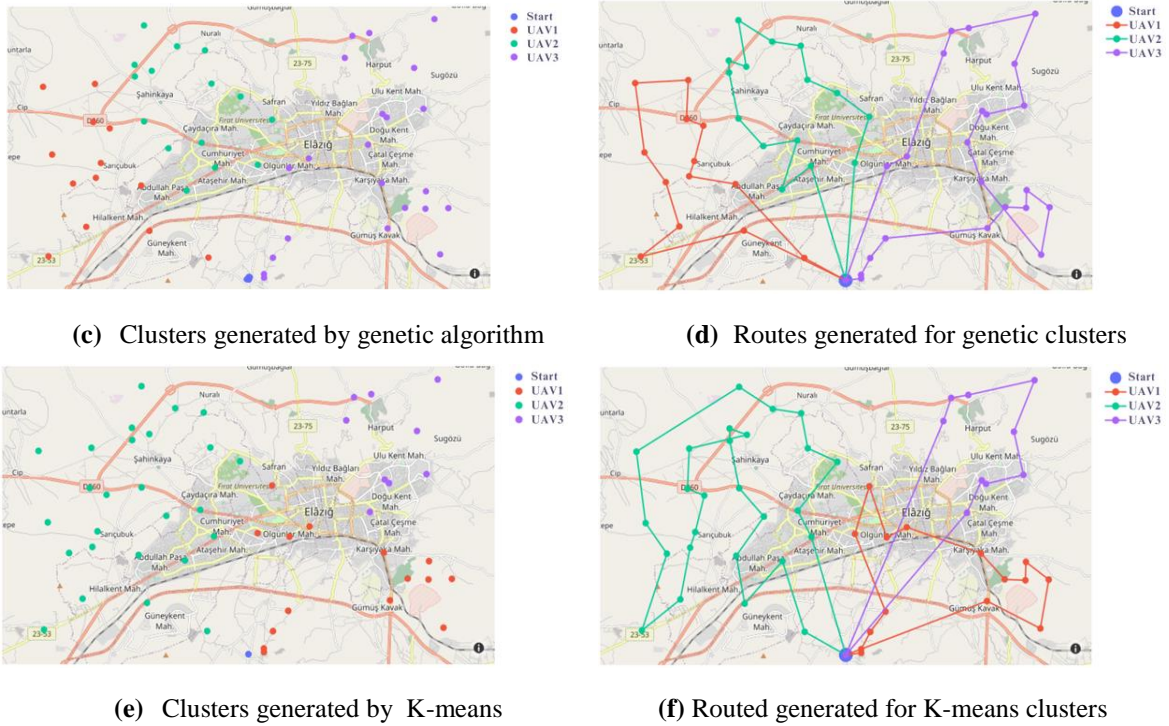
Figure 8. Clusters and route planning in two-dimensional space

In Figure 8, when the clusters created with GA and k-means are considered, it is seen that the routes overlap with each other in the clusters created with k-means. On the other hand, the routes generated with GA appear more disjoint. In addition, the total path taken with the proposed clustering method for the three UAVs is 1.04 units, while the path taken with k-means is calculated as 1.13 units. The proposed approach was also tested in the Gazebo simulation environment for 5 UAVs. Five UAVs with Ardupilot flight controllers were added to the simulation environment via ROS software and are shown in Figure 9.

Figure 9. Multiple UAVs in Gazebo environment

MAVProxy ground station software was used to control the UAVs. A ground station software was run for each UAV and a connection was established with the UAVs. Instant command sending and data

retrieval operations were performed with DroneKit, a Python library that allows application development for UAVs connected in a 3D simulation environment. In order to scan the field in the shortest time with the number of available UAVs, which is the aim of the study, clusters were created as many as the number of UAVs to be activated with the proposed clustering method. The clusters are shown in Figure 10.
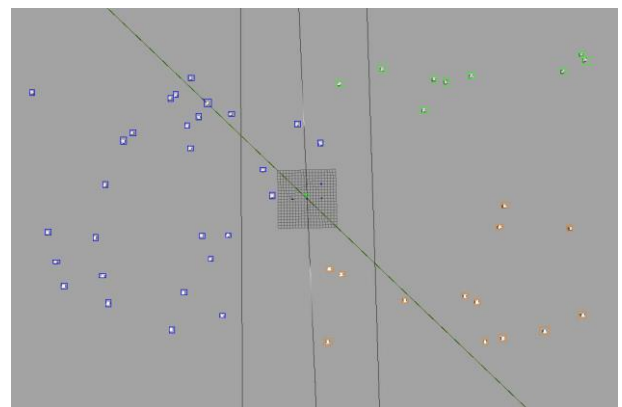
Figure 10. Coordinates clustered with the proposed method

Those marked with blue boxes represent the first cluster, i.e. the coordinates to be reached by UAV 1, those marked with orange boxes represent the second cluster, i.e. the coordinates to be reached by UAV 2, and those marked with green boxes represent the third cluster, i.e. the coordinates to be reached by

UAV 3. In order to control the points within the determined clusters by the UAVs in the fastest and shortest way, the route generated by the ACO was used. The front side of the UAV points to the +x axis and the right side points to the +y direction. Since it is different from the classical coordinate system, there is a difference in location information. The cluster created in the Gazebo simulation environment and the route structure within the cluster are given in Figure 11.
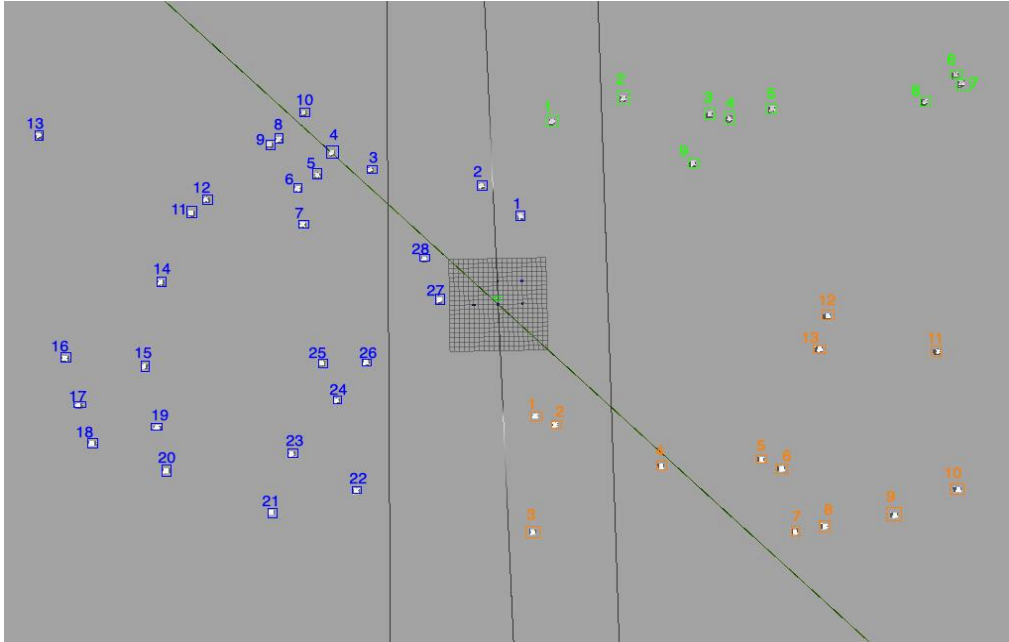
Figure 11. Routes generated for clusters in the simulation environment

The routes created cannot be uploaded to the UAVs at once. Therefore, the coordinate information will be sent to the UAV as a message and the DroneKit library is used to query whether the UAV has reached the target or not. In order to manage multiple UAVs at the same time in this way, multi-threading method was used. A thread was created for each UAV, location information was queried instantly for each UAV, and if the UAV reached the desired target, new location information was sent and the mission was tried to be performed. Thus, multiple UAVs were managed with a single software. The image of the UAV's progress to the target in the Gazebo environment is given in Figure 12.
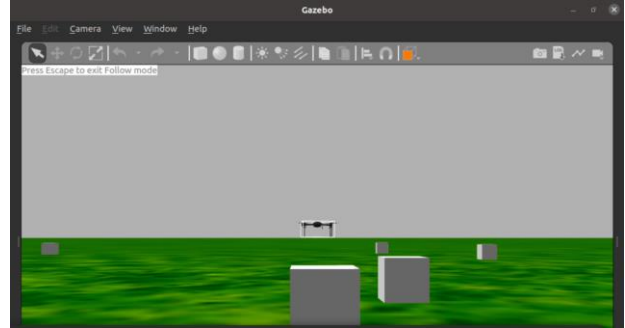
Figure 12. UAV's progress to the target in a gazebo environment

Table 3 shows the distances covered by each method for scenarios with different number of points, number of UAVs and starting points.

Table 3. Routed coordinates for UAVs

Example scenario	Number of points	Number of UAVs	Starting point	Total distance traveled with K-Means Clustering	Total distance traveled with the proposed clustering method
1	100	5	(50, 50)	970.39	955.96
2	100	3	(50, 0)	1000.97	947.40
3	100	4	(0, 50)	1068.11	1018.43
4	50	5	(39.1890, 38.6728)	1.27	1.14
5	50	3	(39.1890, 38.6228)	1.13	1.05
6	50	4	(39.2690, 38.6728)	1.42	1.25

According to the results obtained, the proposed coordinate sharing method for UAVs sent from a starting point to reach the assigned coordinates works more efficiently than clustering methods such as K-Means, which only performs a standard grouping in terms of distance similarity. Subsequently, successful results were obtained in the routing process performed with RDA for each UAV to reach their assigned coordinates from the shortest distance. This method is expected to be used to perform operations such as taking images and transferring cargo in order to quickly determine the situation during and after the disaster until detailed mapping with satellite images or aerial vehicles.

In the literature, different approaches have been used for task allocation and route planning of swarm UAVs. Some studies aim to reach the target with the shortest path in an environment with obstacles. For this purpose, route planning of a single UAV was mostly performed. In studies conducted with swarm UAVs, on the other hand, multiple UAVs were used for shortest route planning. The routes to be traveled by each UAV were determined by clustering approach. Table 4 shows the comparison between the methods in the literature and the proposed approach.

Table 4. Comparison of the proposed method with other studies

Reference	The method	Simulation tool	Results
[7]	Clustering with k-means and distributed route planning	Display on a map	- Decentralized control - Low real-time applicability
[19]	Exponential rank differential evolution algorithm	Representation in two and three dimensional space	- Route planning in the presence of obstacles - Single destination
[20]	Route planning with multi-objective swarm optimization	Representation in two and three dimensional space	- Route planning for a single destination - Avoiding obstacles
[28]	Integer linear optimization	Representation in two dimensional space	- UAV positioning in a distributed environment - Protection of inter-UAV communication
[32]	Adaptive full coverage and intelligent route planning	Representation in two dimensional space	- Preventing intersection of routes - Quality of service and establishment of minimum routes
[33]	Deep Q learning based route planning	Representation in two dimensional space	- Minimum service time - Attention-based deep reinforcement approach - Mathematical modeling
This study	Multiple route planning with genetic algorithm based clustering and ant colony algorithm	Two-dimensional environment, map and representation in Gazebo simulation environment	- Route planning of multiple UAVs with minimum distance - Preventing crossing of routes - Suitable for real life application

Considering the results in Table 4, it is evident that many methods only use two-dimensional graphical representations. Although some studies have applied three-dimensional environments, the main focus has been on guiding to a target in an obstacle-rich environment [19-20]. In multi-route planning with swarm UAVs, only study [32] proposed a method to prevent route intersections. Due to the complexity of the mathematical structures of some models, there is a need to adjust specific parameters [28, 33]. This study offers two main contributions compared to the existing literature. The first contribution is the creation of non-intersecting routes for UAVs using a genetic algorithm, resulting in a low intersection rate. The second contribution is the demonstration of the algorithm in three different platforms: a two-dimensional space, on a map, and in the Gazebo simulation environment. The Gazebo environment models UAVs in a way that accurately reflects real-world scenarios, providing a reliable simulation of actual field conditions.

5. Conclusions

This study proposes an innovative method combining Genetic Algorithm and Ant Colony Optimization techniques for task allocation and route planning of swarm UAVs in disaster situations. Firstly, k-means and GA based clustering techniques are used to determine the mission regions of UAVs. Genetic-based clustering creates more discrete and clear clusters, thus avoiding overlaps between the mission areas of UAVs. This allows for a more efficient and faster scanning of disaster areas. In addition, operational efficiency is increased by ensuring that the routes of the UAVs do not intersect. Route planning using Ant Colony Optimization helped to minimize the total path distance of the UAVs. Thus, energy consumption is reduced and the UAVs can operate for longer periods of time. The proposed approach was tested both on a two-dimensional coordinate system and on Google Maps and Gazebo simulation environment. In particular, the tests in the Gazebo simulation environment demonstrated the applicability and effectiveness of the method in real-world conditions. Similar simulation environment tests have not been conducted before, which emphasizes the novelty of this study in the literature. With real-time data integration, the route planning of UAVs can be updated instantaneously and quickly adapted to emergency situations. This contribution is a great advantage when time is of the essence in disaster response. As a result, the proposed method successfully solves the problem of task sharing and route planning of swarm UAVs in disaster situations and improves operational efficiency. The results of the study provide an important contribution to the optimization of UAV use in future disaster response operations.

Conflict of Interest Statement

There is no conflict of interest between the authors.

Author Contribution Statement

Conceptualization: IA, ÇK, GA
Methodology: ÇK, GA, IA
Manuscript writing reviewing editing: IA, ÇK, MUS
Supervision: IA

References

[1] G. C. Deepak, A. Ladas, Y. A. Sambo, H. Pervaiz, C. Politis, and M. A. Imran, "An overview of post-disaster emergency communication systems in the future networks," *IEEE Wireless Communications*, vol. 26, no. 6, pp. 132-139, Dec. 2019.

[2] L. D. Nguyen, K. K. Nguyen, A. Kortun, and T. Q. Duong, "Real-time deployment and resource allocation for distributed UAV systems in disaster relief," in *Proc. IEEE 20th Int. Workshop Signal Process. Advances Wireless Commun. (SPAWC)*, Cannes, France, Jul. 2019, pp. 1-5.

[3] M. Erdelj and E. Natalizio, "UAV-assisted disaster management: Applications and open issues," in *Proc. Int. Conf. Comput., Netw. Commun. (ICNC)*, Kauai, HI, USA, Feb. 2016, pp. 1-5.

[4] H. Ijaz, R. Ahmad, R. Ahmed, W. Ahmad, Y. Kai, and W. Jun, "A UAV assisted edge framework for real-time disaster management," *IEEE Trans. Geosci. Remote Sens.*, 2023.

[5] D. Erdos, A. Erdos, and S. E. Watkins, "An experimental UAV system for search and rescue challenge," *IEEE Aerosp. Electron. Syst. Mag.*, vol. 28, no. 5, pp. 32-37, May 2013.

[6] A. Nedjati, G. Izbirak, B. Vizvari, and J. Arkat, "Complete coverage path planning for a multi-UAV response system in post-earthquake assessment," *Robotics*, vol. 5, no. 4, pp. 26-41, 2016.

[7] S. Değirmen, F. Çavdur, and A. Sebatlı, "Afet Operasyonları Yönetiminde İnsansız Hava Araçlarının Kullanımı: Gözetleme Operasyonları için Rota Planlama," *Uludağ Üniversitesi Mühendislik Fakültesi Dergisi,* vol. 23, no. 4, pp. 45-55, 2018.

[8] M. Kwong, "Nepal earthquake: Drones used by Canadian relief team," CBC News, Apr. 27, 2015. [Online]. Available: https://www.cbc.ca/news/world/nepal-earthquake-drones-used-by-canadian-relief-team-1.3051106. [Accessed: Jul. 08, 2024].

[9] N. Nikhil, S. M. Shreyas, G. Vyshnavi, and S. Yadav, "Unmanned Aerial Vehicles (UAV) in Disaster Management Applications", in *2020 Third International Conference on Smart Systems and Inventive Technology (ICSSIT), Tirunelveli, India*, 2020, pp. 140-148.

[10] STM ThinkTech, "Savunma ve Güvenlik Bilim ve Teknoloji Özel Dosya: Kahramanmaraş Merkezli Depremler Odağında Doğal Afetlerde Teknoloji Kullanımı," May 5, 2023. [Online]. Available:

https://thinktech.stm.com.tr/tr/kahramanmaras-merkezli-depremler-odaginda-dogal-afetlerde-teknoloji-kullanimi. [Accessed: Jul. 08, 2024].

[11]   B. Yang, X. Xiong, H. Liu, Y. Jia, Y. Gao, A. Tolba, and X. Zhang, "Unmanned Aerial Vehicle Assisted Post-Disaster Communication Coverage Optimization Based on Internet of Things Big Data Analysis", *Sensors*, vol. 23, no. 6795, 2023.

[12]   Y. Chen, D. Yang, and J. Yu, "Multi-UAV Task Assignment With Parameter and Time-Sensitive Uncertainties Using Modified Two-Part Wolf Pack Search Algorithm," *IEEE Transactions on Aerospace and Electronic Systems*, vol. 54, no. 6, pp. 2853-2872, 2018.

[13]   L. Zhu, Y. Wang, and Z. Wu, "An Adaptive Priority Allocation for Formation UAVs in Complex Context," *IEEE Transactions on Aerospace and Electronic Systems*, vol. 57, no. 2, pp. 1002-1015, 2021.

[14]   N. M. Elfatih, E. S. Ali, and R. A. Saeed, "Navigation and Trajectory Planning Techniques for Unmanned Aerial Vehicles Swarm," in Artificial Intelligence for Robotics and Autonomous Systems Applications, A. T. Azar and A. Koubaa, Eds., vol. 1093, Studies in Computational Intelligence. Cham: Springer, 2023.

[15]   D. Xie, R. Hu, C. Wang, C. Zhu, H. Xu, and Q. Li, "A Simulation Framework of Unmanned Aerial Vehicles Route Planning Design and Validation for Landslide Monitoring," *Remote Sens.*, vol. 15, no. 24, Art. no. 5758, Dec. 2023.

[16]   S. Zhang and J. Liu, "Analysis and optimization of multiple unmanned aerial vehicle-assisted communications in post-disaster areas," *IEEE Trans. Veh. Technol.*, vol. 67, no. 12, pp. 12049-12060, Dec. 2018.

[17]   İ. Aydın and G. Altun, "Hesapsal Zekâ Yöntemleri ile İnsansız Hava Araçları için Rota Planlaması," *Dicle Üniversitesi Mühendislik Fakültesi Mühendislik Dergisi*, vol. 12, no. 1, pp. 37-45, 2021.

[18]   X. Wang, T. M. Choi, H. Liu, and X. Yue, "A novel hybrid ant colony optimization algorithm for emergency transportation problems during post-disaster scenarios," *IEEE Trans. Syst., Man, Cybern. Syst.*, vol. 48, no. 4, pp. 545-556, Apr. 2016.

[19]   X. Zhang, X. Yu, and X. Wu, "Exponential rank differential evolution algorithm for disaster emergency vehicle path planning," *IEEE Access*, vol. 9, pp. 10880-10892, 2021.

[20]   Y. Wan, Y. Zhong, A. Ma, and L. Zhang, "An accurate UAV 3-D path planning method for disaster emergency response based on an improved multiobjective swarm intelligence algorithm," *IEEE Trans. Cybern.*, vol. 53, no. 4, pp. 2658-2671, Apr. 2023.

[21]   J. Scherer et al., "An Autonomous Multi-UAV System for Search and Rescue," in *Proc. 1st Workshop Micro Aerial Vehicle Netw., Syst., Appl. Civ. Use*, May 2015, pp. 33-38.

[22]   M. Silvagni, A. Tonoli, E. Zenerino, and M. Chiaberge, "Multipurpose UAV for search and rescue operations in mountain avalanche events," *Geomatics, Nat. Hazards Risk*, vol. 8, no. 1, pp. 18-33, Jan. 2017.

[23]   R. Arnold, J. Jablonski, B. Abruzzo, and E. Mezzacappa, "Heterogeneous UAV Multi-Role Swarming Behaviors for Search and Rescue," in *Proc. 2020 IEEE Int. Conf. Cogn. Comput. Asp. Situat. Manag. (CogSIMA)*, 2020, pp. 122-128.

[24]   E. Karaköse, "Sürü İnsansız Hava Araçlarının Görev Paylaşımı için Genetik Algoritma Tabanlı Bir Yaklaşım," *Fırat Üniversitesi Mühendislik Bilim. Derg.*, vol. 34, no. 1, pp. 351-360, Mar. 2022.

[25]   L. M. Gladence, V. M. Anu, A. Anderson, I. Stanley, and S. Revathy, "Swarm Intelligence in Disaster Recovery," in *Proc. 2021 5th Int. Conf. Intell. Comput. Control Syst. (ICICCS)*, 2021, pp. 1-8.

[26]   W. Alawad, N. Ben Halima, and L. Aziz, "An Unmanned Aerial Vehicle (UAV) System for Disaster and Crisis Management in Smart Cities," *Electronics*, vol. 12, no. 4, p. 1051, Feb. 2023.

[27]   M. Bakirci and M. M. Ozer, "Post-Disaster Area Monitoring with Swarm UAV Systems for Effective Search and Rescue," in *Proc. 2023 10th Int. Conf. Recent Advances Air Space*, 2023.

[28]   R. Masroor, M. Naeem, and W. Ejaz, "Efficient deployment of UAVs for disaster management: A multi-criterion optimization approach," *Comput. Commun.*, vol. 177, pp. 185-194, 2021.

[29]   J. Wang, Y. Sun, B. Wang, & T. Ushio, "Mission-Aware UAV Deployment for Post-Disaster Scenarios: A Worst-Case SAC-Based Approach," *IEEE Transactions on Vehicular Technology*, 2023

[30]   M. Ashraf, A. Gaydamaka, B. Tan, D. Moltchanov, & Y. Koucheryavy, "Low Complexity "Algorithms for Mission Completion Time Minimization in UAV-Based Emergency Response," *IEEE Transactions on Intelligent Vehicles*, 2024.

[31]   P. Mahajan, P. Balamurugan, A. Kumar, G. S. S. Chalapathi, V. Chamola, & M. Khabbaz, "Multi-"Objective MDP-based Routing In UAV Networks For Search-based Operations," *IEEE Transactions on Vehicular Technology,* 2024.

[32] X. Li, M. Tao, S. Yang, M. A. Jan, J. Du, L.Liu, & C. Wu, "AI Empowered Intelligent Search for Path Planning in UAV-Assisted Data Collection Networks," *IEEE Internet of Things Journal*, 2024

[33] P. Wan, G. Xu, J. Chen, & Y. Zhou, "Deep Reinforcement Learning Enabled Multi-UAV Scheduling for Disaster Data Collection With Time-Varying Value," *IEEE Transactions on Intelligent Transportation Systems*, 2024

[34] M. Mitchell, "An Introduction to Genetic Algorithms," in *MIT Press,* Cambridge, MA, USA, 1998.

[35] M. Dorigo and G. Di Caro, "Ant colony optimization: a new meta-heuristic," in *Proc. 1999 Congr. Evol. Comput.-CEC99*, Washington, DC, USA, Jul. 1999, vol. 2, pp. 1470-1477.

[36] M. Quigley et al., "ROS: an open-source Robot Operating System," in *ICRA Workshop Open Source Software*, 2009, vol. 3, no. 3.2, p. 5.

[37] P. Y. O. Yoonseok, C. HanCheol, J. RyuWoon, and L. TaeHoon, "ROS Robot Programming," in *Robot Co.,* Seoul, South Korea, *Ltd.,* 2017.

[38] C. Bernardeschi, A. Fagiolini, M. Palmieri, G. Scrima, and F. Sofia, "Ros/gazebo based simulation of co-operative uavs," in *Modelling and Simulation for Autonomous Systems: 5th International Conference, MESAS 2018,* Prague, Czech Republic, Oct. 2018, Revised Selected Papers, 2019, pp. 321-334.

[39] K. Conley, "ROS/Introduction - ROS Wiki," *ROS Wiki*, 2011. [Online]. Available: http://wiki.ros.org/ROS/Introduction. [Accessed: Mar. 20, 2024].

[40] Open Robotics, "Gazebo: Tutorial: Beginner: Overview," *Gazebo Sim*, 2014. [Online]. Available: https://classic.gazebosim.org/tutorials?cat=guided_b&tut=guided_b1. [Accessed: Mar. 20, 2024].

Generation of Solitary Waves with Analytical Solution for The (3+1)-dimensional pKP-BKP Equation and Reductions

Fatma Nur KAYA SAĞLAM[1*]

[1]*Tekirdağ Namık Kemal University, Department of Mathematics, Faculty of Arts and Science, 59030 Tekirdağ, Turkey*
(ORCID: 0000-0001-7488-3254)

Abstract

In this study, new solitary wave solutions are obtained for the combination of the B-type Kadomtsev-Petviashvili (BKP) equation and the potential Kadomtsev-Petviashvili (pKP) equation, called the integrable (3+1)-dimensional pKP-BKP equation, and its two reduced forms. For this purpose, the Bernoulli auxiliary equation method, which is an ansatz-based method, is used. As a result, kink, lump, bright soliton and breather wave solutions are observed. It is concluded that this method and the results obtained for the considered pKP -BKP equations are an important step for further studies in this field.

1. Introduction

Nonlinear partial differential equations (NPDEs) are used to model the complexity of many physical, engineering, and mathematical systems [1-10]. These equations, which allow nonlinear effects to be taken into account, are essential for more accurately describing many real-world phenomena. NPDEs arise in many fields, including fluid mechanics, electromagnetism, wave propagation, and chemical reactions [11-13]. It is important that these equations are integrable because this makes them more mathematically accessible and solvable, making them easier to use in various applications [14]. It also means that these equations can have analytical solutions. Analytical solutions represent the general solution of the equations and are often useful for understanding the behavior of the system. By combining one integrable system with another, many different unexpected results can be seen [15]. There are many examples in the literature [16-20,31-33]. Recently, the pKP-BKP equation also remains important for researchers to obtain more insights and solitary wave results [20-26].

The nonlinear pKP-BKP equation is obtained by considering the potential Kadomtsev-Petviashvili (pKP) equation and the B-type Kadomtsev-Petviashvili (BKP) equation [26]. The pKP (potential Kadomtsev–Petviashvili) equation [29], which models nonlinear and nonlinear waves in two-dimensional space with an additional degree of freedom, has been used in fields as diverse as plasma physics, fluid dynamics, and nonlinear optics [20,21]. The BKP (B-type Kadomtsev–Petviashvili) equation, which describes the interactions between exponentially localized structures, is an important model for the shallow water wave in fluids and the electrostatic wave potential in plasmas [27,28]. The pKP-BKP Eq.(1), which shows the double effect of the newly developed pKP equation and the BKP equation, has been a subject of curiosity and interest to researchers [20,21].

In this paper, the Bernoulli equation method is utilized to obtain solitary wave solutions for a general form of the (3+1)-dimensional pKP-BKP equation [26] as follows:

$$\Delta_{xt} + \alpha \left(15 \left(\Delta_x \right)^3 + 15 \Delta_x \Delta_{xxx} + \Delta_{xxxxx} \right)_x$$

$$+ \beta \left(6 \Delta_x \Delta_{xx} + \Delta_{xxxx} \right) + \gamma \left(\Delta_{xxxy} + 3 \left(\Delta_x \Delta_y \right)_x \right) \tag{1}$$

$$+ a \Delta_{xx} + b \Delta_{xy} + c \Delta_{xz} - \frac{\gamma^2}{5\alpha} \Delta_{yy} = 0,$$

where some extra terms are inserted into the pKP-BKP equation, such as $b\Delta_{xy}$ and $c\Delta_{xz}$ and $\Delta = \Delta(x, y, z, t)$. When

a. $\gamma = 0$

$$\Delta_{xt} + \alpha\left(15(\Delta_x)^3 + 15\Delta_x\Delta_{xxx} + \Delta_{xxxxx}\right)_x \qquad (2)$$
$$+\beta\left(6\Delta_x\Delta_{xx} + \Delta_{xxxx}\right) + a\Delta_{xx} + b\Delta_{xy} + c\Delta_{xz} = 0,$$

eliminating three expressions from the pKP-BKP equation,

b. $\beta = 0$

$$\Delta_{xt} + \alpha\left(15(\Delta_x)^3 + 15\Delta_x\Delta_{xxx} + \Delta_{xxxxx}\right)_x \qquad (3)$$
$$+\gamma\left(\Delta_{xxxy} + 3\left(\Delta_x\Delta_y\right)_x\right)$$
$$+a\Delta_{xx} + b\Delta_{xy} + c\Delta_{xz} + \mu\Delta_{yy} = 0,$$

eliminating two expressions from the pKP-BKP equation, reduction to two equations will be investigated.

Wazwaz [26] obtained breath-wave solutions for the (3+1)-dimensional pKP-BKP equation using the Hirota bilinear method for Eq.(1). In the study of Ma [21], multiple soliton solutions and lumped solutions were determined. And these newly designed equations were verified to be Painlevé integrable, yielding multiple soliton solutions and lumped solutions for each model developed [26]. For the (3+1)-dimensional pKP-BKP model, several studies have been conducted in the literature [20-26] and the aim of this study is to obtain new results to improve the previous findings.

In summary, the structure of this paper is as, In Section 2 the fundamental properties of the utilized method are desribed and the steps to be used. In Section 3, solutions for the (3+1)-dimensional pKP-BKP equation and its two reduced forms are presented and supported by figures for a better understanding of the dynamics of these solutions. In Section 4, we have given a comparison. In Section 5 the gained results are presented.

2. Bernoulli Auxiliary Equation Method

3. Implementation Of Generalized (3+1)-Dimensional pKP-BKP Equation And Reduced Forms
3.1. The application of Eq. (1)

First of all, to reduce Eq.(1) to an ODE, using the classical wave transformation

$\Delta(x, y, z, t) = u(\xi), \quad \xi = \tau x + \rho y + \varphi z - dt$ where $\tau \neq 0$, $\rho \neq 0$, $\varphi \neq 0$ and $d \neq 0$, the Eq.(1) becomes:

In this part of the study, we will use the Bernoulli auxiliary equation method to obtain analytical solutions to nonlinear equations. To obtain a solution using this method, the following steps must be followed. Suppose to solve the nonlinear partial differential equation given in the following form:

$$P\left(\Delta, \Delta_x, \Delta_y, \Delta_z, \Delta_t, \Delta_{xx}, \ldots\right) = 0, \qquad (4)$$

where P is a function of $\Delta(x, y, z, t)$. Assume the following solitary wave transform structure:
$\Delta(x, y, z, t) = u(\xi), \quad \xi = \tau x + \rho y + \varphi z - dt$, $d \neq 0$,
Eq. (4) reduces to the following ordinary differential equation (ODE) using the above transformation,

$$O\left(u, \frac{\partial u}{\partial \xi}, \frac{\partial u}{\partial \xi^2}, \frac{\partial u}{\partial \xi^3}, \ldots\right) = 0. \qquad (5)$$

Assume that the Eq. (5) has the exactly the following solution:

$$u(\xi) = \sum_{i=0}^{N} g_i z^i(\xi), \qquad (6)$$

where g_i are the parameters to be determined later. According to the homogeneous equilibrium principle, the value of N is found by adjusting the nonlinear term and the highest order subterms in Eq. (5). The Bernoulli auxiliary equation method [30] is used to determine the function $z(\xi)$ in Eq. (6):

$$\frac{dz}{d\xi} = Pz(\xi) + Qz^2(\xi), \qquad (7)$$

where P and Q are constants other than zero and its solution is $z(\xi) = -\dfrac{P}{e^{-P\xi}PC_1 - Q}$ where C_1 is a constant of integration. Substituting Eq. (6) and Eq. (7) into Eq. (5) and setting the coefficients of $z(\xi)$ equal to zero gives a set of algebraic equations that, when solved, give the values of the elements. By calculating the results of these algebraic equations and substituting the aforementioned solution sets into Eq. (6), we can easily obtain the explicit solutions of Eq. (4).

$$\alpha(45\tau^4\Delta'^2\Delta'' + 15\tau^5\Delta''\Delta''' + 15\tau^5\Delta'\Delta^{iv} + \tau^6\Delta^{vi}) \quad (8)$$
$$+\beta(6\tau^3\Delta'\Delta'' + \tau^4\Delta^{iv}) + \gamma(\tau^3\rho\Delta^{iv} + 6\tau^2\rho\Delta'\Delta'')$$
$$+\left(a\tau^2 + b\tau\rho + c\tau\varphi - \frac{\gamma^2\rho^2}{5\alpha} - \tau d\right)\Delta'' = 0.$$

When the $\Delta^{(v)} = N+5$ and $(\Delta')^3 = 3(N+1)$ terms in Eq.(1) are balancing, $N = 1$ is obtained. And from here we found,

$$z^6(\xi): 8Q^2\tau^2 + 6Q\tau g_1 + g_1^2 = 0,$$

$$z^5(\xi): (2Q\tau + g_1)(560P^2Q\tau^3\alpha + 135P^2\tau^2\alpha g_1 + 4Q\tau\beta + 4Q\rho\gamma) = 0,$$

$$z^4(\xi): (2Q\tau + g_1)(70P^2Q\tau^3\alpha + 15P^2\tau^2\alpha g_1 + 2Q\tau\beta + 2Q\rho\gamma) = 0,$$

$$z^3(\xi): 24\left(\frac{25P^2Q\tau^3\beta}{12} + \left(\frac{25}{12}P^2\gamma Q\rho + P^2 g_1\beta\right)\tau^2 + \left(P^2 g_1\rho\gamma + \frac{Qa}{12}\right)\tau + \frac{Q(b\rho + c\varphi - d)}{12}\right)Q\tau$$

$$+45\left(\frac{602}{45}Q^2\tau^2 + \frac{26}{3}Q\tau g_1 + g_1^2\right)\tau^4 P^4\alpha - \frac{2Q^2\gamma^2\rho^2}{5\alpha} = 0,$$

$$z^2(\xi): 10\left(\frac{21Q\tau}{10} + g_1\right)\tau^5 P^4\alpha + -\frac{Q\gamma^2\rho^2}{5\alpha}$$

$$+2\tau\left(\frac{5P^2Q\tau^3\beta}{2} + \left(\frac{5}{2}P^2 Q\gamma\rho + P^2 g_1\beta\right)\tau^2 + \left(P^2\gamma\rho g_1 + \frac{Qa}{2}\right)\tau + \frac{Q(b\rho + c\varphi - d)}{2}\right) = 0,$$

$$z^1(\xi): P^4\tau^6\alpha + \tau\left(P^2\beta\tau^3 + P^2\gamma\rho\tau^2 + a\tau + b\rho + c\varphi - d\right) - \frac{\gamma^2\rho^2}{5\alpha} = 0.$$

$$u(\xi) = \sum_{i=0}^{1} g_i z^i(\xi) = g_0 + g_1 z(\xi), \quad (9)$$

where g_0 and g_1 are constants. Substituting Eq.(7) and Eq.(9) into Eq.(8), equating all coefficients of $z^i(\xi)$, $i = 1,\ldots,7$ to zero, gives the following set of algebraic equations:

The following results are obtained by solving the above equations:

Case 1:

$$d = -\frac{20\alpha^2 P^4\tau^6 - 5a\tau^2\alpha - 5b\tau\rho\alpha - 5c\tau\varphi\alpha + \gamma^2\rho^2}{5\alpha\tau}, \quad P = \frac{\sqrt{-5\tau\alpha(\beta\tau + \gamma\rho)}}{5\tau^2\alpha}, \quad (10)$$

$$\Delta(x,y,z,t) = g_0 - \frac{2Q\sqrt{-5\tau\alpha(\beta\tau + \gamma\rho)}}{5\tau\alpha\left(\exp\left(-P(-dt + \rho y + \tau x + \varphi z)\right)\frac{C_1\sqrt{-5\tau\alpha(\beta\tau + \gamma\rho)}}{5\tau^2\alpha} - Q\right)}. \quad (11)$$

Figure 1 plots the 3D and contour profiles of solution Eq. (11) with various values of parameters

(a) $y = 1$, $z = 2$, $\tau = 0.05$, $\alpha = 0.5$, $g_1 = 1$, $a = 1$, $b = 1.8$, $c = 1.3$, $g_0 = 1$, $C_1 = 0.1$, $Q = 1.7$, $\gamma = -1$, $\beta = 0.78$, $\rho = 1.5$, $\varphi = 0.07$ and (b) is a contour map

that can be useful for analysis of the difference between two shapes. The resulting shape is a kink soliton, which shows a localized perturbation of the wave along a phase shift.

(a)   (b)
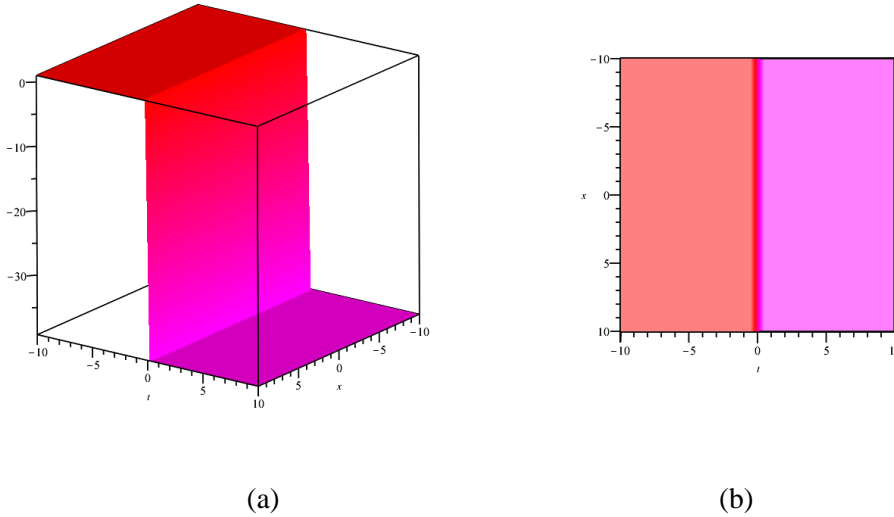
Figure 1. (a) 3D and (b) contour plots of the kink solution.

Case 2:

$$g_1 = -2Q\tau , \quad d = -\frac{-5\alpha^2 P^4 \tau^6 - 5\alpha\beta P^2 \tau^4 - 5\alpha P^2 \gamma\rho\tau^3 - 5a\tau^2\alpha - 5b\tau\rho\alpha - 5c\tau\varphi\alpha + \gamma^2\rho^2}{5\alpha\tau} , \tag{12}$$

$$\Delta(x, y, z, t) = g_0 - \frac{2QP\tau}{\exp(-P(-dt + \rho y + \tau x + \varphi z)C_1 P - Q)} . \tag{13}$$

Figure 2 shown the 3D and contour profiles of solution Eq.(13) with various values of parameters (a) $y = 1$, $z = 2$, $\tau = 0.05$, $\alpha = 0.5$, $P = 2$, $a = 1$, $b = 1.8$, $c = 1.3$, $g_0 = 1$, $C_1 = 0.1$, $Q = 1.7$, $\gamma = -1$, $\beta = 0.78$, $\rho = 1.5$, $\varphi = 0.07$ and (b) is a contour plot

that can be useful for analysis of the difference between two shapes. The resulting shape is a lump soliton.

(a)	(b)
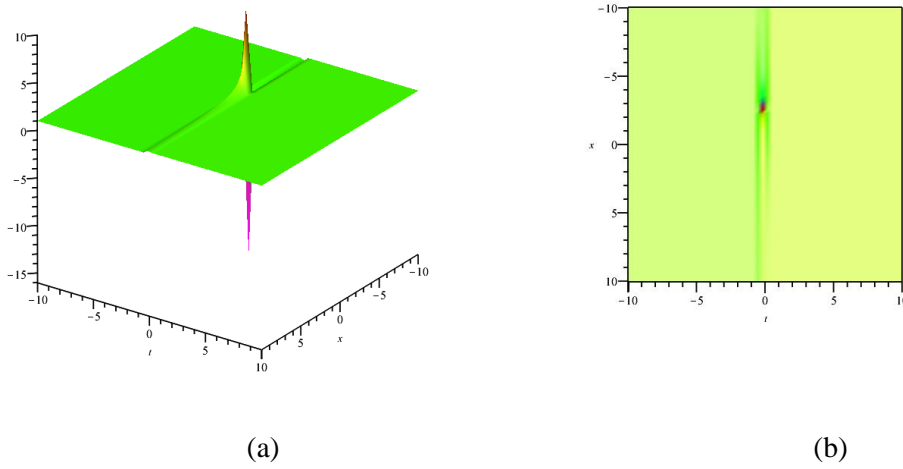
Figure 2. (a) 3D and (b) contour plots of the lump solution.

Case 3:

$$\alpha = \frac{4\beta^2\tau^2 + 8\beta\gamma\rho\tau + 9\gamma^2\rho^2}{25\tau(a\tau + b\rho + c\varphi - d)}, \quad Q = -\frac{g_1}{4\tau}, \quad P = \frac{\sqrt{-5\tau\alpha(\beta\tau + \gamma\rho)}}{5\tau^2\alpha}, \quad (14)$$

$$\Delta(x, y, z, t) = g_0 + \frac{4g_1\sqrt{-5\tau\alpha(\beta\tau + \gamma\rho)}}{4\exp(-P(-dt + \rho y + \tau x + \varphi z))C_1\sqrt{-5\tau\alpha(\beta\tau + \gamma\rho)} + 5g_1\tau\alpha}. \quad (15)$$

Figure 3 shown the 3D and contour profiles of solution Eq.(15) with various values of parameters (a) $y = 0$, $z = 0$, $\tau = 0.5$, $\alpha = 0.02$, $g_1 = 2$, $a = 3$, $b = 1.8$, $c = 1.3$, $g_0 = 1$, $C_1 = 0.5$, $\gamma = -1.1$, $\beta = 0.78$, $\rho = 1.5$, $\varphi = 0.07$, $d = 1.1$ and (b) is a contour plot that can be useful for analysis of the between two shapes. Such solitons is determined by the local structure of the soliton.

(a)   (b)
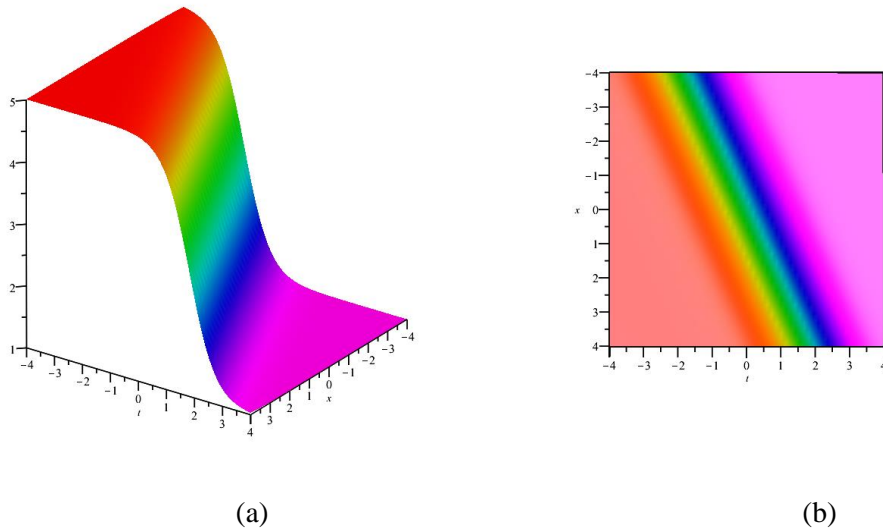
Figure 3. (a) 3D and (b) contour plots of the solution Eq.(15).

3.2. The application of Eq. (2)

To reduce Eq.(2) to an ODE, using the classical wave transformation

$\Delta(x, y, z, t) = u(\xi)$, $\xi = \tau x + \rho y + \varphi z - dt$ where

$\tau \neq 0$, $\rho \neq 0$, $\varphi \neq 0$ and $d \neq 0$, the Eq.(2) becomes:

$$\alpha(45\tau^4\Delta'^2\Delta'' + 15\tau^5\Delta''\Delta''' + 15\tau^5\Delta'\Delta^{iv} + \tau^6\Delta^{vi}) \quad (16)$$
$$+\beta(6\tau^3\Delta'\Delta'' + \tau^4\Delta^{iv})$$
$$+(a\tau^2 + b\tau\rho + c\tau\varphi - \tau d)\Delta'' = 0.$$

$$g_1 = -2Q\tau, d = P^4\alpha\tau^5 + P^2\beta\tau^3 + a\tau + b\rho + c\varphi, \quad (18)$$

Balancing Eq.(8), we found $N = 1$. Apply the transform,

$$u(\xi) = g_0 + g_1 z(\xi), \quad (17)$$

where g_0 and g_1 are constants. Inserting Eq. (7) and Eq. (17) into Eq. (16) and setting all coefficients of $z^i(\xi)$, $i = 1, \ldots, 7$ to zero results in the set of algebraic equations. Three cases of the parameters obtained by solving this algebraic equation are discussed as follows:

Case 1:

$$\Delta(x, y, z, t) = g_0 + \frac{4Q\beta}{5\alpha P\tau\left(\exp\left(-\frac{\sqrt{-\frac{5\beta}{\alpha}}(-dt + \rho y + \tau x + \varphi z)}{5\tau}\right)\frac{C_1\sqrt{-\frac{5\beta}{\alpha}}}{5\tau} - Q\right)}. \quad (19)$$

Figure 4 shown the 3D and contour profiles of solution Eq.(19) with various values of parameters (a) $y = 1$, $z = 2$, $\tau = 0.5$, $\alpha = 0.5$, $a = 1$, $b = 1.8$, $c = 1.3$, $g_0 = 1$, $C_1 = 0.1$, $Q = 1.7$, $\gamma = -1$, $\beta = 0.78$, $\rho = 1.5$, $\varphi = 0.07$ and (b) is a contour plot that can be useful for analysis of the between two shapes. Breather wave solution is obtained for the (3 + 1) dimensional pKP - BKP Eq.(2).

<div align="center">(a)   (b)</div>
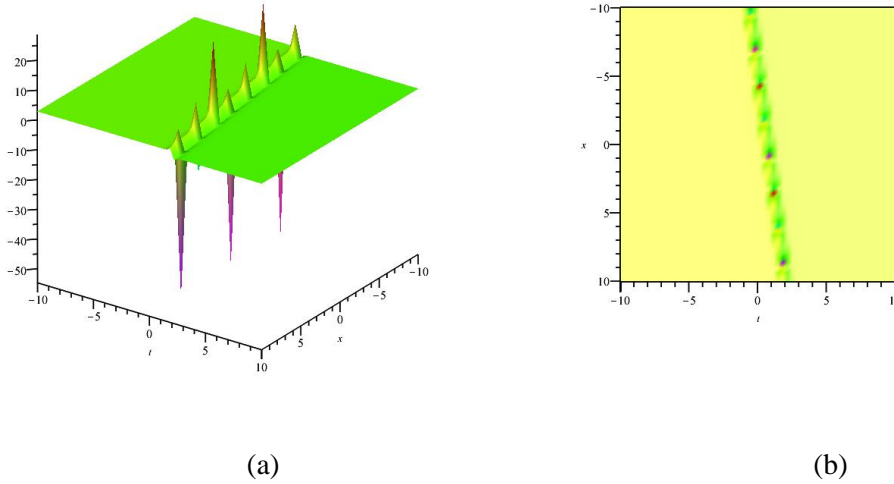
Figure 4. (a) 3D and (b) contour plots of the breather solution.

Case 2:

$$d = \frac{25P\alpha b\rho + 25P\alpha c\varphi + 25a\alpha\sqrt{-\dfrac{\beta}{5\alpha}} - 4\beta^2\sqrt{-\dfrac{\beta}{5\alpha}}}{25\alpha P}, \quad P = \frac{\sqrt{-\dfrac{5\beta}{\alpha}}}{5\tau}, \quad g_1 = -\frac{4Q\sqrt{-\dfrac{\beta}{5\alpha}}}{P}, \tag{20}$$

$$\Delta(x,y,z,t) = g_0 + \frac{4Q\beta}{\alpha\sqrt{-\dfrac{5\beta}{\alpha}}\left(\exp\left(-\dfrac{\sqrt{-\dfrac{5\beta}{\alpha}}\,(-dt + \rho y + \tau x + \varphi z)}{5\tau}\right)\dfrac{C_1\sqrt{-\dfrac{5\beta}{\alpha}}}{5\tau} - Q\right)}. \tag{21}$$

Figure 5 plots the 3D and contour maps of solution Eq.(17) with different values of parameters (a) $y = 0$, $z = 0$, $\tau = 0.82$, $\alpha = 0.5$, $a = 1$, $b = 1.8$, $c = 1.3$, $g_0 = 1$, $C_1 = 0.3$, $Q = 1.7$, $\gamma = 1$, $\beta = -0.78$, $\rho = 1.5$, $\varphi = 0.07$ and (b) is a contour plot that can be useful for analysis of the between two shapes. One bright soliton solution is found for the (3+ 1) dimensional pKP - BKP Eq.(2).

<div style="text-align:center">(a)</div> <div style="text-align:center">(b)</div>
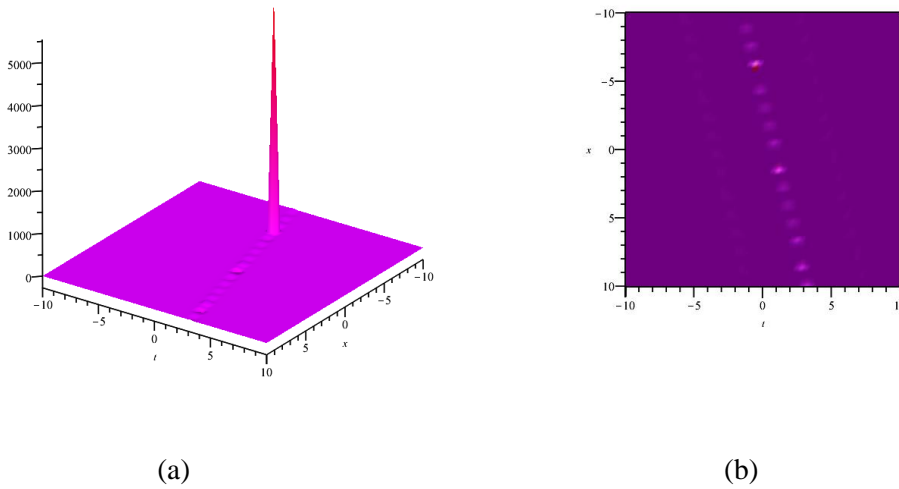
Figure 5. (a) 3D graph of the solution Eq.(17) and (b) contour graph of the solution Eq.(21).

Case 3:

$$\alpha = \frac{4\beta^2}{25(a\tau + b\rho + c\varphi - d)}, \quad Q = -\frac{g_1}{4\tau}, \quad P = \frac{\sqrt{-5\alpha\beta}}{5\tau\alpha}, \tag{22}$$

$$\Delta(x, y, z, t) = g_0 - \frac{4g_1\beta}{-4\exp\left(-\dfrac{\sqrt{-5\alpha\beta}\,(-dt + \rho y + \tau x + \varphi z)}{5\alpha\tau}\right)C_1\beta + \sqrt{-5\alpha\beta}\,g_1}. \tag{23}$$

Figure 6 shows the 3D and contour maps of solution Eq.(23) with different values of parameters (a) $y = 0$, $z = 5$, $\tau = 0.08$, $d = 0.5$, $a = 1$, $b = 1.8$, $c = 1.3$, $g_0 = 1$, $C_1 = 0.1$, $Q = 1.7$, $\gamma = -1$, $\beta = -0.78$, $\rho = 0.5$, $\varphi = 0.04$, $g_1 = 1$ and (b) is a contour plot that can be useful for analysis of the between two shapes. Kink solution is obtained for the (3+ 1) dimensional pKP - BKP Eq.(2).

(a)   (b)
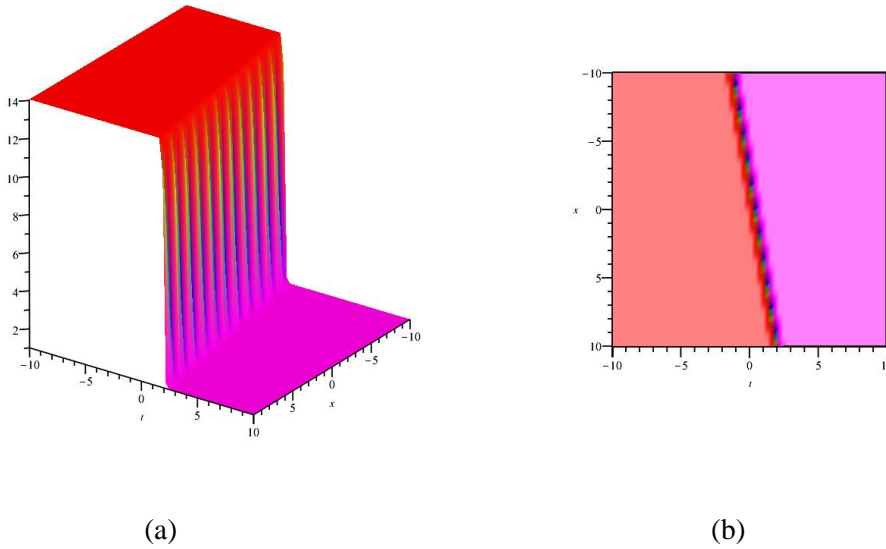
Figure 6. (a) 3D graph of the kink solution Eq.(23) and (b) contour graph of the kink solution Eq.(23).

3.3. The application of Eq. (3)

Reducing Eq.(3) to an ODE, using the classical wave transformation

$\Delta(x, y, z, t) = u(\xi)$, $\xi = \tau x + \rho y + \varphi z - dt$ where $\tau \neq 0$, $\rho \neq 0$, $\varphi \neq 0$ and $d \neq 0$, the Eq.(3) is transformed into:

$$\alpha(45\tau^4\Delta'^2\Delta'' + 15\tau^5\Delta''\Delta''' + 15\tau^5\Delta'\Delta^{iv} + \tau^6\Delta^{vi})$$
$$+\gamma(\tau^3\rho\Delta^{iv} + 6\tau^2\rho\Delta'\Delta'') \tag{24}$$
$$+\left(a\tau^2 + b\tau\rho + c\tau\varphi + \mu\rho^2 - \tau d\right)\Delta'' = 0.$$

If we balance Eq.(8), we find $N = 1$. The use of the conversion,

$$u(\xi) = g_0 + g_1 z(\xi), \tag{25}$$

where g_0 and g_1 are constants. Exchange Eq.(7) and Eq.(25) into Eq.(24), equating all coefficients of $z^i(\xi)$, $i = 1,\ldots,7$ to zero, provides the set of algebraic equation systems. We found parameters corresponding to the following cases when solving these systems:

Case 1:

$$g_1 = -2Q\tau, d = \frac{P^4\alpha\tau^6 + P^2\gamma\rho\tau^3 + a\tau^2 + b\tau\rho + c\tau\varphi + \mu\rho^2}{\tau}, \tag{26}$$

$$\Delta(x, y, z, t) = g_0 - \frac{2QP\tau}{\exp\left(-P(-dt + \rho y + \tau x + \varphi z)C_1P - Q\right)}. \tag{27}$$

Figure 7 plots the 3D and contour profiles of solution Eq.(27) with various values of parameters (a) $y = 1$, $z = 2$, $\tau = 0.05$, $\alpha = 0.5$, $g_1 = 2$, $a = 1$, $b = 1.8$, $c = 1.3$, $g_0 = 1$, $C_1 = 0.1$, $Q = 2$, $\gamma = -1$, $\mu = 0.06$, $\rho = 1.5$, $\varphi = 0.07$, $d = 1.1$ and (b) is a contour map that can be useful for analysis of the difference between two shapes. Two lump soliton solution is found for the $(3 + 1)$ dimensional pKP - BKP Eq.(3).

(a)   (b)
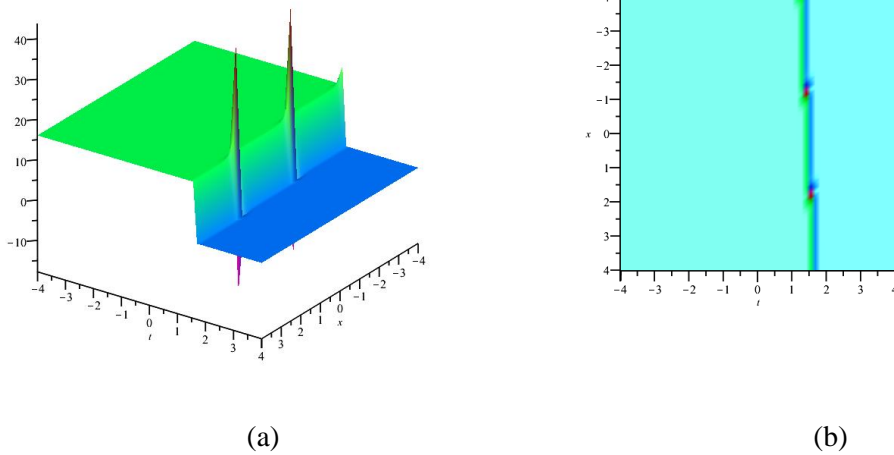
Figure 7. (a) 3D and (b) contour plots of the two lump solution Eq.(27).

Case 2:

$$g_1 = -4Q\tau \, , \, d = -\frac{-25P^4\alpha^2\mu\tau^5 + 4P^4\alpha\gamma^2\tau^5 + 5P^2\alpha b\gamma\tau^3 - a\tau\gamma^2 - c\gamma^2\varphi}{\gamma^2} \, , \, \rho = -\frac{5P^2\alpha\tau^3}{\gamma} \, , \tag{28}$$

$$\Delta\left(x, y, z, t\right) = g_0 - \frac{2QP\tau}{\exp\left(-P\left(-dt - \frac{5P^2\alpha\tau^3}{\gamma} y + \tau x + \varphi z\right)C_1 P - Q\right)}. \tag{29}$$

Figure 8 plots the (a) 3D and (b) contour maps of solution Eq.(29) with different values of parameters for $y = 0$, $z = 0$, $P = 2$, $\tau = 0.05$, $\alpha = 0.5$, $g_1 = 1$, $a = 2$, $b = 1.8$, $c = 1.3$, $g_0 = -1$, $C_1 = 0.5$, $Q = 2$, $\gamma = -1$, $\mu = 0.06$, $\varphi = 0.07$, $d = 1.1$. The one bright soliton shape and amplitude modulation of the soliton are shown in the graph.

(a)   (b)
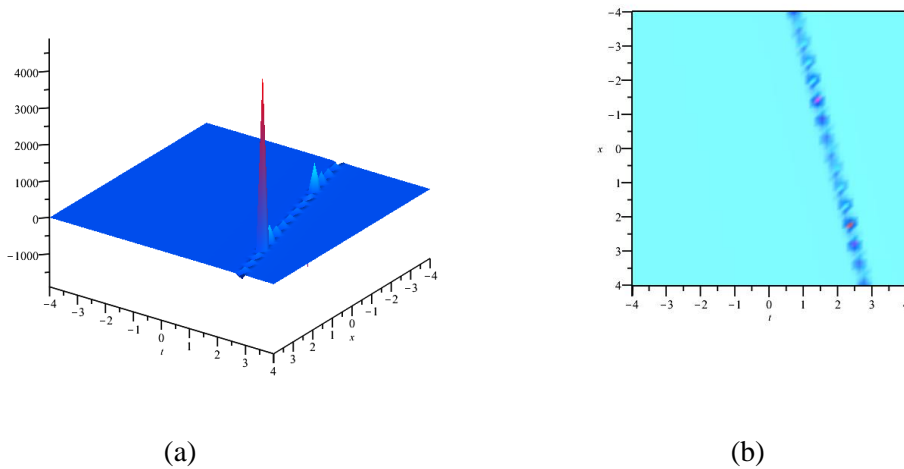
Figure 8. (a) 3D and (b) contour plots of Eq.(29) when $y = 0$, $z = 0$, $P = 2$, $\tau = 0.05$, $\alpha = 0.5$, $g_1 = 1$, $a = 2$, $b = 1.8$, $c = 1.3$, $g_0 = -1$, $C_1 = 0.5$, $Q = 2$, $\gamma = -1$, $\mu = 0.06$, $\varphi = 0.07$, $d = 1.1$.

Case 3:

$$a = \frac{-25\alpha b\rho\tau - 25\alpha c\tau\varphi - 25\alpha\mu\rho^2 + 4\gamma^2\rho^2 + 25\alpha d\tau}{25\alpha\tau^2}, \quad Q = -\frac{g_1}{4\tau}, \quad P = \frac{\sqrt{-5\alpha\tau\gamma\rho}}{5\tau^2\alpha}, \tag{30}$$

$$\Delta(x, y, z, t) = g_0 - \frac{4g_1\sqrt{-5\alpha\tau\gamma\rho}}{4\exp\left(-\dfrac{\sqrt{-5\alpha\tau\gamma\rho}\,(-dt + \rho y + \tau x + \varphi z)}{5\alpha\tau^2}\right)C_1\sqrt{-5\alpha\tau\gamma\rho} + 5\alpha\tau g_1}. \tag{31}$$

Figure 9 shows the (a) 3D and (b) contour maps of solution Eq.(31) with different values of parameters for $y = 0$, $z = 2$, $\tau = 0.07$, $\alpha = 1.7$, $g_1 = 2$, $a = 3$, $b = 0.02$, $c = 2$, $g_0 = 1$, $C_1 = 0.8$, $Q = 1$, $\gamma = -1$, $\mu = 0.2$, $\varphi = 0.07$, $d = 1.7$, $\rho = 0.5$. The obtained kink solution is important for the understanding of the dynamics and the explanation of complex phenomena such as phases and pattern formation.
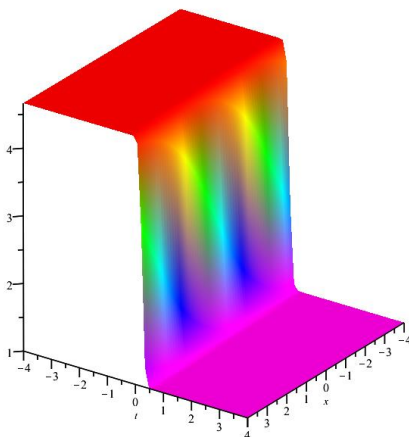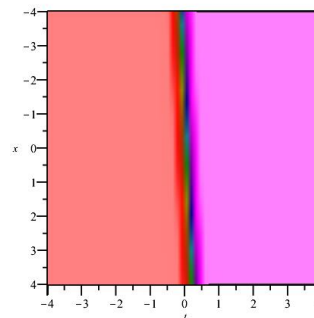
(a)   (b)

Figure 9. Select $y = 0$, $z = 2$, $\tau = 0.07$, $\alpha = 1.7$, $g_1 = 2$, $a = 3$, $b = 0.02$, $c = 2$, $g_0 = 1$, $C_1 = 0.8$, $Q = 1$, $\gamma = -1$, $\mu = 0.2$, $\varphi = 0.07$, $d = 1.7$, $\rho = 0.5$ for (a) 3D and (b) contour plots of Eq.(31).

4. Comparison

In this section, we compare the obtained solutions with the solutions obtained by Wazwaz [26] using the Hirota bilinear method, the tan method, and the tanh method. Wazwaz used the Hirota bilinear method, the tan method, and the tanh method to search for soliton solutions of the (3+1) dimensional pKP-BKP equation for which the kink, singular, periodic, and exponential solutions exist. In this context, new solutions with many physical properties such as kink, lump, breather and bright soliton have been shown. On the other hand, using the Bernoulli auxiliary equation method, we found nine exact solutions of the (3+1) dimensional pKP-BKP equation. [26] shows that there are significant differences between them. This proves the superiority of the Bernoulli auxiliary equation method over other computational methods.

Also a new extended direct algebraic method proposed in [34] focuses on providing closed-form solutions for a wide class of nonlinear pseudo-parabolic models by direct algebraic manipulations, while the Bernoulli auxiliary equation method can provide fast and efficient solutions for specific models and conditions, since it is usually applied under specific conditions. Thus, we can state that this method provides a powerful, efficient and easy-to-use option for all NPDEs.

5. Conclusion

In this study we derive solutions for the (3+1)-dimensional pKP-BKP equation and its two reduced forms. We derive different types of wave solutions for each of the equations studied. Solitons are types of waves in which energy is transported in a localized form that remains unchanged in time and space. They include bright solitons, dark solitons, and kink solitons. By giving different values to the parameters in the master equation, different types of soliton solutions are obtained. Bright soliton waves, which occur in many nonlinear systems and are waves in which the energy or intensity increase is localized in a specific region, are constructed in Figs. 5 and 8. Kink soliton waves that result from changes in the environment or from local changes in the structure of the object are observed in Figs. 1, 6, and 9. Also

breather waves, which are waves that occur in a given medium and spontaneously change their wavelength or form certain periodic or quasiperiodic shapes, are observed in Figure 4. Figure 7 shows a lump wave, which is defined as a wave with a solitonic structure, usually carrying a localized energy density. It is believed that these solutions will make an important contribution to the understanding of nonlinear phenomena. 3D and contour plots are presented together to understand the dynamics of these wave solutions. 3-D graphs show how the wave varies in space and time, while contour graphs show the wave as an array of lines connecting points of the same magnitude. It has been observed that different solutions emerge from those obtained in previous studies [20-26]. This will provide a basis for future studies on the pKP-BKP equation.

Acknowledgment

The author would like to thank the reviewers who have contributed to the improvement of the article with their valuable opinions and assessments.

Statement of Research and Publication Ethics

The study complies with the ethics of research and publication.

References

[1]   I. R. Rahmonov, J. Tekić, P. Mali, A. Irie, A. Plecenik, and Y. M. Shukrinov, "Resonance phenomena in an annular array of underdamped Josephson junctions," *Physical Review B*, vol. 101, no. 17, p. 174515, 2020.

[2]   L. F. Guo and W. R. Xu, "The traveling wave mode for nonlinear Biswas–Milovic equation in magneto-optical wave guide coupling system with Kudryashov's law of refractive index," *Results in Physics*, vol. 27, p. 104500, 2021.

[3]   J. J. Su, Y. T. Gao, and C. C. Ding, "Darboux transformations and rogue wave solutions of a generalized AB system for the geophysical flows," *Applied Mathematics Letters*, vol. 88, pp. 201–208, 2019.

[4]   S. Kumar and S. K. Dhiman, "Lie symmetry analysis, optimal system, exact solutions and dynamics of solitons of a (3+ 1)-dimensional generalised BKP–Boussinesq equation," *Pramana*, vol. 96, no. 1, p. 31, 2022.

[5]   Y. Liu and Y. Yang, "Rogue wave solutions for the 3+ 1-dimensional generalized Camassa–Holm–Kadomtsev–Petviashvili equation," *Chinese Journal of Physics*, vol. 86, pp. 508-514, 2023.

[6]   K. Dysthe, H. E. Krogstad, and P. Müller, "Oceanic rogue waves," *Annu. Rev. Fluid Mech.*, vol. 40, pp. 287-310, 2008.

[7]   J. M. Dudley, G. Genty, A. Mussot, A. Chabchoub, and F. Dias, "Rogue waves and analogies in optics and oceanography," *Nature Reviews Physics*, vol. 1, no. 11, pp. 675-689, 2019.

[8]   H. Chen and J. L. Bona, "Periodic traveling-wave solutions of nonlinear dispersive evolution equations", 2013.

[9]   Y. Zhang, J. W. Yang, K. W. Chow, and C. F. Wu, "Solitons, breathers and rogue waves for the coupled Fokas–Lenells system via Darboux transformation," *Nonlinear Analysis: Real World Applications*, vol. 33, pp. 237-252, 2017.

[10] B. Frisquet, B. Kibler, and G. Millot, "Collision of Akhmediev breathers in nonlinear fiber optics," *Physical Review X*, vol. 3, no. 4, p. 041032, 2013.

[11] K.-J. Wang, "Soliton molecules and other diverse wave solutions of the (2+1)-dimensional Boussinesq equation for the shallow water," *Eur. Phys. J. Plus*, vol. 138, article number 891, 2023.

[12] J. Ahmad and Z. Mustafa, "Analysis of soliton solutions with different wave configurations to the fractional coupled nonlinear Schrödinger equations and applications," *Opt. Quantum Electron.*, vol. 55, article number 1228, 2023.

[13] A. Ali, J. Ahmad, and S. Javed, "Investigating the dynamics of soliton solutions to the fractional coupled nonlinear Schrödinger model with their bifurcation and stability analysis," *Opt. Quantum Electron.*, vol. 55, article number 829, 2023.

[14] M. Wadati, K. Konno, and Y. H. Ichikawa, "New integrable nonlinear evolution equations," *Journal of the Physical Society of Japan*, vol. 47, no. 5, pp. 1698-1700, 1979.

[15] A. M. Wazwaz, "Two kinds of multiple wave solutions for the potential YTSF equation and a potential YTSF-type equation," *J Appl Nonlinear Dyn*, vol. 1, pp. 51–8, 2012.

[16] R. Hirota, "The direct method in soliton theory," Cambridge University Press, 2004.

[17] A. M. Wazwaz, "Partial differential equations and solitary waves theory," *Springer and HEP*, Berlin, 2009.

[18] A. M. Wazwaz, "Two kinds of multiple wave solutions for the potential YTSF equation and a potential YTSF-type equation," *J Appl Nonlinear Dyn*, vol. 1, pp. 51–8, 2012.

[19] S. Y. Zhu, D.-X. Kpng, and Lou, "Dark KortewegDe Vrise System and its higher-dimensional deformations," *Chin Phys Lett*, vol. 40, p. 080201, 2023.

[20] A. M. Wazwaz, "New painlevé integrable (3+1)-dimensional combined pKP-BKP equation: Lump and multiple soliton solutions," *Chinese Phys Lett*, vol. 40, p. 12050, 2023.

[21] W. X. Ma, "N-soliton solution of a combined pKP–BKP equation," *J Geom Phys*, vol. 165, p. 104191, 2021.

[22] Y. Feng and S. Bilige, "Resonant multi-soliton, M-breather, M-lump and hybrid solutions of a combined pKP–BKP equation," *J Geom Phys*, vol. 169, p. 104322, 2021.

[23] Z.-Y. Ma, J.-X. Fei, W.-P. Cao, and H.-L. Wu, "The explicit solution and its soliton molecules in the (2+1)-dimensional pKP-BKP equation," *Results Phys*, vol. 35, p. 105363, 2022.

[24] K. U. Tariq, A. M. Wazwaz, and R. N. Tufail, "Lump, periodic and travelling wave solutions to the (2+1)-dimensional pKP–BKP model," *Eur Phys J Plus*, vol. 137, p. 1100, 2022.

[25] F. N. K. Sağlam and S. Ahmad, "Stability analysis and retrieval of new solitary waves of (2+ 1)-and (3+ 1)-dimensional potential Kadomtsev–Petviashvili and B-type Kadomtsev–Petviashvili equations using auxiliary equation technique," *Modern Physics Letters B*, vol. 2450413, 2024.

[26] A. M. Wazwaz, "Breather wave solutions for an integrable (3+ 1)-dimensional combined pKP–BKP equation," *Chaos, Solitons & Fractals*, vol. 182, p. 114886, 2024.

[27] A. M. Wazwaz, "Abundant solutions of distinct physical structures for three shallow water waves models," *Discontinuity Nonlinearity Complex*, vol. 6, pp. 295–304, 2017.

[28] A. M. Wazwaz, "A variety of distinct kinds of multiple soliton solutions for a (3+1)-dimensional nonlinear evolution equations," *Math Methods Appl Sci*, vol. 36, pp. 349–57, 2013.

[29] A. R. Adem and C. M. Khalique, "New exact solutions and conservation laws of a coupled Kadomtsev–Petviashvili system," *Comput & Fluids*, vol. 81, pp. 10–6, 2013.

[30] Z. Pinar, "Analytical studies for the Boiti–Leon–Monna–Pempinelli equations with variable and constant coefficients," *Asymptotic Analysis*, vol. 117, no. 3-4, pp. 279-287, 2020.

[31] V. Ala, "Exact solutions of nonlinear time fractional Schrödinger equation with beta-derivative," *Fundamentals of Contemporary Mathematical Sciences*, vol. 4, no. 1, pp. 1-8, 2023.

[32] F. S. V. Causanilles, H. M. Baskonus, J. L. G. Guirao, and G. R. Bermúdez, "Some important points of the Josephson effect via two superconductors in complex bases," *Mathematics,* vol. 10, no. 15, article 2591, 2022.

[33] H. M. Baskonus, A. A. Mahmud, K. A. Muhamad, and T. Tanriverdi, "A study on Caudrey–Dodd–Gibbon–Sawada–Kotera partial differential equation," *Mathematical Methods in the Applied Sciences*, vol. 45, no. 14, pp. 8737-8753, 2022.

[34] A. Hussain, H. Ali, F. Zaman, and N. Abbas, "New closed form solutions of some nonlinear pseudo-parabolic models via a new extended direct algebraic method*," International Journal of Mathematics and Computer in Engineering*, vol. 2, no. 1, pp. 35-58, 2023.

Predicting the Number of Visitors with Artificial Neural Networks to Support Strategic Decision-Making for Science Centers

Ali ÇETİNKAYA[1*], Havva KIRGIZ[2], Ferzan KARA[3]

[1]*Konya Science Center*
[2]*Konya Science Center*
[3]*Konya Food and Agriculture University*
(ORCID: 0000-0002-7747-6854) (ORCID: 0000-0003-0985-024X) (ORCID:0009-0001-0057-5010)

Keywords: Science center, Prediction, Neural Networks, Visitor, Bayesian, Machine Learning.

Abstract

Accurately predicting visitor attendance has become increasingly vital for science centers to optimize operations, improve visitor experiences, and stay competitive in attracting and engaging global audiences. As the demand for advanced predictive analytics grows, this study explores the use of artificial neural networks (ANNs) to forecast visitor numbers at science centers. In order to achieve this objective, data pertaining to the number of visitors to the Konya Science Centre was utilized. By analyzing a dataset of ten input factors, such as weather conditions and past visitor behavior, the study develops predictive models capable of accurately estimating future attendance patterns. The best-performing model, utilizing Scaled conjugate gradient, 0.93739 for the training set, 0.90645 for the test set, 0.92376 for the validation and 0.93069 overall. These findings underscore the transformative potential of predictive analytics in science center management. Leveraging machine learning techniques, the study provides valuable insights into visitor preferences and behavior. This knowledge can empower science centers to make data-driven decisions, optimize resource allocation, and adapt their offerings to meet the evolving needs of their target audience. Ultimately, the study highlights how predictive analytics can enhance the long-term sustainability and global competitiveness of science center operations.

1. Introduction

Science centers are informal learning environments where the public can engage with science and technology and where science festivals, workshops, special day events and science shows are held for participants from different age groups. There are more than 3,000 science centers in the world. It is estimated that these centers welcome in excess of 200 million visitors each year [1]. Scientific and Technologic Research Council of Turkiye (TUBITAK) opens large and small scale science centers in many provinces within the scope of science and society activities. Konya Science Center, which is the first TUBITAK-supported science center among science centers, is a science and technology complex located on a total area of 100,000 m2 [2]. According to architectural analyses, Konya Science Centre has the feature of being an "icon building" for the city in parallel with the developing trends in the fields of design and construction technology [1].

To estimate the number of visitors to places such as museums, zoos, etc., many different methods are used [3-9]. In the case of science centers, there is a big gap in the literature for studies conducted for predicting the number of visitors using ANN. For this reason, a literature review will be given for the studies conducted for visitor number prediction of museums.

Normal et al. applied the CRISP-DM methodology to perform the research. They developed and built four different types of regression

models using R and its machine learning packages to model number of visitors. Predictions of visitor number were then generated from each of the four models, and forecast accuracy was measured. The extreme gradient boost model was found to be the most effective, with an average forecast accuracy of 93% and the lowest forecast variability when benchmarked against the actual visitor number from the test data set. [10].

The number of museum visitors in Turkey between 2001 and 2019 and the probable number of museum visitors in 2037 were estimated using time series. According to research, it can be said that number of visitors of museums and ruins have an increasing trend. The number of visitors is estimated to be 84.641.851 in 2037. It is concluded that the Box-Jenkins models, which is generated for the number of visitors to museums and ruins, were statistically significant (p<0.05). The MAPE value (7.8694) showed that the series contains highly usable estimates [6].

By selecting 3 different museums in Thailand, the average number of visitors was estimated according to the number of visitors of 3 museums with a newly created method. Four different methods were used in this study. The RF and XGBoost models have average accuracy of 56.99% and 58.08%, respectively. Regarding the proposed method, the highest average accuracy was 85.14 and 83.13% for proposed method D [11].

The number of visitors was estimated by applying a GIS-based method for open-air museums in Denmark. The results of the correlation analysis must be read with considerable caution, as the model is based on data with very low spatial resolution, which can be mitigated by using higher-resolution demographic, economic, and social data, but at prohibitive costs. The data were analyzed using multiple linear regression (R2=0.94) [12].

Recent studies have focused on predicting visitor numbers using advanced machine learning techniques. In this context, a comprehensive prediction model was developed to identify key factors influencing the visitation patterns of both local and foreign tourists to these protected regions in Sarawak, Malaysia. The study employed a range of machine learning methods, including k-NN, Naive Bayes, and Decision Tree, to forecast whether visitor arrivals would be high, medium, or low. The dataset comprised visitor arrival information from 2015 to 2019, covering eighteen totally protected areas such as national parks, nature reserves, and wildlife centers. Performance evaluation based on accuracy,

precision, and recall highlighted that the Decision Tree method, particularly using Gain Ratio, yielded the highest prediction accuracy for both local (80.65%) and foreign visitors (84.35%) [13].

Another research has focused on leveraging machine learning techniques to forecast visitor numbers to tourist attractions along the Moche Route in northern Peru. The data, spanning from January 2011 to May 2022. The research evaluated the performance of four machine learning algorithms: linear regression, KNN regression, decision tree, and random forest. The findings revealed that linear regression provided the most accurate predictions for both domestic and international tourists [14].

Utilizing monthly tourist data spanning 2012 to 2018, employed XGB and GM learning models to examine the tourist volume in Sanya over the past seven years. The forecast accuracy of these models is compared both demonstrating high prediction accuracy. Based on these fitting results, a combined model is proposed to predict the tourist volume, number of overnight transit tourists, and tourist income in Sanya, China for 2019 and 2020 [15].

The capacity to accurately forecast visitor numbers has become increasingly vital for science centers aiming to optimize operations and enhance visitor experiences.

In the digital era, the ability to predict visitor attendance plays a pivotal role in enabling science centers to efficiently allocate resources and compete globally in attracting and engaging audiences. Looking forward, the demand for advanced predictive analytics continues to surge, offering the potential to revolutionize the strategic decision-making processes of science centers worldwide.

In alignment with this vision, this study aims to explore the potential of artificial neural network (ANN) algorithms to forecast the influx of visitors in science centers. By examining factors such as weather conditions, special occasions, and historical visitor behavior, predictive models are developed to provide an accurate understanding of future attendance trends. The study utilizes extensive data analytics and cutting-edge machine learning techniques to offer science centers insights into visitor behavior and preferences.

While previous research has concentrated on forecasting visitor numbers in a variety of contexts, this study aims to differentiate itself in the field of science centers by striving to comprehensively optimize strategic decision-making processes. This study aims to conduct a forecasting study using

artificial intelligence techniques with visitor data from Konya Science Centre, thus drawing a new route aiming to improve visitor experiences, promote sustainability and increase public interest in science and technology.

The following sections of this article summarize the methodology used (Section 2), present the findings and conclusions (Section 3), and conclude with reflections on the transformative potential of predictive analytics in science center management (Section 4).

The following research questions (RQs) were stated by taking into account the research gap on this topic:

RQ1: How can science centers and cultural institutions accurately forecast visitor numbers to optimize resource allocation and enhance visitor experiences in an increasingly dynamic and technology-driven world?
RQ2: What new techniques can be utilized to overcome the limitations of traditional methods in predicting visitor behaviors and supporting strategic decision-making processes in science centers?

2. Material and Method

Understanding visitor behavior in science centers requires a rigorous approach to data collection and analysis. In this section, we outline the methodologies used to collect, process, and analyze data.

2.1. Data Collection

In this study, analysts played a key role in forecasting visitor numbers at science center using a variety of methods, including both Konya Science Center's visitor data between 2020 and 2023 and other types of data such as meteorological data. Analysts worked on collecting, processing and analyzing visitor data. Daily, monthly and annual visitor numbers were collected from the Konya Science Center. In addition, meteorological data from government agencies were used to understand the impact of weather conditions and special events on visitor flow.

2.2. Data Analysis

The data analysis phase involved creating and evaluating a neural network model to predict visitor numbers at science centers.

Feature engineering involved converting meteorological data into measurable measurements suitable for predictive modeling. This conversion process increased the accuracy and reliability of predictions by converting raw data into a format that can be easily interpreted by machine learning algorithms [16]. To achieve this, the following steps were taken:

Temperature data was converted from continuous values into discrete categories to simplify analysis and capture the varying impacts of different temperature ranges on visitor numbers. The categories were defined as follows:

- Very Hot: 30°C and above = 6
- Hot: 25°C - 30°C = 5
- Warm: 20°C - 25°C = 4
- Cool: 15°C - 20°C = 3
- Cold: 10°C - 15°C = 2
- Very Cold: Below 10°C = 1

Precipitation data, which can significantly influence visitor behavior, was also categorized to capture different levels of rainfall:

- Heavy Rain: 15 mm and above = 6
- Moderate Rain: 5 mm - 15 mm = 5
- Light Rain: 1 mm - 5 mm = 4
- No Rain: 0 mm (dry) = 3

Wind speed data was categorized to reflect varying degrees of wind conditions, which could affect the comfort and safety of visitors.

- Very Strong Wind: 20 km/h and above = 6
- Strong Wind: 15 km/h - 20 km/h = 5
- Moderate Wind: 10 km/h - 15 km/h = 4
- Light Wind: 5 km/h - 10 km/h = 3
- Calm: Below 5 km/h = 2

The model consisted of 9 input nodes representing factors such as weather conditions, events, and historical visitation patterns, and a single output node for estimated visitor numbers.

Input parameters: 9 input parameters were used for each ANN model. The input parameter distributions are as follows: holidays (two), seasons (four), meteorological data (three).

Target parameters: daily visitor numbers
For categorical variables such as holidays, and seasons, a binary coding scheme was adopted, where a value of 1 indicates the presence of the condition and a value of 0 indicates its absence (Figure 1). Meteorological data such as daily air temperature, precipitation amount, and

wind speed were divided into high, medium and low levels to facilitate analysis. These adjustments were made to optimize the modeling process and increase the accuracy of predictions. With the implementation of these improvements, the models were finalized and ready for analysis.

HOLIDAY	SCB	WINTER	SPRING	SUMMER	AUTUMN	HEAT	WIND	RAIN	NU. OF VISITORS
1	0	1	0	0	0	1	2	3	271
0	0	1	0	0	0	1	3	3	562
0	0	1	0	0	0	1	3	3	800
0	0	1	0	0	0	1	2	3	614
0	0	1	0	0	0	1	2	3	477
0	0	1	0	0	0	1	3	6	719
0	0	1	0	0	0	1	3	5	715
0	0	1	0	0	0	1	3	3	626
0	0	1	0	0	0	1	3	3	1.056
0	0	1	0	0	0	1	2	3	1.008
0	0	1	0	0	0	1	2	3	523
0	0	1	0	0	0	1	2	3	488
0	0	1	0	0	0	1	2	3	1.019
0	0	1	0	0	0	1	2	3	975
0	0	1	0	0	0	1	2	4	301
0	0	1	0	0	0	1	2	3	561

Figure 1. Input and target parameters.

Data were cleaned, inconsistencies and missing values were removed, and normalized for uniformity. Three optimization algorithms (Levenberg-Marquardt, Bayesian Regularization, and Scalar Conjugate Gradient) with various hidden layers (2 to 20) were used and trained iteratively for 10 epochs. These are the hyperparameter values used for the scaled conjugate: maximum number of epochs 1000; performance goal 0; minimum performance gradient 1e-6; maximum validation failures 6; epochs between displays 25. These are the hyperparameter values used for the Bayesian regularization maximum number of epochs to train 1000; decrease factor for mu 0.1; increase factor for mu 10; minimum performance gradient 1e-7; maximum validation failures 0. These are the hyperparameter values used for the Levenberg-Marquardt Maximum number of epochs to train 1000; performance goal 0; maximum validation failures 6; minimum performance gradient 1e-7; initial mu 0.001; increase factor for mu 10; maximum value for mu 1e-10.

Training, validation, and testing subsets were produced by randomly splitting the data in the ANN.

Each model was trained using the chosen algorithm and hidden layers, and the parameters were set to minimize the difference between predicted and actual visitor numbers. Measurements such as mean square error was used in the evaluation.

3. Results and Discussion

The analysis of results from this study provides valuable insights into the performance of various optimization algorithms and neural network architectures in predicting visitor numbers to science centers. By meticulously comparing the effectiveness of different model variants, configurations that offer precise predictions were pinpointed, illuminating the critical factors shaping visitor flows.

The employed ANN models consisted of one hidden layer, 9 inputs, and one target (Figure 2).
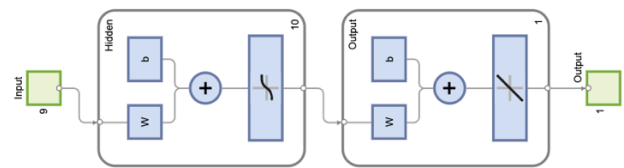
Figure 2. Neural network diagram.

Each model was executed 10 times for between 2 and 20 neurons to find the optimal number of neurons in its hidden layer. The best execution results were given in Table 1 for each algorithm.

Table 1. Analysis of the results

Algorithm	R	MSE	MAPE
Bayesian regularization	0.9281	16271.73	15.0594
Levenberg-Marquardt	0.9272	16311.58	13.5158
Scaled conjugate gradient	0.9306	15565.52	13.9231

Moreover, the best results' training, testing, and validation values are given in Fig. 2, Fig. 3, Fig. 4 for Levenberg–Marquardt, Bayesian regularization, and scaled conjugate gradient algorithms, respectively.

Figure 3. Best results of the Bayesian regularization algorithm (Layer 12).
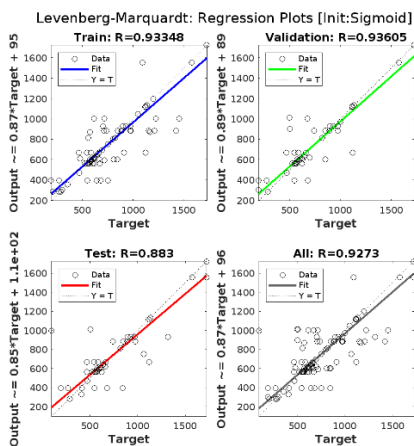
Figure 4. Best results of the Levenberg–Marquardt algorithm (Layer 11).
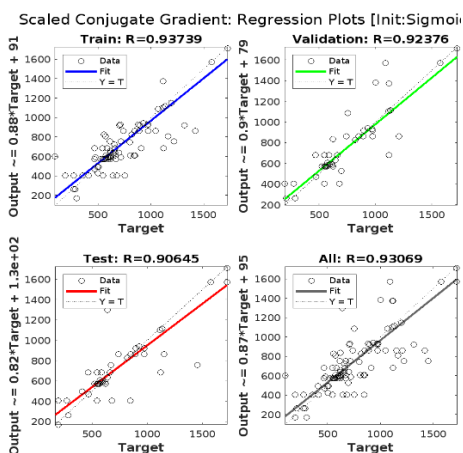
Figure 5. Best results of the scaled conjugate gradient algorithm (Layer 19).

The error histogram graphics are given in Fig. 6, Fig. 7, Fig. 8 for the three algorithms.
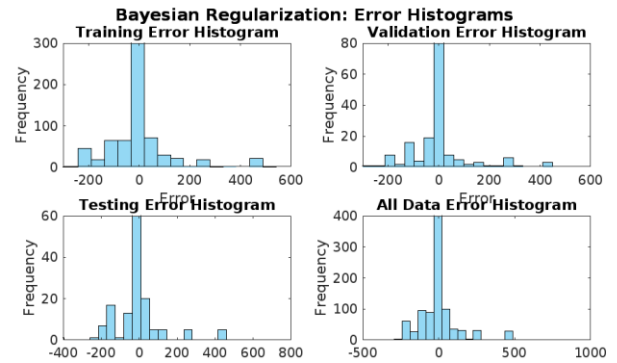
Figure 6. Bayesian regularization algorithm's error histogram values.
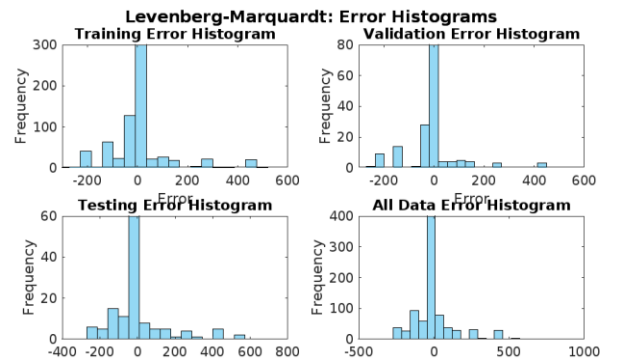
Figure 7. Levenberg–Marquardt algorithm's error histogram values.
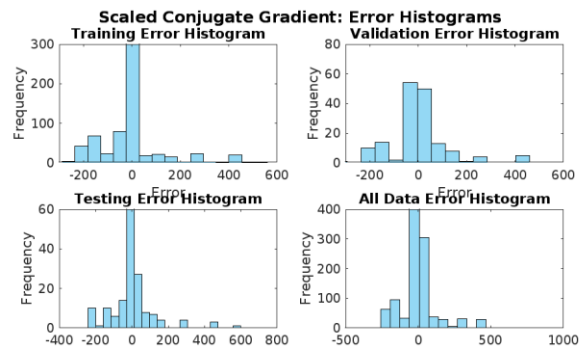
Figure 8. Scaled conjugate gradient algorithm's error histogram values

The error histogram, with blue bars representing training data, green bars for validation data, and red bars indicating testing data, offers a visual representation of outliers. These outliers are data

points where the fit deviates significantly from the majority of the data.

The performance graphics are presented in Fig. 9, Fig. 10, Fig. 11 for the Levenberg–Marquardt, Bayesian regularization, and scaled conjugate gradient algorithms, respectively.
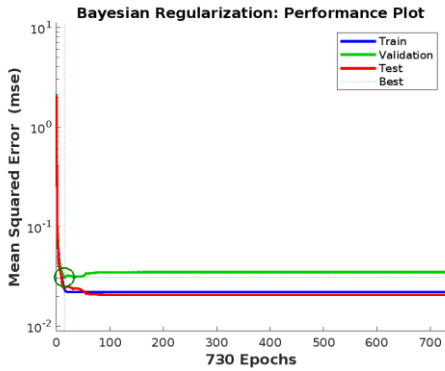
Figure 9. Bayesian regularization algorithm's performance values
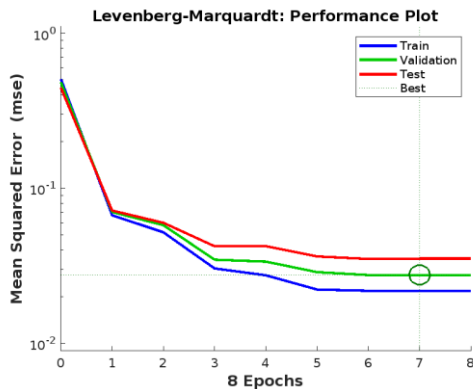
Figure 10. Levenberg–Marquardt algorithm's performance values
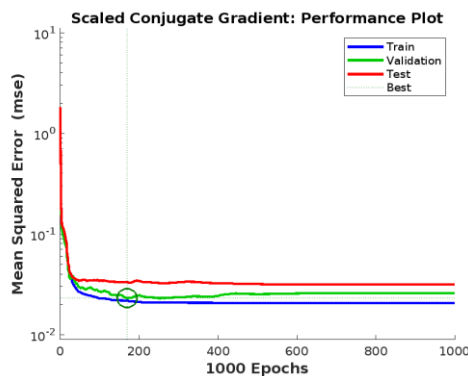
Figure 11. Scaled conjugate gradient algorithm's performance values

Among the ANN training algorithms, it has been observed that the scaled conjugate gradient algorithm gives the best effect in layer 19 of the hidden layer. The results of the scaled conjugate gradient algorithm are as follows: Training R=0.93739, Test R= 0.90645, Validation R=0.93069, All R=0.93069.

4. Conclusion and Suggestions

In conclusion, this study highlights the important role that predictive analytics plays in the management of science centers, particularly in predicting visitor numbers to optimize resource allocation and improve visitor experiences. Through the use of artificial neural network (ANN) algorithms, this research found that: The effectiveness of predictive models in accurately predicting future attendance trends by taking into account a variety of factors such as weather conditions, special occasions, and historical visitor behavior.

The integration of comprehensive data analytics and advanced machine learning techniques has provided insights into visitor behavior and preferences, allowing science centers to make informed, data-driven decisions and adapt their offerings to meet changing audience needs. These findings illuminate the transformative potential of predictive analytics in shaping the landscape of visitor engagement strategies, thereby contributing to the enduring sustainability and prosperity of science center operations.

As science centers continue to adapt to changing technological and societal dynamics, adopting advanced analytical methodologies and leveraging the capabilities of ANN algorithms will continue to be imperative. Predictive analytics remains an indispensable tool to guide strategic decision-making and ensure continued relevance in an increasingly competitive environment.

In the study conducted for 3 museums in Sinop, which is included in the literature, the best result was achieved with the Levenberg - Marquardt method with an R value of 0.99 [3]. Our study was conducted specifically for the science centers, and the best result was obtained with the scaled conjugate algorithm with an R value of 0.93.

This study is of significant value to science centers in their operational activities, such as determining the days on which a science center will be closed based on the number of visitors at any given

time or identifying the most suitable days for planning science events. The lack of visitor estimates for science centers using this method in the literature makes the study more important. It would be beneficial for science center curators and for visitors or schools who wish to plan or book a visit to the museum if the calendar heat map could be displayed on the museum website. Such a feature would provide visitors with information that could influence their decision to visit the museum.

It might be worth considering whether the proposed method could be applied to other science centers as well. It would also be helpful to bear in mind that all science centers must be in a similar situation, such as similar weather conditions.

The data that support the findings of this study are available from the corresponding author, upon reasonable request.

Contributions of the authors

A.Ç., H.K. and F.K. contributed to the design and implementation of the research, to the analysis of the results and to the writing of the manuscript. A.Ç. and H.K. methodology; F.K. and A.Ç. software; A.Ç. and H.K. data collection; A.Ç. writing—original draft preparation; A.Ç. and H.K. writing—review and editing; H.K. and F.K.; visualization.

Conflict of Interest Statement

There is no conflict of interest between the authors.

Statement of Research and Publication Ethics

The study is complied with research and publication ethics.

References

[1]   E. Y. Kuyrukçu, "The importance of iconic buildings for city image: Konya Science Center example," *ICONARP International Journal of Architecture and Planning,* vol. 6, no. 2, pp. 461-481, 2018.

[2]   TÜBİTAK. "About the Call for Large Scale Science Centres." https://bilimmerkezleri.tubitak.gov.tr/Icerik/buyuk-olcekli-bilim-merkezi-projeleri-cagrisi-hakkinda-146 (accessed 11.06.2024.

[3]   Ö. Alcan, M. Demir, and Y. Alcan, "Prediction of the Numbers of Visitors at the Sinop Museums by Artificial Neural Networks," *Karadeniz Fen Bilimleri Dergisi,* vol. 9, no. 1, pp. 70-81, 2019.

[4]   M. Çuhadar, İ. Güngör, and A. Göksu, "Turizm Talebinin Yapay Sinir Ağları İle Tahmini Ve Zaman Serisi Yöntemleri İle Karşılaştırmalı Analizi: Antalya İline Yönelik Bir Uygulama," *Süleyman Demirel Üniversitesi İktisadi Ve İdari Bilimler Fakültesi Dergisi,,* vol. 14, no. 1, pp. 99-114, 2009.

[5]   S. Wahyuni, A. D. Nasution, and H. Hermansyah, "Optimization Of Data Mining In Predicting Tourist Visits At The Deli Serdang Museum," in *International Conference on Sciences Development and Technology*, 2023, vol. 3, no. 1, pp. 115-120.

[6]   S. Öztemiz and M. A. Tekindal, "Forecasting the number of visitors of the museums and ruins by Using time series analysis: The case of Turkey," *Türk Kütüphaneciliği,* vol. 35, no. 2, pp. 232-248, 2021.

[7]   J. Beresford, "Mind the Gap: Prediction and Performance in Respect to Visitor Numbers at the New Acropolis Museum," *Museum & Society,* vol. 12, no. 3, pp. 171-190, 2014.

[8]   G. Trinh and D. Lam, "Understanding the attendance at cultural venues and events with stochastic preference models," *Journal of Business Research,* vol. 69, no. 9, pp. 3538-3544, 2016.

[9]   E. S. Silva, H. Hassani, S. Heravi, and X. Huang, "Forecasting tourism demand with denoised neural networks," *Annals of Tourism Research,* vol. 74, pp. 134-154, 2019.

[10]   N. Yap, M. Gong, R. K. Naha, and A. Mahanti, "Machine learning-based modelling for museum visitations prediction," in *2020 International Symposium on Networks, Computers and Communications (ISNCC)*, 2020: IEEE, pp. 1-7.

[11]   W. Limpornchitwilai and P. Suksompong, "Analysis of visitor data prediction of National Science Museum Thailand (NSM)," Thammasat University, 2021.

[12]   B. Ejstrud, "Visitor numbers and feasibility studies. Predicting visitor numbers to danish open-air museums using GIS and multivariate statistics," *Scandinavian Journal of Hospitality and Tourism,* vol. 6, no. 4, pp. 327-335, 2006.

[13]   A. Z. Abang Abdurahman, W. F. Wan Yaacob, S. A. Md Nasir, S. Jaya, and S. Mokhtar, "Using Machine Learning to Predict Visitors to Totally Protected Areas in Sarawak, Malaysia," *Sustainability,* vol. 14, no. 5, p. 2735, 2022.

[14]   J. Bravo, R. Alarcón, C. Valdivia, and O. Serquén, "Application of Machine Learning Techniques to Predict Visitors to the Tourist Attractions of the Moche Route in Peru," *Sustainability,* vol. 15, no. 11, p. 8967, 2023.

[15]   X. Liu, Y.-n. Chen, Z. Qiu, and M.-r. Chen, "Forecast of the tourist volume of Sanya city by XGBoost model and GM model," in *2019 International Conference on Cyber-Enabled Distributed Computing and Knowledge Discovery (CyberC)*, 2019: IEEE, pp. 166-173.

[16]   G. Dong and H. Liu, *Feature engineering for machine learning and data analytics*. CRC press, 2018.

Bitlis Eren Üniversitesi Fen Bilimleri Dergisi

Automatic Classification of Melanoma Skin Cancer Images with Vision Transform Model and Transfer Learning

Alper Talha KARADENIZ[*]

Department of Computer Engineering, Faculty of Engineerin and Architecture, Kahramanmaras Sutcu Imam University, Kahramanmaras, TR (ORCID: 0000-0003-4165-3932)

Abstract

Melanoma is one of the most aggressive and lethal forms of skin cancer. Therefore, early diagnosis and correct diagnosis are very important for the health of the patient. Cancer diagnosis is made by field experts and this increases the possibility of error. Today, with the developing deep learning technology, it has been seen that automatic detection of Melanoma skin cancer can be performed with high accuracy by computer systems.

One of the latest technologies developed in the field of deep learning is the Vision Transformer (ViT) model. This model was produced by Google and has achieved very successful results in the field of classification. This study aims to detect melanoma skin cancer with high accuracy using the ViT model.

In the study, the melanoma skin cancer dataset consisting of 9600 training and 1000 test images in the Kaggle library was used. In order to use the data set more effectively, some pre-processing methods were first applied. Model performance was evaluated using the transfer learning approach together with the ViT model on this data set. Training and experimental testing of the model was carried out with Python language on the Colab platform.

As a result of the experimental studies carried out on the test data set, it was seen that the model reached 93.5% accuracy rate. This rate is competitive and promising when compared to existing models in the literature.

1. Introduction

Melanoma, a malignant tumor arising from melanocytes, is one of the most aggressive and lethal forms of skin cancer. Early diagnosis and accurate diagnosis are of great importance for effective treatment and improving patient survival rates. Traditional methods include visual examinations and dermoscopy performed by dermatologists. However, these methods rely heavily on the expertise and experience of the practitioner. This increases the potential for human error and calls for more reliable diagnostic tools. The development of computer-aided diagnostic systems is crucial to meet this need [1]. In recent years, advances in machine learning and deep learning technologies are opening new avenues for automatic detection and classification of melanoma from skin lesion images. These technologies show promise in improving diagnostic accuracy and efficiency. Deep learning models are comparable to human experts, especially when trained on large data sets [2].

Vision Transformer (ViT) is a model developed by Google that achieves revolutionary results in the field of computer vision processing. ViT processes these tokens with the Transformer encoder by dividing the images into fixed-size patches and embedding each patch into a linear token. This method effectively captures spatial relationships and contextual information within the image. It shows superior performance, especially in large-scale data sets [3]. However, the success of Transformer-based models

---

[*] Corresponding author: *alperkaradeniz5@gmail.com*

in natural language processing has encouraged the application of these models to image processing tasks. Vision Transformer (ViT), developed by Dosovitskiy et al., has emerged as an alternative to CNNs in image classification tasks. ViT has shown state-of-the-art results, outperforming traditional CNN architectures, especially when pre-trained on large datasets [4].

Many studies have been conducted on automatic diagnosis and classification of melanoma skin cancer. Among traditional approaches, image processing and machine learning methods stand out. In the literature, deep learning methods have been widely used in the classification of skin lesions and successful results have been obtained.

Kaur et al demonstrated that they achieved dermatologist-level accuracy in skin cancer classification using deep CNNs. In the study, dermoscopic images containing different cancer samples were obtained from the International Skin Imaging Cooperation data repositories (ISIC 2016, ISIC2017 and ISIC 2020). The proposed DCNN classifier achieved 81.41%, 88.23% and 90.42% accuracy on ISIC 2016, 2017 and 2020 datasets, respectively [5].

Prakhar Shobhit et al. He applied the Vision Transformer Attention method on the melanoma skin cancer data set and achieved a 91% accuracy rate as a result of the classification [6]. Another study proposes an alternative method based on ready-to-use ViT to identify various skin cancer diseases. To evaluate its performance, the proposed method was compared with 11 CNN-based transfer learning methods that are known to perform better than deep learning techniques in the literature. The proposed model achieved an accuracy of 92.14%, outperforming CNN-based transfer learning models [7].

In our study, after pre-processing the data set, classification of melanoma skin cancer was carried out by fine-tuning it with the google/vit-large-patch32-384 transfer learning method suggested by the ViT model. The rest of this study is as follows: In the second section, the data set and the methods used are mentioned. In the third section, the proposed model is explained. The fourth section includes the results of experimental studies. The last section contains the discussion and conclusion section.

2. Material and Method

2.1. Dataset

The Kaggle melanoma skin cancer dataset was used in the study. The dataset contains two different classes: benign and malignant. The dataset includes 9600 training images and 1000 test images. Each image in the data set was prepared with a size of 300x300 pixels. The purpose of creating the data set is to help deep learning methods to be developed for the detection of melanoma skin cancer [8]. An example image of the data set is shown in Figure 1 [9].
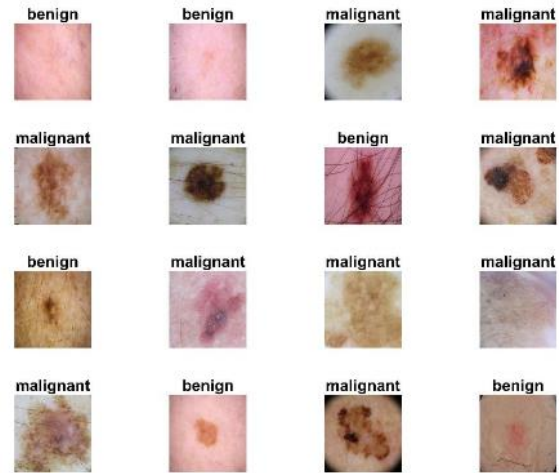
Figure 1. Sample image of the dataset.

2.2. Vision Transformer Model

In this study, the Vision Transformer (ViT) architecture was used for melanoma classification.

Vision Transformers (ViTs) have been produced by Google as an alternative to convolutional neural networks (CNN) in various computer vision processes. After first attracting attention with its superior performance in natural language processing, ViTs have also achieved success in image studies [10].

ViT has demonstrated state-of-the-art results in image classification, object detection, and segmentation tasks, often outperforming traditional CNNs.

ViT transforms an input image into a fixed-size, non-overlapping array of patches, each linearly embedded in a token. These tokens are then processed by a standard Transformer encoder, which uses a self-attention mechanism to capture global dependencies and contextual information across the entire image. This mechanism allows ViT to understand spatial relationships within the image more effectively than the local receptive fields typically used in CNNs. Positional coding is added to patch placements to preserve spatial information, allowing the model to distinguish the position of each patch within the original image [11].

ViT is pre-trained on extensive datasets, especially ImageNet, and then fine-tuned for specific tasks. It shows superior performance on various large-scale image classification criteria. The model's scalability and ability to capture long-range

dependencies make it highly effective for a variety of computer vision applications, including object detection and image segmentation. Leveraging the global context understanding provided by the self-attention mechanism, ViT demonstrates the potential to revolutionize the field of computer vision by often exceeding the performance of traditional CNN architectures. This innovative use of Transformer architecture in visual tasks promises to be improved, highlighting a significant shift in the design of image classification models [12].

The working architecture of ViT is shown in figure 2 [13].
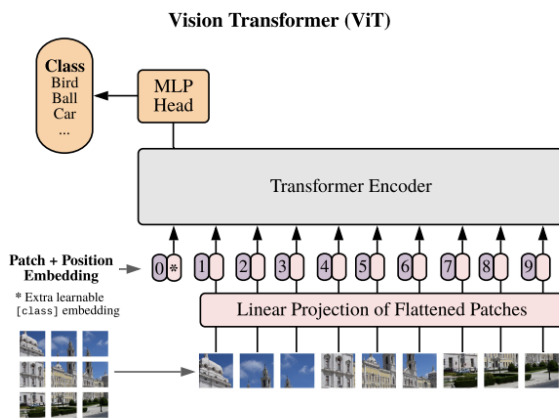
Figure 2. ViT Architecture.

2.3. Transfer Learning Approach
Large data sets and powerful computers are often needed for a complete model training process. Also, the training process takes a long time. Determining the architecture of the model to be created and changing its hyperparameters are quite difficult operations, as well as requiring large amounts of data and powerful computing power. The transfer learning approach is therefore widely applied in the literature. The process of adapting a pre-trained model to a specific task or data collection is known as transfer learning. New data is trained only in the final stage, using the weights of a previously trained model. Thus, the pre-trained model is prepared for a new task. There are many advantages to using a pre-trained model. It allows you to use the latest models without having to start from scratch and reduces transaction costs [14] [15].

3. Model
In the study, classification was performed on the Melonoma image dataset. In the first stage, it was aimed to increase the training success by applying pre-processing on the images. In the second stage,

pre-trained weights were given to the pre-processed data set during the transfer learning phase with the ViT model. Transfer learning of the ViT model was prepared by pre-training on the ImageNet dataset. The ImageNet dataset contains more than 14 million images and 21,000 classes. A wide variety of learning is provided as a result of training on such a large data set. After applying many preprocessing methods for skin cancer classification, transfer learning was used on images with fine tuning [16]. The classification process was carried out in 3 stages by coding the gogle/vit-large-patch32-384 method in the ViT model with the Python programming language in the Colab environment. This model is part of the ViT method produced by Dosovitskiy et al. This particular variant of the model uses a basic configuration with a patch size of 32x32 and an input resolution of 384x384 pixels [13].

The model architecture is shown in figure 3.
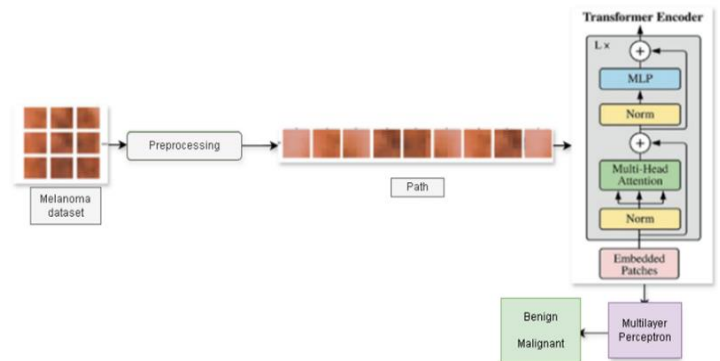
Figure 3. Model Architecture.

4. Experimental Tests

4.1. Performance Metrics

There are two different classes in our data set: malignant and benign. Confusion matrix was used to measure classification performances. The values obtained from this matrix are True Positive (TP), True Negative (TN), False Positive (FP) and False Negative (FN).

The performance criteria used in the study are Accuracy (Acc), F-Score, Recall (Rec) and Precision (Pre). The formulas of these performance metrics are shown in equations 1-4 [17] [18].

$$Rec = \frac{TP}{TP+FN} \tag{1}$$

$$F1 = 2 * \frac{Pre*Rec}{Pre+Rec} \qquad (2)$$

$$Acc = \frac{TP+TN}{TP+TN+FN+FP} \qquad (3)$$

$$Pre = \frac{TP}{TP+FP} \qquad (4)$$

4.2. Preprocessing

Pre-processing was applied to the data set before the training process. In the first stage, all images were resized to 384x384 and brought to the appropriate input size for the ViT model used in the study. In the second stage, Variance Stabilization, which is frequently used in classifying medical images, was applied to the data set. Variance Stabilization is the process of applying transformations to fix the variance of the data before analysis. This preprocessing method increases the performance of statistical analyzes and models by making the data more homogeneous [19]. Finally, the data set was normalized and made suitable for training. Normalization process is one of the basic methods used to increase model performance in deep learning.

4.3. Training

In the study, the data set was divided into 9600 and 1000 images as training and test data sets, respectively. Hyperparameters were tuned by trial and error. The hyperparameters used in coding were determined as batch_size=32, epoch=10, lr=1e-5, optimizer=man, loss function=CrossEntropyLoss, GELU activation function. The gogle/vit-large-patch32-384 model was used in the pre-training (Transfer Learning) phase of the training. In this model, patch sizes are set to 32x32. There is a 24-layer transformer encoder in the encoder part of the model. Transformer's attention mechanism, ViTSdpaSelfAttention consists of 1024 inputs and 1024 outputs, ViTSelfOutput consists of 1024 inputs and 1024 outputs, ViTIntermediate consists of 1024 inputs and 4096 outputs, and the ViTOutput layer consists of 4096 inputs and 1024 outputs. The layer that comes after the Encoder is the LayerNorm layer. Finally, there is a linear layer with 2 class outputs from 1024 features. In the study carried out with Python code in the Colab environment, training times were significantly reduced by using "CUDA" and "GPU".

5. Results and Discussions

In this study, automatic classification of melanoma skin cancer was performed using the Google Vision Transformer (ViT) model. In the first stage, all images are set to 384x384 (Resize). Secondly, Variance Stabilization, which is frequently used for medical images, was applied. Then, experimental tests were carried out by applying the ViT model and transfer learning to the data set.

As a result of the experimental tests performed on the test data of the study, an accuracy rate of 93.5% was achieved. As a result of the experimental tests of the classification process, the Precision, Recall and F1 Score values were calculated as 95.2%, 92.1% and 93.5%, respectively. We can say that these results are quite successful for image classification studies. The complexity matrix is given in figure 4 to see the success of the experimental test results in detail.
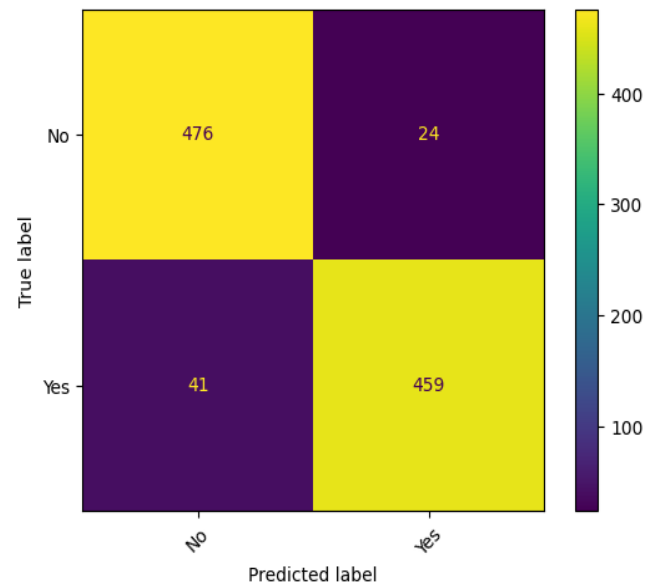
Figure 4. Confusion Matrix.

It is known in the literature that deep learning methods are widely used in skin cancer diagnosis and provide successful results. In particular, the study by Kaur et al. achieved very good levels of accuracy using deep CNNs. These results suggest that the ViT model can outperform traditional CNN-based models in diagnosing skin cancer.

A comparison table with popular studies in the literature on automatic classification of melanoma skin cancer is given below.

Table 1. Comparative Analysis for Automated Classification of Melanoma Skin Cancer.

Paper	Year	Model	Acc
[20]	2022	Transfer learning with AlexNet	%87.1
[21]	2022	VGG16, ResNet50, and Xception	%86.5 in VGG16, %81.6 in Resnet50 and 90.9 in Xception
[5]	2022	DCNN	%90,42
[7]	2023	Transfer learning with ViT and CNN	%92.14 with ViT, %82 in ResNet50
[6]	2023	Vision Transformer Model	%91
[22]	2024	Transfer learning with ViT, Swin transformers and CNN	%88.6 with ViT and %88.8 with ResNet50
This study	2024	Preprocessing, Transfer learning with ViT and Fine Tuning	%93.5

Table 1 shows that the study gives better results than popular studies in the literature.

Instead of operating on pixels like CNN methods, ViT transforms the input image into a fixed-size, non-overlapping, linear array of patches embedded in a token. It is then processed by a standard Transformer encoder, which uses a self-attention mechanism to capture global dependencies and contextual information across the entire image. Positional coding is added to patch placements to preserve spatial information, allowing the model to distinguish the position of each patch within the original image. This mechanism allows ViT to understand spatial relationships within the image more effectively than the local receptive fields typically used in CNNs [11]. Additionally, ViT is pre-trained on extensive datasets, especially ImageNet, and then fine-tuned and used for specific tasks. These mentioned structures make the ViT model more successful than other methods in the literature in image classification applications.

6. Conclusions

The Kaggle melanoma skin cancer dataset used in our study consists of benign and malignant samples and consists of 9600 training and 1000 test images. The breadth and diversity of the data set increased the generalization ability of the model. In addition,

the applied pre-processing played an important role in achieving high accuracy rates. As a result of experimental tests performed on test data, it has proven that it can be used for the diagnosis of Melenoma skin cancer by reaching an accuracy rate of 93.5%.

In future studies, it is recommended to expand the data set and compare it with different deep learning models to further improve the performance of the model. Additionally, further research is needed to test the model in real-world applications and make it suitable for use in clinical settings. In conclusion, this study demonstrates that the ViT model is a promising tool in skin cancer diagnosis and lays a solid foundation for future research.

References

[1]   R. Deepa, G. ALMahadin, and A. Sivasamy, "Early detection of skin cancer using AI: Deciphering dermatology images for melanoma detection," *AIP Adv.*, vol. 14, no. 4, 2024.

[2]   I. H. Sarker, "Deep learning: a comprehensive overview on techniques, taxonomy, applications and research directions," *SN Comput. Sci.*, vol. 2, no. 6, p. 420, 2021.

[3]   K. Al-Hammuri, F. Gebali, A. Kanan, and I. T. Chelvan, "Vision transformer architecture and applications in digital health: a tutorial and survey," *Vis. Comput. Ind. Biomed. Art*, vol. 6, no. 1, p. 14, 2023.

[4]   A. Sriwastawa and J. A. Arul Jothi, "Vision transformer and its variants for image classification in digital breast cancer histopathology: A comparative study," *Multimed. Tools Appl.*, vol. 83, no. 13, pp. 39731–39753, 2024.

[5]   R. Kaur, H. GholamHosseini, R. Sinha, and M. Lindén, "Melanoma classification using a novel deep convolutional neural network with dermoscopic images," *Sensors*, vol. 22, no. 3, p. 1134, 2022.

[6]   P. Shobhit and N. Kumar, "Vision Transformer and Attention-Based Melanoma Disease Classification," in *2023 4th International Conference on Communication, Computing and Industry 6.0 (C216), IEEE*, 2023, pp. 1–6.

[7]   M. A. Arshed, S. Mumtaz, M. Ibrahim, S. Ahmed, M. Tahir, and M. Shafi, "Multi-class skin cancer classification using vision transformer networks and convolutional neural network-based pre-trained models," *Information*, vol. 14, no. 7, p. 415, 2023.

[8]   S. Ghosh, S. Dhar, R. Yoddha, S. Kumar, A. K. Thakur, and N. D. Jana, "Melanoma Skin Cancer Detection Using Ensemble of Machine Learning Models Considering Deep Feature Embeddings," *Procedia Comput. Sci.*, vol. 235, pp. 3007–3015, 2024.

[9]   S. R. Waheed et al., "Melanoma skin cancer classification based on CNN deep learning algorithms," *Malaysian J. Fundam. Appl. Sci.*, vol. 19, no. 3, pp. 299–305, 2023.

[10]   Z. Chen et al., "Vision transformer adapter for dense predictions," arXiv Prepr. arXiv2205.08534, 2022.

[11]   A. Parvaiz, M. A. Khalid, R. Zafar, H. Ameer, M. Ali, and M. M. Fraz, "Vision transformers in medical computer vision—A contemplative retrospection," *Eng. Appl. Artif. Intell.*, vol. 122, p. 106126, 2023.

[12]   X. Su et al., "Vitas: Vision transformer architecture search," *in European Conference on Computer Vision, Springer*, 2022, pp. 139–157.

[13]   A. Dosovitskiy et al., "An image is worth 16x16 words: Transformers for image recognition at scale," arXiv Prepr. arXiv2010.11929, 2020.

[14]   G. Mesnil et al., "Unsupervised and transfer learning challenge: a deep learning approach," in *Proceedings of ICML Workshop on Unsupervised and Transfer Learning, JMLR Workshop and Conference Proceedings*, 2012, pp. 97–110.

[15]   S. Ghosal and K. Sarkar, "Rice Leaf Diseases Classification Using CNN With Transfer Learning," in *2020 IEEE Calcutta Conference (CALCON), IEEE*, 2020, pp. 230–236.

[16]   A. Rahmouni, M. A. Sabri, A. Ennaji, and A. Aarab, "Skin Lesion Classification Based on Vision Transformer (ViT)," in *The International Conference on Artificial Intelligence and Smart Environment, Springer*, 2023, pp. 472–477.

[17]   A. T. Karadeniz, Y. Çelik, and E. Başaran, "Classification of walnut varieties obtained from walnut leaf images by the recommended residual block based CNN model," *Eur. Food Res. Technol.*, pp. 1–12, 2022.

[18]   E. Başaran, Z. Cömert, and Y. Celik, "Timpanik Membran Görüntü Özellikleri Kullanılarak Sınıflandırılması," *Fırat Üniversitesi Mühendislik Bilim. Derg.*, vol. 33, no. 2, pp. 441–453, 2021.

[19]   S. M. Lin, P. Du, W. Huber, and W. A. Kibbe, "Model-based variance-stabilizing transformation for Illumina microarray data," *Nucleic Acids Res.*, vol. 36, no. 2, pp. e11–e11, 2008.

[20]   T. M. Ghazal, S. Hussain, M. F. Khan, M. A. Khan, R. A. T. Said, and M. Ahmad, "Detection of benign and malignant tumors in skin empowered with transfer learning," *Comput. Intell. Neurosci.*, vol. 2022, no. 1, p. 4826892, 2022.

[21]   A. Bassel, A. B. Abdulkareem, Z. A. A. Alyasseri, N. S. Sani, and H. J. Mohammed, "Automatic malignant and benign skin cancer classification using a hybrid deep learning approach," *Diagnostics*, vol. 12, no. 10, p. 2472, 2022.

[22]   G. H. Dagnaw, M. El Mouhtadi, and M. Mustapha, "Skin cancer classification using vision transformers and explainable artificial intelligence," J. *Med. Artif. Intell.*, vol. 7, 2024.

Determining the Suction Capacity of Compacted Clays with Fuzzy-Set Theory

Ömür ÇİMEN[1*], S.Nilay KESKİN[1]

[1]Department of Civil Engineering, Faculty of Engineering and Natural Sciences,
Süleyman Demirel University, Isparta, 32260, Türkiye
(ORCID:0000-0002-6138-6029) (ORCID: 0000-0002-0367-943X)

Abstract
Water suction capacity is an important parameter affecting soil's swelling properties and volumetric change. The water suction capacity is determined through time-consuming laboratory experiments. However, this has random errors due to the heterogeneous and anisotropic structure of the soil sample together with the error caused by the operator made the experiment. Solving such an estimation problem including error can be easily achieved using fuzzy-set theory. In this study, we use fuzzy-set theory to predict the suction capacity of compacted clayey soils. For this reason, the engineering properties of clayey soil (plasticity index, dry density, initial water content, and suction capacity) are partitioned into fuzzy subsets, and fuzzy rules are formed. Later, a computer program in the Fortran language is written to estimate the suction capacity of compacted clayey soil from these properties. It is shown that there is a good similarity between the results of the tests and the proposed fuzzy logic model.

1. Introduction

The suction of soils is known as the free energy of soil water. The water suction capacity of soil is also described as water holding ability [1], [2], [3]. In clays with high absorption capacity, a significant increase in volume and pressure occurs due to soil-water reaction. Engineering structures built on these soils may suffer important damage from soil water, such as a few floored light structures, highway and airport pavements, pipelines, or retaining walls. In such cases, determining the suction capacity and pressure of clayey soil at the start of construction allows necessary precautions to be taken, reducing potential problems. For this reason, many researchers have worked to determine the suction capacity and pressure by experimental and theoretical studies.

In general soil suction has two components; namely matric and osmotic suction. For many practical studies in geotechnical engineering, a variation in total suction is equivalent to a variation in the matric suction [4]. Suction is a parameter that

shows the mechanical behavior of soil, controlled by the matric suction. [5]. An increase in soil suction increases the shear strength of soil based on the effective angle of internal friction and cohesion [6]. In addition, the deformation modulus of soil is a function of effective stress and suction [7]. In the literature, there is a significant amount of research on predicting the shear strength, deformation modulus, and permeability of soils for soil suction [8], [9].

Suction pressure and capacity of soils depend on soil properties such as soil type, dry density, initial water content, plasticity index, consistency limits, fabric, void ratio, flow velocity, etc. [10]. It was stated that the value of suction capacity rises with increasing liquid limit in the studies that searched for a relationship between the suction capacity and liquid limit [11], [12]. In studies searched the relationship among soil suction, dry density, and void ratio, it is shown that suction rises with an increase in dry density, and that suction falls with the increase in void ratio [13]. Studies between suction capacity and initial water content show that suction capacity falls

with increasing water content [14]. In addition, the water retention curves at different temperatures show that suction tends to reduce with increasing temperature of constant water content [15].

The literature shows the effects of soil suction on factors such as initial water content, dry density, and consistency limits. Therefore, initial water content, dry density, and plasticity index are selected as the main factors affecting suction capacity for estimation of suction capacity in this study. These factors can be determined with the experiments in the laboratory, easily.

There is a risk factor, caused by uncertainty, in geotechnical engineering practice [16]. Soil is composed of solids, liquids, and gases. The solid phase may be mineral, organic matter, or both. Thus, soil has a heterogeneous and anisotropic structure. Due to these properties, soil media involves uncertainties and unknown engineering parameters. In uncertainty problems, the fuzzy-set theory has been used recently. First, Zadeh [17] introduced the concept of fuzzy sets to describe uncertainty. The works used the fuzzy-set theory also exist in geotechnical engineering. Fuzzy sets were used to determine the capacity of single piles into sand [18]. Juang et al. [19] presented a qualitative evaluation scheme for mapping the slope failure potential using a fuzzy-set analysis. Juang et al. [20], explained how to determine the relative density of sands from the cone penetration test (CPT) using the fuzzy sets. They implied that there is a good agreement between the results of the fuzzy model and CPT. A fuzzy approach was used to determine soil classification from CPT results [21]. A fuzzy-set-based approach was used for determining characteristic values of measured geotechnical parameters [22], [23]. Researchers implied that a nonlinear model and non-unimodal functions with the fuzzy-deviation method provided the most conservative results.

The intelligent learning algorithms of ANN, Fuzzy Logic, GEP, ANFIS, ANOVA, and other nature-inspired algorithms have been reviewed as they are applied in predicting geotechnical and geo-environmental problems and systems. They are complex exercises conducting experimental protocols for the design of earthwork infrastructures. Mostly, such experimental exercises don't meet the required conditions for sustainable design and construction. At other times, certain errors resulting in experimental setup and human misjudgment, may mar the accuracy of measurements and release unexpected emissions. Most lapses encountered in repeated laboratory measurements may be solved using evolutionary learning methods [24].

There are a lot of studies using fuzzy logic in the geotechnical engineering literature: Landslide risk assessment [25], slope stability analysis of earth dams [26], tunneling geomechanics [27], rock slope stability analysis [28], retaining wall stability [29], safe bearing capacity for settlement criteria for clayey soils [30], suitability of soils in airfield applications [31], engineering properties of granular soil with wastes for environment protection and road base use [32], prediction of unconfined compressive strength of microfine cement injected sands [33] can be given as examples.

This paper aims to determine the suction capacity of compacted clay using the fuzzy-set theory. For this reason, suction capacity tests were made on compacted clayey soil samples using the oedometer test equipment. The parameters affecting the suction capacity are considered as initial water content, dry density, and plasticity index of the clay. The input and output parameters are divided into fuzzy subsets. A fuzzy rule base with if-than rules has been created. The rule base is modeled in the Fortran language. The results obtained from modeling were compared with the experimental results.

2. Material and Method

2.1. Experimental Study

Sieve and hydrometer analysis, consistency limits, pycnometer, and standard compaction tests are made on the three clay samples at ASTM Standards. Soil classes are determined and some engineering properties of the soils are given in Table 1. The Table shows that the classification of samples is high plasticity clay and that the plasticity index of samples is 54%, 47%, and 38%, respectively.

Table 1. Properties of soil samples [34]

Properties	Sample 1	Sample 2	Sample 3
Liquid limit (%)	75	73	66
Plastic limit (%)	21	26	28
Plasticity index (%)	54	47	38
Shrinkage limit (%)	7	13	10
Specific gravity	27.4	27.7	28.1
Max. dry density (kN/m^3)	16.1	16.0	15.2
Opt. water content (%)	23	23	27
Gravel (%)	1	1	0
Sand (%)	6	3	2
Silt + Clay (%)	93	96	98
Color	Grey	Red	Red
Soil classification	CH	CH	CH

Clay soil samples are sieved using a No. 40 sieve and dried in an oven for 24 hours. Samples are

mixed with the pure water at different initial water contents. Prepared samples with various water contents are compacted at different dry densities in oedometer rings having 7.1 - 7.5 cm in diameter and $1.6 - 2$ cm in height. It is capillary-provided saturating the samples that are placed into an oedometer cell. Hence, the final water content is determined and so this water content is considered as a suction capacity. The suction capacity test results are presented in Table 2. In this table, it is seen that 6 different dry densities (11.5 kN/m^3, 13.0 kN/m^3, 14.0 kN/m^3, 15.0 kN/m^3, 16.0 kN/m^3, 17.0 kN/m^3) and 6 different initial water contents (15%, 20%, 25%, 30%, 35%, 40%) exist. As seen from Table 2, the value of suction capacity reduces with the increase of the dry density and initial water content while it rises with the increasing plasticity index.

Table 2. Results of tests [34]

γ_d (kN/m^3)	W_0 (%)	W_{suc} (%)		
		Sample 1	Sample 2	Sample 3
11.5	15	65	56	50
	20	60	55	49
	25	58	50	44
	30	50	46	40
	35	48	42	36
	40	44	40	34
13.0	15	62	51	45
	20	57	50	43
	25	55	45	42
	30	49	42	40
	35	46	41	35
	40	42	39	32
14.0	15	61	50	42
	20	56	48	41
	25	54	45	39
	30	48	42	36
	35	43	39	33
	40	42	36	27
15.0	15	60	48	42
	20	52	46	40
	25	50	43	38
	30	44	40	35
	35	40	36	30
	40	36	33	25
16.0	15	57	46	41
	20	50	44	40
	25	47	40	38
	30	42	36	34
	35	38	34	30
17.0	15	54	44	37
	20	48	42	35

2.2. Fuzzy-Set Theory

Sets are collections of objects with the same properties. In crisp sets, the objects may belong to the set, or may not. In practice, the characteristic value for an object belonging to the set considered is coded as 1 and if it is outside, the set then the coding is 0. In crisp sets, there is no ambiguity or vagueness as to the belonging of each object to the set concerned. On the other hand, in daily life people are always confronted with objects that may be similar to each other with different properties, therefore, there arises uncertainty as to their belonging to a common set with membership values 0 or 1. Of course, logically some of the similar objects may partially belong to the same set. Therefore, an ambiguity emerges in the decision of belonging or not. To alleviate such situations Zadeh [17], generalized the crisp set membership degree as having any value continuously between 0 and 1. The greater the membership degree the more the object belongs to the set.

Any linguistic feature variation can be shown with the fuzzy rules, and represented with general words and fuzzy numbers. For instance, Figure 1 shows a typical membership function for fuzzy subsets of clays' liquid limit values such as "very few", "few", "medium", "high", and "very high". Membership degree and membership function at fuzzy sets are determined by personal intuition, sense, and experience. The triangle, trapezoidal, gaussian, sigmoidal, and π-shaped membership functions are used in literature. However, the most popular membership functions are triangle and trapezoidal membership functions [20].
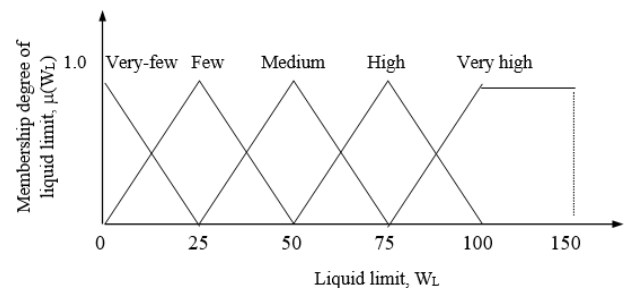
Figure 1. Fuzzy subsets of liquid limit [34]

2.3. Fuzzy Rules

Any solution to uncertainties has three interdependent steps. Successful implementation of these steps leads to a problem's solution in a fuzzy environment, i.e., the solution procedure digests any uncertainty in the basic evolution of the event concerned. The fuzzification step is the first step to the problem's solution with fuzzy rules. It needs to fuzzification the problem and its factors. The inference step systematically relates all factors, pairwise, which take place in the solution depending on the purpose of the problem. This part includes many fuzzy conditional

statements to describe a certain situation. For instance, if two events A and B are interactive, then they are dependent on each other. Conditional statements express the dependence verbally, as follows, without any equation as used in the classical approaches,

$$
\begin{aligned}
&IF\ A\ is\ x(1)\ THEN\ B\ is\ y(1)\\
&\qquad\qquad ALSO\\
&IF\ A\ is\ x(2)\ THEN\ B\ is\ y(2)\\
&\qquad\qquad ALSO\\
&\quad\ldots\ldots\ldots\ldots\ldots\ldots\ldots\\
&\quad\ldots\ldots\ldots\ldots\ldots\ldots\\
&IF\ A\ is\ x(n)\ THEN\ B\ is\ y(n)
\end{aligned}
\qquad (1)
$$

where x(.) and y(.) are linguistic descriptions of A and B respectively. The fuzzy conditional statements in Eq. (1) can be formalized in the form of the fuzzy relation R (A, B) as R (A, B) = ALSO (R_1, R_2, R_3, …, R_n), where ALSO is a sentence connection which combines Ri's into the fuzzy relation R (A, B) and Ri denotes the fuzzy relation between A and B determined by the Eq. (1) fuzzy conditional statement. After having the fuzzy relationship R (A, B) the compositional rule of inference is applied to infer the fuzzy subset y for B, given a fuzzy subset x for A as y = x o R (A, B). Where 'o' is the compositional operator [35], [36].

Lots of fuzzy implication relations are used in the literature. Lee [37] pointed out that there are implication relations of more than 40 reported in the literature. Tsoukalas and Uhrig [38] signified that the preference of implication operator depends on sense and intuition. Implication operators used in literature are the following: Zadeh max-min implication operator, Mamdani min implication operator, Larsen product implication operator, Arithmetic implication operator, and Boolean implication operator. In this study, Mamdani's [39] implication operator which is the most popular in fuzzy sets, is preferred due to the most appealing one to employ in engineering problems.

Defuzzification shows the final result from the previous step. The defuzzification method must be applied to calculate the deterministic value of a linguistic variable B. Several defuzzification techniques have been suggested. The most frequently used ones are the centroid or center of area (COA), the center of sums (COS), and the mean of maxima (MOM) [36]. Problem type, problem property, and user opinion affect the choice of the method to be used. The centroid or center of the area (COA) defuzzification technique, which is one of the most common techniques, is applied in this study. In this

technique, the crisp suction capacity is taken as the geometric center of the output fuzzy value.

2.4. Why is the Fuzzy-Set Theory Used?

Fuzzy-set theory provides a practicable way to understand and manually influence the mapping behavior. In general, fuzzy logic uses simple rules to describe the system of interest, rather than analytical equations, making it easy to implement [40]. Fuzzy cognitive maps are used as an automated decision aid to assess better how change in one component of a system affects the other components of the same system [41]. If an investigated phenomenon is very confusing and there is no sufficient knowledge, the fuzzy logic method provides a good way to solve problems based on ideas and the standard judgment of a person. In solving engineering problems with the fuzzy logic method, knowing the complexity of a phenomenon is a useful source of information.

In geotechnical engineering, it is generally possible that the results of tests and empirical equations are not in good agreement. Moreover, we watch that the results of the many tests done under, even the same conditions on the same sample, can be similar but not equal. These observations lead us to conclude that tested values scatter in wide spectra. From finite measures, we obtain knowledge about the dimensions of the spectra. But even though we generally know the boundaries of the result of another test within this event, we do not know where it will be placed in the spectra. Thus, this is fuzziness.

According to the Casagrande plasticity card, soils with a liquid limit greater than 50% are called high plasticity soils. But, if we apply fuzzy logic to this card, different degrees of high plasticity can be obtained. For example, if we take a soil with high plasticity as a criterion and compare the other soils with the criterion, soils with lower plasticity can be called low-plasticity soils, and soils with higher plasticity can be called very high-plasticity soils.

3. Results and Discussion

Expert knowledge is the most common technique for determining rules and limit sets. The expert is asked to summarize the knowledge about the system in the form of cause-and-effect relationships, and the rules are formulated. In this study, the factors affecting compacted clays' suction capacity are the plasticity index, water content, and dry density. Any of these factors are considered in fuzzy sets and separated subsets. Literature and results of tests are used to limit these subsets [10], [42], [43], [44].

The dry density, water content, and plasticity index set considered as inputs are divided into the subsets 7, 6, and 10, respectively. In this study, the triangle membership function that is used most in literature is selected. These sets are shown in Figures 2, 3, and 4. The membership functions for dry density, initial water content, and plasticity index fuzzy subsets occurred concerning numbers because many subsets exist. In these figures, $(\gamma_d(i))$, $\mu(W_0(j))$, $\mu(PI(k))$ are membership degrees of dry density, water content, and plasticity index, respectively. $\gamma_d(i)$, $W_0(j)$, and $PI(k)$ are fuzzy subsets of dry density, water content, and plasticity index, respectively. The indexes i, j, and k indicate the number of dry density, water content, and plasticity index fuzzy subsets.
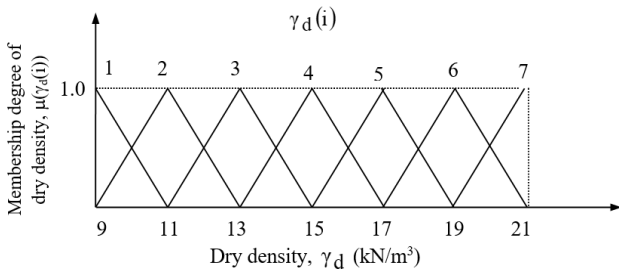

Figure 2. Fuzzy subsets of dry density [34]
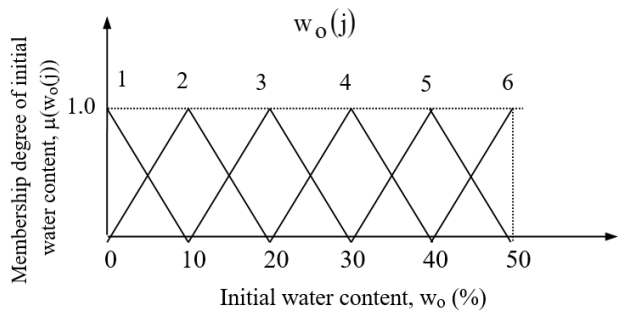
Figure 3. Fuzzy subsets of initial water content [34]

The 14-subset suction capacity set shown in Figure 5 can be obtained as an output If the sets of dry density, initial water content, and plasticity index are taken as input. Here, $\mu(W_{suc}(z))$ is the membership degree for the suction capacity. $W_{suc}(z)$ is the fuzzy subsets of suction capacity and the z index indicates the number of suction capacity subsets The database of subsets is shown in Table 3. As shown in Figure 5, the suction capacity has 14 subsets (5%~400%).
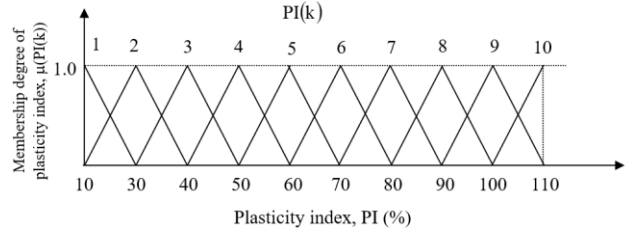
Figure 4. Fuzzy subsets of plasticity index [34]

The rules in Table 3 are formed depending on the results of the suction capacity tests seen in Table 2 and the literature's knowledge. 7x6x10=420 rules are formed for 7 different dry density ($9.0kN/m^3$~$21kN/m^3$), 6 different initial water content (0~50%), and 10 different plasticity indexes (10%~110%) fuzzy subsets. For example, for the 1st dry density fuzzy subset ($9.0kN/m^3$~$11kN/m^3$) shown in Figure 2, 2nd initial water content fuzzy subset (0~20%) shown in Figure 3, and 3rd plasticity index fuzzy subsets (20%~40%) shown in Figure 4, the predicted suction capacity of the sample consists of number 5 (Wsuc=40%~60%), number 6 (Wsuc=50%~80%), and number 7 (Wsuc=60%~105%) suction capacity fuzzy sets as shown in Figure 5. These rules are written in the Fortran language. Thus, the suction capacity may be predicted depending on compacted clays' dry density, initial water content, and plasticity index. The fuzzy output to estimate suction capacity numerically needs to be fuzzified by a Centroid fuzzification method. The results of the fuzzy logic model are shown in Table 4.

Figure 5. Fuzzy subsets of suction capacity [34]

Table 3. Fuzzy rules to determine the suction capacity [34]

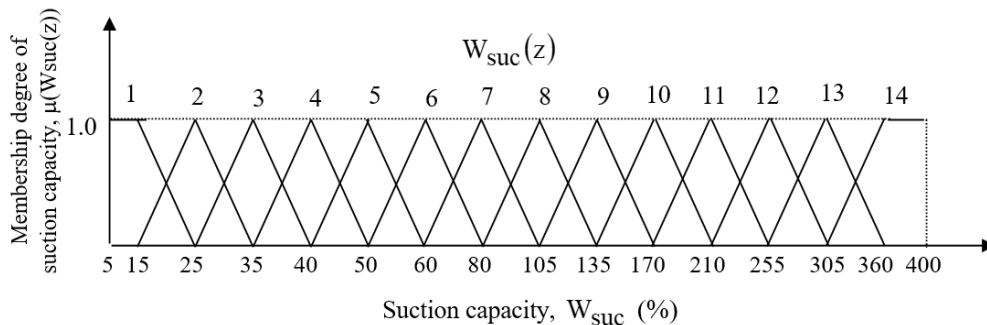| γ_d Subsets number	W_0 Subsets number	PI Subsets number 1	2	3	4	5	6	7	8	9	10
1	1	4-5	5-6	6-7	6-8	7-9	8-10	9-11	10-12	11-13	12-14
	2	3-5	4-6	5-7	6-7	7-8	8-9	9-10	10-11	11-12	12-13
	3	3-4	4-5	5-6	5-7	6-8	7-9	8-10	9-11	10-12	11-13
	4	2-3	3-4	4-5	5-6	6-7	7-8	8-9	9-10	10-11	11-12
	5	1-2	2-3	3-4	4-5	5-6	6-8	7-9	8-10	9-11	10-12
	6	1	1-3	2-4	3-5	4-6	6-7	7-8	8-9	9-10	10-11
2	1	3-5	4-6	5-7	5-8	6-9	7-10	8-11	9-12	10-13	11-14
	2	3-4	4-5	5-6	5-7	6-8	7-9	8-10	9-11	10-12	11-13
	3	2-4	3-5	4-6	4-7	5-8	6-9	7-10	8-11	9-12	10-13
	4	1-3	2-4	3-5	4-6	5-7	6-8	7-9	8-10	9-11	10-12
	5	1	1-3	2-4	3-5	4-6	5-8	6-9	7-10	8-11	9-12
	6	1	1-2	1-4	2-5	3-6	5-7	6-8	7-9	8-10	9-11
3	1	2-5	3-6	4-7	4-8	5-9	6-10	7-11	8-12	9-13	10-14
	2	2-4	3-5	4-6	4-7	5-8	6-9	7-10	8-11	9-12	10-13
	3	1-4	2-5	3-6	3-7	4-8	5-9	6-10	7-11	8-12	9-13
	4	1-3	1-4	2-5	3-6	4-7	5-8	6-9	7-10	8-11	9-12
	5	1	1-2	1-4	2-5	3-6	4-8	5-9	6-10	7-11	8-12
	6	1	1	1-3	2-4	3-5	4-7	5-8	6-9	7-10	8-11
4	1	2-4	3-5	4-6	5-7	6-8	7-9	8-10	9-11	10-12	11-13
	2	1-4	2-5	3-6	4-7	5-8	6-9	7-10	8-11	9-12	10-13
	3	1-3	2-4	3-5	4-6	5-7	6-8	7-9	8-10	9-11	10-12
	4	1-2	1-3	2-4	3-5	4-6	5-8	6-9	7-10	8-11	9-12
	5	1	1	1-3	2-4	3-5	5-7	6-8	7-9	8-10	9-11
	6	1	1	1-2	1-4	2-5	4-7	5-8	6-9	7-10	8-11
5	1	1-4	2-5	3-6	4-7	5-8	6-9	7-10	8-11	9-12	10-13
	2	1-4	1-5	2-6	3-7	4-8	5-9	6-10	7-11	8-12	9-13
	3	1-2	1-4	2-5	3-6	4-7	5-8	6-9	7-10	8-11	9-12
	4	1	1-2	1-4	2-5	3-6	4-8	5-9	6-10	7-11	8-12
	5	1	1	1-2	1-4	2-5	4-7	5-8	6-9	7-10	8-11
	6	1	1	1	1-3	1-5	3-7	4-8	5-9	6-10	7-11
6	1	1-3	1-5	2-6	3-7	4-8	5-9	6-10	7-11	8-12	9-13
	2	1-2	1-4	1-6	2-7	3-8	4-9	5-10	6-11	7-12	8-13
	3	1	1-3	1-5	2-6	3-7	4-8	5-9	6-10	7-11	8-12
	4	1	1	1-3	1-5	2-6	3-8	4-9	5-10	6-11	7-12
	5	1	1	1	1-3	1-5	3-7	4-8	5-9	6-10	7-11
	6	1	1	1	1-2	1-4	2-7	3-8	4-9	5-10	6-11
7	1	1-3	2-4	3-5	4-6	5-7	6-8	7-9	8-10	9-11	10-12
	2	1-2	1-4	2-5	3-6	4-7	5-8	6-9	7-10	8-11	9-12
	3	1	1-3	2-4	3-5	4-6	5-7	6-8	7-9	8-10	9-11
	4	1	1	1-3	2-4	3-5	4-7	5-8	6-9	7-10	8-11
	5	1	1	1	1-3	2-4	4-6	5-7	6-8	7-9	8-10
	6	1	1	1	1-2	1-4	3-6	4-7	5-8	6-9	7-10

The results of the fuzzy logic model with three inputs (dry density, initial water content, and plasticity index) and suction capacity tests are compared as shown in Figure 6. It is shown that the results of the fuzzy logic model and experiments are similar. In the prediction of suction capacity, the maximum error is $\pm10\%$ and the average error is $\pm2.69\%$.

4. Conclusion and Suggestions

Suction capacity tests done on clayey soil take a long time. The test results of the initial water content, initial dry density, and plasticity index are considered to predict the suction capacity by the fuzzy-set theory in this study. Fuzzy-set theory provides a methodology for describing complex systems using qualitative relationships like quantitative equations such as in geotechnical engineering. A computer

program in the Fortran language has been written to estimate the suction capacity of compacted clayey soils using fuzzy sets. The program uses values of dry density, initial water content, and plasticity index fuzzy subsets of compacted soil. A comparison of the results of the experiments and the program that used fuzzy sets was made and a good harmony is obtained between the results of the tests and the results of the fuzzy logic model. Therefore, it is stated that the suggested approach can reliably determine the suction capacity of compacted clayey soils.

Table 4. Results of fuzzy logic model [34]

γ_d (kN/m³)	W_0 (%)	W_{suc}^* (%) Sample 1	Sample 2	Sample 3
	15	66.2	55.2	50.7
	20	62.7	53.4	49.4
	25	58.8	48.8	43.4
11.5	30	54.2	45.6	38.9
	35	49.3	40.8	35.1
	40	44.0	39.2	33.8
	15	62.0	52.6	45.7
	20	58.6	51.0	44.5
	25	55.2	46.7	41.5
13.0	30	50.8	43.6	39.9
	35	46.3	40.7	34.9
	40	41.0	38.5	33.1
	15	61.1	51.3	43.6
	20	57.6	48.7	41.5
	25	52.9	44.7	38.3
14.0	30	48.3	40.8	35.2
	35	43.8	37.6	32.0
	40	41.2	32.4	27.9
	15	60.3	50.1	41.5
	20	55.3	47.5	40.0
	25	50.6	42.7	35.8
15.0	30	45.0	39.2	33.8
	35	41.2	34.5	29.1
	40	36.7	31.0	23.3
	15	57.8	48.0	39.4
	20	51.6	44.9	37.2
16.0	25	48.5	40.7	36.0
	30	43.4	36.5	31.6
	35	39.1	32.3	27.1
17.0	15	55.2	45.9	37.4
	20	48.8	41.6	35.9

W_{suc}^* (%): Suction capacity obtained by fuzzy logic
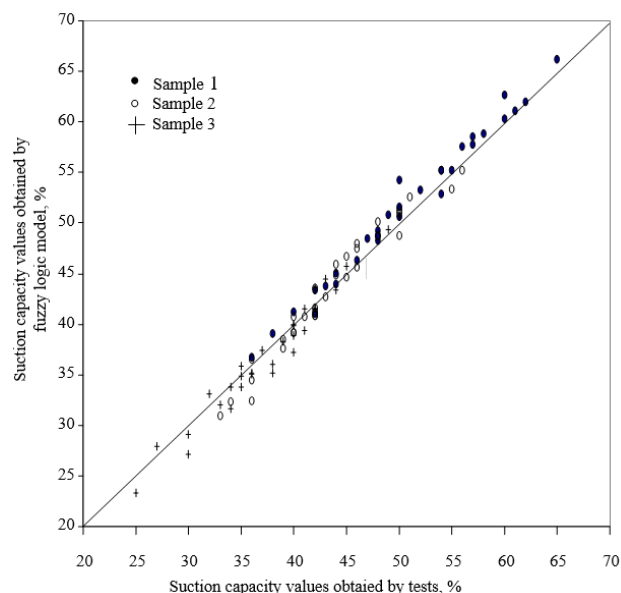
Figure 6. Comparison of the results of fuzzy logic model and tests [34]

Contributions of the authors

Ömür Çimen: Experiment, Methodology, Conceptualization, Writing-Reviewing and Editing.
S.Nilay Keskin: Conceptualization, Methodology.

Conflict of Interest Statement

There is no conflict of interest between the authors.

Statement of Research and Publication Ethics

The study is complied with research and publication ethics

References

[1] D. G. Fredlund and H. Rahardjo, *Soil Mechanics For Unsaturated Soils*. New York, USA: John Wiley & Sons. Inc., 1993.

[2] S. S. Agus, E. C. Leong, and H. Rahardjo, "Soil-water characteristic curves of Singapore residual soils," *Geotech. Geol. Eng.*, vol. 19, pp. 285-309, 2001.

[3] S. Uzundurukan, S. N. Keskin, H. Yıldırım, T. S. Göksan, and Ö. Çimen, "Suction and swell characteristics of compacted clayey soils," *Arabian J. Sci. Eng.*, vol. 39, pp. 747-752, 2013.

[4]   J. Krahn and D. G. Fredlund, "On total matric and osmotic suction," *J. Soil Sci.*, vol. 114, no. 5, pp. 339-348, 1972.

[5]   J. A. Jimenaz-Salas, "Foundation and pavements on unsaturated soils - Part two: Expansive clays," presented at the Proc. the first international conference on unsaturated soils, / Unsat'95 / Paris / France / 6-8 September 1995, 3, Presses Del L'ecole Nationale Des Ponts Et Chaussees, pp. 1441-1464, 1995.

[6]   N. Khalili and M. H. Khabbaz, "A unique relationship for χ the determination of the shear strength of unsaturated soils," *Geotech.*, vol. 48, no. 5, pp. 681-687, 1998.

[7]   J. F. T. Juca and V. Escario, "Variation of the modulus of determination of unsaturated soils with suction," *presented at the Proc. the Tenth European Conference on Soil Mechanics and Foundation Engineering*, Florence, pp. 121-124, 1991.

[8]   S. K. Vanapalli, D. G. Fredlund, D. E. Pufahl, and A. W. Clifton, "Model for the prediction of shear strength with respect to soil suction," *Can. Geotech. J.*, vol. 33, pp. 379-392, 1996.

[9]   D. W. Rassam and D. J. Williams, "Bearing capacity of desiccated tailings", *J. Geotech. Geoenv. Eng.*, vol. 125, no. 7, pp. 600-609, 1999.

[10]   J. D. Nelson and D. J. Miller, *Expansive Soils Problem and Practice in Foundation and Pavement Engineering*, New York, USA: John Wiley & Sons, 1992.

[11]   J. M. Fleureau, S. K. Saoud, R. Soemitro, and S. Taibi, "Behaviour of clayey soils on drying- wetting paths," *Can. Geotech. J.*, vol. 30, pp. 287-296, 1993.

[12]   L. N. Reddi and R. Poduri, "Use of liquid limit state to generalize water retention properties of fine-grained soils," *Geotech.*, vol. 47, no. 5, pp. 1043-1049, 1997.

[13]   S. M. Rao and K. Revanasidappa, "Role of matric suction in collapse of compacted clay soil," *J. Geotech. Geoenv. Eng.*, vol. 126, no. 1, pp. 85-90, 2000.

[14]   S. K. Vanapalli, D. G. Fredlund, and D. E. Pufahl, "The influence of soil structure and stress history on the soil-water characteristics of a compacted till," *Geotech.*, vol. 49, no. 2, pp. 143-159, 1999.

[15]   E. Romero, A. Gens, and A. Lloret, "Temperature effects on the hydraulic behaviour of an unsaturated clay," *Geotech. Geol. Eng.*, vol. 19, pp. 311-332, 2001.

[16]   A. Casagrande, "Role of calculated risk in earthwork and foundation engineering," *J. Soil Mech. Found. Div., ASCE*, vol. 91, no. 4, pp. 1-40, 1965.

[17]   L. A. Zadeh, "Fuzzy Sets," *Inform. Cont.*, vol. 8, pp. 338-353, 1965.

[18]   C. H. Juang, J. L. Wey, and D. J. Elton, "Model for capacity of single piles in sand using fuzzy sets," *J. Geotech. Eng.*, vol. 17, no. 12, pp. 1920-1931, 1991.

[19]   C. H. Juang, D. H. Lee, and C. Sheu, "Mapping slope failure potential using fuzzy sets," *J. Geotech. Eng.*, vol. 118, no. 3, pp. 475–494, 1992.

[20]   C. H. Juang, X. H. Huang, R. D. Holtz, and J. W. Chen, "Determining relative density of sands from CPT using fuzzy sets," *J. Geotech. Eng.*, vol. 122, no. 1, pp. 1-6, 1996.

[21]   Z. Zhang and M. T. Tümay, "Statistical to fuzzy aprrroach toward CPT soil classification," *J. Geotech. Geoenv. Eng.*, vol. 125, no. 3, pp. 179-186, 1999.

[22]   N. O. Nawari and R. Liang, "Fuzzy-based approach for determination of characteristic values of measured geotechnical parameters," *Can. Geotech. J.*, vol. 37, pp. 1131-1140, 2000.

[23]   A. Sujatha, L. Govindaraju, N. Shivakumar, and V. Devaraj, "Fuzzy Expert System for Engineering Classification of Soils," *Geotechnical Characterization and Modelling Conf.*, pp. 85-101, 2020.

[24]   K. C. Onyelowe, F. F. Mojtahedi, A. M. Ebid, A. Rezaei, K. J. Osinubi, A. O. Eberemu, B. Salahudeen, E. W. Gadzama, D. Rezazadeh, H. Jahangir, P. Yohanna, M. E. Onyia, F. E. Jalal, M. Iqbal, C. Ikpa, I. I. Obianyo, and Z. U. Rehman, "Selected AI optimization techniques and applications in geotechnical engineering," *Cogent Eng.*, vol. 10, 2153419, 2023.

[25]   M. Rahal, S. Soleiman, and B. Hussein, "Comprehensive Methodology for Landslide Risk Assessment Using Fuzzy Logic Systems: A Step-by-Step Approach," *presented at the Proc. the 9th World Congress on Civil, Structural, and Environmental Engineering (CSEE 2024), London*, United Kingdom, Paper No.152, April 14-16, 2024.

[26]   A. Flamaki, A. H. Shafiee, and M. Esfandiyari, "Feasibility study of fuzzy method in slope stability analysis of earth dams with respect to the uncertainty of geotechnical parameters," *J. Hydrau. Struct.*, vol. 10, no. 3, pp.34-50, 2024.

[27] V. C. Madanda, F. Sengani, and F. Mulenga, "Applications of fuzzy theory-based approaches in tunnelling geomechanics: a state-of-the-art review," *Mining, Metal. & Explor.*, vol. 40, pp.819–837, 2023.

[28] Y. Mao, L. Chen, Y. A. Nanehkaran, M. Azarafza, and R. Derakhshani, "Fuzzy-based intelligent model for rapid rock slope stability analysis using Qslope," *Water*, vol. 15, 2949, 2023.

[29] E. A. Çubukçu, E. Uray, and V. Demir, "Fuzzy logic based prediction of retaining wall stability," *Chall. J. Struct. Mech.*, vol. 9, no. 4, pp. 145–152, 2023.

[30] V. Phani Kumar and C. Sudha Rani, "Prediction of safe bearing capacity for settlement criteria using neuro-fuzzy inference system for Clayey soils", *Adv. Sustain. Mater. Infras., IOP Conf. Series: Earth Envir. Sci.*, 1086, 012023, 2022.

[31] A. Sujatha, L. Govindaraju, N. Shivakumar, and V. Devaraj, "Fuzzy Knowledge Based System for Suitability of Soils in Airfield Applications," *Civ. Eng. J.*, vol. 7, no. 1, 2021.

[32] I. Zorluer and U. S. Cavus, "Fuzzy logic assessment of engineering properties of granular soil with wastes for environment protection and road base use," *Case Stud. Const. Matrl.*, vol. 15, e00774, 2021.

[33] E. Yıldırım, E. Avcı, and N. A. Tanbay, "Prediction of unconfined compressive strength of microfine cement injected sands using Fuzzy Logic method," *Academic Platf. J. Eng. Smrt. Sys.*, vol. 11, no. 2, pp.87-94, 2023.

[34] Ö. Çimen, "Determination of swelling and suction properties of clay soils with fuzzy logic," PhD dissertation, Dept. Civil Eng., Süleyman Demirel Univ., Isparta, Türkiye, 2002.

[35] S. H. Lee, R. J. Howlett, C. Crua, and S. D. Walters, "Fuzzy logic and neuro-fuzzy modeling of diesel spray penetration: A comparative study," *J. Intelligent Fuzzy Syst.*, vol. 18, pp. 43-56, 2007.

[36] S. Fons, G. Achari, and T. Ross, "A fuzzy cognitive mapping analysis of the impacts of an eco-industrial park," *J. Intelligent Fuzzy Syst.*, vol. 15, no. 2, pp. 43-56, 2004.

[37] B. Kosko, *Neural Networks and Fuzzy Systems*, Englewood Cliffs, N.J., USA: Prentice Hall, 1992.

[38] Z. Sen, *Bulanik Mantık ve Modelleme İlkeleri*, İstanbul, Türkiye: Publications of Water Foundation, (in Turkish), 2001.

[39] C. C. Lee, "Fuzzy logic in control systems: fuzzy logic controller- part 1," *IEEE Trans. Sys. Man Cyber.*, vol. 20, no. 2, pp. 404-418, 1990.

[40] L. H. Tsoukalas and R. E. Uhrig, *Fuzzy and Neural Approaches in Engineering*, New York, USA: John Wiley & Sons, Inc., 1997.

[41] E. H. Mamdani, "Applications of Fuzzy set theory to control systems: A survey," in *Fuzzy Automata and Decision Processes*, M.M. Gupta, G.N. Saridis and B.R. Gaines, Eds., Amsterdam, North-Holland, 1977, pp. 1-13.

[42] F. H. Chen, *Foundations on Expansive Soil*, New York, USA: Elsevier, 1975.

[43] J. K. Mitchell, *Fundamentals of Soil Behavior*, New York, USA: John Wiley & Sons, Inc., 1976.

[44] D. R. Snethen, "Evaluation on expedient methods for ıdentification on classification of potentially expansive soils", *presented at the Proc. 5th Int. Conf. on expansive soils*, Adelaide, 1984.

Bitlis Eren Üniversitesi Fen Bilimleri Dergisi

A Machine Learning Prediction Model for Myelitis and Multiple Sclerosis Based on Fourier Transform Features from MRI Images

Züleyha YILMAZ ACAR[1*]

[1]Selçuk University, Department of Computer Engineering, Faculty of Technology, Konya, Türkiye
(ORCID: 0000-0002-4488-478X)

Abstract

Myelitis is a neurodegenerative disease positioned in the spinal cord, with multiple sclerosis (MS) being a common subtype. Radiological indicators enable the diagnosis of these diseases. This study proposes a classification framework to detect myelitis, MS, and healthy control (HC) groups using magnetic resonance imaging (MRI) images. The feature extraction step involves applying the fast Fourier transform (FFT) to MRI images. FFT is important because it converts spatial data into the frequency domain, making it easier to identify patterns and abnormalities that indicate these diseases. Then, statistical features (mean, minimum, maximum, standard deviation, skewness, kurtosis, and total energy) are extracted from this frequency information. These features are then used to train support vector machine (SVM), k-nearest neighbor (KNN), and decision tree algorithms. In multi-class classification (myelitis vs. MS vs. HC), the proposed method achieves a classification accuracy of 99.31% with SVM, with average precision, recall, and F1-score values of 99.27%, 99.21%, and 99.24%, respectively, indicating effective classification across all classes. In the binary class classification (HC vs. MS, MS vs. myelitis, HC vs. myelitis), the SVM achieves an outstanding classification accuracy of 99.36%, 99.71%, and 100% respectively. This study highlights the efficiency of FFT-based feature extraction in forming detection patterns for classifying HC, MS, and myelitis classes.

1. Introduction

Myelitis is a neurodegenerative disorder caused by inflammation of the myelin sheath surrounding the nerves in the spinal cord. The disease can cause motor symptoms, sensory symptoms, and autonomic involvement [1]. Various presentations are depending on the site of inflammation [2], [3]. Since multiple sclerosis (MS) is in the common myelitis subgroup, it is important to distinguish between myelitis-non-MS and MS in the diagnosis of the disease. In some cases, it has been observed that myelitis has been observed to be the first sign of MS and may progress to MS [4]. Radiological differentials are known to be more useful in diagnosing the disease [3]. Automatic analysis of radiological images obtained by magnetic resonance imaging (MRI) based on artificial intelligence helps experts in useful aspects such as shortening the diagnosis time and early diagnosis of the disease.

Looking at the studies on automatic diagnosis based on artificial intelligence in the context of neurological diseases, we can see that a wide range of topics have been addressed from the past to the present. Some studies use spatial features extracted by applying wavelet transform to MRI images [5]-[8]. The histogram of oriented gradients (HOG) method has been used to discriminate different structures based on texture shape or gradient change representations in images [9]-[11]. Transfer learning, a type of deep learning, has been used for both feature extraction and classification of raw data in some studies [12]-[15]. In addition to these, there are studies on neurological disease diagnosis by using

*Corresponding author: *zuleyhayilmaz@selcuk.edu.tr*

various models of deep learning models as classifiers [16]-[19]. Finally, studies using deep learning models as a feature extraction method followed by traditional machine learning algorithms as classifiers are also common [20]-[22].

This paper presents a classification framework for the detection of myelitis, MS, and healthy control (HC) classes. For the first step of feature extraction, which is the most important pre-step of classification, it is proposed to apply the fast Fourier transform (FFT) to the MRI dataset and extract statistical features from the frequency spectrum. The Fourier transform provides frequency information about the signal to which it is applied, allowing the analysis of the image in frequency domain. Then, the machine learning algorithms are fed by the feature set created by extracting statistical features (mean value, minimum value, maximum value, standard deviation, skewness, kurtosis, and total energy) from the resulting two-dimensional FFT output. Support vector machine (SVM), k-nearest neighbor (KNN), and decision tree algorithms are used as classifiers in the study. Multi-class classification based on three classes (HC vs. MS vs. myelitis) and binary class classification (MS vs.

myelitis, HC vs. MS, HC vs. myelitis) are evaluated and analyzed. Since, to the author's knowledge, no study has applied a fast Fourier transform to MRI images in this manner. Therefore, this study makes a significant and valuable contribution to the literature, demonstrating high classification success using FFT.

2. Material and Method

The classification framework for myelitis, MS and healthy control groups proposed in the study is depicted in Figure 1. Detailed information about the stages is presented following sections.

2.1. Dataset

A public dataset downloaded from the Kaggle website is used in the study [20]. The myelitis dataset consists of a total of 2,746 spinal MRI images categorized into myelitis-non-MS patients, MS patients, and a healthy control group. Detailed information about the dataset is provided in Table 1.
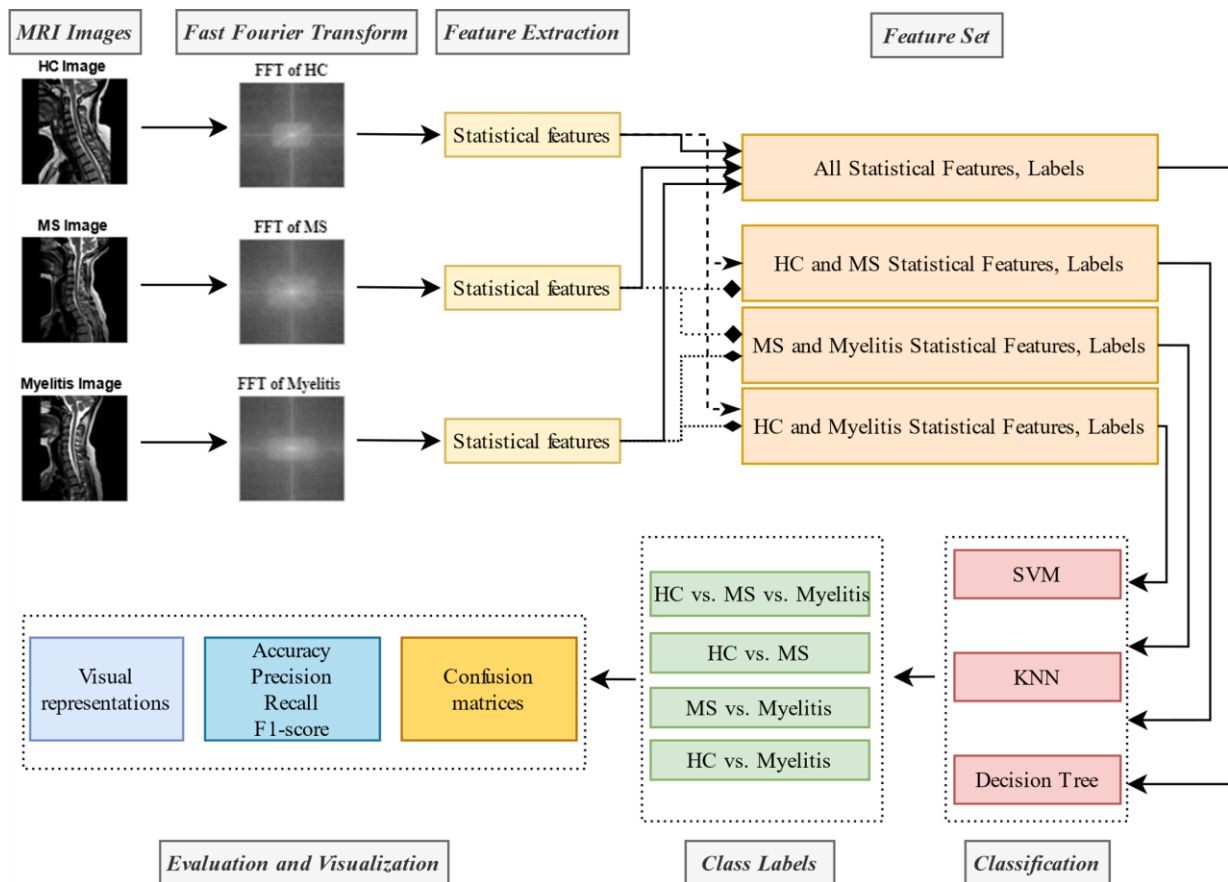

Figure 1. Proposed process of the paper.

Table 1. Details about dataset

Class	Number of images	The class percentages
Myelitis	706	25.71%
MS	667	24.29%
Healthy Control	1,373	50%
Total	2,746	100%

The dataset consists of spinal MRI images. To differentiate between HC, MS, and myelitis classes, the presence of spinal lesions and, if present, vertebral lengths are analyzed. Therefore, spinal MRI images are used in both sagittal and axial planes. Sample images from the dataset are shown in Figure 2.

(a)   (b)
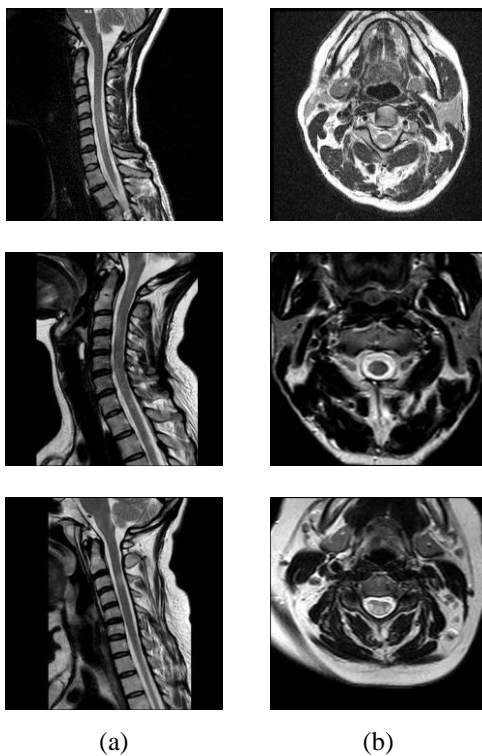
Figure 2. Dataset sample images on (a) sagittal (b) axial planes

2.2. Proposed Approach

2.2.1. Feature extraction model based on FFT

Since the presence and length of lesions in MRI data vary, it is proposed that these patterns are preserved when the images are transformed into the frequency domain. Subsequently, fast Fourier transform (FFT) is applied to the MRI images. The Fourier transform captures the signal's frequency spectrum, enabling analysis and signal processing [23]. This transform provides frequency components of the signal, applied in two dimensions to the image to obtain horizontal and vertical spatial frequencies. In the resulting Fourier-transformed matrix, spectral components are concentrated based on where meaningful information is located, either at low or high frequencies [24].

In this study, frequency spectrum is extracted from MRI images using 2-D FFT. After applying 2-D FFT, a complex value matrix is obtained. The magnitude spectrum for each image is then calculated by taking the absolute value of this matrix. The different MRI data, which are shifted in the spatial domain, display different phase angles in the frequency domain [25]. By using absolute values, the spectrum remains unaffected by these shifts, effectively eliminating spatial differences in the MRI images. The steps involved in applying 2-D FFT are outlined below [26]:

Step 1. 2-D FFT application:

$$FT_{p,q} = \tag{1}$$
$$\sum_{j=0}^{M-1} \sum_{k=0}^{N-1} \left(e^{-\frac{2\pi i}{M}} \right)^j \left(e^{-\frac{2\pi i}{N}} \right)^k X_{j+1,k+1}$$

Step 2. Absolute value calculation of the matrix obtained with 2D FFT:

$$MagnitudeSpectrum_{p,q} = \left| FT_{p,q} \right| \tag{2}$$

Figure 3 illustrates how the Fourier transform utilizes both the spatial arrangement and pixel values within the image.
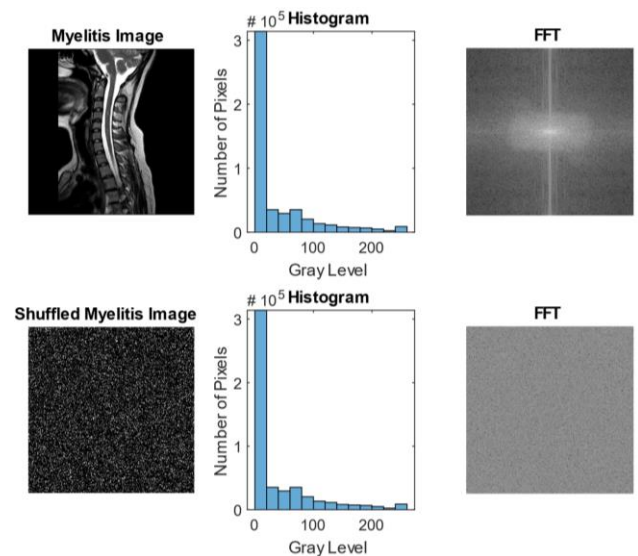
Figure 3. Histogram and FFT representation of a myelitis MRI image (first row) and the same image with pixels shuffled (second row)

Figure 3 displays an original myelitis image and the same image with shuffled pixels, their respective histograms, and the FFT results. The histograms of these images remain unchanged because the pixel values do not change. However, the FFT output differs as it utilizes spatial frequencies of pixels. This figure also illustrates the FFT's capability to extract meaningful information across pixel relationships.

2.2.1. Machine Learning with FFT

Machine learning methods rely on effective feature engineering techniques to achieve high performance, as they involve extracting underlying patterns from the data. In this study, frequency components are extracted using FFT, and their statistical features—mean value, minimum value, maximum value, standard deviation, skewness, kurtosis, and total energy— are utilized as inputs for machine learning algorithms. The equations for the skewness, kurtosis, and total energy features are provided below as (3), (4), and (5) respectively:

$$Skewness = \frac{E(x-\mu)^3}{\sigma^3} \tag{3}$$

$$Kurtosis = \frac{E(x-\mu)^4}{\sigma^4} \tag{4}$$

$$Total\ energy = \sum x^2 \tag{5}$$

In the equations, x is the vector form of the magnitude spectrum matrix. μ is the mean of x, σ is its standard deviation. E(n) is the expected value of the quantity n. The total energy magnitude is the sum of the squares of all values in the vector form of the magnitude spectrum matrix.

Support vector machine, k-nearest neighbor, and decision tree algorithms are used as machine learning classifiers. Each classifier is fed using seven normalized features extracted from the images and along with class labels for myelitis, MS or HC. As a result, the trained models are then used to predict classes for a test set that it is not previously seen. Through 10-fold cross-validation, every data point in the dataset is included in the test set at least once, ensuring robust validation of the proposed method generalization ability.

3. Experimental Results

In the study, multi-class classification is performed for HC vs. MS vs. myelitis, alongside binary class classification for HC vs. MS, MS vs. myelitis, and HC vs. myelitis. The results of these classifiers are shown using the confusion matrices, where the values in the diagonal represent the number of instances correctly classified by the respective class. The confusion matrices used in the study are illustrated in Figure 4.
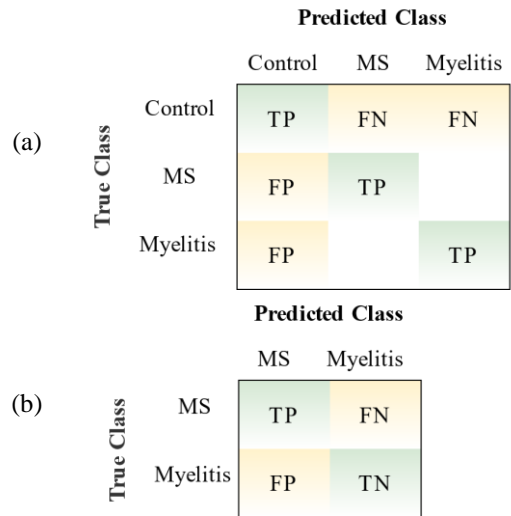
Figure 4. Confusion matrices for (a) multi-class and (b) binary class classification

Evaluation metrics are calculated with true positive (TP), false negative (FN), false positive (FP), and true negative (TP) values in the confusion matrix

3.1. Evaluation Metrics

The performance of the classifiers is evaluated by calculating accuracy, precision, recall, and F1-score values using the confusion matrix. The equations for these metrics are provided in (6) - (9) respectively:

$$Accuracy = \frac{\sum True\ Predictions}{All\ Predictions} \tag{6}$$

$$Precision = \frac{TP}{TP+FP} \tag{7}$$

$$Recall = \frac{TP}{TP+FN} \tag{8}$$

$$F1\text{-}score = \frac{2*Precision*Recall}{Precision+Recall} \tag{9}$$

When calculating the multi-class classification results, the accuracy metric is determined by the proportion of correctly predicted instances represented on the diagonal of the confusion matrix. Precision and recall metrics are computed class-wise using TP, FN, and FP values. This means that each class in the matrix is assumed to be a positive class respectively when calculating the metrics. Classifier comparisons are based on average precision and recall values.

3.2. Results for Machine Learning Models

Using FFT, frequency components are extracted and the images are re-visualized in the frequency domain. The resulting images from applying FFT to the HC, MS, and myelitis classes are shown in Figure 5.
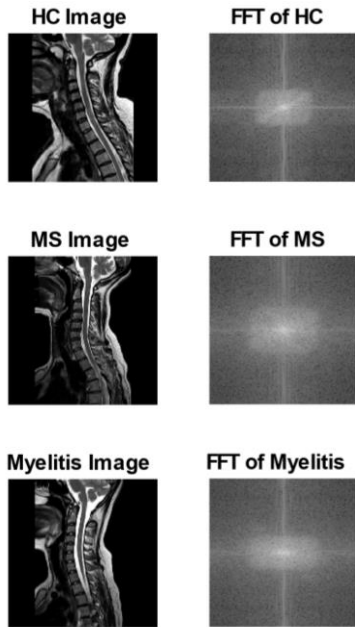
Figure 5. The example images and their FFT results in the dataset

After applying the FFT process, seven statistical features are extracted from each image. As a result, the dataset consisting of 2,746 images is transformed into a 2746x8 numerical matrix, including class labels. The training and testing phases of the classifiers are performed using 10-fold cross-validation. SVM, KNN, and decision tree classifiers are used as machine learning algorithms. By trial-and-error, the hyperparameters for SVM are set to use a cubic kernel and a box constraint level of 1. For KNN, the number of neighbors is set to 1, with the Euclidean distance metric. Lastly, the decision tree is configured with 100 splits and Gini's diversity index as the split criterion.
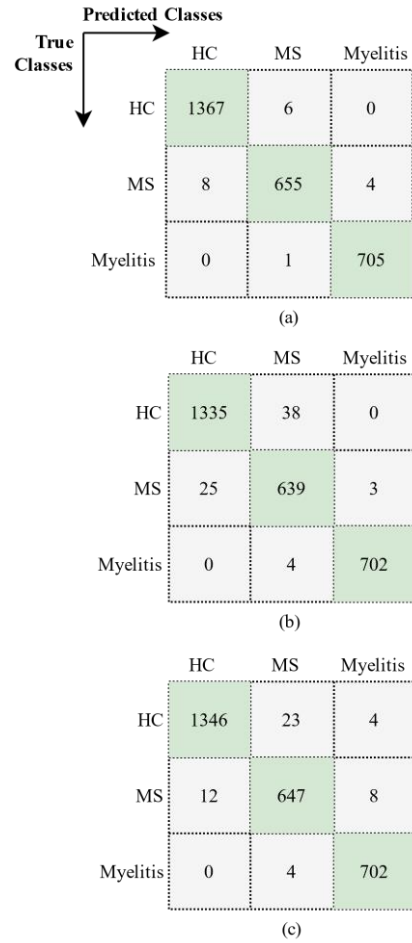
3.3. Multi-class Classification Results for HC, MS, and Myelitis Classes

The confusion matrices obtained by SVM, KNN, and decision tree classifiers for multi-class classification over HC, MS, and myelitis are illustrated in Figure 6.

Figure 6. Confusion matrices of (a) SVM, (b) KNN, and (c) Decision Tree classifiers on multi-class classification

The diagonal values in Figure 6 indicate the number of correctly predicted instances, while outliers represent misclassified data points. Confusion matrix values indicate that the misclassification values in HC and myelitis classes are very low, and there are difficulties in distinguishing between MS and myelitis classes for all classifiers. The total misclassification costs are visualized in Figure 7.
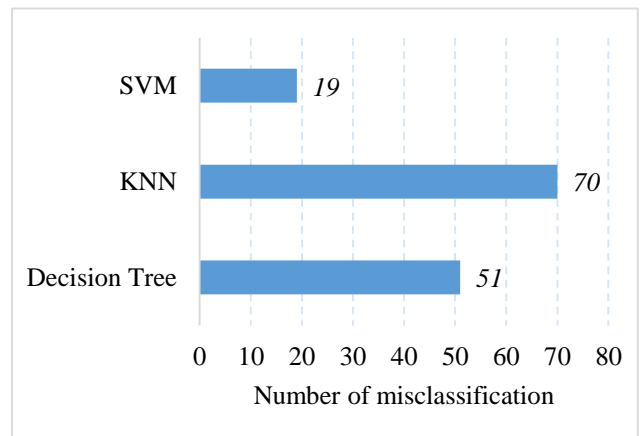
Figure 7. Total misclassification costs of the classifiers

Figure 7 shows that SVM has the lowest error with a misclassification value of 19. On the other hand, decision tree has a cost of 51, while KNN has a cost of 70.

In Table 2, the evaluation metrics calculated from the confusion matrices generated by the classifiers are presented, and precision, recall, and F1-score metrics are calculated for each class individually. Additionally, average precision, recall, and F1-score values are provided to compare the overall performance of the classifiers. Accuracy is presented as a single value, calculated based on the classifiers' correct predictions of the class labels.

Overall, the SVM classifier achieves the highest classification rate with 99.31% accuracy, along with an average precision of 99.27%, average recall of 99.21%, and average F1-score of 99.24%. The KNN classifier achieves 97.45% accuracy, with average precision, recall, and F1-score values of 97.19%, 97.49%, and 97.34% respectively. The decision tree obtains an accuracy of 98.14%, along with average precision, recall, and F1-score values of 97.81%, 98.16%, and 97.98% respectively.

Table 2. Multi-class classification evaluation results

Classifiers	Classes	Evaluation metrics (%)			
		Precision	Recall	F1-score	Accuracy
SVM	Healthy Control	99.42	99.56	99.49	
	MS	98.94	98.20	98.57	99.31
	Myelitis	99.44	99.86	99.65	
	Average values	*99.27*	*99.21*	*99.24*	
KNN	Healthy Control	98.16	97.23	97.69	
	MS	93.83	95.80	94.81	97.45
	Myelitis	99.57	99.43	99.50	
	Average values	*97.19*	*97.49*	*97.34*	
Decision Tree	Healthy Control	99.12	98.03	98.57	
	MS	95.99	97.00	96.50	98.14
	Myelitis	98.32	99.43	98.87	
	Average values	*97.81*	*98.16*	*97.98*	

Figure 8. Confusion matrices of (a) SVM, (b) KNN, and (c) Decision Tree classifiers on binary class classification

3.4. Binary Class Classification Results

In addition to multiclass classification, the performance of the FFT method on binary classification is evaluated. This analysis involves using the feature set created in t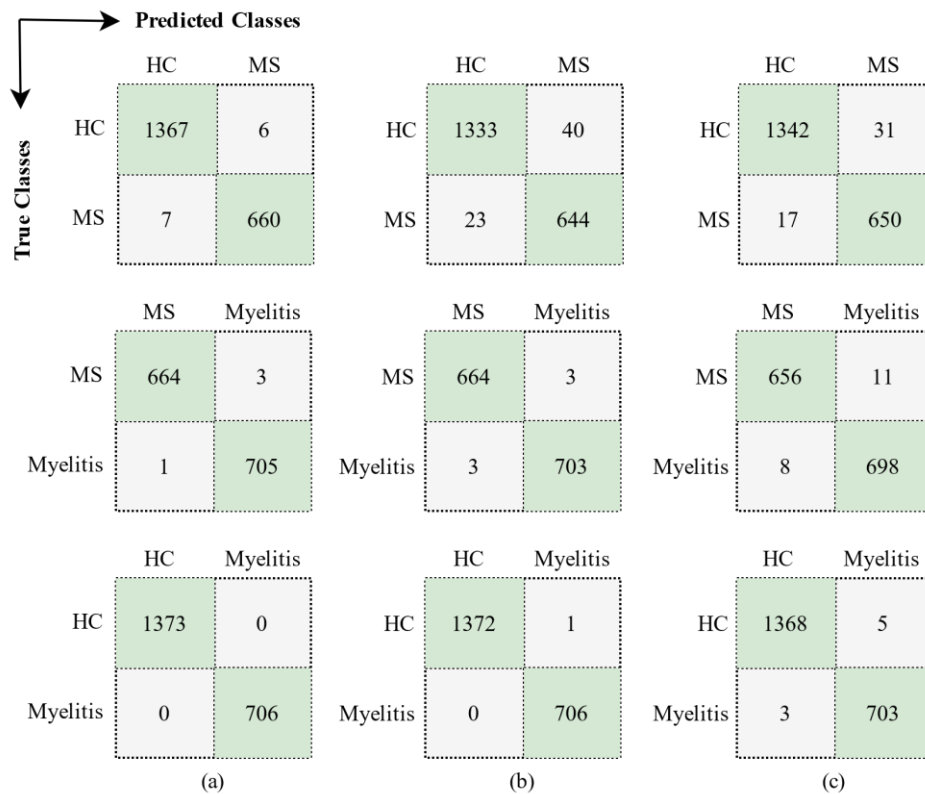he study to classify between two classes. Binary class classification is performed for HC vs. MS, MS vs. myelitis, and HC vs. myelitis. The confusion matrices generated by SVM, KNN, and decision tree classifiers are shown in Figure 8.

According to Figure 8, among 2,040 images, SVM has 13 misclassification cost, the KNN has a cost of 63, and the decision tree has a cost of 48 for HC vs. MS classification. Among 1,343 images for MS vs. myelitis classification, SVM has 4 misclassification cost, the KNN has a cost of 6, and the decision tree is a cost of 19. Among 2,079 images for HC vs. myelitis classification, SVM has zero misclassification cost, the KNN has a cost of 1, and the decision tree is a cost of 8. Visual representations of misclassification costs are illustrated in Figure 9.
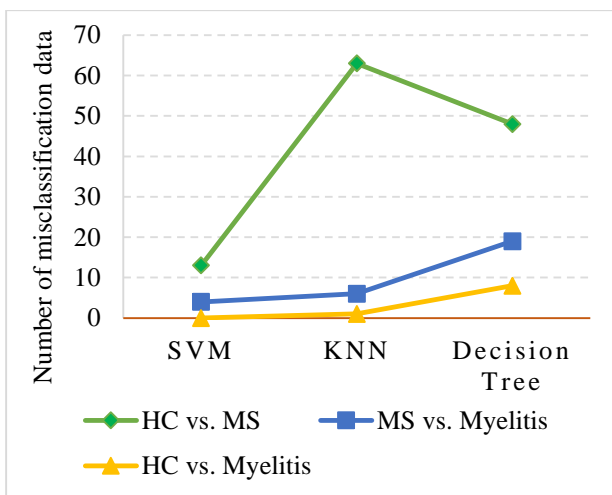
Figure 9. Confusion matrices of (a) SVM, (b) KNN, and (c) Decision Tree classifiers on binary class classification

The calculated evaluation metrics are detailed in Table 3. The results demonstrate that SVM achieves the highest accuracy values across all binary classifications. It gets an accuracy of 99.36% for HC vs. MS, 99.71% for HC vs. MS, and 100% for HC vs. MS. KNN also shows successful evaluation metrics, performing better than the decision tree in all categories except HC vs. MS classification. These results indicate that FFT combined with statistical features exhibits superior performance as a feature extraction method, resulting in minimal misclassification costs, particularly with the SVM classifier. Notably, SVM achieves perfect predictions

for HC vs. myelitis classes. The general results obtained can be summarized as follows: (1) Proposed FFT+statistical features model achieves the highest successful results on HC and myelitis classes, (2) the highest misclassification cost is observed between HC and MS classes, (3) SVM displays the highest evaluation metric results, (4) the decision tree outperforms KNN in predicting HC and MS classes.

4. Discussion

### 4.1. Analysis of the proposed approach's performance results

The dataset for myelitis, MS, and healthy control classes, consisting of axial and sagittal MRI images, is re-visualized in the frequency domain using FFT. Subsequently, seven statistical features—mean value, minimum and maximum values, skewness, kurtosis, and total energy—are extracted from the frequency spectrum.

Multi-class classification and binary class classification are performed and the results are analyzed separately. According to the results obtained by SVM, KNN, and decision tree classifiers, it is observed that the MRI data in the frequency domain with FFT preserved the distinctive features of the classes. Among the classifiers, the SVM achieves the highest accuracy. While calculating the evaluation metrics, each class is selected as a positive class in turn, and class-wise metrics are averaged to analyze the method's success. In the classification of the three classes, the SVM algorithm correctly classified 2,727 data out of 2,746 images, misclassifying 19 images. As a result, SVM achieves 99.31% accuracy, 99.27% precision, 99.21% recall, and a 99.24% F1-score. The decision tree performs better than KNN, with an accuracy of 98.14%. When analyzed on the class-wise basis, the decision tree is particularly successful in classifying healthy control and MS classes, while KNN shows higher success in myelitis classification. Another outcome of the study is the relatively lower classification success in the MS class. Nevertheless, the feature set generated by the proposed method enables SVM and KNN to effectively discriminate healthy control and myelitis classes, achieving a satisfactory success rate.

When the FFT method is applied to MRI data, low-frequency components are located in the center of the spectrum, providing information about the overall structure of the image. High-frequency components, which spread out to the edges, represent distinctive details, thereby analyzing intensity variations between pixels.

Table 3. Binary class classification evaluation results

Classifiers	Classes	Evaluation metrics (%)			
		Precision (average)	Recall (average)	F1-score (average)	Accuracy
SVM	HC vs. MS	99.29	99.26	99.28	99.36
	MS vs. myelitis	99.71	99.70	99.71	99.71
	HC vs. myelitis	100	100	100	100
KNN	HC vs. MS	96.23	96.82	96.51	96.91
	MS vs. myelitis	99.56	99.56	99.56	99.56
	HC vs. myelitis	99.93	99.96	99.95	99.95
Decision Tree	HC vs. MS	97.10	97.60	97.34	97.65
	MS vs. myelitis	98.62	98.61	98.61	98.62
	HC vs. myelitis	99.54	99.61	99.57	99.62
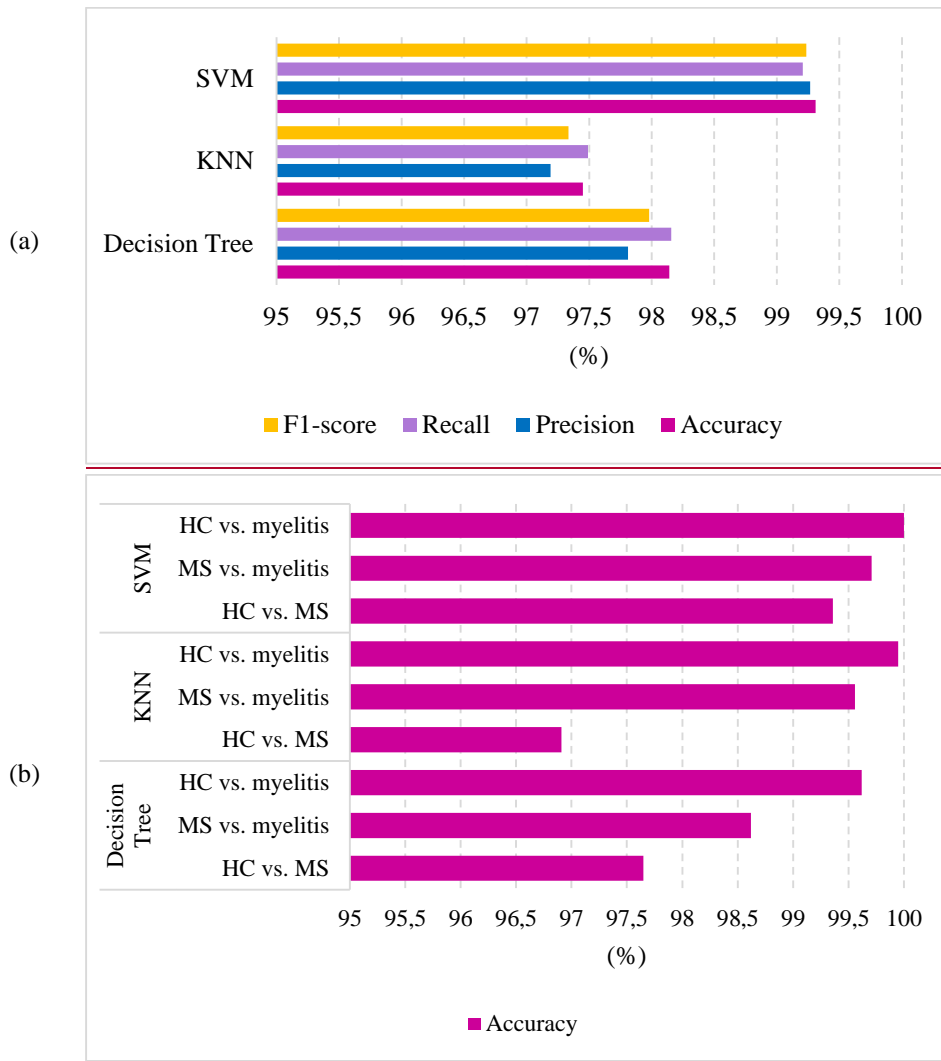
Figure 10. Visual comparison of evaluation metrics for (a) multi-class (b) binary class classification

The results of both multi-class and binary class classification show high accuracies for the healthy control and myelitis classes, with relatively lower accuracies for MS. This is likely due to the vertebral length of the lesions in the spinal cord; more extensive lesions cause stronger pixel intensity changes, making the easier for the FFT to distinguish. An analysis of the binary class classification results reveals that the most confusion for the classifiers occurs between healthy control and MS classes. In contrast, SVM and KNN almost perfectly detects healthy control and myelitis classes, achieving 100%

and 99.95% accuracy, respectively. These results imply that the FFT combined with statistical features effectively extracts image patterns and preserves the distinguishing features between classes. As a result, balanced evaluation metrics are achieved without any class dominance. Figure 10 shows summarized visualizations of performance metrics for multi-class and binary class classification.

Figure 10(a) illustrates for multi-class classification that the proposed FFT+statistical features model shows the highest success with SVM for HC vs. myelitis. The classifiers achieve lower classification success for HC vs. MS among all binary class classification. The proposed method achieves over 96.5% classification success in all classifiers for all binary classes. Figure 10(b) illustrates for binary classification that SVM achieves over 99% success in all metrics. Decision tree obtains better results than KNN, and all classifiers gets balanced/proportional success in all metrics.

4.2. Comparative analysis with other studies and alternative dataset

In order to detect myelitis, MS, and healthy control, the performance of the FFT+statistical features method proposed in this study is compared with another study [20], which utilizes on the same dataset (Myelitis Dataset).

Additionally, the proposed FFT+statistical features model is applied to another dataset from Kaggle [27], containing MRI data of MS and healthy control classes. This dataset comprises both axial and sagittal images, totaling 3,427 images, including 1,411 MS images and 2,016 healthy control images (MS Dataset). All the steps applied to the Myelitis dataset are also applied to this MS dataset, and the results obtained by SVM are listed in Table 4.

Table 4. Overall performance comparison with other studies

Datasets	Method	Evaluation metrics			
		Accuracy	Precision	Recall	F1-score
Myelitis Dataset	Tatli et al. [20]	97.63	97.23	97.23	97.23
(HC vs. MS vs. myelitis)	The proposed model	99.31	99.27	99.21	99.24
MS Dataset	Macin et al. [27]	98.22	99.27	96.39	97.81
(HC vs. MS)	Ekmekyapar and Taşcı [28]	98.02	98.31	97.63	97.94
	The proposed model	99.91	99.93	99.89	99.91
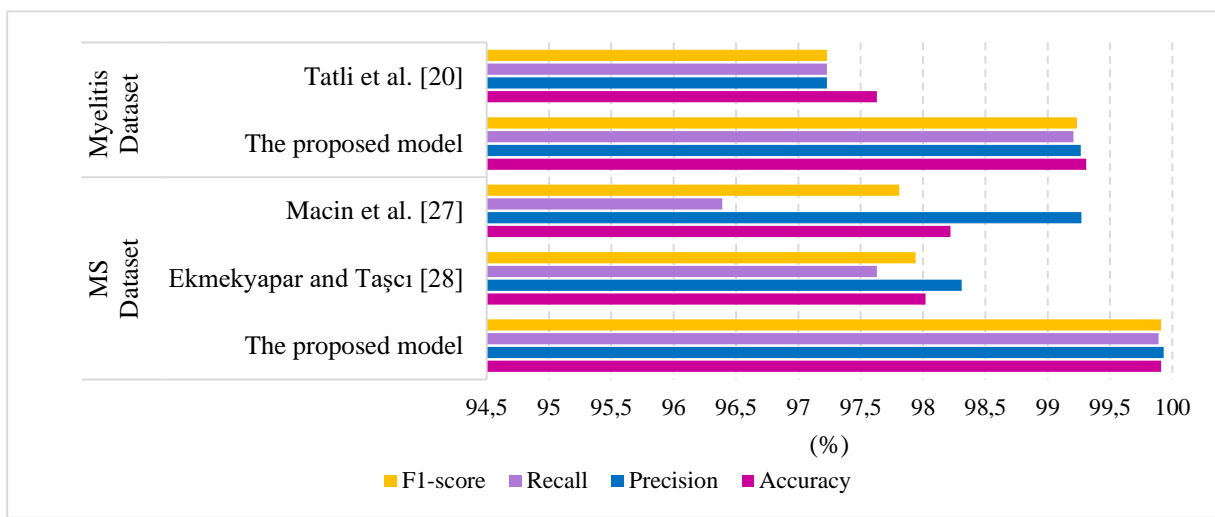
Figure 11. Evaluation metrics comparisons with other studies and datasets

According to Table 4, the method proposed in this paper achieves higher success in all metrics across both datasets. As shown in Figure 11, the bar graph illustrates that the proposed method in this study outperforms the other studies on all evaluated metrics.

5. Conclusion

In this study, it is proposed that visualizing myelitis, MS, and HC MRI images in the frequency domain using FFT is preserve important patterns in statistical features of these images, aiding in class detection. The effectiveness of the proposed feature extraction method is tested using classifiers. SVM, KNN, and decision tree, which are commonly used machine learning algorithms in biomedical image classification, are employed to detect myelitis, MS, and healthy control classes. According to the results, SVM achieves 99.31% correct classification accuracy for multiclass classification after applying the FFT method to MRI images. The method's average precision (99.27%), recall (99.21%), and F1-score (99.24%) values indicate balanced classification across all classes. Additionally, for binary class classification, the proposed FFT+statistical features combination demonstrates superior performance with the SVM classifier, achieving 99.36% accuracy (HC vs. MS), 99.71% accuracy (MS vs. myelitis), 100% accuracy (HC vs. myelitis). These results show that the statistical features of the FFT-transformed images effectively formed patterns that characterize the classes, confirming their utility as a highly successful feature extractor. As a future work, the FFT method can be applied to different biomedical data sets, or its performance can be analyzed by combining it with deep learning models.

References

[1] E. Glucksman, C. Medina, J. Phillips, R. Schlussel, and S. Glucksman, "New onset urinary incontinence in a pediatric patient with transverse myelitis," *Urol Case Rep*, vol. 46, p. 102322, January 2023.

[2] Y. S. Abuzneid, H. Al-Janazreh, M. Haif, S. T. Idais, B. Asakrah, S. M. Ajwa, et al., "Radiation induced delayed transverse myelitis and neurological deficit at tertiary care center," *Ann Med Surg (Lond),* vol. 69, p. 102728, September 2021.

[3] S. Lopez Chiriboga and E. P. Flanagan, "Myelitis and Other Autoimmune Myelopathies," *Continuum (Minneap Minn)*, vol. 27, pp. 62-92, February 2021.

[4] S. Presas-Rodríguez, L. Grau-López, J. V. Hervás-García, A. Massuet-Vilamajó, and C. Ramo-Tello, "Myelitis: Differences between multiple sclerosis and other aetiologies," *Neurología (English Edition),* vol. 31, 2016, pp. 71-75.

[5] Z. Yılmaz Acar, F. Başçiftçi, and A. H. Ekmekci, "Future activity prediction of multiple sclerosis with 3D MRI using 3D discrete wavelet transform," *Biomedical Signal Processing and Control*, vol. 78, p. 103940, September 2022.

[6] M. K. Yagnavajjula, K. R. Mittapalle, P. Alku, S. R. K, and P. Mitra, "Automatic classification of neurological voice disorders using wavelet scattering features," *Speech Communication*, vol. 157, p. 103040, February 2024.

[7] K. Hackmack, F. Paul, M. Weygandt, C. Allefeld, and J.-D. Haynes, "Multi-scale classification of disease using structural MRI and wavelet transform," *NeuroImage*, vol. 62, pp. 48-58, August 2012.

[8] J. Feng, S.-W. Zhang, and L. Chen, "Identification of Alzheimer's disease based on wavelet transformation energy feature of the structural MRI image and NN classifier," *Artificial Intelligence in Medicine*, vol. 108, p. 101940, August 2020.

[9] Z. Ding, Y. Liu, X. Tian, W. Lu, Z. Wang, X. Zeng, et al., "Multi-resolution 3D-HOG feature learning method for Alzheimer's Disease diagnosis," *Computer Methods and Programs in Biomedicine*, vol. 214, p. 106574, February 2022.

[10] E. Kaplan, M. Baygin, P. D. Barua, S. Dogan, T. Tuncer, E. Altunisik, et al., "ExHiF: Alzheimer's disease detection using exemplar histogram-based features with CT and MR images," *Medical Engineering & Physics*, vol. 115, p. 103971, May 2023.

[11] S. Abbasi and F. Tajeripour, "Detection of brain tumor in 3D MRI images using local binary patterns and histogram orientation gradient," *Neurocomputing*, vol. 219, pp. 526-535, January 2017.

[12] Z. Yılmaz Acar, F. Başçiftçi, and A. H. Ekmekci, "A Convolutional Neural Network model for identifying Multiple Sclerosis on brain FLAIR MRI," *Sustainable Computing: Informatics and Systems*, vol. 35, p. 100706, September 2022.

[13] P. Varalakshmi, B. Tharani Priya, B. Anu Rithiga, R. Bhuvaneaswari, and R. Sakthi Jaya Sundar, "Diagnosis of Parkinson's disease from hand drawing utilizing hybrid models," *Parkinsonism & Related Disorders*, vol. 105, pp. 24-31, December 2022.

[14] I. K. Veetil, D. E. Chowdary, P. N. Chowdary, V. Sowmya, and E. A. Gopalakrishnan, "An analysis of data leakage and generalizability in MRI based classification of Parkinson's Disease using explainable 2D Convolutional Neural Networks," *Digital Signal Processing*, vol. 147, p. 104407, April 2024.

[15] S. E. Sorour, A. A. A. El-Mageed, K. M. Albarrak, A. K. Alnaim, A. A. Wafa, and E. El-Shafeiy, "Classification of Alzheimer's disease using MRI data based on Deep Learning Techniques," *Journal of King Saud University - Computer and Information Sciences*, vol. 36, p. 101940, February 2024.

[16] M. Menagadevi, S. Devaraj, N. Madian, and D. Thiyagarajan, "Machine and deep learning approaches for alzheimer disease detection using magnetic resonance images: An updated review," *Measurement*, vol. 226, p. 114100, February 2024.

[17] A. Basher, B. C. Kim, K. H. Lee, and H. Y. Jung, "Volumetric Feature-Based Alzheimer's Disease Diagnosis From sMRI Data Using a Convolutional Neural Network and a Deep Neural Network," *IEEE Access*, vol. 9, pp. 29870-29882, 2021.

[18] A. Ebrahimi, S. Luo, and A. s. D. Neuroimaging Initiative, "Convolutional neural networks for Alzheimer's disease detection on MRI images," *Journal of Medical Imaging*, vol. 8, p. 024503, 2021.

[19] D. Venkatesan, A. Elangovan, H. Winster, M. Y. Pasha, K. S. Abraham, S. J, et al., "Diagnostic and therapeutic approach of artificial intelligence in neuro-oncological diseases," *Biosensors and Bioelectronics: X*, vol. 11, p. 100188, September 2022.

[20] S. Tatli, G. Macin, I. Tasci, B. Tasci, P. D. Barua, M. Baygin, et al., "Transfer-transfer model with MSNet: An automated accurate multiple sclerosis and myelitis detection system," *Expert Systems with Applications*, vol. 236, p. 121314, February 2024.

[21] J. Kunhoth, S. Al Maadeed, M. Saleh, and Y. Akbari, "CNN feature and classifier fusion on novel transformed image dataset for dysgraphia diagnosis in children," *Expert Systems with Applications*, vol. 231, p. 120740, November 2023.

[22] F. Hassan, S. F. Hussain, and S. M. Qaisar, "Fusion of multivariate EEG signals for schizophrenia detection using CNN and machine learning techniques," *Information Fusion*, vol. 92, pp. 466-478, April 2023.

[23] Q. Gao, A. H. Omran, Y. Baghersad, O. Mohammadi, M. A. Alkhafaji, A. K. J. Al-Azzawi, et al., "Electroencephalogram signal classification based on Fourier transform and Pattern Recognition Network for epilepsy diagnosis," *Engineering Applications of Artificial Intelligence*, vol. 123, p. 106479, August 2023.

[24] M. S. Nixon and A. S. Aguado, "Chapter 2 - Images, sampling, and frequency domain processing," in Feature Extraction & Image Processing for Computer Vision (Third Edition), M. S. Nixon and A. S. Aguado, Eds., ed Oxford: Academic Press, 2012, pp. 37-82.

[25] P. Han, *Feature extraction and descriptor based on Fourier transform of local images*, Master Thesis, Department of Computer Science, The University of Regina (Canada), 2022.

[26] M. Li and W. Chen, "FFT-based deep feature learning method for EEG classification," *Biomedical Signal Processing and Control*, vol. 66, p. 102492, April 2021.

[27] G. Macin, B. Tasci, I. Tasci, O. Faust, P. D. Barua, S. Dogan, et al., "An Accurate Multiple Sclerosis Detection Model Based on Exemplar Multiple Parameters Local Phase Quantization: ExMPLPQ," *Applied Sciences*, vol. 12, p. 4920, 2022.

[28] T. Ekmekyapar and B. Taşcı, "Exemplar MobileNetV2-Based Artificial Intelligence for Robust and Accurate Diagnosis of Multiple Sclerosis," *Diagnostics*, vol. 13, p. 3030, 2023.

Deep Learning Based Offline Handwritten Signature Recognition

Bahar ÇİFTÇİ[1*], Ramazan TEKİN[2]

[1]Siirt University, Distance Education Application and Research Center
[2]Batman University, Faculty of Engineering and Architecture, Department of Computer Engineering
(ORCID: 0000-0001-5976-6236) (ORCID: 0000-0003-4325-6922)

Abstract

In our digitalized world, the need for reliable authentication methods is steadily increasing. Biometric authentication methods are divided into two main categories: physiological and behavioral. While physiological biometrics include features such as face, iris, and fingerprint, behavioral biometrics encompass dynamics such as gait, speech, and signature. Most of these methods require specialized equipment, whereas signatures can be easily obtained without additional tools, making them ideal for verifying the legality of documents. Although manual signature recognition is effective, it is resource-intensive, slow, and susceptible to errors. With advancements in technology, the need to automate the signature recognition process to enhance accuracy and efficiency has become increasingly important. Based on this need, in this study, five different DL techniques (GoogLeNet, MobileNet-V3 Large, Inception-V3, ResNet50 and EfficientNet-B0) are used to classify signature images with detailed analyses. DL methods have outperformed traditional techniques by leveraging the power of CNNs to automatically learn and extract complex features from signature data. The dataset used consists of a total of 12,600 images belonging to 420 individuals, each contributing 30 original signatures. The dataset is divided into training, validation, and test sets in different proportions to analyze classification performance. The pre-trained DL models were fine-tuned to optimize their parameters for the signature dataset. The results demonstrate that DL models achieve high accuracy in signature classification, with the GoogLeNet and Inception-V3 models reaching an accuracy of 98.77% at a 20% test rate. The study also highlights the impact of different test rates on model performance.

1. Introduction

In our digitalized world, the need for reliable authentication methods is increasing. Biometric authentication methods are divided into two main categories: physiological and behavioral. Physiological biometrics include features such as face, iris, and fingerprint, while behavioral biometrics encompass dynamics such as gait, speech, signature, and keystroke dynamics [1], [2]. Although other techniques, such as fingerprint, iris/retina scanning, facial recognition, and voice recognition, are more precise, they require specialized equipment. In contrast, signatures can be easily obtained without additional tools, making them indispensable for daily transactions and verifying the legality of documents such as certificates, checks, letters, approvals, visas, and passports. Traditional signature verification has been a manual process involving the comparison of a sample signature with previously obtained genuine signatures. With advancements in technology, there has been an increasing need to automate the signature verification process to enhance accuracy and efficiency. Handwritten signature recognition is divided into two primary categories according to the method of signature acquisition: online and offline. Online signature recognition involves capturing dynamic features such as ink pressure and writing

---

speed during the signing process using devices like electronic handwriting pads or touch screens [3], [4]. Offline signature recognition, on the other hand, involves writing the signature on paper, scanning it, and digitally processing the image [5]. Additionally, signature analysis encompasses two methods: signature verification and signature recognition. Signature recognition is a classification process where the signatory is identified from among many signatures. Signature verification, however, involves comparing two signatures to determine their similarity and conclude whether a signature is genuine or forged. Signature recognition studies require datasets with multiple signatures from different individuals, whereas signature verification necessitates the presence of both genuine and forged signatures for each individual.

Studies on offline signature recognition and verification date back to the early 1990s [6]. In their work, Sabourin and Drouhard Jean-Pierre classified offline signature images using Feedforward Neural Networks (FFNN) and the Probability Density Function (PDF) [6]. Ismail and Gad used various preprocessing techniques to classify 220 genuine and 110 forged Arabic signature images using different algorithms based on fuzzy concepts [7]. Deore and Handore's study utilized Discrete Wavelet Transform (DWT) and Principal Component Analysis (PCA) for extracting features, followed by Artificial Neural Networks (ANN) to implement an offline signature recognition system [8]. As technology advances, the methods we use to verify signatures must also evolve to remain robust against ever-progressing forgery techniques. The integration of ML and DL techniques into signature recognition systems has proven to be highly effective, enhancing accuracy and efficiency while preserving the authenticity of documents and the integrity of transactions. Calik and colleagues used the SUSIG-Visual dataset for classification with CNNs [9]. Gumusbas and Yildirim achieved high accuracy with CapsNet using the CEDAR [10] dataset, which contains genuine and forged signatures Gumusbas & Yildirim, 2019). In another study, the same authors used CapsNet for signature verification with different datasets (GPDS-100 and MCYT) [12]. Tarek and Atia used various CNN models, including VGG-16, ResNet50, Inception-v3, and Xception, to classify genuine and forged signatures from two separate datasets [13].
For the recognition and verification of offline signatures, various feature extraction processes are performed before proceeding to the classification stage with ML and DL. In their study, Jain et al. used GoogLenet for feature extraction and then used SVM method for classification [14]. Foroozandeh et al., in

their study, used SigNet, SigNet-F, VGG16, VGG19, InceptionV3, and ResNet50 for feature extraction, and then preferred the Support Vector Machine (SVM) method for classification [15]. Özyurt et al., in their study, performed feature extraction using the MobileNetV2 method on the large dataset they obtained. During the feature selection phase, they used Neighborhood Component Analysis (NCA), Chi-Square (Chi2), and Mutual Information (MI) methods for classification. Their evaluation employed various ML classifiers, including Support Vector Machine (SVM), K-Nearest Neighbors (KNN), Decision Tree (DT), Linear Discriminant Analysis (LDA), and Naïve Bayes. The study results showed that the highest accuracy of 97.7% was achieved using SVM with NCA feature selection [16]. Pokharel et al., in their signature recognition application, used GoogLeNet for both feature extraction and classification [17].

The drive to develop and improve signature classification systems arises from the need to ensure the security of identities and transactions in an environment where the boundaries between the physical and digital worlds are increasingly blurred. The main motivation of this work is to develop efficient and reliable authentication systems that can respond to the growing demands of modern society, while ensuring that signatures remain a reliable means of authentication

2. Material and Method

2.1. Dataset

The dataset used in this study consists of 12,600 images from 420 different individuals, with each participant contributing 30 genuine signatures (Özyurt et al., 2024). The signatures were obtained from students and faculty members at Raparin University in Ranya, Iraq, and Firat University in Elazig, Turkey. Collected within two months, the signatures were cropped using MATLAB and then resized to 500x600 pixels.

Figure 1. Signature samples from six different users in the dataset

2.2. Proposed Method

The classification of the signature images in this dataset was performed using five DL techniques, considering the remarkable success of DL in various fields.

In the approach proposed for the study, the dataset was divided into different proportions to analyze the performance of classification accuracy. The dataset was split into 20% test and 80% (train + validation) sets. The validation data was then split from the training data as 20%. Thus, in the first scenario, the dataset was divided into 20% test, 16% validation, and 64% train. In the second scenario, the dataset was split into 30% test and 70% (train + validation) sets. The validation data was then split from the training data as 30%. Thus, the second scenario consisted of 30% test, 21% validation, and 49% train. In the third scenario, the dataset was split into 40% test and 60% (train + validation) sets. The validation data was then split from the training data as 40%. Thus, the third scenario consisted of 40% test, 24% validation, and 36% train. Various preprocessing methods were then applied to the train-validation and test datasets. The DL models used were pretrained DL models. The pretrained weights were applied to the dataset, and parameters were optimized for new models. Subsequently, each of these models was fine-tuned individually to enhance their performance. For each classification scenario, train-validation, and test

success, loss, and weights were recorded for all epochs. The flowchart of the proposed method is shown in detail in Figure 2.

2.3. Preprocessing

Preprocessing is essential in classification tasks, including signature classification, as it cleans and standardizes raw data, which often contains inconsistencies and irrelevant information. This step enhances DL classifier models' effectiveness and helps prevent overfitting, leading to more accurate results. (James & Koresh, 2023). The preprocessing methods used in this study include Resize, CenterCrop, ColorJitter, GaussianBlur, Grayscale, and Normalize. Resize is used to resize images to a fixed size. CenterCrop; makes a crop of a certain size from the center of the image. For the Inception-V3 model used in the study, Resize 299 and CentreCrop value 299 were used. For EfficientNet-B0, MobileNet-V3-Large, GoogLeNet and ResNet50 models, Resize 299 and CenterCrop 299 were used. Normalization is a pre-processing step in which the pixel values of the images are scaled to a certain range or distribution. Since the DL models used in the study are Pretrained models previously trained with ImageNet; Normalization values are used as [0.485, 0.456, 0.406] and [0.229, 0.224, 0.225].
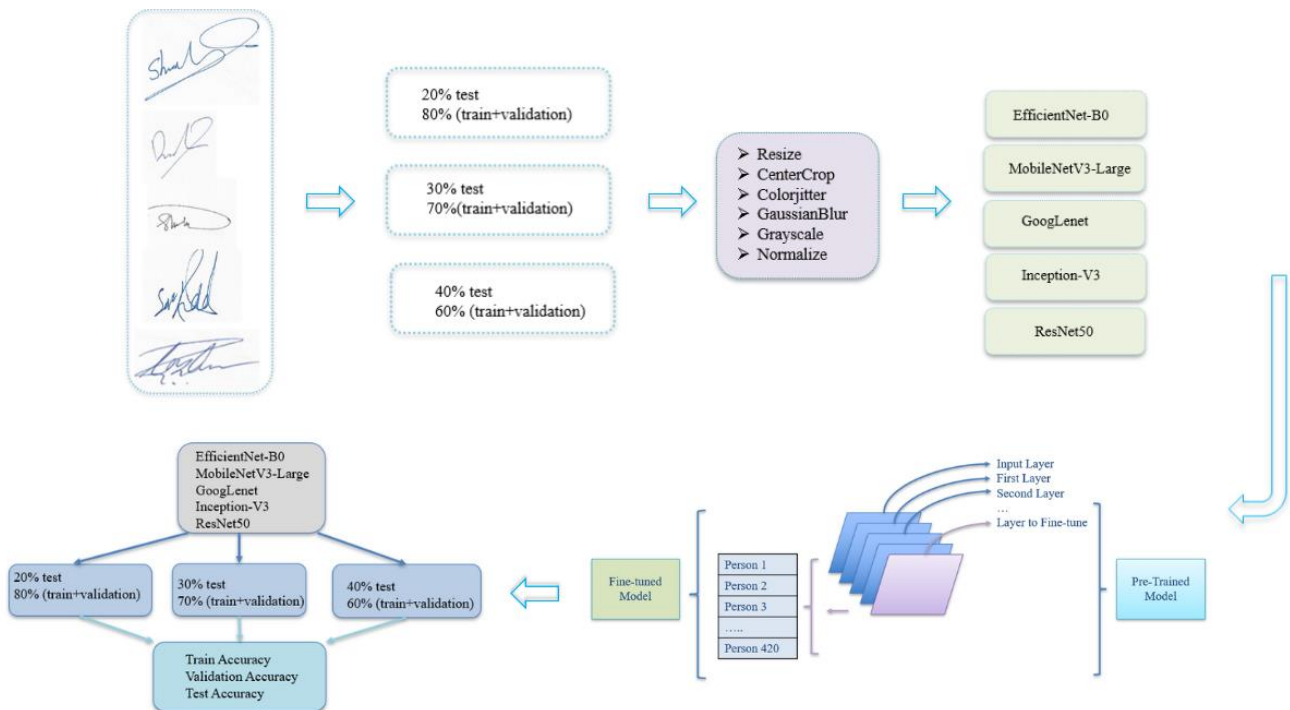

Figure 2. Flowchart of the Implemented Signature Recognition Application

Colourjitter is a preprocess that adjusts the brightness, contrast, saturation and hue of the image. GaussianBlur applies a Gaussian blur to the image. For this study, p=0.1 was chosen for the Colourjitter and GaussianBlur methods, and the transformations were applied with a 10% probability. In the GaussianBlur method, a Gaussian blur with a kernel size of 3x3 was applied. The GrayScale method converts the image to gray scale. Below in Figure 3, the appearance of several different signature samples from the dataset is shown after applying each of the preprocessing steps used in the study individually.

Figure 3. Preprocessing Steps Applied to Several Different Signature Samples from the Dataset

2.4. Classification

In this study, a signature classification application was implemented using advanced DL architectures. CNN architectures were selected for this task because of their superior capabilities in image processing. The CNN architectures used are GoogLeNet [18], MobileNet-V3 Large [19], Inception-V3 [20], ResNet50 [21] and EfficientNet-B0 [22].

In the approach proposed for the study, the data set was divided into train, validation and test. By using a validation set, the possibility of overfitting a model that performs well on the training data and poorly on the unseen data is avoided. The separation of train, validation and test provides an unbiased assessment of the performance of the final model, ensuring that the success of the model is not due to overfitting in the validation set. The CNN architectures used are pre-trained on the ImageNet dataset. ImageNet is a massive dataset ctable3ontaining over 14 million images (Deng et al.,

2010). These models can be repurposed for other tasks without requiring training from scratch, as they have learned a rich set of features from millions of images (Zhuang et al., 2019). This significantly shortens the training time, provides higher accuracy and performance, reduces the computational resources required for training, and offers better generalization capability, making them extremely valuable for practical applications (Zhuang et al., 2019). By fine-tuning the final layers of the models, they were better adapted to the signature classification task, resulting in higher accuracy and performance during the training process. Below in Table 2, the original and modified states of the final layer of each model and their total number of parameters are shown. In the implementation, the highest number of parameters is found in the Inception-V3 model, with 27,481,128 parameters, while the MobileNet-V3-Large model has the lowest number of parameters, with 4,714,196. Detailed information about the layers was accessed using the 'torchscan' and 'torchstat' libraries provided by PyTorch.

Table 1. Modifications and total number of parameters applied to the final layers of the classification models before and after fine-tuning

	The original state of the last layer	Modified last layer	Total parameters
EfficientNet- B0	[0]: Linear (in =1280, out = 1000)	[0]: Dropout(p=0.2) [1]: Linear (in =1280, out =1024 [2]: ReLU () [3]: Linear (in =1024, out =420)	6,185,248

Model	Column 1	Column 2	Parameters
GoogLeNet	[0]: Linear (in =2048, out =1000)	[0]: Dropout(p=0.2) [1]: Linear (in =2048, out =1024 [2]: ReLU () [3]: Linear (in =1024, out =420)	5,288,548
MobileNet-V3-Large	[0]: First Linear (in = 960, out = 1280) [1]: Hardswish [2]: Dropout (p = 0.2) [3]: Last Linear (in = 1280, out = 1000)	[0]: Dropout(p=0.2) [1]: Linear (in =1280, out =1024 [2]: ReLU () [3]: Linear (in =1024, out =420)	4,714,196
Inception-V3	[0]: Linear (in =2048, out =1000)	[0]: Dropout(p=0.2) [1]: Linear (in =2048, out =1024 [2]: ReLU () [3]: Linear (in =1024, out =420)	27,481,128
ResNet50	[0]: Linear (in =2048, out =1000)	[0]: Dropout(p=0.2) [1]: Linear (in =2048, out =1024 [2]: ReLU () [3]: Linear (in =1024, out =420)	26,036,708

EfficientNet-B0

EfficientNet-B0 is a member of the EfficientNet family of architectures (B0, B1, B2, ..., B7, B8), developed to provide a more fluid and effective approach to scaling DL models (Tan & Le, 2019). This model is distinguished by its use of a systematic method called Compound Scaling, which scales CNNs in a balanced way across all dimensions. It emerged from the idea that balancing the depth, width, and input resolution of a network can provide better efficiency and effectiveness. The core components of the EfficientNet-B0 model are MBConv Blocks, which are previously known as bottlenecks in MobileNetV2. These blocks include expansion and squeeze layers that recalibrate feature maps, further enhancing performance (Sandler et al., 2018). In this study, the use of the EfficientNet-B0 model was preferred based on its balance of time and performance efficiency. The schematic diagram of the fine-tuned EfficientNet-B0 model architecture used in this study is shown in Figure 4. a.

GoogLeNet

Inception V1, also known as GoogLeNet, is a deep convolutional neural network developed by Google (Szegedy et al., 2014). The distinguishing feature of GoogLeNet is the Inception module. This module includes multiple convolutions of different sizes (1x1, 3x3, and 5x5) and a 3x3 max pooling operation, all performed in parallel. The outputs from these operations are concatenated to form the final output of the module. In this study, GoogLeNet achieved effective classification with an average of only 5.2 million parameters. For this study, the GoogLeNet model, previously trained on the ImageNet dataset, was fine-tuned with the modifications shown in Table
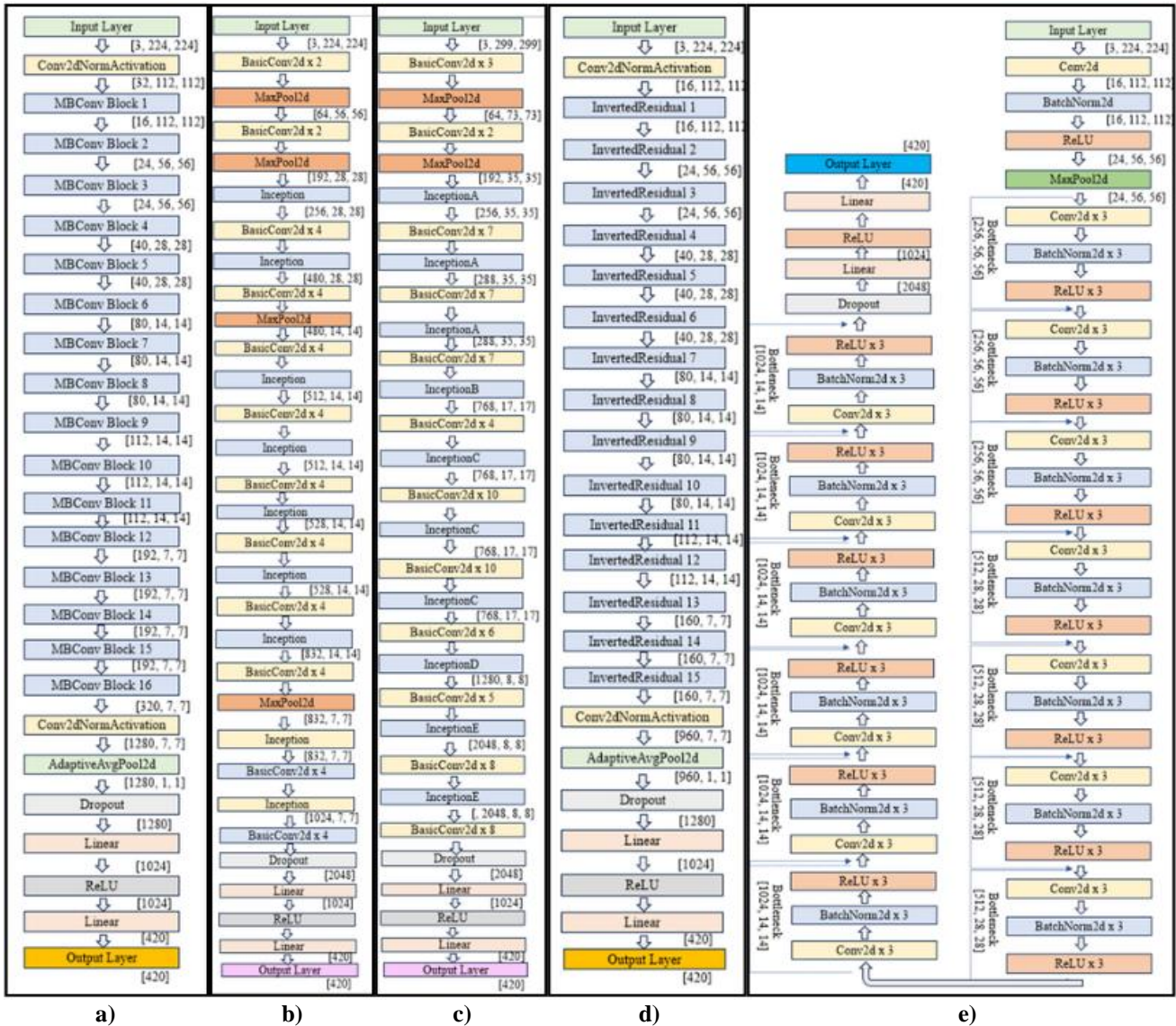
1. The schematic diagram of the fine-tuned GoogLeNet model architecture used in this study is shown in Figure 4. b.

Inception-V3

Developed by researchers at Google, Inception-V3 is designed to provide high accuracy with efficient computation by optimizing the structure of convolutional networks (Szegedy et al., 2015). Inception-V3 introduces the idea of factorizing convolutions into smaller operations to reduce computational load while maintaining or enhancing the network's ability to capture critical features. Inception-V3 also employs Auxiliary Classifiers placed at intermediate points in the network during training. These classifiers add additional regularization, helping to prevent overfitting. While the outputs of these classifiers are not used during inference, they play a crucial role during the training phase. A schematic diagram of the fine-tuned Inception-V3 model architecture used in this study is shown in Figure 4. c.

MobileNet-V3-Large

MobileNetV3-Large is part of the MobileNet family of neural network models. The main purpose of MobileNets is to design a lightweight CNN for efficient performance on mobile and edge devices with lower capacity than computers (Sandler et al., 2018). MobileNet V1 has a structure that uses width and resolution multipliers. MobileNet V2, in addition to the structure of the MobileNet V1 model, used inverted residual structures that provide more efficient memory usage (Sandler et al., 2018).

Figure 4. Schematic diagram of the fine-tuned a) EfficientNet-B0, b) GoogLeNet, c) Inception-V3, d) MobileNetV3-Large, e) ResNet50 model architecture used in this study

MobileNet V3 is a more optimized and improved version of the architectures (Howard et al., 2019). The efficiency of the network is increased by removing complex layers. With approximately 4.7 million parameters, MobileNetV3-Large is both lightweight and fast. A schematic diagram of the fine-tuned MobileNetV3-Large model architecture used in this study is shown in Figure 4.d.

ResNet50

The Residual Network with 50 layers, abbreviated as ResNet-50, is a CNN architecture widely used in image processing tasks, including signature recognition. Developed by Microsoft Research, ResNet-50 has significantly impacted the field of computer vision due to its innovative design that addresses the vanishing gradient problem often encountered in deep networks (He, Zhang, & Ren, 2015). The core idea behind ResNet is the introduction of residual learning. The convolutional layers of ResNet-50 effectively extract hierarchical features from signature images, ranging from simple edges and textures in the initial layers to more complex patterns and shapes in the deeper layers.

The ResNet50 architecture, previously trained on the ImageNet dataset, was used for this study. It accepts input images of 224x224 pixels. A schematic diagram of the fine-tuned ResNet50 model architecture used in this study is shown in Figure 4.e.

2.5. Performance Metrics

Performance metrics provide a comprehensive evaluation of the effectiveness of a classification model [23]. The performance metrics used in this study are Accuracy, Precision, Recall, F1-Score.

Accuracy is a fundamental metric for evaluating classification models and refers to the proportion of correctly predicted samples (both true positives and true negatives) in the total samples. It is calculated as shown in Equation 1.

$$Accuracy(\%) = 100 * \frac{\sum Number\ of\ Correct\ Predictions}{Total\ Number\ of\ Predictions} \quad (1)$$

Precision is a metric that quantifies the number of accurate positive predictions made by the model relative to the total number of positive predictions. It is calculated as shown in Equation 2.

$$Precision = \frac{True\ Positives}{True\ Positives + False\ Positives} \quad (2)$$

Recall is also known as precision or true positive rate. It measures the proportion of true positive samples that the model correctly identifies. It is calculated as shown in Equation 3.

$$Recall = \frac{True\ Positives}{True\ Positives + False\ Negatives} \quad (3)$$

The F1-Score is a widely used metric in ML and statistics that combines precision and recall into a single measure. It is particularly useful when you need to balance the trade-off between these two metrics. It is calculated as shown in Equation 4 below:

$$F1 - Score = 2 * \frac{Precision * Recall}{Precision + Recall} \quad (4)$$

3. Results and Discussion

In this section, the signature dataset has been classified in several experiments and the results are presented. All tests were performed with Pytorch. PyTorch is an open-source ML library written in Python and developed by Facebook's Artificial Intelligence Research Lab (FAIR). It is widely used to develop and train DL models due to its flexibility, ease of use and dynamic computational graph feature. The experiments were conducted on a computer with a 13th Gen Intel(R) Core (TM) i9-13900HX processor, 64 GB RAM, and an Nvidia GeForce RTX

4060 graphics card. In the implemented application, the model was evaluated with three different train-validation and test ratios. In the first scenario, the dataset was divided into 20% test and 80% (train + validation). In the second scenario, the dataset was divided into 30% test and 70% (train + validation). In the third scenario, the dataset was divided into 40% test and 60% (train + validation). The dataset was evaluated using five different CNN models: EfficientNet-B0, ResNet50, MobileNet-V3-Large, Inception-V3, and GoogLeNet. The parameters and methods determined for the classification process were optimized in detail. Firstly, the Batch Size, which determines the amount of data to be used in each epoch, was selected as 32. This value ensures that the model receives sufficient information during training while balancing memory usage. For optimization, the AdamW algorithm was chosen. AdamW effectively regularizes weight decay, enhancing the model's overall performance. AdamW improves the overall performance of the model by regulating the weight decay more efficiently. Learning Rate was initially set as 0.001. However, in order for the model to have a more stable and efficient learning process, it was considered to decrease the learning rate gradually. For this purpose, Step_size was set to 3 and Gamma to 0.8. These parameters ensure that the learning rate is reduced every 3 epochs by multiplying the Learning Rate by a certain coefficient, Gamma. Thus, the Learning Rate is updated as shown in equation 5:

$$LR_{new} = LR_{old} \times (gamma)^{floor(epoch/step\_size)} \quad (5)$$

This equation allows the model to learn rapidly at first, but then to progress in smaller steps over time and to get closer to the result. All tests performed were run for 50 epochs. This allows the model to complete the learning process on the data with a sufficient number of iterations. Cross-entropy was chosen as the loss function used in the study. A Label Smoothing value of 0.11 was chosen. Label Smoothing is a technique used to prevent overconfident predictions in classification problems. After each train and validation step, the tests performed using the test dataset and the corresponding model parameters were copied to memory. This is vital for monitoring the generalization ability and actual performance of the model. In Table 2 and Table 3, it is seen that Inception-V3 and GoogLeNet models have the highest test accuracy (98.77%) at 20% test rate. The result values of GoogLeNet for Precision, Recall and F1-Masure were found to be 0.99 for all three criteria.

However, in Inception-V3, Precision and F1-Score results were 0.98 and Recall result was 0.99 as in GoogLeNet.

Table 2. Test results of Inception-V3 at different Train-Validation-Test ratios

Train-Test Ratio	Test Accuracy (%)	Precision	Recall	F1-Score
20% Testing, 80% (Train +Validation)	98.77	0.98	0.99	0.98
30% Testing, 70% (Train +Validation)	98.17	0.98	0.98	0.98
40% Testing, 60% (Train +Validation)	97.64	0.98	0.98	0.98

Table 3. Test results of GoogLeNet at different Train-Validation-Test ratios

Train-Test Ratio	Test Accuracy (%)	Precision	Recall	F1-Score
20% Testing, 80% (Train +Validation)	98.77	0.99	0.99	0.99
30% Testing, 70% (Train +Validation)	98.36	0.99	0.98	0.98
40% Testing, 60% (Train +Validation)	97.30	0.97	0.97	0.97

Figure 5 presents a comparative graphical representation of the accuracy performance of the five different models used in the study at varying test ratios. The accuracy of GoogLeNet at a 30% test ratio dropped from 98.77% to 98.36%. In contrast, Inception-V3 showed a more significant decrease to 98.17% compared to GoogLeNet at the same 30% test ratio. At a 40% test ratio, GoogLeNet's accuracy fell to 97.30%, whereas Inception-V3 experienced a lesser decline to 97.64%. As the test ratio increased, a performance drop was observed in both models. The second most successful model, EfficientNet-B0, achieved the highest test accuracy of 98.65% at a 20% test ratio. For EfficientNet-B0, the Precision and Recall values were both determined to be 0.99, while the F1-Score was 0.98. Performance declined slightly in the other two scenarios, with an accuracy of 98.25% at a 30% test ratio and 97.76% at a 40% test ratio.

Table 4. Test results of EfficientNet-B0 at different Train-Validation-Test ratios

Train-Test Ratio	Test Accuracy (%)	Precision	Recall	F1-Score
20% Testing, 80% (Train +Validation)	98.65	0.99	0.99	0.98
30% Testing, 70% (Train +Validation)	98.25	0.98	0.98	0.98
40% Testing, 60% (Train +Validation)	97.76	0.98	0.98	0.98

The third most successful model, ResNet50, had the highest test accuracy (98.10%) at 20% test rate (Table 5). The result values of ResNet50 for Precision, Recall and F1-Score were found to be 0.98 for all three criteria. In the other two scenarios, with 30% and 40% test ratios, a slight decline in performance was observed. At the 30% test rate, the accuracy value was 97.96%, while at the 40% test rate it showed a greater decrease (2.30%) compared to the other four models and was obtained as 95.26%. It achieved the highest test accuracy of 97.14% at a 20% test ratio.

Table 5. Test results of ResNet50 at different Train-Validation-Test ratios

Train-Test Ratio	Test Accuracy (%)	Precision	Recall	F1-Score
20% Testing, 80% (Train +Validation)	98.10	0.98	0.98	0.98
30% Testing, 70% (Train +Validation)	97.96	0.98	0.98	0.98
40% Testing, 60% (Train +Validation)	95.26	0.95	0.95	0.95

The result values of MobileNet-V3-Large for Precision, Recall and F1-Score were 0.97 for all three criteria (Table 6). In the other two scenarios, i.e. 30% and 40% test rates, it was observed that the performance decreased slightly. While the accuracy value was 96.61% at 30% test rate, the accuracy value decreased to 95.14% at 40% test rate.

Table 6. Test results of MobileNet-V3-Large at different Train-Validation-Test ratios

| Train-Test Ratio	Test Accuracy (%)	Precision	Recall	F1-Score
20% Testing, 80% (Train +Validation)	97.14	0.97	0.97	0.97
30% Testing, 70% (Train +Validation)	96.61	0.97	0.97	0.96
40% Testing, 60% (Train +Validation)	95.14	0.96	0.96	0.95
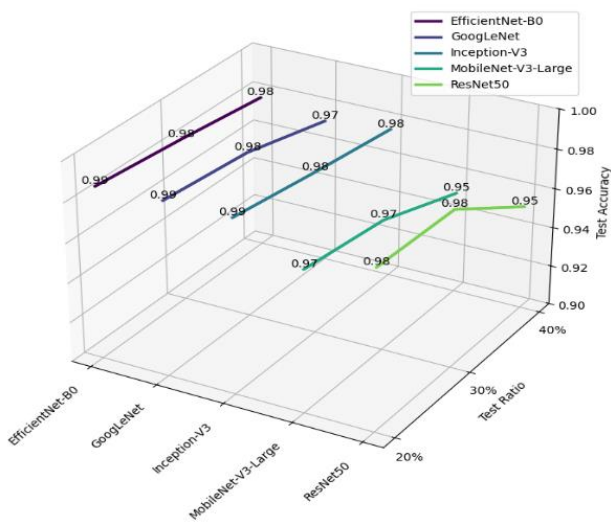
Figure 5. Classifier test accuracies at different Test Ratios for dataset

Figure 6 shows the Training and Validation accuracy graphs of the models over 50 epochs on the dataset divided with a 20% test ratio. We observe a rapid increase in accuracy during the early epochs for all models, indicating efficient learning. Inception-V3 and GoogLeNet show the best performance with minimal gaps between training and validation accuracy, suggesting good generalization and minimal overfitting, highlighting their stable and robust performance. This observation is further supported by their highest test performance as shown in Table 2 and Table 3. EfficientNet-B0 and ResNet50 also show no significant gaps between training and validation accuracy, indicating the absence of significant overfitting. Conversely, the MobileNet-V3-Large model, which is less successful compared to the other four models, shows a relatively larger gap between training and validation accuracy, suggesting potential overfitting.

The dataset used in our study was previously has only been utilized in a single study in the literature [16]. In their signature recognition application, they employed Transfer Learning for feature extraction, followed by classification using various ML methods. The researchers primarily focused on the feature extraction phase. As seen in Table 3, the highest accuracy achieved in their application was 97.7% using the SVM method. The other ML methods used included KNN, Decision Tree (DT), Linear Discriminant Analysis (LDA), and Naïve Bayes. They obtained accuracy rates of 92.54% with LDA, 90.28% with KNN and DT, and 82.50% with Naïve Bayes. In this study, instead of ML techniques, we fine-tuned five different pre-trained DL models, saving time and cost while enhancing performance. The results of the EfficientNet-B0, ResNet50, Inception-V3, and GoogLeNet models surpassed those obtained in the study by Özyurt et al. Only the MobileNet-V3-Large model used in this study performed slightly less successfully than the SVM result from their research but outperformed the other models (KNN, DT, LDA, Naïve Bayes) in terms of accuracy Compared to our study, the direct use of a pre-trained DL model, as well as fine-tuning the model, provided both time and cost savings and higher accuracy values. The data preprocessing methods used in our study are largely similar to those in other studies in the literature. However, additional methods such as ColorJitter and GaussianBlur were used to enrich the data. The use of these methods, in addition to commonly used techniques like resizing, grayscale, and normalization, contributed to the improved performance of the model. Table 3 shows that DL methods, especially CNN models, have been widely used in signature recognition applications in the literature in recent years. Researchers such as Calik et al.[9], Jampour et al. [24], Kancharla et al. [25], Noor et al. [26], Pokharel et al. [17] and Tarek and Atia [13] have achieved high accuracy values using CNN models in their studies. With the use of DL models, the need for the feature extraction stage has decreased and accuracy rates have increased. For example, Kancharla et al., integrated CNN and Jampour et al. integrated CapsNet and ResNet models and achieved very high accuracy values such as 100 %.
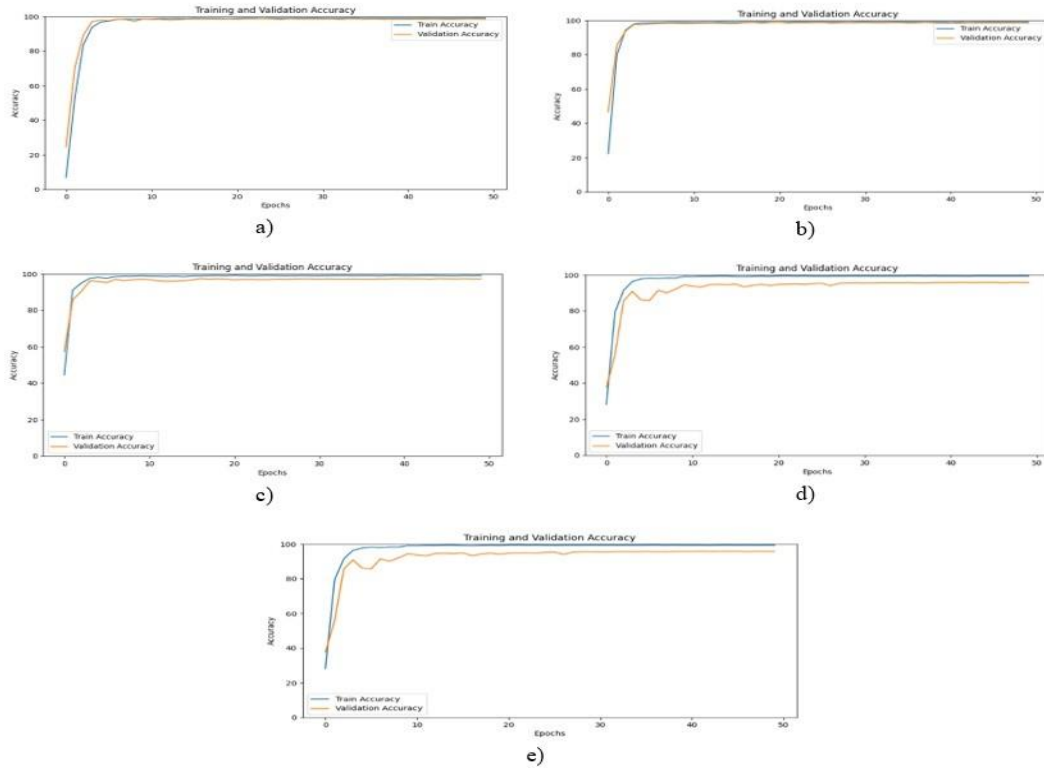
Figure 6. Training and validation accuracy on the signature dataset for a) Inception-V3, b) GoogleNet, c) EfficientNet-B0 and d) MobileNet-V3-Large e) ResNet50

The dataset used in this study has a considerably larger data volume compared to other studies in the literature. Large datasets improve the overall performance of DL models by allowing them to learn more features (Lecun et al., 2015). This is a crucial factor behind the high accuracy values obtained in our study. In the literature, datasets created by researchers, which are not widely available, typically consist of a relatively smaller number of signature images [13], [27], [28]. The extensive size of the dataset in our study allowed the DL models to learn more features and improve their performance [29].

Table 7. Literature summary of offline signature recognition applications using ML and DL

Authors (year)	Database/Number of people / Number of samples	Data pre-processing	Feature extraction	ML techniques	Signature application	Accuracy
[30]	GPDS/2106 signature	Boundary extraction	Modified Direction Feature (MDF) centroid, surface area, length, skew	RBP Neural Network (Resilient Backpropagation), RBF Network (Radial Basis Function)	Classification	91.21%, 88%
[31]	Self-built/100/3000 signature	Conversion to Binary Images, Normalization, Reshaping	Global Features Extraction (Signature Height, Image Area, Pure Width and Pure Height)	ANN, MLP	Classification	75.20%
[9]	SUSIG-Visual/100/2000 signature	Resizing, Grayscale conversion	-	CNN	Classification	92%

[25]	SigComp 2011 Dutch/10/240 signature, SigComp 2011 Chinese/10/240 signature, UTsig Farsça/10/240 signature	Grayscale Conversion, Finalization, Erosion, Dilation, Image Resizing	-	CNN	Classification	100%, 85.11%, 96.29%
[11]	CEDAR/55/2640 signature	Image Resizing, Otsu thresholding, binarizing	-	CapsNet	Verification	98.8%
[12]	CEDAR/55/2640 signature, GPDS-100/400/216,000 signature, MCYT/75/2250	Image Resizing, Otsu thresholding, binarizing	-	CapsNet	Verification	97.96%, 94.89%, 91%
[26]	Self-built/4/10 signature Self-built/10/240 signature Self-built/54/648 signature Self-built/33/165 signature	Grayscale Conversion, Normalization, Inverting, Image Resizing	-	CNN	Classification	99%, 89.1%, 80.8%, 72.7%
[15]	GPDS Senthtetic/4000/216000 signatures, MCYT-75/75/2250 signatures, UTSig/115/7935 signatures, FUM-PHSD/20/600 signatures	Binarization (Otsu's algorithm), Noise removing, Gussian filter, Normalization	SigNet, SigNet-F, VGG16, VGG19, InceptionV3, ResNet50	SVM	Classification	99.7%, 100%, 98.71%, 100%
[17]	Self-built/25/2,500 signature	Cropping image, Scaling dimension,	GoogLeNet	GoogLeNet	Classification	95,2%
[27]	Self-built/30/450 signature	Decoding, Resizing, Padding	CNN	Siamese Network	Classification	84%
[24]	CEDAR/55/2640 signature, MCYT/75/2250 signature UTSig/115/8280 signature	Centralized padding, Image Resizing	-	CapsNet, ResNet	Classification	100%, 99.66%, 99.38%
[14]	MCYT-75/75/2250 signatures, BHSig260(Bengali)/100/5400 signatures, BHSig260(Hindi)/160/8640 signatures, MCYT-75/75/2250 signatures	Image Resizing	GoogLeNet	SVM	Classification	96.5%, 95.7%, 93%
[32]	4NSigComp2012/5/300, SigComp2011/10/576, BHSig260(Bengali)/100/5400 signatures, BHSig260(Hindi)/160/8640 signatures,	Bounding Box Method, Resizing, Binary Thresholding, Inversion, Normalization	-	Siyam Ağlar	Verification	93.23%, 92.11%, 89.78%, 91.3%
[28]	Self-built/20/200 signature	Image acquisition, Grayscaling, Segmentation, Area filtering, Object bounding areas.	Local Binary Pattern (LBP), Uniform LBP, LBP 8 rotation,	Learning Vector Quantization (LVQ)	Classification	90%

			uniform LBP 8 rotation			
[13]	Self-built/30/300 signature Self-built/140 images	Grayscale Conversion, Resizing	-	VGG-16, ResNet50, Inception-v3, Xception, modified CNN	Classification	75%, 86%, 77%, 70%, 75%
[16]	Self-built/420/12,600 signature	Cropping, Resizing	MobileNetV2, Neighborhood Component Analysis (NCA), Chi-Square (Chi2), Mutual Information (MI)	SVM, KNN, Decision Tree (DT), Linear Discriminant Analysis (LDA), Naïve Bayes	Classification	97.7%, 90.28%, 90.28%, 92.54%, 82.50%
This Study	Built by [16] /420/12,600	Resize, CenterCrop, ColorJittter, GaussianBlur, Grayscale, Normalize	-	EfficientNet-B0, ResNet50, Inception-V3, GoogLeNet, MobileNet-V3-Large	Classification	98.65%, 98.10%, 98.77%, 98.77%, 97.14%

4. Conclusion and Suggestions

The proposed methodology offers a robust and efficient approach for signature recognition, with potential applications in various fields such as banking, law, and security systems. However, since the focus of this study is on offline handwritten signatures, further research is needed for other types of signatures, such as digital signatures. For future studies, the application of larger and more diverse datasets, as well as the use of next-generation DL techniques like transformers and attention mechanisms, could allow for the capture of more complex and variable signature features.

Additionally, incorporating dynamic information from the signing process (e.g., pressure, speed) along with signature images could lead to the development of multimodal learning models. This would further enhance the reliability of signature verification systems.

In conclusion, this study demonstrates the potential of DL in the field of signature recognition. Future research, in parallel with technological advancements, will contribute to the emergence of more advanced and reliable signature recognition systems.

Conflict of Interest Statement

There is no conflict of interest between the authors.

Statement of Research and Publication Ethics

The study is complied with research and publication ethics

References

[1] A. K. Jain, K. Nandakumar, and A. Ross, "50 years of biometric research: Accomplishments, challenges, and opportunities," *Pattern Recognit Lett*, vol. 79, pp. 80–105, Aug. 2016, doi: 10.1016/J.PATREC.2015.12.013.

[2] M. A. Ferrer, J. F. Vargas, A. Morales, and A. Ordóñez, "Robustness of offline signature verification based on gray level features," *IEEE Transactions on Information Forensics and Security*, vol. 7, no. 3, pp. 966–977, 2012, doi: 10.1109/TIFS.2012.2190281.

[3] N. S. Kamel, S. Sayeed, and G. A. Ellis, "Glove-Based Approach to Online Signature Verification," *IEEE Trans Pattern Anal Mach Intell*, vol. 30, no. 6, pp. 1109–1113, Jun. 2008, doi: 10.1109/TPAMI.2008.32.

[4] Z. Wang, M. Muhammat, N. Yadikar, A. Aysa, and K. Ubul, "Advances in Offline Handwritten Signature Recognition Research: A Review," *IEEE Access*, vol. 11, pp. 120222–120236, 2023, doi: 10.1109/ACCESS.2023.3326471.

[5]   A. Rıza Yılmaz et al., "İmza Tanıma Uygulaması için Çok Katmanlı Algılayıcıların Diferansiyel Gelişim Algoritması ile Eğitimi Training Multilayer Perceptron Using Differential Evolution Algorithm for Signature Recognition Application," 2013.

[6]   R. Sabourin and Drouhard Jean-Pierre, "Offline signature verification using directional pdf and neural networks," *International Conference on Pattern Recognition*, 1994.

[7]   M. A. Ismail and S. Gad, "Off-line arabic signature recognition and verification," *Pattern Recognit*, vol. 33, no. 10, pp. 1727–1740, Oct. 2000, doi: 10.1016/S0031-3203(99)00047-3.

[8]   M. R. Deore and S. M. Handore, "Offline signature recognition: Artificial neural network approach," in *2015 International Conference on Communications and Signal Processing (ICCSP)*, 2015, vol. 2, pp. 1708–1712..

[9]   NN. Calik, O. C. Kurban, A. R. Yilmaz, L. D. Ata, and T. Yildirim, "Signature recognition application based on deep learning," *in 2017 25th Signal Processing and Communications Applications Conference (SIU)*, 2017, vol. 20, pp. 1–4..

[10]   MM. K. Kalera, S. Srihari, and A. Xu, "Offline signature verification and identification using distance statistics," *Intern. J. Pattern Recognit. Artif. Intell.*, vol. 18, no. 07, pp. 1339–1360, 2004.

[11]   D. Gumusbas and T. Yildirim, "Offline signature identification and verification using capsule network," in *2019 IEEE International Symposium on INnovations in Intelligent SysTems and Applications (INISTA),* 2019.

[12]   D. Gumusbas and T. Yildirim, "Offline signature identification and verification based on capsule representations," *Cybernetics and Information Technologies*, vol. 20, no. 5, pp. 60–67, Dec. 2020, doi: 10.2478/CAIT-2020-0040.

[13]   OO. Tarek and A. Atia, "Forensic handwritten signature identification using deep learning," in *2022 IEEE 9th International Conference on Sciences of Electronics, Technologies of Information and Telecommunications (SETIT)*, 2022, vol. 39, pp. 185–190..

[14]   A. Jain, S. K. Singh, and K. Pratap Singh, "Multi-task learning using GNet features and SVM classifier for signature identification," *IET Biom*, vol. 10, no. 2, pp. 117–126, Mar. 2021, doi: 10.1049/BME2.12007.

[15]   A. Foroozandeh, A. Askari Hemmat, and H. Rabbani, "Offline handwritten signature verification and recognition based on deep transfer learning," in *2020 International Conference on Machine Vision and Image Processing (MVIP)*, 2020.

[16]   F. Özyurt, J. Majidpour, T. A. Rashid, and C. Koç, "Offline Handwriting Signature Verification: A Transfer Learning and Feature Selection Approach," *Traitement du Signal* vol.40, no.6, 2024.

[17]   S. Pokharel, S. Giri, and S. Shakya, "Deep Learning Based Handwritten Signature Recognition," *NCE Journal of Scince and Engineering*, vol.1, no.1, pp. 21-24, 2020.

[18]   C. Szegedy et al., "Going deeper with convolutions," in *2015 IEEE Conference on Computer Vision and Pattern Recognition (CVPR),* 2015.

[19]   A. Howard et al., "Searching for MobileNetV3," in *2019 IEEE/CVF International Conference on Computer Vision (ICCV),* 2019.

[20]   C.C. Szegedy, V. Vanhoucke, S. Ioffe, J. Shlens, and Z. Wojna, "Rethinking the inception architecture for computer vision," in *2016 IEEE Conference on Computer Vision and Pattern Recognition (CVPR)*, 2016.

[21]   K.K. He, X. Zhang, S. Ren, and J. Sun, "Deep residual learning for image recognition," in *2016 IEEE Conference on Computer Vision and Pattern Recognition (CVPR),* 2016.

[22]   M. Tan and Q. V. Le, "EfficientNet: Rethinking Model Scaling for Convolutional Neural Networks," 36th International Conference on Machine Learning, ICML 2019, vol. 2019-June, pp. 10691–10700, May 2019, Accessed: Jul. 25, 2024. [Online]. Available: https://arxiv.org/abs/1905.11946v5

[23]   OO. El Melhaoui, S. Said, A. Benlghazi, and S. Elouaham, "Improved signature recognition system based on statistical features and fuzzy logic," *e-Prime - Advances in Electrical Engineering, Electronics and Energy*, vol. 8, no. 100505, p. 100505, 2024.

[24]   M. Jampour, S. Abbaasi, and M. Javidi, "CapsNet regularization and its conjugation with ResNet for signature identification," *Pattern Recognit*, vol. 120, p. 107851, Dec. 2021, doi: 10.1016/J.PATCOG.2021.107851.

[25]   K. Kancharla, V. Kamble, and M. Kapoor, "Handwritten signature recognition: A convolutional neural network approach," in *2018 International Conference on Advanced Computation and Telecommunication (ICACAT),* 2018, vol. 2709, pp. 1–5..

[26]   F. Noor, A. E. Mohamed, F. A. S. Ahmed, and S. K. Taha, "Offline handwritten signature recognition using convolutional neural network approach," *in 2020 International Conference on Computing, Networking, Telecommunications & Engineering Sciences Applications (CoNTESA)*, 2020, pp. 51–57.

[27]   S. Mshir and M. Kaya, "Signature Recognition Using Machine Learning," in *2020 8th International Symposium on Digital Forensics and Security (ISDFS),* 2020.

[28]   E. K. D. Kette, D. R. Sina, and B. S. Djahi, "Digital image processing: Offline handwritten signature identification using local binary pattern and rotational invariance local binary pattern with learning vector quantization," *J. Phys. Conf. Ser.*, vol. 2017, no. 1, p. 012011, 2021.

[29]   YY. LeCun, Y. Bengio, and G. Hinton, "Deep learning," *Nature*, vol. 521, no. 7553, pp. 436–444, 2015.

[30]   S. Armand, M. Blumenstein, and V. Muthukkumarasamy, "Off-line signature verification using the enhanced modified direction feature and neural-based classification," in *The 2006 IEEE International Joint Conference on Neural Network Proceedings*, 2006, pp. 684–691.

[31]   A.A. A. M. Abushariah, T. S. Gunawan, J. Chebil, and M. A. M. Abushariah, "Automatic person identification system using handwritten signatures," in *2012 International Conference on Computer and Communication Engineering (ICCCE)*, 2012, pp. 560–565.

[32]   M. V. Arısoy, "Signature verification using siamese neural network one-shot learning," *International Journal of Engineering and Innovative Research*, vol. 3, no. 3, pp. 248–260, Sep. 2021, doi: 10.47933/IJEIR.972796.